ISSN 0370—8691

NATIONAL ACADEMY OF SCIENCES OF THE REPUBLIC OF ARMENIA

Communications of the Byurakan Astrophysical Observatory

2

Erevan 2022

Communications of BAO, Vol. 69, Issue 2, 2022, pp. 140-150

Evolution of spectral lines under time-dependent illumination of an absorbing and scattering atmosphere

A. Nikoghossian*

NAS RA V.Ambartsumian Byurakan Astrophysical Observatory, Byurakan 0213, Aragatsotn Province, Armenia

Abstract

This is a continuation of the author's research on the temporal variations in the spectral line profiles formed in absorbing and scattering atmospheres illuminated by non-stationary energy sources. The line radiation transfer in an atmosphere of finite optical thickness is considered under assumption of complete frequency redistribution. We treat two types of illumination of the medium: the sources of the form of Dirac $\delta(t)$ and Heaviside $H(t)$ unit jump functions. The goal of the work is to identify the dependence of the dynamics of changes in the spectral line profiles on frequency redistribution and the values of various optical parameters such as the optical thickness of the medium and the value of scattering coefficient. It is shown that in some cases this dependence allows to use observational material on dynamics of the burst phenomena to estimate some of these characteristics.

1. Introduction

In previous works of this research (Nikoghossian, 2021a,b) we limited ourselves to considering time variations of spectral line profiles under the simple assumption of invariance of the quantum frequency in an elementary act of scattering. In this connection, there is a need to handle the problems of the evolution of the observed spectra in their more general formulation, in which the role of redistribution of radiation by frequency is taken into account. In this paper we find natural to turn to the case important from the point of view of numerous astrophysical applications, considering that diffusion of the line radiation occurs with complete frequency redistribution. As we know, this widely accepted assumption leads to rather good results for opaque usually resonant lines formed at relatively high temperatures and densities.

The medium is assumed to be of finite optical thickness one of boundaries of which is illuminated by non-stationary energy sources. Two types of these sources are considered: those of the form of Dirac $\delta(t)$ and Heaviside $H(t)$ unit jump functions. Solution of the transfer problem for finite medium allows, in particular, to trace the asymptotical behavior of the studied time-dependent phenomenon in passing to the semi-infinite limit. The speed and duration of each evolution phase of profiles besides the redistribution law essentially depend also on the optical parameters such as the scattering (or destruction) coefficient which control the level of the diffusion process in the medium. All of these relationships will be discussed at length.

The outline of the paper is as follows: we begin in the opening Sect.2 by constructing the Neumann series for the stationary problem of diffuse reflection and transmission of a medium with finite optical thickness. Next section treats the corresponding time-dependent version of the problem under assumption that the medium is illuminated by non-stationary fluxes of radiation. The proper PDF (probability density function) and CDF (cumulative distribution function) are derived. The results of numerical calculations for a number of cases of interest are given. A qualitative analysis of the numerical calculations carried out is given. The final section discusses the influence of the frequency redistribution law as well as some physical parameters, such as the thickness of the medium and the scattering coefficient, on the evolution curve of the spectral line profiles.

*nikoghoss@yahoo.com

doi:https://doi.org/10.52526/25792776-22.69.2-140

2. Neumann series

Central to our theory is the representation of the desired physical quantities in the form of expansions in powers of the scattering coefficient λ. In this case, for reflection and transmission coefficients $\rho(x', x, \tau_0)$ and $q(x', x, \tau_0)$, they are

$$\rho\left(x', x, \tau_0\right) = \sum_{n=1}^{\infty} \rho_{\mathrm{n}}\left(x', x, \tau_0\right) \lambda^n, \qquad q\left(x', x, \tau_0\right) = \sum_{n=1}^{\infty} q_{\mathrm{n}}\left(x', x, \tau_0\right) \lambda^n. \tag{1}$$

where x' and x are the dimensionless frequencies of incident quantum and reflected or transmitted quanta. The terms in the expansions obviously have a probabilistic meaning similar to that of reflection and transmission coefficients, relating however to a certain number of scattering events n. The latter satisfy the functional equations obtained by the well-known invariant imbedding technique (Bellman & Wing, 1973, Casti & Kalaba, 1976)

$$\frac{d\rho}{d\tau_0} = -\left[v\left(x\right) + v\left(x'\right)\right] \rho\left(x', x, \tau_0\right) + \frac{\lambda}{2}\left[r\left(x', x\right) + \int_{-\infty}^{\infty} r\left(x', x''\right) \rho\left(x', x, \tau_0\right) dx'' + \right.$$

$$\left. \int_{-\infty}^{\infty} \rho\left(x', x'', \tau_0\right) r\left(x'', x\right) dx'' + \int_{-\infty}^{\infty} \rho\left(x', x'', \tau_0\right) dx'' \int_{-\infty}^{\infty} r\left(x'', x'''\right) \rho\left(x''', x, \tau_0\right) dx''' \right] \tag{2}$$

and

$$\frac{dq}{d\tau_0} = -v\left(x\right) q\left(x', x, \tau_0\right) + \frac{\lambda}{2}\left[\int_{-\infty}^{\infty} r\left(x', x''\right) q\left(x', x, \tau_0\right) dx'' + \right.$$

$$\left. \int_{-\infty}^{\infty} q\left(x', x'', \tau_0\right) dx'' \int_{-\infty}^{\infty} r\left(x'', x'''\right) \rho\left(x''', x, \tau_0\right) dx''' \right], \tag{3}$$

where the following notations are adopted: $r(x', x)$ is the frequency redistribution function, $v(x) = \alpha(x) + \beta$. We retain the commonly accepted designation the $\alpha(x)$ for the profile of absorption coefficient and β for the ratio of absorption coefficient in continuum to that in the center of the spectral line. The equations are solved under initial conditions $\rho(0, x', x) = 0$ and $q(0, x', x) = \delta(x - x')$. The above equations allow, in principle, the construction of a calculation scheme for determining the required components of the reflection and transmittance functions. The task is greatly simplified if one resorts to the approach proposed in our previous papers. It consists in pre-determining the first two simplest components of the reflection and transmittance functions associated with either the absence or the least number of scattering events

$$\rho_1\left(x', x, \tau_0\right) = \frac{\lambda}{2} \frac{r\left(x', x\right)}{v\left(x\right) + v\left(x'\right)} \left\{1 - \mathrm{e}^{-\left[v(x) + v(x')\right]\tau_0}\right\}, \qquad q_0\left(x', x, \tau_0\right) = \delta\left(x - x'\right) \mathrm{e}^{-\mathrm{v(x)}\tau_0}, \tag{4}$$

The remaining required components are found by solving the following first-order linear inhomogeneous differential equations

$$\frac{d\rho_n}{d\tau_0} = -\left[v\left(x\right) + v\left(x'\right)\right] \rho_n\left(x', x, \tau_0\right) + \Phi_{\mathrm{n}}\left(x', x, \tau_0\right), \tag{5}$$

$$\frac{dq_n}{d\tau_0} = -v\left(x\right) q_n\left(x', x, \tau_0\right) + \Psi_{\mathrm{n}}\left(x', x, \tau_0\right), \tag{6}$$

where

$$\Phi_2\left(x', x, \tau_0\right) = \frac{\lambda}{2}\left(\int_{-\infty}^{\infty} r\left(x', x'',\right) \rho_1\left(x'', x, \tau_0\right) dx'' + \int_{-\infty}^{\infty} \rho_1\left(x', x'', \tau_0\right) r\left(x'', x\right) dx''\right), \tag{7}$$

doi:https://doi.org/10.52526/25792776-22.69.2-140

$$\Psi_1\left(x',x,\tau_0\right)=\frac{\lambda}{2}\int\limits_{-\infty}^{\infty}q_0\left(x',x'',\tau_0\right)r\left(x'',x\right)dx''. \tag{8}$$

and for higher values of n

$$\Phi_n\left(x',x,\tau_0\right)=\Phi_2\left(x',x,\tau_0\right)+$$

$$\frac{\lambda}{2}\sum_{k=1}^{n-2}\int\limits_{-\infty}^{\infty}\rho_k\left(x',x'',\tau_0\right)dx''\int\limits_{-\infty}^{\infty}r\left(x'',x'''\right)\rho_{n-k-1}\left(x''',x,\tau_0\right)dx''', \tag{9}$$

$$\Psi_{\mathrm{n}}\left(x',x'',\tau_0\right)=\Psi_1\left(x',x'',\tau_0\right)+$$

$$\frac{\lambda}{2}\sum_{k=0}^{n-1}\int\limits_{-\infty}^{\infty}q_k\left(x',x'',\tau_0\right)dx''\int\limits_{-\infty}^{\infty}r\left(x'',x'''\right)\rho_{n-k-1}\left(x''',x,\tau_0\right)dx'''. \tag{10}$$

Thus, each of the components of the reflection and transmittance functions is found as a result of solving differential equations (5) and (6), which assume knowledge of all previous such components. As is not difficult to see, implementing a numerical solution to the problem is generally very time consuming. Nevertheless, it can be somewhat simplified due to the following considerations. The first one concerns the reflection function and its components and is that they are determined separately as it follows from Eq.(2). The number of determinable coefficients in the Neumann series needed to achieve satisfactory accuracy depends on the optical thickness of the medium and the value of the scattering coefficient λ. It is evident that closer to the conservative state $\lambda = 1$ the convergence of the series slows down. However, this fact starts to play a role in the line profiles at relatively high optical thicknesses, e.g. starting from a $\tau_0 = 3$ where the required accuracy still does not exceed 1 per cent. The volume of numerical calculations is considerably reduced by limiting the consideration to complete frequency redistribution, when the frequency redistribution law may be written in the form

Table 1.

x_i	R_1	R_2	R_3	R_4	R_5	R_6
0.0000	0.295840	0.132594	0.030205	0.015939	0.010014	0.006790
0.3158	0.283697	0.130920	0.031725	0.017206	0.010925	0,007428
0.6319	0,245898	0.124040	0,035821	0.021156	0,013923	0,009583
0.9486	0,182869	0.107053	0,039881	0.027230	0,019237	0,013732
1.2664	0,108693	0.077409	0,037955	0.031127	0,024526	0,018936
1.5854	0,049275	0.043453	0,026935	0.026202	0,023214	0,019847
1.9061	0,017022	0.018343	0,013416	0.014718	0,014207	0,013159
2.2289	0,004575	0.005815	0,004706	0.005531	0,005592	0,005409
2.5542	0,000971	0.001375	0,001172	0.001423	0,001467	0,001445
2.8824	0,000163	0.000241	0,000210	0.000257	0,000267	0,000264
3,2141	0.000022	0.000032	0.000028	0.000035	0.000036	0.000036
3.5499	0.000002	0.000003	0.000003	0.000004	0.000004	0.000004

$$r(x',x)=\alpha_0\left(x'\right)\alpha_0\left(x\right), \tag{11}$$

and $\alpha_0\left(x\right)=\pi^{-1/4}\alpha\left(x\right)$.

In this case, the calculations include the moments of the quantities being sought, thereby reducing the number of independent variables. On the other hand, since we are interested in spectral line profiles, instead of reflection and transmission coefficients it is sufficient to know the integrals

doi:https://doi.org/10.52526/25792776-22.69.2-140

Table 2.

x_i	Q_1	Q_2	Q_3	Q_4	Q_5	Q_6
0.0000	0.049638	0.073712	0.113676	0.061489	0.037741	0.026191
0.3158	0.065989	0.088693	0.11706	0.061317	0.037995	0, 026424
0.6319	0, 133268	0.132753	0, 106953	0.059244	0, 038067	0, 026750
0.9486	0, 294402	0.177762	0, 089281	0.051058	0, 035582	0, 025830
1.2664	0, 545273	0.162882	0, 058524	0.034976	0, 027701	0, 021596
1.5854	0, 781959	0.094040	0, 028157	0.017593	0, 015907	0, 013622
1.9061	0, 921009	0.036146	0, 009996	0.006443	0, 006374	0, 005876
2.2289	0, 976413	0.010087	0, 002713	0.001773	0, 001833	0, 001754
2.5542	0, 992624	0.002164	0, 000577	0.000380	0, 000398	0, 000386
2.8824	0, 996268	0.000365	0, 000097	0.000064	0, 000067	0, 000065
3, 2141	0.996907	0.000048	0.000013	0.000008	0.000009	0.000009
3.5499	0.996994	0.000005	0.000001	0.000001	0.000001	0.000001

$$R_n(x,\tau_0) = \int\limits_{-\infty}^{\infty} \rho_n\left(x',x,\tau_0\right)dx', \qquad Q_n(x,\tau_0) = \int\limits_{-\infty}^{\infty} q_n\left(x',x,\tau_0\right)dx'. \tag{12}$$

Tables 1 and 2 demonstrate the values of the first six quantities $R_n(x,\tau_0)$ and $Q_n(x,\tau_0)$ for a medium with of optical thickness $\tau_0 = 3$ as a function of the frequency in the line. The values of the latter are the nodes of the 49th order Hermite polynomial.

3. Time dependent problem

As we have shown in recent papers (Nikoghossian, 2021a,b) the probability density function (PDF) of the total time taken by a quantum at a certain number of n scattering events has the form

$$F_n\left(z\right) = \frac{z^{2n-1}}{(2n-1)!}\mathrm{e}^{-z}, \qquad n = 1,2,... \tag{13}$$

where the dimensionless time z is read in units of the mean time $\bar{t} = t_1 t_2/\left(t_1+t_2\right)$ expressed in terms of t_1 and t_2 representing respectively the frequency-averaged mean time taken by a quantum to fly between two successive acts of scattering and the mean time for an atom to be in an excited state. A remarkable property of the family of functions $F_n(z)$, which is a special case of the $Erlang - n$ distribution, their extremum (maximum) taken at $z = 1$. It is also important to emphasize that the value of t_1 depends on the density of scattering centres, which in turn is determined by the physical conditions in the medium.

Let us now introduce the PDF functions $\bar{R}(x,\tau_0,z)$, $\bar{Q}(x,\tau_0,z)$ such that $\bar{R}dz$ and $\bar{Q}dz$ are respectively the probabilities of observing the given reflected and transmitted lines profiles in the time interval $(z, z+dz)$. They are obviously represented as

$$\bar{R}\left(x,\tau_0,z\right) = \sum_{n=1}^{\infty} R\left(x,\tau_0\right)F_n\left(z\right)\lambda^n \qquad \bar{Q}\left(x,\tau_0,z\right) = \sum_{n=1}^{\infty} Q\left(x,\tau_0\right)F_n\left(z\right)\lambda^n \tag{14}$$

These functions describe the evolution of the spectral line profiles formed at the boundaries of the medium when it is illuminated by a δ-function shaped pulse. We see that all components of the Neumann series, and hence the profiles themselves, take their maximal values, as it was said, at $z = 1$ to which some real time $t = \bar{t}$ corresponds. Knowledge of $\bar{t}$ allows to estimate the value of t_1 and making then an idea about some physical characteristics of the medium such as the level of ionization of some atoms or ions.

In addition, we consider also the establishment of the equilibrium state regime under prolonged illumination of the medium by a source of the unit jump form given by the Heaviside H-function. The

doi:https://doi.org/10.52526/25792776-22.69.2-140

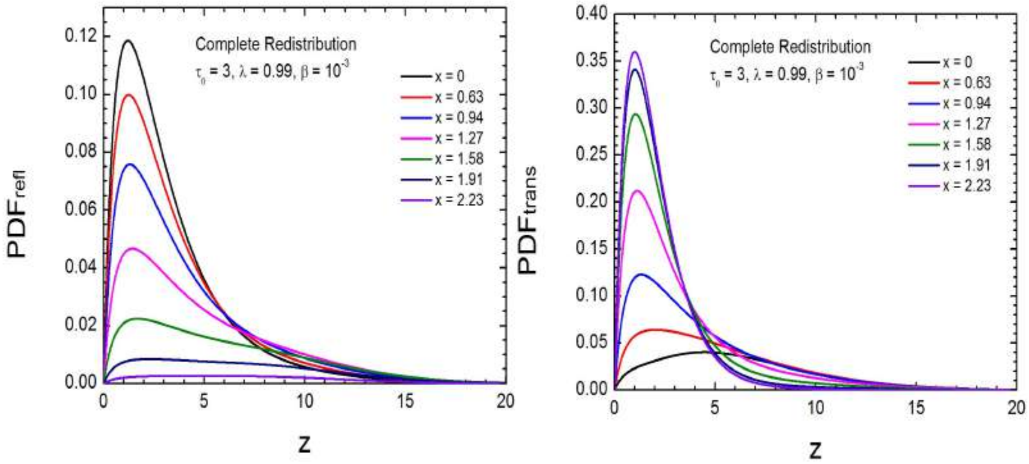

Figure 1. Probability density functions for radiation reflected from the medium (left panel) and transmitted radiation (right panel) for the medium of optical thickness $\tau_0 = 3$ and $\lambda = 0,99$

evolution of the line profiles in this case is described by the cumulative distribution function (CDF) given by

$$C_R(x, \tau_0, z_0) = \mathrm{e}^{-z_0} \sum_{n=1}^{\infty} R_n(x, \tau_0) \lambda^n \sum_{k=0}^{\infty} \frac{z^{2n+k}}{(2n+k)!}, \tag{15}$$

$$C_Q(x, \tau_0, z_0) = \mathrm{e}^{-z_0} \sum_{n=1}^{\infty} Q_n(x, \tau_0) \lambda^n \sum_{k=0}^{\infty} \frac{z^{2n+k}}{(2n+k)!} \tag{16}$$

In both illumination cases it is assumed that the incident radiation has a unit intensity at all frequencies within the line.

4. The evolution of the line profiles

Now we consider in detail changes of spectral line profiles separately for two following cases: lines generated when the medium is illuminated by a $\delta(z)$ pulse as a result of a. reflection from the medium and b. due to transmission through it. In both cases, the intensity of incident radiation is assumed equaled to unity. Figs.1-3 show the probability density functions for the radiation reflected from the medium (left panels) and for radiation transmitted through it (right panels). Here and below, the values of the optical medium parameters are chosen so as to show as clearly as possible the differences in evolution of the strong and weak lines.

Obviously, the picture of the processes in both reflection and transmission cases depends on both the optical thickness of the medium and the value of the scattering coefficient. In particular, the duration of changes in the observed spectral lines essentially depends on the value of the scattering coefficient. As one would expect, the greater the role of multiple scattering in the medium, the longer duration of the line evolution (cf. Fig.1,2). For the same reason the process is comparatively short in a medium of smaller optical thickness. (cf. Fig.3). The absorption lines produced by the passage of radiation through a medium also have a faster time course, which is due to the possibility of transmittance without scattering.

It is easy to note the independence of the maximum of PDF values of these lines attained at $z = 1$ from the value of the scattering factor. At the media thicknesses we are considering ($\tau_0 \leq 3$), it is also weakly dependent on the optical thickness (cf. Fig.3). The physically weak dependence of the mentioned value on the parameters λ and τ_0 is explained by the asymptotic tendency of the line profile in the far wings to unity. As a result, the maximum value of the PDF becomes approximately $\mathrm{e}^{-1} = 0.35$. It follows that the numerical value of this quantity depends only on the intensity of the primary radiation incident on the medium in the continuum, which is taken as one in the paper.

doi:https://doi.org/10.52526/25792776-22.69.2-140

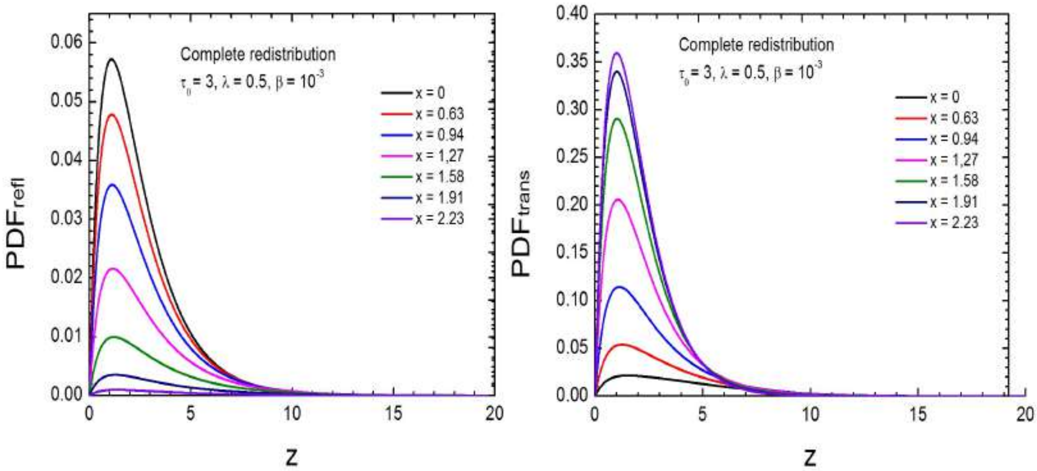

Figure 2. The same as in Fig.1 for $\lambda = 0,5$.

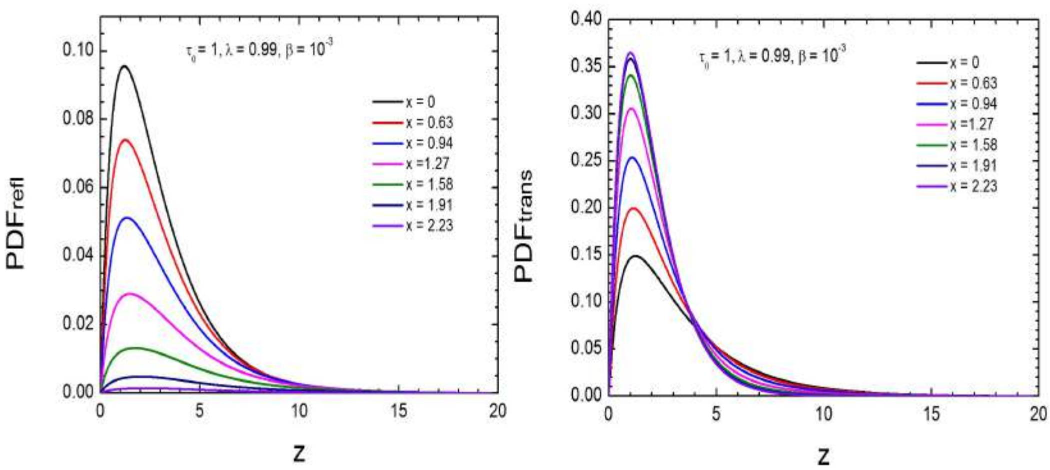

Figure 3. The same as in Fig.1 for $\tau_0 = 1$ and $\lambda = 0,99$.

doi:https://doi.org/10.52526/25792776-22.69.2-140

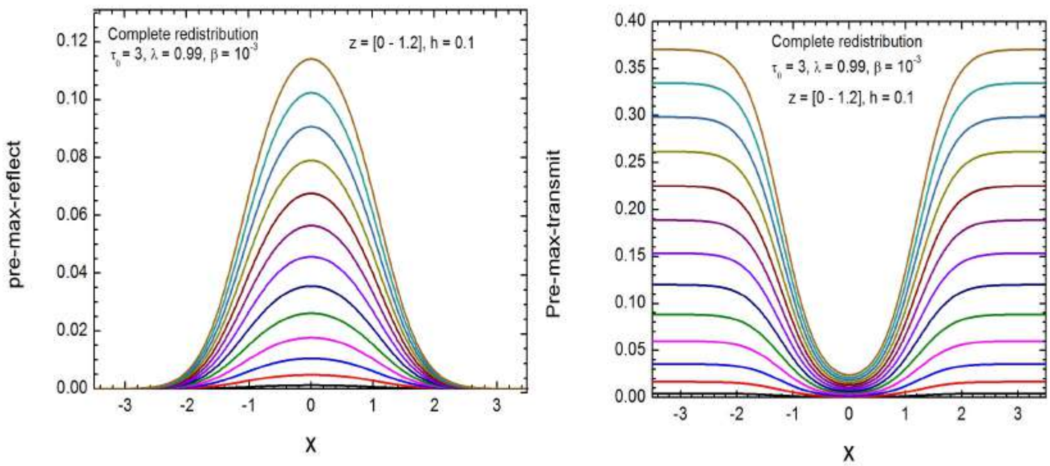

Figure 4. Evolution of the reflected (left) and transmitted spectral lines profiles formed as a result of reflection (left) and transmission (right) before PDF maximum. The value of the time variable z grows from the bottom to top in increment $h = 0.1$

Therefore, a comparison of the theoretical and observed values of the maximum allows us to judge about the intensity of the radiation falling on the medium.

Then, by following the evolution of the absorption line profiles arising as the result of transmittance through the medium, it is possible to gain insight into both the optical thickness of the medium and the role of diffusion in the medium in the observed spectra. This can be done by comparing the different parameters of the theoretically derived distributions and the profiles of the observed lines. For example, the relative fraction of the total energy absorbed in the line during the period up to the maximum is calculated to be weakly dependent on the scattering coefficient over the whole interval of $0 < \lambda \leq 1$ and is accurately 22 per cent at $\tau_0 = 1$, and 19 per cent at $\tau_0 = 3$. Therefore these values can serve as an indicator of the optical thickness of the medium.

It is somewhat more difficult to estimate similar parameters when studying the evolution of the emission line-spectrum formed due to reflection from the medium. In this case, as it follows from Figs 1-3, the maximum value of the reflection probability density function, as well as the duration of the whole process, are significantly dependent on the value of the scattering factor. Instead, these values for equal λ are weakly dependent on the optical thickness.of the medium, what gives an indication of the value of the scattering coefficient.

Figs. 4,5 illustrate the evolution of the spectral line profiles both before and after the PDF maximum is reached. The time variable grows with the increment $h = 0.1$. In the immediate vicinity of the maximum, profile changes slow down. After this, the decline begins, shown in Fig.4. The time variable z varies here from top to bottom in ten times greater steps $h = 1$. What draws attention is the fact that after a long time the 'information' of the initial illumination of one of the boundaries of the medium is gradually lost and it radiates at the expense of a small number of still diffusing quanta. In this case, as it follows from Fig. 4, double-peaked emission lines appear at both boundaries of the medium.

5. Illumination by radiation of the form of Heaviside's unit-jump H-function. Establishment of a stationary regime in the medium

Let us now proceed to next problem, important from the point of view of astrophysical applications. We assume now that the finite atmosphere is illuminated continuously after its onset until the steady state field of radiation is established. As above, we are interested both in evolution of emission lines of reflected spectrum and absorption lines arising from the passage of radiation through the medium. The time dependence of the line profiles are described by cumulative distribution functions (CDF) given by Eqs.(15) and (16).

doi:https://doi.org/10.52526/25792776-22.69.2-140

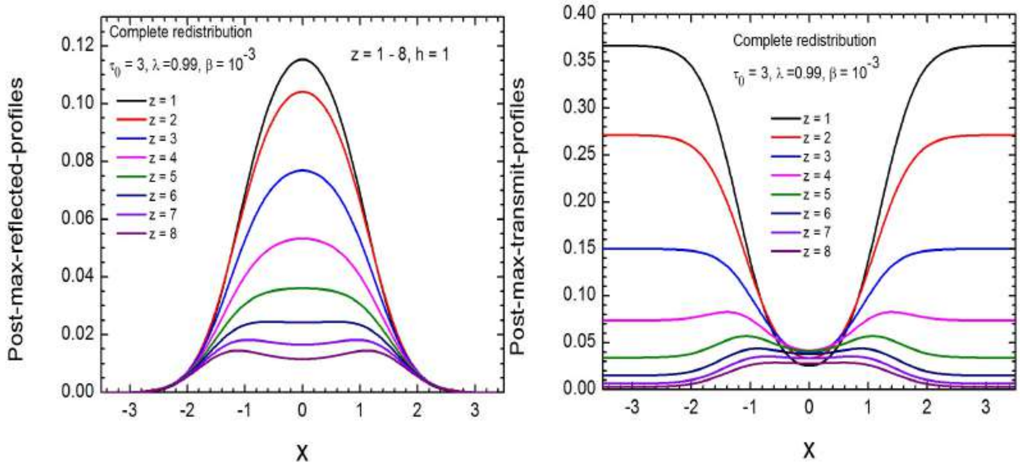

Figure 5. Evolution of the reflected (left) and transmitted (right) spectral lines profiles formed after PDF maximum. The value of the time variable z grows from the bottom to top in increment $h = 1$

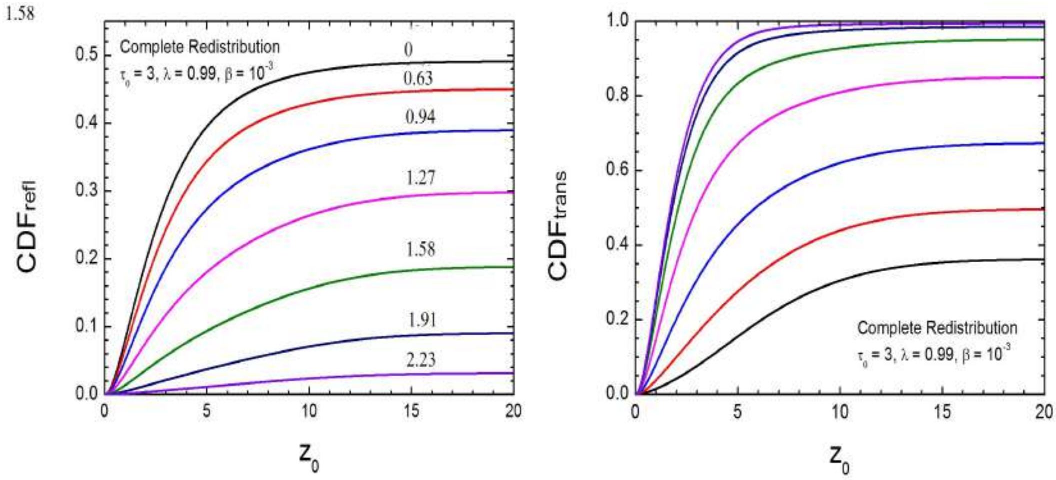

Figure 6. Evolution of the reflected (left) and transmitted (right) spectral lines profiles intending towards stationary regime for $\tau_0 = 3$ and $\lambda = 0.99$ and indicated values of frequencies within a line.

Here, in addition to the initial phase of the appearance of the line spectra, we will be interested in their evolution and the rate at which the steady state is established, which as above depends both on the thickness of the medium and on the value of the scattering coefficient. Typical curves showing the variation of the spectral line profiles before reaching the stationary regime are shown in Figs. 6-8. They are characterised by a plateau due to an asymptotic tendency of the line radiation towards their limiting values. As should be expected, the rate of the tendency towards stationary regime in the optically thin media we consider is sufficiently high. In fact, the curves achieve their limit values within the time interval $[5 \leq z_0 \leq 10]$. The illustrations above clearly show that the absorption lines formed as a result of transmission through the medium are established faster than the emission lines in the reflected spectrum. Another feature of the processes under study is their longer duration when the role of multiple scattering in the medium increases, i.e. at larger values of λ.

The absorption spectrum, as can also be seen in Figures 9-11, provides rich material for estimating both the optical thickness of the medium and the value of the scattering coefficient. The central residual line intensities together with equivalent widths provide important time-dependent information about these quantities, and, as a consequence, to study the physics of the observed phenomenon.

The spectrum formed by the reflection of the medium can, of course, also be used to obtain all sorts of information about its physical characteristics. For this purpose one can use the limiting values of the quantities under consideration known as solutions of the classical stationary transfer problem. In this case, the values of the optical thickness of the medium and the scattering coefficient are found

doi:https://doi.org/10.52526/25792776-22.69.2-140

0

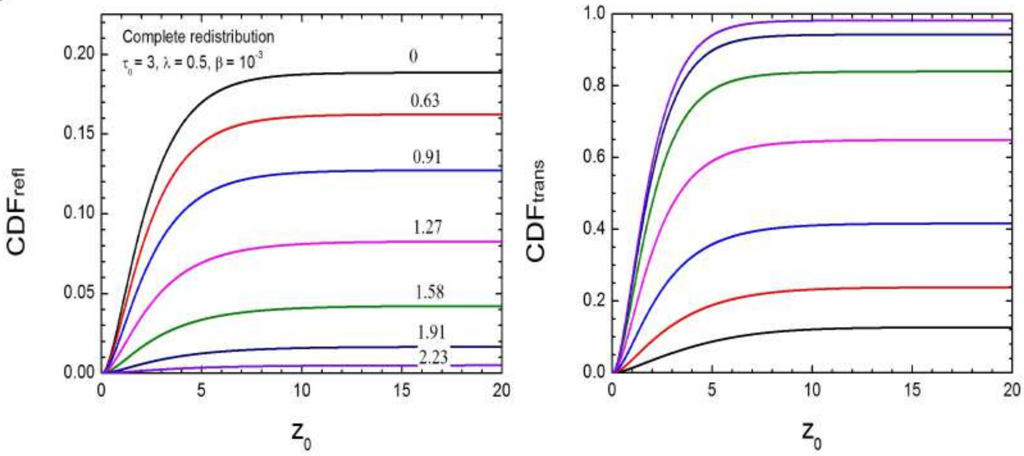

Figure 7. The same as in Fig.6 for $\tau_0 = 3$ and $\lambda = 0.5$.

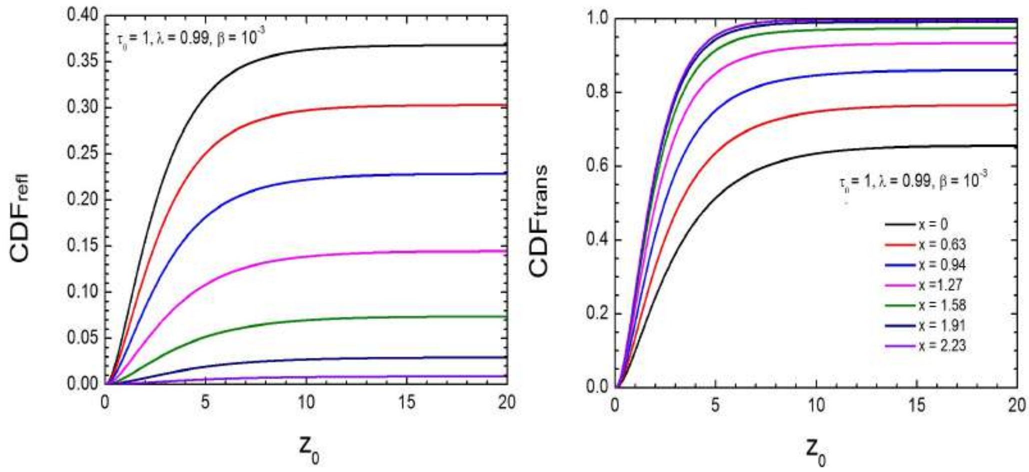

!

Figure 8. The same as in Fig.6 for $\tau_0 = 1$ and $\lambda = 0.99$.

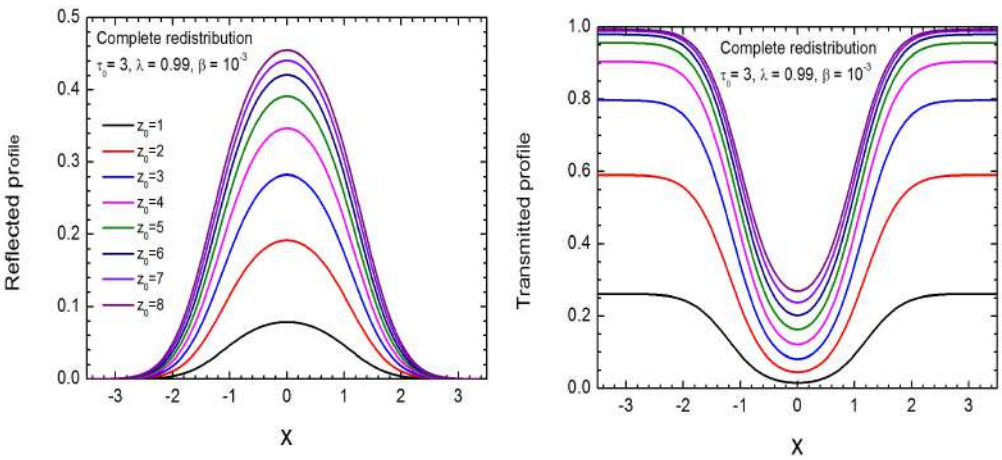

Figure 9. Evolution of the reflected (left) and transmitted (right) spectral lines profiles intending towards stationary regime for $\tau_0 = 3$ and $\lambda = 0.99$ during indicated time intervals.

doi:https://doi.org/10.52526/25792776-22.69.2-140

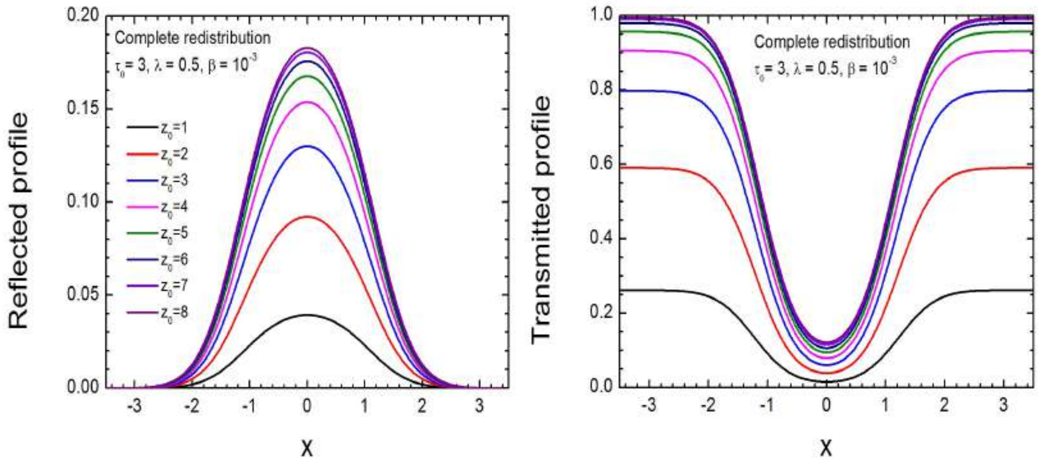

Figure 10. The same as in Fig.9 for $\tau_0 = 3$ and $\lambda = 0.5$.

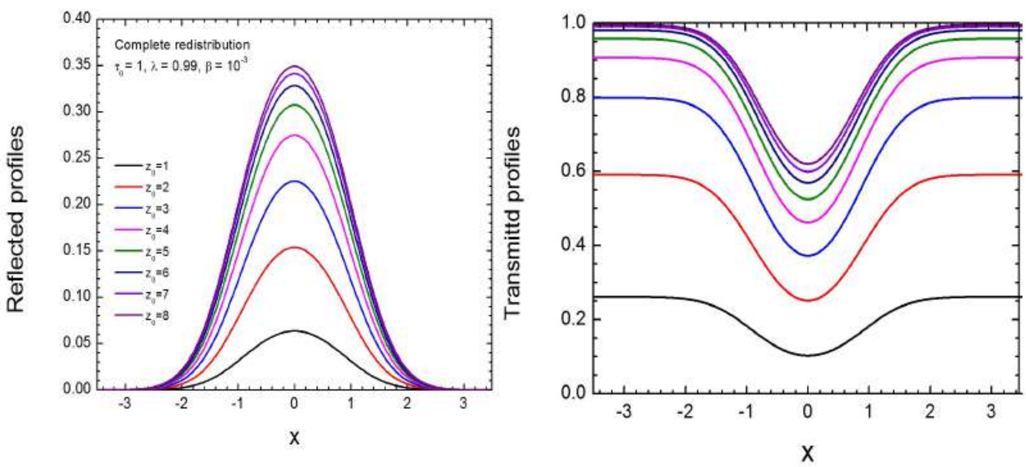

Figure 11. The same as in Fig.9 for $\tau_0 = 1$ and $\lambda = 0.99$.

doi:https://doi.org/10.52526/25792776-22.69.2-140

jointly from the known solution of the stationary problem. The identification of the spectral line and its assignment to a certain chemical element together with the dynamics of change and saturation rate, as in the case of the absorption spectrum, reveal the physical picture of the dynamic process under study.

6. Concluding remarks

The paper solves the problem of spectral line formation in a finite medium illuminated from one side by non-stationary radiation. Two possible types of non-stationarity of the sources are considered: $\delta(t)$-shaped energy radiation and that of the form of a unit-jump given by the Heaviside $H(t)$ function. This choice is due to the fact that knowledge of the solutions of the problem for these two cases makes it possible, if necessary, to refer to problems with a more general formulation involving more complex laws of variation of the incident radiation over time. Separately, we considered the problem of establishing a stationary radiation field under continuous illumination of the medium.

One of the main goals of this work was to identify the possibility of using data on the dynamics of changes in the observed spectra to obtain additional information about the properties of the radiating medium and the optical parameters of the lines contained in them. It has been shown that the specific type of probability distributions describing the temporal variations of spectral lines provides this possibility because of a number of its characteristics. One of them is the location of their maximum value taken at $z = 1$. The comparison of this time value with the real time for a given line makes it possible to estimate a number of characteristics of the emitting medium, such as the degree of ionisation of the atom or ion concerned. To determine the optical thickness of the medium and the scattering coefficient by comparing theoretical results with observational data, line-dependent values of various parameters characterising the evolution of spectral lines can be used. These include the knowledge of the maximum value of the temporal distribution, the amplification and subsequent attenuation rates of the spectral lines, the relative values of the energy emitted by reflection as well as the energy absorbed due to the passage through the medium both in the pre-maximal and post-maximal periods.

References

Bellman R., Wing J. M., 1973, An Introduction to Invariant Imbedding. New York, Wiley and Sons

Casti J., Kalaba R., 1976, Imbedding Methods in Applied Mathematics (Russian transl). M., Mir

Nikoghossian A. G., 2021a, Astrophysics, 64, 490

Nikoghossian A. G., 2021b, Communications of the Byurakan Astrophysical Observatory, 68, 32

Nikoghossian A. G., 2022, Communications of the Byurakan Astrophysical Observatory, 69, 25

doi:https://doi.org/10.52526/25792776-22.69.2-140

Relative velocity in pseudo-Riemannian spacetime

G.Ter-Kazarian*

Byurakan Astrophysical Observatory, 378433, Aragatsotn District, Armenia

Abstract

We give a coordinate independent definition of relative velocity of test particle in pseudo-Riemannian spacetime as measured along the observer's line-of-sight in general and several instructive cases. In doing this, the test particle is considered as a luminous object, otherwise, if it is not, we assume that a light source is attached to it, which has neither mass nor volume. Then we utilize the general solution of independent definition of relative velocity of a luminous source in generic pseudo-Riemannian spacetime. As a corollary, we discuss the implications for the Minkowski metric, the test particle and observer at rest in an arbitrary stationary metric, the uniform gravitational field, the rotating reference frame, the Schwarzschild metric, the Kerr-type metrics, and the spatially homogeneous and isotropic Robertson-Walker (RW) spacetime of standard cosmological model. In the last case, it leads to cosmological consequence that the resulting, so-called, *kinetic* recession velocity of an astronomical object is always subluminal even for large redshifts of order one or more, so that it does not violate the fundamental physical principle of *causality*. We also calculate the measure of carrying away of a galaxy at redshift z by the expansion of space, which proves, in particular, that cosmological expansion of a flat 3D–space is fundamentally different from a kinematics of galaxies moving in a non-expanding flat 3D-space. So, it is impossible to mimic the true cosmological redshift by a Doppler effect caused by motion of galaxies in a non-expanding 3D-space, flat or curved. We also give a reappraisal of the `standard´ kinematic interpretation of redshifts in RW spacetime as accumulated Doppler-shifts.

Keywords: *Classical general relativity; Fundamental problems and general formalism; Riemannian geometries; Relative velocity; Classical black holes*

1. Introduction

This article is an extended version of (Ter-Kazarian, 2023), where we have studied the question of a coordinate independent relative velocity in pseudo-Riemannian spacetime. Here, in addition to more detailed exposition, we also include some relevant topics. In particular, Appendix A provides a reappraisal of the `standard´ kinematic interpretation of redshifts in RW spacetime as accumulated Doppler-shifts.

The relative velocity of test particles and observers, which is fundamental notion in physics, has been an open question in general relativity (GR). From almost its very outset there has been an ongoing quest for determining the relative velocity of test particles and observers, which does not depend on coordinates. There is no unique way to compare the four-vectors of their velocities at widely separated spacetime events in curved pseudo-Riemannian spacetime, because GR provides no *a priori* definition of relative velocity. This inability to compare vectors at different points was the fundamental feature of a curved spacetime. Different coordinate reference frames and notions of relative velocity yield different results for the motion of distant test particles relative to a particular observer.

Perhaps the most convincing example of this is Milne's universe (Milne, 1934). Against the background of empty Minkowski space M_4 and complete disregard for gravity, Milne considered an infinite number of test particles (no mass, no volume) shot out in all directions and with all possible speeds, in a unique event of creation occurred in his origin point O at $T = 0$. All the particles, being free,

*gago_50@yahoo.com

doi:https://doi.org/10.52526/25792776-22.69.2-151

will move uniformly and radially away from O, with all possible speeds short of c. The particles in this idealized model each stay at fixed comoving coordinates $\chi(x, y, z)$ as their proper time t increases. The physical distance between two particles, as measured along a geodesic of a comoving hypersurface of constant t, grows at the Hubble expansion rate of the universe at the time t. So the Milne universe is the Minkowski spacetime described from an expanding reference frame. The picture in some particular inertial frame $S(X, Y, Z, T)$ of arbitrarily chosen reference particle P will be that of a ball of dust whose unattained boundary expands at the speed of light. Milne's model satisfies the Cosmological Principle of homogeneity and isotropy. The Minkowski coordinates are the coordinates of a rigid inertial reference frame of the expanding cloud of particles defining the Milne universe model. The time T is the private time of comoving inertial reference frame of an arbitrary particle P in the Milne universe. All the clocks at rest in this frame show the same time T as the clock at the spatial origin of the reference frame. The coordinate R is the distance from the origin particle measured at T=const. The fan of lines is the set of world lines of the reference particles defining the Milne universe. The cosmic time t is the time measured by clocks following all of the test particles. The space at a fixed cosmic time t is called the public space of the Milne universe. Each public map in Milne's model is a 3-space of constant negative curvature. The coordinate transformation between the Minkowski coordinates $(R(X, Y, Z), T)$ and the Milne coordinates (t, χ), is $R = ct\sinh(\chi/ct_0)$, $T = t\cosh\cosh(\chi/ct_0)$, which leads to the line element $ds^2 = c^2dt^2 - d\sigma^2$, where $d\sigma^2 = a^2(t)dl^2$ is the metric of public space with scale factor $a(t) = t/t_0$. By Schur's theorem, dl^2 represents a 3D-space of constant curvature. For the spatially flat model, there is no upper limit to the comoving coordinate distance χ, and that also to the proper distance $L(t) = a(t)\chi$, at any fixed t. For the Milne universe, at any time t and at sufficiently large proper distance, the `proper´ recession velocity $\dot{L}(t, z) = HL$, where $h = \dot{a}(t)/a(t)$ is the Habble parameter necessarily exceeds the local speed of light for the observer. Although in the Milne coordinates the 3D comoving hypersurface of constant t (constant proper time) does have an extrinsically non-zero curvature, nevertheless the 4D curvature is zero. Therefore, simple coordinate transformations to the Minkowski coordinates as above, transform the metric to the standard Minkowski form. In these coordinates there are no superluminal speeds.

The ambiguity illustrated by this example has analogs in all spacetimes. This feature led to consideration of the need for a strict definition of `radial velocity´ within the solar system at the General Assembly of the International Astronomical Union (IAU), held in 2000 (Lindegren & Dravins, 2003, Soffel, 2003). Whereas, the metric tensors and gravitational potentials of both the Barycentric Celestial Reference System and the Geocentric Celestial Reference System are defined and discussed. The necessity and relevance of the two celestial reference systems are explained. The transformations of coordinates and gravitational potentials are discussed. Potential coefficients parameterizing the post-Newtonian gravitational potentials are expounded. Simplified versions of the time transformations suitable for modern clock accuracies are elucidated.

Several papers appeared that study the general question of relative velocities. The result of such efforts was the introduction of four geometrically defined inequivalent concepts of relative velocity. The three distinct coordinate charts are employed by Bolós (2006, 2007), Bolós & Klein (2012), Bolós et al. (2002), Klein & Collas (2010), Klein & Randles (2011), each with different notions of simultaneity, to calculate the Fermi, kinematic, astrometric, and spectroscopic relative velocities. The four definitions of relative velocities depend on two different notions of simultaneity: `spacelike simultaneity´ (or `Fermi simultaneity´) (Klein & Randles, 2011, Walker, 1935) as defined by Fermi coordinates of an observer, and `lightlike simultaneity´ as defined by optical (or observational) coordinates of an observer (Ellis, 1985). The Fermi and kinematic relative velocities can be described in terms of the `Fermi simultaneity´, according to which events are simultaneous if they lie on the same space slice determined by Fermi coordinates. Thereby, for an observer following a timelike worldline in Riemannian spacetime, Fermi-Walker coordinates provide a system of locally inertial coordinates. If the worldline is geodesic, the coordinates are commonly referred to as Fermi or Fermi normal coordinates. Useful feature of Fermi coordinates was that the metric tensor expressed in these coordinates is Minkowskian to first order near the path of the Fermi observer, with second order corrections involving only the curvature tensor (Manasse & Misner, 1963). Klein & Randles (2011) find explicit expressions for the Fermi coordinates for Robertson-Walker (RW) spacetimes and show that the Fermi

doi:https://doi.org/10.52526/25792776-22.69.2-151

chart for the Fermi observer in non-inflationary RW spacetimes is global. However, rigorous results for the radius of a tubular neighborhood of a timelike path for the domain of Fermi coordinates are not available. The spectroscopic (or barycentric) and astrometric relative velocities, which can be derived from spectroscopic and astronomical observations, mathematically, both rely on the notion of light cone simultaneity. According to the latter, two events are simultaneous if they both lie on the same past light cone of the central observer. It is shown that the astrometric relative velocity of a radially receding test particle cannot be superluminal in any expanding RW spacetime. Necessary and sufficient conditions are given for the existence of superluminal Fermi speeds. Note that for the Hubble velocity, the proper distance is measured along non geodesic paths, while for the Fermi velocity, the proper distance is measured along spacelike geodesics. In this respect the Fermi velocity seems to be more natural, but the Hubble velocity is defined at all spacetime points, whereas the Fermi velocity makes sense only on the Fermi chart of the central observer. Although these four definitions of relative velocities have own physical justifications, all they are subject to many uncertainties, and the ambiguity still remains.

In this article, we are looking for a solution by considering the test particle as a luminous object, otherwise, if it is not, we assume that a light source is attached to it, which has neither mass nor volume. In such case, a hope appears that a relative velocity of luminous source as measured along the observer's line-of-sight (speed) can be defined in coordinate independent way directly from general kinematic spectral shift rule (Synge, 1960):

$$z = \frac{\triangle\, \tau_O}{\triangle\, \tau_S} - 1 = \frac{p_{\mu(S)} V^{\mu}_{(S)}}{p_{\mu(O)} V^{\mu}_{(O)}} - 1, \tag{1}$$

which is generally valid for pseudo-Riemannian manifold, and thus, the definitions will be free of the above mentioned ambiguities. Here $V^{\mu}_{(S)}$ and $V^{\mu}_{(O)}$ are respective unit tangent vectors of four-velocity vectors of source S and observer O, $p^{\mu}_{(S)}$ and $p^{\mu}_{(O)}$ are respective four-momenta of light ray as seen by the source and observer. An aforementioned inability to immediately compare the four-velocity vector V^{μ}_{S} with the four-velocity vector V^{μ}_{O} in pseudo-Riemannian spacetime necessitates to seek a useful definition of the relative velocity by bringing both vectors to a common event. Historically, Synge subjected the vector $V^{\mu}_{(S)}$ to parallel transport along the null geodesic to the observer and obtained a relativistically invariant form of global Doppler shift. Narlikar (Narlikar, 1994) has proved this rule in other context of standard cosmological model of expanding universe.

It is well known that null geodesics are peculiar, in a sense that they lie in a metric space wherein they are being only 1D-affine spaces, so that only a parallel displacement, not a metric distance is defined along them. As a corollary, their geometric properties become a rather unexpected mixture of affine and metric properties. At first glance, we seem to have attractive proposal of choosing a null geodesics for the parallel transport since it does not require any additional structures, like particular foliation of spacetime, which in turn is applicable to any spacetime. However, a resulting Doppler effect is inconclusive, because a definition of relative velocity has disadvantage that there is no unique way to compare four-vectors of the velocities at widely separated spacetime events by parallel transport.

Our primary interest, in (Ter-Kazarian, 2021b) is rather to extend those geometrical ideas developed by (Synge, 1960), to build a series of infinitesimally displaced `relative´ spectral shifts and then sum over them in order to give a coordinate independent definition of the relative velocity of luminous source, without subjecting it to a parallel transport, as measured along the observer's line-of-sight in generic pseudo-Riemannian spacetime. These peculiarities deserve careful study, because they furnish valuable theoretical clues about the interpretation of velocity of test particle relative to observer in GR, a systematic analysis of properties of which happens to be surprisingly difficult by conventional methods. The parallel transport of four-velocity vector has not been discussed in this article, although the actual formulation of theory has made the task easier. A resulting general relationship between the spectral shift and relative velocity is utterly distinct from a familiar global Doppler shift. In particular case when adjacent observers are being in free fall and populated along the null geodesic, such a performance is reduced to a global Doppler velocity as studied by Synge (Synge, 1960).

Utilizing this general solution, in present article we discuss the implications for several instructive cases: the Minkowski metric, the test particle and observer at rest in an arbitrary stationary metric,

doi:https://doi.org/10.52526/25792776-22.69.2-151

the uniform gravitational field, the rotating reference frame, the Schwarzschild metric, the Kerr-type metrics, and the spatially homogeneous and isotropic Robertson-Walker spacetime of standard cosmological model. In the last case, the general solution gives a coordinate independent definition of *kinetic* recession velocity, so that, reconciles the cosmological interpretation of redshift with the kinematical interpretation of redshifts as accumulation of a series of `relative´ infinitesimal spectral shifts. Such a practical implementation leads to important cosmological consequence that the *kinetic* recession velocity is always subluminal even for large redshifts of order one or more (Ter-Kazarian, 2021a, 2022), and thus, it does not violate the fundamental physical principle of *causality*. This provides a new perspective to solve startling difficulties of superluminal `proper´ recession velocities, which the conventional scenario of expanding universe of standard cosmological model presents (see e.g. (Bolós & Klein, 2012, Bunn & Hogg, 2009, Chodorowski, 2011, Davis & Lineweaver, 2004, Grøn & Elgarøy, 2007, Harrison, 1993, 1995, 2000, Kaya, 2011, Klein & Collas, 2010, Klein & Randles, 2011, Murdoch, 1977, Narlikar, 1994, Page, 2009, Peacock, 1999, 2008, Peebles, 1993, Peebles et al., 1991, Whiting, 2004). In some instances (in earlier epochs), the distant astronomical objects are observed to exhibit redshifts in excess of unity, and only a consistent theory could tackle the key problems of a dynamics of such objects.

With this perspective in sight, we will proceed according to the following structure. To start with, section 2 deals with both the coordinate independent definition and calculation of relative velocity of test particle as measured along the observer's line-of-sight in generic pseudo-Riemannian spacetime. We defer a derivation of a Doppler velocity from a general solution of relative velocity of source along the null geodesic, as it is studied by (Synge, 1960), to the section 3. We use the general solution as a backdrop to explore in section 4 the special cases of the Minkowski metric, the test particle and observer at rest in an arbitrary stationary metric, the uniform gravitational field, the rotating reference frame, the Schwarzschild metric, the Kerr-type metrics, and the spatially homogeneous and isotropic Robertson-Walker spacetime of standard cosmological model. Concluding remarks are given in section 5. Appendix A provides a reappraisal of the `standard´ kinematic interpretation of redshifts in RW spacetime as accumulated Doppler-shifts. Unless otherwise stated, we are not using the $c = 1$ convention here, so the light velocity c appears in all formulae where it should.

2. The relative velocity of luminous source in generic pseudo-Riemannian spacetime, revisited

For a benefit of the reader, in this section we necessarily revisit a general solution for relative velocity of luminous source, an early version of which is given in (Ter-Kazarian, 2021b). In this section much more will be done to make the early results and formulations clear and rigorous, which are in use throughout the present paper. Therein, we divide the spectral shift into infinitesimally shifted `relative´ spectral intervals, measured at infinitesimally separated points of spacetime between neighboring adjacent observers, and sum them over to remove the ambiguity that represents the parallel transport of the four-velocity of source to the observer. To clarify our setup, it should help a few noteworthy points of Fig. 1. The (o) and (s) are two world lines respectively of observer O and source S in pseudo-Riemannian spacetime. The passage of light signals from S to O is described by a single infinity of null geodesics $\Gamma(v)$ connecting their respective world lines. The $S_{(1)}$ and $S_{(2)}$ are two neighboring world points on (s). The parametric values for these geodesics are $v, v+\triangle v$, respectively, where $v = const$ and $\triangle v$ is infinitesimally small. Accordingly, the world line (s) is mapped pointwise on the (o) by a set of null geodesics $\Gamma(v)$. That is, a set of null geodesics are joining (s) to (o), each representing the history of a wave crest. The totality of these null geodesics forms a 2-space with equation $x^\mu = x^\mu(u, v)$, which is determined once (s) and (o) are given. The u denote the affine parameter on each of these geodesics running between fixed end-values $u = 0$ on (s) and $u = 1$ on (o). The $O_{(1)}$ and $O_{(2)}$ are corresponding world points on (o), where the null geodesics from $S_{(1)}$ and $S_{(2)}$ meet it. Also the proper times of the observer and the source are, respectively, denoted by τ_O and τ_S, and $\triangle\tau_O$ and $\triangle\tau_S$ are the elements of proper time corresponding to the segments (the clock measures of) $O_{(1)}O_{(2)}$ and $S_{(1)}S_{(2)}$. A dense family of adjacent observers O_j $(j = 1, ..., n-1)$ with the world lines (o_j) are populated between the two world lines (o) and (s). Each observer O_j

doi:https://doi.org/10.52526/25792776-22.69.2-151

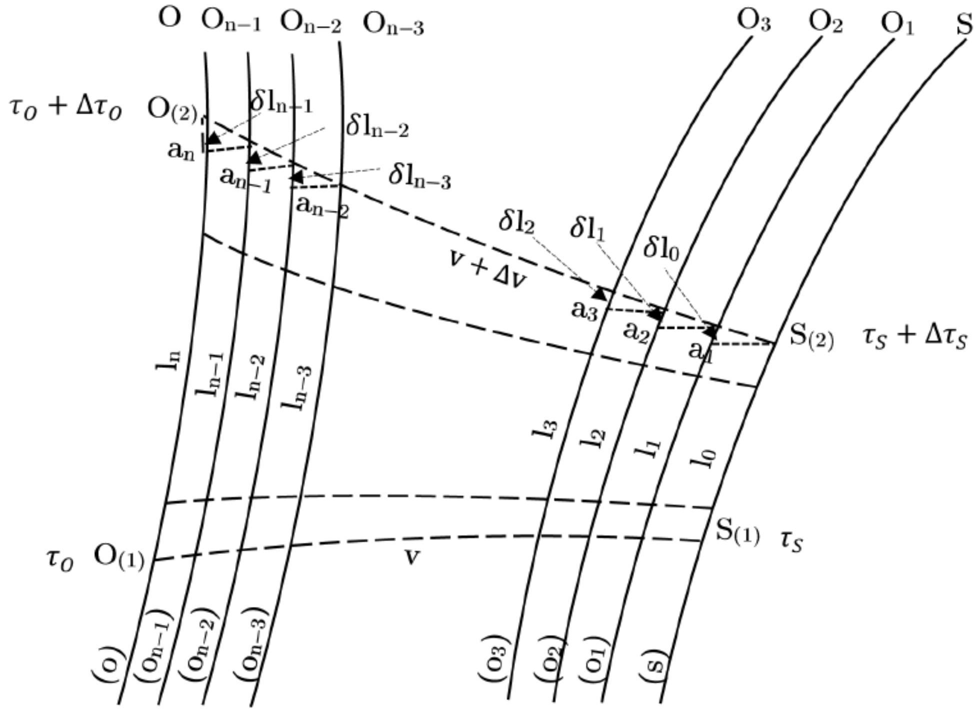

Figure 1. The infinitesimal spectral shifts as measured locally by emitter and adjacent receivers in generic pseudo-Riemannian spacetime. The (o) and (s) are two world lines respectively of observer O and source S. A dense family of adjacent observers O_j $(j = 1, ..., n-1)$ with the world lines (o_j) populated between the two world lines (o) and (s). A set of null geodesics (the dotted lines) is mapping (s) on (o), each representing the history of a wave crest. Each line segment l_{i-1} of proper space scale factor (at the affine parameter u_{i-1}) is identically mapped on the line segment $(l_i - \delta l_{i-1})$ of proper space scale factor (at infinitesimally close affine parameter u_i), such that $l_{i-1} \equiv (l_i - \delta l_{i-1})$, where δl_i denotes infinitesimal segment $a_i O_{i(2)}$. The null geodesic light signals travelling from an adjacent observer (O_{a_n}), located at point a_n, to the observer $(O_{(2)})$, is also schematically depicted with large dashed line.

measures the frequency of light rays emitted by the source S as it goes by. The $O_{j(1)}$ and $O_{j(2)}$ are two neighboring world points on (o_j) where the null geodesics from $S_{(1)}$ and $S_{(2)}$ meet it. The u_j denote the values of affine parameter on each of the null geodesics chosen at equal infinitesimally small δu_j, so that $u = u_j$ on (o_j). The τ_{O_j} denotes the proper times of the adjacent observers, i.e. $\triangle\ \tau_{O_j}$ are the elements of proper time corresponding to the segment $O_{j(1)}O_{j(2)}$. Here and throughout, for a mere convenience, we use the proper space scale factor l_i $(i = 0, 1, 2, ..., n)$ which encapsulates the beginning and evolution of the elements of proper time: $l_0 = c\ \triangle\ \tau_S$, $l_1 = c\ \triangle\ \tau_{O_{(1)}}$, $\cdots$, $l_{n-1} = c\ \triangle\ \tau_{O_{n-1}}$, $l_n = c\ \triangle\ \tau_O$. Each line segment l_{i-1} of proper space scale factor (at the affine parameter u_{i-1}) is identically mapped on the line segment $(l_i - \delta l_{i-1})$ of proper space scale factor (at infinitesimally close affine parameter u_i), such that $l_{i-1} \equiv (l_i - \delta l_{i-1})$, where δl_i denotes infinitesimal segment $a_i O_{i(2)}$. The null geodesic light signals travelling from an adjacent observer (O_{a_n}), located at point a_n, to the observer $(O_{(2)})$, is also schematically depicted with large dashed line. The wavelength λ_i of light ray is varied on the infinitesimal distance between the observers O_{i+1} and O_i in a general Riemannian spacetime in proportion to the proper space scale factor l_i :

$$\frac{\lambda_{i+1}}{\lambda_i} = \frac{\triangle\ \tau_{O_{i+1}}}{\triangle\ \tau_{O_i}} = \frac{l_{i+1}}{l_i}, \tag{2}$$

such that the spectral shift z_i is defined as the fractional shift in wavelength

$$z_i = \frac{\lambda_i}{\lambda_S} - 1 = \frac{l_i}{l_0} - 1 = \frac{\triangle\ \tau_{O_i}}{\triangle\ \tau_S} - 1. \tag{3}$$

doi:https://doi.org/10.52526/25792776-22.69.2-151

Following (Ter-Kazarian, 2021b), the spectral shift z_i, in general, can be evaluated straightforwardly in terms of the world function $\Omega(SO_i)$ for two points $S(x')$ and $O_i(x_{(i)})$ $(i = 1, ..., n)$ through an integral defined along the geodesic $\Gamma_{SO_i}(v)$ joining them (Synge, 1960), taken along any one of the curves $v = const$. The world function $\Omega(SO_i)$ can be defined for any of the geodesics in the family linking points on (o_i) and (s):

$$\Omega(SO_i) = \Omega(x'x_{(i)}) \equiv \Omega_i(v) = \frac{1}{2}(u_{Oi} - u_S)\int_{u_S}^{u_{Oi}} g_{\mu\nu}U^\mu U^\nu du, \tag{4}$$

taken along $\Gamma_{SO_i}(v)$ with $U^\mu = \dfrac{dx^\mu_{(i)}}{du}$, has a value independent of the particular affine parameter chosen. The holonomic metric $g = g_{\mu\nu}\,\vartheta^\mu \times \vartheta^\nu = g(e_\mu,\, e_\nu)\,\vartheta^\mu \times \vartheta^\nu$, of signature $+2$ (a chronometric interpretation), is defined in the Riemannian spacetime, with the components, $g_{\mu\nu} = g(e_\mu, e_\nu)$ in the dual holonomic basis $\{\vartheta^\mu \equiv dx^\mu\}$. We have taken $u_S = 0$ and $u_{Oi} \leq 1$ for given world function $\Omega_{(i)}(v)$, which becomes

$$\Omega_{(i)}(v) = \frac{1}{2}u_{Oi}\int_0^1 g_{\mu\nu}U^\mu U^\nu du. \tag{5}$$

By virtue of $\delta U^\mu/\delta u = 0$, we have $g_{\mu\nu}U^\mu U^\nu = const$ along $\Gamma_{SO_i}(v)$, therefore, (4) is reduced to

$$\Omega_{(i)}(v) = \frac{1}{2}(u_{O_{(i)}} - u_S)^2 g_{\mu\nu}U^\mu U^\nu, \tag{6}$$

with the last part evaluated anywhere on $\Gamma_{SO_i}(v)$. Taking $u_S = 0$ and $u_{Oi} = 1$, and applying conventional methods **?**, we then have

$$\Omega_{(i)}(v) = \frac{1}{2}g_{\mu\nu}U^\mu U^\nu = \frac{1}{2}\varepsilon L_i^2, \quad L_i = \int_S^{O_i} ds, \tag{7}$$

that is, to within the factor $\varepsilon = \pm 1$, the world-function is half the square of the measure, L_i, of geodesic joining S and O_i. Synge has proved that the following relations hold in general:

$$\left.\frac{\partial\Omega_{(i)}(v)}{\partial x^\mu}\right|_S = -u_{Oi}\; g_{\mu\nu}\left.\frac{\partial x^\nu}{\partial u}\right|_S, \quad \left.\frac{\partial\Omega_{(i)}(v)}{\partial x^\mu}\right|_{O_i} = u_{Oi}\; g_{\mu\nu}\left.\frac{\partial x^\nu}{\partial u}\right|_{O_i}. \tag{8}$$

The right hand sides are invariant under transformation of the affine parameter. If the geodesic is not null, one has

$$\frac{\partial\Omega_{(i)}}{\partial x'^\mu} = -L_i\tau_{\mu(S)}, \quad \frac{\partial\Omega_{(i)}}{\partial x^\mu_{(i)}} = L_i\tau_{\mu(O_i)}, \tag{9}$$

where $\tau_{\mu(S)}$ and $\tau_{\mu(O_i)}$ are the unit tangent vectors to the geodesic at S and O_i.

For null geodesics $\Gamma_{S_{(1)}O_{i(1)}}(v)$ and $\Gamma_{S_{(2)}O_{i(2)}}(v+\vartriangle v)$, in particular, the world functions $\Omega_{(i)}(v)$ does not change in the interval v and $v+\vartriangle v$, therefore

$$\left.\frac{\partial\Omega_{(i)}(v)}{\partial x^\mu}\frac{dx^\mu}{dv}\right|_{O_i} + \left.\frac{\partial\Omega_{(i)}(v)}{\partial x^\mu}\frac{dx^\mu}{dv}\right|_S = 0, \tag{10}$$

which yields

$$p_{\mu(i)}V^\mu_{(i)} \vartriangle \tau_{O_i} - p_{\mu(S)}V^\mu_{(S)} \vartriangle \tau_S = 0, \tag{11}$$

where $V^\mu_{(i)} = dx^\mu/d\tau_{O_i}|_{O_{i(1)}}$ and $V^\mu_{(S)} = dx^\mu/d\tau_S|_{S_{(1)}}$ are the respective four-velocity vectors of observer O_i and source S (or world lines (o_i) and (s)) at points $O_{i(1)}$ and $S_{(1)}$, $p^\mu_{(i)} = dx^\mu_{(i)}/du_i$ and $p^\mu_{(S)} = dx'^\mu/du_0$ are respective four-momenta of light ray (tangent to null geodesic) at the end points. Then, by virtue of (2), we obtain

$$1 + z_i = \frac{l_i}{l_0} = \frac{p_{\mu(S)}V^\mu_{(S)}}{p_{\mu(i)}V^\mu_{(i)}}. \tag{12}$$

At $i = n$, the equation (12) becomes a general coordinate independent definition of spectral shift (1).

doi:https://doi.org/10.52526/25792776-22.69.2-151

In studying further a set of null geodesics $\Gamma(v)$ with equations $x^\mu(u_i, v)$ (where $v = const$), we may deal with the deviation vector $\eta^\mu_{(i)}$ drawn from $O_{i(1)}S_{(1)}$ to $O_{i(2)}S_{(2)}$, and that we have along null geodesic

$$\eta_{\mu(i)}\frac{\partial x^\mu}{\partial u_i} = const. \tag{13}$$

The equation (13) yields

$$\eta_{\mu(i+1)}p^\mu_{(i+1)} = \eta_{\mu(i)}p^\mu_{(i)}. \tag{14}$$

Then

$$\begin{aligned} &\eta_{\mu(i+1)} = V^\mu_{(i+1)}l_{i+1}, \quad \eta_{\mu(i)} = V^\mu_{(i)}l_i, \\ &\eta_{\mu(i+1)}p^\mu_{(i+1)} = -E_{i+1}l_{i+1}, \quad \eta_{\mu(i)}p^\mu_{(i)} = -E_i l_i, \end{aligned} \tag{15}$$

where $E_i = -p_{\mu(i)}V^\mu_{(i)}$ is the energy of light ray relative to an observer O_i. Combining (2) and (15), we may write the ratio $(\lambda_{i+1}/\lambda_i)$ in terms of energy of photon and the world-function

$$\frac{\lambda_{i+1}}{\lambda_i} = \frac{l_{i+1}}{l_i} = \frac{E_i}{E_{i+1}} = \frac{p_{\mu(i)}V^\mu_{(i)}}{p_{\mu(i+1)}V^\mu_{(i+1)}} = \frac{\Omega_{\mu(i)}V^\mu_{(i)}}{\Omega_{\mu(i+1)}V^\mu_{(i+1)}}, \tag{16}$$

where $\Omega_{\mu(i)} = (u_{Oi} - u_S)U_\mu$. Therefore, the infinitesimal `relative´ spectral shift δz_i between the observers O_{i+1} and O_i will be

$$\begin{aligned} &\delta z_i = \frac{\delta\lambda_i}{\lambda_i} = \frac{\lambda_{i+1}-\lambda_i}{\lambda_i} = \frac{\delta l_i}{l_i} = \frac{l_{i+1}-l_i}{l_i} = \frac{p_{\mu(i)}V^\mu_{(i)}}{p_{\mu(i+1)}V^\mu_{(i+1)}} - 1 = \frac{\Omega_{\mu(i)}V^\mu_{(i)}}{\Omega_{\mu(i+1)}V^\mu_{(i+1)}} - 1 = \\ &\frac{\tilde{\delta} z_i}{1+z_i} \equiv \frac{z_{i+1}-z_i}{1+z_i}. \end{aligned} \tag{17}$$

For definiteness, let consider case of $l_n > l_0$ (being red-shift, Fig. 1). In similar way, of course, we may treat a negative case of $l_n < l_0$ (being blue-shift), but it goes without saying that in this case a source is moving towards the observer. In first case, the observers at the points $O_{i(2)}$ $(i = 1, ..., n)$ should observe the monotonic increments of `relative´ spectral shifts $(\delta z_0, \delta z_1, \delta z_2, ..., \delta z_{n-1})$ when light ray passes, respectively, across the infinitesimal distances $(O_{1(2)}, S_{(2)}), (O_{2(2)}, O_{1(2)}), ..., (O_{n(2)}, O_{(n-1)(2)})$. Thus, the wavelength of light emitted at $S_{(2)}$ is stretched out observed at the points $O_{i(2)}$. While weak, such effects considered cumulatively over a great number of successive increments of `relative´ spectral shifts could become significant. The resulting spectral shift is the accumulation of a series of infinitesimal shifts as the light ray passes from luminous source to adjacent observers along the path of light ray. This interpretation holds rigorously even for large spectral shifts of order one or more. If this view would prove to be true, then it would lead to the chain rule for the wavelengths:

$$\frac{\lambda_{O_{(n2)}}}{\lambda_0} \equiv \frac{\lambda_n}{\lambda_0} = \frac{\lambda_n}{\lambda_{n-1}} \cdot \frac{\lambda_{n-1}}{\lambda_{n-2}} \cdots \frac{\lambda_2}{\lambda_1} \cdot \frac{\lambda_1}{\lambda_0} = \prod_{i=0}^{n-1}(1+\delta z_i), \tag{18}$$

where $\lambda_0 \equiv \lambda_{S_{(2)}}$, such that

$$1 + z = \frac{\lambda_n}{\lambda_0} = \prod_{i=0}^{n-1}(1+\delta z_i) = \prod_{i=0}^{n-1}\frac{p_{\mu(i)}V^\mu_{(i)}}{p_{\mu(i+1)}V^\mu_{(i+1)}} = -\prod_{i=0}^{n-1}\frac{\Omega_{\mu(i)}V^\mu_{(i)}}{\Omega_{\mu(i+1)}V^\mu_{(i+1)}}, \tag{19}$$

where $\Omega_{\mu(0)} = -(u_{O1} - u_S)U_{\mu(S)}$.

With no loss of generality, we may of course apply the equation (19) all the way to $n \to \infty$. Let us recast the increment of the proper space scale factor, $l_i = l(u_i)$, over the affine parameters $u_i \quad (i = 1, 2, ..., n)$, into the form $l_i = l_0 + i\varepsilon$, where ε can be made arbitrarily small by increasing n. In the limit $n \to \infty$, all the respective adjacent observers are arbitrarily close to each other, so that $\delta z_i = \delta l_i/l_i \simeq \varepsilon/l_0 \to 0$. This allows us to write the following relation for the infinitesimal `relative´ redshifts:

$$\lim_{n\to\infty}(\delta z_{n-1} = \delta z_{n-2} = \cdots = \delta z_1 = \delta z_0 = \varepsilon/l_0) = \lim_{n\to\infty}\left(\delta z^{(a)}_{(n)} \equiv \frac{1}{n}\sum_{i=0}^{n-1}\delta z_i\right), \tag{20}$$

doi:https://doi.org/10.52526/25792776-22.69.2-151

provided, $\delta z^{(a)}_{(n)}$ is the average infinitesimal increment of spectral shift. There does not seem to be any reason to doubt a validity of (20). Certainly, the identification adopted here can be readily proved as follows. The relation (19) then becomes

$$\begin{gathered}1+z=\lim_{n\to\infty}\prod_{i=0}^{n-1}(1+\delta z_i)=\lim_{n\to\infty}\left(1+\delta z^{(a)}_{(n)}\right)^n=\lim_{n\to\infty}\left(1+\frac{1}{n}\sum_{i=0}^{n}\frac{\delta l_i}{l_i}\right)^n=\\ \lim_{n\to\infty}\left(1+\frac{1}{n}\ln\frac{l_n}{l_0}\right)^n=\frac{l_n}{l_0}=\frac{p_{\mu(S)}V^{\mu}_{(S)}}{p_{\mu(O)}V^{\mu}_{(O)}},\end{gathered}\tag{21}$$

and hence

$$\begin{gathered}1+z=\frac{\triangle\,\tau_O}{\triangle\,\tau_S}=\frac{p_{\mu(S)}V^{\mu}_{(S)}}{p_{\mu(O)}V^{\mu}_{(O)}}=-\frac{\Omega_{\mu(S)}V^{\mu}_{(S)}}{\Omega_{\mu(O)}V^{\mu}_{(O)}}=1+\sum_{i=0}^{n-1}\tilde{\delta}z_i=\lim_{n\to\infty}\prod_{i=0}^{n-1}(1+\delta z_i)=\\ \lim_{n\to\infty}\left(1+\delta z^{(a)}_{(n)}\right)^n,\end{gathered}\tag{22}$$

where $\Omega_{\mu(O)}=(u_O-u_S)U_{\mu(O)}$ and $\Omega_{\mu(S)}=-(u_O-u_S)U_{\mu(S)}$. The first line of equation (22) is the overall spectral shift rule (1), which proves a validity of the relation (20).

It is worth emphasizing that the general equation (22) follows from a series of infinitesimal stretching of the proper space scale factor in Riemannian spacetime, whereas the path of a luminous source appears nowhere, thus this equation does not relate to the special choice of transport path. Therefore, to remove the ambiguity of parallel transport of four-velocities in curved spacetime, we advocate exclusively with this proposal. To obtain some feeling about this statement, below we give more detailed explanation. Imagine a family of adjacent observers $(O_{a_i}(u_i))$ situated at the points a_i $(i=1,...,n)$ on the world lines (o_i) at infinitesimal distances from the observers $(O_{i(2)})$, who measure the wavelength of radiation in relative motion caused by a series of infinitesimal stretching $(\delta l_0,...,\delta l_{n-1})$ of the proper space scale factor. Let $v_{O_{i(2)}O_{a_i}}(u_i)\equiv c\delta\beta_{i-1}=c(\beta_i-\beta_{i-1})$ be an infinitesimal increment of the velocity, $c\beta_i$, of observer $O_{i(2)}$ with respect to the velocity, $c\beta_{i-1}$, of a neighboring observer O_{a_i} at the point a_i, due to infinitesimal stretching of the proper space scale factor δl_{i-1}. Since each line segment l_{i-1} of proper space scale factor (at the affine parameter u_{i-1}) is identically mapped on the line segment $(l_i-\delta l_{i-1})$ (where δl_i denotes infinitesimal segment $a_iO_{i(2)}$) of proper space scale factor (at the affine parameter $u_i=u_{i-1}+\delta u_{i-1}$), the relative velocity $v_{O_{i(2)}O_{a_i}}(u_i)$ of observer $(O_{i(2)}(u_i))$ to adjacent observer $(O_{a_i})(u_i)$ should be the same as it is relative to observer $(O_{(i-1)(2)}(u_{i-1}))$, that is $v_{O_{i(2)}O_{(i-1)}}(u_{i-1})\equiv v_{O_{i(2)}O_{a_i}}(u_i)$. Taking into account that the infinitesimal velocities of source (S) relative to observers $(O_{i(2)})$ arise at a series of infinitesimal stretching of the proper space scale factor δl_i $(i=0,1,2,...,n-1)$ as it is seen from the Fig. 1, we may fill out the whole pattern of monotonic increments of \`relative´ spectral shifts $(\delta z_0,\delta z_1,\delta z_2,...,\delta z_{n-1})$ by, equivalently, replacing the respective pairs $(O_{1(2)},S_{(2)}),(O_{2(2)},O_{1(2)}),...,(O_{n(2)},O_{(n-1)(2)})$ with new ones $(O_{1(2)},O_{a_1}),(O_{2(2)},O_{a_2}),...,(O_{n(2)},O_{a_n})$, which attribute to the successive increments of relative velocities $v_{O_{1(2)}S}(u_1),...,v_{O_{n(2)}O_{(n-1)(2)}}(u_n)$ of the source (S) away from an observer $(O_{n(2)})$ in the rest frame of $(O_{n(2)})$, viewed over all the values $(i=1,...,n)$. This framework provides the following definition.

Definition: The velocity $v_n\equiv v_{O_{n(2)}S_{(2)}}$ given in the limit $n\to\infty$ to be referred to as the relative velocity, $v_{r.v.}(z)$, of test particle (a source (S)) with respect to observer $(O_{n(2)})$ along the line of sight. That is

$$v_{r.v.}(z)=c\lim_{n\to\infty}\beta_n(z)\equiv\lim_{n\to\infty}v_{O_{n(2)}S_{(2)}}.\tag{23}$$

By virtue of the relation (20), at the limit $n\to\infty$, the relative infinitesimal velocities tends to zero, $v_{O_{i(2)}O_{a_i}}(u_i)=c\delta\beta_i=c\delta z_i(1-\beta_{i+1}\beta_i)\simeq(c\varepsilon/l_0)(1-\beta_{i+1}\beta_i)\to 0$, such that

$$\lim_{n\to\infty}\delta\beta_0=\lim_{n\to\infty}\delta\beta_1=\lim_{n\to\infty}\delta\beta_2=\cdots=\lim_{n\to\infty}\delta\beta_{n-1}=\lim_{n\to\infty}\left(\delta\beta^{(a)}_{(n)}\equiv\frac{1}{n}\sum_{i=0}^{n-1}\delta\beta_i\right)=\lim_{n\to\infty}\frac{1}{n}\beta_n.\tag{24}$$

doi:https://doi.org/10.52526/25792776-22.69.2-151

We are free to deal with any infinitesimal `relative´ spectral shift δz_i for the pair $(O_{i(2)})$ and (O_{a_i}), in local tangent inertial rest frame of an observer $(O_{i(2)})$, where we may approximate away the curvature of space in the infinitesimally small neighborhood.

Remark: In this case, although the corresponding infinitesimal relative velocities arise as the first-order Doppler velocities, $\delta\beta_i^{(r)} = \delta z_i$, we cannot summing them over. Actually, the infinitesimal relative velocities arise in generic pseudo-Riemannian spacetime at a series of infinitesimal stretching of the proper space scale factor as alluded to above, so that the *SR law of composition of velocities cannot be implemented globally along non-null geodesic* because these velocities are velocities at the different events, which should be in a different physical frames, and cannot be added together.

To facilitate further calculations of the relative velocity in quest, we can address the pair of observers at points $O_{(n)2}$ and a_n. Suppose $V^\mu_{O_{n(2)}}$ and $V^\mu_{O_{a_n}}$ be the unit tangent four-velocity vectors of observers $(O_{n(2)})$ and (O_{a_n}) to the respective world-lines in a Riemannian spacetime, thus in their respective rest frame we have $V^0_{O_{n(2)}} = 1$ and $V^0_{O_{a_n}} = 1$, as the only nonzero components of velocity. The ray passes an observer $O_{a_n}(u_n)(\equiv O_{(n-1)(2)}(u_{n-1}))$ with the proper space scale factor l_{n-1} who measures the wavelength to be λ_{n-1}. The ray passes next observer $O_{n(2)}(u_n)$ with the proper space scale factor $l_n = l_{n-1} + \delta l_{n-1}$. The ray's wavelength measured by observer $O_{n(2)}(u_n)$ is increased by $\delta\lambda_{n-1} = \lambda_n - \lambda_{n-1}$ leading to infinitesimal `relative´ spectral shift δz_{n-1}. For comparing the vectors $V^\mu_{O_{n(2)}}$ and $V^\mu_{O_{a_n}}$ at different events, it is necessary to seek a useful definition of the relative velocity by bringing both vectors to a common event by subjecting one of them to parallel transport. Since all the paths between infinitesimally separated spacetime points $O_{(n)2}$ and a_n are coincident at $n \to \infty$, for comparing these velocities there is no need to worry about specific choice of the path of parallel transport of four-vector. Therefore, we are free to subject further the unit tangent four-velocity vector $V^\mu_{O_{a_n}}$ to parallel transport along the null geodesic $\Gamma_{a_n O_{n(2)}}$ to the point $O_{n(2)}$. A parallel transport yields at $O_{n(2)}$ the vector $\beta_{\mu(O_{n(2)})} = \mathrm{g}_{\mu\nu'}(O_{(n)2}, O_{a_n})V^{\nu'}_{O_{a_n}}$, where the two point tensor $\mathrm{g}_{\mu\nu'}(O_{(n)2}, O_{a_n})$ is the parallel propagator, which is determined by the points O_{a_n} and $O_{(n)2}$. At $O_{a_n} \to O_{(n)2}$, we have the coincidence limit $[\mathrm{g}_{\mu\nu}](O_{n(2)}) = g_{\mu\nu}(O_{n(2)})$. As we have at point $O_{n(2)}$ two velocities $V^\mu_{O_{n(2)}}$ and $\beta^\mu_{(O_{n(2)})} = g^{\mu\nu}\beta_{\nu(O_{n(2)})}$, we may associate Doppler shift δz_{n-1} to four-velocity $\beta^\mu_{(O_{n(2)})}$ of observer O_{a_n} observed by an observer $O_{n(2)}$ with four-velocity $V^\mu_{O_{n(2)}}$ as measured by the latter. Then, following (Synge, 1960), the infinitesimal Doppler shift can be written:

$$\delta z_{n-1} = \frac{\delta\lambda_{n-1}}{\lambda_{n-1}} = \frac{p_{\mu(O_{n(2)})}\beta^\mu_{(O_{n(2)})}}{p_{\mu(O_{n(2)})}V^\mu_{(O_{n(2)})}} - 1 = \left[(1+\beta^2_{(O_{n(2)})})^{1/2} + \beta_{R(O_{n(2)})}\right] - 1, \tag{25}$$

where $c\beta^\mu_{(O_{n(2)})} = v^\mu_{(O_{n(2)})}$, $c\beta_{(O_{n(2)})} = v_{(O_{n(2)})}$, $c\beta_{R(O_{n(2)})} = v_{R(O_{n(2)})}$, and

$$\begin{aligned} &v^2_{(O_{n(2)})} = v_{(\alpha)(O_{n(2)})}v^{(\alpha)}_{(O_{n(2)})}, \quad v_{(\alpha)(O_{n(2)})} = v_{\mu(O_{n(2)})}\xi^\mu_{(\alpha)(O_{n(2)})}, \\ &v_{R(O_{n(2)})} = v_{\mu(O_{n(2)})}r^\mu_{(O_{n(2)})} = v_{(\alpha)(O_{n(2)})}v^{(\alpha)}_{(O_{n(2)})}. \end{aligned} \tag{26}$$

Reviewing notations the three-velocity of an observer (O_{a_n}) relative to observer at $(O_{n(2)})$ is $v_{(\alpha)(O_{n(2)})}$, the relative speed is $v_{(O_{n(2)})}$, and $v_{R(O_{n(2)})}$ is the speed of recession of (O_{a_n}). Whereas $\xi^\mu_{(\alpha)(O_{n(2)})}$ is the frame of reference on world-line (o) with $\xi^\mu_{0(O_{n(2)})} = V^\mu_{(O_{n(2)})}$, the unit vector $r^\mu_{(O_{n(2)})}$ at $O_{n(2)}$ is orthogonal to world-line (o) $(r_{\mu(O_{n(2)})}V^\mu_{(O_{n(2)})} = 0)$ and lying in the 2-element which contains the tangent at $O_{n(2)}$ to (o) and $S_{(2)}O_{(2)}$.

In the local inertial rest frame $\xi^\mu_{(\alpha)(O_{n(2)})}$ of an observer $(O_{n(2)})$, the velocity vector $\beta^\mu_{O_{n(2)}}$ takes the form $(\gamma, \gamma\delta\beta_{(O_{n(2)})}, 00)$, where an observer (O_{a_n}) is moving away from the observer $(O_n(2))$ with the relative infinitesimal three-velocity $\delta\beta_{(O_{n(2)})}$ (in units of the speed of light) in a direction making an angel $\theta_{(O_{n(2)})}$ with the outward direction of line of sight $\Gamma_{O_{a_n}O_{n(2)}}$ from O_{a_n} to $O_{(n)2}$, and $\gamma =$

doi:https://doi.org/10.52526/25792776-22.69.2-151

$(1-\delta\beta^2_{(O_{n(2)})})^{-1/2}$. Therefore, the equation (25) is reduced to

$$\delta z_{n-1} = \frac{1+\delta\beta_{(O_{n(2)})}\cos\theta_{(O_{n(2)})}}{\sqrt{1-\delta\beta^2_{(O_{n(2)})}}} - 1 = \beta_{R(O_{n(2)})} + \cdots \simeq \beta_{R(O_{n(2)})} = \frac{p_{(\alpha)(O_{n(2)})}v^{(\alpha)}_{(O_{n(2)})}}{E_{O_{n(2)}}} = \delta\beta_{(O_{n(2)})}\cos\theta_{(O_{n(2)})}. \tag{27}$$

Thus, at $n\to\infty$, the wavelength measured by the observer $O_{n(2)}$ is increased by the first-order Doppler shift caused unambiguously by the infinitesimal relative speed $\delta\beta^{(r)}_{n-1} \equiv \delta\beta_{(O_{n(2)})}\cos\theta_{(O_{n(2)})}$ along the line of sight with end-points O_{a_n} and $O_{n(2)}$:

$$\delta z_{n-1} = \frac{\delta l_{n-1}}{l_{n-1}} = \delta\beta^{(r)}_{n-1}. \tag{28}$$

The SR law of composition of velocities along the line of sight can be implemented in the tangent inertial rest frame of an observer $O_{n(2)}$:

$$\delta\beta^{(r)}_{n-1} = \frac{\beta_n - \beta_{n-1}}{1-\beta_n\beta_{n-1}} \simeq \frac{\delta\beta_{n-1}}{1-\beta^2_{n-1}}, \tag{29}$$

where $v_{n-1} = c\beta_{n-1}$ and $v_n = c\beta_n$ are, respectively, the three-velocities of observers O_{a_n} and $O_{n(2)}$ along the line of sight with end-points O_{a_n} and $O_{n(2)}$. According to (24), at $n\to\infty$, a resulting infinitesimal increment δz_{n-1} of spectral shift reads

$$\lim_{n\to\infty}\delta z_{n-1} = \lim_{n\to\infty}\frac{\delta\beta_{n-1}}{1-\beta^2_{n-1}} = \lim_{n\to\infty}\frac{\beta_n}{n(1-\beta^2_n)}, \tag{30}$$

A convenient form of relation (22), due to (20), can be written

$$1+z = \frac{p_{\mu S}V^\mu_S}{p_{\mu O}V^\mu_O} = -\frac{\Omega_{\mu(S)}V^\mu_{(S)}}{\Omega_{\mu(O)}V^\mu_{(O)}} = \lim_{n\to\infty}(1+\delta z_{n-1})^n. \tag{31}$$

This, combined with (30), gives a finite spectral shift

$$1+z = \frac{p_{\mu S}V^\mu_S}{p_{\mu O}V^\mu_O} = -\frac{\Omega_{\mu(S)}V^\mu_{(S)}}{\Omega_{\mu(O)}V^\mu_{(O)}} = \lim_{n\to\infty}\left[1+\frac{1}{n}\left(\frac{\beta_n}{1-\beta^2_n}\right)\right]^n = \exp\left(\frac{\beta_{r.v.}}{1-\beta^2_{r.v.}}\right). \tag{32}$$

where the subscript $()_{r.v.}$ designates relative velocity $\beta_{r.v.} \equiv \lim_{n\to\infty}\beta_n$. The equation (32) directly yields the relative velocity of test particle (a luminous source) as measured along the observer's line-of-sight in generic pseudo-Riemannian spacetime:

$$\beta_{r.v.} = \frac{\sqrt{1+4\left[\ln\left(p_{\mu S}V^\mu_S\right)-\ln\left(p_{\mu O}V^\mu_O\right)\right]^2}-1}{2\left[\ln\left(p_{\mu S}V^\mu_S\right)-\ln\left(p_{\mu O}V^\mu_O\right)\right]} = \frac{\sqrt{1+4\left[\ln\left(-\Omega_{\mu(S)}V^\mu_{(S)}\right)-\ln\left(\Omega_{\mu(O)}V^\mu_{(O)}\right)\right]^2}-1}{2\left[\ln\left(-\Omega_{\mu(S)}V^\mu_{(S)}\right)-\ln\left(\Omega_{\mu(O)}V^\mu_{(O)}\right)\right]}. \tag{33}$$

The relative velocity of test particle is plotted on the Fig. 2 for spectral shifts $-1\le z\le 4$.

2.1. A global Doppler velocity along the null geodesic

A final point should be noted. Suppose the velocities of observers say $O_{i(2)}$ $(i = 1, ..., n-1)$, being in free fall, populated along the null geodesic $\Gamma_{S_{(2)}O_{(2)}}(v+\vartriangle v)$ of light ray (Fig. 1), vary smoothly along the line of sight with the infinitesimal increment of relative velocity $\delta\beta^{(r)}_i$. The (i)-th observer situated at the point $i(2)$ of intersection of the ray's trajectory $\Gamma_{S_{(2)}O_{(2)}}(v+\vartriangle v)$ with the world line (o_i) at affine parameter u_i, and measures the frequency of light ray as it goes by. According to the equivalence principle, we may approximate away the curvature of space in the infinitesimally small neighborhood

doi:https://doi.org/10.52526/25792776-22.69.2-151

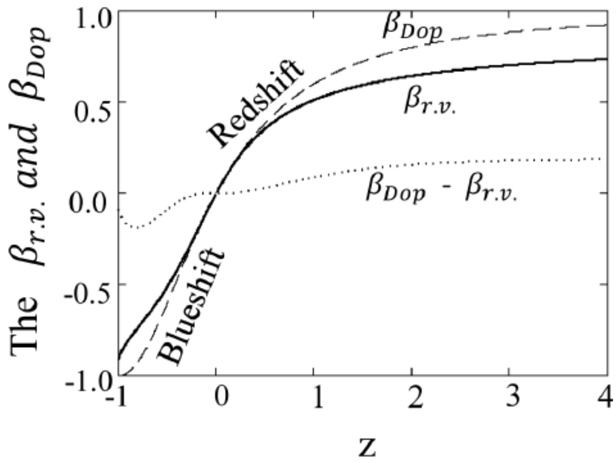

Figure 2. The relative velocity along the line of sight ($\beta_{r.v.}$) vs. z. The global Doppler velocity (β_{Dop}), and their difference (in units of the speed of light) are also presented.

of two adjacent observers. If we approximate an infinitesimally small neighborhood of a curved space as flat, the resulting errors are of order $(\delta l_i/l_n)^2$ in the metric. If we regard such errors as negligible, then we can legitimately approximate spacetime as flat. The infinitesimal increment of spectral shift δz_i is not approximated away in this limit because it is in that neighborhood of leading order $(\delta l_i/l_i)$. That is, approximating away the curvature of space in the infinitesimally small neighborhood does not mean approximating away the infinitesimal increment δz_i. Imagine a thin world tube around the null geodesic $\Gamma_{S_{(2)}O_{(2)}}(v+\bigtriangleup v)$ within which the space is flat to arbitrary precision. Each observer has a local reference frame in which SR can be taken to apply, and the observers are close enough together that each one $O_{i(2)}$ lies within the local frame of his neighbor $O_{(i+1)(2)}$. This implies the vacuum value of a velocity of light to be universal maximum attainable velocity of a material body found in this space. Such statement is true for any thin neighborhood around a null geodesic. Only in this particular case, the relative velocity of observers can be calculated by the SR law of composition of velocities globally along the path of light ray. We may apply this law to relate the velocity β_i to the velocity β_{i+1}, measured in the $(i+1)$-th adjacent observer's rest frame. The end points of infinitesimal distance between the adjacent observers $O_{i(2)}$ and $O_{(i+1)(2)}$ will respectively be the points of intersection of the ray's trajectory with the world lines $o_i(u_i)$ and $(o_{i+1})(u_{i+1})$. This causes a series of infinitesimal increment of the proper space scale factor from $l_i =\bigtriangleup \tau_i$ to $l_{i+1} =\bigtriangleup \tau_{i+1}$, which in turn causes a series of infinitesimal increment of spectral shift $\delta z_i = \delta\lambda_i/\lambda_i = \delta l_i/l_i$. Within each local inertial frame, there are no gravitational effects, and hence the infinitesimal spectral shift from each observer to the next is a Doppler shift. Thus, at the limit $n\to\infty$, a resulting infinitesimal frequency shift δz_i, can be unambiguously equated to infinitesimal increment of a fractional SR Doppler shift $\delta\bar{z}_i$ from observer $O_{i(2)}$ to the next $O_{(i+1)(2)}$ caused by infinitesimal relative velocity $\delta\bar{\beta}^r_i$:

$$\left(\delta z_i = \frac{\delta l_i}{l_i}\right)_{n\to\infty} = \left(\delta\bar{z}_i = \delta\bar{\beta}^r_i = \frac{\bar{\beta}_{i+1}-\bar{\beta}_i}{1-\bar{\beta}_{i+1}\bar{\beta}_i} \simeq \frac{\delta\bar{\beta}_i}{1-\bar{\beta}^2_i}\right)_{n\to\infty}, \tag{34}$$

where by $\bar{()}$ we denote the null-geodesic value, as different choices of geodesics yield different results for the motion of distant test particles relative to a particular observer. The relation (34), incorporated with the identity (20), yield

$$\left(\delta z_{n-1} = \delta\beta^{(r)}_{n-1}\right)_{n\to\infty} = \left(\frac{\delta\beta_{n-1}}{1-\beta^2_n}\right)_{n\to\infty} = \left(\delta\bar{z}^{(a)}_{(n)} = \delta\bar{\beta}^{r(a)}_{(n)} \equiv \frac{1}{n}\sum_{i=0}^{n-1}\frac{\delta\bar{\beta}_i}{1-\bar{\beta}^2_i}\right)_{n\to\infty}, \tag{35}$$

which, by virtue of (24), for sufficiently large but finite n gives

$$\frac{\beta_n}{1-\beta^2_n} = \sum_{i=0}^{n-1}\frac{\delta\bar{\beta}_i}{1-\bar{\beta}^2_i} = \int_0^{\bar{\beta}_n}\frac{d\bar{\beta}}{1-\bar{\beta}^2}, \tag{36}$$

doi:https://doi.org/10.52526/25792776-22.69.2-151

or

$$\bar{\beta}_n = \frac{e^{\varrho_n} - 1}{e^{\varrho_n} + 1}, \quad \varrho_n \equiv \frac{2\beta_n}{1 - \beta_n^2}. \tag{37}$$

Hence the general solution (39), by means of relation (36), is reduced to a global Doppler shift along the null geodesic:

$$1 + z = \sqrt{\frac{1 + \bar{\beta}_{r.v.}}{1 - \bar{\beta}_{r.v.}}} = \frac{p_{\mu(O2)} V^{\mu}_{(S2)}}{p_{\mu(O2)} V^{\mu}_{(O2)}}, \tag{38}$$

where $\bar{\beta}_{r.v.} = \lim\limits_{n\to\infty} \bar{\beta}_n$, $V^{\mu}_{(S2)}$ and $V^{\mu}_{(O2)}$ are the four-velocity vectors, respectively, of the source $S_{(2)}$ and observer $O_{(2)}$, $p_{\mu(S2)}$ and $p_{\mu(O2)}$ are the tangent vectors to the typical null geodesics $\Gamma_{S_{(2)}O_{(2)}}(v)$ at their respective end points. This procedure, in fact, is equivalent to performing parallel transport of the source four-velocity in a general Riemannian spacetime along the null geodesic to the observer. Note that any null geodesic from a set of null geodesics mapped (s) on (o) can be treated in the similar way.

In Minkowski space a parallel transport of vectors is trivial and mostly not mentioned at all. This allows us to apply globally the SR law of composition of velocities to relate the velocities $\bar{\beta}_i$ to the $\bar{\beta}_{i+1}$ of adjacent observers along the path of light ray, measured in the $(i+1)$-th adjacent observer's frame. Then, according to (34)-(38), a global Doppler shift of light ray emitted by luminous source as it appears to observer at rest in flat Minkowski space can be derived by summing up the infinitesimal Doppler shifts caused by infinitesimal relative velocities of adjacent observers.

3. The several special cases

The equation (32) directly yields the relative velocity of test particle (a luminous source) as measured along the observer's line-of-sight in generic pseudo-Riemannian spacetime:

$$\beta_{r.v.} = \frac{\sqrt{1 + 4\left[\ln\left(p_{\mu S} V^{\mu}_{S}\right) - \ln\left(p_{\mu O} V^{\mu}_{O}\right)\right]^2} - 1}{2\left[\ln\left(p_{\mu S} V^{\mu}_{S}\right) - \ln\left(p_{\mu O} V^{\mu}_{O}\right)\right]} = \frac{\sqrt{1 + 4\left[\ln\left(-\Omega_{\mu(S)} V^{\mu}_{(S)}\right) - \ln\left(\Omega_{\mu(O)} V^{\mu}_{(O)}\right)\right]^2} - 1}{2\left[\ln\left(-\Omega_{\mu(S)} V^{\mu}_{(S)}\right) - \ln\left(\Omega_{\mu(O)} V^{\mu}_{(O)}\right)\right]}. \tag{39}$$

In this section we discuss the implications of the general solution (39) for several instructive cases of potential interest, that is the Minkowski metric, the test particle and observer at rest in an arbitrary stationary metric, the uniform gravitational field, the rotating reference frame, the Schwarzschild metric, the Kerr-type metrics, and the spatially homogeneous and isotropic Robertson-Walker spacetime of standard cosmological model. We use the term `Doppler shift´ in a generalized sense, to refer to any effect that causes a photon's frequency at detection to differ from that which it had. Unless otherwise stated we take, for convenience natural, units, $h = c = G = 1$.

Suppose the metric $g_{\mu\nu}$ is stationary, i.e. there exists a coordinate system such that the metric tensor is independent of the time coordinate x^0. Let also $\mathbf{U} = d\mathbf{x}/d\tau$ be the four-velocity of an observer carrying the clock, which in general is written

$$\mathbf{U} = (-g_{00} - 2g_{i0}v^i - g_{ij}v^i v^j)^{1/2}(1, \vec{v}), \tag{40}$$

where $d\tau = (-g_{\mu\nu}dx^{\mu}dx^{\nu})^{1/2}$ is the proper time, measured on a clock moving with three-velocity $\vec{v} = d\vec{x}/dx^0$ in an arbitrary coordinate system:

$$d\tau = (-g_{00} - 2g_{i0}v^i - g_{ij}v^i v^j)^{1/2}, \tag{41}$$

provided, dx^0 is the coordinate time interval. The energy $\hat{E}$ of test particle relative to an observer, with four-momentum $\mathbf{P} = E(1, \vec{w})$, can be written

$$\hat{E} = -\mathbf{U}\cdot\mathbf{P} = \frac{(g_{00} + g_{i0}v^i + g_{i0}w^i + g_{ij}v^i w^j)P^0}{(-g_{00} - 2g_{i0}v^i - g_{ij}v^i v^j)^{1/2}}, \tag{42}$$

doi:https://doi.org/10.52526/25792776-22.69.2-151

where E and $\vec{w}$ are the energy and spatial coordinate velocity of an observer. If test particle is freely moving in a time-independent metric, then from the equations of motion it follows that the covariant momentum P_0, conjugate to the time coordinate, is a constant of motion for the particle. The equation (42) then becomes

$$\hat{E} = \frac{(g_{00} + g_{i0}v^i + g_{i0}w^i + g_{ij}v^i w^j)P_0}{(-g_{00} - 2g_{i0}v^i - g_{ij}v^i v^j)^{1/2}(g_{00} + g_{i0}w^i)}. \tag{43}$$

By virtue of (43) and that P_0 is a constant of motion, the spectral shift rule (1) gives the frequency shift $\omega_O D_O = \omega_S D_S$ (Grøn, 1980), where D is a general Doppler shift factor:

$$D = \frac{(-g_{00} - 2g_{i0}v^i - g_{ij}v^i v^j)^{1/2}(g_{00} + g_{i0}w^i)}{(g_{00} + g_{i0}v^i + g_{i0}w^i + g_{ij}v^i w^j)}. \tag{44}$$

Therefore, we may recast the general solution (39) into the form

$$\beta_{r.v.} = \frac{\sqrt{1 + 4\left(\ln D_O - \ln D_S\right)^2} - 1}{2\left(\ln D_O - \ln D_S\right)}, \tag{45}$$

3.1. The Minkowski metric

In case at hand, there is no deflection of the light, and the magnitude of the velocity of light is constant, so $\vec{w}_O = \vec{w}_S = \vec{n}$, where $\vec{n}$ is a unit vector in the direction of propagation of the light. Then $D = \gamma(1 - \vec{v} \cdot \vec{n})$, where $\gamma = (1 - v^2)^{-1/2}$ (see Grøn, 1980). Hence the general solution (45) reduced to

$$\beta_{r.v.} = \frac{\sqrt{1 + 4\left[\ln(\gamma_S(1 - \vec{v}_S \cdot \vec{n}) - \ln(\gamma_O(1 - \vec{v}_O \cdot \vec{n})\right]^2} - 1}{2\left[\ln(\gamma_S(1 - \vec{v}_S \cdot \vec{n}) - \ln(\gamma_O(1 - \vec{v}_O \cdot \vec{n})\right]}. \tag{46}$$

In the rest frame of observer $\vec{v}_O = 0$, the equation gives

$$\beta_{r.v.} = \frac{\sqrt{1 + 4\left[\ln(1 - \vec{v}_S \cdot \vec{n}) - \ln(1 - v_S^2)^{1/2}\right]^2} - 1}{2\left[\ln(1 - \vec{v}_S \cdot \vec{n}) - \ln(1 - v_S^2)^{1/2}\right]}. \tag{47}$$

The condition $\vec{v}_S \cdot \vec{n} = 0$ reveals the transverse Doppler effect - the SR time dilation. The case $\vec{v}_S \cdot \vec{n} = v_S$, describes the longitudinal Doppler shift (38).

3.2. The source and observer at rest in an arbitrary stationary metric

The spectral shift at $v_S = v_O = 0$ is known as the gravitational Doppler effect, such that the rate of time at the position of the absorber is different from that at the position of the emitter. Thereby (45) reduced to

$$\beta_{r.v.} = \frac{\sqrt{1 + \left(\ln g_{00}^O - \ln g_{00}^S\right)^2} - 1}{\ln g_{00}^O - \ln g_{00}^S}. \tag{48}$$

3.3. The uniform gravitational field

The case of uniform gravitational field can be identified with a rigidly accelerated reference frame in flat spacetime (Greenberger & Overhauser, 1979, Grøn, 1979). The metric in this frame with constant acceleration g along the z axis, as measured in its instantaneous rest inertial frames, is (Möller, 1952)

$$ds^2 = -(1 + gz)^2 dt^2 + dx^2 + dy^2 + dz^2. \tag{49}$$

Thereby the time passes more slowly closer to the source in the gravitational field.

doi:https://doi.org/10.52526/25792776-22.69.2-151

The equations (45), for metric (49), yields

$$\beta_{r.v.} = \frac{\sqrt{1 + 4\ln^2 \left\{ \frac{[(1+gz_O)^2 - v_O^2]^{1/2}(1+gz_O)^2[(1+gz_S)^2 - v_S \cdot w_S]}{[(1+gz_S)^2 - v_S^2]^{1/2}(1+gz_S)^2[(1+gz_O)^2 - v_O \cdot w_O]} \right\}} - 1}{2\ln \left\{ \frac{[(1+gz_O)^2 - v_O^2]^{1/2}(1+gz_O)^2[(1+gz_S)^2 - v_S \cdot w_S]}{[(1+gz_S)^2 - v_S^2]^{1/2}(1+gz_S)^2[(1+gz_O)^2 - v_O \cdot w_O]} \right\}}. \tag{50}$$

Then, for both the test particle and observer at rest, the equation (50) gives

$$\beta_{r.v.} = \frac{\sqrt{1 + 4\left[\ln(1+gz_O) - \ln(1+gz_S)\right]^2} - 1}{2\left[\ln(1+gz_O) - \ln(1+gz_S)\right]}. \tag{51}$$

3.4. The rotating reference frame

Consider a reference frame Σ_r, with cylindrical coordinates (t, r, θ, z) rotates with constant angular velocity ω. The cylindrical coordinates are defined by the transformation from coordinates (T, R, Θ, Z) of inertial frame Σ_0, in which the axis of Σ_r, is permanently at rest: $T = t, \quad R = r, \quad \Theta = \theta + \omega t, \quad Z = z$. This gives for the line element in Σ_r

$$ds^2 = -(1 - r^2\omega^2)dt^2 + dr^2 + r^2 d\theta^2 + dz^2 + 2\omega r^2 d\theta dt. \tag{52}$$

If the test particle and observer are both at rest in Σ_r, at distances r_S and r_O. from the axis, respectively, equation (45) gives

$$\beta_{r.v.} = \frac{\sqrt{1 + \left[\ln(1 - r_O^2\omega^2) - \ln(1 - r_S^2\omega^2)\right]^2} - 1}{\ln(1 - r_O^2\omega^2) - \ln(1 - r_S^2\omega^2)}. \tag{53}$$

Note that:

(i) As v^i and w^i are components of coordinate velocities, so they need not have the dimension of (length/time). For example v^i is an angular velocity with dimension time^{-1}. When given in an inertial frame Σ_0, they may be found in the arbitrary frame Σ by using the coordinate transformation from Σ_0 to Σ.

(ii) The $\vec{w}$ is a spatial tangent vector along the path of a photon. Although $\vec{w}$ is always a unit vector in an inertial frame, this is not generally the case.

(iii) As shown by (Möller, 1952) it is not possible by a simple change of rate of coordinate clocks to introduce a time-orthogonal system of coordinates in the rotating reference frame. The non-vanishing g_{02} component represents a genuine physical effect, and may be regarded as a component of a gravitational spatial vector potential, giving rise to a Coriolis acceleration for a moving particle in Σ_r.

3.5. The Schwarzschild metric

The line element in the usual Schwarzschild coordinates has the form

$$ds^2 = -B(r)dt^2 + A(r)dr^2 + r^2 d\theta^2 + r^2 \sin^2\theta d\phi^2, \tag{54}$$

where $B(r) = 1 - 2m/r$, $A(r) = 1/B(r)$. In this case the expression (44) becomes

$$\begin{aligned} \frac{D_O}{D_S} = & \frac{\left[B - A(v^r)^2 - r^2(v^\theta)^2 - r^2\sin^2\theta(v^\phi)^2\right]_O^{1/2} B_O}{\left[B - A(v^r)^2 - r^2(v^\theta)^2 - r^2\sin^2\theta(v^\phi)^2\right]_S^{1/2} B_S} \times \\ & \frac{\left(-B + Av^r w^r + r^2 v^\theta w^\theta + r^2\sin^2\theta v^\phi w^\phi\right)_S}{\left(-B + Av^r w^r + r^2 v^\theta w^\theta + r^2\sin^2\theta v^\phi w^\phi\right)_O}. \end{aligned} \tag{55}$$

doi:https://doi.org/10.52526/25792776-22.69.2-151

In case $v_S^\phi = w_O^\phi = w_S^\phi = w_O^\phi = 0$, the equation (55) can be written in the form (see Jaffe & Vessot, 1976)

$$\beta_{r.v.} = \frac{\sqrt{1+4\left[\ln\left(\frac{\left[B-A(v^r)^2-r^2(v^\theta)^2\right]_O^{1/2}\left[1-(A/B)^{1/2}(1-Bl^2/r^2)^{1/2}v^r-lv^\theta\right]_S}{\left[B-A(v^r)^2-r^2(v^\theta)^2-\right]_S^{1/2}\left[1-(A/B)^{1/2}(1-Bl^2/r^2)^{1/2}v^r-lv^\theta\right]_O}\right)\right]^2}-1}{2\left[\ln\left(\frac{\left[B-A(v^r)^2-r^2(v^\theta)^2\right]_O^{1/2}\left[1-(A/B)^{1/2}(1-Bl^2/r^2)^{1/2}v^r-lv^\theta\right]_S}{\left[B-A(v^r)^2-r^2(v^\theta)^2-\right]_S^{1/2}\left[1-(A/B)^{1/2}(1-Bl^2/r^2)^{1/2}v^r-lv^\theta\right]_O}\right)\right]}, \tag{56}$$

where l is the impact parameter of the photon, as measured at infinity (Misner et al., 1973).

3.6. The Kerr-type metrics

Various frequency-shift effects have to be taken into account in a wide array of astrophysical contexts. The Kerr–Doppler effect has been studied in (Asaoka, 1989, Cisneros et al., 2015, Cunningham, 1998, Fanton et al., 1997, Li et al., 2005, Schönenbach, 2014). A formula for Kerr–Doppler effect for Kerr-type, (i.e. stationaryand axisymmetric) space–times, e.g. the coarse-grained, diffuse internal space–time of a spiral galaxy, is derived by (Cisneros et al., 2015), for the combined motional and gravitational Doppler effect in general stationary axisymmetric metrics for a photon emitted parallel or antiparallel to the assumed circular orbital motion of its source. In obtaining the formula, the authors utilized two seemingly different approaches, an eikonal approximation solution to a scalar wave equation in the Kerr-type metric, and a KV representation of both the source circular motion and the photon motion. Killing vector approach derivation will take advantage of the conserved quantities of time-like and null geodesic motion which result from the one parameter families of symmetries of the space–time, described by the KV fields. The two approaches produced the same formula, because despite apparent dissimilarities the underlying physics is the same. For example, the local propagation, or wave 3-vector used in the eikonal approach is (proportional to) the local photon 3-momentum used in the KV approach. While the KV approach is limited to the particular highly symmetric application that we treated, that of a photon emitted tangentially to the circular orbit of a source, it allows analysis in a more modern relativistic context, in which the relationship between the orbital velocity, Ω, and the radius is determined by the conserved quantities of the Lagrangian. On the other hand, the eikonal method should be applicable for a local photon propagation 3-vector in any direction relative to the source motion, for the special case of the exterior Kerr metric. The wave equation would then yield a different expression for the local effective refractive index than it is obtained for tangential emission Note that the eikonal method should be applicable for a local photon propagation 3-vector in any direction relative to the source motion, for the special case of the exterior Kerr metric. This analysis extends to arbitrary Kerr-type (i.e. stationary and axisymmetric) space–times, e.g. the coarse-grained, diffuse internal space–time of a spiral galaxy. The formula yields expected results in the limits of a moving or stationary source in the exterior Kerr and Schwarzschild metrics and is useful for broad range astrophysical analyses.

The geometries under consideration comprise all stationary axisymmetric metrics of the Kerr type, i.e. all metrics independent of time t and azimuthal angle φ in polar (Boyer–Lindquist) coordinates (t, r, θ, φ), with $g_{0\varphi} = g_{\varphi 0}$ the only non-vanishing off-diagonal elements. In such metrics, the source was restricted to be moving in the φ-direction (which is the case for emitters in circular orbits in the equatorial plane, and also for emitters at the apsides of other orbits in that plane), and emitting in (or against) that same direction. For stable, circular, equatorial orbits that most closely approximate those in spiral galaxies, the relevant KV are the time-like $\xi = (1, 0, 0, 0)$ and the axial $\eta = (0, 0, 0, 1)$, for Kerr type metrics in Boyer–Lindquist-type coordinates. In this setting, the Doppler shift observed by a receiver in asymptotic flat space can be given without recourse to a perturbative expansion. Based on this analysis, the general formula (45), for a relative velocity of test particle moving directly

doi:https://doi.org/10.52526/25792776-22.69.2-151

towards or directly away from the asymptotic observer, can be recast into the form

$$\beta_{r.v.}=\frac{\sqrt{1+4\ln^2\left(\dfrac{g_{00}\sqrt{-g_{00}-2\Omega g_{0\varphi}-\Omega^2 g_{\varphi\varphi}}}{g_{00}+\Omega\left(g_{0\varphi}+\sqrt{g_{t\varphi}^2-g_{\varphi\varphi}g_{00}}\right)}\right)}-1}{2\ln\left(\dfrac{g_{00}\sqrt{-g_{00}-2\Omega g_{0\varphi}-\Omega^2 g_{\varphi\varphi}}}{g_{00}+\Omega\left(g_{0\varphi}+\sqrt{g_{t\varphi}^2-g_{\varphi\varphi}g_{00}}\right)}\right)}, \tag{57}$$

where Ω is the angular velocity $\Omega = d\varphi/dt = u^\varphi/u^t$, which is a constant for a circular orbit. In the case of Kerr black hole (Chandrasekhar, 1983, O'Neill, 1995), the metric components are written

$$\begin{aligned}
&g_{00}=-(1-2Mr/\Sigma), \quad g_{\varphi\varphi}=\big[(r^2+a^2)^2-\\
&a^2\Delta\sin^2\theta\big]\frac{\sin^2\theta}{\Sigma}, \quad g_{\theta\theta}=\Sigma, \quad g_{rr}=\Sigma/\Delta,\\
&g_{0\varphi}=g_{\varphi 0}=-2Mar\frac{\sin^2\theta}{\Sigma},
\end{aligned} \tag{58}$$

where

$$\Sigma=r^2+a^2\cos^2\theta, \quad \Delta=r^2+a^2-2Mr, \tag{59}$$

and for an emitter in the equatorial plane, $\theta=\pi/2$, Doppler formula derived in (Cisneros et al., 2015) coincides with the expression given in (Asaoka, 1989, Cunningham, 1998, Fanton et al., 1997, Li et al., 2005). To obtain the Schwarzschild metric limit we set $a=0$ with $M=M_S/c^2$ for a source of mass M_S, then equation (57) yields

$$\beta_{r.v.}=\frac{\sqrt{1+4\ln^2\left[(1-2M/r)\left(\dfrac{(1-2M/r)^{1/2}+\Omega r/c}{(1-2M/r)^{1/2}-\Omega r/c}\right)\right]^{-1/2}}-1}{2\ln\left[(1-2M/r)\left(\dfrac{(1-2M/r)^{1/2}+\Omega r/c}{(1-2M/r)^{1/2}-\Omega r/c}\right)\right]^{-1/2}}, \tag{60}$$

where the velocity of light, c, is recovered. As expected, the equation (60) leads to the correct limits: the familiar gravitational redshift for non-moving optical sources ($\Omega=0$), and the usual longitudinal Lorentz–Doppler ratio for $M=0$ but $\Omega r/c=v/c$, where the relative source–observer velocity $v\approx\Omega r$ can be positive or negative. For a source in circular orbit, $M/r\approx v^2/c^2$, the equation (60) yields the usual Lorentz–Doppler formula to first order in v/c.

3.7. The Robertson-Walker spacetime

In the framework of standard cosmological model, one assumes that the universe is populated with comoving observers. In the homogeneous, isotropic universe comoving observers are in freefall, and obey Wayl's postulate: their all worldlines form a 3-bundle of non-intersecting geodesics orthogonal to a series of spacelike hypersurfaces, called comoving hypersurfaces. In case of expansion, all worldlines are intersecting only at one singular point. The clocks of comoving observers, therefore, can be synchronized once and for all. Let the proper time, t, of comoving observers be the temporal measure. Suppose $R(t)$ is the scale factor in expanding homogenous and isotropic universe. One considers in, so-called, cosmological rest frame a light that travels from a galaxy to a distant observer, both of whom are at rest in comoving coordinates. As the universe expands, the wavelengths of light rays are stretched out in proportion to the distance $L(t)$ between co-moving points ($t>t_1$), which in turn increase proportionally to $R(t)$ (Harrison, 1993, 1995):

$$\frac{\lambda(t)}{\lambda(t_1)}=\frac{dt}{dt_1}=\frac{R(t)}{R(t_1)}=\frac{L(t)}{L(t_1)}. \tag{61}$$

Reviewing notations in this `cosmic wavelength stretching´ relation with a fixed comoving coordinate χ ($d\chi=0$), $L_1\equiv L(t_1)=cR_1\chi$ is the proper distance to the source at the time when it emits light,

doi:https://doi.org/10.52526/25792776-22.69.2-151

$L(t) = cR(t)\chi$ is the same distance to the same source at light reception. Integration of differential equation (61) gives $\chi = \tau_1 - \tau$, where the interval of conformal time $d\tau \equiv dt/R(t) = \chi dt/L(t)$ is constant, i.e. at emission $d\tau_1$ equals $d\tau$ at reception.

In what follows, the mathematical structure has much in common with those constructions used for deriving of (17)-(39). After making due allowances for (61), particularly, the infinitesimal `relative´ increment δz_j $(j = 1, ..., n-1)$ of redshift reads

$$\delta z_j = \frac{\delta\lambda_j}{\lambda_j} = \frac{\lambda_{j+1} - \lambda_j}{\lambda_j} = \frac{\delta L_j}{L_j} = \frac{L_{j+1} - L_j}{L_j} = \frac{\tilde{\delta} z_j}{1 + z_j} \equiv \frac{z_{j+1} - z_j}{1 + z_j}, \quad 1 + z_j = \frac{\lambda_j}{\lambda_1}, \tag{62}$$

where, the role of proper space scale factor l_i is now destined to the scale factor $R(t_i) \propto L(t_i)$. As a corollary, the general relation (39) straightforwardly yields the particular solution for the case of expanding RW spacetime of standard cosmological model, i.e. the so-called *kinetic* recession velocity v_{rec} of luminous source, which can be written in terms of scale factor $R(t)$:

$$v_{rec}(R) = \frac{\sqrt{1 + 4[\ln R(t) - \ln R_1]^2} - 1}{2[\ln R(t) - \ln R_1]}, \tag{63}$$

agreed with the result obtained by quite different study of, so-called, `lookforward´ history of expanding universe (Ter-Kazarian, 2021a, 2022). This interpretation so achieved has physical significance as it agrees with a view that the light waves will be stretched by travelling through the expanding universe, and in the same time the *kinetic* recession velocity of a distant astronomical object is always subluminal even for large redshifts of order one or more. It, therefore, does not violate the fundamental physical principle of *causality*. Moreover, the general solution is reduced to global Doppler shift (38) along the null geodesic, studied by Synge (Synge, 1960) (see also (Bunn & Hogg, 2009, Narlikar, 1994).

Once we are equipped with the general solution (63), we may define the most important parameter $\zeta(z, \dot{L})$ of practical measure of sweeping up of test particle with redshift z, in expanding universe:

$$\zeta(R, \dot{L}) \equiv \frac{v_{rec}(R)}{\dot{L}} = \frac{\sqrt{1 + 4[\ln R(t) - \ln R_1]^2} - 1}{2\dot{L}[\ln R(t) - \ln R_1]}, \tag{64}$$

where $\dot{L}(t, z)$ is the `proper´ recession velocity. The general solution (63) and parameter $\zeta(z, \dot{L})$ are plotted on the Fig. 3 for the distances at which the Hubble empirical linear `redshift-distance´ law $(cz = HL)$ is valid. (*Top panel(a):* for redshifts $0 \leq z \leq 25$; and *Bottom panel(b):* for redshifts $0 \leq z \leq 800$), where the global Doppler velocity, and their difference are also presented to guide the eye. As it is seen from the Fig. 3, the $\zeta(z) = 0.034$ at $z = 25$, and it declines in magnitude to $\zeta(z) = 1.16 \times 10^{-3}$ at $z = 800$. In particular, this offers a clear way out of ambiguity of the meaning of `expansion of flat 3D space´. Indeed, since the concept of 3D `space´ is not a well-defined (invariant) concept in general relativity, this arises the question whether the cosmological redshift in expanding universe can be distinguished from a purely kinematic Doppler effect resulting from the motion of test particles (galaxies) in stationary spacetime. The measure $\zeta(z)$, which declines in magnitude, uniquely distinguishes between real cosmological expansion and the hypothetical motion of galaxies in stationary spacetime. It proves that cosmological expansion of a flat 3D–space is fundamentally different from a kinematics of galaxies moving in a non-expanding flat 3D-space, in agreement with (Abramowicz et al., 2007). According to them, the rather wide-spread belief that cosmological expansion of a flat 3D–space (with spatial curvature k = 0) cannot be observationally distinguished from a kinematics of galaxies moving in a flat and non-expanding space is erroneous. The authors show that the expanding universe is necessarily a curved spacetime, so that the interpretation of the observed cosmological redshift as being due to the expansion of the cosmological 3D–space is observationally verifiable. Thus it is impossible to mimic the true cosmological redshift by a Doppler effect caused by motion of galaxies in a non-expanding 3D-space, flat or curved.

4. Concluding remarks

Let us briefly summarize the main results of this work. This report is about the much-discussed in literature question of the velocity of test particle relative to the observer in curved spacetime. We

doi:https://doi.org/10.52526/25792776-22.69.2-151

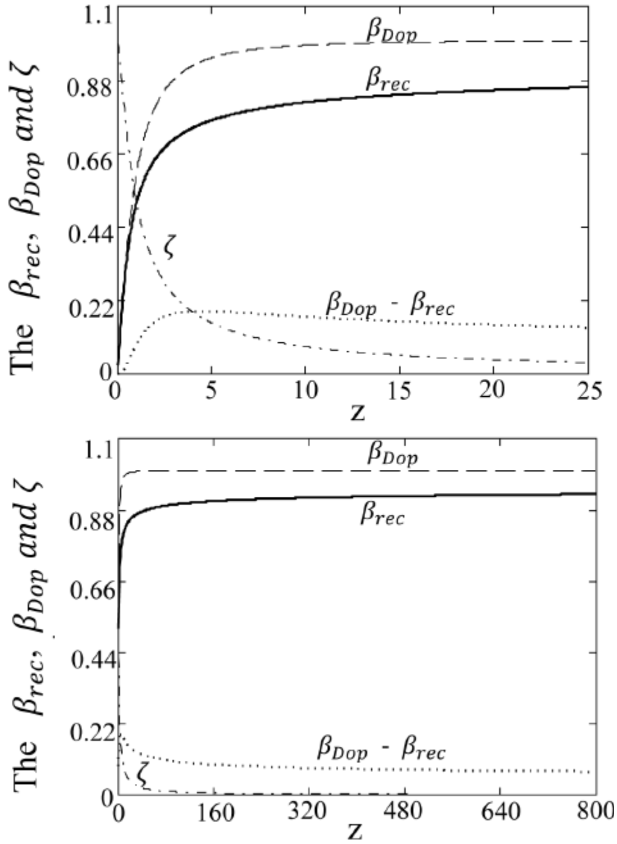

Figure 3. The parameter ζ, the *kinetic* recession velocity (β_{rec}), the Doppler velocity (β_{Dop}), and their difference vs. z.
Top panel: $0 \leq z \leq 25$; *Bottom panel:* $0 \leq z \leq 800$.

aim to give a unique (coordinate independent) definition of relative velocity between test particle and observer as measured along the observer's line-of-sight in generic pseudo-Riemannian spacetime. In doing this, the test particle is considered as a luminous object, otherwise, if it is not, we assume that a light source is attached to it, which has neither mass nor volume. Then, extending those geometrical ideas of well-known kinematic spectral shift rule to infinitesimal domain, we try to catch this effect by building a series of infinitesimally displaced shifts and then sum over them in order to find the proper answer to the problem that we wish to address. Thereby, the general equation (22) follows from a series of infinitesimal stretching of the proper space scale factor in Riemannian spacetime, whereas the path of a luminous source appears nowhere, thus this equation does not relate to the special choice of transport path. A resulting general expression (39) of relative velocity of test particle (a luminous source) as measured along the observer's line-of-sight in generic pseudo-Riemannian spacetime is utterly distinct from a familiar Doppler velocity. In particular case only, when adjacent observers are being in free fall and populated along the null geodesic, the relative velocity of luminous source is reduced to global Doppler velocity (38) as studied by Synge. We discuss the implications for several instructive cases of the Minkowski metric, the test particle and observer at rest in an arbitrary stationary metric, the uniform gravitational field, the rotating reference frame, the Schwarzschild metric, the Kerr-type metrics, and the spatially homogeneous and isotropic Robertson-Walker spacetime of standard cosmological model. The last case leads to cosmological consequence that resulting *kinetic* recession velocity of a distant astronomical object is always subluminal even for large redshifts of order one or more and, thus, it does not violate the fundamental physical principle of *causality*. This provides a new perspective to solve startling difficulties, which the conventional scenario of standard cosmological model presents. We calculate the measure, $\zeta(z, \dot{L})$, of carrying away of a galaxy at redshift z by the expansion of space, such that it declines in magnitude to the $\zeta(25) = 0.034$, and then up to $\zeta(800) = 1.16 \times 10^{-3}$. This proves that cosmological expansion of a flat 3D–space is fundamentally different from a kinematics of galaxies moving in a non-expanding flat 3D-space.

doi:https://doi.org/10.52526/25792776-22.69.2-151

Appendices

Appendix A A reappraisal of the `standard´ kinematic interpretation

Finally, it is our purpose to give a reappraisal of the `standard´ kinematic interpretation. One source of alternative understanding of a complex problem is the `standard´ kinematic interpretation that cosmological redshift of distant galaxy is the recession effect of the accumulation of a series of infinitesimal Doppler shifts due to infinitesimal relative velocities of the Hubble flow along the line of sight (Bunn & Hogg, 2009, Chodorowski, 2011, Grøn & Elgarøy, 2007, Padmanabhan, 1993, Peacock, 1999, 2008, Peebles, 1993, Whiting, 2004). Within the `stretching of space´ point of view, one assumes that an observer at the origin at the present epoch time measures the redshift of a galaxy at some comoving distance. Consider a light ray that travels from a galaxy to this observer, both of whom are at rest in comoving coordinates. Imagine a family of comoving observers along the path of light ray, each of whom measures the frequency of light ray as it goes by. It was assumed that each observer is close enough to his neighbor so that we can accommodate them both in one inertial reference frame and use SR to calculate the change in frequency from one observer to the next. If adjacent observers are separated by the infinitesimal proper distance δL, then their relative velocity in this frame is $\delta v = H\delta L$. This infinitesimal recessional velocity should cause a fractional shift given by the non-relativistic Doppler formula:

$$\frac{\delta\nu}{\nu} = -\frac{H\delta L}{c} = -H\delta t. \tag{65}$$

And hence, as it was concluded, the relation (65) for redshift, by means of $H = \dot{R}/R$, becomes $\delta\nu/\nu = -\delta R/R$. This integrates to give the main result of expansion scenario that the frequency decreases in inverse proportion to the scale factor, $\nu \propto 1/R$.

However, a hard look at the basic relation (65) reveals the following three objections, which together constitute a whole against the claim.

(i) The equation (65) would lead to the relation $\delta\nu/\nu = -\delta R/R$ if, and only if, $\dot{L}(t,z) = c$, i.e. when galaxy situates on the Hubble sphere: $L = L_H \equiv c/H$, where L_H is the Hubble length. But in general case of $\dot{L}(t,z) \neq c$ ($L \neq L_H$), it was in conflict because the infinitesimal time interval $\delta t' = \delta L/c$ does not equal to the infinitesimal epoch time interval $\delta t = \delta L/\dot{L}$ ($\delta t'/\delta t = \dot{L}/c$):

$$\frac{H\delta L}{c} = \frac{1}{R}\left(\frac{dR}{dt}\delta t\right)\frac{\delta L}{c\delta t} = \frac{\dot{L}(t,z)}{c}\frac{\delta R}{R}, \tag{66}$$

and hence (65) leads to

$$\frac{\delta\nu}{\nu} = -\frac{\dot{L}(t,z)}{c}\frac{\delta R}{R}. \tag{67}$$

This can readily be integrated to give

$$\delta \ln\nu = \delta\left[\ln\left(\frac{1}{R}\right)^{\dot{L}/c}\right] + \frac{\delta\dot{L}}{c}\ln R. \tag{68}$$

As it is clearly seen, (68) is utterly distinct from the simple behavior of $\nu \propto 1/R$.

(ii) If adjacent observers (i+1) and (i), separated by the infinitesimal proper distance δL_i, are situated at the distances $(L_i + \delta L_i)$ and (L_i) from the observer at the origin at the present epoch, then not an infinitesimal difference in their velocities $\delta\beta_i$, but their SR relative velocity $\delta\beta_i^r$ should contribute to an infinitesimal Doppler shift. That is,

$$\frac{\delta\nu_i}{\nu_i} = -\delta\beta_i^r = -\frac{\delta\beta_i}{1-\beta_{i+1}\beta_i} = -\frac{H\delta L_i/c}{1-\left[H(L_i+\delta L_i)/c\right](HL_i/c)} \approx -\frac{H\delta L_i/c}{1-(HL_i/c)^2}, \tag{69}$$

the integration of which along path of light ray yields the Doppler shift:

$$\frac{\nu_1}{\nu} = \sqrt{\frac{1+\dot{L}/c}{1-\dot{L}/c}}, \tag{70}$$

which has nothing to do with the main result of expansion scenario $\nu \propto 1/R$. Moreover, the equation (70) limits the values of $\dot{L}$ to $\dot{L} \leq c$, which shows that it is incorrect to use $\dot{L}$ in equation (65).

(iii) As we have seen from the Fig. 3, the $\zeta(z)$ declines in magnitude to zero, which once more shows that it is incorrect to use in (65) the `proper´ recession velocity $\dot{L}$.

References

Abramowicz M. A., Bajtlik S., Lasota J.-P., Moudens A., 2007, Acta Astr., 57, 139

Asaoka I., 1989, PASJ, 41, 763

Bolós V. J., 2006, J. Geom. Phys., 56, 813

Bolós V. J., 2007, Commun. Math. Phys., 273, 217

Bolós V. J., Klein D., 2012, Gen Relativ Gravit., 44, 1361

Bolós V. J., Liern V., Olivert J., 2002, Int. J. Theor. Phys., 41, 1007

Bunn E. F., Hogg D. W., 2009, Am. J. Phys., 77, 6888

Chandrasekhar S., 1983, The Mathematical Theory of Black Holes. Oxford Univ. Press, New York

Chodorowski M. J., 2011, MNRAS, 413, 585

Cisneros S., Goedecke G., Beetle C., EngeLlhardt M., 2015, MNRAS, 448, 2733

Cunningham C. T., 1998, Astrophys. J., 202, 788

Davis T. M., Lineweaver C. H., 2004, PASAu, 21, 97

Ellis G. F. R. e. a., 1985, Phys. Rep., 124, 315

Emtsova E., Toporensky A., 2019, arXiv:[gr-qc], 1901.03602, 1

Fanton C., Calvani M., de Felice F., Cadez A., 1997, PASJ, 49, 159

Greenberger D. M., Overhauser A. W., 1979, Rev. Mod. Phys., 51, 43

Grøn Ø., 1979, Found. Phys., 9, 501

Grøn Ø., 1980, Eur. J. Phys., 11, 186

Grøn Ø., Elgarøy Ø., 2007, Am. J. Phys., 75, 151

Harrison E. R., 1993, ApJ, 403, 28

Harrison E. R., 1995, ApJ, 446, 63

Harrison E. R., 1981 and 2000, Cosmology: the science of the universe, 1 and 2 edn. Cambridge U. Press, Cambridge

Jaffe J., Vessot R. F. C., 1976, Phys. Rev. D, 14, 3294

Kaya A., 2011, Am. J. Phys., 79, 1151

Klein D., Collas P., 2010, Phys. Rev. D, 81, 063518

Klein D., Randles E., 2011, Ann. Henri Poincaré, 12, 303

Li L. X., Zimmerman E. R., Narayan R., McClintock J. E., 2005, Astrophys. J. Sup., 157, 335

Lindegren L., Dravins D., 2003, Astron. Astrophys., 401, 1185

Manasse F. K., Misner C. W., 1963, J. Math. Phys., 4, 735

Milne E. A., 1934, Quarterly J. of Math., 5, 64

Misner C. W., Thorne K. S., Wheeler J. A., 1973, Gravitation. Freeman, San Francisco

Möller C., 1952, The Theory of Relativity. OUP, Oxford

doi:https://doi.org/10.52526/25792776-22.69.2-151

Murdoch H. S., 1977, QJRAS, 18, 242

Narlikar J. V., 1994, Am. J. Phys., 62, 903

O'Neill B., 1995, The Geometry of Kerr Black Holes. Peters, A K, Wellesley, MA

Padmanabhan T., 1993, Structure Formation in the Universe. Cambridge Univ. Press, Cambridge

Page D. N., 2009, Class. Quantum Grav., 26, 127001

Peacock J. A., 1999, Cosmological Physics. Cambridge Univ. Press (Ninth printing with corrections 2010), address = Paris

Peacock J. A., 2002, in Modern Cosmology, Proceedings of the Como School 2000, ed. by Bonometto, S and Gorini, V and Moschella U. IOP, Bristol

Peacock J. A., 2008, arXiv:[astro-ph], 0809.4573, 1

Peebles P. J. E., 1993, Principles of Physical Cosmology. Princeton Univ.Press.

Peebles P. J. E., Schramm D., Turner E., Kron R., 1991, Nature, 352, 769

Pirani F., 1962, Le Theories relativistes dee la Gravitation

Robertson H. P., 1935, ApJ, 82, 284

Schönenbach T. e. a., 2014, MNRAS, 442, 121

Soffel M. e. a., 2003, Astron. J., 126, 2687

Synge J. L., 1960, Relativity: The General Theory. North-Hollaand, Amsterdam

Ter-Kazarian G., 2021a, ComBAO, 68, issue 1, 12

Ter-Kazarian G., 2021b, ComBAO, 68, issue 1, 38

Ter-Kazarian G., 2022, Gravitation & Cosmology, 28, No 2, 186

Ter-Kazarian G., 2023, To appear in Gravitation & Cosmology, 29, No 1

Walker A. G., 1935, Proc. Lond. Math. Soc., 4, 170

Walker A. G., 1936, Proc. Lond. Math. Soc., 42, 90

Whiting A. B., 2004, The Observatory, 124, 174

doi:https://doi.org/10.52526/25792776-22.69.2-151

On mass-loaded accretion during high mass star formation

A. G. Yeghikyan *[1], A. L. Samsonyan[1], N. A. Harutyunyan[2], N. M. Azatyan[1], D. H. Andreasyan[1], D. S. Baghdasaryan[1], and E. H. Nikoghosyan[1]

[1]Byurakan Astrophysical Observatory, Byurakan, Aragatsotn Province, Armenia
[2]Yerevan State University, Yerevan, Armenia

Abstract

Analytical formulae of the dependence of the velocity and density on the radius during spherical accretion with both mass and momentum inputs, as well as the rate of mass inflow are presented. Some features of gas inflow near the star are discussed, and details of mass loading are presented and calculated as caused by hydrodynamical ablation and conductivity. It looks like that in one example velocities of inflow are in the range from 10-20 km/s (free fall) to 40-50 km/s and the densities are in the range from $2 \cdot 10^8$ (free fall) to $6 \cdot 10^6$ cm^{-3} at 10^{17} cm when mass-loading accretion is taken place during formation of $10 M_\odot$ mass star.

Keywords: *ISM: star formation via mass-loading accretion flows*

1. Introduction

Massive stars (with masses M$\geq 8 M_\odot$) are more interesting in terms of their environmental impact, as compared to the formation of low-mass stars described in detail in Bodenheimer (2011),Stahler & Palla (2005). Being powerful sources of hydrogen-ionizing L_c radiation and stellar wind, the formation of massive stars have a significant impact on the vicinity of the molecular cloud, the source of matter for such stars, and bring a large amount of mass, momentum and energy into the interstellar medium.

Comparing the estimate of time to reach MS (main sequence) (that is a Kelvin-Helmholz time) to the time it takes for the protostar to collect matter (accretion time), Dyson (1994) noted that massive stars should continue to gain mass, i.e., accrete, already reaching the MS, the nuclear reactions mode, that can serve as energy sources, since this time is clearly shorter. For example, for $10 M_\odot$ one may got 5-10 megayears for accretion times and only $\sim$ 400 kiloyears for Kelvin-Helmholz time.

As a result, the protostar (with a reservation of about the beginning of nuclear reactions) remains immersed in a gas-dust shell-cocoon, which is very sensitive to the onset of hard radiation and the stellar wind, analyzed in detail in Kahn (1974).

Further the density distribution at this accretion phase is given by the obvious formula

$$\rho(r) = \dot{M}/(4\pi \cdot r^2 v) = (\dot{M} r^{-3/2})/(4\pi(2GM_*)^{1/2}), \tag{1}$$

together with free fall velocity,

$$v(r) = \sqrt{\frac{2GM_*}{r}} \tag{2}$$

This formula determines the behavior of the main gas-dynamic parameters at the accretion stage (Fig. 1). Here $\dot{M}$ is the mass accretion rate, M_* is the protostar mass and other quantities have their usual meanings.

When the protostar reaches the MS (and radiative equilibrium), but still continues to gain mass, the star (protostar) loses mass (via stellar wind) and ionizes the surrounding gas (by means of the stellar photon radiation), and the so-called ultra-compact HII region (UCHII) is formed Kahn (1974).

The present article is devoted to the features of mass accumulation by a protostar, by means of mass-loaded flows, described first in Hartquist et al. (1986) in relation to WR nebulae, and, in the formation of massive stars, in Dyson (1994).

*ayarayeg@gmail.com

doi:https://doi.org/10.52526/25792776-22.69.2-172

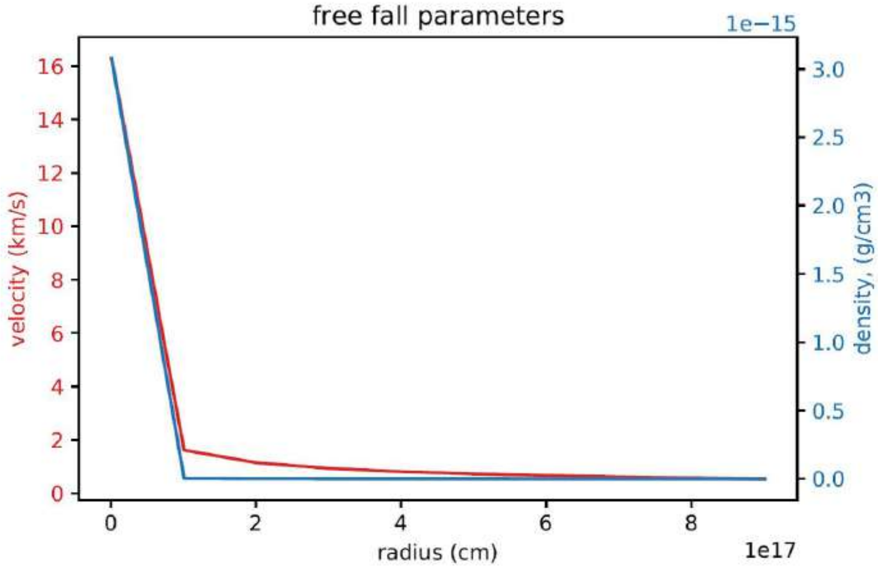

Figure 1. Distribution of velocity and density along the radius, according to free-fall dependencies for spherically symmetric accretion, $M_* = 10M_\odot, \dot{M} \approx 10^{22} g/s \approx 10^{-3} M_\odot/yr$

.

2. Mass-loading accretion and the formation of massive stars

We will divide this process of additional mass gain into two types - the first one is the one through clumps of the molecular cloud (clumps) via photoionization, and the second one - through the same clumps, but already via the stellar wind, and the mass injection rate will vary.

When a molecular cloud is compressed, followed by the formation of a star, flows with continuously added gas along the way are possible. The source of this gas can be condensations, having 3-4 orders of magnitude higher density than usual, for example, in this case, in the region of star formation. It is also possible that the influence of the stellar wind is insignificant, which is typical for not very massive stars. We should be interested in a period with an intense wind, on the order of $\sim 10^{-6}M_\odot$, when UCHII is formed under the influence of both hard radiation and a sufficiently powerful wind. In this case, the wind flow itself can be considered isothermal, since the loaded mass is excited and immediately radiate, and the emission measure is proportional to the square of the density. As a result, a uniform temperature of the order of 10000 K is established in the region of intense HII emission. The hard radiation of a protostar is responsible for the ionization because thermonuclear reactions are already taking place, the radiation energy propagates to the outer layers and is radiated through the photosphere into the environment, in the first approximation, as an absolutely black body with an effective temperature inherent in massive O, B stars. In the case of mass-loaded flows, taking into account stationarity and isothermality, the gas-dynamic equations of conservation of mass and momentum should be written as:

$$\frac{d}{dr}(\rho v r^2) = S r^2, \tag{3}$$

$$\frac{1}{r^2}\frac{d}{dr}(\rho v^2 r^2) = -S v_c - \frac{dP}{dr} - \frac{G M_* \rho}{r^2}, \tag{4}$$

and instead of conservation of energy, we use the relationship between pressure and density in an isothermal process:

$$P = \rho c^2. \tag{5}$$

The first term on the right in (4) takes into account the momentum of the gas portions that have entered the flow from moving clumps, and the minus sign is the direction towards the wind. Our goal is to show that an arbitrary combination of the observed parameters of fast winds leads to the establishment of protostar parameters that do not contradict the observations. Because

$$\frac{1}{r^2}\frac{d}{dr}(\rho v^2 r^2) = S v + \rho v \frac{dv}{dr} = -S v_c - \frac{dP}{dr} - \frac{(G M_* \cdot \rho)}{r^2}, \tag{6}$$

doi:https://doi.org/10.52526/25792776-22.69.2-172

then after some algebric transformations we bring the system to the form:

$$\frac{dv}{dr}(v^2 - c^2) = -\frac{S}{\rho}(v^2 + c^2 + vv_c) + \frac{(2uc^2)}{r} - \frac{(GM_* v)}{r^2}, \tag{7}$$

$$\frac{d\rho}{dr} = -\frac{\rho}{v}\frac{dv}{dr} - \frac{2\rho}{r} + \frac{S}{v}. \tag{8}$$

Let us first neglect the term on the right in (7), which takes into account gravity, and exclude ρ by means of

$$\dot{M} \cdot 4\pi r^2 \rho v = const, \tag{9}$$

which in this case is written as

$$4\pi r^2 \rho v = \dot{M}_s + 4\pi \int_{r_0}^{r} S r'^2 dr', \tag{10}$$

where $\dot{M}_s$ is the mass loss rate of the central star,

$$\dot{M}_s = 4\pi r_0^2 \rho_0 v_\infty. \tag{11}$$

The values with the index 0 refer to the inner boundary of the cloud from the side of the star and v_∞ is the ultimate speed of the fast wind, and further we denote

$$4\pi \int_{r_0}^{r} S r'^2 dr' \equiv I(r). \tag{12}$$

After subsequent integration, we finally get:

$$v = \frac{v_s I(r) + v_\infty \dot{M}_s}{M_s + I(r)}, \tag{13}$$

and

$$\rho = \frac{[\dot{M}_s + I(r)]^2}{[4\pi r^2 (v_s I(r) + v_\infty \dot{M}_s)]}. \tag{14}$$

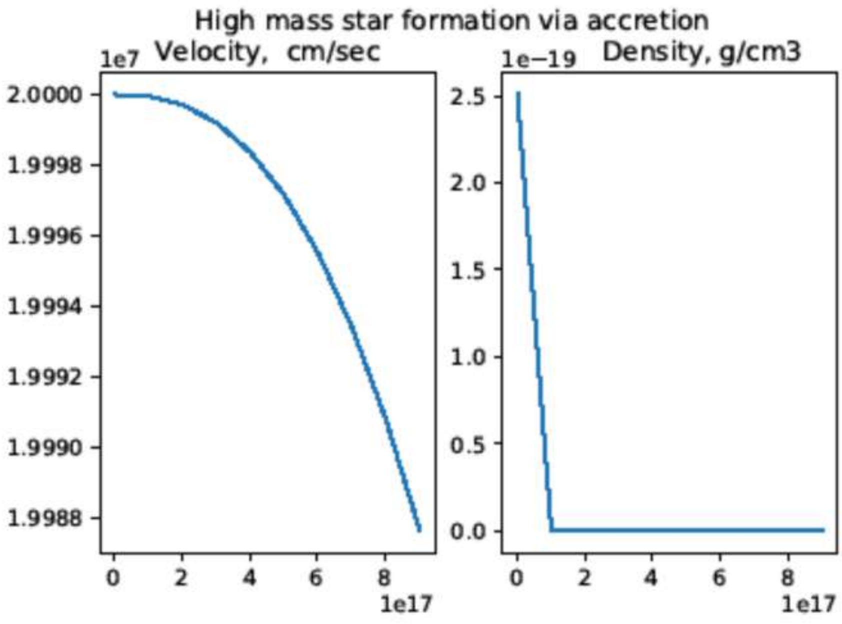

Figure 2. The distribution of velocity and density (13, 14) along the radius, when $M_* = 10M_\odot$, for spherical-simmetrical accretion with constant mass-loading rate about $\dot{M} \approx 10^{22} g/s \approx 10^{-3} M_\odot/yr$ when gravitation is not taken into account. Here we choose $S \sim 10^{-3} M_\odot/yr$.

doi:https://doi.org/10.52526/25792776-22.69.2-172

Gravity is not taken into account here, but the momentum introduced during the loaded mass from condensations is taken into account. They were first used in analytical theories of the planetary nebulae Yeghikyan (1999) and now are used in the description of formation of massive stars (Fig. 2).

It should be also mentioned the work of Johnson & Axford (1986), where the same equations are used to describe the galactic wind. Distribution (15, 16) for one set of parameters when mass-loading sources are constant, that is are not radius-dependent, is shown in Yeghikyan (2022).

With a uniform distribution of mass loading centers, $S(r) = S_0 = const$, and $v_s = 20km/s = const$, we have $I(r = r_m) = (4/3)S_0\pi r_m^3$, where $r_m^3 = 10^{18}$ cm is the maximum value of the radius from which accretion starts. With a power dependence of the form $S(r) = S_0(r_0/r)^\alpha, I(r) = 4\pi S_0(r^{3-\alpha} - r_0^{3-\alpha})/(3-\alpha)$.

Finally, in the general case, according to Pittard et al. (2004), one should distinguish the possibility of mass loading from cloud clumps (due to conductivity - S_c) and through hydrodynamic ablation - S_a), then the equations will be written in the form

$$\frac{d\rho}{dr} = -\frac{\rho}{v}\frac{dv}{dr} - \frac{2rho}{r} + \frac{(S_c + S_a)}{v} \tag{15}$$

$$\frac{dv}{dr} = \frac{v}{\rho(v^2 - c^2)}[S_a(v_c - v) - S_c(v + v_c)] - \frac{(GM_* v)}{((v^2 - c^2)r^2)} - \frac{(c^2(S_c + S_a))}{\rho(v^2 - c^2)} + \frac{(2uc^2)}{(r(v^2 - c^2))}. \tag{16}$$

Here, $S_c = S_{c0} \cdot (T/T_m)^{5/2} \cdot e^{(-r/r_m)}, S_a = S_{a0} \cdot (v/c)^{4/3} \cdot e^{(-r/r_m)}$ – expressions for terms describing mass loading Pittard et al. (2004). S_c is due to the conductivity of the electron gas formed during the interaction of a high-speed stellar wind with condensation in the cloud and causing photoevaporation with subsequent addition of the mass of the protostar. S_a, in turn, is the rate of mass input caused by hydrodynamic ablation (Bernoulli effect) in supersonic flow, and $S_a = S_{a0} \cdot (v/c)^{4/3}$ in subsonic flow, both mechanisms are described in Hartquist et al. (1986), Pittard et al. (2004). The solutions of the system of differential equations (15, 16), for one set of parameters are shown in Fig. 3, 4.

As can be seen, with these data, the density and initial velocity decrease with increasing radius, and the velocity at the protostar of about 100 km/s drops to several km/s only at a distance of about 10^{17} cm. The density decreases from 10^7 cm^{-3} to 70 cm^{-3} at a radius of the order of 10^{18} cm. However, these values were obtained at radius-independent mass-loading rates (Fig. 3).

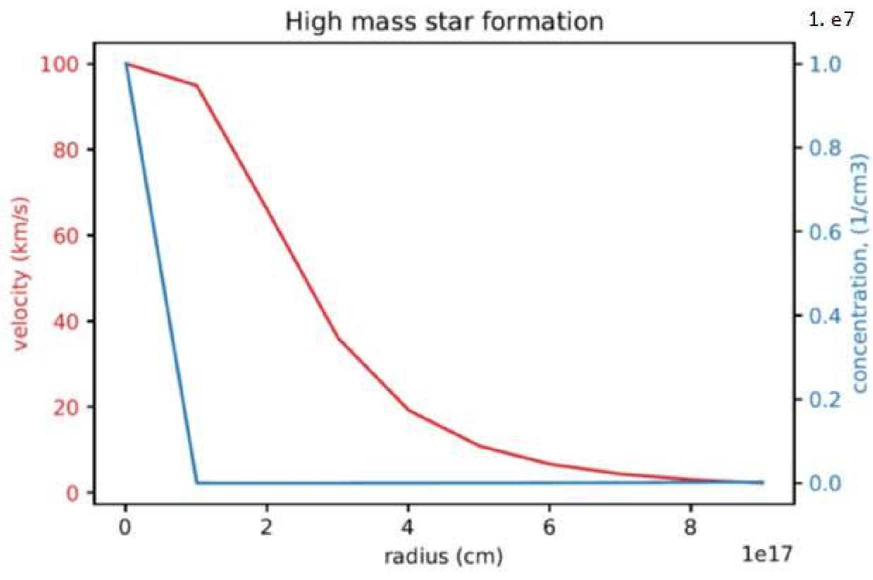

Figure 3. The distribution of velocity and density (concentration), solution of (15, 16), along the radius, when $M_* = 10M_\odot$, for spherical-simmetrical accretion with equal radius-independent mass-loading rates about $\dot{M} \approx 10^{22}g/s \approx 10^{-3}M_\odot/yr$ and $G \neq 0$.

In the opposite case, for the radius-dependent loading speed, we get the picture Fig. 4.

As you can see, with approximately the same density behavior, the speed almost everywhere remains about 40-50 km/s, while density (concentration) is around $6 \cdot 10^6$ cm^{-3} and then decrease, both at 10^{17} cm, which can be verified by observations and further refined by numerical models that take into account many various parameters. In this sense, the proposed analytical model should be regarded as preliminary.

doi:https://doi.org/10.52526/25792776-22.69.2-172

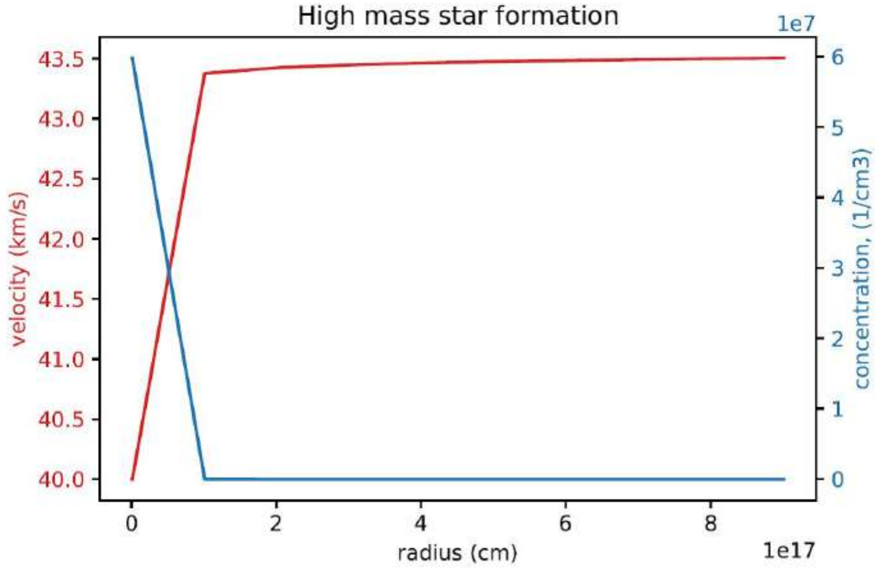

Figure 4. The distribution of velocity and density (concentration) along the radius, solution of (15, 16) for spherically symmetric accretion with loaded mass, $G \neq 0$, primary $(10^{-3} M_{\odot}/\mathrm{yr})$ via ablation, and secondary $10^{-6} M_{\odot}/\mathrm{yr})$ via conductivity, $M_{*} \approx 10 M_{\odot}, v_{\infty} = 2000$ km/s, $v_s = 20$ km/s. Initial conditions: $v = 100$ km/s, $n = 10^9$ cm^{-3} at $r_0 = 10^{15}$ cm.

.

3. Conclusion

This article describes some details of the formation of massive stars, where the mass of protostars is gained by accretion and is carried out by loading through hydrodynamic ablation and electronic conduction. In the spherically symmetric case, the mass and angular momentum conservation equations are written, with the source terms given as functions depending on the radius. The gas-dynamic equations of gas flow with the loaded mass are analyzed, taking into account the momentum introduced by the loaded mass. In the simplest case of neglecting gravity, analytical formulas for the distribution of the velocity and density of matter in the vicinity of a protostar are obtained, in a more general case, when gravity is taken into account, the resulting system of differential equations is solved numerically. We emphasize that in this case, the sources of the accreted mass are cloud clumps, which are 3-4 orders of magnitude higher than density of the cloud, while the mechanisms for adding mass can be hydrodynamic ablation and electronic conduction, each, to the extent of its applicability. Numerical solutions of these equations can be verified by observations. Of course, the analytical description given in the article should be considered as preliminary, subject to refinement by means of numerical models.

References

Bodenheimer P., 2011, Principles of star formation. Springer

Dyson J., 1994, in T.Ray, S. Beckwith (Eds.) Star Formation and Techniques in Infrared and mm-Wave Astronomy. Springer

Hartquist T., Dyson J., Pettini M., Smith L., 1986, MNRAS, 221, 715

Johnson H., Axford W., 1986, Astrophys.J., 165, 381

Kahn F., 1974, Astronom. and Astrophys., 37, 149

Lizano S., Canto G., Garay G., Hollenbach D., 1996, Astrophys.J., 468, 739

Pittard J., Hartquist T., Ashmore I. e. a., 2004, Astron. Astrophys., 414, 399

Stahler S., Palla F., 2005, The formation of stars. Wiley-VCH

Yeghikyan A. G., 1999, Astrophysics, 42, 391

Yeghikyan A. G., 2022, Communications of the Byurakan Astrophysical Observatory, 69, 32

doi:https://doi.org/10.52526/25792776-22.69.2-172

Acknowledgements

This work was made possible by a research grant number 21AG-1C044 from Science Committee of Ministry of Education, Science, Culture and Sports RA. Calculations were performed using the equipment of the AvH.

Introduction

Editorial board *

NAS RA V. Ambartsumian Byurakan Astrophysical Observatory (BAO)

For many years Armenia had leading positions both in astronomy (Byurakan Astrophysical Observatory (BAO), Viktor Ambartsumian, Beniamin Markarian and other Armenian astronomers) and space technology (Grigor Gurzadian, Hrant Tovmasyan). Particularly, Gurzadyan designed, developed and prepared the first Soviet space observatories, “Orion” and “Orion-2”. Soviet cosmonautics training courses were organized in BAO in 1970-1980s. BAO had and now restored the Department of Applied Astronomy. Currently, on a contractual basis with Russian Space Agency “Roscosmos”, BAO participates in a project to monitor the space debris, according to which 3 small telescopes have been installed in BAO Saravand station. It is also worth noting that Virtual Observatories are of great importance in modern astronomy, when research is performed using all telescopes, different times, different modes, and the results of observations at all electromagnetic waves. The Armenian Virtual Observatory (ArVO) is part of the International Virtual Observatory Alliance (IVOA) and also participates in the International Planetary Data Alliance (IPDA), where space agencies of the major countries are members.

Today, the Byurakan Astrophysical Observatory (BAO) hosts a number of medium-size optical telescopes, the most important being the 2.6 m classical telescope and 1 m Schmidt telescope and is an important observatory with modern facilities in the region. Furthermore BAO has several departments related to inter- and multi- disciplinary sciences, such as the research departments of Astrochemistry, Astrobiology and Exoplanets, High-Energy Astrophysics, Astroinformatics, and Archaeoastronomy and Cultural Astronomy. And that is why,in this year the International conference Space Sciences and Technologies” was organized and successfully held.

The main objectives of this meeting of representatives of various scientific fields are the exchange of information and discussion of the latest achievements in astrophysics and instrumentation necessary for astronomical observations. The prospects for combining the efforts of representatives of such scientific disciplines as astrophysics, chemistry, biology, programming, etc. were also actively discussed.

Symposium Topics

- Space Sciences and Space Astronomy
- Multiwavelength Astronomical Surveys, Catalogues, Archives and Databases
- Exoplanets and Planetary Science
- Virtual Observatories and Astroinformatics
- Space Technologies
- Interdisciplinary and Multidisciplinary Sciences

This issue of ”Communications of BAO” includes the proceedings presented on the International conference Space Sciences and Technologies”. All the papers passed relevant peer-review

*combao@bao.am

Astronomical Surveys, Catalogues, Archives, Databases and Virtual Observatories

A. M. Mickaelian*, H. V. Abrahamyan, G. M. Paronyan, and G. A. Mikayelyan

NAS RA V. Ambartsumian Byurakan Astrophysical Observatory (BAO), Byurakan 0213, Aragatzotn Province, Armenia

Abstract

Astronomical surveys and catalogs are the main sources for the discovery of new objects, both Galactic and extragalactic. Archives and Databases maintain billions of astronomical objects; planets, comets, stars, exoplanets, nebulae, galaxies, and quasars. We will review the current background in astronomy for further all-sky or large-area studies. Modern astronomy is characterized by multiwavelength (MW) studies (from gamma-ray to radio) and Big Data (data acquisition, storage, mining and analysis). Present astronomical databases and archives contain billions of objects observed at various wavelengths, and the vast amount of data on them allows new studies and discoveries. Surveys are the main source also for accumulation of observational data for further analysis, interpretation, and achieving scientific results. We review the main characteristics of astronomical surveys (homogeneity, completeness, sensitivity, etc.), compare photographic and digital eras of astronomical studies (including the development of wide-field observations), and describe the present state of MW surveys. Among others, Fermi-GLAST, INTEGRAL (gamma-ray), ROSAT, Chandra, XMM (X-ray), GALEX (UV), DSS1/2, SDSS, Hubble, Gaia (optical), 2MASS, IRAS, AKARI, WISE, Herschel (IR), NVSS and FIRST (radio) surveys and major astronomical archives and databases will be presented and discussed, as well as surveys and databases for variable and transit objects.

Keywords: *astronomical surveys – multiwavelength astronomy – catalogs – archives – databases – Virtual Observatories – Big Data – Data Science*

Astronomical Surveys and Catalogs

Astronomical surveys and catalogs are the main source for astronomical data, for discovery of astronomical objects and various parameters related to them. Surveys are quite different and have a number of parameters defining their tasks and needs. For an astronomical survey, it is most important to define the task and corresponding parameters. Main parameters of astronomical surveys:

- **Wavelength range.** You find different objects at various wavelengths (from gamma-rays to longest radio), depending of what astronomical objects radiate at what wavelengths and the strength of their radiation. As this depends on the mechanisms of radiation and for the thermal one, mainly the temperature (as well as some other parameters), we find different objects and physical conditions, hence depending of what we search, corresponding wavelengths should be used.

- **Method.** Methods may be direct imaging, photometry, spectroscopy, variability, polarimetry, etc., also depending on which of them efficiently reveal what we search for.

- **Sensitivity.** The sensitivity of the survey (**limiting magnitude** in optical range) is the parameter defining the deepness of the survey and the number of expected objects, i. e. we may select between relatively surface studies and deep ones.

- **Resolution.** The resolution is another limitation depending on the task of the survey; if we need to have faster collection of well resolved objects or detailed studies of small features. Two types of resolution may be regarded; **spatial** (for resolving of close objects or morphological details) and **spectral** (for resolving close spectral lines and other features).

*aregmick@yahoo.com

doi:https://doi.org/10.52526/25792776-22.69.2-179

- **Sky area.** Ground based surveys have always been limited to the sky area depending on the geographical location of the telescopes, mainly geographical latitude but also very often the longitude. Space telescopes do not have such limitations. Nevertheless, any survey is solving some task and for this, definite sky area is being used.

- **Coverage.** Surveys are being accomplished at various surfaces; from very small deep surveys (ex. 2 arcmin by 2 arcmin) to large area (thousands of sq. degrees) and all-sky ones (mostly from Space observatories). Typically, the coverage is somehow anticorrelated to the sensitivity, as the capabilities of accumulating data are limited; the deeper the survey, the smaller the coverage and vice-versa, the larger the coverage the smaller the sensitivity.

- **Time domain.** The Universe is changing and observations give data for the definite moment (epoch, given the astronomical changes are slower). Time domain astronomy appeared after accumulation of many observations at different epochs during dozens of years. It is important to compare data from different time domains and obtain understanding on their variability. Some objects have very fast variability, so that even seconds are important. In such cases fast photometers are needed.

- **Completeness.** This is one of the most important parameters of the surveys, as the observers should provide an understanding on what can be expected from the point of view of detection and the nature of the discoveries. Thus, completeness of the **detection** and the **classification** are quite different. E. g., the detection limit of Markarian Survey for galaxies is almost 18^m, however by Markarian criteria objects brighter than 17^m can be selected as UV-excess galaxies.

One of the most famous astronomical surveys, Sloan Digital Sky Survey (SDSS) was started in 2000 and is still active (Figure 1). Its main goals are cosmological, detecting and studying numerous galaxies and quasars, however many stars and other objects are also being detected. The total unique area covered is 14,555 sq. deg. In the photometric part, the number of catalog objects is 1,231,051,050, among them unique detections are 932,891,133. The number of unique, primary sources: total 469,053,874; stars 260,562,744, galaxies 208,478,448, unknown 12,682. In spectroscopy, the total number of spectra is 4,851,200, including useful spectra 4,151,126; galaxies 2,541,424, QSOs 680,843, stars 928,859, sky spectra 394,231, standards 88,788, and unknown objects 217,055. We give in Table 1 the list of the most important astronomical

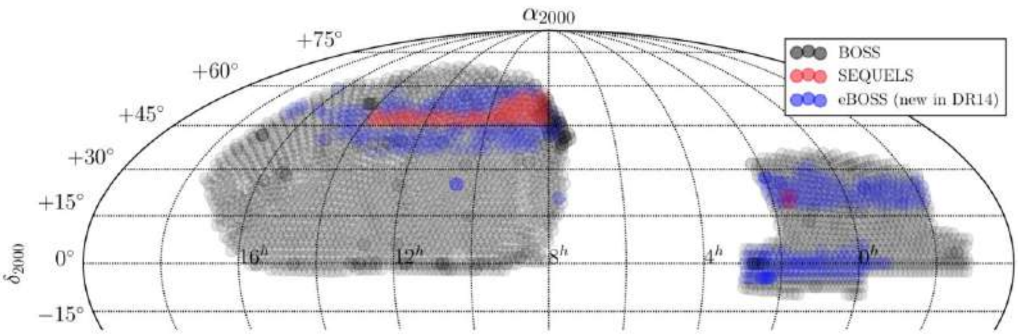

Figure 1. Sloan Digital Sky Survey (SDSS).

surveys in all wavelengths, from gamma-ray to radio.

Some understanding on the distribution of surveys, their data and their importance is given in Figures 2-4. In Figure 4, only extragalactic surveys are taken into consideration.

We give in Figure 5 the numbers of catalogued objects in astronomical catalogues of different wavelength ranges, from gamma-rays to radio. The difference is so big that even at logarithmic scale the numbers for gamma- X-rays, FIR, submm/mm and radio are almost negligible. We give in Table 2 the numbers by wavelength ranges.

Astronomical Archives and Databases

Astronomical observations, hence data are maintained in astronomical archives, mostly organized by the observatories, where the observations have been carried out. Later on, Space observations appeared and dedicated astronomical archives and databases appeared to maintain and share the data.

doi:https://doi.org/10.52526/25792776-22.69.2-179

Table 1. Most important all-sky or large area astronomical surveys in multiwavelength astronomy.

Survey	Years	Wavelength	Results	Number of sources
Fermi-GLAST	2014	10 MeV-100 GeV	Sky survey	3 033
ROSAT	1999	0.07–2.4 keV	Sky survey	124 730
Galaxy Evolution Explorer (GALEX)	2013	1350–2800 Å	Sky survey	82 992 086
USNO B1.0	2003	visible	Sky survey	1 045 913 669
Guide Star Catalog (GSC 2.3.2)	2003	visible	Sky survey	945 592 683
Sloan Digital Sky Survey (SDSS)	2000-pres.	visible	Sky survey	1 231 051 050
HIgh Precision PARallax COllecting Satellite (HIPPARCOS) (Tycho-2)	1993	visible	Astrometry	2 539 913
Global Astrometric Interferom. for Astrophysics (Gaia)	2022	3200–10000 Å	Astrometry	1 811 709 771
DENIS	2001	0.8-2.4 μm	Sky survey	355 220 325
Two Micron Astronomical Sky Survey (2MASS)	2003	1.24, 1.66, 2.16 μm	Sky survey	470 992 970
Wide-field Infrared Survey Explorer (WISE), AllWISE catalog	2013	3–28 μm	Sky survey	747 634 026
Infrared Astronomical Satellite (IRAS)	1988-1990	8–120 μm	Sky survey	405 769
AKARI	2006	7–180 μm	Sky survey	1 298 044
NRAO/VLA Sky Survey (NVSS)	1998	21 cm	Sky survey	1 773 484
Faint Images of the Radio Sky at Twenty Centimeters (FIRST)	1999	21 cm	Sky survey	946 432

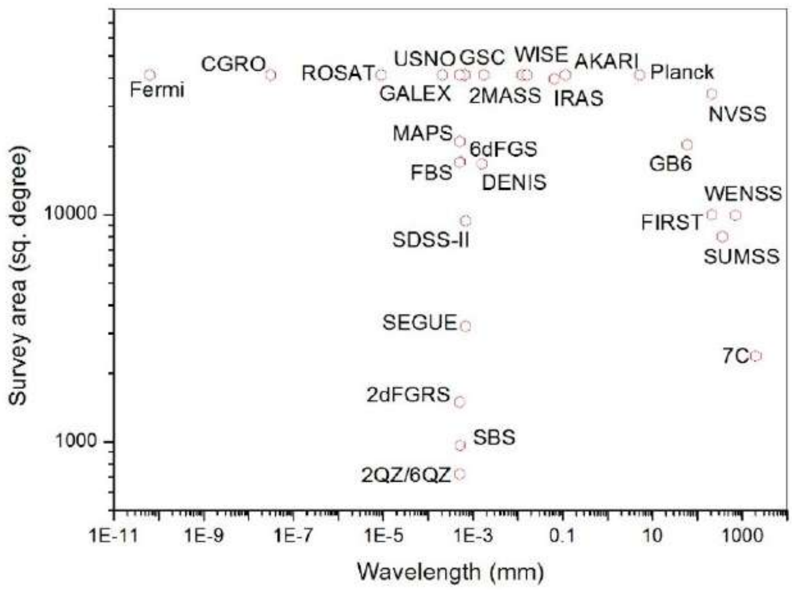

Figure 2. Survey area vs. wavelength (in mm) for most important astronomical surveys.

One of the oldest and most important astronomical databases is the **Wide-Field Plate Data Base** (**WFPDB**, http://www.skyarchive.org) created and maintained by Milcho Tsvetkov (Bulgaria). It contains 414 astronomical archives, in total 2,204,725 photographic plates from 125 observatories obtained between 1879 and 2002. The database includes 2,128,330 direct and 64,095 objective prism plates. The largest archives involved are: Harvard (USA) – 600,000 plates, Sonneberg (Germany) – 270,000 plates, Italian archive – 87,000 plates, Ukrainian archive – 85,000 plates; SAI (Moscow, Russia) – 50,000 plates. Among the objective prims Schmidt telescope observations, some 2500 First and Second Byurakan Surveys (FBS and SBS) plates are listed, plates that provided numerous astronomical discoveries. We give in Fig. 6 images from the digitized version of the FBS (**DFBS**), the software bSpec for extraction and analysis of DFBS spectra and webpage interface for working with DFBS images and spectra.

Among the multimission archives, most famous are:

- **High Energy Astrophysics Science Archive** (**HEASARC**; http://heasarc.gsfc.nasa.gov). It is the primary archive for HEA missions in gamma-rays, X-rays and extreme UV. Available data from ASCA, BeppoSAX, Chandra, EUVE, GLAST, HETE-2, INTEGRAL, ROSAT, RXTE, Astro-E2, Swift, XMM-Newton, etc.

- NASA/IPAC **Infrared Science Archive** (**IRSA**; http://irsa.ipac.caltech.edu). A multi-mission archive for NASA's IR and submm (IR/SM) astronomy data. Available data from 60 source catalogs, 22 image data sets and 7 spectroscopic data sets.

- **Multimission Archive at Space Telescope** (**MAST**; http://archive.stsci.edu). Supports a variety of astronomical data archives with a primary focus on scientifically related data sets in the

doi:https://doi.org/10.52526/25792776-22.69.2-179

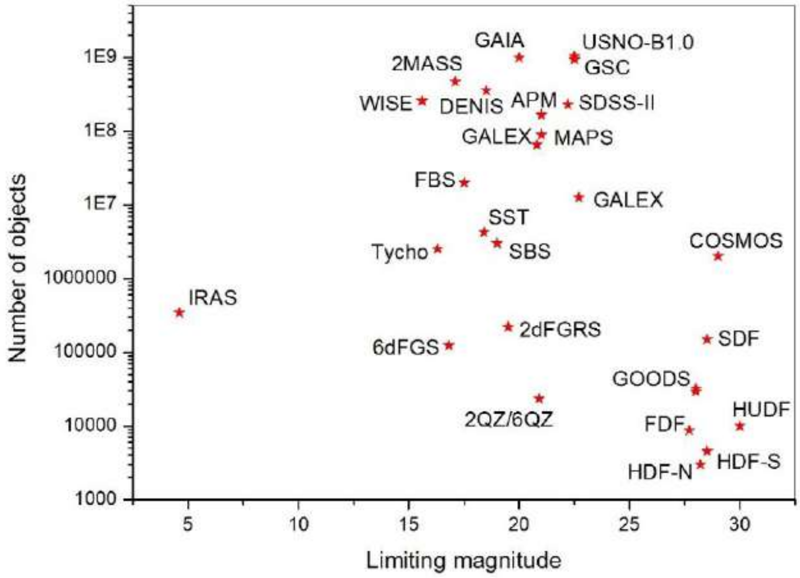

Figure 3. Number of objects in different astronomical surveys given by the limiting magnitude of surveys. Deep surveys are located in the right bottom, as relatively smaller number of objects have been discovered in them.

Table 2. Numbers of catalogues astronomical objects in different wavelengths and the main surveys and catalogs providing these numbers.

Wavelength range	Wavelengths	Main surveys and catalogs	Number of catalogued objects
Gamma-rays	<0.1 Å	Fermi, INTEGRAL	10 000
X-rays	0.1 – 100 Å	ROSAT, Chandra, XMM	1 500 000
UV	100 – 3000 Å	GALEX, Hubble	100 000 000
Optical	3000–10000 Å	DSS1/2, SDSS, Gaia	2 400 000 000
NIR	1 – 10 μm	2MASS, DENIS	600 000 000
MIR	10 – 100 μm	WISE, Spitzer	600 000 000
FIR	100 – 300 μm	IRAS, AKARI, Spitzer	4 000 000
Submm/mm	0.3 – 10 mm	Herschel, ALMA	1 000 000
Radio	1 cm – kms	NVSS, FIRST	2 000 000

optical, UV and near-IR parts of the spectrum. Available data from wide variety of space missions (including HST) and integrated ground-based surveys (DSS, FIRST, etc.).

Another database in Strasbourg (France), VizieR, maintains all published astronomical catalogs and lists and tables from the published papers. Some 30,000 catalogs and tables are available and cross-correlation tools (X-Match service) are provided as well. Most of the data are VO compliant and are given in VO format.

Astrophysical Virtual Observatories

Various useful tasks and tarnsformations are being done by Vos, such as combining data from different wavelengths and building multiwavelength Spectral Energy Distributions (SED, Fig. 7, left panel), overlapping images and comparing objects and sources from different databases (Aladin, Fig. 7, right panel), overlapping spectra for the same object to compare changes (Fig. 8, left panel), combining spectral data for the same object from observations of different telescopes and building combined spectra (VOSpec, Fig. 8, right panel), etc.

There is the **International Virtual Observatory Alliance (IVOA)** created in 2002 and unifying 23 VO projects (21 national and 2 European ones). The **Armenian Virtual Observatory (ArVO)** created in 2005 is part of this consortium.

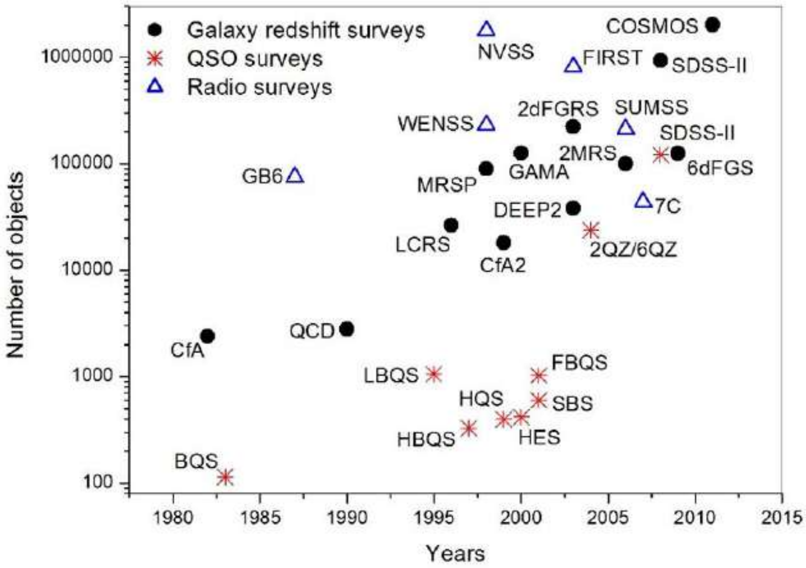

Figure 4. Number of objects in different astronomical surveys given by the years of surveys. Galaxy redshift surveys, QSO and radio surveys are given in different icons.

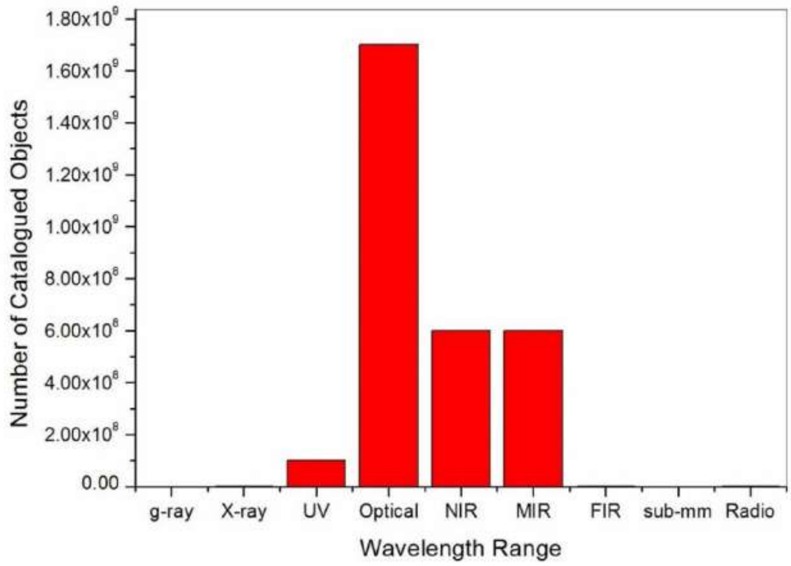

Figure 5. Numbers of astronomical objects so far discovered in different wavelength ranges, from gamma-rays to radio.

Summary

Astronomy is one of the science disciplines related to Big Data and Data Science. **Big Data** are often characterized as 4 Vs, namely:

1) **Volume.** Quantity of generated and stored data. The size of the data determines the value and potential insight, whether it can be considered big data or not. In Astronomy, this condition is well maintained, as the Universe provides the Biggest Data. At present some 3 billion objects have been catalogued and each has numerous data related to its spatial and physical characteristics; astrometry, photometry, variability, spectroscopy, polarimetry, etc. E. g., some spectra show hundreds of spectral lines with line parameters and overlapped profiles totaling thousands of data.

2) **Variety.** The type and nature of the data. This helps people who analyze it to effectively use the resulting insight. Big Data draws from text, images, audio, video; plus it completes missing pieces through data fusion. In Astronomy, most of the data is in the form of images and spectra, as well as photometric, polarimetric data, etc. And these are quite different as well.

3) **Velocity.** In this context, the speed at which the data is generated and processed to meet the demands

doi:https://doi.org/10.52526/25792776-22.69.2-179

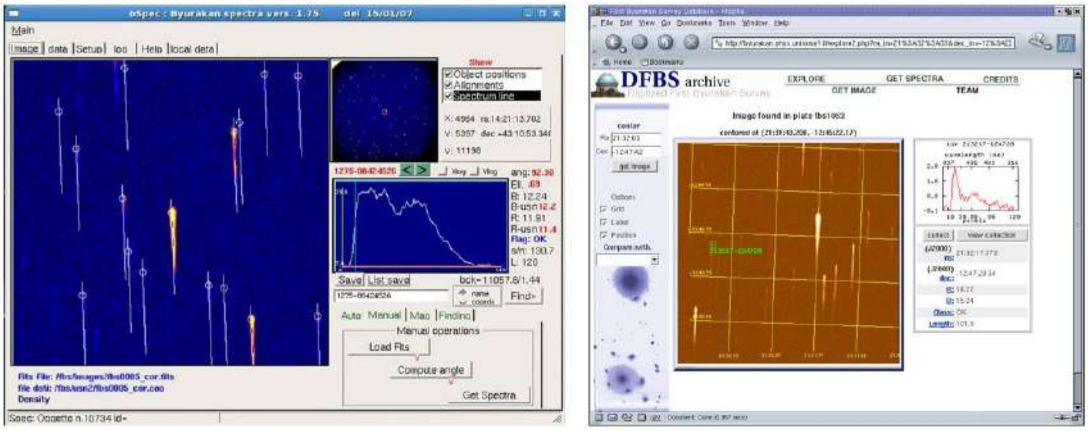

Figure 6. Dedicated software bSpec for extraction and analysis of the DFBS spectra (left panel) and DFBS webpage interface (right panel)

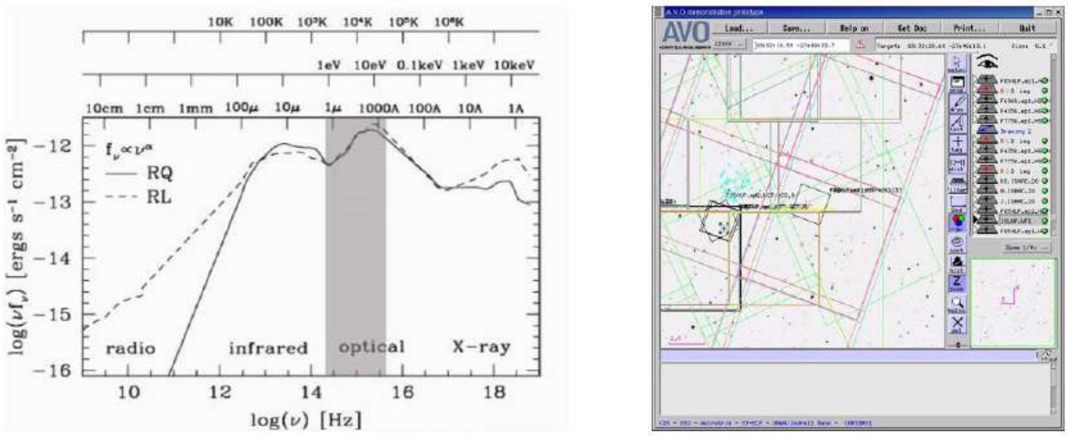

Figure 7. VO methods in astronomy: SEDs and image overlapping.

and challenges that lie in the path of growth and development. Big Data is often available in real-time. There are astronomical telescopes and receivers giving terabytes of data per night, accumulating peta and at present also exa bytes per year.

4) **Veracity.** The data quality of captured data can vary greatly, affecting the accurate analysis. Especially important is that many astronomers permanently verify data and each discovery is being checked by many others. Moreover, in VOs, various data are being combined and used together. This way, data become more homogenous and confident.

In Table 3, we give data volumes in different astronomical survey projects, showing the correspondence of astronomical data to the definition of Big Data.

Table 3. Data volumes in different astronomical projects.

Surveys, Projects	**Short**	**Range**	**Information Volume**
Digitized First Byurakan Survey	DFBS	opt	400 GB
Digital Palomar Observatory Sky Survey	DPOSS	opt	3 TB
Two Micron All-Sky Survey	2MASS	NIR	10 TB
Green Bank Telescope	GBT	radio	20 TB
Galaxy Evolution Explorer	GALEX	UV	30 TB
Sloan Digital Sky Survey	SDSS	opt	140 TB
SkyMapper Southern Sky Survey	SkyMapper	opt	500 TB
Panoramic Survey Telescope and Rapid Response System, expected	PanSTARRS	opt	~40 PB
Large Synoptic Survey Telescope, expected	LSST	opt	~200 PB
Square Kilometer Array, expected	SKA	radio	~4.6 EB

doi:https://doi.org/10.52526/25792776-22.69.2-179

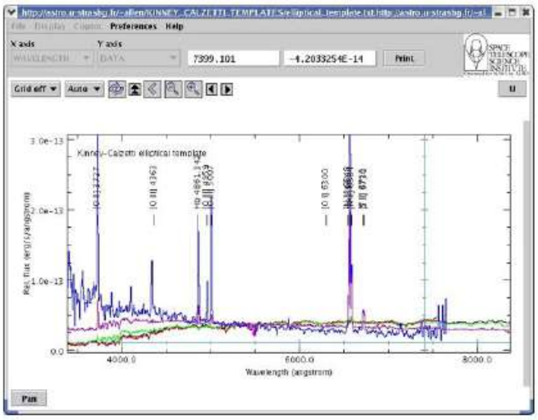
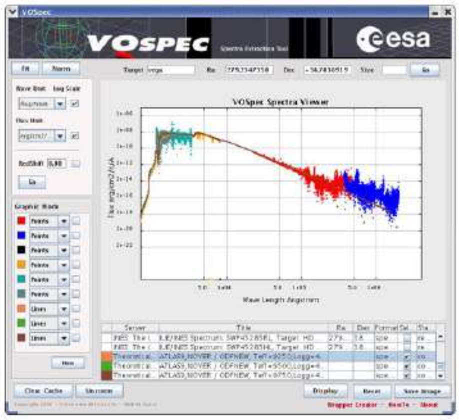

Figure 8. VO methods in astronomy: spectra overlapping and spectra combining and analysis.

Acknowledgements

This work was partially supported by the Republic of Armenia Ministry of Education, Science, Culture, and Sports (RA MESCS) Committee of Science, in the frames of the research projects No. 15T-1C257 and 21AG-1C053. This work was made possible in part by research grants from the Armenian National Science and Education Fund (ANSEF) based in New York, USA (grants astroex-4193, astroex-4195, astroex-2347 and astroex-2597).

References

1988, Infrared Astronomical Satellite (IRAS) Catalogs and Atlases.Volume 1: Explanatory Supplement. Vol. 1

Abrahamyan H. V., Mickaelian A. M., Knyazyan A. V., 2015, Astronomy and Computing, 10, 99

Acero F., et al., 2015, Astrophys. J. Suppl. Ser. , 218, 23

Ahumada R., et al., 2020, Astrophys. J. Suppl. Ser. , 249, 3

Bianchi L., Herald J., Efremova B., Girardi L., Zabot A., Marigo P., Conti A., Shiao B., 2011, Astrophys. Space. Sci. , 335, 161

Bird A. J., et al., 2010, Astrophys. J. Suppl. Ser. , 186, 1

Cabanela J. E., Humphreys R. M., Aldering G., Larsen J. A., Odewahn S. C., Thurmes P. M., Cornuelle C. S., 2003, Publ. Astron. Soc. Pac. , 115, 837

Calchi Novati S., et al., 2017, VizieR Online Data Catalog, p. J/ApJ/814/92

Colless M., et al., 2001, Mon. Not. R. Astron. Soc. , 328, 1039

Condon J. J., Cotton W. D., Greisen E. W., Yin Q. F., Perley R. A., Taylor G. B., Broderick J. J., 1998, Astron. J. , 115, 1693

Cutri R. M., et al., 2003, 2MASS All Sky Catalog of point sources.

Cutri R. M., et al., 2013, Explanatory Supplement to the AllWISE Data Release Products, Explanatory Supplement to the AllWISE Data Release Products, by R. M. Cutri et al.

DENIS Consortium 2005, VizieR Online Data Catalog, p. B/denis

D'Elia V., et al., 2013, Astron. Astrophys. , 551, A142

Evans I. N., et al., 2010, Astrophys. J. Suppl. Ser. , 189, 37

Gaia Collaboration et al., 2021, Astron. Astrophys. , 649, A1

Garn T., Green D. A., Hales S. E. G., Riley J. M., Alexander P., 2007, Mon. Not. R. Astron. Soc. , 376, 1251

Gold B., et al., 2011, Astrophys. J. Suppl. Ser. , 192, 15

Gregory P. C., Scott W. K., Douglas K., Condon J. J., 1996, Astrophys. J. Suppl. Ser. , 103, 427

Hagen H. J., Engels D., Reimers D., 1999, Astron. and Astrophys. Suppl. Ser. , 134, 483

Hartman R. C., et al., 1999, Astrophys. J. Suppl. Ser. , 123, 79

Helfand D. J., White R. L., Becker R. H., 2015, Astrophys. J. , 801, 26

Helou G., Walker D. W., 1985, IRAS small scale structure catalog

Høg E., et al., 2000, Astron. Astrophys. , 355, L27

Huchra J. P., Vogeley M. S., Geller M. J., 1999, Astrophys. J. Suppl. Ser. , 121, 287

Ishihara D., et al., 2010, Astron. Astrophys. , 514, A1

Lane W. M., Cotton W. D., van Velzen S., Clarke T. E., Kassim N. E., Helmboldt J. F., Lazio T. J. W., Cohen A. S., 2014, Mon. Not. R. Astron. Soc. , 440, 327

Lasker B. M., Doggett J., McLean B., Sturch C., Djorgovski S., de Carvalho R. R., Reid I. N., 1996, in Jacoby G. H., Barnes J., eds, Astronomical Society of the Pacific Conference Series Vol. 101, Astronomical Data Analysis Software and Systems V. p. 88

Lasker B. M., et al., 2008, Astron. J. , 136, 735

Markarian B. E., Lipovetsky V. A., Stepanian J. A., Erastova L. K., Shapovalova A. I., 1989, Soobshcheniya Spetsial'noj Astrofizicheskoj Observatorii, 62, 5

Massaro E., Mickaelian A. M., Nesci R., Weedman D., 2008, The Digitized First Byurakan Survey

Mauch T., Murphy T., Buttery H. J., Curran J., Hunstead R. W., Piestrzynski B., Robertson J. G., Sadler E. M., 2003, Mon. Not. R. Astron. Soc. , 342, 1117

McGlynn T. A., White N. E., Scollick K., 1994, in American Astronomical Society Meeting Abstracts #184. p. 27.08

McMahon R. G., Irwin M. J., Maddox S. J., 2000, VizieR Online Data Catalog, p. I/267

Mickaelian A. M., 2016a, Baltic Astronomy, 25, 75

Mickaelian A. M., 2016b, Astronomy Reports, 60, 857

Mickaelian A. M., et al., 2007, Astron. Astrophys. , 464, 1177

Monet D., 1998, USNO-A2.0

Monet D., Canzian B., Harris H., Reid N., Rhodes A., Sell S., 1998, VizieR Online Data Catalog, p. I/243

Monet D. G., et al., 2003, Astron. J. , 125, 984

Moshir M., 1989a, IRAS Faint Source Survey, Explanatory supplement version 1 and tape

Moshir M., 1989b, in Bulletin of the American Astronomical Society. p. 768

Oliver S. J., et al., 2012, Mon. Not. R. Astron. Soc. , 424, 1614

Pojmanski G., 1998, ACTAA, 48, 35

Simpson J. M., et al., 2015, Astrophys. J. , 807, 128

Skrutskie M. F., et al., 2006, Astron. J. , 131, 1163

Stepanian J. A., 2005, Rev. Mex. Astron. Astrofis. , 41, 155

Tsvetkov M. K., Stavrev K. Y., Tsvetkova K. P., Mutafov A. S., 1994, IAU Commission on Instruments, 5, 47

Vlemmings W. H. T., Ramstedt S., O'Gorman E., Humphreys E. M. L., Wittkowski M., Baudry A., Karovska M., 2015, Astron. Astrophys. , 577, L4

Voges W., et al., 1999, Astron. Astrophys. , 349, 389

Wisotzki L., Christlieb N., Bade N., Beckmann V., Köhler T., Vanelle C., Reimers D., 2000, Astron. Astrophys. , 358, 77

Xmm-Newton Survey Science Centre C., 2013, VizieR Online Data Catalog, p. IX/44

Yamamura I., Makiuti S., Ikeda N., Fukuda Y., Oyabu S., Koga T., White G. J., 2010, VizieR Online Data Catalog, p. II/298

doi:https://doi.org/10.52526/25792776-22.69.2-179

On the Place and Role of Astronomy and Astrophysics in the Emerging New Model of Education

L.A. Gheonjian *[1, 2]

[1]Tamar the King University, Tbilisi, Georgia
[2]Ivane Javakhishvili Tbilisi State University, Faculty of exact and Natural Sciences, Faculty Institute of Electrical and Electronics Engineering, Tbilisi, Georgia

Abstract

Developing digital technologies as an evolutionary leap, we are clearly facing a crisis in traditional education system. We are close, or are already at the bifurcation point of techno-cultural evolution. Systems Theory (Bertalanffy (1968)) and the concept of Purposeful Systems (Ackoff & Emery (2009), Ackoff et al. (2006)) focuses on the design of a new model of education. The main difficulty of education is caused by contradictions between the fuzzy logic (Zadeh (1973)) of the humanities and the clear logic of natural sciences. Lingvistic variables of fuzzy logic, reflecting and classifying the multiplicity of objects and connections, allow fuzzy interpretation of reality. The concepts of number and measure achieve convergence in the identification of objects, in their study and in the creation of new objects of reality. Problems arise in the process of combining these two logics in education. Psychology, responsible for understanding of teaching-learning processes, encounters difficulties in solving these problems. Ethology, studying the social behavior of animals and humans, firmly argue that without solving the problems of education as a form of intelligence development, we become an endangered biological species if the environment we have created will be destroyed. We will return to the primitive, animal form of social behavior, since the form of social organization are transmitted genetically and lie deep in our subconscious (Dolnik (2009), Lorenz (1963, 1971)). The digitalization and standardization of education started replacing part, or all of the intelligence with the ability to use databases of "recipes" for recognizing situations and appropriate behavior. Repetitions of each such recipe creates a fixed set of unconscious behavior (Uznadze (1995)) turning people into state of cybernetic organism. This perspective causes some blurred models of the present and gloomy forecasts and plans of social reconstruction. There is the need to clearly describe the reality in which our biological species exists and to transfer this knowledge into the process of education in the form of intellectual development.

Astronomy and astrophysics have created the most fully formulated model of the Universe, that becomes an essential part of culture and practice. The analysis of the intellectual activity of our civilization identifies astronomers and astrophysicists as a special group of purposeful and advanced carriers of intellect whith the great potential for formation of a new model of education. The development of astronomy and astrophysics can be represented as a continuous process of transforming the concepts of fuzzy logic into constructing the model the Universe as observable, measurable and clearly described system. The specificity of the subject of study, the need to constantly develop complex specific technologies for remote research and the need to use the most advanced methods for describing, interpreting and understanding the results, created conditions for specific Cerebral Sorting (Saveliev (2016)) and formation of advanced intellectual, professional and social community.

All significant results in General Psychology have been achieved in cooperation with exact and natural sciences. It is reasonable to offer astronomers and astrophysicists ideas explaining their intellectual activity and consistent with the concepts and ideas of General Psychology. This knowledge may became the part of activity technology and motivation to form a system based on astronomy and astrophysics as a model of cognition and education. Such a model based on General Psychological Theory of Set (Nadirashvili (2007), Uznadze (1995)) is proposed for discussion and use.

Keywords: *Astronomical knowledge, Astronomical Education, Uznadze Theory of Set.*

*lev.gheonjian@gmail.com,

1. Introduction

Education is a natural continuation of human scientific activity, a kind of processed product and a system for disseminating knowledge gained by science. Taking care on education, science strengthens the foundation on which it relies, on which its future state and development prospects depend. The formulation of the goals and objectives of scientific research, the determination of an adequate methodology and research tools, the systematization of the results of observations and experiments, the formulation of the discovered patterns using the language of known ideas - is an ideal plan and algorithm of scientific activity. Publication of the results for rigorous verification and confirmation by other members of the scientific community, and the practice of applying knowledge is the only criterion for the reliability and usefulness of scientific activity results. This activity should be considered only as part of the comprehension of the existing reality and its laws in order to create new reality objects. Science has become a tool for designing a new reality, first in our imagination in a certain language of ideas, then in planning and technology for creating the future.

If the process is well documented, as soon as the future becomes present, we have the opportunity to compare the result of activities with the original intent. Creating systems as formations consisting of many elements and connections between them (Bertalanffy (1968)), in most cases, a difference between the result and the intention is found. We have learned to create systems and to identify as systems many phenomena to explore them. In the first case, having discovered a discrepancy, we try redesign the system by replacing elements and reconfiguring connections. In the second case, we try to predict its behavior and try to improve its performance or prevent undesirable consequences of its functioning. If this can be done, practice shows that our identification is adequate to the phenomenon of reality.

The concept of the system turned out to be very productive. On this basis developed the concept of Purposeful systems (Ackoff & Emery (2009)) and the concept of Self-organizing systems (Kapitsa et al. (1997)). Social systems of varying complexity and scale became the subject of research in these areas. There are some results in the form of approaches to forecasting and designing their future by intervening in the system at the stage of its current development (Ackoff (1974), Ackoff et al. (2006)). These ideas began to be projected onto education as a system, and on its elements and connections (Pribram & King (1996)).

The concept of instability appeared as a systems property to behave in an unpredictable way under external influence, unforeseen destruction of elements or connections. The Catastrophe Theory was created and instability was generalized as a property of the Universe. The idea pushed determinism and made it possible to include human activity, including educational activities, in the field of study of natural science. Iinstability, unpredictability and, ultimately, time as an essential variable began to play an important role in overcoming the disunity that has always existed between social and natural sciences (Prigogine (1989)).

Self-organizing Criticality (Bak (1996), Bak et al. (1988)) belongs to the field of Catastrophe Theory. We only recently understand this phenomenon, although it has long been observed and known as flicker noise. Such systems have large number of identical elements and should be classified as stochastic. They are systems of relaxers, can be synchronized and synchronization can even be controlled (Lursmanashvili et al. (2010)). In science and education, we are dealing with a spectrum of diverse changing intellectual states of elements, which is a product of current state of education system and, as we will see below, two types of social relationships that come into conflict.

The general systems patterns found in some scientific areas can be transferred to systems of other areas. In such cases, we often observe an intellectual breakthrough in understanding the phenomena. A retrospective analysis of intellectual breakthroughs shows that the process begins in exact and natural sciences, where understanding is brought to simple primary models of phenomena easily accepted by various fields of research and activity. For example, systems and self-organization ideas (Bertalanffy (1968), Nicolis & Prigogine (1977)) have been consistently developed in natural sciences useing mathematical formulations. Authors of discoveries find the simplest formulations for the dissemination of this knowledge and projection to other areas of human activity (Prigogine (1978), Prigogine & Stengers (1997, 2018)).

If science reaches the level of understanding of phenomenon, the impact on education is reached if linguistic variables of fuzzy logic (Zadeh (1973)) are combined with clear logic of measure and number. Such case is a condition for al breakthrough as a form of instability. Some turn out to be so significant that starts self-organization changing the form of existence and activity of the entire civilization. This transformation lasts 50-100 years (Dyson (1988)). Generations change and the duration of transformation in many ways depends on the effectiveness of the impact of science on education. Sometimes breakthrough waits technology to be realized. Developing information and digital technologies as a stage in the evolutionary leap of humanity, it should not be forgotten that Boolean algebra about a century was waiting for its first

doi:https://doi.org/10.52526/25792776-22.69.2-187

implementation. It took about 70 more years for the technology to develop so much that we began to realize its unpredictable impact on evolution and fear our transformation into cybernetic organisms.

We are clearly facing a crisis in the traditional education system. It cannot be excluded that we are already at the bifurcation point of techno-cultural evolution, although the formulation of systems approach to education as a societal problem, was the part of breakthrough in understanding systems. The following requirements were formulated for the education of the Systems Age (Ackoff (1974)): should focus on the learning process, not the teaching process; should not be organized around rigidly scheduled quantized units of classified subject matter, but rather around development of the desire to learn and the ability to satisfy the desire; should individualize students and preserve their uniqueness by tailoring itself to fit them, not by requiring them to fit it; should be organized as a continuing, if not a continuous process; should be carried out by educational systems that can and do learn to adapt.

From these requirements follows a number of properties and objects that the system must satisfy and contain, arises a number of questions. Apparently the requirements, as well as the requirements for an ideal university (Ortega y Gasset, (1991)), were waiting for the technology of their implementation. This approach was later developed by the same author in the form of the so-called Idealized Design (Ackoff et al. (2006)). This is really good tool to design the future ideal education system. Apparently, in both cases, only a part of the necessary invariant formulations of the properties was found. The system approach clearly implies that the identification and creation of a future system is impossible without a clear formulation of both its purpose and the current state.

2. Is it possible to measure the intelligence of our civilization as a system?

Is it possible to assess current state of science and education as the complex self-organizing system, consisting of many carriers of intelligence interacting with each other by exchanging information? What should be the sample and indicators to make a conclusion about its state? It turned out that the scientific activity of universities, reflected in scientific publications, is suitable for assessing their intellectual state. For many years, author has been using data of international indices, collected and published without interpretation by the University Ranking by Academic Performance (URAP) Research Laboratory of Informatics Institute of Middle East Technical University of Turkey. Transformation of these data in the form of a diagnostic diagram allows to draw a number of significant conclusions and generalizations.

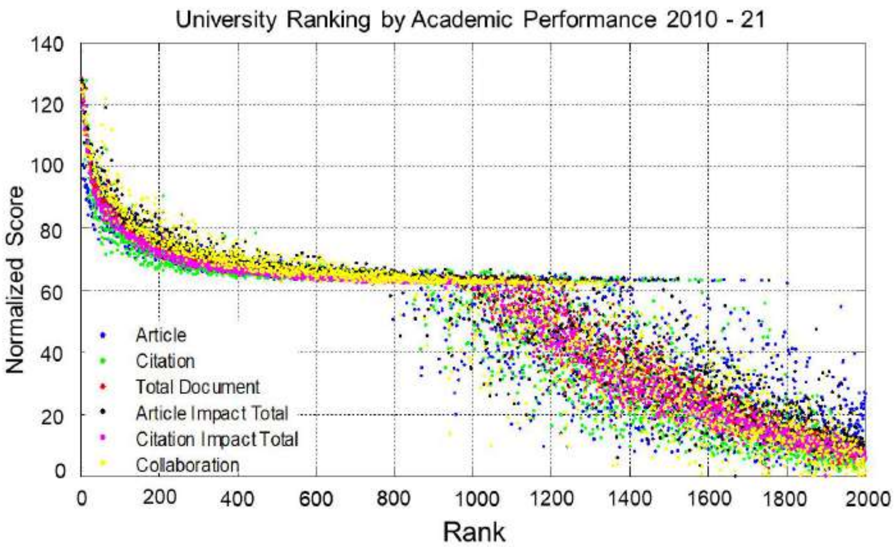

Figure 1. Diagnostic diagram.

.

The curves of the ranking indices of about a thousand of first universities are in good correlation with each other. The shape of each curve corresponds to the phenomenon of self-organizing criticality. By normalizing each index in such a way that the data of the first thousand universities match as much as possible, it is possible to bring all the data into one diagram. The general view of the diagram shown in Figure 1 has not changed for 12 years. This indicates the fundamental nature of regularities.

doi:https://doi.org/10.52526/25792776-22.69.2-187

The diagram indicates the presence of two self-organizing types of intellectual "population" - two types of universities classified by the effectiveness of scientific activity. The indices of the second group weakly correlate, create significant noise indicating a relatively low scientific, and therefore intellectual efficiency of activity. This state is traced further for the three thousand universities whose data is published. Considering that the world system of higher education is represented by approximately thirty thousand universities, we can state that we are a weakly intellectually developed civilization. This diagram is the argument confirming the existence of Cerebral Sorting mechanism as a factor of social self-organization (Saveliev (2016)).

The data on the intellectual activity of universities can be regrouped by country.The diagram is presented in Figure 2. It turns out that countries can be classified as having intelligent education systems, and countries with education systems in disaster. Diagram shows that some countries have both types of university "population", and some, mostly European, only the first type. This is another argument in favor of the Cerebral Sorting mechanism. It also becomes obvious why many perfect models of education (Ackoff et al. (2006), Ortega y Gasset, (1991)) have not been implemented for many decades.

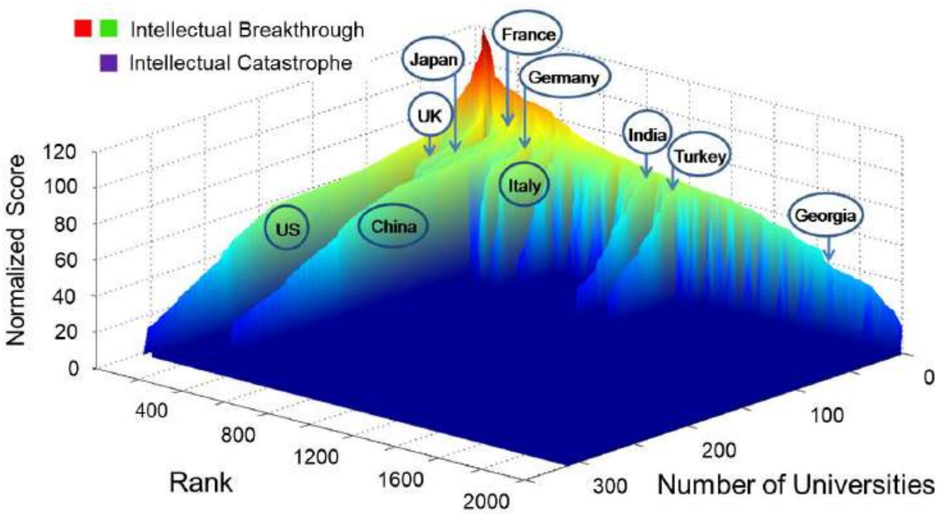

Figure 2. 3D Diagnostic diagram.

.

We canl see two categories of development: ability to form attitudes of imitation and learning borrowing models from the information environment; ability to create effective attitudes of behavior in new, previously unknown situations (Nadirashvili (2007), Saveliev (2016)).

3. How to solve the problem of intellectual development

It is proposed to consider the picture of the Universe created by astronomy and astrophysics as a result of human intellectual development, which has, had, has and will have a significant impact on the development of civilization. The scientific activity accompanying this development continuously formulated and solved the most complex problems in the fields of engineering and technology using the language of clear logic. We have almost completed the construction of a model of the Universe, but have not yet fully figured out what place to assign in it to the human as a carrier of intelligence. The intellectual development of the human is a continuous process of interaction between science and education. Every achievement of science is an achievement of education, preparing the basis for an intellectual breakthrough. And every achievement of science returns to education. The system has own peculiar hysteresis of the transition from education to science and vice versa. It seems to the author that the existing knowledge about the Universe can best be transformed into new digital and systems forms of education if this process will be carried out on the basis of knowledge about human psychology and ethology.

Simplistically, education can be represented as a kind of renewable environment for storing and using information, as a library of informational messages of varying degrees of complexity. "Consumers" learn to use it and turn to it in search of recipes for their life needs. If we take into account the achievements of ethology (Dolnik (2009), Lorenz (1963, 1971, 1981)), these basic needs are the simplest needs of a biological species, the satisfaction of which has turned out to be very complicated as a result of our social and technocultural

doi:https://doi.org/10.52526/25792776-22.69.2-187

development. The models of social behavior necessary to satisfy these primary needs have been developed in the course of biological evolution, are part of the genetic code and are transmitted from generation to generation. This is part of our subconscious social behavior, responsible for building hierarchies in the ownership and distribution of life resources. The history of our civilization can be represented as a continuous process of growing and resolving conflicts of this subconscious behavior in a continuously developing technocultural environment (Dolnik (2009), Lorenz (1963)). Moreover, the subconscious, coming into conflict with the consciousness, builds self-organizing social hierarchies, selecting its members according to their intellectual abilities and regulating access to education (Saveliev (2016)). Such established hierarchies, as a rule, for the purpose of self-preservation, begin to hinder the development of science and its impact on education. The demand for science and education arises when there is a threat from another, more developed hierarchy.

The situation gets more complicated by two factors of this self-organization. One is the presence of significant differences in the morphological parameters of the brain that determine the intellectual potential of each person (Saveliev (2018), Zworykin (1992)). The second - childhood and adolescence is the period of deployment of subconscious programs of social behavior and at the same time the period of mastering the skills to turn on and exercise consciousness and intellect. This is that crucial period of life when the first personal library of behavior programs in the already existing techno-cultural environment is consciously formed in the memory and brought to automatic, unconscious behavior (Uznadze (1995)). Some of these programs begin to form and are fixed as a counterbalance to the primary subconscious programs, oppose fear and aggressiveness in the natural behavior of a human as a biological phenomenon. Obviously, the state of the education system and its impact on this age group can shape the fate of generations and the community as a whole. By transforming education systems in a certain way, one can create and preserve entire behavioral communities for a long time. These considerations must be taken into account when we talk about education, designing the future and a systems approach to social problem (Ackoff (1974)).

Turning over the pages of the history of science and relying on the idea of the Cerebral Sorting (Saveliev (2016)) as a factor in the self-organization of social communities, one can come to the conclusion that the Universe, as a special subject of research, has formed a special social group of its researchers. The main feature and the argument of Cerebral Sorting of this social group is intellectual activity to study phenomena and objects that are not directly a part of life resources.

Darwin's theory of the evolution of species has received significant support from ethologists who study the social behavior of animals and humans[1] (Lorenz (1963, 1971, 1981)). We have pointed that *two forms* of behavior in human social behavior. One, ancient, subconscious is successively deployed in the form of a set of programs for future adulthood during the initial development of the organism until its puberty (Dolnik (2009), Lorenz (1963)). These programs establish and maintain hierarchies of strong individuals in the possession/distribution of food and reproduction in the animal world. This is a set of physiological sorting programs. It is important that in this set of programs for enimals, there are programs for "bloodless" maintenance of subordination in the process of change and maintenance of the hierarchical rank.

The second, later form of social behavior is the product of conscious social behavior and social evolution. This set of behavioral programs includes a variety of forms of learning reduced to a simple formula - fixing in memory a set of social situations and contacts with the environment, the skills of their unconscious recognition, and unconscious response in accordance with the program (set) alredy fixed in memory by previous experience of being in situations or contacts. This is what we may call the mechanism of our psychics in accordance with the Uznadze General Psychological Theory of Set (Uznadze (1995)). It is difficult to imagine ourself as a robot learning automatically by trial and error, approaching the desired result in each new situation and fixing it in memory in order to respond if it is repeated. It is also difficult to accept the idea that the education system is only a realized way of creating attitudes of behavior not from one's own, but from someone else's experience. But there is no other theory that claims to be General Psychological, is confirmed experimentally and explains a significant part of psychological processes, and one have to come back to it again and again (Nadin (2015), Parjanadze (2015)). This second form of behavior is responsible for cerebral sorting (Saveliev (2016)). We differ significantly from each other in terms of memory capacity, speed of recognizing situations and accuracy of recognizing situations.

Both forms, interacting, competing and conflicting in different situations, explain all psychological phenomena without exception. It is very important that by developing this second form of social behavior, evolution weakened in our species the protective subconscious "bloodless" mechanisms of the first model.

[1] In 1973 Lorenz K., Frisch K. and Tinbergen N. were awarded the Nobel Prize for Physiology or Medicine for their discoveries concerning animal behavioral patterns.

doi:https://doi.org/10.52526/25792776-22.69.2-187

As a result, our social reality and the entire history of our civilizations have turned into a bizarre conglomeration of hierarchical pyramids of various sizes being built and destroyed. It is easy to guess that we are dealing with a system and a phenomenon of self-organizing criticality (Bak (1996), Bak et al. (1988)).

Researcher experienced in systems approach and seeking in psychology a clue to his motives and incentives for research behavior, comes to conclusion that he is dealing with a poorly organized system of young, emerging field of science with the most difficult object of study. The only working definition of intelligence he will find has long been present in psychology (Piajet (1950)) and is analogous to the basic concept of Operations Research (Ackoff & Sasieni (1968)). The exact and natural sciences already understand and build in their own way what psychologists are trying to define and formulate. Every unsolved problem in psychology is a challenge for the entire scientific community.

References

Ackoff R. L., 1974, Redesigning the Future, a Systems Approach to Societal Problems. WILEY AND SONS.

Ackoff R. L., Emery F. E., 2009, On purposeful systems: An Interdisciplinary Analysis of Individual and Social Behavior as a System of Purposeful Events. Transaction Publishers, Rutgers - The State University.

Ackoff R. L., Sasieni M. W., 1968, Fundamentals of Operations Research. WILEY AND SONS.

Ackoff R. L., Magidson J., Addison H., 2006, Idealized Design: How to Dissolve Tomorrow's Crisis Today . Prentice Hall, Upper Saddle River, New Jersey.

Bak P., 1996, How Nature Works. Springer.

Bak P., Tang C., Wiesenfeld K., 1988, Self-organized criticality. Physical review A, vol. 38, pp. 364-374.

Bertalanffy L., 1968, General system theory: Foundations, development, applications. G. Braziller.

Dolnik V. R., 2009, Naughty child of the biosphere. Conversations about human behavior in the company of birds, animals and children. Petroglyph.

Dyson J., 1988, Infinite in All Directions. Harper and Row.

Kapitsa S. P., Kurdyumov S. P., Malinetsky G. G., 1997, Synergetics and future forecasts. Nauka.

Lorenz K. Z., 1963, On Aggression (First ed.). Routledge.

Lorenz K. Z., 1971, Evolution and Modification of Behavior. University of Chicago Press.

Lorenz K. Z., 1981, The Foundations of Ethology. Springer Nature.

Lursmanashvili O., Paatashvil N., Gheonjian L., 2010, Detecting quasi-harmonic factors synchronizing relaxation processes: application to seismology. Synchronization and triggering: from fracture to Earthquake Processes. Springer, pp. 305-322.

Nadin M., 2015, Anticipation: Learning from the Past: The Russian/Soviet contributions to the science of anticipation. Springer.

Nadirashvili S., 2007, Basic Points of the Antropic Attitude Theory. Bulletin of the Georgian National Academy of Sciences, V. 175, No 4, pp. 146-153.

Nicolis G., Prigogine I., 1977, Self Organization in Nonequilibrium Systems. WILEY AND SONS.

Ortega y Gasset, 1991, Mission of the University. Routledge. (First published in 1944)

Parjanadze D. S., 2015, Dimitri Uznadze's Theory of Set: Problems of Anticipation and Unconscious Forms of Memory. Anticipation: Learning from the Past. Springer, pp. 341-348.

Piajet F., 1950, The Psychology of Intelligence. Routledge.

Pribram K. H., King J., 1996, Editors, Learning as Self-Organization. Lawrence Erlbaum Associates, Inc., Publishers

Prigogine I., 1978, Time, structure, and fluctuations. Science 201.4358, pp. 777-785.

Prigogine I., 1989, The Philosophy of instability. Futures, Vol. 21, № 4, pp. 396–400.

Prigogine I., Stengers I., 1997, The end of certainty. Simon and Schuster.

Prigogine I., Stengers I., 2018, Order out of chaos: Man's new dialogue with nature. Verso Books.

Saveliev S. V., 2016, Cerebral sorting (in russian). VEDI.

Saveliev S. V., 2018, Morphology of consciousness (in russian). VEDI, Vol I and II

Uznadze D. N., 1995, Psychology of Set. Springer, first published in english in 1966

Zadeh L. A., 1973, The concept of a linguistic variable and its application to approximate reasoning. Elsevier.

Zworykin V. P., 1992, Morphofunctional foundations of individuality, as well as human spirituality (in Russian). Advances in the physiological sciences, Vol. 23, pp. 107-123.

doi:https://doi.org/10.52526/25792776-22.69.2-187

On the Stability of “Stable Systems” in the Presence of Dark Energy

H.A.Harutyunian *

Byurakan Astrophysical Observatory, Armenia

Abstract

The influence of dark energy on baryon objects and their system is considered. For such an analysis, the concept is adopted, according to which the entire baryonic Universe interacts with dark energy on all cosmic scales. It is shown that the interaction of baryonic objects with a carrier of dark energy inevitably leads to the injection of energy into the baryonic world with tangible physical consequences. The consequences seem quite dramatic, since the accumulation of energy in the baryonic world changes the virial theorem for all objects and systems, making them more and more unstable. This process of stability loss takes place at all spatial scales, including the micro world, where baryonic matter experiences the dark energy influence. It results decaying of all cosmic objects beginning with atomic nuclei and reaching the clusters of galaxies. Evolution under the influence of dark energy can take place in two different ways depending on the existence of the angular momentum of the body and its value. If the angular momentum is small, the object under the influence of dark energy obtains a more regular shape, otherwise at the equatorial plane would appear a structure consisting of less evolved matter.

Keywords: *dark energy, baryon matter, interaction, energy exchange, virial theorem, instability, objects' formation, evolution, metallicity*

1. Introduction

At any stage of the evolution of science, researchers have a certain set of tools with the laws of Nature that can be used for physical research. This toolkit is enriching constantly over time due to new discoveries. Any new discovery has the potential to change the basic ideas underlying our knowledge. Therefore, any new discovery requires special detailed studies for the introduction of needed changes and corrections. At the same time, newly discovered laws of nature can have very far-reaching consequences that do not clarify our ideas, but completely change them. This is the only way for the evolution of our scientific paradigms.

The history of science shows that researchers always try to keep all established ideas intact. They usually prefer to add new loose parameters to fit new observable facts or patterns to existing models and ideas. Major changes in beliefs that are highly valued by different paradigms occur very rarely and slowly when the inertia of the old type of thinking is reduced to a negligible level. Perhaps this approach underlies cognition through the human psyche. Undoubtedly, this is a question more philosophical than physical or astrophysical. However, when choosing a methodology for ongoing research, existing implicit trends should be taken into account.

Interestingly, from the very beginning of more or less serious cosmogonic studies of space objects and their systems, everything was considered stable and dynamically balanced. Even for the universe as a whole, Einstein introduced an anti-gravitational constant to keep it in a stationary state. All cosmogonic models based on the Kantian-Laplacian primitive hypothesis require stability at the final stage of the formation of an object/system. Apparently, this state of affairs is subconsciously more acceptable to a person. However, since this is not always true, researchers have often encountered paradoxes that have arisen because of this.

Then, as you know, it turned out that the Universe is actually non-stationary and it is expanding (Hubble, 1929). Very soon, the researchers decided that the expansion of the universe is exactly the effect that was predicted by Friedman (1922) and Lemaître (1927). In a strange way, most researchers did not even think that the real Universe had either homogeneity or isotropy, as the authors assumed when solving the corresponding problem.

*hhayk@bao.sci.am

doi:https://doi.org/10.52526/25792776-22.69.2-193

Moreover, detailed observations later showed that the Moon is rapidly moving away from the Earth (Dickey et al., 1994), and the Earth is moving away from the Sun (Krasinsky & Brumberg, 2004). In both cases, the observed data does not fit into our traditional scientific understanding. Nevertheless, tidal effects are certainly noted as the removal mechanism, although in the first case, they do not correspond to the observed speed, and in the second case, there are no data on the change in the Sun's spin at all.

Finally, at the end of the millennium, instead of the expected measurement of the deceleration of the expansion of the Universe, the scientific community encountered its accelerated expansion (Perlmutter et al., 1999, Riess et al., 1998). Of course, it was impossible to predict such behavior within the framework of the simple big bang hypothesis. Therefore, the discovery of an accelerating expansion should be recognized as a very dramatic change in our understanding of physical reality. Is the scientific community ready for such an unprecedented change? This seems very unlikely. However, most researchers accepted this change readily and without hesitation.

2. Dark energy

The most intriguing issue brought into consideration due to the universe acceleration phenomenon should be the possible consequences of the interaction between the baryonic matter and the carrier of the acceleration energy whatever it is. There is no doubt that the carrier of dark energy interacts with baryonic matter. The very discovery of dark energy took place because this interaction causes to accelerate the recession of galaxies. In other words, we learned about the existence of dark energy only because of how it interacts with baryonic objects, which are galaxies. So, one arrives at an inevitable conclusion that the carrier of dark energy interacts with the baryonic objects. This conclusion has far-reaching effects, which are very essential for the correct understanding of the going on processes. First, one should consider the physical consequences for the interacting systems using the available toolkit of the relevant physical laws. Therefore, one should apply the second law of thermodynamics here describing the process energetically. This law insists that due to the interaction of two various systems of objects the exchange of energy takes place in such a way that the system possessing lower energy gains some portion of energy from the other side of the interaction. Dark energy is positive since it implements physical work. On the other hand, all objects and their systems considered stable possess negative energy. What does it mean? The stability of a system (object) is a well-defined concept. Such a system has negative total energy and the null virial theorem:

$$E = T + U < 0 \tag{1}$$

and

$$W = 2T + U = 0. \tag{2}$$

What do we know about dark energy and its carrier? Frankly, no more than what we could determine from the very beginning of the discovery of dark energy. The part of researchers who accept the existence of dark energy (the majority) also believes that it fills all space uniformly on all scales. The homogeneity of distribution and excessively low density are probably the most significant characteristics of dark energy. It is precisely its low density that is often cited as an argument against the possible influence of dark energy on a small scale. However, at the same time, one essential detail is forgotten, namely, that the energy of a substance is cumulative and has the property of accumulation if the interaction continues in time. Therefore, a qualitatively different mechanism works, about which the proverb "a drop wears away a stone" was invented. Let us suggest that due to the interaction between the carrier of dark energy and any system of baryonic objects the latter gains some small non-zero portion of energy per unit of time. Then the relation (2) will change and will have

$$W = \Delta E > 0. \tag{3}$$

This is correct for any system, which obeys the relations (1)-(2) and interacts with any system with positive energy. In parallel with the accumulation of energy in the system, the latter sequentially passes into other energy states, which can be considered quasi-stationary, but in no way - stable. If the virial theorem is positive, it leads to the increase of the geometrical sizes of the given system of objects to reach an equilibrium. In other words, the expansion effect in the systems of cosmic objects is the natural reaction of the system to the interaction with the carrier of dark energy. The Universe as a whole shows this effect more clearly than all its subsystems with its accelerating expansion. To detect the expansion of systems of lower hierarchical classes, special methods of measurement are usually needed, and sometimes the courage

doi:https://doi.org/10.52526/25792776-22.69.2-193

to reject the hypotheses that prevail due to historical reasons. Taking into account the physical properties of dark energy that we have adopted, it is possible to determine a certain characteristic parameter that somehow shows the ratio of destructive dark energy and gravitational or other energy responsible for the integral existence of a given object or system. The spatial distribution of dark energy is uniform, meaning that the amount of energy is proportional to the volume considered. For the sake of simplicity, we will use the ratio of these energies in a given volume:

$$\eta = E_{de}/E_{\text{int}} \,. \tag{4}$$

It is clear from the physical meaning of this parameter that the system we are considering is the more easily subject to the influence of dark energy, the greater the value of this parameter. Any system consisting of objects with masses possesses gravitational energy given by the relation

$$E_{gr} = -G \sum_{i \neq j} \frac{M_i M_j}{R_{ij}}, \tag{5}$$

where R_{ij} is the mutual distance between i -th and j -th objects. If, in order to simplify the picture, we assume that all objects have the same mass M , and instead of mutual distances we take some average value R, then for rough estimates we obtain

$$E_{gr} \approx -G\frac{N(N-1)M^2}{R} \approx -G\frac{(NM)^2}{R}. \tag{6}$$

For the particular case of one homogeneous spherical object, the more correct calculations give a similar result:

$$E_{gr} = -\frac{3}{5}G\frac{M^2}{R}, \tag{7}$$

where R is the radius and M is the mass of the spherical object: The examples given show that the gravitational energy in these cases grows as the second power of the mass of the system or object, divided by the size. If we assume that the mass is proportional to the volume of the object, then we get that at the same density, the gravitational energy is proportional to the fifth power of the size. The amount of dark energy in the same volume is proportional to the third power of the size. It follows from what has been said that relation (4) for objects of the same type decreases with an increase in the size of the objects. And this, in turn, means that in objects or systems of the same type, the effect of dark energy on the physical characteristics of an object or system decreases with increasing mass (size). However, if we consider objects and systems that belong to different hierarchical levels of the universe, this regularity will not be preserved. Here we estimate the parameter (4) for various structural units. As a first example, let us take clusters of galaxies. Suppose our hypothetical cluster consists of 1000 galaxies with masses $\sim 10^{11} M_\odot$, and the size of the cluster is about 5 Mpc. We first transform (4) into the relation

$$\eta = k\frac{R^4}{(NM)^2}, \tag{8}$$

where

$$k = \frac{4\pi}{3}\frac{\rho_{de}}{G} \tag{9}$$

is a constant. Putting the corresponding values into the relation (8), one can easily obtain

$$\eta_{cl} = 6 \times 10^4 k. \tag{10}$$

The next hierarchical level is occupied by galaxies. Therefore, the same ratio should be estimated for galaxies as well. Masses of galaxies vary in a wider range than for the clusters of galaxies. Their mass range is wider for the elliptical galaxies. Actually, there are dwarf galaxies, which do not differ from the globular star clusters and the largest ones have masses of hundreds of Milky Way. Their masses span from several hundred thousand up to tens of trillions of solar masses. If we assume the normal galaxy possessing a mass of $\sim 10^{11} M_\odot$ and radius 25kpc, we find for the introduced parameter

$$\eta_{gal} = 6 \times 10^2 k. \tag{11}$$

doi:https://doi.org/10.52526/25792776-22.69.2-193

On the other hand, when this parameter is calculated for a dwarf galaxy, characterized by a radius 0.5 kpc and a mass $\sim 10^7 M_\odot$, we find

$$\eta_{dgal} = 10^4 k. \tag{12}$$

Obviously, this parameter is useable only for rough estimates. Nevertheless, it gives some idea of the variation of dark energy/gravitational energy ratio for various cosmic objects. The general physical approach to the problem under discussion tells us that this ratio is responsible for the time scales if we consider the evolutionary changes in the gravitational systems due to the dark energy influence. We again emphasize here that we hypothesized the above inevitable interaction between dark energy carriers and baryonic objects on all spatial scales, which could be studied using modern research toolkits, including all empirical and theoretical tools. There is one issue, we would like to stress as well. While estimating the parameter introduced in this section, we would like to mention that for the baryonic objects, namely, galaxies larger masses are used. In the clusters, obviously, not all the galaxies have a mass $\sim 10^{11} M_\odot$, the majority have much fewer masses. Moreover, masses of galaxies are given with their hypothetical component of dark matter. For example, dwarf spheroidal galaxies, have luminosities in the range $10^5 \div 10^7 L_\odot$ as though possess the masses$10^7 \div 10^9 M_\odot$. One can find easily that the reason for such a high mass-to-luminosity ratio is the big value of the velocity dispersion and, consequently, the forced involvement of dark matter. This situation is kind of confusing. Within the framework of our hypothesis or paradigm, which states that all baryonic objects participate in interaction with a dark energy carrier, which, in turn, inevitably leads to the transfer of energy to baryonic objects and their systems, an expansion of these systems must occur, since the virial theorem becomes essentially positive, even if before it was zero. The fact is that our hypothesis appears owing to the existing observational data and known laws of physics. On the other hand, the idea of the existence of dark matter was dictated by the unproven Kant-Laplace hypothesis, which to this day regulates all the mechanisms of the formation of space objects. Moreover, if the existence of dark energy is an observational fact and apparently accepted by the scientific community, then the need for dark matter simply disappears.

3. Clusters of galaxies and galaxies

Clusters of galaxies are the largest baryonic structures in the observable universe, which yield some categorization. Of course, larger structures exist as well, called superclusters, but those are simply some kind of conglomerates, composed of clusters and groups of galaxies. We will not dwell on the analysis of the advantages and disadvantages of these classifications, but I would like to mention one classification - simple and visual, which was one of the first. We are talking about regular and irregular clusters, which differ from each other not only in appearance but also in composition. In short, regular clusters have more ”regular galaxies”, which are elliptical and lenticular galaxies, while irregular clusters are dominated by spiral and irregular galaxies.

The estimate we obtained in the previous section is more suitable for regular clusters. However, it can also be used for irregular clusters. In both cases, there is a rather large velocity dispersion, which is usually a sign of the instability of any system. The estimate we obtained in the previous section is more suitable for regular clusters. However, it can also be used for irregular clusters. In both cases, there is a rather large velocity dispersion, which is usually a sign of the instability of any system.

Nevertheless, the idea of the existence of dark matter first appeared due to studies of kinematical conditions in clusters of galaxies (Zwicky, 1933, 1937). Nearly a century ago Zwicky was the first to notice that galaxies in clusters possess an extremely high-velocity dispersion, which makes these structures non-stable and predicts their expansion. That was the real situation, shown by the observational data. Zwicky could make the most evident inference, dictated by the relevant observational data, Moreover, the scientific community was aware of the expansion of the universe already, and it was obvious that clusters’ kinematics resembled actually the kinematical situation at the larger scales of the universe structure.

Zwicky, a very famous and professional astrophysicist, was unable to overcome the inertia of thinking that the clusters were the result of the condensation of more rarefied matter and reached a balanced state due to compression. If we take such a formation mechanism as a basis, then obviously the cluster formed in this way cannot expand. It is this approach and belief in the existing hypothesis that led to the introduction of the idea of dark matter. Nothing more. If Zwicky had been a little more daring and believed more in observational facts than in the speculative conclusions of authoritative predecessors, there would not have been an almost century-long search for dark matter.

doi:https://doi.org/10.52526/25792776-22.69.2-193

However, he preferred to come up with an artificial possibility of reconciling new data with old ideas and introduced a new free parameter called dark matter. The virial theorem when the dispersion of velocities is used instead of velocities has the following form:

$$\sigma^2 = \frac{1}{5}\frac{GM}{R}, \tag{13}$$

for example, represents the relation between velocity dispersion σ and particles (galaxies) total mass M and system's radius R for the spherical homogeneous distribution of particles. Putting here for Coma cluster $\sigma = 1000 km/s$, $2Mpc$ one can find easily $M = 2 \times 10^{15} M_\odot$. Assuming that there are two thousand galaxies in the Coma cluster, we obtain the average mass of a galaxy $\sim 10^{12} M_\odot$ which is a very large value.

Anyway, a long time passed after the introduction of dark matter, and many new discoveries took place during this period, including the most relevant one for the issue under consideration. Undoubtedly, saying most relevant we bear in mind dark energy, which drastically changed the situation. Unfortunately, the majority of researchers take this discovery as the next simple tool to fit observational data the old cosmogonic ideas. Nevertheless, this discovery showed, first of all, the big defects of the vulgar big bang hypothesis.

The next hierarchical class after clusters of galaxies, of course, are the galaxies themselves. Let us turn again to the "regular" objects of this class, which are elliptical galaxies. As is known, normal elliptical galaxies show a velocity dispersion of about 200 km/sec. The velocity dispersion of dwarf spheroids can reach up to 80 km/sec. These values together with accepted values of their radiuses give huge values of the mass equal to $10^{12} M_\odot$ and $8 \times 10^9 M_\odot$, correspondingly.

Guided by the same ideas, we also obtain huge values for the masses of galaxies. This is a long-established technique, and the majority of researchers have no doubts about its correctness. However, once again it is worth repeating that the cornerstone for using this formula is the assumption that all given systems are gravitationally bound and in a stationary or balanced state.

4. The nearest space.

Let us consider the immediate vicinity of the Earth, namely, the Earth-Moon and the Sun-Earth systems. For both systems, the available observational data show a gradual increase in the distances between objects. The Moon removal velocity is 3.82 ± 0.07 cm per year (Dickey et al., 1994) and the Earth's recession velocity amounts to 15 ± 4 cm per year (Krasinsky & Brumberg, 2004). Researchers traditionally attribute these expansion phenomena to tidal effects in the said system. We have repeatedly mentioned in our articles that in the Earth-Moon system, where the corresponding observational data are available with the required accuracy, the calculations do not confirm the tidal mechanism or support it as a second auxiliary tool when applying the Hubble expansion effect to smaller scales.

As for the change in the distance between the Sun and the Earth, there is no observational data on a decrease in the Sun's spine. Therefore, no calculations to test the correctness of the proposed hypothesis is possible. Based on this, and also taking into account the paradigm that the carrier of dark energy interacts with baryon objects at all scales and constantly transfers a certain amount of energy to them, we, remaining within the framework of this paradigm, considered this issue and found, in our opinion, self-consistent solution (Harutyunian & Grigoryan, 2018). In our interpretation, there are two main mechanisms at work, and both are associated with the impact of dark energy.

The fact is that in our approach when the interaction of the carrier of dark energy with baryonic matter is assumed on all scales, such interaction also includes atomic nuclei. Due to this interaction, they constantly absorb some, apparently, an extremely small amount of energy per unit of time. But in view of the cumulative property of energy, the "mastered" amount of energy is gradually growing. This process is accompanied by two very important phenomena that are interconnected. Excess energy reduces the binding energy of atomic nuclei, thereby increasing their mass by reducing the mass defect. But, on the other hand, a decrease in the binding energy destabilizes the atomic nucleus, gradually bringing it closer to the state of radioactive decay.

Naturally, all this is based on known observational data and the laws of physics, which today are well known to us and have been empirically tested many times. However, this is not yet sufficient to prove that in the situation we are considering these laws operate in exactly the way we assume. Therefore, various empirical schemes are required to test the validity of our reasoning, as well as observational data that

doi:https://doi.org/10.52526/25792776-22.69.2-193

contain ”fingerprints” of those physical processes that occur according to our scenario of the evolution of water matter under the influence of dark energy.

One such ”fingerprint” is the chemical content of space objects. We will return to this issue in the next section. Here we just intended to remind the reader about the removal of the Earth from the Sun, which is the result of the injection of dark energy into the gravitational system, on the other hand, is slowed down by the same injection of energy into atomic nuclei and an increase in the mass of the Sun.

The parameter η , introduced above for a qualitative assessment of the ”strength of influence” of dark energy on the gravitational system, can also be calculated for small scales, which are the distances of the Earth from the Sun and the Moon. But in these cases, instead of spherical formations, we are dealing with systems that are geometrically flat. To put it mildly, it is not very clear how dark energy affects baryon objects, and what part of it has a direct impact. Therefore, we will assume that this process involves that part of the volume of space, the points of which are between space objects. These parts of space are enclosed in volumes of truncated cones, the bases of which in one case are the Sun and the Earth, and in the second case - the Earth and the Moon. It is clear that the height is given by the distance of these objects. Thus, we have the volume

$$V_{de} = \frac{\pi R}{2}\left(r_1^2 + r_2^2\right), \tag{14}$$

where r_1 and r_2 are the radii of two interacting objects (Sun and Earth or Earth and Moon) and R is the average distance between them. The gravitational energy of two-body system, which we consider here, will have the following simple form:

$$E_{gr} = -G\frac{M_1 M_2}{R}, \tag{15}$$

and consequently the parameter η should will be

$$\eta = -\frac{V_{de}\rho_{de}}{E_{gr}} = \frac{3k}{8}\frac{R^2\left(r_1^2 + r_2^2\right)}{M_1 M_2}, \tag{16}$$

where k is given by the relation (9).

Calculations give the following tiny values for required parameter: $\sim 10^{-13}k$ for the Sun-Earth system, and $\sim 10^{-15}k$ for the Earth-Moon system. It is easy to see, that for the Earth-Moon system the parameter η is about 10^{19} times less than for clusters of galaxies. However, when we calculate the ratio

$$\mu = \frac{\sigma}{R}, \tag{17}$$

where σ is dispersion for clusters of galaxies and increase of the radius of lunar orbital radius per second, we obtain more or less similar values, which are close to the Hubble constant value, being larger for clusters.

5. Evolutionary scenarios.

Various phenomena of the activity of space objects in the form of instability and non-stationarity are undoubtedly associated with the appearance of excess energy, from which the object must be freed in various ways. As the primary cause of evolutionary processes, active phenomena were first indicated in the works of Ambartsumian. Along with this, the question of the source of energy that controls these phenomena was very non-trivial. After the discovery of dark energy, this question gets its natural and logical answer. Indeed, the amount of dark energy is considered to be the largest in comparison with all other types of energy-mass, and also the carrier of dark energy interacts with baryon objects of all hierarchical levels. And finally, when interacting, energy always flows in one direction - toward baryonic objects.

Any object has some ”limit of stability” in relation to the amount of internal (excess) energy. We keep in mind that the interaction of baryonic objects with a carrier of dark energy occurs continuously. Even with very small portions of energy transfer per unit of time, over time, the amount of ”mastered” energy increases unhindered and can reach the ”stability limit” if the object is somehow not simultaneously released from all the received energy. This process destabilizes the object, which leads to the need to release the accumulated energy.

An essential issue relevant to the problem under consideration could be the dependence of the evolution rate on the mass of the given object. This is not a trivial issue, since our knowledge concerning the carrier of dark energy is extremely scant or practically zero. We have only some incomplete information on the

doi:https://doi.org/10.52526/25792776-22.69.2-193

external manifestation of its interaction with the baryonic objects and that is all. Therefore, one needs using of some circuitous way for finding a more or less realistic solution. Above, we assumed that the ratio η of the amount of dark energy in the volume occupied by an object to the gravitational energy of a baryonic object can serve as an indicator of the object's compliance under the influence of dark energy. The greater the ratio, the stronger the process of evolution is forced by dark energy.

It varies from object to object for two reasons. First, the amount of dark energy is considered to be strictly proportional to volume, and gravitational energy is proportional to the second power of mass, which means proportional to the second power of volume. Second, the density of a baryonic object varies from object to object and within the same object. With the same density, it turns out that objects of smaller mass are more easily amenable to the evolutionary influence of dark energy. But one thing remains unchanged. This is that the given body receives a certain amount of energy, which must be mastered according to the laws of physics.

Let us test it for the spherical object. The gravitational energy of a homogeneous object of mass M and radius R as follows from the relation (7) is proportional to the second order of the mass:

$$E_{gr} \sim -G\frac{M^2}{R}. \tag{18}$$

where

$$M = \frac{4\pi}{3}R^3\rho = V\rho. \tag{19}$$

What does mean energy injection into the object? It changes the total energy of the object, but we do not know yet how it would distribute in the body. The body is made up of atoms, and we assume that they are also affected by dark energy. Such an impact, according to the second law of thermodynamics, increases the energy of atomic nuclei, which leads to a decrease in the binding energy and an increase in the masses of the nuclei.

We repeat that it does not matter how much the mass increases per unit of time, since this process continues as long as there is a given nucleus and it interacts with the carrier of dark energy. We are still interested in the fact that the mass of atomic nuclei increases, thereby increasing the mass of the given object. This further reduces the energy of the object, instead of increasing it. This means that the radius should increase or the mass ejection from the object should happen.

No doubt, the situation is not an easy one for comprehensive understanding. Various changes can happen when permanent energy injection is going on. The mass increase changes the quasi-stability between compressing and expanding pressures. We do not have any calculated model to estimate quantitatively all processes taking place during the energy injection. This excessive energy partially can transfer into heat, which in its turn will increase the inner pressure against mass growth.

Let us make here one more important remark, which may help to understand how some features of the structure of cosmic structures are formed. We are talking about the existence of two types of the stellar population in galaxies and their relationship with the regular and non-regular forms of the distribution of objects, namely, stars in galaxies and galaxies in clusters.

Even a superficial study of the mentioned structures allows us to come to the conclusion that all regular structures are devoid of or have only an insignificant rotational moment, while irregular ones, on the contrary, have a significant rotational moment. Therefore, it is not unreasonable to assume that in the absence of rotation, the proto-structure (proto-galaxy, proto-cluster), under the influence of dark energy, in order to free itself from excess energy, ejects clumps of matter isotropically from the surface layers of the proto-object.

However, if the latter has a significant rotational moment, then in the equatorial region, mechanical centrifugal force is also added to the ejection mechanism due to the influence of dark energy. At the same time, matter can be ejected not only from the outer layers but also from deeper layers, where the matter has gone through a shorter evolutionary path than in the outer layers (Harutyunian, 2022). The shorter the evolutionary path, the higher the metallicity. Such a scenario quite accurately explains the existence of two types of population, their striking difference in metallicity, and the existence of a metallicity gradient in galaxies.

6. Concluding remarks.

Based on our hypothesis of a continuous interaction between baryonic matter and a carrier of dark energy, we considered the possibility of the existence of stable structures of baryonic objects with the virial

doi:https://doi.org/10.52526/25792776-22.69.2-193

theorem equal to zero. This question is very important from the point of view of choosing the concept of cosmogonic models.

In the model accepted by most researchers at the present time, all cosmic structures are in an equilibrium state, and, according to the model, they have reached this state due to the compression of a more rarefied substance. This state of affairs excludes the possibility of the existence of such systems with the virial theorem greater than zero. Here we argue the opposite, based on the fact that any even equilibrium system of baryon objects, interacting with a carrier of dark energy, no doubt continuously receives a certain amount of energy from it and passes into the class of unstable ones with energy-increasing with time.

We also briefly reviewed Ambartsumyan’s well-known assertion that the evolution of cosmic objects is due to active processes, which show that everywhere active processes are accompanied by excess energy. We hypothesize that various manifestations of excess energy are portions of dark energy transformed into baryon structures.

A lot of observational facts fit our ideas on these subjects. We consider very briefly here the scenario of galaxy formation to show how can be explained first and second type stellar populations and also the metallicity difference between them. We are going to continue our research in this direction and carry out a more comprehensive analysis of relevant observational data.

References

Dickey J. O., et al., 1994, Science, 265, 482

Friedman A., 1922, Zeitschrift f¨ur Physik, 10, 377

Harutyunian H. A., 2022, Communications of the Byurakan Astrophysical Observatory, 69, 1

Harutyunian H. A., Grigoryan A. M., 2018, Communications of the Byurakan Astrophysical Observatory, 65, 268

Hubble E., 1929, Proceedings of the National Academy of Science, 15, 168

Krasinsky G. A., Brumberg V. A., 2004, Celestial Mechanics and Dynamical Astronomy, 90, 267

Lemaître G., 1927, Annales de la Société Scientifique de Bruxelles, 47, 49

Perlmutter S., et al., 1999, Astrophys. J. , 517, 565

Riess A. G., et al., 1998, Astron. J. , 116, 1009

Zwicky F., 1933, Helvetica Physica Acta, 6, 110

Zwicky F., 1937, Astrophys. J. , 86, 217

doi:https://doi.org/10.52526/25792776-22.69.2-193

Semi-detached double-lined eclipsing binaries with Gaia DR3 data

O.Yu. Malkov *[1], A.D. Grinenko†[2], and A.M. Sachkov‡[1,2]

[1]Institute of Astronomy RAS, Moscow, Russia
[2]Faculty of Physics MSU, Moscow, Russia

Abstract

Semi-detached double-lined eclipsing binaries (SD DLEB) play an important role in our understanding of basic properties of interacting binaries. We have collected data on semi-detached systems with available light and radial velocity curve solutions, and have compiled the most comprehensive list of SD DLEB, containing astrophysical and orbital parameters. The goal of this work was to make a cross-identification of the catalogued objects with Gaia DR3 archive. We have supplied our catalogue with data from Gaia DR3 as well as multicolor photometry from SIMBAD, and make a preliminary analysis of the results.

Keywords: *binaries: close – binaries: eclipsing – stars: evolution*

1. Introduction

Semi-detached eclipsing systems provide a unique opportunity to derive basic properties of interacting binaries. In our previous work we collected data on semi-detached systems with available light and radial velocity curve solutions, and compiled the most comprehensive list of SD DLEB, containing astrophysical and orbital parameters. We considered the classification of semi-detached binaries and discussed gaps between various classes in the HR diagram. We listed systems with component parameters that are inverted and briefly discussed their evolutionary state. A special analysis was conducted for systems with controversial data on parallaxes (Malkov (2020)). We compiled useful empirical relations between parameters of the accretor and the donor (Malkov (2021)). We also compared the catalogued data with models of low and intermediate-mass interacting binaries (Zeleke et al. (2022)).

In the present work we cross-identify a revised version of our catalogue with Gaia DR2/DR3 archives (Gaia Collaboration et al. (2016, 2022)), with the main purpose of providing the objects with triginometric parallax. We also supply our objects with multicolor photometry driven for SIMBAD database.

2. Cross-identification with Gaia DR3 and analysis of the results

Cross-identification of the catalogued objects with Gaia archive was carried out with the help of the service `https://gea.esac.esa.int/archive/`. Some special cases are described below.

Flamsteed identifier 68 Her was used for the star u Her in the current version of the catalogue. This is done so that the Gaia archive does not confuse it with another star, U Her.

The prototype of the class, β Per itself, was not found in the Gaia DR3 archive. It is included in Gaia DR2, however, parallax and proper motion are not measured by Gaia. The values, given in our catalogue, are taken from van Leeuwen (2007).

The only catalogued star with unknown parallax is GG Cas. It is included both in Gaia DR2 and DR3 archives, but the parallax is not determined. According to SIMBAD, ground based parallax for this star is also inavailable.

*malkov@inasan.ru, Corresponding author
†alenagr4622@mail.ru
‡asachkov2003@yandex.ru

doi:https://doi.org/10.52526/25792776-22.69.2-201

The majority (105) of the catalogued objects are marked as variable in Gaia DR3. We did not find a dependence of the probability of recognising the star as a variable on the period or on other parameters. Apparently it should depend on the maximum amplitude.

According to the non-single-star flags, Gaia recognize two catalogued stars as spectroscopic binaries (flag=2), sixteen others as eclipsing binaries (flag=4), three others as eclipsing+spectroscopic binaries (flag=6), and the rest remain single (flag=1) or unclassifed stars. The stars with flag=6 (YY Cet, RW CrB, RZ Dra) are among the shortest period binaries in our sample, they all have period less than 0.8 day.

It is known that besides the data, based on the coordinates of the input object, Gaia DR3 archive also displays data (coordinates, parallax, proper motion, radial velocity) provided by the CDS Name resolver. The target-distance parameter, containing the on-sky angular separation (in units of degrees) between the target coordinates provided by the Name resolver and the target coordinates of the Gaia DR3 archive, is also calculated and provided. For the majority of the catalogued objects these two sets of parameters are the same, and target-distance does not exceed 1.5×10^{-8}. However, seven objects from our sample (QS Aql, AB Per, δ Pic, V Pup, λ Tau, GG Cas, IU Aur) demonstrate a suspiciously high value (5.8×10^{-6} to 1.5×10^{-5}) of target-distance and/or a large difference between parallaxes provided by the Name resolver and ones driven from the Gaia DR3 archive. Obviously in these cases one should rely upon the data, provided by the Name resolver. In fact, QS Aql, AB Per, δ Pic, V Pup, λ Tau are absent in Gaia DR3 archive (but they are included in Gaia DR2).

Consequently, for these five stars and for β Per Gaia DR2 names are included in the current version of the catalogue, rather than Gaia DR3 names. Also, parameters teff-val and a-g-val are taken for these stars from Gaia DR2 instead of teff-gspphot and ag-gspphot, provided by Gaia DR3.

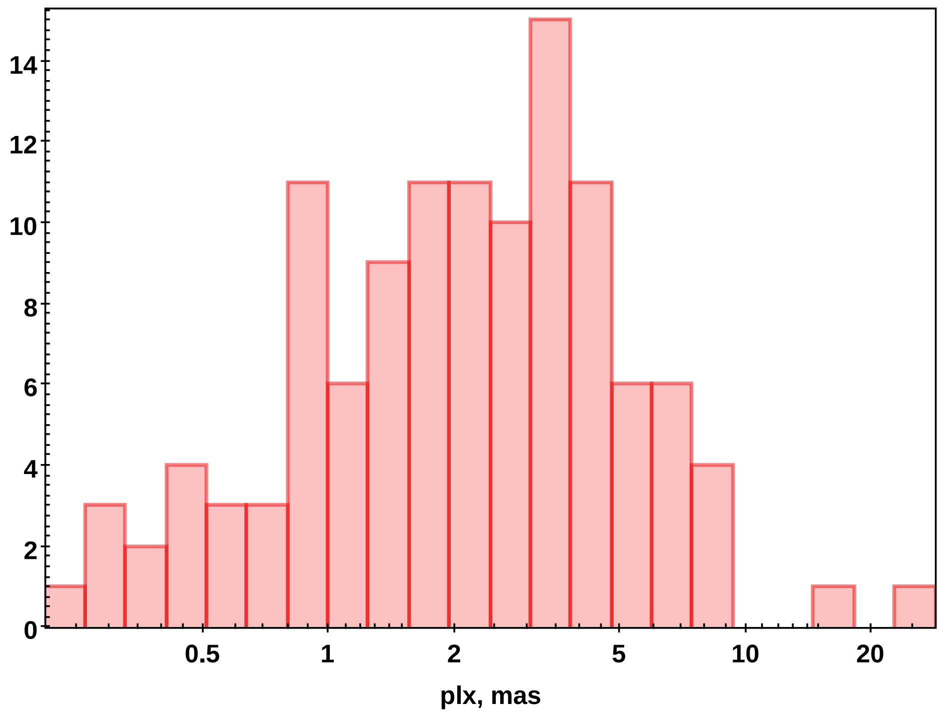

Figure 1. Distribution of the catalogued objects by parallax (target-parallax, see text for explanation). Two nearest objects are R CMa (ϖ= 23.16 mas) and RZ Cas (ϖ= 15.31 mas).

Distribution of the catalogued objects by target-parallax is shown in Fig. 1.

Position of the catalogued objects in the Hertzsprung-Russell diagram is shown in Fig. 2. B and V magnitudes are taken from SIMBAD, and absolute V-magnitude (M_V) is calculated from V and parallax; no correction for interstellar extinction is made.

3. Conclusion

Objects from a refined version of the Catalogue of semi-detached double-lined eclipsing binaries were cross-matched with Gaia DR3 archive (with the main purpose of providing the objects with triginometric parallax), and the results were analysed. Among 120 catalogued objects, two stars have no Gaia parallax.

doi:https://doi.org/10.52526/25792776-22.69.2-201

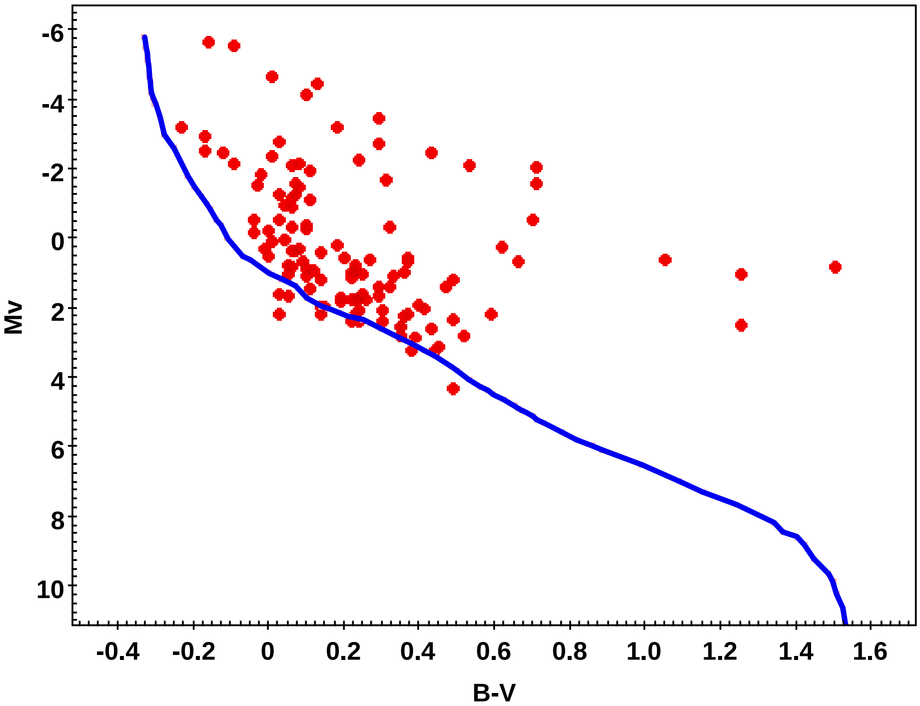

Figure 2. Catalogued objects in the Hertzsprung-Russell diagram (red points). M_V is calculated from V and parallax, no correction for interstellar extinction is made. $B-V$ is taken from SIMBAD. Blue curve represents the main sequence (see Mamajek's data available at `http://www.pas.rochester.edu/~emamajek/EEM_dwarf_UBVIJHK_colors_Teff.txt` and published in (Pecaut et al., 2012)).

GG Cas, being included both in Gaia DR2 and DR3 archives, has no parallax at all, while β Per, being included in Gaia DR2 archive but not in DR3 archive, has only Hipparcos parallax. Five more stars were not found in Gaia DR3, but present in Gaia DR2.

The majority of the catalogued stars remain single objects for Gaia DR3 from photometric and/or spectroscopic point of view. Shorter period systems ($P < 0.8$ day) have the best chance of being recognised as eclipsing+spectroscopic binary stars.

In addition, multicolor photometry from SIMBAD is added, and the Hertzsprung-Russell diagram of the catalogued objects is constructed.

Acknowledgements

This research has made use of NASA's Astrophysics Data System, of the SIMBAD database and VizieR catalogue access tool, operated at CDS, Strasbourg, France. This work has made use of data from the European Space Agency (ESA) mission *Gaia* (`https://www.cosmos.esa.int/gaia`), processed by the *Gaia* Data Processing and Analysis Consortium (DPAC, `https://www.cosmos.esa.int/web/gaia/dpac/consortium`). Funding for the DPAC has been provided by national institutions, in particular the institutions participating in the *Gaia* Multilateral Agreement. This research made use of TOPCAT, an interactive graphical viewer and editor for tabular data (Taylor, 2005) The acknowledgements were compiled using the Astronomy Acknowledgement Generator.

References

Gaia Collaboration et al., 2016, Astron. Astrophys. , 595, A1

Gaia Collaboration et al., 2022, arXiv e-prints, p. arXiv:2208.00211

Malkov O. Y., 2020, Mon. Not. R. Astron. Soc. , 491, 5489

Malkov O. Y., 2021, Astronomical and Astrophysical Transactions, 32, 111

Pecaut M. J., Mamajek E. E., Bubar E. J., 2012, Astrophys. J. , 746, 154

Taylor M. B., 2005, in Shopbell P., Britton M., Ebert R., eds, Astronomical Society of the Pacific Conference Series Vol. 347, Astronomical Data Analysis Software and Systems XIV. p. 29

Zeleke D. B., Negu S. H., Malkov O. Y., 2022, Research in Astronomy and Astrophysics, 22, 105013

van Leeuwen F., 2007, Astron. Astrophys. , 474, 653

doi:`https://doi.org/10.52526/25792776-22.69.2-201`

Appendices

Appendix A List of 120 semi-detached double-lined eclipsing binaries with Gaia and SIMBAD data

The table contains name, orbital period (in day), spectral type, Gaia DR2/DR3 ID, parallax with error (mas), G, B, V magnitudes, absolute V magnitude M_V. Not all parameters are shown in the table. Some values are rounded.

doi:https://doi.org/10.52526/25792776-22.69.2-201

Table 1. Semi-detached binaries in Gaia archive

Name	P	Sp	Gaia ID	plx	plx er	G	B	V	Mv
TW And	4.1227	FV+KIV	2874199987159664384	3.8517	0.0282	9.0082	9.48	9.07	1.99
WW And	23.2852	A5+F3p	1926891142676374656	0.8376	0.0767	10.8320	11.44	11.07	0.68
RY Aqr	1.9665	A7+G8III	6892535685232812032	6.2888	0.0178	8.8099	9.26	8.87	2.86
XZ Aql	2.1391	A2	4216146640300354048	1.9380	0.0223	10.0654	10.43	10.18	1.61
KO Aql	2.8640	AV+[G8IV]	4503821320738678016	4.0808	0.0250	8.3135	8.51	8.4	1.45
QS Aql	2.5132	B5V+[A8IV]	5517171678268362880	1.4729	0.9233	5.9610	5.91	6.0	-5.54
V337 Aql	2.7338	B0V+B3V	4261802284445511808	0.5371	0.0216	8.5272	9.32	8.89	-2.45
TT Aur	1.3327	B2V+B4	188555356425677184	0.9153	0.0239	8.5869	8.67	8.6	-1.59
IM Aur	1.2472	B7V+A5V	211807141136171136	1.8746	0.0422	7.9879	8.07	8.11	-0.52
IU Aur	1.8114	O9.5V+B0.5IV-V	182856896896621952	-1.1878	0.3224	8.3034	8.57	8.39	-3.21
Y Cam	3.3056	A7V+gK5	1136680382131779584	1.2510	0.0140	10.4755	10.93	10.6	1.08
S Cnc	9.4845	B9.5V+G8IV	661017766324783360	2.9054	0.0311	8.2423	8.44	8.35	0.66
RZ Cnc	21.6429	K0-2III+K4	709587249372597760	2.6995	0.0222	8.7417	10.17	8.67	0.82
R CMa	1.1359	F1V+G8IV	3030977013710528768	23.1637	0.0814	5.6195	6.05	5.7	2.52
HH Car	3.2314	8V+BIII	5338423042200185472	0.2273	0.0146	10.2249	10.79	10.5	-2.71
QZ Car	5.9986	late-OV+O8III	5350346970905044480	0.7356	0.1086	6.2499	6.37	6.24	-4.42
RZ Cas	1.1952	A(2-3)V+K1IV	541801332594262912	15.3142	0.0259	6.2293	6.40	6.26	2.18
SX Cas	36.561	midB+K3III	420596084197761920	1.2557	0.0168	8.7538	9.67	8.97	-0.53
TV Cas	1.8125	B9V+G5IV	428246623544412416	4.1720	0.0205	7.2029	7.29	7.22	0.32
TW Cas	1.4283	B9V+F6IV	516316302333109248	3.4822	0.0247	8.3126	8.48	8.38	1.08
ZZ Cas	1.2435	B3+[B9]	430730248515346560	0.3228	0.0296	10.9492	11.10	10.79	-1.66
AQ Cas	11.7210	B0.5II-III+B3II	511009646904766336	0.3265	0.0107	9.9073	10.84	10.31	-2.11
GG Cas	3.7587	B5V+KIII-IV	413230043488454656			9.7578	10.70	10.03	
SV Cen	1.6585	B1V+B6.5III	5335388664983921024	0.3875	0.0283	9.0943	9.71	9.7	-2.35
BF Cen	3.6933	B7V+[A]	5335710886269762688	0.5606	0.0242	8.6047	8.51	8.48	-2.77
MP Cen	2.9934	B3+B6/7	5334906700945688448	0.3570	0.0148	10.0490	10.40	10.29	-1.94
V716 Cen	1.4900	B5.5V+A2V	5895765142704352640	3.9426	0.0532	6.0934	6.13	6.09	-0.93
U Cep	2.4930	B8Ve+G8IV	566936237123439360	5.1938	0.0238	6.9091	6.92	6.92	0.49
RS Cep	12.4200	AVe+G8III-IV	556832549897897984	1.0822	0.0204	10.1544	10.76	10.39	0.56
XX Cep	2.3373	A8V+K1IV	2016972824676318336	3.1342	0.0138	9.1332	9.47	9.18	1.66
XY Cep	2.7745	B8+G4	2211230514682716288	1.7797	0.0607	9.7904	10.43	9.94	1.19
XZ Cep	5.0972	BII+B2III	2224860133836098560	0.9586	0.0156	8.1451	9.22	8.51	-1.58
GT Cep	4.9087	B2V+A0IV	2213360032485424768	0.7995	0.0248	8.0550	8.49	8.25	-2.23
LZ Cep	3.0705	O9III+ON9.7V	2199161386015469312	0.9070	0.0524	5.4814	5.55	5.54	-4.67
YY Cet	0.7904	A8V+G2IV	5138409988587248896	1.8792	0.0184	10.6365	10.98	10.68	2.04
U CrB	3.4522	B6V+F8-GIII-IV	1277156564676743552	2.4859	0.0301	7.7809	7.79	7.83	-0.19
RW CrB	0.7264	A9V+[K1IV]	1272944026393513088	3.7501	0.0202	10.1402	10.67	10.22	3.09
AB Cru	3.4133	O8Vn	6071508298145817344	0.2973	0.0192	8.4991	8.59	8.49	-4.14
AI Cru	1.4177	B2IVe	6058510765049380096	0.4963	0.0212	9.6074	9.67	9.69	-1.83
SW Cyg	4.5731	A2Ve+[KI]	2082658577035787392	2.1113	0.0134	9.2604	9.57	9.35	0.97
WW Cyg	3.3177	B7V+[G0IV]	2074464462324115456	0.8268	0.0149	9.9862	10.16	10.1	-0.31
KU Cyg	38.4394	A7V+M2III	2084134705758394112	0.8439	0.0180	10.9972	11.70	11.04	0.67
V448 Cyg	6.5197	O9.5V+B1Ib	2059011376158159488	0.4784	0.0193	8.0259	8.45	8.16	-3.44
V548 Cyg	1.8052	AV+[K]	2137780359106512640	1.6809	0.0307	8.5322	8.71	8.61	-0.26
W Del	4.8061	B9.5Ve+G5IV	1812558769663138176	1.2537	0.0273	9.7321	9.89	9.81	0.30
AV Del	3.8534	F8	1751749213935107456	1.2178	0.0224	11.4667	12.36	11.77	2.19
Z Dra	1.3574	A5V+gK2	1074900468737991552	3.2042	0.0234	10.3786	11.11	10.67	3.19
RZ Dra	0.5508	A5V+K2IV	2157561187465024896	2.6096	0.0152	10.4037	10.55	10.31	2.39
TW Dra	2.8068	A6V+KIII	1640708022815757568	6.0571	0.0179	7.3932	7.75	7.46	1.37
AI Dra	1.1988	A0V+G4V	1413786483748744960	6.0080	0.0832	7.0939	7.18	7.13	1.02
OO Dra	1.2383	A4V	1079310648531984000	1.4474	0.0152	11.0420	11.42	11.39	2.19
S Equ	3.4360	B8V+G8IV-III	1734709738640800256	2.4961	0.0280	8.3479	8.43	8.37	0.35
TZ Eri	2.6061	A6V+KIV	3202234883261674368	3.3372	0.0236	9.5287	9.97	9.61	2.22
AS Eri	2.6641	A3V+[G6IV]	3249135719973670528	4.7505	0.0354	8.2548	8.49	8.3	1.68
RW Gem	2.8654	B5V+[F5]	3424637773136532224	0.9177	0.0426	9.5709	9.89	9.79	-0.39
RX Gem	12.2086	AVe+K2IV	937758765659068288	1.5332	0.0212	9.1586	9.42	9.24	0.16
RY Gem	9.3005	A2Ve+K2IV	3168597794613114240	2.3807	0.0257	8.6340	8.88	8.68	0.56
AF Gem	1.2435	B9V+GIV	3378297756072107392	0.9693	0.0266	10.6398	11.05	10.82	0.75
UX Her	1.5488	A3V+KIV	4502802210861958272	3.9608	0.0196	8.8560	9.12	8.97	1.95
AD Her	9.7665	A4V+K2	4530807837182604800	1.7738	0.0193	9.5517	10.08	9.72	0.96

doi:https://doi.org/10.52526/25792776-22.69.2-201

Table 2. Semi-detached binaries in Gaia archive (continued)

Name	P	Sp	Gaia ID	plx	plx er	G	B	V	Mv
68 Her	2.0510	B2.5V+B8IV	1334035606852913536	3.4356	0.1164	4.8159	4.63	4.8	-2.51
RX Hya	2.2816	A2V+G5IV	5756165167814720512	3.6326	0.0190	9.4405	9.78	9.56	2.36
SX Hya	2.8957	A3+[G9IV]	6178229164451588352	3.8830	0.0261	8.7134	9.09	8.83	1.77
TT Hya	6.9534	B9.5V+KIII-IV	3532612598122182272	5.2365	0.0287	7.2110	7.43	7.31	0.90
RT Lac	5.0739	G5IV+G9IV	1961028607902617216	5.3695	0.0150	8.6038	10.09	8.84	2.48
TW Lac	3.0374	A3+[KIV]	2006361437964416128	0.9231	0.0179	11.4418	11.90	11.85	1.67
Y Leo	1.6861	A5V+G9IV	645963390556163456	2.5167	0.0582	10.0209	10.31	10.07	2.07
T LMi	3.0198	A3V+G7IV	793600868428166912	1.2835	0.0339	10.8380	11.09	11.06	1.60
SS Lib	1.4379	A5+[F5]	6261900040823123584	1.9312	0.0147	10.3447	10.87	10.47	1.89
del Lib	2.3273	AV+[G5IV]	6332277920392457472	9.2824	0.4724	4.8772	4.93	4.93	-0.23
RW Mon	1.9060	B9V+[G7IV]	3326370605032161664	1.9843	0.0252	9.2772	9.38	9.32	0.80
TU Mon	5.0490	B3V+A5III	3080938169233453312	0.6955	0.0493	9.2859	9.21	9.24	-1.54
UX Mon	5.9044	A5+G2III	3042861291292225280	1.7989	0.0212	8.2635	8.74	8.42	-0.30
AR Mon	21.2081	K0+K3	3058418895491950336	2.2975	0.0264	8.3985	9.84	8.79	0.59
AU Mon	11.1130	B3Ve+F8III	3112305895950166784	1.1534	0.0369	8.2367	8.46	8.43	-1.25
FW Mon	3.8735	B5+[F2IV]	3043073462677166976	0.6062	0.0352	9.9080	10.08	9.97	-1.11
BP Mus	3.3204	A0.5/1.5V+G5III	5842184360518202880	1.7848	0.0159	10.0832	10.43	10.11	1.36
UU Oph	4.3968	AV+[G6IV]	6034454000384147072	0.9841	0.1073	10.2306	10.58	10.44	0.40
KZ Pav	0.9498	F0V+K1	6375292709353220992	8.8818	0.0198	7.7369	8.28	7.85	2.59
TY Peg	3.0922	A2+[G6IV]	2812756459901030528	1.4461	0.0270	10.2518	10.46	10.21	1.01
AQ Peg	5.5485	A2e+G5IV	1770170564888184704	1.2063	0.0201	10.3072	10.57	10.47	0.87
AT Peg	1.1460	A4V+[G8IV]	2722801840219112448	3.5751	0.0333	8.9415	9.21	9.02	1.78
DI Peg	0.7118	F4+K4	2813513473657289088	3.6634	0.6702	9.4460	10.00	9.51	2.32
RT Per	0.8494	F5V+G7IV	242962936981732608	5.1901	0.0188	10.3327	11.22	10.73	4.30
RW Per	13.1989	B9.6e+K2III-IV	229136921858228096	2.1630	0.0342	9.4959	10.19	9.72	1.39
RY Per	6.8635	B4V+F7III	438165588512859008	1.1025	0.0273	8.4580	8.69	8.63	-1.15
ST Per	2.6483	A3V+K1IV	143580413107943680	2.6899	0.0265	9.4909	9.83	9.61	1.75
AB Per	7.1602	A5V+[G9IV]	237076873279709184	-1.7937	0.6592	9.5248	10.10	9.72	3.19
DM Per	2.7277	B5V+A5III	457464770661735296	1.3117	0.0273	7.8909	8.03	7.95	-1.46
IZ Per	3.6876	B8V+A5IV	407553608544043520	0.9596	0.0466	7.9390	8.07	8.01	-2.07
bet Per	2.8673	B8V+K2IV	239863001382455424	36.27	1.4	4.3403	2.07	2.12	
del Pic	1.6725	B0.5+B0.5-3	5499415974230271488	1.9695	0.2022	5.0749	4.58	4.81	-3.19
Y Psc	3.7657	A3V+KIV	2758178523763705856	2.1968	0.0265	9.2869	9.62	9.4	1.10
V Pup	1.4544	B1V+B3	5517171678268362880	0.8945	0.7329	8.2493	4.24	4.41	-2.93
XZ Pup	2.1923	AV+[G2IV]	5699396282969664256	2.7172	0.0290	7.7676	7.88	7.84	0.01
U Sge	3.3806	B8V+G4III-IV	4516549576568929408	3.7591	0.0283	6.4794	6.61	6.58	-0.54
RS Sgr	2.4156	B5V+A2	4044610255085884800	2.2917	0.0977	6.0343	5.94	6.03	-2.16
XZ Sgr	3.2755	A3V+G5IV	4053182253880893824	5.2533	0.0341	8.7903	9.29	8.94	2.54
V356 Sgr	8.8961	B3V+A2II	4079974569075292032	1.4783	0.0289	6.9040	7.07	6.99	-2.16
V505 Sgr	1.1828	A2V+G5IV	6878492245987853568	8.6674	0.1446	6.6395	6.62	6.48	1.16
mu01 Sco	1.4462	B0V+B2V	5971289565647972608	1.8732	0.7354	3.0698	2.82	2.98	-5.65
U Sct	0.9549	F+[G7IV]	4102730405305344128	3.1540	0.0172	10.0876	10.81	10.29	2.78
RZ Sct	15.1902	B3Ib+F5IV	4156190653517727360	1.2160	0.0208	7.3003	8.24	7.53	-2.04
RW Tau	2.7688	B8V+KIV	163742260906017024	3.4691	0.0428	8.0243	8.13	8.08	0.78
HU Tau	2.0563	B8V+GIV	3411229847309096704	7.8722	0.0466	5.8619	5.83	5.84	0.32
V1251 Tau	18.8988	G8III+K1-2III	3282677181172799104	1.9869	0.0209	9.2640	10.80	9.55	1.04
lam Tau	3.9529	B3V+A4IV	3305012316783145728	8.2174	0.5324	3.3871	3.29	3.41	-2.44
X Tri	0.9715	A3V+G5IV	298268990328628224	4.7529	0.0420	8.8134	9.30	9.0	2.38
TX UMa	3.0633	B8V+F7IV	829685534384441344	4.1849	0.0841	6.9228	6.99	6.98	0.08
VV UMa	0.6873	A1V+[G5IV]	1024762227410763264	2.1769	0.0394	10.1370	10.42	10.28	1.96
IO UMa	5.5201	A3	1567133171450548480	3.5249	0.0680	8.1156	8.44	8.21	0.94
W UMi	1.7011	A3V+[G2IV]	1727726671573301120	2.4373	0.0168	8.5609	8.92	8.65	0.58
RU UMi	0.5249	F0V+[G8IV]	1686621699950649344	3.5335	0.0144	10.0314	10.39	10.04	2.78
S Vel	5.9336	A5V+[K4IV]	5423067604782946432	6.0632	0.0207	7.7048	8.05	7.81	1.72
UW Vir	1.8107	A4+[K3IV]	3511171223730060672	4.1013	0.0508	8.9400	9.36	9.13	2.19
UY Vir	1.9945	A7V+[G6IV]	3508999005366339200	6.8690	0.2053	7.9309	8.36	7.99	2.17
BD Vir	2.5485	A5+[KIV]	3604868379129516160	2.3171	0.0247	9.8015	10.18	9.95	1.77
DL Vir	1.3154	A3V+KIV	6293889335197400064	4.5204	0.1266	6.7795	7.61	6.99	0.26
Z Vul	2.4549	B3V-A2III	2023954311223665536	1.9243	0.0207	7.3716	7.40	7.33	-1.24
RS Vul	4.4776	B5V+G1III-IV	2022188873509795200	2.7974	0.0233	6.7802	6.91	6.85	-0.91

doi:https://doi.org/10.52526/25792776-22.69.2-201

Communications of BAO, Vol. 69, Issue 2, 2022, pp. 207-216

First Byurakan Spectral Survey. Late-Type Stars. Dwarfs

K. S. Gigoyan *[1], K. K. Gigoyan[1], A. Sarkissian[2], G. R. Kostandyan[1], E. Karapetyan[3], M. Meftah[2], N. Azatyan[1], and F. Zamkotsian[4]

[1]INAS RA V. Ambartsumian Byurakan Astrophysical Observatory (BAO), Byurakan 0213, Aragatzotn Province, Armenia
[2]Universite de Versailles Saint -Quentin, CNRS/INSU, LATMOS-IPSL, France
[3]Yerevan State University, Astronomy Department, 0025, Alex Manoogian 1, Yerevan, Armenia
[4]Laboratoire d Astrophysique de Marseille, CNRS-AMU, 13388, Marseille Cedex 13, France

Abstract

A total of 18 lists of the First Byurakan Survey of Late-Type Stars (FBS LTS) were published between 1990 and 2016. The stars were found on FBS low-dispersion spectral plates. A systematic search and selection were carried out on a surface of $\sim$16 000 deg^2 on almost the whole area of the FBS. Since 2007, all FBS low-resolution spectral plates have been digitized. The second version of the "Revised And Updated Catalogue of the First Byurakan Survey of Late-Type Stars", containing data for 1471 M and C (carbon) stars (130 C-type giants, 1105 M – giants, and 236 M dwarfs) was generated. Among the 236 M dwarfs selected, 176 are new discoveries. The *Gaia* EDR3 G broad-band magnitudes are in the range $11.3 < G < 17.1$. New distance information by Bailer-Jones et al. (2021), which is based on the EDR3 parallaxes are used to estimate the G-band absolute magnitudes for M dwarfs. 9 FBS M dwarfs (out of 176 new discovered) lie within 25 pc of the Sun. The object FBS 0909-082 is more distant (r = 780ṗc) M dwarf among the sample considered, for which G-band absolute magnitude M(G) = 9.18, M = 0.59 M_{Sun}, L = 0.13597 L_{Sun}, and T_{eff} = 3844 K. This object can be classified as M1-M2 subtype dwarf. The nearest object is FBS 0250+167, a M7 subtype dwarf with very high proper motion (5.13 arcsec/yr) and is located at 3.83 pc from the Sun. The TESS estimated masses lie in the range 0.095 ($\pm$0.02) $M_\odot \leq M \leq 0.7\,(\pm\,0.1)\,M_\odot$ and T_{eff} in the range $4000K < T_{eff} < 2790K$ for FBS M dwarfs. Color-absolute magnitude (CaMD) diagrams are constructed for the FBS M dwarfs based on Gaia EDR3 and TESS data.

Keywords:*surveys-stars: late-type -stars, dwarf M stars, TESS and Gaia data*

1. Introduction

More than 75% of all stars within our Galaxy are M dwarfs (Henry et al., 2006, 2018), dominating the stellar populations by number, having a very low mass range $0.075\,M_\odot \div 0.50\,M_\odot$ and effective temperature (T_{eff}) less than 4000 K (Delfosse et al., 2000). M dwarfs are main-sequence stars whose spectra display bands of TiO and other molecules such as CaH, CaOH, VO, FeH, and CrH (Johnson et al., 1986, Kirkpatrick et al., 1993).

The great majority of the M dwarfs discoveries was based on the study of the proper motion catalogues, such as Lowell Observatory Proper Motion (Giclas et al., 1971), proper motion "Catalogue of Nearby Stars, 3rd edition- CNS3" (Gliese & Jahreiss, 1991), the "New Luyten Two Tenths"(NLTT) catalogue of Luyten (1979-80), which includes 58 845 stars with proper motions larger than 0.18 arcsec/yr. Numerous of the M dwarfs was confirmed among the proper motion objects in the catalogue by Lépine & Shara (2005).

Spectra of M dwarfs increases dramatically with the development of modern astronomical facilities. West et al. (2011) presented the spectroscopic catalog of 70841 M dwarfs from Sloan Digital Sky Survey (SDSS) Data Release 7. Zhong et al. (2019) presented catalog of M dwarfs from the LAMOST (Large Sky Area Multi-Objects Fiber Spectroscopic Telescope, (Cui et al., 2012), Data Release 5).

M dwarfs are in the focus of many astronomers in the recent two decades for their application to exoplanet research (Tarter et al., 2007). The small radii, low mass, low luminosity facilitate the discovery of orbiting low-mass planets via radial velocity (RV) and transiting photometry (Mann et al., 2018, Martinez et al., 2017, Muirhead et al., 2012). Recently, the Calar Alto High-Resolution search for M dwarfs with Exoearth

*kgigoyan@bao.sci.am, Corresponding author

doi:https://doi.org/10.52526/25792776-22.69.2-207

with Near-infrared and optical Echelle Spectrog- raph (CARMENES; Quirrenbach et al., 2014), and HARPS (Astudillo-Defru et al., 2017) surveys is searching for planets around M dwarfs (Alonso-Floriano et al., 2015, Cifuentes et al., 2020, Espinoza et al., 2022). CARMENES is a high-resolution, double-channel spectrograph at the 3.5 m Calar Alto telescope, which is monitoring M dwarfs to detect exoplanets with the RV method.

The main goal of the present paper is the characterization of a Galactic M dwarfs sample selected on First Byurakan Survey (FBS) plates (Gigoyan et al., 2019), using modern astronomical data bases, such as *Gaia* EDR3 (Brown et al., 2021) and TESS (Transiting Exoplanet Survey Satellite, Stassun et al. (2019). In this paper we present some important parameters for FBS M dwarfs and is structures as follows: First, we introduce the FBS for late-type stars (LTSs) and its digitized version, we characterize our sample of 236 M dwarfs. In Section 3, for selected M dwarfs we present spectroscopic observations. Cross-correlations with Gaia EDR3, TESS, GALEX, and ROSAT catalogues, color-absolute magnitude diagrams (CaMD) of FBS M dwarfs are considered in Section 4, giving a special attention on star FBS 025+167. In Section 5 we discuss possible multiplicity and companions around M dwarfs. Finally, in Section 6, we discuss the results obtained for the FBS M dwarfs, and we provide concluding remarks.

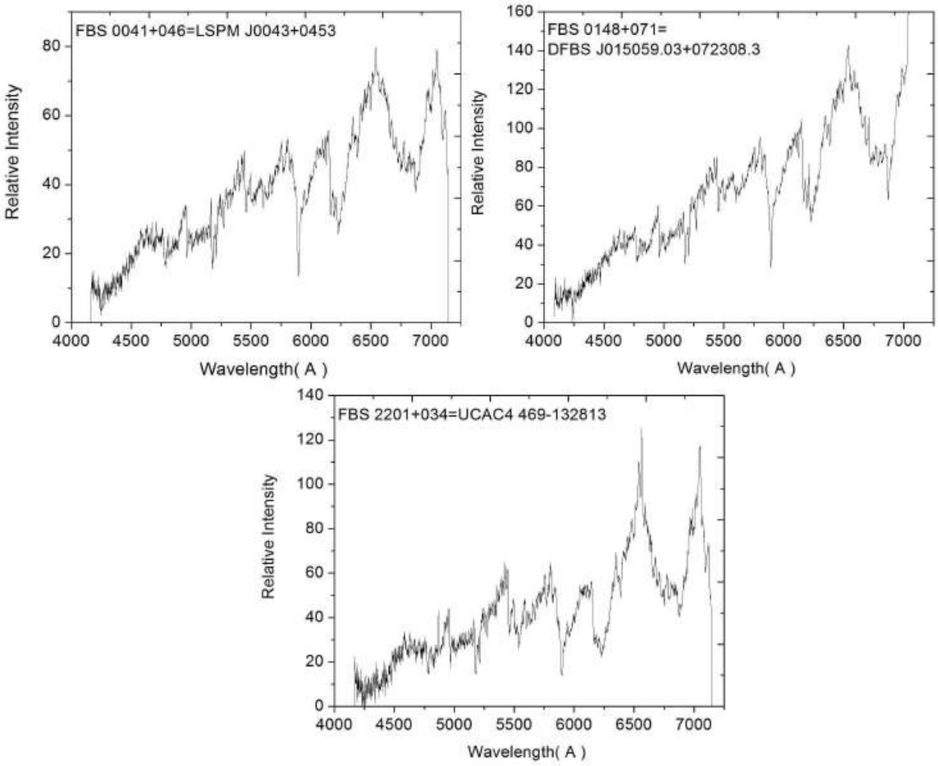

Figure 1. BAO 2.6-m telescope spectra for three FBS M dwarfs, obtained on September 8/9 2018 with the SCORPIO spectrograph, using a 600 line/mm grism and CCD EEV 42-40 in spectral range λ4000-7000 Å (pixel size 13.5 μm, resolution ~6 Å).

2. FBS Late-Type Stars Catalog

All M dwarfs analyzed in this paper are presented in "The Second Revised and Updated Version of the FBS Late-Type Stars (LTSs) Catalogue", which is a comprehensive list of 1471 objects (130 C (carbon) giants, 1105 M giants, and 236 M dwarfs, Gigoyan et al. (2019), CDS VizieR Catalogue J/MNRAS/489/2030). LTSs are selected on the Digitized First Byurakan Survey (DFBS)(its spectra are available on the DFBS web portal in Trieste `https://www.ia2-byurakan.oats.inaf.it/` plates, which is a digitized version of the FBS (Markarian et al., 1989). From the 236 M dwarfs, 176 are new discoveries. 60 M dwarfs are proper motion objects, known mainly from the NLTT catalogue (CDS VizieR Catalog I/98A), and from Catalogue by Lépine & Shara (LSPM; 2005). Spectral types as M dwarfs for a large number of these 60 known proper motion objects was reported also by Gigoyan et al. (2019).

doi:https://doi.org/10.52526/25792776-22.69.2-207

Table 1. CAFOS spectral types for 6 FBS M dwarfs

FBS Number	"Karmn" Number	SIMBAD association	J mag	Sp. type	Data
0444-113	J04468-112AB	1RXS J044652.0-111658	8.14	M4.9V	2013-02-14
0928+026	J09308+024	1RXS J093051.2+022741	9.42	M4.0V	2012-01-04
1040-089	J10430-092AB	WT1827	9.67	M5.5V	2012-01-09
1527+469	J1529.0+4646	1RXS J152902.1+464627	9.94	M4.5V	2012-02-09
1652+631	J16528+610	LSPM J1652+6304	9.59	M6.0V	2012-08-06
2201+034	J22035+036AB	1RXS J220330.8+034001	9.74	M4.0V	2012-01-04

3. Spectroscopy

For FBS LTSs, medium-resolution CCD spectra were obtained at different epochs with the Byurakan Astrophysical Observatory (BAO, Armenia) 2.6-m telescope. Figure 1 present optical spectra for three FBS M dwarfs obtained with the SCORPIO spectrograph and an EEV 42-40 2048 × 2048 pixel CCD as examples.

Moderate-resolution CCD spectra for 44 FBS M dwarfs (out of 236, presented by Gigoyan et al. (2019) was secured by LAMOST (Large Sky Area Multi-Object Fiber Spectroscopic Telescope) observations Luo et al. (2019), LAMOST DR7, spectra available on-line at http://dr7.lamost.org/search/.

Spectra for 12 M dwarfs were secured also with Calar Alto Focal Reductor and Spectrograph (CAFOS) mounted on the Ritchey-Chretien focus of the Zeiss 2.2 m Calar Alto telescope (wavelength range of $\lambda 4200-8300 \mathring{A}$, CDS Vizier Catalogue J/A+A/577/A128/Mstars/).We list in Table 1 CAFOS observations of 6 FBS M dwarfs (out of the 12 stars observed).

Table 1 presents FBS name, CARMENCITA identifier follows the nomenclature format "Karmn" (CARMENCITA CARMENES Cool dwarf Information and data Archive, (Alonso-Floriano et al., 2015), other associations in SIMBAD database, 2MASS (Two Micron All-Sky Survey, Skrutskie et al. (2006) J magnitude, spectral subclasses estimated and data of observations.

4. Photometric Data

4.1. Gaia EDR3 Data

Gaia EDR3 (Gaia Collaboration; Brown et al., 2021) provides high-precision astrometry, three-band photometry, effective temperatures, and information on astrophysical parameters for about 1.8 billion sources over the full sky brighter than G = 21.0 magnitude. All FBS M dwarfs were cross-matched with the Gaia EDR3 catalogue source. These objects are relatively bright, so that G-band brightnesses were in the range $11.3 < G < 17.1$.

4.2. TESS Observations

NASA's Transiting Exoplanet Survey Satellite (TESS) is an all-sky space-based mission designed to search for planets transiting around nearby M dwarfs (Ricker et al., 2014). We have cross-matched our list of 236 M dwarfs with the TESS Input Catalog (TIC), Version 8.2, Paegert et al. (2021), CDS VizieR catalogue IV/39/tic82, Stassun et al. (2018). This catalogue includes numerous of important physical parameters for stars, parallaxes, proper motions, TESS (T) magnitudes, temperatures, masses and luminosities in solar units, etc.

4.3. GALEX Ultraviolet Detection

We have cross-correlated the FBS M dwarfs against the GR6+7 data release of the GALEX. To match with the FBS M dwarf sample we queried GALEX (VizieR Catalogue II/335/galex-ais, Bianchi et al., 2017) data to identify UV sources within 5 arcsec. We found GALEX counterparts for 43 FBS M dwarfs (out of 176 new discovered) using 5" search radius.

doi:https://doi.org/10.52526/25792776-22.69.2-207

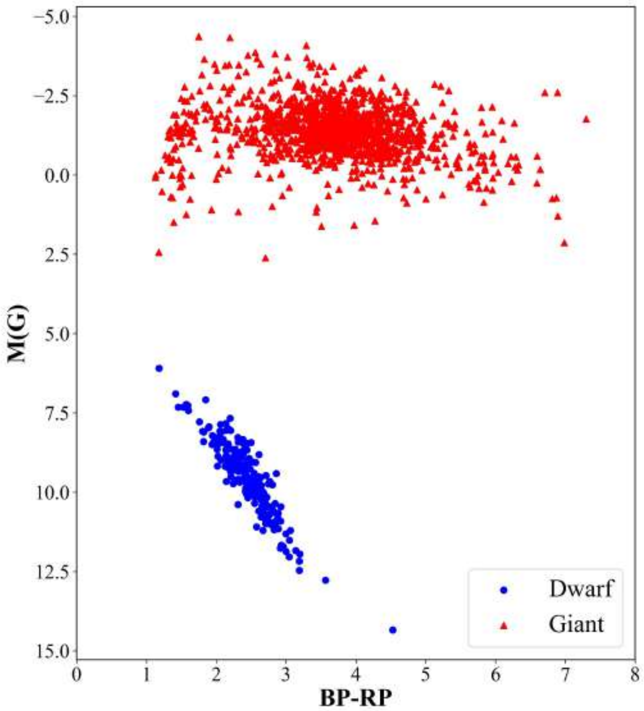

Figure 2. *Gaia* EDR3 absolute magnitude M(G) vs. BP-RP color for FBS M dwarfs (blue circles) and giants (M and N giants – red triangles) for comparison. The faintest object among the sample is M dwarf FBS 0250+167 (M(G) = 14.35).

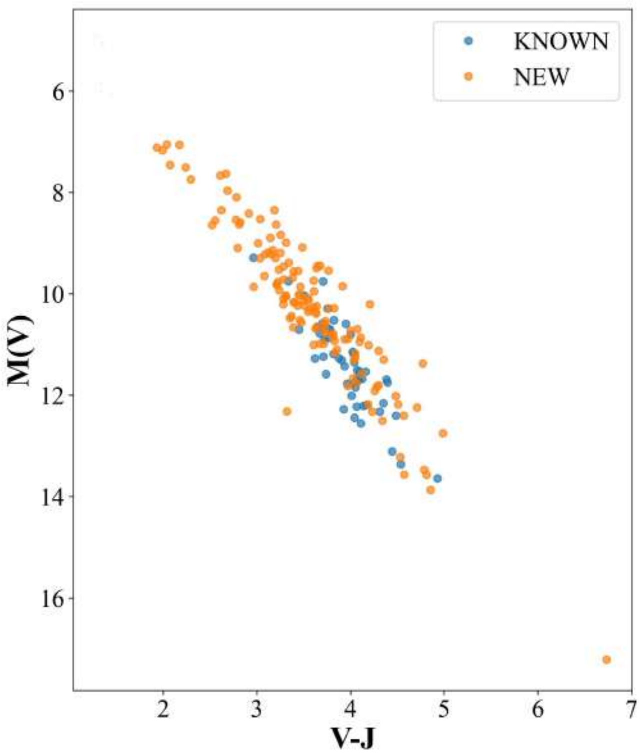

Figure 3. Observational HR diagram for FBS M dwarfs (M_V vs. V-J and V-K color based on TIC catalogue data with measured trigonometric parallaxes). Symbols are: orange dots-FBS M dwarfs (NEW), blue dots–M dwarfs KNOWN.

doi:https://doi.org/10.52526/25792776-22.69.2-207

4.4. ROSAT Data

Our list of all FBS M dwarfs was cross-correlated also with both the ROSAT All-Sky Survey Faint Source Catalog (Voges et al., 2000) and the Second ROSAT All-Sky Survey (2RXS) Source Catalog (Boller et al., 2016). We used a search radius of 15 arcsec, which is on the order of the astrometric precision of the ROSAT catalog. Our search identified 20 M dwarfs with the X-ray counterparts.

4.5. 2MASS Data

The 2MASS J-H versus H-Ks color-color plots for all 1471 FBS M-and C-type stars are presented in paper by Gigoyan et al. (2019). A special interest among all FBS M dwarfs present the extremely high proper motion star FBS 0250+167 (2MASS 02530084+1652532, J – H = 0.511, H – Ks = 0.298). In our XIV – th list of the LTSs, we present this object as M7-M8 subtype star (Gigoyan et al., 2003). The finder chart and the direction of the motion of this object is presented in Figures 9 and 10 by Gigoyan (2022, in press).

As part of CARMENES search for exoplanets around M dwarfs, Zechmeister et al. (2019) obtained more than 245 RV measurements for FBS 0250+167 and analyzed them for planetary signals. Authors find periodic variability in the RV and evident for two planet candidates, orbiting at periods of 4.91 and 11.4 d, respectively. TIC v8.2 catalogue gives the following data for FBS 0250+167, TIC Identifier is 257870150, M = 0.095M_{Sun}, L = 0.00077L_{Sun}, T_{eff} = 2790 K, and V = 15.13 mag.

4.6. Color-Absolute Magnitude (CaMD) diagrams based on *Gaia* DR3 and TESS

Figure 2 present the observational Gaia absolute magnitude (M(G)) versus BP-RP color, or Hertzsrung-Russell Diagram-HRD) for all FBS detected M dwarfs. For comparison on the same diagram we present FBS M and C giants (Gigoyan et al., 2019) also.

We used the distance information derived from *Gaia* EDR3 by Bailer-Jones et al. (2021). We estimate the absolute G-band magnitude via the usual equation:

$$M(G) = G - 5Logr + 5 - A(G) \tag{1}$$

We assume that A(G) is very low for our objects, because they are at high Galactic latitudes.

Figure 3 shows the absolute M(V) magnitude vs. optical-to-infrared V-J color diagrams for FBS M dwarfs (J and K magnitudes are from the 2MASS) based on TIC catalog data.

5. Possible Companions. Multiplicity

Stellar multiplicity among low-mass stars within 15 pc is presented by Ward-Duong et al. (2015). Winters et al. (2019), surveyed a volume-limited sample of 1120 M dwarfs within 25 pc. In many studies, authors explored the regions around M dwarfs in search of different types of objects at different separation from the star to study substellar companions. Finding and characterizing M dwarf multiples is useful for studying transiting exoplanets, and multiplicity trends among them can yield insight into stellar formation and evolution (Lamman et al., 2020).

There are no direct and high-angular-resolution CCD imaging observations to search companions around FBS sample of the new detected M dwarfs. This type of observations is required to resolve the faint and close companions. Therefore, for a preliminary information about companions around FBS sample of the new detected M dwarfs, we used high accuracy photometric data mainly from the Gaia EDR3 and TESS (TIC) catalogues. We search also possible data for multiplicity in the Gaia Catalogue of Nearby Stars (GCNS) for FBS M dwarfs up to 100 pc distances. As a supplement information, we check visually POSS II I-band direct images for FBS M dwarfs in STScI Digitized Sky Survey database (on-line via `https://stdatu.stsci.edu:cgi-bin/dss-form`).

5.1. Gaia EDR3 Search

Gaia DR3 has the potential for extensive multiplicity studies. Gaia can resolve most companions down to 1 arcsec. at magnitude contrast as large as six; closer systems are not resolved, regardless of secondary brightness (Lamman et al., 2020, Ziegler et al., 2018). From 176 of our cross-matched FBS new M dwarf

doi:https://doi.org/10.52526/25792776-22.69.2-207

Table 2. Some Important *Gaia* ERD3 Catalogue Data For Three FBS M Dwarfs

FBS Number	*Gaia* EDR3 Number	G mag	BP-RP mag	r (pc)
0041+046	(bright) 2554308108533636992	13.68	2.44	56.04
	(faint) 2554308108534379264	20.57	1.58	
0820+035	(bright) 3092033444148132224	13.48	2.68	49.23
	(faint) 3092030489210218240	20.83	1.66	
0828-087	(bright) 5752169164602798336	12.37	2.50	61.30
	(faint) 5752169160308040960	16.92	0.46	

Table 3. Some Important TESS Catalog Data For Three FBS M Dwarfs

FBS Number	TESS Input Catalog Identifier	TESS T mag	T_{eff} K	Mass ($M_{\odot}$)	Lumonosity ($L_{\odot}$)
0041+046	(bright) 336565415	12.52	3464.0	0.366 (0.020)	0.01847(0.00448)
	(faint) 610931424	18.99			
0820+035	(bright) 455236039	12.23	3340.0	0.386(0.020)	0.01751(0.00437)
	(faint) 804051355	19.76			
0828-087	(bright) 51039965	11.18	3433.0	0.641(0.021)	0.05586(0.01311)
	(faint) 51039966	16.70			

targets, 27 had second Gaia EDR3 object within 5 arcsecond search radius. In 19 cases from 27, Gaia EDR3 database gives nearly equal-magnitudes in G-band. Three objects, mainly FBS 0041+046, FBS 0820+035, and FBS 0828-087 deserve a special attention. There are very close to primary M star and extremely faint in G-band second object (see detail below).

5.2. TESS Catalog Search

TESS Input Catalog-v8.2 gives data for two objects in search radius 5 arcsec around position for 27 FBS M dwarfs also, from which in 12 cases this catalogue comprises two objects with nearly-equal T magnitudes (Stassun et al., 2019). In this catalogue also three objects noted above, are exceptional, having the bright primary star, and very faint secondary object.

In Tables 2 and 3 consequently, *Gaia* EDR3 and TESS catalogue important data are presented for three FBS M dwarfs and for very close and faint companions in 5" search radius around them.

There are no distance information (only positional data) about the very faint and very close objects around these M dwarfs in Gaia EDR3 and TESS databases. If these objects are gravitationally bound, i. e. they are physical companions at the same distances, therefore absolute magnitudes can be obtained M (G) = 16.83, 17.37 and 13.00 for FBS 0041+046, FBS 0820+035, and for FBS 0828-087 consequently. Such BP-RP colors and absolute G-band magnitudes placed them on White Dwarfs (WD) sequence on HRD (for detail see Fig. 13 by Babusiaux et al., 2018).

Table 4. GCNS Data For Three New FBS M Dwarfs As A Binary Systems

FBS Number	*Gaia* EDR3 Identifier	G mag.	G mag. diff	BP-RP color	Angul. sep.(arcsec.)	Proj. sep. (AU)
1009+350A	753259752444224000	14.28	2.62	2.41	3.431	249.95
B	753259748150042752	16.91		3.08		
1107+350A	761700565771564416	11.54	2.03	1.68	3.170	190.000
B	761700565771564032	13.58		2.34		
1136-082A	3591834837013732096	12.73	3.00	3.00	4.250	192.411
B	3591834871372295040	15.74		2.69		

doi:https://doi.org/10.52526/25792776-22.69.2-207

5.3. Gaia Catalogue of Nearby Stars Search

To search companions around new discovered FBS M dwarfs we have cross-matched with the Gaia Catalogue of Nearby Stars (GCNS, Gaia Collaboration; Smart et al., 2019). This catalogue gives information about 19176 resolved multiple systems.

Table 4 present data for three FBS M dwarfs, which are presented as resolved binary systems in the GCNS data base. These table present FBS Name (A, B) for the bright, primary source and B for the secondary component, Gaia EDR3 source identifier, Gaia EDR3 G –band magnitude, BP-RP color, G-band magnitude differences, angular separation of both objects, projected separation in AU.

Figure 4 illustrates secondary physical components around three FBS M dwarfs on DSS2 I charts according to GCNS database.

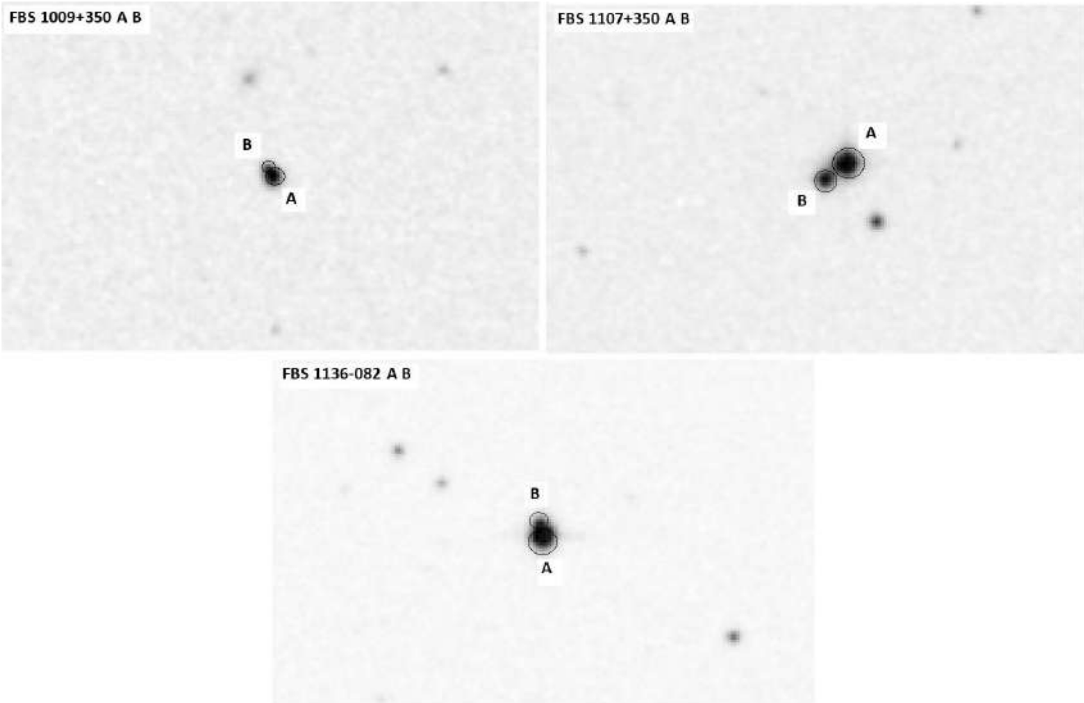

Figure 4. POSS2 I images for three FBS M dwarfs, which are included in GCNS catalogue as a binary systems. Physical components are circled and noted as B. They all are within 100 pc from the Sun. Very important note, the *Gaia* BP-RP colors for all components are typical for dwarf M stars. Field is 15 arcmin × 15 arcmin.

5.4. Washington Visual Double Star Catalog

We have cross-matched also all FBS M dwarfs with the "Washington Visual Double Star Catalogue" (WDS) objects (SIMBAD VizieR Catalog B/wds/wds, Mason et al., 2001) to find publications with information on multiple systems. Four objects out of 236, namely FBS 0115-095, FBS 0913-103, FBS 1345+796, and FBS 1513+796, are associated with the visual doubles. FBS 1345+796, is EA type eclipsing binary.

5.5. Visual Inspection of the POSS2 I Images

With help of the data visualization software SAOImage ds9, we search the POSS2 I-band images for new detected FBS M dwarfs, aiming to look companions around these objects. Such visualization allowed to detect very close and comparatively bright possible physical companions around dwarfs FBS 0756+234, FBS 1010+205, FBS 1016+142, FBS 1340-049, FBS 1412-058, and FBS 1719+829. Only in case of FBS 0756+234 we have very good matched Gaia EDR3 catalogue distances (Bailer-Jones et al., 2021) for primary M dwarf star and for very close companion. For the remaining FBS M dwarfs above noted, the distance values for the faint close objects and primary star are very different.

In Figure 5 we illustrate the POSS2 I - band image and second companion around M dwarf star FBS 0756+234. Spectra in the range 3900-9100 A for this object was secured by LAMOST telescope and classified as dM4 type star (identifier is LAMOST J075935.66+232039.5).

doi:https://doi.org/10.52526/25792776-22.69.2-207

Table 5. *Gaia* EDR3 and TESS Catalogue Data For Dwarf M Star FBS 0756+234

FBS Number	*Gaia* EDR3 Identifier	G mag	BP-RP color	*Gaia* EDR3 distance(pc)	TIC Number	Mass ($M_\odot$)	Lum ($L_\odot$)	TESS T_{eff} (K)
0756+234A	680421917468548608	13.09	2.49	44.8166	54233548	0.389(±0.021)	0.01992(±0.004888)	3437.0
B	680421917468548480	14.58	2.82	44.7298	54233549	0.224(±0.02)	0.00658(±0.00167)	3267.0

Table 5 include Gaia EDR3 and TESS data for dwarf M star FBS 0756+234 and for very close companion. The BP-RP color and Teff of the second and very close object is also typical for M dwarfs, therefore most probably, we have pair of M dwarfs. High-angular-resolution CCD is required to resolve very well the second component of FBS 0756+234 and faint companions around FBS M dwarfs in general.

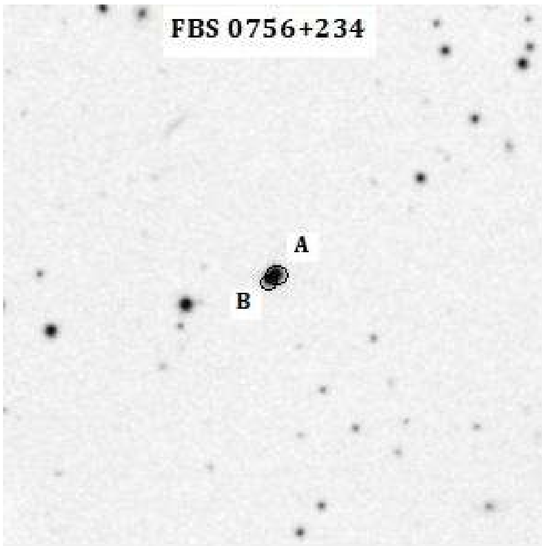

Figure 5. POSS2 I image of dwarf M star FBS 0756+234 (primary star-A), which we present as a binary system (companion-B). Angular separation is 1.74´ arcsec on I-image. Field is 5´ × 5´.

6. Summary And Future Works

In an effort to characterize the new M dwarfs found in the FBS, we used Gaia EDR3 and TESS monitored data to search M dwarfs and their possible multiplicity. These objects are relatively bright, 2MASS Ks magnitude lie in range between 7.3 and 14.4. For this purpose, we search visually POSS II I-images, also cross-matched all M dwarfs with the GCNS and with the Washington Visual Double Star Catalogue. The Gaia EDR3 G broad-band magnitudes are in the range $11.3 < G < 17.1$. The TESS estimated masses lie in the range $0.095\,(\pm\,0.02)\,M_\odot \le M \le 0.7\,(\pm\,0.1)\,M_\odot$ and T_{eff} in the range $4000K > T_{eff} < 2790K$ for FBS M dwarfs. For 27 FBS M dwarfs Gaia EDR3 and TESS catalogues gives two objects in 5 arcsec search radius. Three objects, namely FBS 0041+046, FBS 0820+035, and FBS 0828-087 most probably are binaries, having the second companion White Dwarf. Four objects FBS 0115-095, FBS 0913-103, FBS 1345+796, and FBS 1513+796 are included in Washington Visual Double Star Catalogue. FBS 1345+796, is EA type eclipsing binary. According to Gaia EDR3 and TESS photometric data, most probably FBS 0756+234 is a close binary. Gaia EDR3 BP-RP color for both objects are typic 0909-082 is a more distant M dwarf (r=780 pc), or which G-wide band absolute magnitude M(G) = 9.18, $M = 0.59\,M_\odot$, $L = 0.13597\ L_\odot$, and $T_{eff} = 3844$ K. This object can be classified as M1-M2 subtype dwarf. The nearest object is FBS 0250+167, a M7 subtype dwarf with extremely high proper motion (5.13 arcs./yr) and is located at 3.83 pc from the Sun. As part of CARMENES search for exoplanets around M dwarfs, two exoplanets was found around this high proper motion object.

In the future, high-angular-resolution CCD observations are necessary for higher-significance detections of the close companions around FBS M dwarfs and their reliable photometry to know more about multiplicity of FBS M dwarfs. Also we plan to download and analyze the TESS light curves for all FBS new detected M dwarfs from the Mikulski Archive for Space Telescopes (MAST-https://mast.stsci.edu/portal/Mashup/

doi:https://doi.org/10.52526/25792776-22.69.2-207

Clients/Mast/Portal.html).

Finally, for the first time we estimate the detection range of survey FBS for early and late-subclasses of M dwarfs adopting the limiting magnitude 17.5-18.0 in V-band. Adopting Mv = 8.0 for early-type M0 dwarfs (Reid et al., 2004), one can estimate the detection range up to $\sim 1000pc$, and adopting Mv = 19.0-20.0 for M8-M9 dwarfs, the detection range can be estimated up to 25 pc for survey FBS.

Acknowledgements

This work is supported by ERASMUS+2019-1-FRO-KA107-061818. KSG and KKG are grateful to Administration of OVSQ Observatory and LATMOS Laboratory (France) for organizing their visit. This research has made use of results from the SAO/NASA Astrophysics Data System Bibliographic Services, as well as the SIMBAD and VizieR databases, operated at CDS, Strasbourg, France, and Two Micron All Sky Survey, which is a joint project of the University of Massachusetts and the Infrared Processing and Analysis Center, funded by NASA and NSF. This research was made possible using the ASAS-SN and Catalina Sky Survey variability data bases. We used LAMOST telescope spectra. The LAMOST is a National Major Scientific project build by the Chinee Academy of Sciences. This work has made use of data from the European Space Agency (ESA) mission *Gaia* (https://cosmos.esa.int/gaia), processed by Gaia Data Processing and Analysis Consortium (DPAC, https://www.cosmos.esa.int/web/gaia.dpac.consortium). This paper includes data collected by the TESS mission, which are publicly available from the Mikulski Archive for Space Telescopes (MAST). This research has made use of the Washington Double Star Catalog maintained at the U.S. Naval Observatory.

References

Alonso-Floriano F. J., et al., 2015, Astron. Astrophys. , 577, A128

Astudillo-Defru N., et al., 2017, Astron. Astrophys. , 602, A88

Babusiaux C., van Leeuwen F., Barstow M. A., Jordi C., Zucker S., Zurbach C., Zwitter T., 2018, Astron. Astrophys. , 616, A10

Bailer-Jones C. A. L., Rybizki J., Fouesneau M., Demleitner M., Andrae R., 2021, Astron. J. , 161, 147

Bianchi L., Shiao B., Thilker D., 2017, Astrophys. J. Suppl. Ser. , 230, 24

Boller T., Freyberg M. J., Trümper J., Haberl F., Voges W., Nandra K., 2016, Astron. Astrophys. , 588, A103

Brown et al., 2021, Astron. Astrophys. , 650, C3

Cifuentes C., et al., 2020, Astron. Astrophys. , 642, A115

Cruz K. L., Núñez A., Burgasser A. J., Abrahams E., Rice E. L., Reid I. N., Looper D., 2018, Astron. J. , 155, 34

Cui X.-Q., et al., 2012, Research in Astronomy and Astrophysics, 12, 1197

Delfosse X., Forveille T., Ségransan D., Beuzit J. L., Udry S., Perrier C., Mayor M., 2000, Astron. Astrophys. , 364, 217

Espinoza N., et al., 2022, Astron. J. , 163, 133

Giclas H. L., Burnham R., Thomas N. G., 1971, Lowell proper motion survey Northern Hemisphere. The G numbered stars. 8991 stars fainter than magnitude 8 with motions ¿ 0".26/year

Gigoyan K. S., Abrahamyan H. V., Azzopardi M., Mauron N., Russeil D., Sinamyan P., 2003, Astrophysics, 46, 475

Gigoyan K. S., Mickaelian A. M., Kostandyan G. R., 2019, Mon. Not. R. Astron. Soc. , 489, 2030

Gliese W., Jahreiss H., 1991, NASA STI/Recon Technical Report A, 224, 161

Guerrero N. M., et al., 2021, Astrophys. J. Suppl. Ser. , 254, 39

Henry G. W., Fekel F. C., Sowell J. R., Gearhart J. S., 2006, Astron. J. , 132, 2489

Henry T. J., et al., 2018, Astron. J. , 155, 265

Jayasinghe T., et al., 2018, Mon. Not. R. Astron. Soc. , 477, 3145

Johnson H. R., Querci F. R., Jordan S., Thomas R., Goldberg L., Pecker J.-C., 1986, The M-type stars

Kirkpatrick J. D., Kelly D. M., Rieke G. H., Liebert J., Allard F., Wehrse R., 1993, Astrophys. J. , 402, 643

Lamman C., et al., 2020, Astron. J. , 159, 139

Lépine S., Shara M. M., 2005, Astron. J. , 129, 1483

Luo A. L., Zhao Y. H., Zhao G., et al. 2019, VizieR Online Data Catalog, p. V/164

Mann A. W., et al., 2018, Astron. J. , 155, 4

Markarian B. E., Lipovetsky V. A., Stepanian J. A., Erastova L. K., Shapovalova A. I., 1989, Soobshcheniya Spetsial'noj Astrofizicheskoj Observatorii, 62, 5

Martinez A. O., et al., 2017, Astrophys. J. , 837, 72

doi:https://doi.org/10.52526/25792776-22.69.2-207

Mason B. D., Wycoff G. L., Hartkopf W. I., Douglass G. G., Worley C. E., 2001, Astron. J. , 122, 3466

Muirhead P. S., et al., 2012, Astrophys. J. , 747, 144

Paegert M., Stassun K. G., Collins K. A., Pepper J., Torres G., Jenkins J., Twicken J. D., Latham D. W., 2021, arXiv e-prints, p. arXiv:2108.04778

Quirrenbach A., et al., 2014, in Ramsay S. K., McLean I. S., Takami H., eds, Society of Photo-Optical Instrumentation Engineers (SPIE) Conference Series Vol. 9147, Ground-based and Airborne Instrumentation for Astronomy V. p. 91471F, doi:10.1117/12.2056453

Reid I. N., et al., 2004, Astron. J. , 128, 463

Ricker G. R., et al., 2014, in Oschmann Jacobus M. J., Clampin M., Fazio G. G., MacEwen H. A., eds, Society of Photo-Optical Instrumentation Engineers (SPIE) Conference Series Vol. 9143, Space Telescopes and Instrumentation 2014: Optical, Infrared, and Millimeter Wave. p. 914320 (arXiv:1406.0151), doi:10.1117/12.2063489

Skrutskie M. F., et al., 2006, Astron. J. , 131, 1163

Smart R. L., Marocco F., Sarro L. M., Barrado D., Beamín J. C., Caballero J. A., Jones H. R. A., 2019, Mon. Not. R. Astron. Soc. , 485, 4423

Stassun K. G., et al., 2018, Astron. J. , 156, 102

Stassun K. G., et al., 2019, Astron. J. , 158, 138

Tarter J. C., et al., 2007, Astrobiology, 7, 30

Voges W., et al., 2000, , 7432, 3

Ward-Duong K., et al., 2015, Mon. Not. R. Astron. Soc. , 449, 2618

West A. A., et al., 2011, Astron. J. , 141, 97

Winters J. G., et al., 2019, Astron. J. , 157, 216

Zechmeister M., et al., 2019, Astron. Astrophys. , 627, A49

Zhong J., Li J., Carlin J. L., Chen L., Mendez R. A., Hou J., 2019, Astrophys. J. Suppl. Ser. , 244, 8

Ziegler C., et al., 2018, Astron. J. , 156, 259

The stellar content of UCHII regions: the molecular cloud GRSMC 045.49+00.05

N. Azatyan *[1], E. Nikoghosyan[1], L. Kaper[2], D. Andreasyan[1], A. Samsonyan[1], A. Yeghikyan[1], D. Baghdasaryan[1], and N. Harutyunyan[3]

[1]Byurakan Astrophysical Observatory, 0213 Aragatsotn Prov., Armenia
[2]Anton Pannekoek Institute for Astronomy, University of Amsterdam,, Science Park 904, 1098 XH Amsterdam, The Netherlands
[2]Department of Physics, Yerevan State University, 1 Alex Manoogian st.,, 0025, Yerevan, Armenia,

Abstract

Ultra-compact H II (UC HII) regions are an important phase in the formation and early evolution of massive stars. The main objectives of this work are to study the stellar content associated with the G045.49+00.04 and G045.14+00.14 star-forming regions located in the GRSMC 45.46+0.05 molecular cloud at a distance of about 8 kpc. Both regions contain a number of UC HII regions. The main objective is to characterize the embedded young stellar objects (YSOs), such as their mass, evolutionary age and age spread, spatial distribution, luminosity function. We used near-, mid-, and far-infrared photometric data to identify and classify the YSOs. Their main parameters were determined by the spectral energy distribution (SED) fitting tool using radiation transfer models. Totally, we identified 2864 YSOs. We also constructed a colour-magnitude diagram to compare the parameters of stellar objects with the results of the radiative transfer models. The density distribution of the identified YSOs showed the presence of dense clusters in the UC HII regions. The parameters of YSOs in the IRAS clusters and non-cluster objects surrounding them show some differences. In general, the YSOs in these clusters have an evolutionary age larger than 10^6 years with an age spread of a few Myr. The clusters include several high- and intermediate-mass zero-age main sequence stellar objects. The small age spread suggests that the clusters may originate from a single triggering event.

Keywords: *stars: pre-main sequence – Stars: luminosity function – Infrared: stars – radiative transfer*

1. Introduction

Massive stars are generally recognised to form inside dense ($n > 10^3\,cm^{-3}$) and cold ($T \sim 10$–$30\,K$) compact clumps in giant molecular clouds (GMCs) (e.g. Lada & Lada, 2003). Based on results obtained for different massive star-forming regions, star formation in these clumps appears to be triggered by compression from external shocks. If star formation is triggered by compression, the age spread of the new generation of stars should be small (Zinnecker et al., 1993).

Massive stars and the star clusters hosting them are thought to play an important role in the evolution of galaxies. They affect their environment by shaping the morphology, energy, and chemistry of the interstellar medium (ISM) through phenomena such as outflows, stellar winds, and supernovae (McKee & Tan, 2003). The energy injected into the surrounding neutral ISM may trigger the formation of new stars (Elmegreen & Lada, 1977).

The main challenges in studying high-mass star formation include: (i) the newly formed massive stars are deeply embedded in GMCs, (ii) massive stars are rare, and (iii) they begin burning their nuclear fuel, i.e. reach the zero-age main sequence (ZAMS) while still accreting (McKee & Tan, 2003, Peters et al., 2010). Understanding the formation and early evolution of massive stars requires detailed knowledge of the environments where star-forming events occur. Massive stars produce powerful Lyman continuum emission that is sufficiently energetic to ionise their surroundings and create observable ionised H II regions (Churchwell, 2002, Keto, 2007). Thus, UC HII regions are the sites of the early stages of massive star formation. These represent ideal natural laboratories to investigate the influence of hot massive stars on their environment.

*nayazatyan@bao.sci.am, Corresponding author

doi:https://doi.org/10.52526/25792776-22.69.2-217

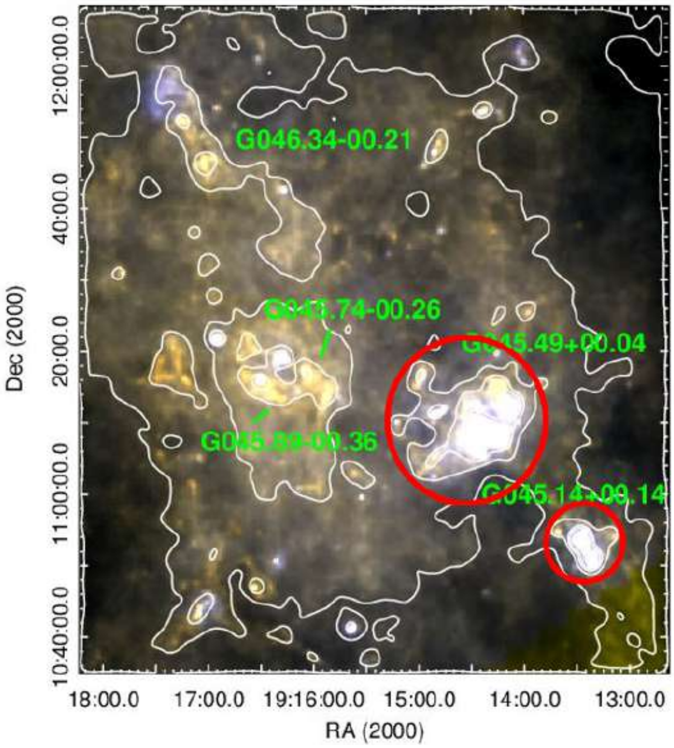

Figure 1. Colour-composite *Herschel* images of GRSMC 45.46+0.05 molecular cloud: 160 μm (blue), 350 μm (green), and 500 μm (red) bands. G045.49+00.04 and G045.14+00.14 star-forming regions are mentioned with red circles.

The main goal of this work is the study of stellar content in G045.49+00.04 and G045.14+00.14 star-forming regions which are part of the Galactic Ring Survey Molecular Cloud (GRSMC) 45.46+0.05 large star formation complex (Simon et al., 2001) at a distance of about 8 kpc (e.g., Wu et al., 2019). This complex is an ideal laboratory to investigate the early stages of massive star formations and their influence on natal environments since it contains a number of H II. Figure 1 shows G045.49+00.04 and G045.14+00.14 star-forming regions by red circles. Both regions also contain UC HIIs. The regions are sites of active star formation and have a complex hierarchical structure, containing a large number of high-mass stars at different stages of evolution. Based on data of stellar groups composition and putative triggers of star formation, we will be able to reconstruct the history of star formation in the regions.

In this paper, we present the results of a near-, mid-, and far-infrared (NIR, MIR, and FIR) study of the UC HIIs in G045.49+00.04 and G045.14+00.14 star-forming regions. We aim to better understand (i) the physical properties of dense molecular and ionised gas in the immediate neighbourhood of UC HII regions; (ii) the properties of embedded massive stars or star clusters; and (iii) whether the formation of the embedded massive stars or star clusters was triggered.

We have organised the paper as follows. Section 2 describes the used data; in Section 3 we present the methods; in Section 4, we analyse the stellar population in the regions. Finally, the study results are summarised in Section 5.

2. Used data

We used data covering a wide range of NIR to FIR wavelengths. The first database is the archival NIR photometric data in the J, H, and K bands of the Galactic Plane Survey DR6 (UKIDSS GPS, Lucas et al., 2008) with a resolution of 0.1″/px. This survey is complete to approximately 18 mag in the K band and provides a percentage probability of an individual object being a star, galaxy, or noise.

Archival MIR observations were obtained from the Galactic Legacy Infrared Midplane Survey Extraordinaire (GLIMPSE, Churchwell et al., 2009), using the *Spitzer* Infrared Array Camera (IRAC, Fazio et al., 2004). The four IRAC bands are centred at approximately 3.6, 4.5, 5.8, and 8.0 μm with a resolution of 0.6″/px. At longer wavelengths, we used data from a survey of the inner Galactic plane using the Multiband Infrared Photometer for *Spitzer* (MIPSGAL). We also used Wide-field Infrared Survey Explorer (WISE,

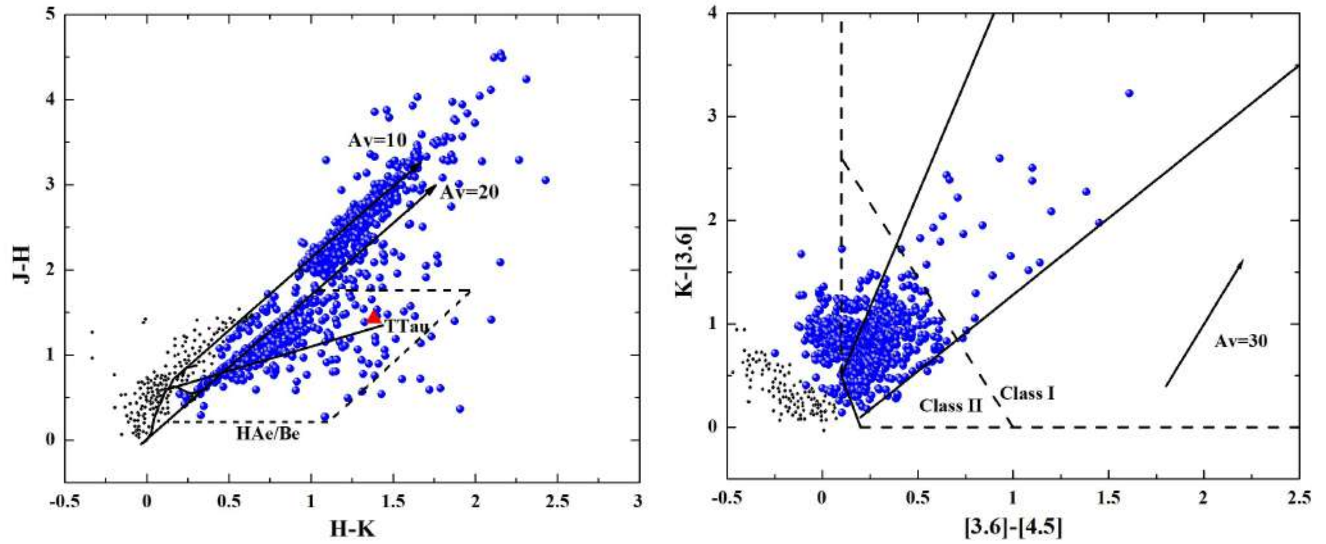

Figure 2. Two colour-colour diagrams of the G045.14+00.14 star-forming region. *Left panel*: (J-H) vs. (H-K) diagram. *Right panel*: K-[3.6] vs. [3.6]-[4.5] diagram. The blue circles are selected YSO candidates and black circles are non-classified ones. Not all non-classified objects are presented in these diagrams. IRAS 19111+1048 source is indicated by a red triangle.

Wright et al., 2010) data in the 3.4, 4.6, 12, and 22 μm bandpasses.

To study deeply embedded point sources, we used FIR observations, in the 70–500 μm range, obtained with the Photodetector Array Camera and Spectrometer (PACS, Poglitsch et al., 2010) and the Spectral and Photometric Imaging Receiver (SPIRE, Griffin et al., 2010) on board the 3.5 m *Herschel* Space Observatory (Pilbratt et al., 2010). For our analyses, we used photometric data and images from the PACS 70 and 160 μm catalogues, in addition to *Herschel* infrared Galactic Plane Survey (Hi-GAL, Molinari et al., 2016) data at 70, 160, 250, 350, and 500 μm.

3. Methods

The identification of stellar objects was performed with GPS UKIDSS-DR6 as the main catalogue, and then other MIR and FIR catalogues were cross-matched with it within 3 σ of the combined error–matching radius. The GPS UKIDSS-DR6 catalogue provides the probability of an object being a star, galaxy, or noise based on its image profile. The UKIDSS team recommends that sources classified as noise should be excluded since most of them are not real sources (Lucas et al., 2008). We selected objects with a < 30 % probability of being noise and a magnitude of $K < 18.02$ mag, taking into account the K band limit of the UKIDSS survey. In addition, we removed objects with zero errors of measured magnitudes in the J, H, and K bands. This yielded a total of approximately 134,000 objects.

One of the main observational characteristics of YSOs is an IR excess due to the presence of circumstellar discs and envelopes (Hartmann, 2009, Lada & Lada, 2003); furthermore, the measure of the IR excess in the NIR and/or MIR ranges can be used to characterise the evolutionary stage of a YSO (Class I and Class II). YSO candidates can be identified based on their position in colour–colour (c-c) diagrams. To confirm the selected YSOs and to determine their parameters, we constructed their SEDs and fitted them with the radiative transfer models of (Robitaille et al., 2007).

4. Results

Since c-c diagrams are useful tools to identify YSO candidates, we constructed six c-c diagrams, namely (J-H) vs. (H-K), K-[3.6] vs. [3.6]-[4.5], [3.6]-[4.5] vs. [5.8]-[8.0], [3.6]-[5.8] vs. [8.0]-[24], [3.4]-[4.6] vs. [4.6]-[12] and [3.4]-[4.6] vs. [4.6]-[22]. Figure 2 shows only two c-c diagrams of G045.14+00.14 star-forming region. The same approach has previously been successfully applied to other star-forming region (Azatyan, 2019, Azatyan et al., 2022).

The left panel of Figure 2 shows the (J-H) versus (H-K) c-c diagram and the distribution of objects.

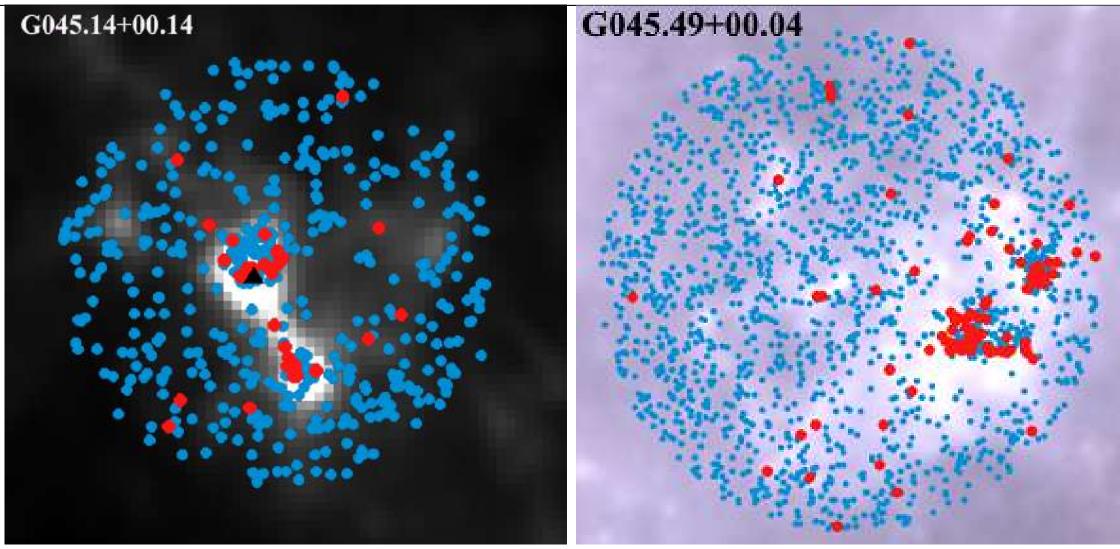

Figure 3. Distribution of YSOs in G045.14+00.14 *(left panel)* and G045.49+00.04 *(light panel)* regions on *Herschel* 500 μm images. Class I and Class II objects are indicated by filled red and blue circles, respectively. IRAS 19111+1048 source is indicated by a black triangle.

The solid and dashed curves represent the loci of the intrinsic colours of dwarf and giant stars (Bessell & Brett, 1988) converted to the CIT system (Carpenter, 2001); the parallel solid lines drawn from the base and tip of these loci are the interstellar reddening vectors (Rieke & Lebofsky, 1985). The locus of unreddened classical T Tauri stars (CTTSs) is taken from Meyer et al. (1997). The region where the intermediate-mass PMS stars, i.e. Herbig Ae/Be stars, are usually found is bounded by dashed lines (Hernández et al., 2005). Objects located to the right of the reddening vectors can be considered YSO candidates, since deviation from the MS and the presence of IR excess can be caused by the existence of a circumstellar disc and envelope. Among the objects located in the reddening band of MS and giants, we classified those that have a (J-K) > 3 mag colour index as Class I evolutionary stage YSOs (Lada & Adams, 1992). These are located in the upper right corner of the diagram.

The other example of our used c-c diagrams is K-[3.6] versus [3.6]-[4.5] which used data from the GLIMPSE catalogue to combine NIR and MIR photometry. This diagram is presented in the right panel of Figure 2, where the diagonal lines outline the YSO location region and the dashed line separates the Class I and Class II object domains. The arrow shows the extinction vector (Flaherty et al., 2007). All lines are taken from Gutermuth et al. (2008).

To minimise the likelihood of making an incorrect selection, we selected YSOs on the criterion of being stars classified as objects with IR excess by at least two c-c diagrams. However, since the region has saturated areas in the MIR band around the IRAS objects, this can lead to the potential loss of objects belonging to the molecular cloud. Accordingly, objects within those areas classified as YSOs based on only the NIR c-c diagram were included in the list of candidate YSOs. The selected YSOs are indicated with blue filled circles and non-classified objects - black circles (Figure 2). Totally, in the two parts of the molecular cloud, we identified 5108 YSO candidates with Class I and Class II evolutionary stages.

To confirm the selected YSOs and to determine their parameters, we constructed their SEDs and fitted them with the radiative transfer models of Robitaille et al. (2007). These models assume an accretion scenario in the star formation process, where a central star is surrounded by an accretion disc, an infalling flattened envelope, and the presence of bipolar cavities. We used the command-line version of the SED fitting tool where numerous precomputed models are available. This procedure was performed using wavelengths ranging from 1.1 μm to 500 μm. For the interstellar extinction, we chose an interval of 10–100 mag that would exceed the results obtained by COBE/DIRBE and IRAS/ISSA maps ($A_v = 10-50$ mag, Schlegel et al., 1998). The distance interval corresponds to the estimates made in the previous studies (6.5–9.5 kpc, see Introduction).

As we selected YSOs in the MIR–saturated regions using only their J, H, and K magnitudes, constructing their SEDs based on only three photometric data points does not provide a reliable basis for any conclusions (302 YSOs). Excluding these objects, we achieved relatively robust parameters for 2562 of the 4806 selected YSOs with χ^2 <100 that composes 53% of the total number. Overall, the final list comprised 2864 YSOs

doi:https://doi.org/10.52526/25792776-22.69.2-217

(2562 with constructed SEDs and 302 YSOs in the saturated regions). The mass range of the YSOs is from 1.5 to 24 $M_{\odot}$.

Figure 3 shows the distribution of the selected YSOs in the two star-forming regions, with Class I and Class II objects shown by filled red and blue circles, respectively. Excluding the regions in the vicinity of the IRAS sources, all types of stellar objects are distributed relatively homogeneously in the molecular cloud. Additionally, in the UC HII regions, close to the IRAS sources, the selected YSOs form relatively dense concentrations or clusters. The evolutionary age spread of the vast majority of stellar objects in the IRAS clusters is small; from ~1 to 7 Myr. Furthermore, the members of the IRAS clusters are more developed than the non-cluster objects.

The distribution of stellar population within the two star-forming regions on K versus J–K colour-magnitude diagram also shows certain different between the IRAS clusters and non-cluster regions. An overwhelming majority (more than 80%) of the non-cluster objects are younger then 0.1 Myr. In contrast, objects in the IRAS clusters are concentrated around the ZAMS.

5. Discussion and Conclusion

The search for and study of the young stellar population of the G045.49+00.04 and G045.14+00.14 star-forming regions located in the GRSMC 45.46+0.05 molecular cloud made it possible to obtain the following results:

- We obtained relatively robust parameters for 2562 YSOs with $\chi^2 < 100$. We also identified 302 YSOs located in the MIR-saturated regions based only on the J, H, and K photometric data.
- The stellar distribution shows the existence of dense clusters in the vicinity of the IRAS sources. The non-cluster objects are uniformly distributed in the molecular cloud.
- The study of the stellar parameters from different samples (i.e. clusters and non-cluster) showed differences between the two populations.
- Around 75% of the YSOs in the IRAS clusters are older than 0.1 Myr isochrone and are concentrated around the ZAMS.
- More than 80% of the non-cluster objetcs are younger than 0.1 Myr isochrone.

Based on the results, we concluded that dense clusters were formed in the UC HII regions, which include high- and intermediate-mass stellar objects. The evolutionary ages of these stars, in most cases, are several million years. The small spread of evolutionary ages suggests that the clusters owe their origin to a triggering shock.

The distribution of the non-cluster objects in the molecular cloud implies that their origin cannot be explained by the activity of the embedded massive star(s) in the UC HII regions. We assume that these uniformly distributed objects are part of the young stellar population of the GRSMC 45.46+0.05 molecular cloud. To understand the tracers of their origins, it is necessary to investigate the star formation history of the GRSMC 45.46+0.05 star-forming region as a whole.

In the coming works, we plan to find the trigger of star formation in the whole molecular cloud as well as the properties of Interstellar medium to reconstruct the star formation history.

Acknowledgements

This work was made possible by a research grant number № 21AG-1C044 from Science Committee of Ministry of Education, Science, Culture and Sports RA.

References

Azatyan N. M., 2019, Astron. Astrophys. , 622, A38

Azatyan N., Nikoghosyan E., Harutyunian H., Baghdasaryan D., Andreasyan D., 2022, Proc. Astron. Soc. Aust. , 39, e024

Bessell M. S., Brett J. M., 1988, Publ. Astron. Soc. Pac. , 100, 1134

Carpenter J. M., 2001, Astron. J. , 121, 2851

Churchwell E., 2002, Ann. Rev. Astron. Astrophys. , 40, 27

doi:https://doi.org/10.52526/25792776-22.69.2-217

Churchwell E., et al., 2009, Publ. Astron. Soc. Pac. , 121, 213

Elmegreen B. G., Lada C. J., 1977, Astrophys. J. , 214, 725

Fazio G. G., et al., 2004, Astrophys. J. Suppl. Ser. , 154, 10

Flaherty K. M., Pipher J. L., Megeath S. T., Winston E. M., Gutermuth R. A., Muzerolle J., Allen L. E., Fazio G. G., 2007, Astrophys. J. , 663, 1069

Griffin M. J., et al., 2010, Astron. Astrophys. , 518, L3

Gutermuth R. A., et al., 2008, Astrophys. J. , 674, 336

Hartmann L., 2009, Accretion Processes in Star Formation: Second Edition. Cambridge University Press

Hernández J., Calvet N., Hartmann L., Briceño C., Sicilia-Aguilar A., Berlind P., 2005, Astron. J. , 129, 856

Keto E., 2007, Astrophys. J. , 666, 976

Lada C. J., Adams F. C., 1992, Astrophys. J. , 393, 278

Lada C. J., Lada E. A., 2003, Ann. Rev. Astron. Astrophys. , 41, 57

Lucas P. W., et al., 2008, Mon. Not. R. Astron. Soc. , 391, 136

McKee C. F., Tan J. C., 2003, Astrophys. J. , 585, 850

Meyer M. R., Calvet N., Hillenbrand L. A., 1997, Astron. J. , 114, 288

Molinari S., et al., 2016, Astron. Astrophys. , 591, A149

Peters T., Banerjee R., Klessen R. S., Mac Low M.-M., Galván-Madrid R., Keto E. R., 2010, Astrophys. J. , 711, 1017

Pilbratt G. L., et al., 2010, Astron. Astrophys. , 518, L1

Poglitsch A., et al., 2010, Astron. Astrophys. , 518, L2

Rieke G. H., Lebofsky M. J., 1985, Astrophys. J. , 288, 618

Robitaille T. P., Whitney B. A., Indebetouw R., Wood K., 2007, Astrophys. J. Suppl. Ser. , 169, 328

Schlegel D. J., Finkbeiner D. P., Davis M., 1998, Astrophys. J. , 500, 525

Simon R., Jackson J. M., Clemens D. P., Bania T. M., Heyer M. H., 2001, Astrophys. J. , 551, 747

Wright E. L., et al., 2010, Astron. J. , 140, 1868

Wu Y. W., et al., 2019, Astrophys. J. , 874, 94

Zinnecker H., McCaughrean M. J., Wilking B. A., 1993, in Levy E. H., Lunine J. I., eds, Protostars and Planets III. pp 429–495

doi:https://doi.org/10.52526/25792776-22.69.2-217

The Precise Individual Masses and Theoretical Stability and Habitability of some Single-lined Spectroscopic Binaries

B. S. Algnamat, [*] A. A. Abushattal, A. F. Kraishan, and M. S. Alnaimat

Department of Physics, Al-Hussein Bin Tala University, P. O. Box 20, 71111, Ma'an, Jordan.

Abstract

Over the past few decades, some Spectroscopic Binaries (SBs) have been resolved using high-resolution techniques. Astrophysics is interested in this subject because we can obtain the mass of each component. By combining a visual solution with a complimentary one, such as the spectroscopic orbit or Edward method, we can determine the individual masses, semimajor axes, magnitudes, spectral types, radii, and temperatures. These provide the most probable physical parameters for some single-lined spectroscopic binaries. Then We can use these parameters to calculate theoretical the stability and habitability of the system. Additionally, we assume the composite spectrum, the apparent global magnitude, and the parallax (generally the Hipparcos, and recently the Gaia). The next step is to obtain the spectrum for each components. The Edwards method will be used in this case. As soon as we have two spectra foe two single-lined spectroscopic binaries (HIP 754 and HIP 3841), we can determine each mass based on the magnitude difference, Δm. For selected samples, we calculate the rest of the physical parameters needed to calculate the theoretical stability and habitability.

Keywords: *binaries, visual, single-lined spectroscopic, stars, physical parameters, stability, habitability*

1. Introduction

Binary systems exhibit periodic oscillations in radial velocity due to their orbital motion. These oscillations are evident in the Doppler shifts of spectral lines. A single-lined spectroscopic binary star has only one set of lines. The peculiar characteristics of their velocity and light curves exclude these from being categorized as single-lined spectroscopic binaries, even though many intrinsic variable stars have cyclic variations in radial velocity. We recognize most stars to be double stars today as single-lined spectroscopic binaries, though a few single stars with unusual characteristics may also qualify. Spectroscopic observations of double stars enable us to study their orbital motions. A BS is an ideal environment for searching for exoplanets. Astrometric, spectroscopic, and eclipsing binary systems are the three main types. Mass determination is a difficult technique. (Al-Wardat et al., 2017, Duquennoy & Mayor, 1991, Raghavan et al., 2010). A stellar mass can be determined from the orbits and parallaxes of binaries and multiple stars, which is one of the reasons why astronomy and astrodynamics are interested in them. The mass of stars affects studies of their evolution fundamentally. Also available are luminosity, parallaxes, sizes, and orbital elements, which can be used to evaluate parameters of interests, and orbital elements.(Al-Tawalbeh et al., 2021, Docobo et al., 2018, Hussein et al., 2022).

The search for stars that are in the main sequence and premain sequence is a method used by missions such as CoRoT, Kepler, and K2 to find exoplanets. In the past 50 years, speckle interferometry has been used by researchers around the world to observe binary stars effectively and accurately. Astrometric parallaxes for bright stars found systematic errors in Gaia, so both types of parallaxes were regarded as effective verification methods. Physical parameters have been determined with this research method in many publications over the years (Abushattal, 2017, Abushattal et al., 2019a, Docobo et al., 2017, Masda et al., 2016).

High resolution techniques have been used to resolve a number of spectroscopic binaries. However, before choosing a particular telescope to resolve SBs, we should consider the following questions. We would like to know how big a telescope we would need for each case. We would like to know what size telescope we would need. In order to prepare a telescope list, what is the best way to do it? The purpose of this paper is to

[*]bilal.s.algnamat@ahu.edu.jo, Corresponding author

doi:https://doi.org/10.52526/25792776-22.69.2-223

answer these questions by considering SBs with known orbits and parallaxes. We propose the maximum and minimum angular separations between these SBs using a three-dimensional model. Furthermore to describe the habitability and stability around single-lined spectroscopic binaries. A description of these systems is provided along with their spectral spectra, magnitudes, and masses. Spectroscopic orbits, composite spectra, and apparent magnitudes of each component can be used to calculate a visual orbit. Find the critical distances between the components by drawing the apparent orbit and calculating the critical angular distances. Additionally, we examine other optically resolvable systems and determine telescope sizes.

Many physical processes can be observed in a binary system, including mass loss, mass exchange, component variability, the Nova phenomenon, the Flare phenomenon, and X-ray binaries. Among the different aspects of the dynamical approach are perturbations, the discovery of dark components, such as brown stars and exoplanets, as well as orbit calculation (Abushattal et al., 2019b, Taani et al., 2019a,b, 2020). CoRoT, Kepler, and TESS are all capable of finding Earth-like planets within BSs, which occur in half of multiple stars. As multiple stars form, they often host the most massive exoplanets. Binary star systems are also powerful hosts of many exoplanets, due to the stages of star formation. Binary stars' properties determine their habitability and stability. A major objective of this work is to determine each planet's mass, semi-major axis, luminosities, and temperatures, which are the most important parameters.

2. Single-lined spectroscopic binaries

The following orbital parameters are known for a SB1 binary with an orbit: P (periastron period), T (periastron epoch), e (eccentricity), $A_1 = a_1.\sin(i)$ (a_1 represents the semimajor axis of the main component's orbit, and i indicates its inclination), Ω (periastron argument for the main component's orbit), and the mass function.

$$f(\mathcal{M}) = \frac{(\mathcal{M}_2.sin(i))^3}{(\mathcal{M}_1 + \mathcal{M}_2)^2} \tag{1}$$

Additionally, we know the global apparent magnitude, the parallax and the spectrum components (typically the Hipparcos and Gaia parallax). It is first necessary to obtain information on each star's individual spectrum before we can analyze its spectrum. In order to accomplish this, we will use the Edwards method (Abushattal et al., 2019a, Edwards, 1976).

The magnitude difference, Δm, must be used to assign the corresponding masses to each star. This necessitates an analysis of the current calibrations. Knowing the masses of components around the center of mass will allow us to determine the three semimajor axes: a (relative orbit), a_1, and a_2 (these last ones represent the orbits of the components around the center of mass). The semimajor axis of the orbit is a$''$ (in arc seconds) and the orbital inclination is i.

A 'visual binary' already exists in these conditions, except for the node. Two points should be noted, however.

- Due to the fact that we will determine the inclination using $\sin(i)$, there are two possible values for this element: i and $i^{'}$=180° - i. It is impossible to determine the direction of motion without optical resolution of the binary.

- Furthermore, we are unsure of the angle of the node (Ω), but this poses no problem. It can be taken as zero for our purposes.

Application of the methodology to the SB1, HIP 754 system

Using the Edward method, we will calculate the physical and orbital properties of binary stars based on their spectral type. In Abushattal (2017) the same method is used, but he began by using astrophysical relationships to calculate apparent magnitude and parallax.

As a single-lined spectroscopic binary system, HIP 754 has the following information, which can be found in Table 1: spectral type, global visual magnitude m, Hipparcos parallax (Gaia did not determine HIP 754 parallax), the orbital elements (P, T, e, $a_1.\sin(i)$, ω_1), and the mass function, ($f(\mathcal{M})$).

Due to the fact that HIP 754 is a SB1, Δm is assumed to equal 1.5. Consequently, the lower limit will be $\Delta m = 1.5$ and the upper limit will be $i = 90$. By using the Edwards process, $\Delta m = 1.5$ and S = 0.30. The absolute magnitude will be M_1 = M - 0.30 = 5.97 - 0.30 = 5.67. By means of our calibrations, the absolute apparent magnitude of 5.67 corresponds to the G8V spectral type with a mass of $\mathcal{M}_1 = 0.928 \pm 0.045\mathcal{M}_{\odot}$.

doi:https://doi.org/10.52526/25792776-22.69.2-223

Table 1. HIP 754. Physical and orbital parameters

Sp type	K0V
V (mag)	7.77$\pm$ 0.01
π_{Hip} (mas)	19.45$\pm$ 1.40
π_{Gaia}(mas)	-
P (days)	463.44 $\pm$ 0.18
T $_{(MJD)}$	56108.7 $\pm$ 0.9
e	0.293 $\pm$ 0.003
$a_1\sin(i)$(Gm)	70.48 $\pm$ 0.29
ω_1(degree)	274.7$\pm$ 0.8
$f(\mathcal{M})(\mathcal{M}_\odot)$	0.0652 $\pm$ 0.0008

Regarding the secondary component, its absolute magnitude will be $M_2 = M_1 + 1.5 = 7.17$. This value corresponds to the K4V spectral type with a mass of $\mathcal{M}_2 = 0.720 \pm 0.024\ \mathcal{M}_\odot$.
According to the expressions (3.14) and (3.15), we obtain the following values of the semi-major axes:

$$a = 1.3855 \pm 0.0076_{A.U},$$

$$a_1 = 0.6064 \pm 0.0294_{A.U}, \text{ and}$$

$$a_2 = 0.7791 \pm 0.0569_{A.U},$$

the orbital inclination is,

$$i = 51.1^\circ \pm 2.9^\circ or 128.9^\circ \pm 2.9^\circ.$$

The following Table shows the corresponding results for different initial values of Δm for HIP 754.

Table 2. Orbital inclination and intermediary parameters as a function of Δm

Δm	S	M_1	M_2	Sp_1	Sp_2	$\mathcal{M}_{1(\mathcal{M}_\odot)}$	$\mathcal{M}_{2(\mathcal{M}_\odot)}$	$a_{(A.U)}$	$\sin(i)$	i
1.5	0.27	5.70$\pm$0.02	7.70$\pm$0.03	G8V	K5V	0.914$\pm$0.045	0.677$\pm$0.019	1.3683$\pm$0.0070	0.810	54.1$\pm$3.0
2.0	0.23	5.74$\pm$0.02	8.24$\pm$0.02	G8V	K7V	0.910$\pm$0.044	0.606$\pm$0.016	1.3475$\pm$0.0067	0.878	61.4$\pm$3.2
2.5	0.18	5.79$\pm$0.02	8.79$\pm$0.02	G9V	K9V	0.901$\pm$0.043	0.559$\pm$0.020	1.3294$\pm$0.0068	0.927	68.0$\pm$3.9
3.0	0.14	5.83$\pm$0.02	9.33$\pm$0.02	G9V	M1V	0.884$\pm$0.042	0.500$\pm$0.024	1.3061$\pm$0.0078	0.999	$\cong$90

When $\sin(i) = 1$, Δm is very close to 3.0. So, the possible scenarios for HIP 754 are between $\Delta m = 1.5$ and $\Delta m = 3.0$.

Now, following the explanations of subsection, we will obtain the maximum and minimum values of ρ'' for different values of Δm (see Table 3).

Table 3. Semimajor axis and the maximum and minimum values of the angular separation, $\rho^{''}$, as a function of Δm

Δm	a"	ρ''_{max}	$\rho^{''}_{min}$
1.5	0.0266$\pm$0.0019	0.0267$\pm$0.0019	0.0081$\pm$0.0006
2.0	0.0262$\pm$0.0019	0.0261$\pm$0.0019	0.0077$\pm$0.0005
2.5	0.0259$\pm$0.0019	0.0255$\pm$0.0018	0.0046$\pm$0.0003
3.0	0.0254$\pm$0.0018	0.0249$\pm$0.0018	0.0014$\pm$0.0003

In conclusion, the most probable values of ρ''_{max} are between $0.''0272 \pm 0.0020$ and $0.''0249 \pm 0.0018$. In these conditions, a telescope of 4.30 m (or larger) of diameter will be necessary to try to optically resolve this system in the epochs when ρ'' is near to the maximum value.

3. Stability

An orbital parameters; eccentricity, semimajor axis, and inclination do not change significantly over time is considered stable system. The purpose of this section is to investigate and determine the likely stable

doi:https://doi.org/10.52526/25792776-22.69.2-223

Table 4. Physical Parameters SB1

Name (HIP)	$\pi_{Hip(mas)}$	$\pi_{Gaia(mas)}$	$m_{(mag)}$	Sp	Sp_1	Sp_2	$\mathcal{M}_1(\mathcal{M}_\odot)$	$\mathcal{M}_2(\mathcal{M}_\odot)$
754	19.45±1.40	-	7.77	K0V	G8V	K4V	0.93±0.05	0.72±0.03
				K0V	G8V	K7V	0.91±0.04	0.61±0.02
				K0V	G9V	M1V	0.88±0.04	0.50±0.02
3841	4.63±1.03	2.55±0.35	8.93	K2III	K4III	A6IV	1.73±0.26	2.09±0.13
				K2III	K2III	G3V	1.79±0.57	1.03±0.04
				K2III	K2III	M1V	1.88±0.40	0.50±0.02

Table 5. Dynamical Parameters For SB1

Name(*HIP*)	$a_{(AU)}$	$a_{1(AU)}$	$a_{2(AU)}$	$i_{(degree)}$	$\rho_{max(mas)}$	D(m)
754	1.386±0.008	0.606±0.029	0.779±0.057	51.1±2.9	0.0272±0.0020	4.3
3841	2.959±0.027	1.618±0.159	1.341±0.226	9.6±0.9	0.0120±0.0020	10.0

regions of two single-lined spectroscopic systems. Based on the empirical expression of (Holman & Wiegert, 1999), we can determine planetary orbit stability around binary systems. Three types of stable orbits were described by Dovark during the 1980s: The satellite orbits (S-type) involve the planet orbiting around one of the binary's components, The planet-type orbits (P-type) when the planet orbits the binary star around both components. Which is a circumbinary planet, and, The librator-type orbits (L- type) where the stable orbit is around the Lagrangian points (Dvorak, 1984).

Holman - Wiegert empirical expression In 2007, Holman and Wigeret came up with the same equation as Dvorak as a function of mass ratio and semimajor axis. This applies to both S- and P-type orbits (Holman & Wiegert, 1999, Wiegert & Holman, 1997).

In the inner region of the S-type, the expression is:

$$\begin{aligned}\frac{a_s}{a} &= (0.464 \pm 0.006) + (-0.380 \pm 0.010)\mu + (-0.631 \pm 0.034)e \\ &+(0.586 \pm 0.061)\mu e + (0.150 \pm 0.041)e^2 + (-0.198 \pm 0.047)\mu e^2.\end{aligned} \tag{2}$$

The expression for the P- type (the outer region) is:

$$\begin{aligned}\frac{a_i}{a} &= (1.60 \pm 0.04) + (4.12 \pm 0.09)\mu + (5.10 \pm 0.05)e + (-4.27 \pm 0.17)\mu e \\ &+(-2.22 \pm 0.11)e^2 + (-5.09 \pm 0.11)\mu^2 + (4.61 \pm 0.36)\mu^2 e^2.\end{aligned} \tag{3}$$

The stability of each orbit around a star is expressed in terms of two distance values, which are important to understand here:a_{max}(A.U) is the distance around a star at which the orbit of an exoplanet remains stable regardless of the presence of the second component. There is also the second value a_{min}(A.U) which represents the distance closest to the star at which the possibility of stable orbits of exoplanets exists, however a guarantee of stability is not available. We have to take into account the spectral type and the size of the star. This is because, in some cases, the radius of the star is very close to the minimum value for stability. Further, there may be a limit to the maximum stability of the star in some cases.

4. Habitability

During his time at the University of Edinburgh, Cockell provided a useful definition of habitability. An environment that is habitable can support metabolic activities for at least one known organism, enabling it to survive, grow, maintain, or reproduce. (Cockell et al., 2016).

It is necessary for the liquid state of water on an exoplanet in order to support life's basic processes; not cold or hot, and its temperature is determined by many factors, including radio activity and atmospheric

Table 6. Physical parameters for the 17 single-lined spectroscopic binaries

Name (HIP)	e	$a_{(A.U)}$	Δm	$\mathcal{M}_1(\mathcal{M}_\odot)$	$\mathcal{M}_2(\mathcal{M}_\odot)$
754	0.293±0.003	1.385±0.008	1.5	0.93±0.05	0.72±0.026
		1.306±0.008	3.0	0.88±0.04	0.50±0.024
3841	0.562±0.010	2.959±0.027	1.5	1.73±0.26	2.09±0.13
		2.526±0.046	9.0	1.88±0.40	0.50±0.02

doi:https://doi.org/10.52526/25792776-22.69.2-223

Table 7. The stability limits for exoplanet orbits around each component and both components, in the 17 single-lined spectroscopic binaries

Name (HIP)	$a_{1S_{max}(A.U)}$	$a_{1S_{min}(A.U)}$	$a_{1P_{min}(A.U)}$	$a_{2S_{max}(A.U)}$	$a_{2S_{min}(A.U)}$
754	0.272	0.230	4.306	0.220	0.175
	0.280	0.242	**4.519**	0.198	0.149
3841	0.319	0.090	**9.904**	0.350	0.138
	0.369	0.224	9.6350	0.202	0.029

Table 8. Stellar parameters used to study the habitable zone for the two single-lined spectroscopic binaries

HD	$a_{(A.U)}$	Sp_1	Sp_2	$T_1(K)$	$T_2(K)$	$L_1(L_\odot)$	L_2 $(L_\odot)$	$\mathcal{M}_1(\mathcal{M}_\odot)$	$\mathcal{M}_2(\mathcal{M}_\odot)$
754	1.386±0.008	G8V	K4V	5486	4798	0.47	0.090	0.93±0.05	0.72±0.03
		G9V	M1V	5384	4144	0.37	0.005	0.88±0.04	0.50±0.02
3841	2.959±0.027	K4III	A6IV	4798	8121	42.07	20.890	1.73±0.26	2.09±0.13
		K2III	M1V	5055	4144	41.69	0.005	1.88±0.40	0.50±0.02

constituents. A parameter's external value depends on where the radiation is coming from depending on its distance from the nearest star. In order to find exoplanets with liquid water, it is first necessary to determine their habitable zones (HZ). The HZ appears as a spherical shell around a single star or a binary star. To determine whether a binary system is habitable, several parameters must be considered: $\mathcal{M}_1(\mathcal{M}_\odot)$, $\mathcal{M}_2(\mathcal{M}_\odot)$, the period (P), the eccentricity (e), and the semimajor axis of the exoplanet's orbit (a)(Mason et al., 2013). As the planet migrates out of the habitable zone due to the tidal force, the semimajor axis and eccentricity can change due to the gravitational force generated by the host star. Because of this, exoplanets are becoming less habitable over time, and habitability is changing (Barnes et al., 2007, Barnes et al., 2008).

In binary systems with fewer than 50 AU between two stars, the gravity of one star perturbs the orbit of an exoplanet and prevents it from containing liquid water (Eggl et al., 2012).

For the purposes of determining a habitable zone for spectroscopic binaries, the following parameters are fixed: temperature derived from the table describing spectral types developed by (Gray, 2005), mass derived from our previous chapter methodology, and luminosity derived from the relation between luminosity and absolute magnitude.

$$\frac{L}{L_\odot} = -\frac{M_v - M_{v\odot} - (BC - BC_\odot)}{2.5}, \tag{4}$$

where, L is the luminosity of the star, M_v is the absolute magnitude ($M_{v\odot} = 4.82$), and BC is the bolometric correction ($BC_\odot$ = -0.08).

Using Tobias Muller and Nader Haghighipour's 2013 website (http://astro.twam.info/hz/), the habitable zone of single, double, and multiple stars is determined (see (Müller & Haghighipour, 2014). This website includes a habitable zone calculator, tables, plots, and videos that simulate the motion of exoplanets around stars. There are four different models available on this website: (Kasting et al., 1993, Kopparapu, 2013, Kopparapu et al., 2014, Selsis et al., 2007). It the HZ calculator on this website describe the stability using the Holman & Wiegert (1999) model.

As we mentioned before, the habitable zone provides the area around each component or around both components in which the existence of liquid water is possible. We have calculated all parameters which allow us to use a methodology of to describe the habitable zone around the stars of our sample of two single-ined spectroscopic binaries.

Our sample of two spectroscopic binaries allows us to describe the habitable zone around the stars using the methodology of (Müller & Haghighipour, 2014).

5. The Graphics of the Stability and Habitable Zones

As we discussed in the previous sections, stable orbits can be identified within habitable zones by combining stability zones and habitable zones see figure 1, and 2. In case the habitable and stable areas are compatible, there is a possibility of having an exoplanet with liquid water.

doi:https://doi.org/10.52526/25792776-22.69.2-223

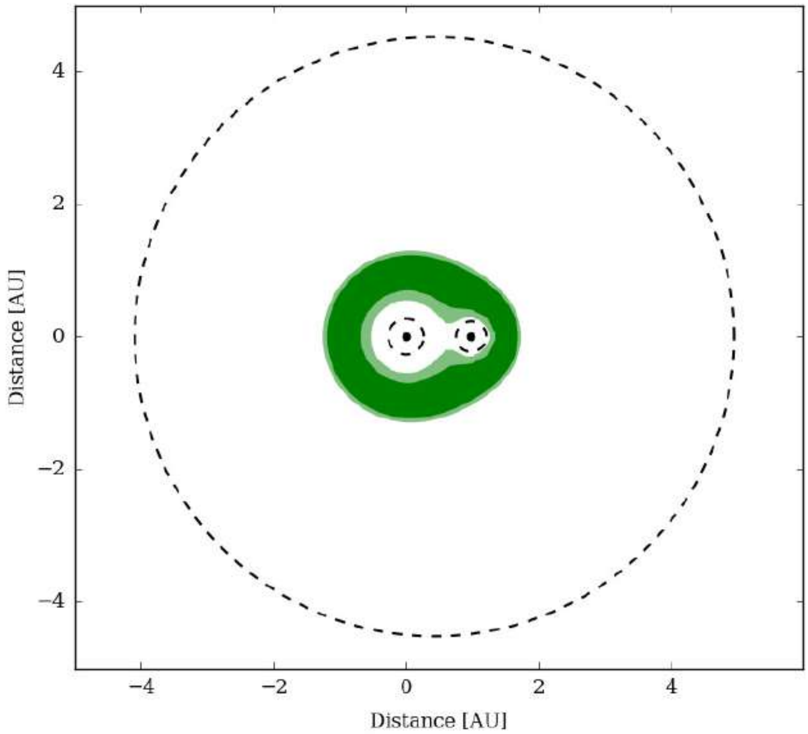

Figure 1.   Stability and Habitable Zones for SB1 HIP 754

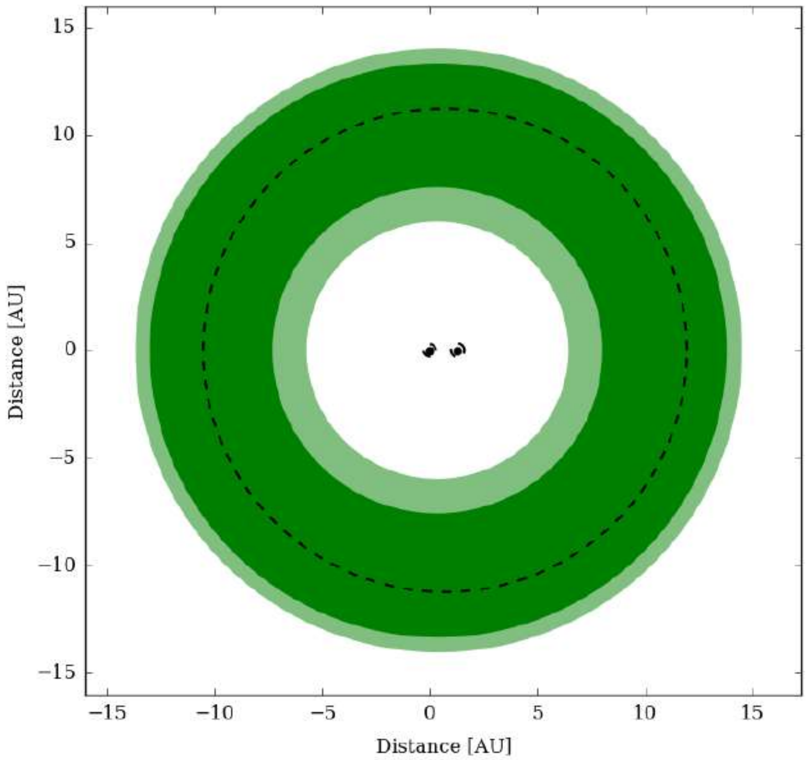

Figure 2.   Stability and Habitable Zones for SB1 HIP 3841

6. Conclusions and Future Work

We analyze two binary stars using the Edward method and perform a spectro-interferometric analysis to determine their physical and orbital properties. With the new method, stability, habitability and astronomical parameters such as orbital parallax and mass, as well as semi-major axis have been calculated for two single-lined spectroscopic systems with recent orbital calculation results. In this way, we can determine whether the host system is stable and habitable enough to host an exoplanet or the existance of earth-like planets.

doi:https://doi.org/10.52526/25792776-22.69.2-223

Acknowledgements

Thanks to Gor Mikayelyan, the Scientific and Local Organizing Committee of the International Conference "Space Sciences and Technologies" at Byurakan Astrophysical Observatory (BAO), Armenia.

References

Abushattal A. A., 2017, PhD thesis, Universidade de Santiago de Compostela

Abushattal A. A., Docobo J. A., Campo P. P., 2019a, The Astronomical Journal, 159, 28

Abushattal A., Al-Wardat M., Taani A., Khassawneh A., Al-Naimiy H., 2019b, in Journal of Physics: Conference Series. p. 012018

Akeson R., et al., 2013, Publications of the Astronomical Society of the Pacific, 125, 989

Akeson R., Christiansen J., Ciardi D. R., Ramirez S., Schlieder J., Van Eyken J. C., et al., 2017, in American Astronomical Society Meeting Abstracts.

Al-Tawalbeh Y. M., et al., 2021, Astrophysical Bulletin, 76, 71

Al-Wardat M., Docobo J., Abushattal A., Campo P., 2017, Astrophysical Bulletin, 72, 24

Baglin A., Auvergne M., Barge P., Michel E., Catala C., Deleuil M., Weiss W., 2007, in AIP Conference Proceedings. pp 201–209

Barlow R. J., 1993, Statistics: a guide to the use of statistical methods in the physical sciences. Vol. 29, John Wiley & Sons

Barnes R., Raymond S. N., Jackson B., Greenberg R., 2007, in AAS /Division for Planetary Sciences Meeting Abstracts #39. p. 468

Barnes R., Raymond S. N., Jackson B., Greenberg R., 2008, Astrobiology, 8, 557

Borucki W. J., et al., 2010, Science, 327, 977

Brescia M., Djorgovski S. G., Feigelson E. D., Longo G., Cavuoti S., 2017, Astroinformatics

Broeg C., et al., 2013, in EPJ Web of Conferences. p. 03005

Catala C., 2009, Experimental Astronomy, 23, 329

Christiansen J. L., 2022, Nature Astronomy, 6, 516

Cockell C. S., et al., 2016, Astrobiology, 16, 89

Docobo J. A., Griffin R. F., Campo P. P., Abushattal A. A., 2017, Monthly Notices of the Royal Astronomical Society, 469, 1096

Docobo J., Balega Y., Campo P., Abushattal A., 2018, Double Stars Information Circular, 196, 1

Duquennoy A., Mayor M., 1991, Astronomy and Astrophysics, 248, 485

Dvorak R., 1984, in , The stability of planetary systems. Springer, pp 369–378

Edwards T., 1976, The Astronomical Journal, 81, 245

Eggl S., Pilat-Lohinger E., Georgakarakos N., Gyergyovits M., Funk B., 2012, The Astrophysical Journal, 752, 74

Feigelson E. D., Babu G. J., 2012, Modern statistical methods for astronomy: with R applications. Cambridge University Press

Gardner J. P., et al., 2006, Space Science Reviews, 123, 485

Gray D. F., 2005, The observation and analysis of stellar photospheres. Cambridge University Press

Griffin R., 2014, The Observatory, 134, 109

Hartkopf W. I., Mcalister H. A., Mason B. D., 2004

Hatzes A. P., 2016, Space Science Reviews, 205, 267

Holman M. J., Wiegert P. A., 1999, The Astronomical Journal, 117, 621

Howell S. B., et al., 2014, Publications of the Astronomical Society of the Pacific, 126, 398

Hussein A. M., Al-Wardat M. A., Abushattal A., Widyan H. S., Abu-Alrob E. M., Malkov O., Barstow M. A., et al., 2022, The Astronomical Journal, 163, 182

Jack D., Hernández Huerta M. A., Schröder K.-P., 2020, Astronomische Nachrichten, 341, 616

Kalirai J., 2018, Contemporary Physics, 59, 251

Kasting J. F., Whitmire D. P., Reynolds R. T., 1993, Icarus, 101, 108

Kopparapu R. K., 2013, The Astrophysical Journal Letters, 767, L8

doi:https://doi.org/10.52526/25792776-22.69.2-223

Kopparapu R. K., Ramirez R. M., SchottelKotte J., Kasting J. F., Domagal-Goldman S., Eymet V., 2014, The Astrophysical Journal Letters, 787, L29

Masda S. G., Al-Wardat M. A., Neuhäuser R., Al-Naimiy H. M., 2016, Research in Astronomy and Astrophysics, 16, 012

Mason P. A., Zuluaga J. I., Clark J. M., Cuartas-Restrepo P. A., 2013, The Astrophysical Journal Letters, 774, L26

Matson R., Williams S., Hartkopf W., Mason B., 2020, United States Naval Observatory, Washington, DC

Müller T. W., Haghighipour N., 2014, The Astrophysical Journal, 782, 26

Muller R., Cersosimo J., Rosado-de Jesus I., Cotto D., Miranda V., Martinez C., Centeno D., 2006, Journal of Double Star Observations, 2, 138

Pourbaix D., et al., 2004, Astronomy & Astrophysics, 424, 727

Raghavan D., et al., 2010, The Astrophysical Journal Supplement Series, 190, 1

Rein H., 2012, arXiv preprint arXiv:1211.7121

Ricker G. R., et al., 2014, Journal of Astronomical Telescopes, Instruments, and Systems, 1, 014003

Schneider J., 2007, http://exoplanet. eu

Schneider J., Dedieu C., Le Sidaner P., Savalle R., Zolotukhin I., 2011, Astronomy & Astrophysics, 532, A79

Selsis F., Kasting J. F., Levrard B., Paillet J., Ribas I., Delfosse X., 2007, Astronomy & Astrophysics, 476, 1373

Straizys V., Lazauskaite R., 2009, arXiv preprint arXiv:0907.2398

Swain M., et al., 2009, The Astrophysical Journal, 704, 1616

Szebehely V., 1984, Celestial mechanics, 34, 49

Taani A., Abushattal A., Mardini M. K., 2019a, Astronomische Nachrichten, 340, 847

Taani A., Karino S., Song L., Mardini M., Al-Wardat M., Abushattal A., Khasawneh A., Al-Naimiy H., 2019b, in Journal of Physics: Conference Series. p. 012029

Taani A., Khasawneh A., Mardini M., Abushattal A., Al-Wardat M., 2020, arXiv preprint arXiv:2002.03011

Tinetti G., Tennyson J., Griffith C. A., Waldmann I., 2012, Philosophical Transactions of the Royal Society of London A: Mathematical, Physical and Engineering Sciences, 370, 2749

Varley R., 2015, Astrophysics Source Code Library, pp ascl–1512

Vavilova I., 2016, Odessa astronomical publications, pp 109–115

Wiegert P. A., Holman M. J., 1997, Astron. J. , 113, 1445

Wolszczan A., Frail D. A., 1992, Nature, 355, 145

Wright J. T., Gaudi B. S., 2012, arXiv preprint arXiv:1210.2471

doi:https://doi.org/10.52526/25792776-22.69.2-223

A planetary resonant effect in Parker stellar dynamo

D.D. Sokoloff *[1, 3], A.Yu. Serenkova†[1], and E.V. Yushkov‡[1,2]

[1]Moscow State University named after 'M. V. Lomonosov', Moscow, Russia.
[2]Space Research Institute of the Russian Academy of Sciences, Moscow, Russia.
[1]IZMIRAN, Moscow, Russia

Abstract

The effect of periodic pumping on dynamo generation in the simplest Parker model is studied in this work. Pumping is understood in the sense that the periodic parameters oscillations in the dynamo system leads to a change in the rate of the exponential growth of the mean magnetic field. And since the Parker model simultaneously describes its time oscillations as the field grows, this phenomenon is very similar to parametric resonance in the classical model of a harmonic oscillator. With the help of asymptotic analysis and numerical simulation, we demonstrate both pump regions similar to parametric resonance, as well as different amplification regions at high driving force frequencies, and suppression regions at low frequencies, find the gain maximum and investigate the behavior of the critical pump frequency separating the regions of generation and suppression.

Keywords: *MHD dynamo, Parker dynamo model, parametric resonance.*

1. Introduction

Solar activity cycle as well as stellar activity cycles are believed to be driven by stellar dynamo action based on stellar differential rotation and mirror asymmetric convection. The point however is that, the length of solar activity cycle (about 11 year) is quite close to the Jupiter orbital period and many astronomers supposed that the physical nature of solar activity cycle is somehow associated with the Jupiter influence on solar magnetohydrodynamics. Obridko et al. (2022) recently demonstrated that solar activity cycle is the only known case among a dozen similar cases accessible for contemporary observations where an activity cycle is observable and its length is closed to the planets orbital period and we have to accept that we face just a coincidence in solar case.

Obridko et al. (2022) stress however that this result do not exclude that a planetary effect on stellar dynamo is possible in principle. The aim of this short paper is to show that a weak periodic modulation of stellar dynamo drivers indeed can affect the dynamo threshold and transform a slightly subcritical dynamo action in a supercritical one.

2. Dynamo model

Obviously, a gravitation of an exoplanet or a star in a binary system leads to a weak modulation of stellar dynamo drivers which can be in principle include in dynamo model (e.g. Moss et al., 2002). The problem is how to separate this weak influence from various nonstationary phenomena associated with dynamo action. Our aim here is to demonstrate a physical phenomena rather to suggest a realistic model of a particular explanatory system and we sole the above problem as follows. We consider the simplest stellar dynamo model originated by Parker (1955) and include a weak periodic modulation of differential rotation.

The model proposed by Parker (1955) to describe the solar dynamo cycle is a direct consequence of the averaged magnetic induction equation written for the poloidal and toroidal components of the magnetic field. In the approximation of azimuthal symmetry - independence of the angle φ, and of a thin spherical layer -

*sokoloff.dd@gmail.com, Corresponding author
†serenkova.ai19@physics.msu.ru
‡yushkov.msu@mail.ru

doi:https://doi.org/10.52526/25792776-22.69.2-231

independence of the radial distance r, the only remaining spatial variable θ can be taken into account through the expansion of the magnetic field components in the first few harmonics. The simplest approximation describing the physical structure of the dynamo cycle can be obtained for only two components and is called the low-mode approximation. This is the minimal set of the Fourier modes sufficient to obtain a growing oscillating solution with nonzero magnetic moment (Nefedov & Sokoloff, 2010). Thus, for a dimensionless average magnetic field expanded in terms of symmetric (for A) and antisymmetric (for B) harmonics with respect to the equator

$$\mathbf{B} = B\mathbf{e}_\varphi + [\nabla, A\mathbf{e}_\varphi] = (b_1 \sin(2\theta) + b_2 \sin(4\theta))\,\mathbf{e}_\varphi + [\nabla, (a_1 \sin(\theta) + a_2 \sin(3\theta))\,\mathbf{e}_\varphi], \tag{1}$$

This yields in the following simple dynamical system

$$\begin{array}{ll} \dot{a}_1 = (R_\alpha/2)b_1 - \mu^2 a_1, & \dot{b}_1 = R_\omega(a_1 - a_2) - \mu^2 b_1, \\ \dot{a}_2 = (R_\alpha/2)(b_1 + b_2) - \mu^2 a_2, & \dot{b}_2 = 2R_\omega a_2 - \mu^2 b_2. \end{array} \tag{2}$$

Two dimensionless control parameters of the system R_α and R_ω are responsible for the hydrodynamic helicity in the convective shell and for the differential rotation, while it is well known that if their product, the dynamo number D, is large enough, then the magnetic field in the system will increase exponentially. The third parameter μ is responsible for diffusion and, in general, must take into account all components of the Laplacian: radial, axial, and crosswise. Depending on the specific model, μ can be considered the same for all four equations (if the main part of diffusion is radial) or different (if the axial part of the Laplacian determines the main contribution, since the second derivatives with respect to θ will be different for different harmonics). Here we assume the equality of all diffusion coefficients, and then we make an assumption about what will change if these coefficients differ for each of the equations of the system.

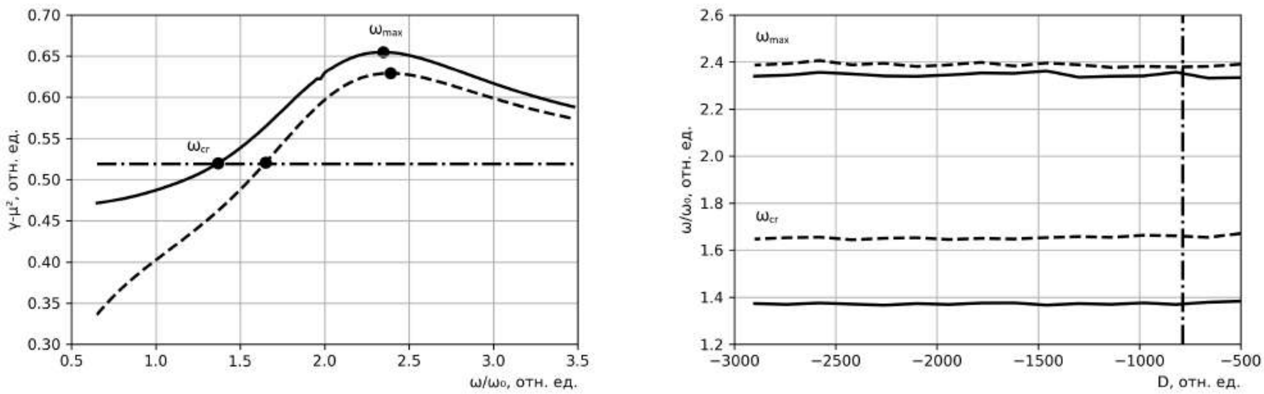

Figure 1. The left panel: dependence of the exponential growth rate $\gamma - \mu^2$ on the parametric excitation frequency ω. The dash-dotted horizontal line is the growth rate without parametric pumping $\sigma = 0$. The right panel: dependence of the critical excitation frequency ω_{cr} and the frequency of maximal growth ω_{max} on the dynamo-number $D = R_\alpha R_\omega$. The dash-dotted vertical line shows the dynamo-number when the dynamo-growth stops. The black solid and dashed lines are the numerical and analytic results respectively. The frequencies are normalised on correspondingly eigenfrequencies ω_0.

Having expressed two components: $b_1(t)$ and $b_2(t)$ from the first two equations, we substitute them into the second two. We obtain a system of two equations of the second order, which, after the replacement $a_{1,2}(t) = f_{1,2}(t)\exp(-\mu^2 t)$, can be reduced to a Mathieu-type system:

$$\begin{array}{l} \ddot{f}_1 - (R_\alpha R_\omega/2)(1 + \sigma \sin(\omega t))(f_1 - f_2) = 0, \\ \ddot{f}_2 - (R_\alpha R_\omega/2)(1 + \sigma \sin(\omega t))(f_1 + f_2) = 0. \end{array} \tag{3}$$

For such a system, in the absence of a periodic force $\sigma = 0$, it is easy to calculate the eigenfrequencies ω_0 and the generation rates γ_0 of the harmonic solution:

$$\lambda_0 = \gamma_0 \pm i\omega_0 = \pm\sqrt{-\frac{R_\alpha R_\omega}{\sqrt{2}}}\exp(\pm 3i\pi/8). \tag{4}$$

doi:https://doi.org/10.52526/25792776-22.69.2-231

For $\sigma \neq 0$, the solution to the system can be sought in the form of a harmonic with a shifted frequency and a changed generation rate, however, unlike the analysis of parametric resonance for a harmonic equation, this method does not give anything. Therefore, we are looking for a solution (3) as a sum of not two, but four complex conjugate exponents with exponents $\gamma \pm i\beta \pm i\omega/2$. Then, if the external periodic action has a double frequency ω, then, neglecting the higher harmonics and collecting the terms from each of the four exponentials, we obtain the solvability of the system for

$$\gamma + i\beta = \pm\sqrt{\lambda_0^2 \pm i\gamma_0\omega\sqrt{1 \pm \frac{iR_\alpha^2 R_\omega^2\sigma^2}{8\lambda_0^2\omega^2}} - \frac{\omega^2}{4}}. \tag{5}$$

For small σ, this asymptotic expression for the exponent of the exponential solution can be approximately written as

$$\gamma + i\beta = \lambda_0 \pm \frac{i\omega}{2} \pm \frac{R_\alpha^2 R_\omega^2\sigma^2}{32\lambda_0\omega(\lambda_0 \pm i\omega/2)} + o(\sigma^2). \tag{6}$$

Thus, periodic pumping of the Parker model selects two harmonics with frequencies shifted by 2β relative to each other and γ generation rates close to γ_0. The appearance of diffusion proportional to μ^2, see the system (2), only leads to a decrease in the generation rate by μ^2 – it transforms in $(\gamma - \mu^2)$ – while the very nature of the beats remains the same. Note that in the course of the analytical evaluation, we neglect the higher harmonics in $i\omega/2$, so in the formula (6), the signs should be chosen such that only the lower harmonics remain. It can be seen that for $\sigma = 0$ the solution completely coincides with λ_0 defined by Eq. (4), while for $\sigma \neq 0$ the real part of the solution (6) is greater than λ_0 for ω is greater than some critical frequency, and less than λ_0 for ω less than this critical frequency. In the region of the doubled frequency of the external force, the positive addition to the generation rate has a local maximum, and then, at $\omega \to \infty$, the generation rate tends to γ_0.

The described features of the dependence of external pumping on the frequency of the driving force are clearly visible in the figure 1, left panel: the analytical results are shown in the figure by dashed line, and the numerical results of calculating the generation rate are shown by a black solid line. The divergence of the solutions is due to the asymptotic nature of the results obtained, therefore, a decrease in σ leads to the fact that the two curves tend to each other and simultaneously converge to the straight line $Re\,\gamma = \lambda_0$, dashed-dotted horizontal line. A distinctive feature of such a response to a parametric action is the absence of a clearly defined narrow resonance maximum at multiple frequencies, which, however, is explained by the degeneracy of the symmetric system and the absence of a pure harmonic solution for the system (3).

By the degeneracy of the system, we mean that the fourth-order equation for the eigenvalues of the system (2) has roots with real parts and frequencies that coincide in absolute value, respectively, among them there is no fastest growing harmonic with a selected frequency, since two equally growing harmonics have the same frequency. As a result, under parametric pumping, they do not have a solution in the form of a quasi-harmonic signal, as in the classical case of parametric resonance, but instead, beats with a specific resonance pattern are observed. If the diffusion μ for each equation of the system (2) differs, then a distinguished frequency will appear with the fastest growing harmonic, and the parametric resonance will acquire classical features with distinguished narrow peaks at doubled and multiple frequencies. Indeed, a numerical test showed that for different diffusion coefficients – the resonance pattern is a superposition of the pattern 1 and sharp peaks at double and multiple frequencies. At the same time, the gain maximum at ω_{max} corresponding to the figure 1 and the presence of the critical frequency ω_{cr} (below which the generation rate is suppressed by the periodic influence, and above which it is enhanced) remain.

Finally, let's pay attention to the resulting asymptotic formula for the exponential growth rate (6), the real part of which is shown in the figure 1. The graph has a wide maximum, in comparison with the classical resonant peak, near the frequency $\omega = 2.4\omega_0$ and a critical boundary $\omega = 1.6\omega_0$, which separates the region of amplification and suppression of generation. The position of these characteristic markers depends on the natural frequency ω_0, and, accordingly, on the dynamo number $D = R_\alpha R_\omega$, but its minimum value is limited by the generation region – see the analytical and numerical estimate of the critical frequency in the figure 1, right panel. In other words, at sufficiently high frequencies of the excitation force, greater than this critical frequency, a periodic change in R_α will lead to an increase in generation at frequencies close to the natural frequency ω_0. Of course, in the case of nonlinear suppression $D = R_\alpha R_\omega$ the natural frequency of the system will also change, but the generation will still be enhanced at sufficiently high frequencies. In this case, it is difficult to predict in advance what kind of amplification - at high frequencies near a wide maximum or

doi:https://doi.org/10.52526/25792776-22.69.2-231

at a doubled frequency near a resonant peak - will be the main one, since this will be determined by the diffusion part, but both can be present in the general formulation.

3. Conclusion and Discussion

We demonstrated that even a weak planetary effect on dynamo drivers can in principle lead to substantial modification of dynamo driven magnetic field, i.e. transform a decaying magnetic field in a growing one and *vice versa*. Indeed, playing with parameter μ responsible for turbulent losses in our dynamical system we can make the dynamo number D for unperturbed system to be just a threshold one and dynamo driven magnetic field to be just marginally stable. Then if the frequency of parametric excitation is large enough we obtain excitation (right part of Fig. 1) and decay if the frequency is low enough (left part of Fig. 1). If the unperturbed dynamo system is slightly subcitical a moderate σ can be still sufficient to get an excitation. Of course, if perturbation is weak the subcritical dynamo should be very close to the excitation level so the effect hardly can happen in many exoplanetary systems.

Acknowledgements

DS acknowledge a financial support from Basis Foundation under grant 21-1-1-4-1 for analytical results, and EY acknowledge a financial support from Basis Foundation under grant 21-1-3-63-1 for the numerical verification.

References

Moss D., Piskunov N., Sokoloff D., 2002, Astron. Astrophys. , 396, 885

Nefedov S. N., Sokoloff D. D., 2010, Astronomy Reports, 54, 247

Obridko V. N., Katsova M. M., Sokoloff D. D., 2022, Mon. Not. R. Astron. Soc. , 516, 1251

Parker E. N., 1955, Astrophys. J. , 122, 293

doi:https://doi.org/10.52526/25792776-22.69.2-231

The Exoplanets Catalogues and Archives: An Astrostatistical Analysis

A.A Abushattal [*], A. F. Kraishan, and O. S. Alshamaseen

Department of Physics, Al-Hussein Bin Tala University, P. O. Box 20, 71111, Ma'an, Jordan.

Abstract

The discovery of more than 5000 exoplanets based on several methods will improve our understanding of the formation and evolution of the exoplanets. Due to the dramatically increases in the amount of the astronomical data in recent decades. Which can be analyzed statistically to extract scientific information and test astrophysical theories. This information is valuable to figure out if there is a life somewhere else on the universe. This work presents a statistical analysis of all these exoplanets based on three primary data sources: NASA Exoplanet Archive, Open Exoplanet Catalogue, and Exoplanet.eu catalogue. Moreover, several parameters are examined, including mass, radius, discovery method, distance, orbital period, and discovery year. As part of our analysis, we have also clarified and summarized the data in the form of graphs based on astrophysical correlations.

Keywords: *extra-solar Planets, statistical Analysis, exoplanet archive, exoplanet catalogues*

1. Introduction

The term extrasolar planet is used to describe any planet that orbits a star other than the Sun and is outside of the solar system. In 1992, extrasolar planets were discovered for the first time by the researchers Wolszczan, as well as D. A Frail, when they confirmed the existence of a planetary system around the PSR 1257+1 millisecond pulsar (Wolszczan & Frail, 1992). More than 5,000 have been identified, and almost 9,000 have yet to be identified. It has become an increasingly relevant research area around the world in recent years to study the possibility of finding a planet similar to our planet, "The Earth".

To find Earth-sized planets near sun-like stars many scientific planet-hunting missions were designed such as CoRoT (Convection, Rotation and planetary Transits), a CNES-led mission launched in 2006, was the first space telescope to detect exoplanets. The transit method was used to uncover exoplanets while focused on studying stars(Baglin et al., 2007), The Kepler mission from NASA in 2009 has been responsible for a quarter of all exoplanet discoveries. Due to the long duration of the scan, it is sensitive to even faint stars over a wide area of sky(Borucki et al., 2010), K2 (Howell et al., 2014), Transiting Exoplanet Survey Satellite (TESS) Launched in April 2018, NASA's Transiting Exoplanet Survey Satellite is a mission to search for exoplanets. As a first-of-its-kind satellite, it conducts transit surveys throughout the sky(Ricker et al., 2014), PLAnetary Transits and Oscillations of stars (PLATO) Planetary Transits and Oscillations of Stars is a mission designed for searching for planets with liquid water within the habitable zone of Sun-like stars. Moreover, it will provide insight into the evolutionary state of the entire extrasolar system by analyzing the planet's host star, including its age(Catala, 2009), and CHaracterising ExOPlanet Satellite (CHEOPS), December 2019 marked the launch of the satellite and April 2020 marked the start of operations. Any bright star, particularly one that hosts exoplanets in the Earth-to-Neptune size range, can be observed. The ability to observe the same targets repeatedly makes CHEOPS the most effective instrument for studying individual exoplanets. This is because it knows exactly where and when to look for transits. These planets will be measured precisely and combined with mass measurements calculated by other observatories, enabling a first characterization of their nature to be made. A CHEOPS mission will also identify candidates for future missions to explore further. As a result, the James Webb Space Telescope will have well-characterized targets to study more thoroughly (Abushattal et al., 2019b, Broeg et al., 2013, Hatzes, 2016).

[*]Ahmad.Abushattal@ahu.edu.jo, Corresponding author

doi:https://doi.org/10.52526/25792776-22.69.2-235

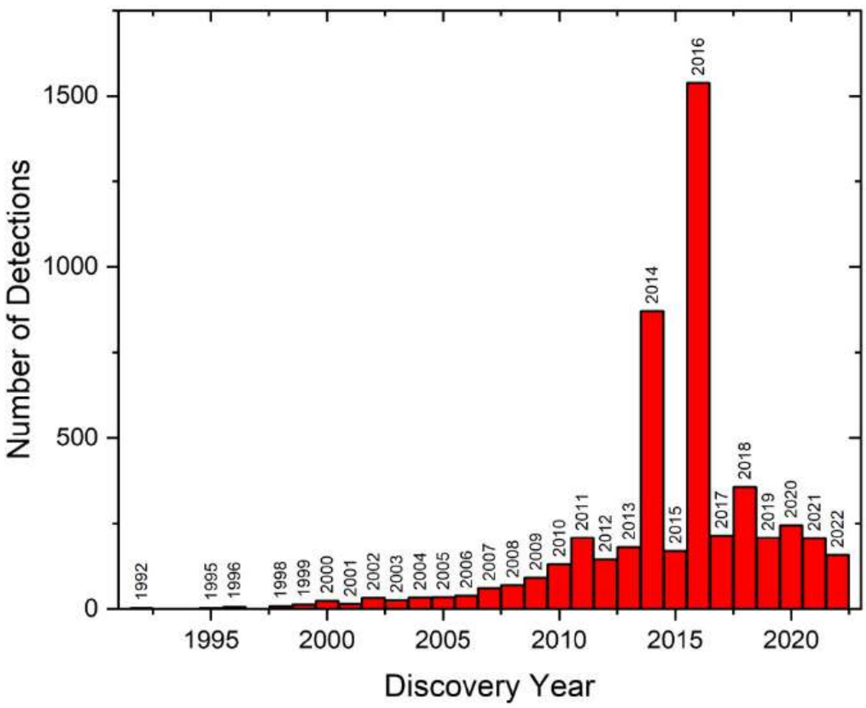

Figure 1. Detection Per Year.

James Webb Space Telescope was launched by NASA, ESA, and CSA in 2021 to study exoplanets and their atmospheres. In order to investigate these extrasolar bodies, Webb will use four instruments operating at infrared wavelengths. The observation of transiting planets with similar size and mass characteristics using highly sensitive spectroscopic methods. Using infrared wavelengths, Webb will measure absorption, reflection, and emission spectra of exoplanet atmospheres. Additionally, some exoplanets that orbit at larger distances from their parent star will be visible directly by it (Gardner et al., 2006, Kalirai, 2018). Detecting extrasolar planets is commonly done using Direct Imaging, Microlensing, Radial Velocity, and Transit techniques (Wright & Gaudi, 2012). Masses, radiuses, densities, and orbital parameters of exoplanets. As well as their orbits, a number of exoplanets were determined around single, double, and multiple systems. The physical properties of the outer planets can be calculated either by astronomical calculations or by imaging. According to astronomy calculations, for example, more than 50% of stars are binary stars (Al-Tawalbeh et al., 2021, Docobo et al., 2018, Hussein et al., 2022), which are observed and then their physical characteristics and orbital characteristics are determined, which allows us to determine when the planets are stable and their eligibility around these systems (Abushattal, 2017, Abushattal et al., 2019a, Docobo et al., 2018). The exoplanets are affected by physical processes, including mass loss and exchange, variability of components, relativistic processes, X-ray Binaries stability.(Abushattal et al., 2019b, Taani et al., 2019a,b, 2020). The Extrasolar Planets Encyclopaedia (Schneider, 2007), NASA Exoplanet Archive (Akeson et al., 2013), and The Open Exoplanet Catalogue (Rein, 2012) are helpful websites that provide a database of extrasolar planets of single stars.

Astrophysics theories can be tested quantitatively using statistical methodology, which has deep roots in probability theory. Statistics has become increasingly sophisticated and comprehensive in recent decades. After introducing mathematical statistics from a historical perspective, this review discusses hypothesis tests, point estimation, and elements of probability theory (Barlow, 1993, Feigelson & Babu, 2012).

Identifying new exoplanets around a wide variety of stars relies on modern astrostatistics to turn huge amounts of information into something useful for astronomers. The goal of this work is to collect data from different sources and analyze them statistically in order to provide a summary of the physical and orbital characteristics of exoplanets.

doi:https://doi.org/10.52526/25792776-22.69.2-235

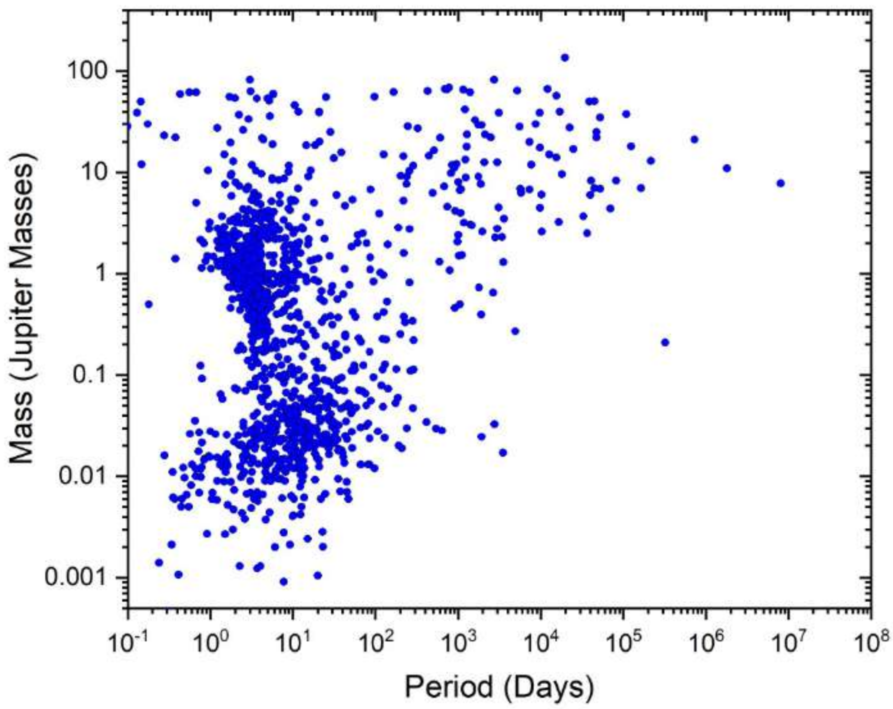

Figure 2. Mass - Period Distribution.

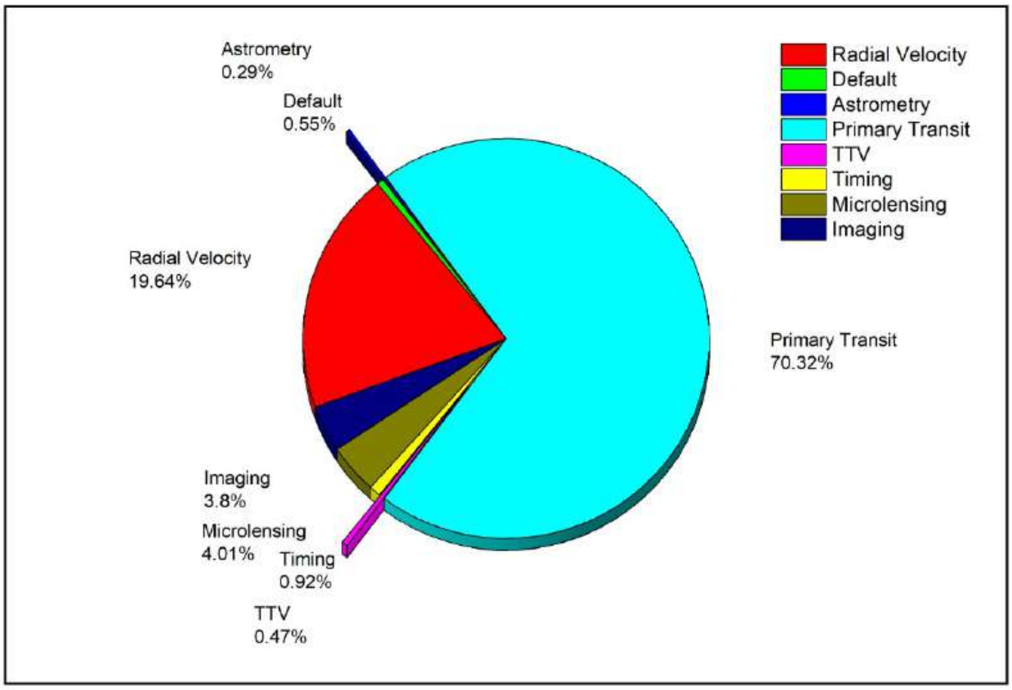

Figure 3. Detection Methods Distribution.

2. Methodology

Exoplanets took us years to discover because we spent so much time studying how our solar system formed before we learned about them. Observing exoplanets, even in our own solar system, can provide information

doi:https://doi.org/10.52526/25792776-22.69.2-235

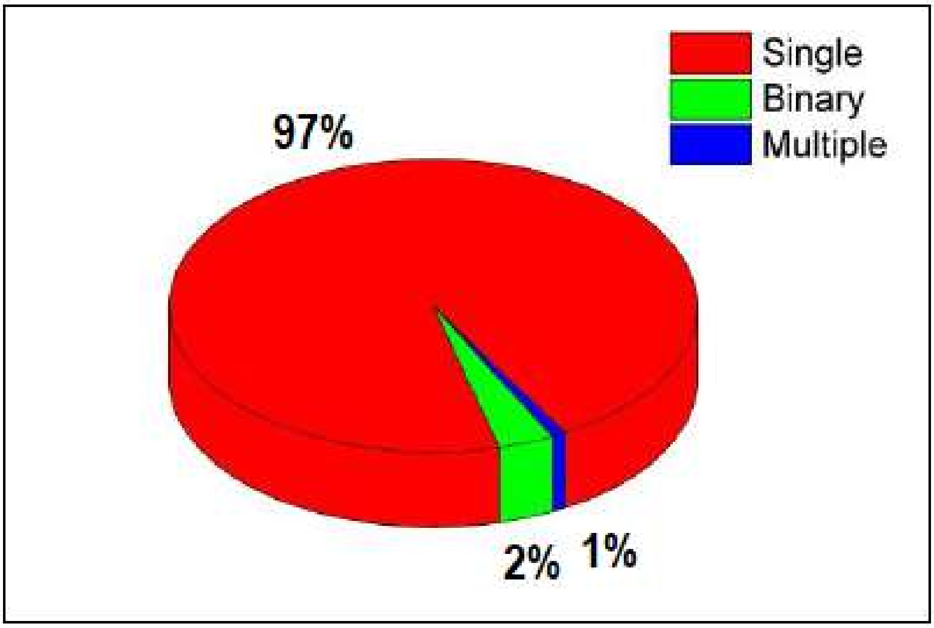

Figure 4. Exoplanets distribution.

about their processes. Discovering exoplanets allows us to imagine life elsewhere more realistically, because we are able to find earth-like planets that might have life. Statistical methods can be used to test astrophysics theories quantitatively. Astronomers need to transform this massive amount of data about exoplanets into something that can help them identify, detect, and discover new candidates. Data for this study are gathered from three main sources:

- **The Extrasolar Planets Encyclopaedia** : A database of all known extrasolar planets and candidate extrasolar planets, as well as an interactive catalog spreadsheet, was founded by Jean Schneider in February 1995 at the Meudon Observatory in Paris, France. Among the main catalogue's features is a database of all confirmed and unconfirmed extrasolar planet detection. All error ranges and the year of discovery of the planet are included, as well as the mass, orbital period, radius, transit time, semi-major axis, eccentricity, inclination, periastron time, maximum variation in time, and longitude of periastron. In addition to providing information about the planet, the planet data pages also provide information about its parent star, including its name, distance in parsecs, apparent magnitude, spectral type, effective temperature, radius, mass, and age. The interactive spreadsheet catalogue does not list all of these figures, and many are blank when Kepler's third law of motion would suffice (Schneider, 2007, Schneider et al., 2011).

- **NASA Exoplanet Archive**

  Exoplanet Archive is an online database that tracks and catalogs extra-solar planets (exoplanets) and their hosts, supporting the search for and characterization of exoplanets. Infrared Processing and Analysis Center at California Institute of Technology owns and operates this facility. The Exoplanet Exploration Program of NASA's Exoplanet Science Institute launched the archive in 2011. A total of 4,000 exoplanets have been confirmed as of June 2019. A total of 5,246 exoplanets have been confirmed in 3,875 planetary systems, with 842 systems having more than one exoplanet. Time-series data from surveys searching for transiting exoplanets are included in the archive along with light curves, spectra, images, and parameters. The archive also develops Web-based tools and services to analyze the data, including displaying and analyzing transit data sets from Kepler and CoRoT missions, whose U.S. data portal is Exoplanet Archive. A number of surveys and telescopes have contributed data to the archive, including SuperWASP, Trans-Atlantic Exoplanet Survey, HATNet Project, and KELT. In the Exoplanet Archive, objects with planetary parameters (transits, radial velocity, microlensing, eclipse timing variations, imaging, transit timing variations, and astrometry) equal to or less than 30 Jupiter masses (or minimum mass) are represented (Akeson et al., 2013, 2017, Christiansen, 2022).

- **The Open Exoplanet Catalogue**

doi:https://doi.org/10.52526/25792776-22.69.2-235

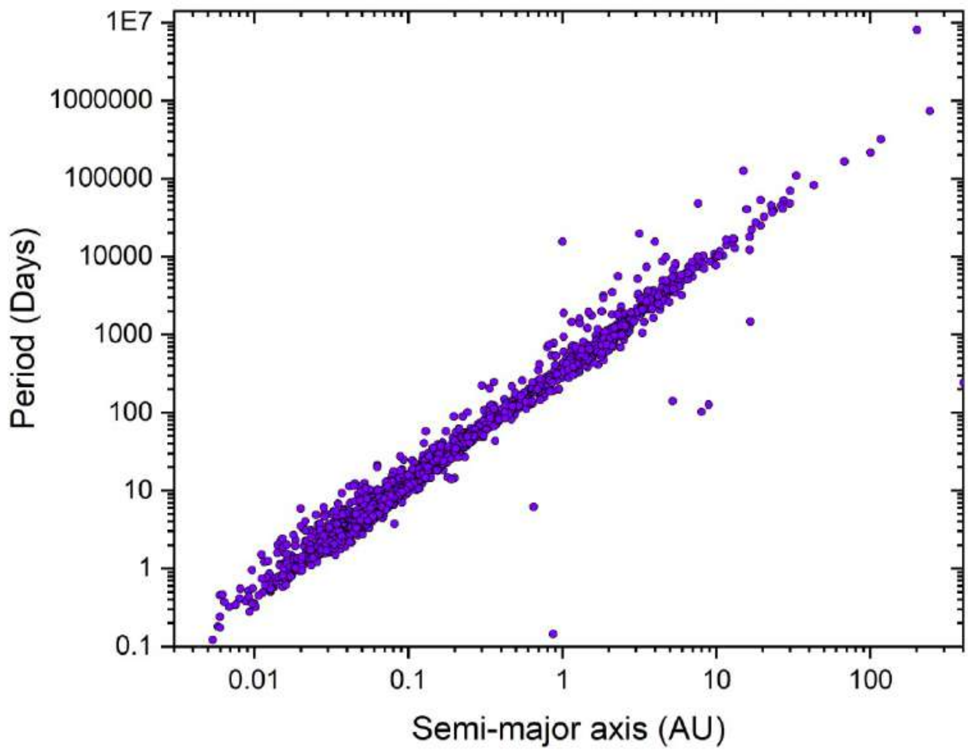

Figure 5. Period with Semi-major axis Distribution .

A catalogue of all extra-solar planets discovered is the Open Exoplanet catalogue. This is a completely decentralized and open astronomical database. With the Extrasolar Planets Encyclopedia, NASA Exoplanet Archive, and Exoplanet Data Explorer, it is considered one of the most widely used exoplanet catalogues. According to Hanno Rein, a distributed version control system and small text files are the basis of a new kind of astronomical database presented in 2012. Varley introduced ExoData in 2016, which provides an exploratory analysis tool and Python interface for the Open Exoplanet Catalogue. An example of a database is the Open Exoplanet catalogue, which is a daily updated list of all discovered extrasolar planets. Furthermore, it is the only catalogue capable of accurately storing and representing planets in any star system (s- or p-type binaries, triples, quads, etc) (Rein, 2012, Varley, 2015).

Data mining, astrophysics, and statistical analysis are all included in the scope of astrostatistics. Astrophysical data can be analyzed using it, complex datasets can be characterized, and astronomical data can be linked with astrophysical theory. In the same way as Astroinformatics, this field studies the stars. The data from all previous catalogues is processed and collected by computer programs in this project. Once the data has been sorted and identified, arrange it so that it is easier to analyze. These sources will be useful to astrophysics researchers and specialists studying exoplanets.

3. Results

A distribution of exoplanet-containing stars over the last decade was determined, as well as the number of exoplanets in single stars, binary systems, and multiple systems. We conclude with a description of the diversity of exoplanets. Here we summaries the statistical analysis of Detection Per the year of the discovery, the Mass - Period Distribution of all 5000 discovered exoplanets, the Mass - Period Distribution, the Period with Semi-major axis Distribution, finally the Exoplanets distribution.

doi:https://doi.org/10.52526/25792776-22.69.2-235

Conclusions and Future Work

New technologies enable more accurate characterization of previously detected extrasolar planets, leading to the detection of smaller and more distant planets. Recent years have seen the discovery of many extrasolar planetary systems, but they are very difficult to detect with current technology because they are similar to those in our solar system. Therefore, most of the surveyed stars have no detectable planets, making it impossible to determine if this is a typical or unusual solar system. In the 1990s, extrasolar planets were discovered, resulting in an explosion in exoplanet searches. Our study presents a statistical analysis of the 5000 exoplanets discovered to date. Several sources were used to compile this information, including the NASA Exoplanet Archive, the Open Exoplanet Catalogue, and the Exoplanet.eu database.

Acknowledgements

Thanks to Gor Mikayelyan, the Scientific and Local Organizing Committee of the International Conference "Space Sciences and Technologies" at Byurakan Astrophysical Observatory (BAO), Armenia.

References

Abushattal A. A., 2017, PhD thesis, Universidade de Santiago de Compostela

Abushattal A. A., Docobo J. A., Campo P. P., 2019a, The Astronomical Journal, 159, 28

Abushattal A., Al-Wardat M., Taani A., Khassawneh A., Al-Naimiy H., 2019b, in Journal of Physics: Conference Series. p. 012018

Akeson R., et al., 2013, Publications of the Astronomical Society of the Pacific, 125, 989

Akeson R., Christiansen J., Ciardi D. R., Ramirez S., Schlieder J., Van Eyken J. C., et al., 2017, in American Astronomical Society Meeting Abstracts.

Al-Tawalbeh Y. M., et al., 2021, Astrophysical Bulletin, 76, 71

Al-Wardat M., Docobo J., Abushattal A., Campo P., 2017, Astrophysical Bulletin, 72, 24

Baglin A., Auvergne M., Barge P., Michel E., Catala C., Deleuil M., Weiss W., 2007, in AIP Conference Proceedings. pp 201–209

Barlow R. J., 1993, Statistics: a guide to the use of statistical methods in the physical sciences. Vol. 29, John Wiley & Sons

Borucki W. J., et al., 2010, Science, 327, 977

Brescia M., Djorgovski S. G., Feigelson E. D., Longo G., Cavuoti S., 2017, Astroinformatics

Broeg C., et al., 2013, in EPJ Web of Conferences. p. 03005

Catala C., 2009, Experimental Astronomy, 23, 329

Christiansen J. L., 2022, Nature Astronomy, 6, 516

Docobo J. A., Griffin R. F., Campo P. P., Abushattal A. A., 2017, Monthly Notices of the Royal Astronomical Society, 469, 1096

Docobo J., Balega Y., Campo P., Abushattal A., 2018, Double Stars Information Circular, 196, 1

Duquennoy A., Mayor M., 1991, Astronomy and Astrophysics, 248, 485

Feigelson E. D., Babu G. J., 2012, Modern statistical methods for astronomy: with R applications. Cambridge University Press

Gardner J. P., et al., 2006, Space Science Reviews, 123, 485

Hartkopf W. I., Mcalister H. A., Mason B. D., 2004

Hatzes A. P., 2016, Space Science Reviews, 205, 267

Howell S. B., et al., 2014, Publications of the Astronomical Society of the Pacific, 126, 398

Hussein A. M., Al-Wardat M. A., Abushattal A., Widyan H. S., Abu-Alrob E. M., Malkov O., Barstow M. A., et al., 2022, The Astronomical Journal, 163, 182

Jack D., Hernández Huerta M. A., Schröder K.-P., 2020, Astronomische Nachrichten, 341, 616

Kalirai J., 2018, Contemporary Physics, 59, 251

Matson R., Williams S., Hartkopf W., Mason B., 2020, United States Naval Observatory, Washington, DC

Muller R., Cersosimo J., Rosado-de Jesus I., Cotto D., Miranda V., Martinez C., Centeno D., 2006, Journal of Double Star Observations, 2, 138

Pourbaix D., et al., 2004, Astronomy & Astrophysics, 424, 727

doi:https://doi.org/10.52526/25792776-22.69.2-235

Raghavan D., et al., 2010, The Astrophysical Journal Supplement Series, 190, 1

Rein H., 2012, arXiv preprint arXiv:1211.7121

Ricker G. R., et al., 2014, Journal of Astronomical Telescopes, Instruments, and Systems, 1, 014003

Schneider J., 2007, http://exoplanet. eu

Schneider J., Dedieu C., Le Sidaner P., Savalle R., Zolotukhin I., 2011, Astronomy & Astrophysics, 532, A79

Taani A., Abushattal A., Mardini M. K., 2019a, Astronomische Nachrichten, 340, 847

Taani A., Karino S., Song L., Mardini M., Al-Wardat M., Abushattal A., Khasawneh A., Al-Naimiy H., 2019b, in Journal of Physics: Conference Series. p. 012029

Taani A., Khasawneh A., Mardini M., Abushattal A., Al-Wardat M., 2020, arXiv preprint arXiv:2002.03011

Varley R., 2015, Astrophysics Source Code Library, pp ascl–1512

Vavilova I., 2016, Odessa astronomical publications, pp 109–115

Wolszczan A., Frail D. A., 1992, Nature, 355, 145

Wright J. T., Gaudi B. S., 2012, arXiv preprint arXiv:1210.2471

doi:https://doi.org/10.52526/25792776-22.69.2-235

The Physical Parameters, Stability, and Habitability of some Double-lined Spectroscopic Binaries

H.A. Alameryeen*, A. A. Abushattal, and A. F. Kraishan

Department of Physics, Al-Hussein Bin Tala University, P. O. Box 20, 71111, Ma'an, Jordan.

Abstract

Large ground telescopes can now resolve most double-lined binaries optically at some point in their orbit due to the improvement of imaging techniques in recent decades. Using additional information about these systems, such as astrometric parallax, even a single precise visual observation can provide a 3D orbit and the primary physical parameters. Furthermore, both the visual and spectroscopic orbits can be determined. We combine the Edward method with the visual solution and the spectroscopic orbit parameters: period (P), periastron epoch (T), eccentricity (e), semimajor axis (a1,2) and inclination (i), we also know the mass ratio of the system. The developed method allows us to select double-lined spectroscopic systems with recently calculated orbits. We calculate the individual masses, orbital parallax, and other fundamental astrophysical parameters. The purpose of these parameters is to verify the reliability of the data received from space missions and to calculate the stability and habitability, which is the primary goal of this study. Astronomical information can be obtained from binary stars. By observing short period binaries using both spectroscopy and interferometry, we can determine the individual masses and orbital parallaxes of the objects based on their corresponding orbits. Spectroscopic binaries with double-lines are therefore fundamentally important to optically resolve. To determine the required telescope aperture for the resolution of a spectroscopic binary, we developed a specific algorithm. We determined the most probable maximum and minimum separations between each spectroscopic binary based on photometric and spectroscopic information. Thus, we also determined the different physical parameters of each system by using the calibrations we obtained in our study. Based on optically resolved spectroscopic binaries with both spectroscopic and visual orbits, the methodology presented here was successfully tested.

Keywords: *binaries: visual, spectroscopic - stars: physical parameters, stability - habitability*

1. Introduction

A binary star consists of two stars orbiting the same mass center due to gravitational attraction. It can be considered a primary movement when a fixed motion is made around the center of mass, whereas a relative motion (secondary movement) can be considered a secondary movement. According to estimates, many stars are binary or multicomponent systems with three to four components (Al-Wardat et al., 2017, Duquennoy & Mayor, 1991, Raghavan et al., 2010). Astrophysics uses binary stars (BSs) for a variety of purposes. The stellar structure model, the star's evolution model, is considered a crucial test-bed for the development of a stellar structure model. There are many reasons why astronomy and astrodynamics are interested in binaries and multiple stars, but the most important reason is that stellar masses can be determined from their orbits and parallaxes. Studies of star evolution are fundamentally affected by their mass. Other physical parameters of interest are also obtainable, including luminosity and orbital elements, as well as sizes, parallaxes, and orbital elements (Al-Tawalbeh et al., 2021, Docobo et al., 2018, Hussein et al., 2022).

Space missions such as CoRoT, Kepler, and K2 can find exoplanets by searching for main sequence and pre-main sequence stars. BSs are ideal environments for looking for exoplanets. The three main types of binary systems are astrometric, spectroscopic, and eclipsing. A technique that determines the mass of a system is difficult. Since speckle interferometry was introduced 50 years ago, it has been used by researchers around the world for effective and accurate observation of binary stars. The astrometric binary and the

*Hatem.a.alameryeen@ahu.edu.jo, Corresponding author

doi:https://doi.org/10.52526/25792776-22.69.2-242

double-lined spectroscopic binary are two types of binary systems that correlate with the masses of their components. We can determine the total mass of the system in AB by determining the orbit solution with known parallax. When the SB2 orbital solution is combined with the SB2 mass ratio, the three-dimensional orbit, mass, and parallax of the orbit can be calculated. Gaia data release (Gaia DR2) found systematic errors in astrometric parallaxes for bright stars, so such parallaxes were thought to be an effective verification method for them. This research method has been used in many publications over the years to determine physical parameters by combining each technique. Two double-lined spectroscopic binaries HD 6840 and HD 130669 were determined with precision in this study (Abushattal, 2017, Abushattal et al., 2019a, Docobo et al., 2017).

A number of spectroscopic binaries, SB, have been resolved using high resolution techniques since the 1970s. As a result of the SB2 orbits and the visual orbits, we can determine the mass and parallax of the components (the ratio using SB2 orbits and the sum using visual orbits).

In spite of this, we should consider the following questions before preparing the SB list to be resolved by a particular telescope. Could you please give us an estimate of what size telescope we would require in each case? How should we prepare a list for our telescope? To answer these questions, SB (double-lined) with a known orbit and parallax will be considered in this paper. As a result of our analysis, we propose the maximum and minimum angular separation for each of these SB using a three-dimensional model. Additionally, we provide the most probable values of these systems' physical parameters (spectral type, magnitude, and mass). In the first place, it is possible to calculate the masses of each component based on their spectroscopic orbits, composite spectrums, and apparent magnitudes of the whole, then the visual orbit can be calculated. Calculate the maximum and minimal angular distances between the components by drawing the apparent orbit and calculating the maximum and minimal angular distances. The tables corresponding to the calibrations used in this study are also described in the same section. In addition, we examine other systems and determine the telescope size necessary to resolve them optically.

The binary system serves as a suitable environment to observe many physical processes: mass loss, mass exchange, component variability the Nova phenomenon, the Flare phenomenon, X-ray binaries, etc. A dynamical approach includes perturbations, discovering dark components, such as brown stars and exoplanets, and calculating orbits (Abushattal et al., 2019b, Taani et al., 2019a,b, 2020). In 50% of multiple stars, the main sequence and pre-main sequence stars form BSs, which make BSs an ideal environment for discovering Earth-like planets via space missions like CoRoT, Kepler, and TESS. Due to the stages of star formation, multiple stars often contain the most massive exoplanets Exoplanets are often found in binary star systems, and binary stars are powerful hosts of many exoplanets. Habitability and stability are two parameters that depend on a binary star's properties. In this work, the main objective is to determine the mass of each planet, the semi-major axis, luminosities, and temperatures, which are the most important parameters for this work

2. Methodology for Double-lined Spectroscopic binaries (SB2)

A double-lined spectroscopic binary is one where two stars are too close together for their spectra to be resolved separately. In this binary, a specific spectral line of some element shows up twice in the (combined) spectrum. Due to their different wavelengths, the Doppler shifts indicate the relative radial velocity of stars, which is characteristic of orbital cycles. Observations show a cyclic pattern of peaks and valleys over time, single during orbital times with no radial velocity difference between the stars, and two during orbital times with radial velocity differences. Based on the relative radial velocities, we can estimate the smaller companion's mass, based on the spectral class.

If the spectral lines of both components are present in the observable spectrum and the orbit and parallax are known. However, we have additional information for the SB2. Indeed, the orbital parameters are P, e, T, $A_1 = a_1\, sin\, i$, $A_2 = a_2$, and ω_1 or $\omega = 180^\circ + \omega_1$. The result is:

$$\frac{A_2}{A_1} = \frac{a_2}{a_1} = \frac{\mathcal{M}_1}{\mathcal{M}_2} = q, \tag{1}$$

and the mass ratio, q, is known.

Hereafter, we will suppose that if the spectroscopic binary is a double-lined SB2, then Δm is less than 1.5 or 2.0 (depending on the observational instrumentation). It is even possible that, in a few cases with $\Delta m = 2.5$, it may also be an SB2. This is not a problem for our methodology because it selects the solution by means of q.

doi:https://doi.org/10.52526/25792776-22.69.2-242

Application of the methodology to the SB2, BD+52 1332 (HD 74089, HIP 42870) We will calculate the physical and orbital properties of binary stars using the Edward method, starting with their spectral type. In **?** the same method was used, but the starting point was to calculate the absolute magnitude based on astrophysical relations for the selected systems using parallax and apparent magnitude.

The double-lined binary BD+52 1332 (HD 74089) has a period of 1231.9 days. A Hipparcos parallax of 1.85±1.05mas and a Gaia parallax of 3.11 ± 0.24mas are the values of the two parallaxes. A late-type giant star has color indices of V = 8.53, B-V = 0.88, J-H = 0.482, and H-K = 0.125. Based on the spectral types of the components, Griffin (2014) identified the binary as G8III and G2III-IV. As reported in the Henry Draper Catalogue, Simbad has a spectral type of K0. Strairzys and Lazauskaite's paper provides a K0III spectral type by analyzing the color indices (Straizys & Lazauskaite, 2009).
In February 2012, the Cambridge Coravel spectrometer used to observe the radial velocity of HD$\dot{7}$4089 for the first time. It took about 11 months of observation were required to establish the radial velocity of the second component. For primary and secondary components, Griffin used 39 and 20 observations, respectively, to determine the orbital elements (Griffin, 2014).

Table 1. HD 74089. Physical and orbital parameters

Sp type	K0III
V_T (mag)	8.53 ± 0.01
π_{Hip} (mas)	1.85± 1.06
π_{Gaia}(mas)	3.11 ± 0.24
P (days)	1321.9126 ± 0.0017
T $_{(MJD)}$	56255.501 ± 0.016
e	0.0 ± 0.0
$a_1$sin(i)(Gm)	14.11± 0.07
$a_2$sin(i)(Gm)	15.36± 0.19
ω_1 (degree)	0.0± 0.0
q($\mathcal{M}_1/\mathcal{M}_2$)	1.0880 ± 0.0144

As a result, we consider HD 74089 to be K0III, with an absolute magnitude of 0.53. In the case of K0III, the mass of each component is 1.91 and the Δm is 0.42 until we reach a value of Δm = 0.0 (Edward's step = 0). This value has an absolute magnitude of 0.53 for both components. In agreement with Griffin: 1.088 ± 0.014, the ratio of the masses is 1.00 ± 0.57. See Table 3.9 for cases where the delta value was different.

According to the inclination, there is a minimum and maximum separation of ρ''_{max} =0.00080±0.00007, and ρ''_{min} = 0.00041±0.00040, respectively. If HD 74089 is to be resolved optically, a much larger telescope array is required than 147m.

Table 2. Orbital inclination and intermediary parameters as a function of Δm for HD 74089

Δm	S	M_1	M_2	Sp$_1$	Sp$_2$	$\mathcal{M}_{1(\mathcal{M}_\odot)}$	$\mathcal{M}_{2(\mathcal{M}\odot)}$	$a_{(A.U)}$	q $(m_1/$ m$_2)$
0.0	0.00	0.50±0.07	0.50±0.07	K0III	K0III	1.90±0.42	1.90±0.41	0.236±0.001	1.000±0.63
0.5	0.19	0.33±0.07	0.81±0.08	K1III	A2IV	1.84±0.40	2.63±0.25	0.255±0.001	0.700±0.31
1.0	0.29	0.23±0.05	1.22±0.06	K2III	A4IV	1.70±0.28	2.29±0.19	0.246±0.007	0.75±0.30

Name	$\pi_{Hip(mas)}$	$\pi_{Gaia(mas)}$	$m_{(mag)}$	Sp	Sp$_1$	Sp$_2$	$\mathcal{M}_1(\mathcal{M}_\odot)$	$\mathcal{M}_2(\mathcal{M}_\odot)$
HIP 12623	41.34±0.43	-	4.92	F9V	F9V	G3V	1.16±0.03	1.04±0.04
HIP 20087	18.50±0.50	-	5.63	F0V	A9V	F4V	1.69±0.03	1.38±0.03
HIP 42870	1.85±1.06	3.11±0.24	8.53	K1III	K1III	K0III	1.89±0.42	1.91±0.42

Table 3. Physical Parameters SB2

Table 4. Dynamical Parameters For SB2

Name (HD)	$a_{(AU)}$	$a_{1(AU)}$	$a_{2(AU)}$	$i_{(degree)}$	ρ(mas)	D (m)
HIP 12623	1.227±0.116	0.572±0.045	0.649±0.061	56.3±3.4	0.0457±0.0032	2.6
HIP 20087	7.380±0.542	3.264±0.246	4.116±0.393	55.9±3.2	0.1576±0.0126	1.0
HIP 42870	0.238±0.001	0.118±0.023	0.118±0.023	59.0±3.6	0.0008±0.0001	147

doi:https://doi.org/10.52526/25792776-22.69.2-242

3. Stability

Stability is a very difficult concept to define. As a result of a variety of initial conditions, physical and mathematical theorems, and different constants, Astronomy has at least 50 concepts related to stability (Szebehely, 1984). Our definition of stability is characterized by the condition of no significant variation of orbital parameters over time (eccentricity, semimajor axis, and inclination). This section investigates three double-lined spectroscopic systems and determines their probable stable regions. We can determine the stability of planetary orbits around binary systems based on the empirical expression of (Holman & Wiegert, 1999) by observing the ratio between the mass and eccentricity of the system for two types of orbits: the inner (S-type) and the outer (P-type) of the orbit. During the 1980s, Dvorak (1984) described three types of stable orbits for planetary systems in binary systems:

- The satellite orbits (S-type) involve the planet orbiting around one of the binary's components,
- The planet-type orbits (P-type). The planet orbits the binary star around both components. We will say that it is a circumbinary planet, and
- The librator-type orbits (L- type). The stable orbit is around the Lagrangian points (which is stable only for the mass ratio, $\mu = \mathcal{M}_2/(\mathcal{M}_1{+}\mathcal{M}_2)$, $\mu \leq 0.04$) (Dvorak, 1984).

Holman - Wiegert empirical expression. Based on two values, the ratio of mass to eccentricity of the system (especially in the case of the P-type) Dvorak determined the stable zone in three-body problems. As a function of the mass ratio and semimajor axis, Holman - Wigeret came up with the same expression as Dvorak in 2007. For both types of orbits, (S-type) and (P-type), they developed the expressions below based on the results of the /*alpha* Centauri system (Wiegert & Holman, 1997). They used least-squares fit data with the binary conditions as 0.1≤ $\mu \leq 0.9$, and 0.0≤ e ≤ 0.8 for the S-type, and 0.1≤ $\mu \leq 0.5$, 0.0≤ e ≤ 0.8 for P-type. The eccentricity (e), the longitude of the ascending node (Ω), the inclination (i), and the argument of perihelion (ω), were considered equal zero (Holman & Wiegert, 1999). The expression for the S- type (the inner region) is:

$$\begin{aligned}\frac{a_s}{a} &= (0.464 \pm 0.006) + (-0.380 \pm 0.010)\mu + (-0.631 \pm 0.034)e \\ &+(0.586 \pm 0.061)\mu e + (0.150 \pm 0.041)e^2 + (-0.198 \pm 0.047)\mu e^2.\end{aligned} \tag{2}$$

The expression for the P- type (the outer region) is:

$$\begin{aligned}\frac{a_i}{a} &= (1.60 \pm 0.04) + (4.12 \pm 0.09)\mu + (5.10 \pm 0.05)e + (-4.27 \pm 0.17)\mu e \\ &+(-2.22 \pm 0.11)e^2 + (-5.09 \pm 0.11)\mu^2 + (4.61 \pm 0.36)\mu^2 e^2.\end{aligned} \tag{3}$$

Table 5. Physical parameters for the 13 double-lined spectroscopic binaries

Name	e	$\mathcal{M}_1(\mathcal{M}_\odot)$	$\mathcal{M}_2(\mathcal{M}_\odot)$	$a_{(A.U)}$
HIP 12623	0.663±0.002	1.18±0.03	1.04±0.04	1.221±0.116
HIP 20087	0.167±0.004	1.74±0.03	1.38±0.03	0.738±0.542
HIP 42870	0.0	1.91±0.42	1.91±0.42	0.237±0.001

Table 6. The stability limits for exoplanet orbits around each component and both components (circumbinary planets), in the 13 double-lined spectroscopic binaries

Name (HD)	$a_{1S_{max}(A.U)}$	$a_{1S_{min}(A.U)}$	$a_{1Pmin(A.U)}$	$a_{2S_{max}(A.U)}$	$a_{2S_{min}(A.U)}$
HIP 12623	0.1134	0.0011	**4.473**	0.1073	- 0.0104
HIP 20087	0.150	0.136	**2.140**	0.175	0.162
HIP 42870	0.065	0.064	**0.539**	0.065	0.064

Exoplanet orbits, especially those in stellar binary systems, are difficult to determine due to their instability

doi:https://doi.org/10.52526/25792776-22.69.2-242

Table 7. Stellar parameters used to study the habitable zone for the 13 double-lined spectroscopic binaries

HD	$a_{(A.U)}$	Sp_1	Sp_2	T_1(K)	T_2(K)	$L_1(L\odot)$	$L_2(L\odot)$	$\mathcal{M}_1(\mathcal{M}_\odot)$	$\mathcal{M}_2(\mathcal{M}_\odot)$
HIP 12623	1.222±0.116	F8V	G2V	6160	5811	2.21	1.30	1.18±0.03	1.04±0.04
HIP 20087	7.380±0.542	A8V	F3V	7682	6782	9.70	4.47	1.74±0.03	1.38±0.03
HIP 42870	0.230±0.001	K0III	K0III	5282	5282	39.81	39.81	1.91±0.42	1.91±0.42

Table 4 shows the following data: Column 1, present the name of the binary (HD number); Column 2, the eccentricity (e); Column 3, the semimajor axis of the binary in astronomical units (A.U); Column 4, includes the minimum and the maximum values of Δm for each binary; Column 5 and 6, the masses for each component in solar mass ($\mathcal{M}_\odot$).

Tables 6, and 7 list, the name of the binary (HD number) in Column 1. Columns 2 and 3 indicate the stability limits of the exoplanets orbits in the case of an S-type orbit around the main component (as a minimum value ($a_{S\,min}$) and maximum value ($a_{S\,max}$)) in astronomical units (A.U), Column 4 shows the stability limits for the exoplanet in the case of a P-type orbits where bold values indicate a minimum value ($a_{P\,min}$) (especially for the SB1 because different Δm are possible) also in astronomical units (A.U); and Columns 5 and 6 contain the same information as Columns 2 and 3 but, in this case, for orbits around the secondary component.

On the other hand, in order to understand the orbit stability around each star, we have to mention here that the stability is given between two values of the distance: the first one is $a_{S\,max\,(A.U)}$, which represents the largest distance around the star at which the orbit of the exoplanet is stable even with the existence of the second component. The second value $a_{S\,min}$ $(A.U)$, represents the closest separation to the star where the existence of the stable orbits of exoplanets is possible in this situation the stability is not guaranteed, we have to take into account the spectral type and the size of the star because, in some cases, the radius of the star is very close to the minimum value for the stability which means that the stability analysis by Holman and Wiegert cannot be used as the restricted three-body problem is not a valid model. Moreover, in some cases, the maximum stability limit might be in side the star.

4. Habitability

An interesting definition of habitability was introduced by Cockell of the UK Centre for Astrobiology, University of Edinburgh, which describes the environment as capable of supporting metabolic activities for at least one known organism, and as such supporting its survival, growth, maintenance, or reproduction processes. (Cockell et al., 2016). The best state for the water to support the basic processes of life, the liquid state, requires suitable temperature on the exoplanet; not cold or hot, and its temperature depends on various parameters, internal parameters such as radio activity and the components of the atmosphere. Depending on the distance from the nearest star, the external parameter depends on the source of the radiation. It is first necessary to determine the habitable zone where liquid water can be found when searching for exoplanets. Around a single star or around a binary star, the HZ appears as a spherical shell. Several parameters must be taken into consideration in order to determine the habitability of a binary system: ($\mathcal{M}_1$, $\mathcal{M}_2$), the period (P), the eccentricity (e), and the semimajor axis of the exoplanet orbit (a)(Mason et al., 2013). Because of the gravitational force generated by the host star, the semimajor axis and eccentricity of the exoplanets can change because it migrates out of the habitable zone due to the tidal force. As a result, it is generally less likely that exoplanets will be habitable in the future (Barnes et al., 2007, Barnes et al., 2008), and Over time, habitability changes..

When two stars are separated by less than 50 AU, especially in cases of binary systems, the gravity of one star affects the HZ and stability around the exoplanet, causing perturbations in its orbit and ability to contain liquid water. (Eggl et al., 2012).

The following parameters are fixed in order to determine a habitable zone for spectroscopic binaries: the temperature derived from the table relating to spectral types developed by (Gray, 2005) , the mass derived from our previous chapter methodology, and the luminosity determined by the luminosity-absolute magnitude relation.

$$\frac{L}{L_\odot} = -\frac{M_v - M_{v\odot} - (BC - BC_\odot)}{2.5}, \tag{4}$$

where, L is the luminosity of the star, M_v is the absolute magnitude ($M_{v\odot}$ = 4.82), and BC is the bolometric correction ($BC_\odot$ = -0.08).

doi:https://doi.org/10.52526/25792776-22.69.2-242

A website http://astro.twam.info/hz/ devised by Tobias Muller and Nader Haghighipour in 2013 determines the habitable zone for single stars, double stars, and multiple stars (Müller & Haghighipour, 2014). As well as a habitable zone calculator, this website contains tables, plots, and videos that simulate the motion of an exoplanet around a star. On this website, you will find four different models: Kasting et al. (1993), Kopparapu (2013), Kopparapu et al. (2014), Selsis et al. (2007). It the HZ calculator on this website describe the stability using the Holman & Wiegert (1999) model. This the same method that we used previously to describe the radii of the stability around single-lined and double-lined spectroscopic binaries.

As we mentioned before, the habitable zone provides the area around each component or around both components in which the existence of liquid water is possible. We have calculated all parameters (see Tables 4.5, 4.6), which allow us to use a methodology of (Müller & Haghighipour, 2014) to describe the habitable zone around the stars of our sample of 30 spectroscopic binaries. Tables 4.5 and 4.6 list in Column 1, the name of the star; Column 2, the semimajor axis of the binary in astronomical units (A.U); Columns 3 and 4; the spectral type for the primary component and the secondary; Columns 5 and 6, the temperature of each component in Kelvin degrees (K); Columns 7 and 8, the luminosity of each component in the solar luminosity ($L_\odot$), and Columns 9 and 10, the mass of the each component in solar mass ($\mathcal{M}_\odot$).

We take into account that liquid water exists in an environment with an atmospheric pressure of 1 atm within a temperature range of 273 K to 373 K which is dependent on the distance from the center-mass of the system and the luminosity of the stars. The habitable zone was calculated using the (Müller & Haghighipour, 2014) method and we classified these results into three subtypes depending on the width of the habitable zone (WHZ) in AU compared with the width of our solar system which is about 0.7 AU (Kopparapu, 2013). Taking into account the difference in the class of each system, 50% of our results show habitable zones within the following ranges: $0.5 \leq$ WHZ ≤ 2.5, 23%, 2.5 ¡ WHZ ≤ 5, and 27 %, 5 ¡ WHZ. This WHZ yields an increased possibility of the existence of liquid water, especially around giants stars. Unfortunately, it also expands the area to search for habitable exoplanets requiring more observing time.

5. The Graphics of the Stability and Habitable Zones

After identifying stability zones and habitable zones in the previous two sections, we combine these two parameters to find stable orbits within habitable zones. The possibility of having an exoplanet with liquid water is possible when there is a match between the habitable and stable areas.

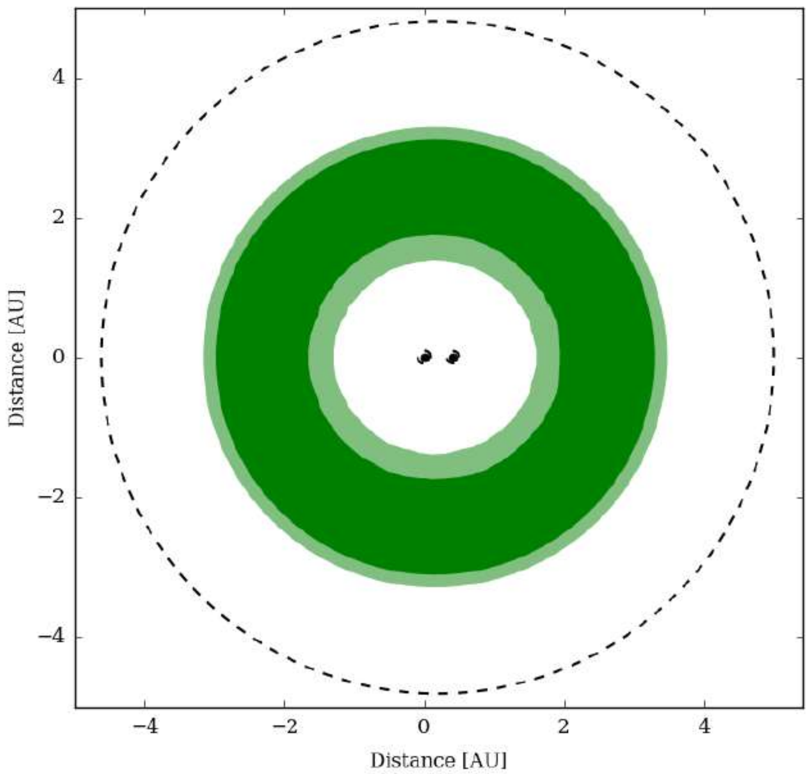

Figure 1. Stability and Habitable Zone for HIP 12623 system

doi:https://doi.org/10.52526/25792776-22.69.2-242

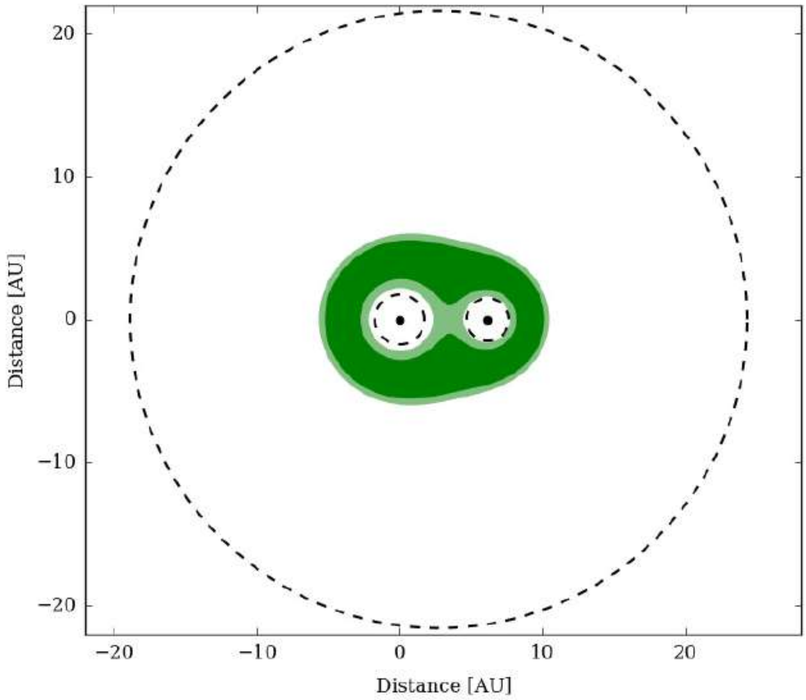

Figure 2. Stability and Habitable Zone for HIP 20087 system

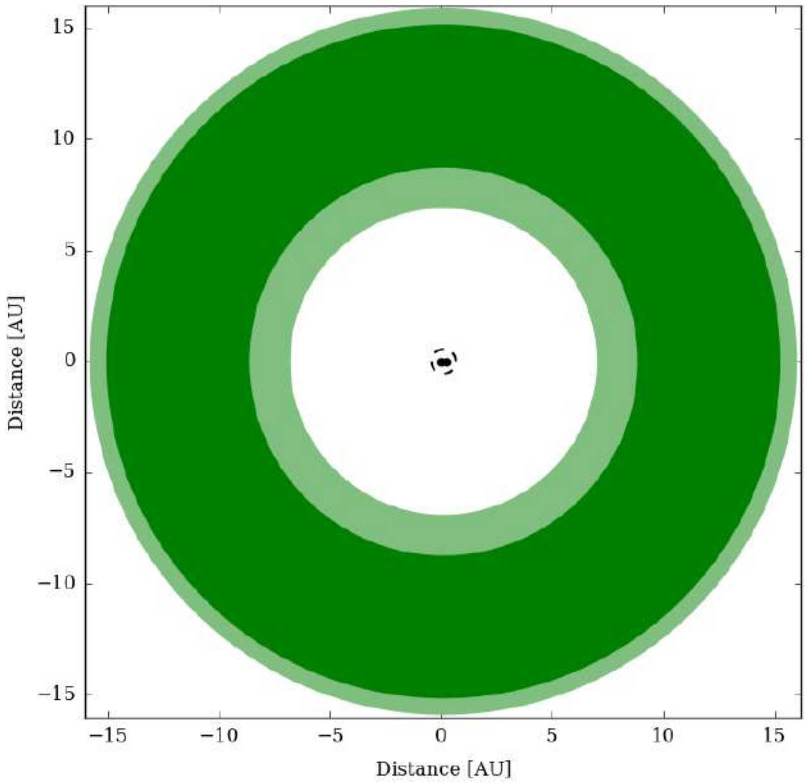

Figure 3. Stability and Habitable Zone for HIP 4287 system

6. Conclusions and Future Work

We present a spectro-interferometric analysis and calculate the physical and orbital properties of three binary stars, starting with their spectral type, and then analyzing them using the Edward method. This new method has been developed for three double-lined spectroscopic systems with recent orbital calculation results to calculate the stability and habitability, astronomical parameters such as orbital parallax and mass

doi:https://doi.org/10.52526/25792776-22.69.2-242

and semi-major axis. In this way, we can determine whether the host system is stable and habitable enough to host an exoplanet or the existence of earth-like planets.

Acknowledgements

Thanks to Gor Mikayelyan, the Scientific and Local Organizing Committee of the International Conference "Space Sciences and Technologies" at Byurakan Astrophysical Observatory (BAO).

References

Abushattal A. A., 2017, PhD thesis, Universidade de Santiago de Compostela

Abushattal A. A., Docobo J. A., Campo P. P., 2019a, The Astronomical Journal, 159, 28

Abushattal A., Al-Wardat M., Taani A., Khassawneh A., Al-Naimiy H., 2019b, in Journal of Physics: Conference Series. p. 012018

Akeson R., et al., 2013, Publications of the Astronomical Society of the Pacific, 125, 989

Akeson R., Christiansen J., Ciardi D. R., Ramirez S., Schlieder J., Van Eyken J. C., et al., 2017, in American Astronomical Society Meeting Abstracts.

Al-Tawalbeh Y. M., et al., 2021, Astrophysical Bulletin, 76, 71

Al-Wardat M., Docobo J., Abushattal A., Campo P., 2017, Astrophysical Bulletin, 72, 24

Baglin A., Auvergne M., Barge P., Michel E., Catala C., Deleuil M., Weiss W., 2007, in AIP Conference Proceedings. pp 201–209

Barlow R. J., 1993, Statistics: a guide to the use of statistical methods in the physical sciences. Vol. 29, John Wiley & Sons

Barnes R., Raymond S. N., Jackson B., Greenberg R., 2007, in AAS /Division for Planetary Sciences Meeting Abstracts #39. p. 468

Barnes R., Raymond S. N., Jackson B., Greenberg R., 2008, Astrobiology, 8, 557

Borucki W. J., et al., 2010, Science, 327, 977

Brescia M., Djorgovski S. G., Feigelson E. D., Longo G., Cavuoti S., 2017, Astroinformatics

Broeg C., et al., 2013, in EPJ Web of Conferences. p. 03005

Catala C., 2009, Experimental Astronomy, 23, 329

Christiansen J. L., 2022, Nature Astronomy, 6, 516

Cockell C. S., et al., 2016, Astrobiology, 16, 89

Docobo J. A., Griffin R. F., Campo P. P., Abushattal A. A., 2017, Monthly Notices of the Royal Astronomical Society, 469, 1096

Docobo J., Balega Y., Campo P., Abushattal A., 2018, Double Stars Information Circular, 196, 1

Duquennoy A., Mayor M., 1991, Astronomy and Astrophysics, 248, 485

Dvorak R., 1984, in , The stability of planetary systems. Springer, pp 369–378

Eggl S., Pilat-Lohinger E., Georgakarakos N., Gyergyovits M., Funk B., 2012, The Astrophysical Journal, 752, 74

Feigelson E. D., Babu G. J., 2012, Modern statistical methods for astronomy: with R applications. Cambridge University Press

Gardner J. P., et al., 2006, Space Science Reviews, 123, 485

Gray D. F., 2005, The observation and analysis of stellar photospheres. Cambridge University Press

Griffin R., 2014, The Observatory, 134, 109

Hartkopf W. I., Mcalister H. A., Mason B. D., 2004

Hatzes A. P., 2016, Space Science Reviews, 205, 267

Holman M. J., Wiegert P. A., 1999, The Astronomical Journal, 117, 621

Howell S. B., et al., 2014, Publications of the Astronomical Society of the Pacific, 126, 398

Hussein A. M., Al-Wardat M. A., Abushattal A., Widyan H. S., Abu-Alrob E. M., Malkov O., Barstow M. A., et al., 2022, The Astronomical Journal, 163, 182

Jack D., Hernández Huerta M. A., Schröder K.-P., 2020, Astronomische Nachrichten, 341, 616

Kalirai J., 2018, Contemporary Physics, 59, 251

Kasting J. F., Whitmire D. P., Reynolds R. T., 1993, Icarus, 101, 108

doi:https://doi.org/10.52526/25792776-22.69.2-242

Kopparapu R. K., 2013, The Astrophysical Journal Letters, 767, L8

Kopparapu R. K., Ramirez R. M., SchottelKotte J., Kasting J. F., Domagal-Goldman S., Eymet V., 2014, The Astrophysical Journal Letters, 787, L29

Mason P. A., Zuluaga J. I., Clark J. M., Cuartas-Restrepo P. A., 2013, The Astrophysical Journal Letters, 774, L26

Matson R., Williams S., Hartkopf W., Mason B., 2020, United States Naval Observatory, Washington, DC

Müller T. W., Haghighipour N., 2014, The Astrophysical Journal, 782, 26

Muller R., Cersosimo J., Rosado-de Jesus I., Cotto D., Miranda V., Martinez C., Centeno D., 2006, Journal of Double Star Observations, 2, 138

Pourbaix D., et al., 2004, Astronomy & Astrophysics, 424, 727

Raghavan D., et al., 2010, The Astrophysical Journal Supplement Series, 190, 1

Rein H., 2012, arXiv preprint arXiv:1211.7121

Ricker G. R., et al., 2014, Journal of Astronomical Telescopes, Instruments, and Systems, 1, 014003

Schneider J., 2007, http://exoplanet. eu

Schneider J., Dedieu C., Le Sidaner P., Savalle R., Zolotukhin I., 2011, Astronomy & Astrophysics, 532, A79

Selsis F., Kasting J. F., Levrard B., Paillet J., Ribas I., Delfosse X., 2007, Astronomy & Astrophysics, 476, 1373

Straizys V., Lazauskaite R., 2009, arXiv preprint arXiv:0907.2398

Swain M., et al., 2009, The Astrophysical Journal, 704, 1616

Szebehely V., 1984, Celestial mechanics, 34, 49

Taani A., Abushattal A., Mardini M. K., 2019a, Astronomische Nachrichten, 340, 847

Taani A., Karino S., Song L., Mardini M., Al-Wardat M., Abushattal A., Khasawneh A., Al-Naimiy H., 2019b, in Journal of Physics: Conference Series. p. 012029

Taani A., Khasawneh A., Mardini M., Abushattal A., Al-Wardat M., 2020, arXiv preprint arXiv:2002.03011

Tinetti G., Tennyson J., Griffith C. A., Waldmann I., 2012, Philosophical Transactions of the Royal Society of London A: Mathematical, Physical and Engineering Sciences, 370, 2749

Varley R., 2015, Astrophysics Source Code Library, pp ascl–1512

Vavilova I., 2016, Odessa astronomical publications, pp 109–115

Wiegert P. A., Holman M. J., 1997, Astron. J. , 113, 1445

Wolszczan A., Frail D. A., 1992, Nature, 355, 145

Wright J. T., Gaudi B. S., 2012, arXiv preprint arXiv:1210.2471

doi:https://doi.org/10.52526/25792776-22.69.2-242

Astroinformatics: The Importance of Mining Astronomical Data in Binary Stars Catalogues

A.A Abushattal [*], A. A Alrawashdeh, and A. F. Kraishan

Department of Physics, Al-Hussein Bin Tala University, P. O. Box 20, 71111, Ma'an, Jordan.

Abstract

The field of Astroinformatics offers exciting new perspectives on astronomical discovery through the implementation of advanced data mining procedures. Data deluges transform research practices and methodologies across various scientific disciplines, including day-to-day astronomical research. It is essential to use innovative algorithms and methods to process astronomical data and its variety. Descriptive Data Mining was used in this study to clarify the importance and effectiveness of obtaining common data between three binary star catalogs. These catalogues are The Ninth Catalogue of Spectroscopic Binary Orbits (SB9), The Sixth Catalog of Orbits of Visual Binary Stars (6COVBS), and The Fourth Catalog of Interferometry Measurements of Binary Stars (4CIMBS). We collect scattered data from the Ninth Catalog in its latest edition in 2021, which contains astronomical information for approximately 4021 binary systems. Then we search for the orbits of these binary systems in the 6COVBS to calculate the physical and the orbital properties with high accuracy. After that, we use the 4CIMBS to look for new observations of these stars in 66,225 resolved stars in its latest edition 2020 to calculate new orbits. As a result of this research, we have found about 600 standard systems among these catalogues, which are valuable data to calculate many physical properties of such binary stars, starting from individual masses, by the combination of the spectroscopic orbital solution with the visual orbital solutions. Furthermore, calculate the orbital parallax for each system with high accuracy compared with those from space missions such as Gaia and Hipparcos give us a new and essential method to verify the validity of the data from those satellites.

Keywords: *astroinformatics, aata Mining, binary Star catalogues, visual and spectroscopic binary star*

1. Introduction

Astroinformatics, which covers a variety of multi-disciplinary applications of e-Astronomy, is now classified as a new academic research field by data-oriented astronomy. There are many computational methods and software for working with astronomical surveys and catalogues. These include data modelling, data mining, data access, digital astronomical database, machine learning, statistics, and other software (Borne, 2009, Brescia et al., 2017, Siemiginowska et al., 2019, Vavilova, 2016).

A binary star consists of two stars whose components are gravitationally bounded, so they orbit the same centre of mass. A fixed movement around the centre of mass can be considered as a primary movement, while a relative movement (the secondary movement) can be considered a secondary movement. The majority of the observed stars appear to be binary or belong to multiple systems with three to four components, according to estimates (e.g., Al-Wardat et al., 2017, Duquennoy & Mayor, 1991, Raghavan et al., 2010). Astrophysics and Astrodynamics are interested in binaries and multiple stars for many reasons. The mass of stars plays a fundamental role in studying their evolutionary tracks. As well as obtaining information on sizes, parallaxes, and orbital elements it is possible to get information on other physical parameters of interest, including aspects such as luminosity and the orbital elements (Al-Tawalbeh et al., 2021, Docobo et al., 2018, Hussein et al., 2022).

Many observatories equipped with large refractors and telescopes were constructed around the world at the beginning of the 20th century, especially in Europe and North America, for the observation of binaries. Due to these various research lines, double stars have drawn the attention of many relevant astronomers. Traditional classifications for the binaries include visual, spectroscopic, and eclipsing binaries, based on the

[*]Ahmad.Abushattal@ahu.edu.jo, Corresponding author

doi:https://doi.org/10.52526/25792776-22.69.2-251

methods used to discover and study them. Four methods are used To establish binary nature: a direct visual observation through an eyepiece, a photographic camera (traditional camera or CCD), or speckle interferometry using modern high resolution techniques. There are other cases when the binary cannot be resolved optically, even with large telescopes. However, other methods are possibly using the Doppler-Fizeau effect (spectroscopic binaries) to observe the periodic variation of spectrum lines. Eclipses are frequently accompanied by periodic variations in the magnitude of the stellar companion (Abushattal et al., 2019a, Docobo et al., 2017, **?**).

Furthermore, binary systems serve as a "shop window" through which many physical processes can be observed : mass loss, mass exchange, variability of components, relativistic processes, the Nova phenomenon, the Flare phenomenon, X-ray Binaries, Wolf-Rayet components, etc. From a dynamical perspective, these include perturbations, the discovery of dark components, such as brown stars and exoplanets, orbit calculation methods, etc (Abushattal et al., 2019b, Taani et al., 2019a,b, 2020). Using two or three different techniques, it has been possible to study a number of binaries thanks to precision devices attached to large telescopes.

The purpose of this paper is to highlight the importance of creating a common database across different catalogues. That will enable us to compare data about binary stars that can serve as a starting point for determining their physical and orbital characteristics will assist in answering questions about the formation and development of stars and searching for Earth-like planets around Sun-like stars.

1.1. The Ninth Catalogue of Spectroscopic Binary Orbits (SB9)

Batten and collaborators continue their series of compilations of spectroscopic binary orbits over the past 55 years with the Ninth Catalogue of Spectroscopic Binary Orbits `http://sb9.astro.ulb.ac.be`. The new Catalogue contains the orbits for 2386 systems as of 2004. In addition, three straightforward applications are presented, highlighting some differences between this catalogue and its predecessors: (1) Completeness assessment: period distribution of SB1s and SB2s, (2) Shortest periods across the H-R diagram; (3) Relationship between periods and eccentricities (Pourbaix et al., 2004). Several contributors from around the world contribute to the compilation of SB9. Data from new orbits should be contributed directly by the authors. In SB8 there was more information included for each new system in the notes, but it will be less in SB9 due to the growing volume of data. In contrast, SB9 provides multiple orbits and individual radial velocities for each system (depending on the system's orbits). ADS bibliographic service is linked to references.

A new automatic grading system is in the process of being developed, which will allow for the entry of grades for new orbits. The grades of old orbits are listed as (5 being the best, 1 being the worst). Some elements (such as centre-of-mass velocity V_0) of double-lined binaries are listed only if they were determined separately for primary and secondary components, since the elements are meant to reflect the actual Keplerian motion of stars rather than the radial velocity curve that they are derived from.In the WEB page of SB9, you can search for your object of interest by identifying it in common catalogues (like HD, BD, HIP), by bibcode, or by coordinates. Enter identifier and number, separated by space, for uncommon identifiers (like nearby stars or cluster members).

1.2. The Sixth Catalog of Orbits of Visual Binary Stars (6COVB)

Over the past three decades, the field of visual double star work has undergone revolutionary changes thanks to the advent and maturation of interferometry. A large telescope equipped with speckle interferometry can produce astrometric results that are much more accurate (down to milliarcseconds) than those available from micrometry and other visual methods. At the time of the Fourth catalog publication, only a few orbits were calculated where Speckle played a significant role, despite Speckle being available since 1970. Many orbits now include speckle results exclusively, despite its popularity growing in the 1980s. In 1983, speckle was at its peak, but now long-baseline interferometry and Navy Precision Optical Interferometry are perhaps in a similar stage of maturity; multi-aperture telescope arrays are being used to observe a growing number of binaries, once considered exclusively spectroscopists' property. In the coming decades, the distinction between spectral and visual regimes will become less significant as new interferometers improve in magnitude sensitivity. In catalogs such as this one, only a subset of a binary's elements will be published, as spectroscopic and visual "combined solutions" become more common.

Creating a new catalogue requires grading each orbit. The Fourth Catalog grading scheme assessed

doi:https://doi.org/10.52526/25792776-22.69.2-251

orbital coverage, the number of observations, and the overall quality of observations on a numerical scale (1 = definitive, 5 = indeterminate). They graded observers numerically based on their qualitative assessment of individual observers and their accumulated experience (Matson et al., 2020).

1.3. The Fourth Catalog of Interferometry Measurements of Binary Stars (4CIMB)

The Georgia State University center for High Angular Resolution Astronomy (CHARA) began tabulating binary star observations made with their speckle camera using the speckle interferometry technique in 1982 using the Fourth Catalogue of Interferometric Measurements of Binary Stars. As time progressed, the Speckle catalog included all published astrometric and photometric data from high-angular-resolution methods for binary stars (and single stars observed by duplicate surveys). The results from various infrared speckle or imaging surveys were also included, even though some are not really considered high resolution. The catalogue includes 24 bands of right ascension. While the catalog is updated regularly, statistics are only updated occasionally. In addition to the astrometric data, this catalogue contains 73,894 photometric observations

2. Methodology

In this work, a large amounts astronomical data are processed and collected from various Spectroscopic and visual catalogues through computer programs. Then sort and identify the commonalities among them and arrange them so that they are easily accessible. In order to benefit from them and to make them accessible to researchers in the field of astrophysics and specialists in studying binary stars.

Ground-based telescopes and space observatories collect a vast amount of data over the electromagnetic spectrum. In this article, we introduce Astroinformatics as a new data-oriented approach and advanced methodology for processing astronomical surveys and catalogues using astroinformation resources. Interoperability between different astronomical archives and data centres allows easy access to astronomical data. Figure 1 illustrates the importance of astroinformation as a link between data science and astronomy.

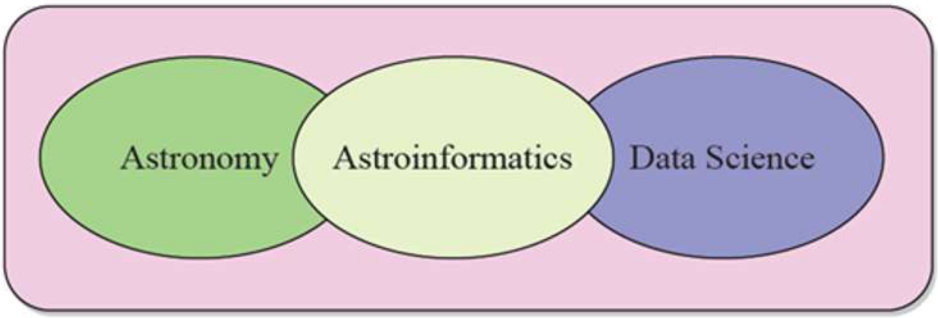

Figure 1. In Astronomy and Data Science, Astroinformatics acts as a bridge.

The Fourth Interferometric catalogue is available in plain text and gzipped plain text formats. In each system, there are two parts: an identification line containing catalogue numbers, followed by individual measurements sorted by observation date. An ID line format change has been made to accommodate longer names. Observations are accompanied by acronyms linked to reference files. Links to notes files are also included with the notes. Additionally, it provides links to pairs with visual or astrometric orbits published in the Sixth Orbit catalogue. WDS, Interferometric, and Orbit catalogues all use the same notes file. In the notes file, additional systems will be included in addition to those in this catalogue. To facilitate faster linking to the files, the notes file was divided into 24 smaller ones because it was much larger than the measurements file. (Hartkopf et al., 2004).

In comparison to prior editions, SB9 is capable of storing unlimited stellar identifiers per system, although important catalogues (HD, HIP, etc.) still remain the preferred sources for stellar identification. To match the level of precision used by other catalogues, this catalogue was built with a different epoch and equinox than 1900.0. Declination and Right Ascension are now given to the hundredth of a second. This catalogue also provides information about uncertainties associated with orbital parameters. NASA Astrophysics Data System (ADS) specifies an orbit's bibliographic reference by its 19-character bibliography code ("bibcode"). In the absence of a bibcode, a special code indicates that the reference appears in the Notes section of

doi:https://doi.org/10.52526/25792776-22.69.2-251

the Catalogue. Using SB9's web interface, you can view specific orbits at your convenience. Both catalog identifiers and coordinates can be used to search for systems. The selection criteria are met by several systems, and users are asked to pick one. The user can choose from several orbits. To help you choose among the orbits, a list of publication years is provided. HTML links are used to display the displayed information. Directly connecting to ADS makes it easy to retrieve the abstract, coordinates, spectral type, apparent magnitude, identifiers, and orbital parameters of a paper. The interface can also automatically generate an orbit plot (if actual observations are available). The corresponding figure has a link to a PostScript version. On the SB9 main page, researchers can also download a compressed version of the SB9 database if they are interested in previewing the properties of a sample of these systems rather than browsing one orbit. It is virtually impossible to limit the distribution of the database when combined with other public access catalogs through Unix-like tools like sort and join, as well as scripting languages like Python and Awk (Pourbaix et al., 2004).

The Sixth Catalogue of Orbits of Visual Binary Stars contains about ten thousand orbits of binary stars. Observations are the ultimate gauge of a model's accuracy, and scientists use them to test predictions. A couple shortcomings in the original format were addressed in March 2005 by extensively modifying the Sixth Orbit catalogue. The first request was that published formal errors for orbital elements be included when they were available in the catalogue. Recent developments in interferometry, such as long-baseline interferometry, have also led to shorter periods and smaller semi-major axes of orbits. Because of this, both formal errors and higher precisions were accommodated in the master file. It is now possible to quote periods in centuries, minutes, milliarcseconds, microarcseconds, and arcseconds, as well as T0 in Julian dates and Julian dates, as well as fractional Besselian years, by using the flags added to the period and semi-major axes columns. In order to decrease the width of the web catalogue, two lines are used per orbit. In addition to the errors, some catalogue names (such as HD and Hipparcos) and other items are stacked along the bottom of the page (Muller et al., 2006).

Therefore, we have used astronomical data science and its specialized programs to process the data in each of the previous three catalogues. Then, we worked on linking them with each other, searching for the stars shared between those catalogues, and forming a unified database containing the visual spectroscopic binaries. The figure 2 represents the Summary of this process.

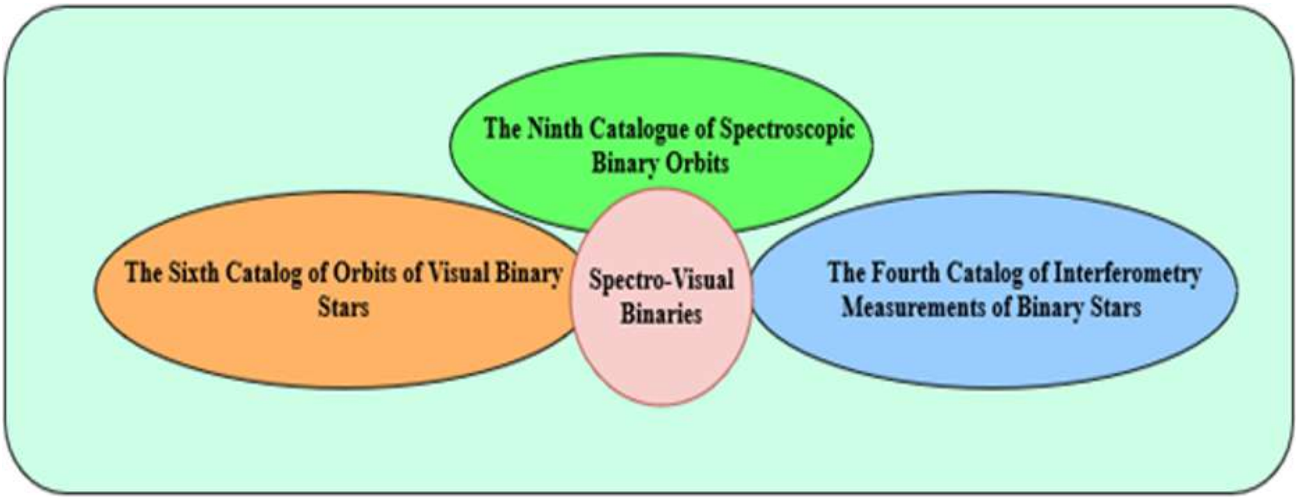

Figure 2. In all catalogues, the common Spectro-visual stars could be found.

3. Results

As a result of this work, two important sciences are brought together: observational astronomy, which studies and monitors many astronomical objects and stores their data, as well as astronomical information, which processes and arranges that data, making it easier for researchers to reach their goals. Research results can be summarized as follows: finding a field of knowledge based on the link between astronomical data, data science, and precision-visual binaries. We combined data from the three catalogues; the Ninth catalogue of Spectroscopic Binary Orbits (SB9), the Sixth catalogue of Orbits of Visual Binary Stars (6COVBS), and the Fourth Catalog of Interferometry Measurements of Binary Stars (4CIMBS). After applying the research

doi:https://doi.org/10.52526/25792776-22.69.2-251

method, more than 600 common systems have been found in the previous three catalogs. These systems provide the starting point for researchers working on binary stars to determine their physical and orbital properties accurately. The data will be published on the official website of Al-Hussein Bin Talal University's, Department of Physics.

4. Conclusions and Future Work

Our study involved processing binary star catalogues with big data programs and identifying spectroscopic binary stars as a common database. Therefore, it is necessary to work on finding joint research groups specializing in data science and observational astronomy that analyze these observed data, which are in different astronomical catalogues, and prepare them for use in the various astrophysical sciences such as observational astronomy and astrobiology.

Acknowledgements

Thanks to Gor Mikayelyan, the Scientific and Local Organizing Committee of the International Conference "Space Sciences and Technologies" at Byurakan Astrophysical Observatory (BAO).

References

Abushattal A. A., 2017, PhD thesis, Universidade de Santiago de Compostela

Abushattal A. A., Docobo J. A., Campo P. P., 2019a, The Astronomical Journal, 159, 28

Abushattal A., Al-Wardat M., Taani A., Khassawneh A., Al-Naimiy H., 2019b, in Journal of Physics: Conference Series. p. 012018

Al-Tawalbeh Y. M., et al., 2021, Astrophysical Bulletin, 76, 71

Al-Wardat M., Docobo J., Abushattal A., Campo P., 2017, Astrophysical Bulletin, 72, 24

Borne K. D., 2009, arXiv preprint arXiv:0909.3892

Brescia M., Djorgovski S. G., Feigelson E. D., Longo G., Cavuoti S., 2017, Astroinformatics

Docobo J. A., Griffin R. F., Campo P. P., Abushattal A. A., 2017, Monthly Notices of the Royal Astronomical Society, 469, 1096

Docobo J., Balega Y., Campo P., Abushattal A., 2018, Double Stars Information Circular, 196, 1

Duquennoy A., Mayor M., 1991, Astronomy and Astrophysics, 248, 485

Hartkopf W. I., Mcalister H. A., Mason B. D., 2004

Hussein A. M., Al-Wardat M. A., Abushattal A., Widyan H. S., Abu-Alrob E. M., Malkov O., Barstow M. A., et al., 2022, The Astronomical Journal, 163, 182

Jack D., Hernández Huerta M. A., Schröder K.-P., 2020, Astronomische Nachrichten, 341, 616

Matson R., Williams S., Hartkopf W., Mason B., 2020, United States Naval Observatory, Washington, DC

Muller R., Cersosimo J., Rosado-de Jesus I., Cotto D., Miranda V., Martinez C., Centeno D., 2006, Journal of Double Star Observations, 2, 138

Pourbaix D., et al., 2004, Astronomy & Astrophysics, 424, 727

Raghavan D., et al., 2010, The Astrophysical Journal Supplement Series, 190, 1

Siemiginowska A., Kuhn M., Graham M., Mahabal A. A., Taylor S. R., 2019

Taani A., Abushattal A., Mardini M. K., 2019a, Astronomische Nachrichten, 340, 847

Taani A., Karino S., Song L., Mardini M., Al-Wardat M., Abushattal A., Khasawneh A., Al-Naimiy H., 2019b, in Journal of Physics: Conference Series. p. 012029

Taani A., Khasawneh A., Mardini M., Abushattal A., Al-Wardat M., 2020, arXiv preprint arXiv:2002.03011

Vavilova I., 2016, Odessa astronomical publications, pp 109–115

doi:https://doi.org/10.52526/25792776-22.69.2-251

Substructures in the Isolated Galaxy Clusters

E.A. Panko *[1,2], S. Yemelianov[1], A. Sirginava[1], and Z. Pysarevskyi[3]

[1]I.I. Mechnikov Odessa National University, Odessa, Ukraine
[2]Pavol Jozef Safarik University in Kosice, Kosice, Slovak Republic
[3]National Centre "Junior Academy of Sciences"under the auspices of UNESCO, Dnipro, Ukraine

Abstract

The isolated clusters are special objects for understanding the ways of forming observed large-scale distributions of matter. One can consider the isolated clusters as objects evolving without any external influence. We present the results of the analysis of the $2D$ distribution of galaxies in 31 isolated galaxy clusters with redshifts $z < 0.15$ and the distance to the nearest neighbor less than $60h^{-1}Mpc$. We defined the morphological types of these clusters accordingly to advance Panko's classification scheme using the "Cluster Cartography" set. The main part of these clusters belongs to the open O-type clusters without any signs of a complex structure. However, we detected the presence of the inner regular substructures for 10 clusters. They are linear substructures, X- and Y-type crosses, and compact short chains. All substructures were detected on a statistically significant level. The detected substructures have special orientations of galaxies, which note to their $3D$ type. Practically all studied galaxy clusters are young.

Keywords: *galaxy clusters: morphology; galaxies: orientation*

1. Introduction

The modern approach to the status of galaxy clusters is the idea that these objects are the elements of the Large Scale Structure (LSC) of the Universe and evolve in interaction with other LCS elements. Observed features in the inner structure of galaxy clusters reflect this interaction and arise due to the global influence of the most massive cluster components – dark matter (DM) and intracluster gas. It was studied in different theoretical works from Zeldovich (1970) and Peebles (1969), numerical simulations (Springel et al. (2005), Vogelsberger et al. (2014), Artale et al. (2017), Cui et al. (2018), Tomoaki et al. (2021)) and observed data analysis (Wen et al. (2009), Dietrich et al. (2012), Parekh et al. (2020)). At the same time, the galaxies were and are confident optical markers of the common inner structure of the clusters. It can be noted from the comparison of the distribution of hot gas and galaxies inside the cluster (Tugay et al. (2016)). It has common characteristics: simple distribution of gas observed in γ- and X-rays corresponds to regular visual morphology of the clusters, or gas disturbed distribution shows the agreement with optically detected cluster substructures, for example, Dietrich et al. (2012). Common characteristics in the DM, hot gas, and galaxies distributions are disturbed in collided clusters Markevitch et al. (2004), where we observe the separation of DM from other cluster components.

The inner structure of galaxy clusters from Abell (1958) and Zwicky et al. (1968) papers is described in the different morphology schemes, based on the positions of the cluster members mainly. The schemes take into account richness, concentration to the cluster's center, and the presence or excess of some special types of galaxies. The Bautz & Morgan scheme (Bautz & Morgan, 1970, BM) is based on the relative contrast (dominance in extent and brightness) of the brightest galaxy to other cluster members. Rood & Sastry (1971) (RS) and later Struble et al. (1987) schemes note the features in the geometry of the distribution of the ten brightest cluster members. Oemler recognized spiral rich and spiral poor galaxy clusters and introduced the special type having giant dominated elliptical cD galaxy in the center. Bahcall (1999) published the common review of morphological schemes. Panko (2013) and AName et al. (2019) based on the different approaches proposed numerical criteria for describing the $2D$ structure of galaxy clusters. This approach also allows detecting the regular linear substructures. Accordingly to Rood & Sastry (1971) and Struble

*panko.elena@onu.edu.ua, panko.elena@gmail.com Corresponding author

doi:https://doi.org/10.52526/25792776-22.69.2-256

et al. (1987) ideas they are the key to the way to the evolution of galaxy clusters: from the open structure without any substructures to the strongly regular concentrated cluster with a giant cD galaxy in the center.

Our study of the detailed morphology of galaxy clusters allowed the detection of some additional kinds of regular substructures, such as crosses, semi-crosses, or curved compact chains (Panko & Emelyanov (2021)). One can assume these substructures as a sign of complex interaction with the underlying DM filaments and the influence of the nearest clusters. One more feature in the detected regular peculiarities is the alignment of galaxies from the brightest and most massive cluster members according to the parent structure to the prevalent orientation of galaxies belonging to the substructure (Panko et al. (2021)). In the second case, we have a the possibility to divide wall-type substructures from filament-type, using the Joachimi et al. (2015) results, even if we have no measured redshifts. Isolated galaxy clusters have influence from the neighbors and we can study the interaction with the underlying LSC elements in pure.

The paper is organized in a standard manner. Section 2 contains the description of the observational data, section 3 explains the cluster mapping and character of substructures, section 4 presents the results and their analysis, and conclusions are given at the end.

2. Observational Data

The main base of our study is the list of galaxies obtained from 216 digitized plates of Muenster Red Sky Survey Ungruhe et al. (2003), hereafter MRSS, and based on the MRSS "A Catalogue of Galaxy Clusters and Groups" (Panko & Flin, 2006, PF hereinafter).

The MRSS plates covered about 5000 square degrees of sky with galactic latitudes $b < -45°$. and contained information on more than 5 million galaxies. For each galaxy except for equatorial coordinates and r_F magnitude, a lot of other parameters are given, particularly, the size of axes of the galaxy image in best-fitted ellipse approximation (in *arcsec*), ellipticity, and the position angle of the major axis. The MRSS list contains only galaxies, the stars and perturbed objects were deleted by an automatic procedure with a posterior visual check of the automatic classification, which considerably diminished the number of objects erroneously classified as galaxies. So, MRSS is a statistically valid input list for further research. The r_F magnitudes of galaxies were obtained with external CCD calibration of the photographic magnitudes. There are about 1.2 million galaxies in MRSS completeness limit $r_F = 18.3^m$. This list was used as input data for the creation of the PF catalogue. Each PF cluster has several parameters including Right Ascension and Declination (2000.0), equivalent radius in *arcsec* for the full area of the structure, the number of galaxies, major and minor semiaxes of the best-fitted ellipse, the ellipticity of the structure ($E = 1–b/a$), the position angle of the major axis of structure (counted clockwise from direction to the North Pole, same as the position angle for galaxies in the MRSS), and also the full list of galaxies in the cluster field. Unfortunately, MRSS was the last photographic survey with corresponding weaknesses, and their galaxies have no redshifts.

The comparison of PF catalogue with ACO Abell et al. (1989) and APM Dalton et al. (1997) catalogues allows to estimate the distances to PF galaxy clusters as the $logz$ vs. m_{10} relation Biernacka et al. (2009), following Dalton et al. (1997).

1711 PF galaxy clusters with $z_{est} < 0.15$ and richness over 50 galaxies allowed to create the list of galaxy superclusters Panko (2011) using *FoF* method in Zeldovich & Einasto (1982). Simultaneously, for each of these clusters, the distance to the nearest neighbor was determined. The distribution of distances is shown in Fig. 1. The clusters from the biggest distances (right "tail" noted in Fig. 1 by the ellipse) were selected for the present study as isolated.

The question about the limit distance allowed assuming the cluster as isolated is not obvious. For example, Lee (2012) studied the relative abundance of isolated clusters as a probe of dark energy under the assumption that those galaxy clusters which do not belong to the superclusters are referred to as the isolated. From another hand, one can assume the nonrandom orientation of galaxy clusters is caused due to interaction with neighbors. Firstly this effect was described in Binggeli (1982) paper as the cluster's tendency to be aligned pointing to each other at the separation of up to $15h^1Mpc$. The effect named after Binggeli was observed at various distances and was detected for ranges from $10h^{-1}Mpc$ till $150h^{-1}Mpc$. It was observed that the strength of the effect diminished with distance (Struble & Peebles (1985), Flin (2019), Ulmer et al. (2019), Biernacka et al. (2015)). It is currently believed that the effect occurs over distances till $60h^{-1}Mpc$ and we selected this value for our study. Moreover, this value is a good criterion for isolated clusters. It is close to another one, which we formally calculated based on the median and standard deviation of the distribution of distances to the nearest neighbor (Fig. 1).

doi:https://doi.org/10.52526/25792776-22.69.2-256

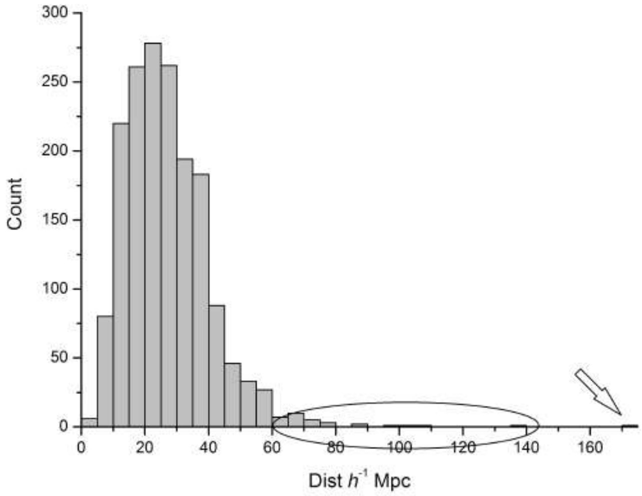

Figure 1. The examples of distribution of the galaxies in the isolated clusters. Right panel to the nearest neighbor for 1711 PF clusters. Isolated clusters are shown by the ellipse. Excluded cluster is marked by the arrow.

We've selected 32 PF galaxy clusters with a richness of 50 and more having neighbors no closer than $60h^{-1}Mpc$, and we checked additionally the presence of the galaxy groups with a richness of less than 50 for selected clusters. We suppose these clusters are placed in relatively low-density environments without any close neighbors. The PF 0540-5764 cluster having the largest distanse ($173.7h^{-1}Mpc$) is located near the boundary of MRSS region and we excluded it from the present study. It is shown in the Fig. 1 by arrow.

Our data set contains 31 PF isolated galaxy clusters with the richness 50 and more galaxies in the cluster field and information about these galaxies. 9 clusters have identifications with ACO, and only 4 with APM catalogues. It can be explained by the lesser depths of the corresponding sky surveys. Only 5 clusters in the data set belong to the rich clusters ($N > 100$), while others contain from 50 to 88 galaxies in the cluster field. The main part of our isolated clusters, 19 ones, have richness from 50 to 60 galaxies, they are poor clusters. 22 isolated clusters have z_{est} in the range 0.10 – 0.14.

3. Cluster Mapping and substructures detection

The criteria of the advanced detail morphology scheme were described in Panko (2013) for base regular features in the clusters, such as the degree of concentration to the cluster center or/and to some line. The first character is noted as C, I, or O for clusters with significant, intermediate, or low concentration to the center correspondingly. The linear substructure is noted as L. The role of the brightest galaxies can be marked too. "Cluster Cartography" tool (hereafter CC) was created for cluster mapping and statistical analysis of the distribution of galaxies in the cluster field (Panko & Emelyanov (2015)). The tool allows for creating the 2D cluster map, the symbol for each galaxy corresponds to MRSS data.

The study of the morphology of PF clusters expanded the list of regular substructures (Panko & Emelyanov (2017)), and respectively CC was upgraded (Panko & Emelyanov (2021)). All CC maps have the same size $4000 \times 4000\,arcsec$. The size, shape, and orientation of symbols for galaxies correspond to MRSS data: magnitude m, ellipticity E, and positional angle of the major axis PA of the galaxy image in the best-fitted ellipse. The size of the symbol m' is calculated from the magnitude as

$$m' = 3 \cdot 2^{0.6(18.5-m)} + 6,$$

And the axes A and B of the ellipse having the same square, as:

$$A = \frac{m'}{\sqrt[4]{(1-2E+E^2)}}, \;\; B = \frac{(m')^2}{A}.$$

The legend of the symbol size is shown in a panel in Fig. 2. The typical value for ellipticity 0.2 and positional angle 45° were used for the legend.

doi:https://doi.org/10.52526/25792776-22.69.2-256

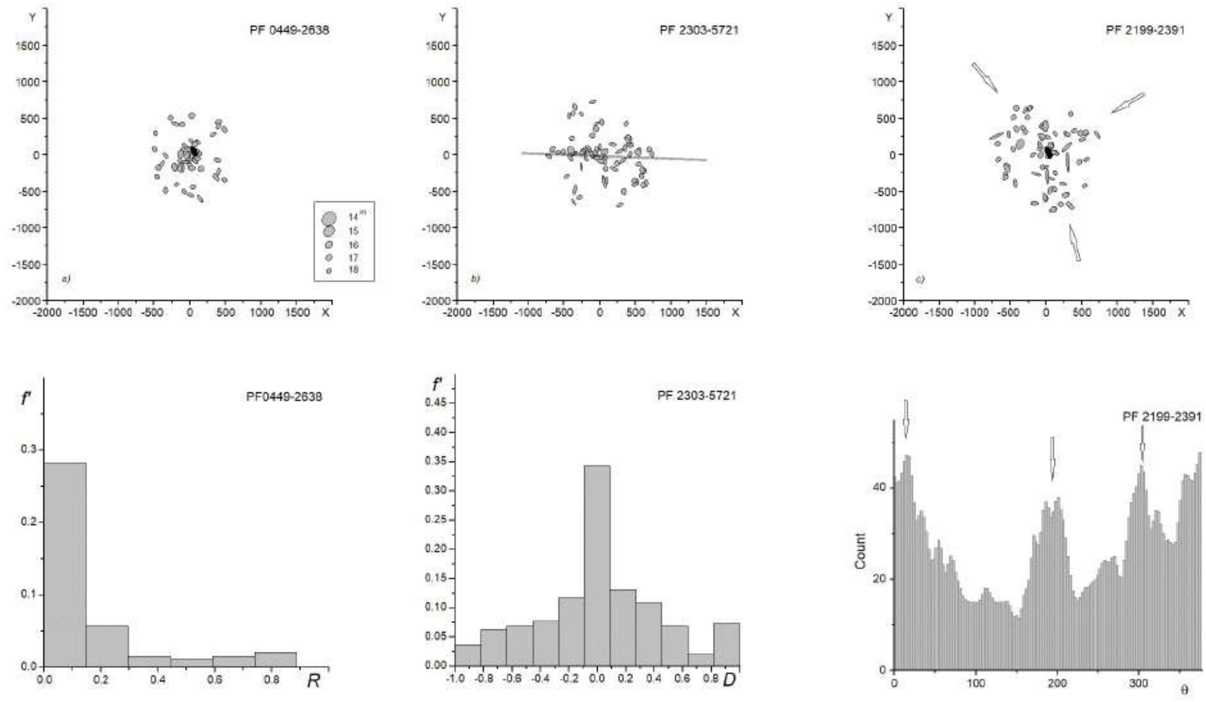

Figure 2. The distribution of galaxies for some isolated clusters: *a)* concentrated cluster, standard case; *b)* linear substructure; and *c)* Y-type substructure. The cluster maps are shown in the upper panel and respective distributions are in the lower one. The brightest galaxy in the C-type cluster is shown as black. The legend of the symbols according to the magnitudes of the galaxies is presented in the *a)* panel.

The numerical analysis of the CC input data is executed automatically and the results can be seen in the Fig. 2. The maps for C-type cluster, OL11- and OY-types are presented in the upper panel as *a*, *b*, and *c*. All clusters are belonged to isolated. The distribution of the density of galaxies is shown in the lower panel for the same map. For PF 0449-2638 the variations of the density along the cluster radius show the significant peak for the central zone. The brightest galaxy of the cluster is shown as black, but the difference between second- and third-ranked galaxies is not significant; it is the brightest cluster member, but not cD galaxy. We attribute this cluster to a typical C-type. Its evolutional status is: greatly evolved. This cluster is not so massive, it is possible cD stage would not be achievable.

The PF 2303-5721 cluster is shown in the *b* map. It has no concentration to the cluster center, it's an open type. The linear substructure is clearly seen in the distributions of densities of galaxies in the stripes. CC automatically detects the direction of the densest stripe. Attribution for PF 2303-5721 is OL11, where 11 is the ratio of the cluster diameter to the width of the overdense stripe. The direction of the linear substructure is shown in the map as the line. The status of the PF 2303-5721: the middle stage of evolution.

The Y-type crumbly substructure in the open cluster is present in *c* part. The crossed substructures can be detected using the "lighthouse beam" diagram. The beam with a width of some part of the diameter (from 1/5 to 1/11), is rotated with step 1°, and the number of galaxies for each position of the beam is shown in the lower part. Three peaks in the distribution correspond to Y-type substructure (pointed by arrows for both panels). PF 2199-2391 cluster we assume as OY type, pertaining to the early stage of evolution.

In this way, the morphological types and presence of features were determined for all 31 isolated clusters.

4. The Morphology, Evolutionary Status and Substructures in the Isolated Galaxy Clusters

The morphological classification of 31 isolated PF galaxy clusters is present in Table 1, Appendix A. Only 1 cluster has a significant concentration to the center and can be considered as evolved. 6 clusters have intermediate concentrations with different levels from clearly seen to possible presence. Other clusters are open, with or without substructures. This common distribution by types corresponds to the assumption that isolated clusters are young structures formed during the general evolution of LCS. The more interesting is the presence of different types of substructures in the isolated clusters. Parts of the filaments with different densities can appear both as elongated clusters and as linear substructures inside a cluster. The interaction of filaments contributes to the appearance of substructures. The rich cluster PF 0413-3091 in which 2 cores are clearly detected, deserves a separate analysis after studying its $3D$ structure when the measured redshifts for its galaxies are obtained.

2 Spiral-rich clusters PF 2188-7165 and PF 2199-2391 are additional evidence of the early stage of cluster evolution. According to the classical work Dressler (1980), spiral (disk) galaxies are destroyed during prolonged interaction with other cluster members. Later papers (Fasano et al. (2000)) note that dependence is ambiguous, and the shapes of galaxies in individual clusters appear to relate to local conditions. X and Y substructures in the PF 2195-7771 and PF 0375-7764 clusters can arise due to crossing the DM underlying filaments. 2 clusters contain special substructures (Fig. 3).

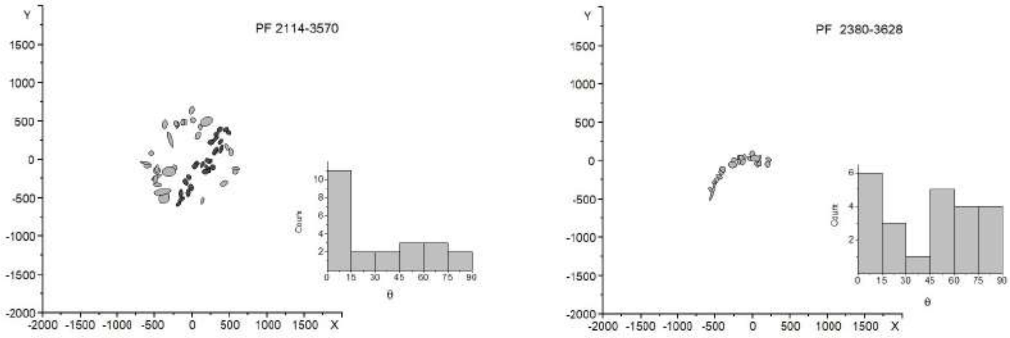

Figure 3. The linear compact chain in PF 2114-3750 (dark symbols), and curved stripe extracted from PF 2380-3628 cluster. The distributions of orientations of the galaxies relative to the common direction of the substructures are shown too in the histograms for both cases.

X and Y substructures in the PF 2195-7771 and PF 0375-7764 clusters can arise due to crossing the DM underlying filaments. 2 clusters containing special substructures are shown in Fig. 3. The compact chain in the PF 2195-7771 contains 23 galaxies that have significant alignment along the parent structure. At less, for galaxies with ellipticity $E > 0.25$ the acute angle between the directions of their major axis and the parent structure less, then $30°$. For the curved stripe in PF 0375-7764 we see another distribution. Half of the galaxies in this structure tend to be perpendicular to the central line of the stripe. Both these cases have z good agreement with Joachimi et al. (2015) modeling. In this approach, elliptical galaxies tend to align their major axes with the filament direction, while disc galaxies tend to align their spin perpendicular to the filament direction, and in $2D$ projection we'll see the general alignment of galaxies according to the filament. In another case, in a two-dimensional structure, elliptical galaxies tend to align their major axes along the structure, while disc galaxies tend to align their spin in the perpendicular direction, and we'll not see prevailing orientations. For our data, the substructure in PF 2195-7771 probably is filament-type, while the curved stripe in PF 0375-7764 is the projection of wall.

5. Conclusion

We determined the morphological types for 31 isolated PF galaxy clusters according to Panko (2013) scheme. We assumed the isolated clusters are formed in relatively low-dense regions and connected with the underlying DM filaments. They formed later than galaxy clusters in the rich regions. Our results confirm this point of view. The majority of the clusters (25 of the 31) are open clusters, 6 have a different level of concentration to the cluster center, and only 1 is a concentrated one. The direction of the evolution is: from an open cluster without a regular inner structure to a cluster with a well-formed core that contains a giant elliptical cD galaxy. The part of the open clusters for isolated ones is bigger than for the common list. 2 Spiral-rich clusters can be recognized as young too. So, our isolated clusters are newly formed young objects. Our observational data confirmed this position.

For 7 clusters of galaxies, we found regular substructures, namely, linear belts, one compact chain, one curved stripe, and the X- or Y-type substructures, without the correlation between the richness and

doi:https://doi.org/10.52526/25792776-22.69.2-256

substructures' presence. The orientations of galaxies in the detected substructures are in agreement with Joachimi et al. (2015) model and confirm the validation of the substructures.

Acknowledgements

This research has (was) made use of (using) NASA's Astrophysics Data System. E. Panko thankful to the SAIA n. o. the National Scholarship Program of the Slovak Republic and Pavol Jozef Safarik University in Kosice for the particular support of this study.

References

AName A. A., Name B. A., Name A. C., et al. 2019, Proc. Polish Astron. Soc., 2, 85

Abell G. O., 1958, Astrophys. J. Suppl. Ser. , 3, 211

Abell G. O., Corwin H. G., Olowin R., 1989, Astrophys. J. Suppl. Ser. , 70, 1

Artale M. C., Pedrosa S. E., Trayford J., et al. 2017, Mon. Not. R. Astron. Soc. , 470, 1771

Bahcall N. A., 1999, in Formation of Structure in the Universe. Cambridge University Press, p. 135

Bautz L. P., Morgan W. W., 1970, Astrophys. J. , 162, L149

Biernacka M., Flin P. A., Panko E., 2009, Astrophys. J. , 696, 1689

Biernacka M., Panko E., Bajan K., et al. 2015, Astrophys. J. , 813, 20

Binggeli B., 1982, Astron. Astrophys. , 107, 338

Cui W., Knebe A., Yepes G., et al. 2018, Mon. Not. R. Astron. Soc. , 473, 68

Dalton G., Maddox S., Sutherland W., et al. 1997, Mon. Not. R. Astron. Soc. , 289, 263

Dietrich J. P., Werner N., Clowe D., et al. 2012, Nature. , 487, 202

Dressler A., 1980, Astrophys. J. , 236, 351

Fasano G., Poggianti B., Couch W., et al. 2000, Astrophys. J. , 542, 673

Flin P., 2019, Mon. Not. R. Astron. Soc. , 228, 941

Hoyle B., Masters K. L., Nichol, R. C., et al. 2012, Mon. Not. R. Astron. Soc. , 423, 3478

Joachimi B., Cacciato M., Kitching T. D., et al. 2015, Space Sci. Rev. , 193, 1

Lee J., 2012, Astrophys. J. , 752, 40

Markevitch M., Gonzalez A. H., Clowe D., et al. 2004, Astrophys. J. , 606, 819

Panko E., 2011, Balt.~Astron., 20, 313

Panko E. A., 2013, Odes.~Astron.~Publ., 26, 90

Panko E. A., Emelyanov S. I., 2015, Odes.~Astron.~Publ., 28, 135

Panko E. A., Emelyanov S. I., 2017, Odes.~Astron.~Publ., 30, 121

Panko E. A., Emelyanov S. I., 2021, Odes.~Astron.~Publ., 34, 35

Panko E., Flin P., 2006, Journal Astron. Data., 12, 1

Panko E. A., Flin P., 2014, Odes. Astron. Publ., 27, 32

Panko E. A., Yemelianov S. I., Korshunov V. M., et al. 2021, Astr. Rep. , 65, 1002

Parekh V., Lagana T. F., Tho K., et al. 2020, Mon. Not. R. Astron. Soc. , 491, 2605

Peebles P., 1969, Astron. J. , 155, 393

Rood H. J., Sastry G. N., 1971, Publ.~Astron.~Soc.~Pacific, 83, 313

Springel V., White S. D., Jenkins A., et al. 2005, Nature. , 435, 629

Struble M. F., Peebles P. J. E., 1985, Astron. J. , 90, 582

Struble M. F., Rood H. J., Name A. C., et al. 1987, Astrophys. J. Suppl. Ser. , 63, 555

Tomoaki A. A., Francisco P., Klypin A. A., et al. 2021, Mon. Not. R. Astron. Soc. , 506, 4210

Tugay A. T., Dylda S. S., Panko E. A., 2016, Odes.~Astron.~Publ., 29, 34

doi:https://doi.org/10.52526/25792776-22.69.2-256

Ulmer M. P., McMillan S. L. W., Kowalski M. P., 2019, Astrophys. J. , 338, 711

Ungruhe R., Seitter W. C., Duerbeck H., 2003, Journal Astron. Data., 9, 1

Vogelsberger M., Genel S., Springel V., et al. 2014, Mon. Not. R. Astron. Soc. , 444, 1518

Wen Z. L., Han J. L., Liu A. C., 2009, Astrophys. J. Suppl. Ser. , 183, 197

Zeldovich Y. B., 1970, Astron. Astrophys. , 5, 84

Zeldovich Y., Einasto J.and Shandarin S., 1982, Nature. , 300, 407

Zwicky F., Herzog E., Wild P., et al. 1961 – 1968, Catalogue of Galaxies and of Clusters of Galaxies. California Institute of Technology, Pasadena

doi:https://doi.org/10.52526/25792776-22.69.2-256

Appendices

Appendix A The Morphology Types of 31 Isolated PF Galaxy Clusters

In Appendix A the results of the morphological classification of 31 isolated PF galaxy clusters according to the Panko (...) scheme are present. The consecutive columns of Table 1 contain the following information:

PF	the structure identification, based on the first digits of *R.A.* and *Dec.* of the cluster center;
R.A., Dec.	Right Ascension, in hours, and Declination, in degrees, of the cluster center for 2000.0;
N	the number of all galaxies in the cluster field;
Dist $(h^{-1})Mpc$	the distance to nearest neighbor
z_{est}	the redshift of the cluster, estimated according to Biernacka et al. (2009);
Panko Type	the result of the detailed classification by the Panko scheme;
note	additional information.

Table 1. **Morphology of 31 Isolated PF Galaxy Clusters**

PF	*R.A.*	*Dec.*	N	z_{est}	Dist (h^{-1} Mpc)	Panko type	Note
0016-5711	0.1670739	-57.107367	88	0.053	68.9	IL7	1
0024-2431	0.2472369	-24.300611	52	0.129	78.5	O	2
0093-3597	0.9354548	-35.969931	51	0.121	62.7	O	
0096-3921	0.9621619	-39.205838	52	0.142	136.9	O	
0115-4600	1.1567254	-45.996573	261	0.04	105.4	O	3
0145-2632	1.4517246	-26.313951	51	0.13	60.1	O	
0200-2252	2.0036788	-22.519040	52	0.133	73.0	O	4
0240-4218	2.4023855	-42.175194	56	0.14	98.3	O	5
0294-2398	2.9476380	-23.972509	52	0.131	64.0	O	
0303-4097	3.0337096	-40.962828	53	0.127	60.5	O	6
0341-3468	3.4138816	-34.671654	50	0.118	60.0	I	
0358-6952	3.5873377	-69.511811	53	0.126	68.8	O	
0375-7764	3.7591708	-77.637521	54	0.126	67.4	OY	
0381-1788	3.8163216	-17.879863	282	0.069	73.5	O	7
0397-6046	3.9736611	-60.450522	75	0.115	71.4	O	
0413-3091	4.1336041	-30.907580	271	0.064	77.0	I P	8
0444-3673	4.4464843	-36.724158	56	0.133	101.0	O	
0449-2638	4.4987465	-26.377217	54	0.124	68.9	C	9
0450-6452	4.5014199	-64.516471	59	0.118	71.4	O	
0501-3610	5.0177646	-36.090484	61	0.123	78.0	O	
2104-4422	21.0417124	-44.215199	56	0.123	66.8	O	
2114-3750	21.1438407	-37.493762	55	0.127	69.0	OL7 cc	10
2169-2686	21.6904909	-26.851294	57	0.130	65.4	O	
2175-1751	21.7500206	-17.503100	79	0.125	87.4	O	
2188-7165	21.8810032	-71.642227	102	0.062	64.3	O	11
2190-6118	21.9097413	-61.171245	58	0.119	73.1	O	12
2195-7771	21.9567135	-77.709296	50	0.144	89.1	OX	
2199-2391	21.9915162	-23.900561	70	0.109	62.6	I L5	13
2204-7192	22.0482039	-71.910053	262	0.051	67.4	O	
2303-5721	23.0319804	-57.207073	70	0.119	65.4	IL11	14
2380-3628	23.8044115	-36.274714	65	0.126	69.7	O cs	15

Types: O – open, I – intermediate, C – compact cluster, according to concentration to the cluster center; L11, etc. — linear substructure; X, Y – X- or Y-type substructure, P – nonstandard feature, cc – compact chain, and cs – curved stripe.

doi:https://doi.org/10.52526/25792776-22.69.2-256

Notes:
[1] PF 0016-5711, identification with ACO 2731
[2] PF 0024-2431, elongated cluster
[3] PF 0115-4600, identification with ACO 2877 and APM 147
[4] PF 0200-2252, identification with ACO S 213
[5] PF 0240-4218, identification with ACO 3014
[6] PF 0303-4097, identification with ACO 3081; negligible concentration to the cluster center, possible classification I?O
[7] PF 0381-1788, identification with ACO 464
[8] PF 0413-3091, double core; identification with ACO 3223 and APM 484
[9] PF 0449-2638, identification with ACO 495 and APM 503
[10] PF 2114-3750, 23 galaxy in the compact chain
[11] PF 2188-7165, Spiral-rich cluster
[12] PF 2190-6118, elongated cluster
[13] PF 2199-2391, 24 galaxy in the compact in the linear substructure, Spiral-rich cluster
[14] PF 2303-5721, possible short chain
[15] PF 2380-3628, curved stripe

doi:https://doi.org/10.52526/25792776-22.69.2-256

Magnetic Field in some Selected Directions of the Galaxy: Sagittarius Spiral Arm

R.R.Andreasyan *[1], G.M.Paronyan†[1], and A.G.Sukiasyan‡[1]

[1]Byurakan Astrophysical Observatory, 0213 Aragatsotn Prov., Armenia

Abstract

Faraday rotation data on 180 pulsars are used in a detail study of the magnetic field in the direction of galactic longitude $40° < l < 70°$, including the Sagittarius spiral arm region. The highly regular magnetic field in northern hemisphere of galaxy is directed to the Sun, when the magnetic field of southern hemisphere is directed from the Sun. We propose that the Sagittarius spiral arm lies mainly to the north of the Galactic plane, while the magnetic field with opposite direction below this plane is the field of the halo of the southern hemisphere of the Galaxy.

Keywords: *magnetic fields – Galaxy: general*

1. Introduction

The study of the magnetic fields of galaxies and, in particular, of our Galaxy has a great importance for explaining many dynamical and active processes taking place in these objects. The presence of the magnetic field of the Galaxy can explain the transportation of cosmic rays through the interstellar medium Fermi (1949), as well as synchrotron background radiation in the Galaxy Kiepenheuer (1950). The magnetic field of the Galaxy was studied using observational data of various types, such as interstellar polarization of starlight, Zeeman splitting of spectral lines of HI and different molecules in the radio range, data on Faraday rotation of extragalactic radio sources and pulsars. It is known that pulsars, for which numerous and diverse observational data were obtained, can be considered probes for studying the interstellar medium. In particular, data on dispersion measures (DM), which practically are known for all known pulsars, and about measures of Faraday rotation (RM) (more than 1300 pulsars) are very important for studying the magnetic field of the Galaxy. These data are directly derived from observations of pulsars. Theoretically they are expressed by the electron density ne in the interstellar medium through which the polarized radio emission of the pulsar passes and the projection of the magnetic field B_L (in Gauss) in this medium, using the following formulas:

$$RM = d\psi/d(\lambda^2) = \alpha \int n_e B_L dL, (\alpha = 8.1 * 10^5), \tag{1}$$

$$t_2 - t_1 = (2\pi e^2/m) * (1/\omega_2^2 - 1/\omega_1^2) * DM, \tag{2}$$

$$DM = \int n_e dL, \tag{3}$$

where dψ – is the difference of plane of polarization in different wavelength λ.

t –is the time of receiving the radio signal from pulsar.

ω – is the frequency of radio wave.

In these formulas, integration is carried out over the entire traversed path L of radiation (in parsecs) from the pulsar to the observer. Formula 1 makes it possible to determine the distance of a pulsar with the

*randreasyan@gmail.com, Corresponding author
†paronyan_gurgen@yahoo.com
‡andranik.suqiasyan.1995@mail.ru

doi:https://doi.org/10.52526/25792776-22.69.2-265

known electron density distribution in the Galaxy, and formula 2 together with formula 1 makes possible to determine the average component of the tension of interstellar magnetic field $< B_l >$ on the line of sight in micro gauss (μG).

$$< B_l >= (1/\alpha) * RM/DM = 1.23 * RM/DM, \tag{4}$$

Rotayion measure and dispersion measure data were used to study the structure and magnitude of the magnetic field of the Galaxy, since the seventies of the last century, when the rotation measures were known for only 3-4 tens of pulsars Manchester (1974). As the amount of RM data increases, more detailed studies have been carried out and various models have been proposed for the plane component of the Galactic magnetic field, as well as for the magnetic field in the Halo of the Galaxy. In particular, in Andreasyan & Makarov (1988, 1989a,b), where the model of the two-component magnetic field of our Galaxy was proposed, for the first time it was shown that the data on the rotation measures of pulsars and extragalactic radio sources are in good agreement with the model when the magnetic field of the plane component of the spiral arms is imbedded in the magnetic field of the Galactic halo with the dipole configuration, which is deformed due to the differential rotation of Galaxy.

It should be noted that in works studying the plane component of Galactic magnetic field are discussed mainly three models: 1) a bisymmetric spiral (BSS), in which the magnetic field in neighbor spiral arms has opposite directions; 2) an axially symmetric (ASS) structure with two changes in the direction of the field inside the solar circle; 3) concentric circular model.

There are also works in which it is shown that none of these models correspond to observational data better than the other Noutsos et al. (2008). We begin more detail investigation of separate regoins of Galaxy.

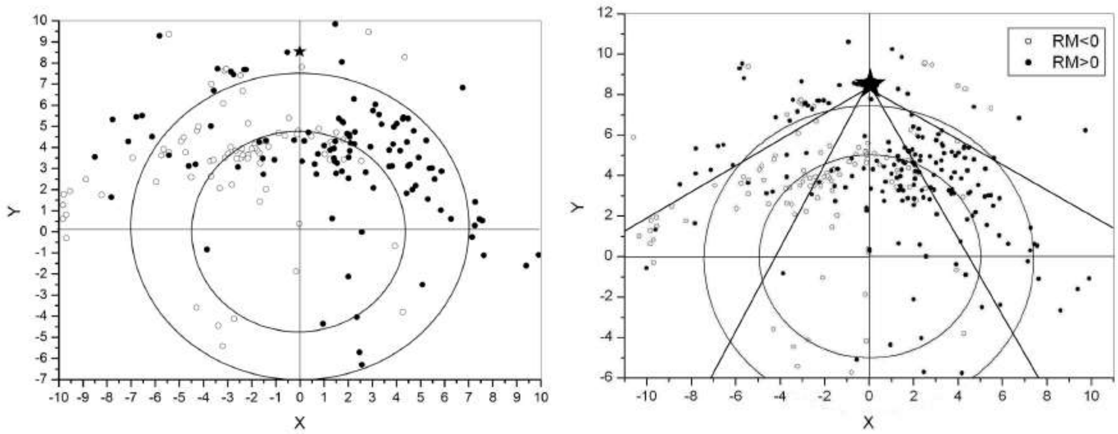

Figure 1. Distribution of rotation measures of pulsars in the plane of the Galaxy. (a) Black circles denote pulsars in which $RM > 300 rad/m^2$ (the projection of the magnetic field on the line of sight is directed toward the observer), white circles - in which $RM < -300 rad/m^2$; (b) The distribution of rotation measures of pulsars with $|RM| > 200 rad/m^2$

.

2. Sagittarius spiral arm region.

In Andreasyan et al. (2020) using pulsars rotation measure data was studied the magnetic field in the plane of Galaxy. It was shown, that distribution of signs of large ($| RM |> 200 rad/m^2$) rotation measures of pulsars are in good agreement with the concentric ring model with the anticlockwise direction of magnetic field in the galactocentric ring with radius $5\,kpc < R < 7\,kpc$ and reversal of direction at the radius 7 kpc (Fig.1a;b).

On the fig1b with black lines there are also divided two regions with about $40° < l < 70°$ and $290° < l < 320°$ (l-is Galactic longitude). In the first region, that includes the Sagittarius spiral arm we have mainly pulsars with $RM > 200 rad/m^2$, while in the second region there are mainly pulsars with $RM < -200 rad/m^2$. It is interesting, that this picture is greatly distorted when we ad pulsars with $|RM| < 200 rad/m^2$. The study of 3-dimensional distribution of rotation measure signs of pulsars may gave some explanation of this phenomenon.

doi:https://doi.org/10.52526/25792776-22.69.2-265

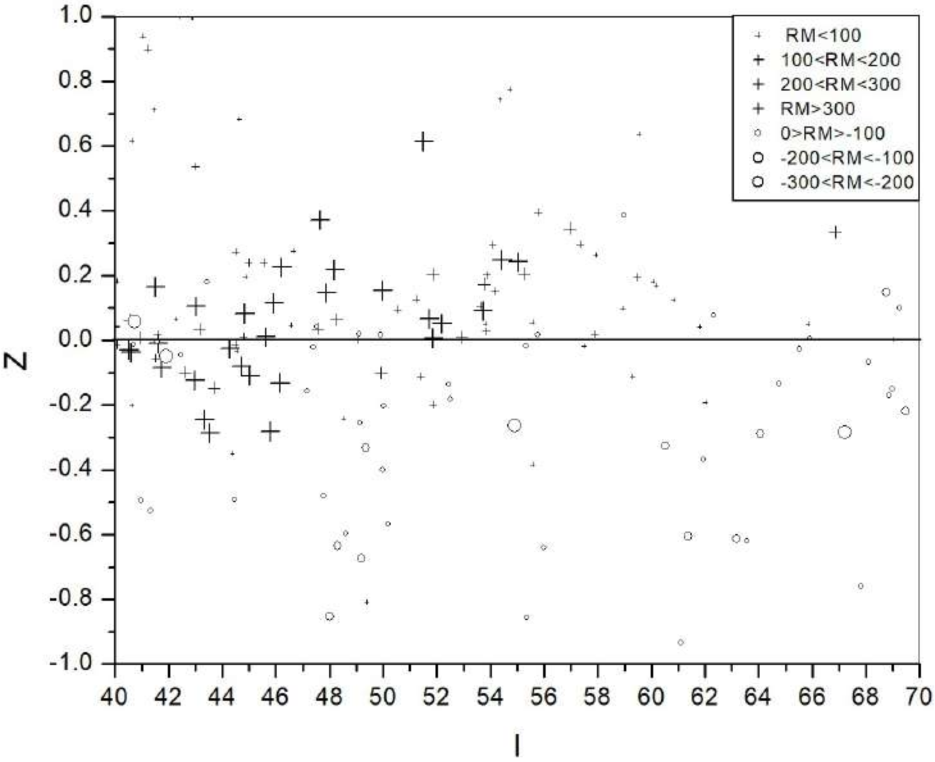

Figure 2. The distribution of RM for the pulsars in the region of galactic longitude $40^\circ < l < 70^\circ$. Z - is the distance of pulsar from the Galactic plane in kpc. The simbols "+" with different sizes indicate pulsars with positive sign and of RM, and the open circles – for the pulsars with negative sign of RM.

In this paper we study the magnetic field of first region more detail using the RM data of 180 pulsars. The data of pulsars were used for the study of Z dependence of rotation measure signs (Z is the distance of pulsar from the Galactic plane). In fig.2 we bring the distribution of RM signs for pulsars in the region with galactic longitude $40^\circ < l < 70^\circ$, which includes the Saggitarius spiral arm. The figure shows that in the Southern hemisphere of Galaxy (where $Z < 0$) the rotation measures are mostly negative, and in the Northern hemisphere they are mostly positive. Moreover, the magnitudes of positive rotation measures in the Northern hemisphere are much larger than the absolute magnitudes of negative rotation measures in the southern hemisphere, where $|RM| < 200 rad/m^2$. Three pulsars of Southern Hemisphere with $Z > 0.2$ kpc and positive RM has distances more than 10 kpc from the Sun, and are located outside of the Sagittarius arm (in the Perseus arm region). All of this can be easily explained if if we assume that Sagittarius' arm is located not symmetrically to the Galactic plane and is mostly located in the Northern hemisphere. The magnetic field of this spiral arm is directed toward the Sun. This direction coincides with the direction of the magnetic field of the Northern Hemisphere Halo Andreasyan & Makarov (1988). The negative rotation measures in the Southern hemisphere are mainly due to the magnetic field of Southern hemisphere halo which is directed opposite to the field of Northern Hemisphere halo and to the Sagittarius spiral arm field.

It must be mentioned that there is an assumption that pulsars are correlated with the spiral arms of the galaxy Kramer et al. (2003) and are born as a result of the evolution of O-stars, galactic distribution of which is well known Bronfman et al. (2000). These stars are highly concentrated in the galactic plane, and in particular O-B stars are distributed asymmetrically relative to the plane of the galaxy, which phenomena is known as the Gould Belt. (See, for example, Biazzo et al. (2012)). According to Gould belt plane of symmetry in the distribution of O-B stars is inclined relative to the plane of the galaxy, and in the direction of the galactic longitude $l = 0^\circ - 180^\circ$ O-B stars are distributed above the plane of the Galaxy (mainly located in the Northern hemisphere of Galaxy). Such an asymmetric distribution has also gas-dust component of the Galaxy Kulikovskij (1985). Above we have shown that the regular magnetic field in the Sagittarius spiral arm region in the direction of the Galactic longitude of about $40^\circ - 70^\circ$ is also distributed asymmetrically relative to the plane of the galaxy, or probably, spiral arm is located mainly in the Northern hemisphere of the Galaxy. This result fits very well into the picture of the Gould Belt phenomenon.

In fig.3 we bring the rotation measure distribution of pulsars in the abowe mentioned region, but in coordinates of the pulsar distance from the Sun (d) and the distance of pulsar from the Galactic plane.

doi:https://doi.org/10.52526/25792776-22.69.2-265

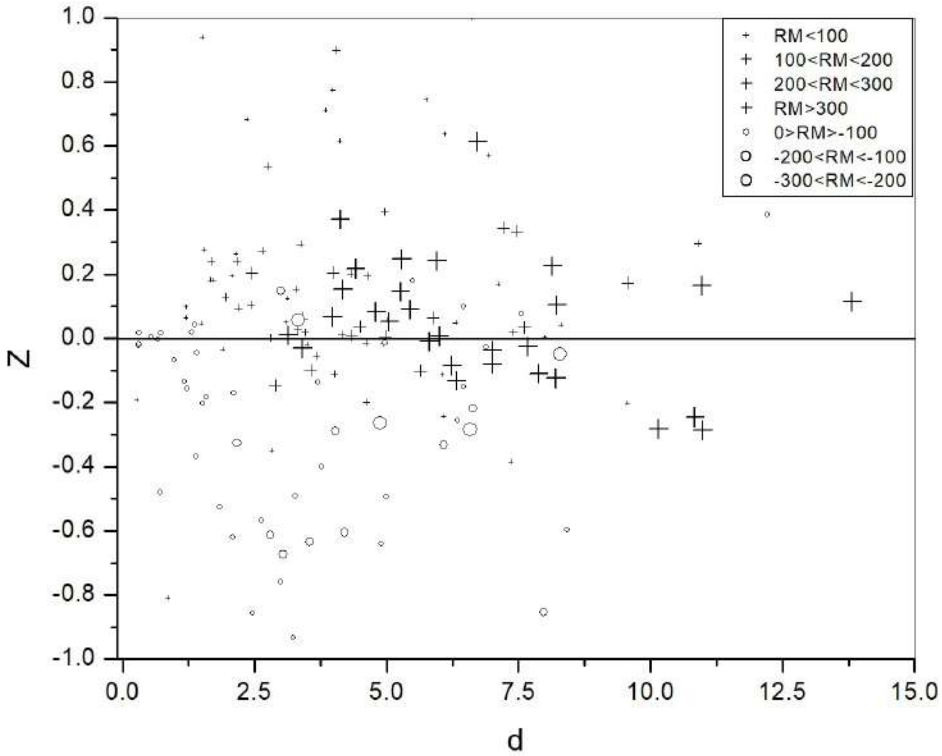

Figure 3. The distribution of RM for the pulsars in the region of galactic longitude 40°< l <70°. d - is the distance of pulsar from the Sun in kpc, and Z - is the distance of pulsar from the Galactic plane in kpc. The simbols "+" and open circles indicate the same as in the fig.2.

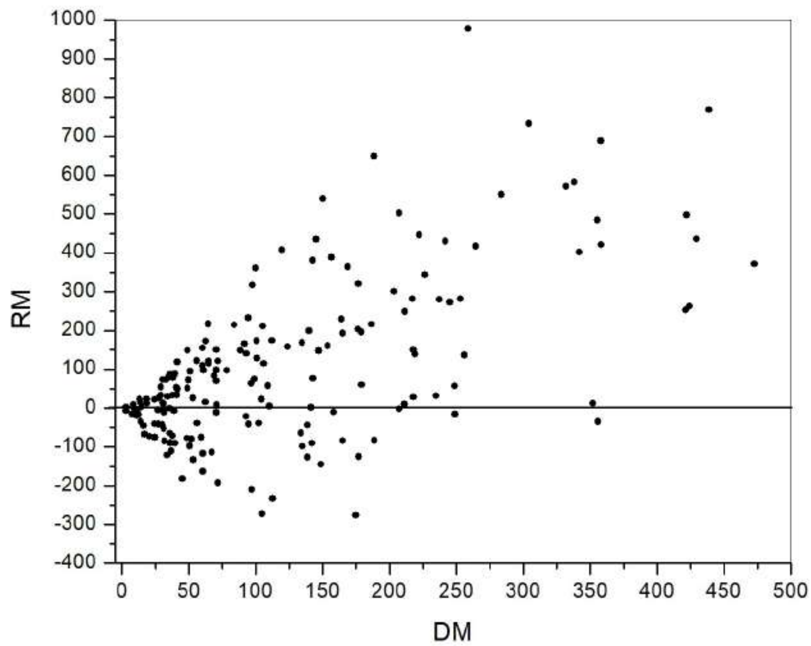

Figure 4. The distribution of pulsars of region 40°< l <70° in coordinates of rotation measures RM and dispersion measures DM.

From the fig.3 we see that, as in the fig.2, pulsars with positive sign of RM mainly are located in the northern hemisphere of Galaxy, and pulsars with negative sign of RM are located in the region southern of the plane of about $Z < -0.2$ kpc. Figure confirms the findings of the previous figure, that 3 pulsars with positive rotation measures and located at $Z < -0.2$ kpc are in the distances more than 10 kpc from the Sun. The negative rotation measures of some Northern hemisphere pulsars at a distance of about $d < 1$ kpc from the Sun are due to the influence of the magnetic field of local Orion arm and also of the interarm space Andreasyan & Makarov (1989a,b).

doi:https://doi.org/10.52526/25792776-22.69.2-265

In fig. 4 we bring the distribution of pulsars of this region in coordinates of rotation measures RM and dispersion measures DM. It can be seen from the figure that the magnitudes of positive rotation measures increase up to the values of $DM \sim 250 - 300$, while the absolute magnitudes of the negative values increase up to the value of $DM \sim 50$ that corresponds to the inter arm distance between the local Orion arm and Sagittarius spiral arm of Galaxy. As discussed above, some of these negative RM values can be due to the magnetic field of Orion's arm and interarm space that probably is the continuation of the magnetic field of Southern hemisphere halo.

Using the formulae 4 it was estimated the value of the strength of the average magnetic field in the Northern hemisphere that include the Sagittarius spiral arm region. It is $< B >\sim 2.5$ microGauss.

3. Conclusion.

Faraday rotation data of 180 pulsars are used in a detail study of the magnetic field in the direction of galactic longitude $40° < l < 70°$, that includes the Sagittarius spiral arm region. We propose that the region of regular magnetic field in the Sagittarius spiral arm at the direction of the Galactic longitude of about $40° - 70°$ is distributed asymmetrically relative to the plane of the galaxy, or probably, spiral arm is located mainly in the Northern hemisphere of the Galaxy, while the magnetic field with opposite direction below this plane is the field of the Halo of the Southern hemisphere of the Galaxy.

References

Andreasyan R. R., Makarov A. N., 1988, Astrophysics, 28, 247

Andreasyan R. R., Makarov A. N., 1989a, Astrophysics, 30, 101

Andreasyan R. R., Makarov A. N., 1989b, Astrophysics, 31, 560

Andreasyan R. R., Mikhailov E. A., Andreasyan H. R., 2020, Astronomy Reports, 64, 189

Biazzo K., Alcalá J. M., Covino E., Sterzik M. F., Guillout P., Chavarría-K. C., Frasca A., Raddi R., 2012, Astron. Astrophys. , 542, A115

Bronfman L., Casassus S., May J., Nyman L. Å., 2000, Astron. Astrophys. , 358, 521

Fermi E., 1949, Physical Review, 75, 1169

Kiepenheuer K. O., 1950, Physical Review, 79, 738

Kramer M., et al., 2003, Mon. Not. R. Astron. Soc. , 342, 1299

Kulikovskij P. G., 1985, Stellar astronomy.

Manchester R. N., 1974, Astrophys. J. , 188, 637

Noutsos A., Johnston S., Kramer M., Karastergiou A., 2008, Mon. Not. R. Astron. Soc. , 386, 1881

Taylor A. R., Stil J. M., Sunstrum C., 2009, Astrophys. J. , 702, 1230

doi:https://doi.org/10.52526/25792776-22.69.2-265

Communications of BAO, Vol. 69, Issue 2, 2022, pp. 270-273

Comparison of [CII] 158μm line widths to luminosities

A.L. Samsonyan *

Byurakan Astrophysical Observatory, Byurakan, Armenia

Abstract

A comparison of [CII] 158μm emission line widths to different luminosities is presented to decide if any luminosity relates to velocity dispersion. [CII] 158 μm emission lines are observed with Herschel PACS for 379 galaxies and the archival data for [CII] line widths are taken from http://cassis.sirtf.com/herschel/. Emission line widths are compared to [CII] luminosities, to near-infrared 1.6μm luminosities and to infrared 22μm luminosities. H magnitudes are taken from 2MASS catalogue, and 22μm fluxes from the WISE catalogue.

Keywords: *infrared:galaxies - galaxies:starburst - galaxies:active - galaxies: distances and redshifts*

1. Introduction

Investigation of early galaxies is crucial for understanding galaxy formation and evolution. A particularly important new capability is the study of the far infrared [CII] 158 μm emission line. Especially in dusty, obscured sources it may be the only line observable with currently available techniques. This [CII] line is the strongest far-infrared line in most sources (Brauher et al., 2008, Luhman et al., 2003, Malhotra et al., 1997, Nikola et al., 1998, Stacey et al., 1991) and is associated with star formation because it arises within the photodissociation region (PDR) surrounding starbursts (Helou et al., 2001, Malhotra et al., 2001, Meijerink et al., 2007, Tielens & Hollenbach, 1985). Numerous observations of the [CII] line have been made (De Looze et al., 2014, Díaz-Santos et al., 2013, 2014, Farrah et al., 2013, Sargsyan et al., 2012, 2014) using the Photodetector Array Camera and Spectrometer (PACS) instrument (Poglitsch et al., 2010) on the *Herschel* Space Observatory (Pilbratt et al., 2010). The [CII] line profiles are often of very high quality, with velocity resolution <250 km s^{-1}, so the line profiles themselves potentially contain diagnostic information. In previous papers (Sargsyan et al., 2011, 2014), we compared the [CII] line with mid-infrared emission lines and with the Polycyclic Aromatic Hydrocarbon (PAH) feature observed with the Infrared Spectrograph ((IRS; Houck et al., 2004) on the *Spitzer* Space Telescope (Werner et al., 2004). These comparisons led to our calibration of the star formation rate (SFR) based on [CII] luminosities such that log(SFR) = log(L[CII])-7.0 for SFR in solar masses/year and L([CII]) in solar luminosities. For those sources also observed at high resolution with the IRS, we compared line widths for various emission lines and confirmed the association of [CII] with the starburst component of 379 sources ((Samsonyan et al., 2016, hereafter S16)). The [CII] line profiles were published in S16. In this paper our primary new result is the comparison of the line widths with various other properties of the galaxies to search for astrophysical mechanisms that control the line widths.

2. Sample selection and data

For the analysis in this paper, the [CII] profiles shown in S16 are used. These profiles arise from the 8" x 8" spaxel of the PACS observation which is most closely aligned with the position of the *Spitzer* IRS observations used for comparisons in S16. All data used for the analysis in section 3 are available in VizieR Online Data Catalog. The full list of the FWHM of the profile from the Gaussian fits illustrated in http://cassis.sirtf.com/herschel/. The FWHM-s listed are intrinsic widths, after correcting for instrumental resolution of 236 km s^{-1}. The FWHM errors are also given in the webpage, the errors are so small, that they can be neglected. Archival data for H band fluxes and luminosities from the Two Micron All Sky Survey (2MASS; Skrutskie et al., 2006) and for 22 μm fluxes and luminosities from the Wide-Field Infrared Survey Explorer (WISE; Wright et al., 2010) are also given.

*anahit.sam@gmail.com

doi:https://doi.org/10.52526/25792776-22.69.2-270

3. Analysis and discussion

The objective of this study is to search for what physical characteristic of the galaxies is primarily responsible for determining the observed [CII] profile widths. Much of the analysis in S16 was designed to compare the [CII] line to mid-infrared forbidden lines observed with the *Spitzer* IRS, with the goal of seeking differences between AGN and starburst sources. As described and reviewed in that paper, the mid-infrared AGN/starburst classification is made using the strength relative to continuum (equivalent width - EW) of the 6.2μm PAH emission feature.

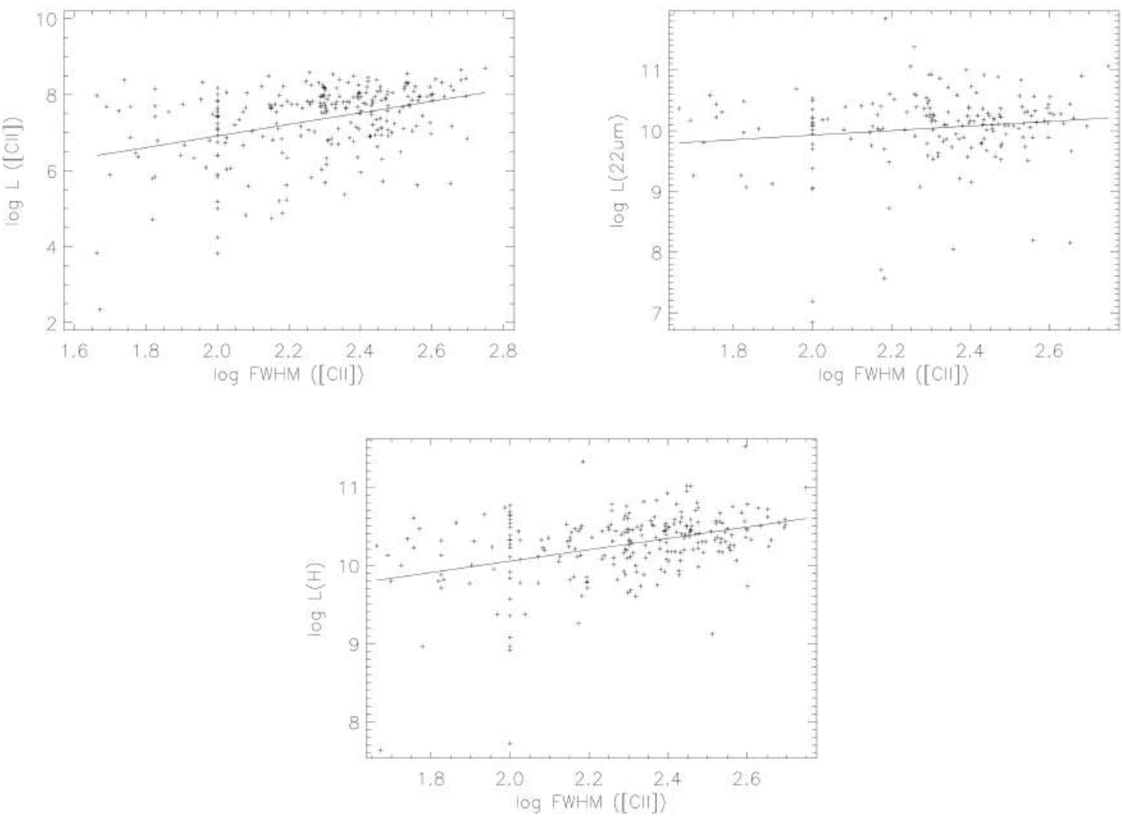

Figure 1. Luminosities in solar luminosities compared to [CII] FWHM in km/s. Top left figure shows [CII] luminosity and line fit is logL([CII]) = 1.52($\pm$0.24)log(FWHM)+3.86. Top right figure shows 22 μm luminosity and line fit is log L(22 μm) = 0.38($\pm$0.20)log(FWHM)+9.17. Lower figure shows H luminosity and line fit is log(L(H)) = 0.73($\pm$0.11)log(FWHM)+8.60.

The objective of this paper is to compare [CII] FWHM to other galactic parameters in search of correlations. It has long been known that stellar velocity dispersions within galactic bulges relate to bulge luminosity with a form L $\propto \sigma^n$ for σ the stellar line of sight velocity dispersion. This relates to the FWHM by FWHM = 2.35 σ, and FWHM is normally used as the measure of velocity dispersion when using optical emission lines (e.g. Feldman et al., 1982, Shields et al., 2003, Whittle, 1992). The initial study (Faber & Jackson, 1976) found that $3 < n < 4$. In a reevaluation of a large sample of galactic bulges, Whittle (1992) found $n = 3.2$. When using the [OIII] optical emission line, primarily for Seyfert galaxies, he found $n = 2.2$. Subsequent studies by Nelson & Whittle (1996) and Shields et al. (2003) determined that even the [OIII] widths from the narrow line region of AGN are controlled primarily by bulge gravity rather than by other sources inputing kinetic energy to the gas. More recent studies of relations between velocity dispersions and bulge gravity emphasized the use of sigma to determine relations among the masses of central black holes, bulge velocity dispersions, and bulge luminosities. The comprehensive summary of Kormendy & Ho (2013) studies yields $n = 3.7$, and that of McConnell & Ma (2013) gives $n = 5.1$. Based on this extensive previous work, it would be expected that any integrated measure of velocity dispersion for a galaxy should show a meaningful correlation with the mass of that galaxy. This is my motive for comparing the FWHM of the [CII] lines with three different measures of galaxy luminosity, each of which measures a different mass. The three parameters are: 1. the luminosity of the [CII] line itself, which scales primarily with the photodissociation regions surrounding starbursts and so scales with the gas mass connected to star formation; 2.

doi:https://doi.org/10.52526/25792776-22.69.2-270

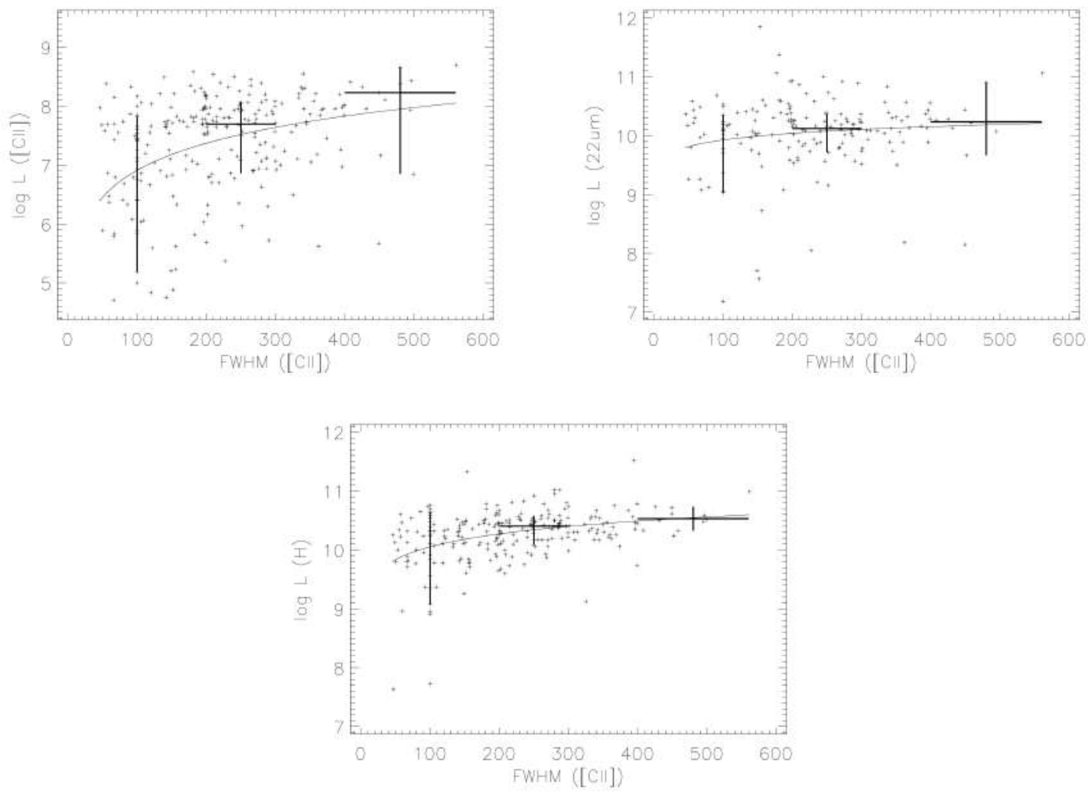

Figure 2. Luminosities compared to FWHM (linear scale). Fits are as in Fig.1. Vertical lines show 1 dispersions for velocities 100 km/s, 200-300 km/s and > 400 km/s.

The luminosity of dust reradiation, taken as 22μm dust luminosity, which scales with the total luminosity of younger, hotter stars that are heating the dust; 3. The near infrared (H band) luminosity of the galaxy, which scales with the total luminosity of the evolved stars. Comparisons of [CII] FWHM with these three measures of luminosity are shown in Fig.1 and 2.

Fig.1 illustrates the results using the conventional comparison of logL with logFWHM. In all cases, the value of n is much smaller than previous studies using stellar velocity dispersions or optical emission lines. For [CII] luminosities, $n = 1.52 \pm 0.24$; for 22 μm luminosities, $n = 0.38 \pm 0.20$; for H luminosities, $n = 0.73 \pm 0.11$. In Fig.2, the fits are shown using linear values for FWHM to compare scatter among the comparisons using the different parameters. These plots show the scatter in the luminosity distributions above and below the formal fits (1 for logL) within three different ranges of FWHM. In all cases, the scatter is extreme. The range of luminosities at a given value of FWHM is comparable in all cases to the full range of FWHM over all luminosities. There can be a factor of 5 range in gas velocities for the same value of luminosity. It does not appear, therefore, that FWHM for [CII] can be used in a meaningful way to predict any kind of galaxy luminosity. Despite the large scatters, the results do imply a meaningful conclusion. The luminosity dispersions are smallest for the H band luminosities, next for the dust luminosities, and largest for the [CII] luminosities. This scaling of luminosity dispersions also progresses the same as the uncertainties in the slopes of the line fits in Fig.1 (smallest uncertainty for H luminosity). In both cases, therefore, the correlation of FWHM with H band luminosity is better than with either other parameter. I conclude from this that the gravity associated with the mass of evolved stars is a factor controlling the widths of the [CII] line. Nevertheless, the large range in gas velocities that can be found at the same value of luminosity remains puzzling. It seems that some unidentified process other than straightforward gravitational forces within the galactic bulge is the primary controller of [CII] gas velocities.

4. Summary

Emission line widths are compared to [CII] luminosities, to near-infrared 1.6 m luminosities and to infrared 22 m luminosities to decide if any luminosity accurately relates to velocity dispersion. The luminosity dispersions are smallest for H band luminosities and the slope uncertainty for the line fit is the smallest for

doi:https://doi.org/10.52526/25792776-22.69.2-270

H luminosities. I conclude from this that the gravity associated with the mass of evolved stars is a weak factor controlling the widths of the [CII] line, but line widths are primarily determined by a mechanism that is still unknown.

Acknowledgements

This work was made possible by a research grant number 21AG-1C044 from Science Committee of Ministry of Education, Science, Culture and Sports RA. I express great appreciation to those who developed the missions responsible for the archival data used in this paper: the PACS instrument on the Herschel Space Observatory, the 2MASS Survey, and the WISE survey. I also thank my colleagues who initially involved me in research with the IRS and PACS: Lusine Sargsyan, Daniel Weedman, Vianney Lebouteiller, Don Barry and James Houck.

References

Brauher J. R., Dale D. A., Helou G., 2008, Astrophys. J. Suppl. Ser. , 178, 280

De Looze I., et al., 2014, Astron. Astrophys. , 568, A62

Díaz-Santos T., et al., 2013, Astrophys. J. , 774, 68

Díaz-Santos T., et al., 2014, Astrophys. J. Lett. , 788, L17

Faber S. M., Jackson R. E., 1976, Astrophys. J. , 204, 668

Farrah D., et al., 2013, Astrophys. J. , 776, 38

Feldman F. R., Weedman D. W., Balzano V. A., Ramsey L. W., 1982, Astrophys. J. , 256, 427

Gallerani S., Fan X., Maiolino R., Pacucci F., 2017, , 34, e022

Helou G., Malhotra S., Hollenbach D. J., Dale D. A., Contursi A., 2001, Astrophys. J. Lett. , 548, L73

Houck J. R., et al., 2004, Astrophys. J. Suppl. Ser. , 154, 18

Kormendy J., Ho L. C., 2013, Ann. Rev. Astron. Astrophys. , 51, 511

Luhman M. L., Satyapal S., Fischer J., Wolfire M. G., Sturm E., Dudley C. C., Lutz D., Genzel R., 2003, Astrophys. J. , 594, 758

Malhotra S., et al., 1997, Astrophys. J. Lett. , 491, L27

Malhotra S., et al., 2001, Astrophys. J. , 561, 766

McConnell N. J., Ma C.-P., 2013, Astrophys. J. , 764, 184

Meijerink R., Spaans M., Israel F. P., 2007, Astron. Astrophys. , 461, 793

Nelson C. H., Whittle M., 1996, Astrophys. J. , 465, 96

Nikola T., Genzel R., Herrmann F., Madden S. C., Poglitsch A., Geis N., Townes C. H., Stacey G. J., 1998, Astrophys. J. , 504, 749

Pilbratt G. L., et al., 2010, Astron. Astrophys. , 518, L1

Poglitsch A., et al., 2010, Astron. Astrophys. , 518, L2

Samsonyan A., Weedman D., Lebouteiller V., Barry D., Sargsyan L., 2016, Astrophys. J. Suppl. Ser. , 226, 11

Sargsyan L., Weedman D., Lebouteiller V., Houck J., Barry D., Hovhannisyan A., Mickaelian A., 2011, Astrophys. J. , 730, 19

Sargsyan L., et al., 2012, Astrophys. J. , 755, 171

Sargsyan L., Samsonyan A., Lebouteiller V., Weedman D., Barry D., Bernard-Salas J., Houck J., Spoon H., 2014, Astrophys. J. , 790, 15

Shields G. A., Gebhardt K., Salviander S., Wills B. J., Xie B., Brotherton M. S., Yuan J., Dietrich M., 2003, Astrophys. J. , 583, 124

Skrutskie M. F., et al., 2006, Astron. J. , 131, 1163

Stacey G. J., Geis N., Genzel R., Lugten J. B., Poglitsch A., Sternberg A., Townes C. H., 1991, Astrophys. J. , 373, 423

Tielens A. G. G. M., Hollenbach D., 1985, Astrophys. J. , 291, 722

Werner M. W., et al., 2004, Astrophys. J. Suppl. Ser. , 154, 1

Whittle M., 1992, Astrophys. J. , 387, 121

Wright E. L., 2006, Publ. Astron. Soc. Pac. , 118, 1711

Wright E. L., et al., 2010, Astron. J. , 140, 1868

doi:https://doi.org/10.52526/25792776-22.69.2-270

Biermann Battery and Magnetic Fields of Accretion Discs

R.R. Andreasyan *[1], I.K. Marchevsky†[2], V.E. Martynova‡[2], and E.A. Mikhailov§[3,4]

[1]V.A. Ambartsumian Byurakan Astrophysical Observatory NAS Armenia, Byurakan, Aragatsotn province, 0213, Armenia
[2]N.E. Bauman Moscow State Technical University, Moscow, 105005, Russia
[3]M.V. Lomonosov Moscow State University, Moscow, 119991, Russia
[4]P.N. Lebedev Physical Institute, Moscow, 119991, Russia

Abstract

Magnetic fields should be studied to understand different processes in accretion discs, such as transition of angular momentum which is closely connected with them. There are different ways to describe the growth of magnetic fields of cosmic objects. One of them is based on Biermann battery mechanism which previously has been used to study the origin of magnetic fields in galaxies. It is based on different masses and same absolute values of charges of protons and electrons, which move across the disc. They interact with rotating medium, get azimuthal velocity and produce circular currents that are associated with the magnetic fields in the disc. Such magnetic field influences the motion of the charged particles that created it, and we should take into account the feedback. Mathematical description of this mechanism leads us to the Fredholm-type integral equation of the 2nd kind. In the presented work it is solved numerically using Galerkin methods. Here we give the solutions of different cases.

Keywords: *magnetic fields, Biermann battery, accretion discs*

1. Introduction

It is well-known that a large variety of astrophysical objects have regular structures of magnetic field Arshakian et al. (2009), Beck et al. (1996). They are studied using both theoretical and observational methods. From the observational point of view, magnetic fields can be measured using Zeeman effect or synchrotron emission, where the field influences spectral parameters of the electromagnetic waves. However, nowadays most of the observational results are obtained using Faraday rotation of the polarization plane of the radio-waves which can be detected on modern radio telescopes Zeldovich et al. (1983). Theoretically, the evolution of magnetic fields is studied basing on different models of magnetohydrodynamics Krause & Raedler (1980).

One of the most interesting objects from the point of view of cosmic magnetism is connected with accretion discs. They surround compact astrophysical objects such as black holes, neutron stars and white dwarfs. Magnetic fields describe a large variety of processes there, such as transition of the angular momentum between different parts of the disc Shakura & Sunyaev (1973). Also there are observational works which prove the magnetic field existence. Some papers describe the Faraday rotation measurements in the accretion disc surrounding the central black hole in M87 Kravchenko et al. (1973). It should be associated with regular magnetic field structures and it is the strong argument for the magnetism of accretion discs.

As for generation of the magnetic field in accretion discs, there are various approaches. First of all, the magnetic field can be connected with transfer of the accreting medium Lubow et al. (1994). Moreover, the magnetic field can be generated by interaction with central body. However, these effects seem to be quite weak to describe strong growth of the magnetic field. Different computational models have shown that they cannot fully describe the field evolution and the strengths which are comparable with the equipartition value. So, we should base our theoretical approaches on generation the magnetic field *in situ*, taking into account the motions in different parts of the disc Brandenburg et al. (1995).

Previously it has been shown that the magnetic field of the accretion disc can be explained by the large-scale dynamo which is quite similar to the mechanism which describes field evolution in galactic discs Boneva

*randreasyan@gmail.com
†iliamarchevsky@mail.ru
‡vasmartynova2001@mail.ru
§ea.mikhajlov@physics.msu.ru, Corresponding author

doi:https://doi.org/10.52526/25792776-22.69.2-274

et al. (2021), Moss et al. (2016). Similar geometry gives us an opportunity to use the same approximations, such as no-z model which is based on small half-thickness of the disc Moss (1995), Phillips (2001). It was obtained that the alpha-effect (which is connected with the helicity of the turbulent motions) and differential rotation (non-uniform angular velocity of the disc) can support exponential growth of the field.

However, the dynamo mechanism does not explain the initial magnetic field which should be connected with another process. Most probable explanation of the seed field is connected with the Biermann battery Biermann & Schluter (1951). It has been used to study initial magnetic field of the galaxies Andreasyan & Mikhailov (2021), Mikhailov & Andreasyan (2021). It is connected with the same absolute values of the charge of protons and electrons, and strictly different masses. The particles move in the raidal direction and interact with surrounding medium. It makes them have rotational movements, which is associated with circular currents. Such currents produce vertical magnetic field which can be the source of regular field structures. One of the most important points is connected with taking into account the feedback. It can be done using the integral equation.

In this work we describe the model of the magnetic field in accretion discs based on the Biermann battery effect. It contains basic physical models, and the approximation for movement of the electrons and protons. After that we obtain the 2nd kind Fredholm-type equation and solve it using the Galerkin methods Marchevskii et al. (2022). After that, the results are shown.

2. Biermann battery

We can describe the motion of the particles which fall on the central body which is surrounded by the accretion disc. Here we are focusing on the ones which are associated with the black holes, but the following results can be easily transferred onto other objects such as neutron stars or white dwarfs.

We assume that the protons move under influence of surrounding media, and we should solve their equations of motion. As for the electrons, we can assume that they are "glued" by the radiation. The protons can produce the circular currents which are associated with magnetic field.

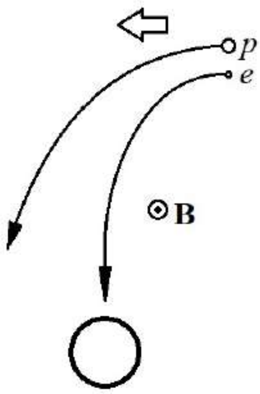

Figure 1. Scheme of the Biermann mechanism in accretion discs.

As for the protons, we can consider the following equation of their motion Mikhailov & Andreasyan (2021):

$$m\frac{d\mathbf{v}}{dt} = \mathbf{F} - \frac{m}{\tau}\left(\mathbf{v} - \mathbf{V}_{rot}\right) + \frac{e}{c}(\mathbf{v} \times \mathbf{B}), \quad (1)$$

where m is the mass of the proton, $\mathbf{v}$ is its velocity, $\mathbf{F}$ describes the force field (can be associated mainly with the gravitational forces), τ is the typical time of interaction between the particle and surrounding medium, $\mathbf{V}_{rot}$ is the rotation velocity of the accretion disc, and $\mathbf{B}$ is the magnetic field. As for our aims connected with the circular currents producing magnetic field, we can reduce this equation to the angular component in the following way:

$$\frac{d\varphi}{dt} = -\frac{2}{r}\frac{dr}{dt}\frac{d\varphi}{dt} - \frac{1}{\tau}\left(\frac{d\varphi}{dt} - \Omega\right) - \frac{e}{rmc}\frac{dr}{dt}B, \quad (2)$$

Taking into account the typical relationship between the parameters (we assume that the typical processes in azimuthal direction are much faster than in the radial one), introducing the value $V = -\frac{dr}{dt}$ and assuming

doi:https://doi.org/10.52526/25792776-22.69.2-274

that $r \approx R$, we can rewrite the equation as:

$$\frac{d^2\varphi}{dt^2} = \frac{2V}{R}\frac{d\varphi}{dt} - \frac{1}{\tau}\left(\frac{d\varphi}{dt} - \Omega\right) + \frac{e}{Rmc}VB, \tag{3}$$

and obtain the following solution that satisfies trivial initial condition:

$$\omega = \frac{d\varphi}{dt} = \frac{\Omega + \frac{e\tau VB}{Rmc}}{1 - \frac{2V\tau}{R}}\left\{1 - \exp\left(-\frac{t}{\tau}\left(1 - \frac{2V\tau}{R}\right)\right)\right\} \tag{4}$$

It can be seen that the exponential term decreases and quite soon the velocity will be very close to the value (we assume that $\frac{V\tau}{R} \ll 1$):

$$\omega \cong \Omega + \frac{V\tau}{R}\left(2\Omega + \frac{eB}{mc}\right) \tag{5}$$

It is obvious that $\frac{eB}{mc}$ is the cyclotron frequency and it is much larger than the angular velocity of the accretion disc. So, taking into account that $\Omega \ll \frac{eB}{mc}$, we can rewrite it as:

$$\omega \cong \Omega + \frac{V\tau}{R}\frac{eB}{mc}. \tag{6}$$

The magnetic field will grow slower if the qualitative formulae is performed:

$$\Omega \sim -\frac{V\tau}{R}\frac{eB}{mc}. \tag{7}$$

So, we can estimate the magnetic field that can be reached, assuming that $\Omega \sim 10^{-6}$ s, $\tau \sim 1$ s, $R \sim 10^{16}$ cm and $V \sim 10^{10}$ cm s^{-1} and obtain the field:

$$B \sim \frac{\Omega Rmc}{V\tau e} \sim 10^{-4}\ \mathrm{G}. \tag{8}$$

This field is quite large to be the source of the seed field. However, it is quite interesting to find the structure of the field.

3. Detailed structure of the field

If there is a flux of protons falling on the central object of the accretion disc, each of them is associated with a circular current. Taking into account that the large-scale frequency is much smaller than the cyclotron one ($\Omega \ll \frac{eB}{mc}$), we shall obtain:

$$I = \frac{e}{2\pi}\left(\Omega - \frac{V\tau}{R}\frac{eB}{mc}\right). \tag{9}$$

According to the Biot – Savart law, the current with radii R will produce at distance r from the center of the disc the field Mikhailov & Andreasyan (2021):

$$b = \frac{I}{cR}\Phi\left(\frac{r}{R}\right), \tag{10}$$

where we have introduced the special function:

$$\Phi(\alpha) = \int_0^{2\pi} \frac{(1 - \alpha\cos x)dx}{(1 + \alpha^2 - 2\alpha\cos x)^{3/2}}, \tag{11}$$

that can be expressed through full elliptic integrals Korn & Korn (2000).

If we have the density of the particles n and the half-thickness h, each ring corresponding to $-h < z < +h$, and distance from the center in the range $(r, r + dr)$, it produces the field:

$$dB(r) = \frac{4neh\Omega}{c}\Phi\left(\frac{r}{R}\right)dR + \frac{2nhe^2V\tau}{mc^2R}\Phi\left(\frac{r}{R}\right)B(R)dR. \tag{12}$$

doi:https://doi.org/10.52526/25792776-22.69.2-274

Taking into account the typical models for the accretion discs Suleimanov et al. (2007), measuring distances at outer radii of the disc and fields in their typical values, we can write an integral equation for the field:

$$B(r) = \int_{R_{min}}^{1} \Phi\left(\frac{r}{R}\right) \frac{dR}{R^{9/4}} + \chi \int_{R_{min}}^{1} \Phi\left(\frac{r}{R}\right) B(R) \frac{dR}{R^{1/8}} \tag{13}$$

where we have introduced the parameter $\chi = \frac{2e^2 n_0 h_0 V_0 \tau_0 R_{max}^{7/8}}{mc^2 R_{min}^{7/8}}$. Here n_0, h_0, V_0 and τ_0 are the density of the medium, half-thickness of the disc, velocity and the interaction time corresponding to the case $r = R_{min}$. It is necessary to take into account that usually this parameter is sufficiently higher than one.

The solution for different cases is shown on figure 2. We can see that the field reaches its maximum values near the inner border of the disc. If we take astrophysically important large values of χ, it monotonously depends on r.

4. Role of the outflows

Also there are flows from the central to the outer parts in the discs. Such mechanism is quite important in galaxies, but as for the accretion discs their influence is much weaker. However, it is quite interesting to study them, too.

As for the outflows, we can take the same models for the accretion disc structure and obtain the following equation in dimensionless variables:

$$B(r) = \int_{R_{min}}^{1} \Phi\left(\frac{r}{R}\right) \frac{dR}{R^{19/8}} + \beta \int_{R_{min}}^{1} \Phi\left(\frac{r}{R}\right) B(R) \frac{dR}{R^{15/4}}, \tag{14}$$

where the parameter $\beta = \frac{2e^2 n_0 h_0 V_0 \tau_0 R_{min}^{11/4}}{mc^2 R_{max}^{11/4}}$ has the same meaning as χ in previous case. The results for this case are presented in the figure 3.

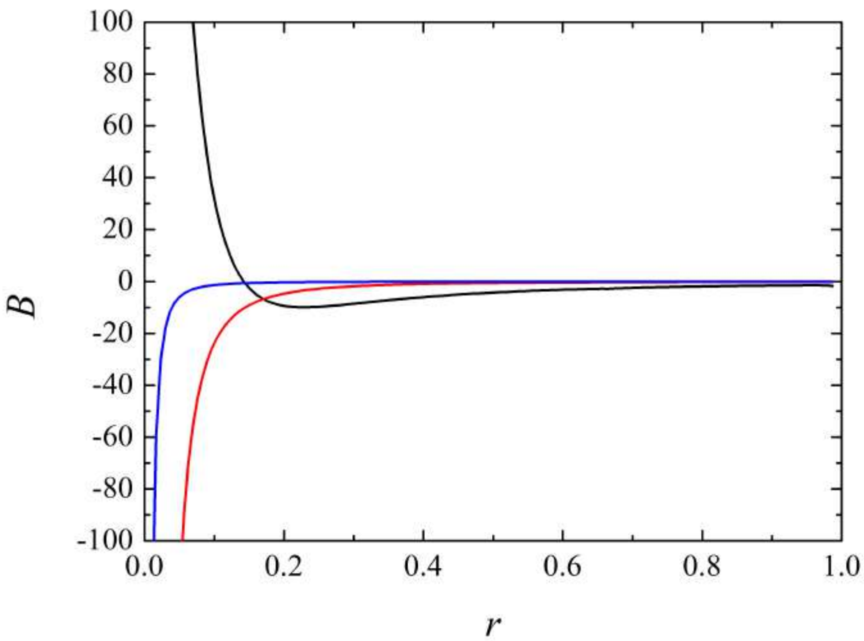

Figure 2. Structure of the magnetic field induced by the radial flows. Black line shows $\chi = 1$, red line – $\chi = 10$, blue line – $\chi = 100$.

5. Conclusion

We have studied the magnetic field produced by the Biermann battery mechanism. It can be very important to generate the vertical magnetic fields in the accretion discs, which are quite comparable with

doi:https://doi.org/10.52526/25792776-22.69.2-274

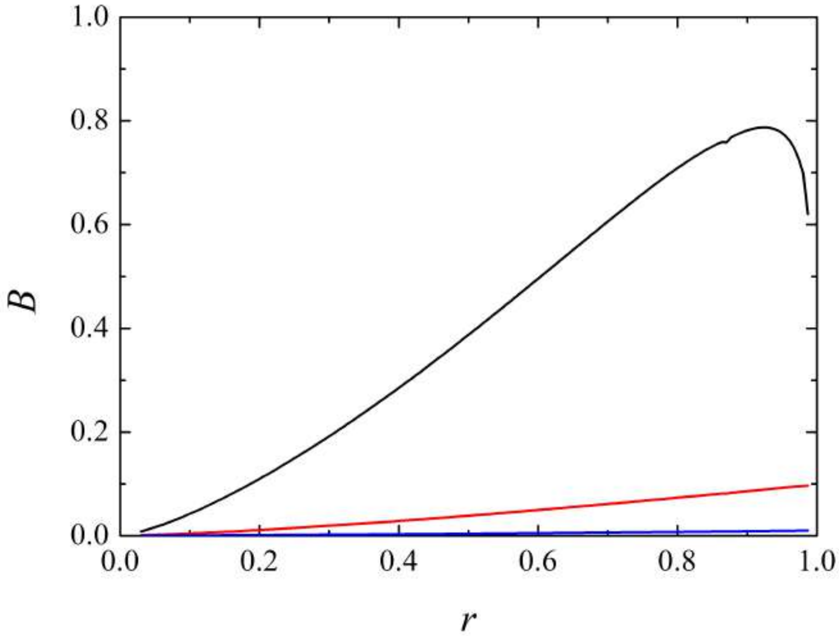

Figure 3. Structure of the magnetic field induced by outflows. Black line shows $\beta = 1$, red line – $\beta = 10$, blue line – $\beta = 100$.

the equipartition one. After that, it can be turned by the turbulent dynamo mechanism and after that strengthened by the large-scale one. So, this step-by-step process can explain the magnetic field generation in the accretion discs from the zero to astrophysically important values.

We have obtained the detailed structure of the field generated by the inflows and the outflows. In our opinion, the inflows are much more important (it is the fundamental difference with the galaxies, where there are no intensive flows towards the center).

Of course, the seed magnetic field can be generated taking into account another mechanisms, such as interaction with the central object or transition with the matter, but the Biermann battery seems to be more important in the generation.

Authors thank the organizers of the conference "Space Sciences and Technologies" for an opportunity to present the work.

References

Andreasyan R., Mikhailov E., 2021, Astronomy Reports, 65, 715

Arshakian T. G., Beck R., Krause M., Sokoloff D., 2009, Astronomy and Astrophysics, 494, 21

Beck R., Brandenburg A., Moss D., et al. 1996, Annual Review of Astronomy and Astrophysics, 34, 155

Biermann L., Schluter A., 1951, Physical Review, 82, 863

Boneva D. V., Mikhailov E. A., Pashentseva M. V., Sokoloff D. D., 2021, Astronomy and Astrophysics, 652, A38

Brandenburg A., Nordlund A., Stein R. F., Torkelsson U., 1995, Astrophysical Journal, 446, 741

Korn G. A., Korn T. M., 2000, Mathematical handbook for scientists and engineers: definitions, theorems, and formulas for reference and review. Dover Publications, New-York

Krause F., Raedler K.-H., 1980, Mean-field magnetohydrodynamics and dynamo theory. Pergamon Press, Oxford

Kravchenko E., Giroletti M., Hada K., et al. 1973, Astronomy and Astrophysics, 637, L6

Lubow S. H., Papaloizou J. C. B., Pringle J. E., 1994, Monthly Notices of the Royal Astronomical Society, 267, 235

Marchevskii I. K., Sokol K. S., A. I. Y., 2022, Herald of the Bauman Moscow State Technical University, Series Natural Sciences, p. 33

Mikhailov E. A., Andreasyan R. R., 2021, Open Astronomy, 30, 127

Moss D., 1995, Monthly Notices of the Royal Astronomical Society, 275, 191

doi:https://doi.org/10.52526/25792776-22.69.2-274

Moss D., Sokoloff D., Suleimanov V., 2016, Astronomy and Astrophysics, 588, A18

Phillips A., 2001, Geophysical and Astrophysical Fluid Dynamics, 94, 135

Shakura N. I., Sunyaev R. A., 1973, Astronomy and Astrophysics, 337, 24

Suleimanov V. F., Lipunova G. V., I. S. N., 2007, Astronomy Reports, 51, 549

Zeldovich I. B., Ruzmaikin A. A., Sokolov D. D., 1983, Magnetic fields in astrophysics. Gordon and Breach Science Publishers, New York

doi:https://doi.org/10.52526/25792776-22.69.2-274

Failure of the hypothesis of accelerated expansion of the universe

A.P. Mahtessian *[1], G.S. Karapetian , M.A. Hovhannisyan [2], and L.A. Mahtessian [2]

[1]NAS RA V. Ambartsumian Byurakan Astrophysical Observatory (BAO), Armenia
[2]NAS RA Institute of Applied Problems of Physics, Armenia

Abstract

Our estimates of the cosmological parameters within the ΛCDM model and the model with zero cosmological constant are very different from other studies. The purpose of this report is to draw attention to the difference between our approach and the approaches of other authors and to evaluate the correctness of these approaches.

Keywords: *cosmological models - supernovae - dark energy - acceleration: general*

1. Introduction

We analyze the Hubble diagram in order to find the best fit between the observational data of type 1a supernovae and cosmological models.

For better fit between theory and observation, Pearson's Chi^2 (Chi-squared) goodness-of-fit test was used. Results are obtained for the ΛCDM model and, for comparison, the model with a zero cosmological constant. In order to improve the fit between the observed data and theory, the optimization is also carried out assuming that the absolute magnitude of supernovae is not constant, but evolves with time. It is assumed that the dependence of the absolute magnitude on the redshift is linear: $M = M_0 + \epsilon_c z$, where ϵ_c is the evolution coefficient of the absolute magnitude of type 1a supernovae and $M_0 = M(z = 0)$. In the case of the flat universe ($\Omega_M + \Omega_\Lambda = 1$), the best fit between theory and observation is $\epsilon_c = 0.304$. In this case, for the cosmological parameters we obtain $\Omega_\Lambda = 0.000$, $\Omega_M = 1.000$. And for the absolute magnitude M_0 of supernovae 1a, we obtain the value -18.875. Naturally, this result exactly coincides with the simulation result for the model with zero cosmological constant ($\epsilon_c = 0.304$, $q_0 = 0.500$, $M_0 = -18.875$). Within the framework of the Friedmann-Robertson-Walker model, without restriction on space curvature ($\Omega_M + \Omega_\Lambda + \Omega_K = 1$), we obtain the following values: $\epsilon_c = 0.304$, $\Omega_\Lambda = 0$, $\Omega_M = 1.000$, $\Omega_K = 0.000$, $M_0 = -18.875$. Therefore, the general case also leads to a flat Universe model ($\Omega_K = 0.000$). Within the framework of this work, the critical impact of the absolute magnitude M of type 1a supernovae on the cosmological parameters is also shown. In particular, it was found that a change in this value by only 0.4m (from -19.11 to -18.71) leads to a change in the parameters from $\Omega_\Lambda = 0.7$ and $\Omega_M = 0.3$ to $\Omega_\Lambda = 0$ and $\Omega_M = 1$.

More details about these results can be found in Mahtessian et al. (2020) and Mahtessian et al. (2022).

2. Discussion

Such a critical difference between the results of ours and other authors must be explained. What is the difference between our approaches and those of other authors? Who is right?

First, about the differences.

First difference. This is due to the rather large width of the distribution of the absolute magnitudes of type Ia supernovae. This issue was studied in the article by Ashall et al. (2016). The average absolute magnitude of 115 studied stars was obtained $\overline{MB} = -19.04 \pm 0.07$, standard deviation $\sigma_{MB} = 0.70$, 89 of

*amahtes@gmail.com, Corresponding author

doi:https://doi.org/10.52526/25792776-22.69.2-280

them have late host galaxies ($Sa - Irr$ or star-forming galaxies, $S - F$), for which $\overline{MB} = -19.20 \pm 0.05$, $\sigma_{MB} = 0.49$, and 26 have early host galaxies ($E - SO$ or passive galaxies), respectively $\overline{MB} = -18.48 \pm 0.19$, $\sigma_{MB} = 0.98$.

Such large standard deviations in the absolute magnitude distributions of type Ia supernovae allow us to conclude that when estimating the values of cosmological parameters, it is wrong to take as a basis the absolute magnitude determined by few stars. In Mahtessian et al. (2020) showed that in this case the obtained cosmological parameters lead to a violation of the initial assumption that the absolute magnitudes of type Ia supernovae do not change with distance. This violation disappears when the absolute magnitude of supernovae is estimated while estimating the cosmological parameters.

Thus, when estimating cosmological parameters, the absolute magnitude of supernovae should also be an estimated parameter. The absence of such an approach can be considered a shortcoming in the works of other authors related to this topic. Note that this approach also improves the fit between the observational data and the theory. Assuming that the absolute magnitude of supernovae is constant with distance, we get that the share of dark energy in a flat universe does not exceed 50%. **In Mahtessian et al. (2020) also obtained another important result that the cosmological model with a zero cosmological parameter describes the universe no worse than the Friedmann-Robertson-Walker model**.

Second difference. The correlation between the absolute magnitude of supernovae and the age of the stellar population of host galaxies indicates that there is an evolution in the absolute magnitude of supernovae (Kang & et al. (2020). It is known that the absolute magnitude of type 1a supernovae correlates with the characteristics of the host galaxy. For example, in Hicken & et al. (2009) found a systematic difference in the absolute magnitude of supernovae of ~ 0.14 magnitude between very early and very late galaxies. Sullivan et al. (2010) and Kelly et al. (2010) found that SNe Ia in less massive galaxies (by a factor of 10) are weaker by ~ 0.08 magnitudes than in more massive galaxies. Rigault et al. (2018) showed that SNe Ia in environments with local star formation (higher local SFR) is about 0.16 magnitudes weaker than in locally passive environments (lower local SFR).

Kang & et al. (2020), converted the features of the host galaxies (morphology, mass and local SFR) to age differences with methods known in the literature. Table 1 is taken from Kang & et al. (2020). The table shows the correlation of the absolute magnitude of supernovae 1a with the properties of the parent galaxies. The last column of Table 1 shows the estimated absolute magnitude evolution over 5.3 Gyr, which corresponds to the difference in age at z=0 and z=1 (see Kang & et al. (2020), for each of the four different studies. The average of these values is ~ 0.25 mag/5.3 Gyr. In this range of redshifts, the observed decrease in supernova brightness in the Hubble diagram is approximately comparable to this value (see, for example, Riess & et al. (998)). And so, this effect may be associated with the evolution of the luminosity of supernovae and has nothing to do with the accelerated expansion of the universe.

We estimate the absolute magnitude of the supernova from simulations, whether we accept its evolution or not.

In order to assess who is right, in a previous work (Mahtessian et al. (2020)) we proposed an absolute magnitude test.

The meaning of the test is that after finding the values of the cosmological parameters, the dependence of the absolute magnitudes of SNe 1a on the distance (on the redshift z) is plotted and its compliance with the initial assumption is checked. If initially it was assumed that the absolute magnitude was independent of the redshift, then the absolute magnitudes calculated from the obtained parameters Ω_Λ and Ω_M should be independent of the redshift.

That is, there must be consistency between the initial guesses and the simulation results.

3. The sample

For the study, we use a subsample from SNIa "Union2" (Amanullah & et al. (2010)). The sample consists of 719 supernovae identified in 17 papers. Following several principles, the authors cleared the sample and left 557 supernovae for further study. We also use the observational material of these 557 stars without making any changes.

doi:https://doi.org/10.52526/25792776-22.69.2-280

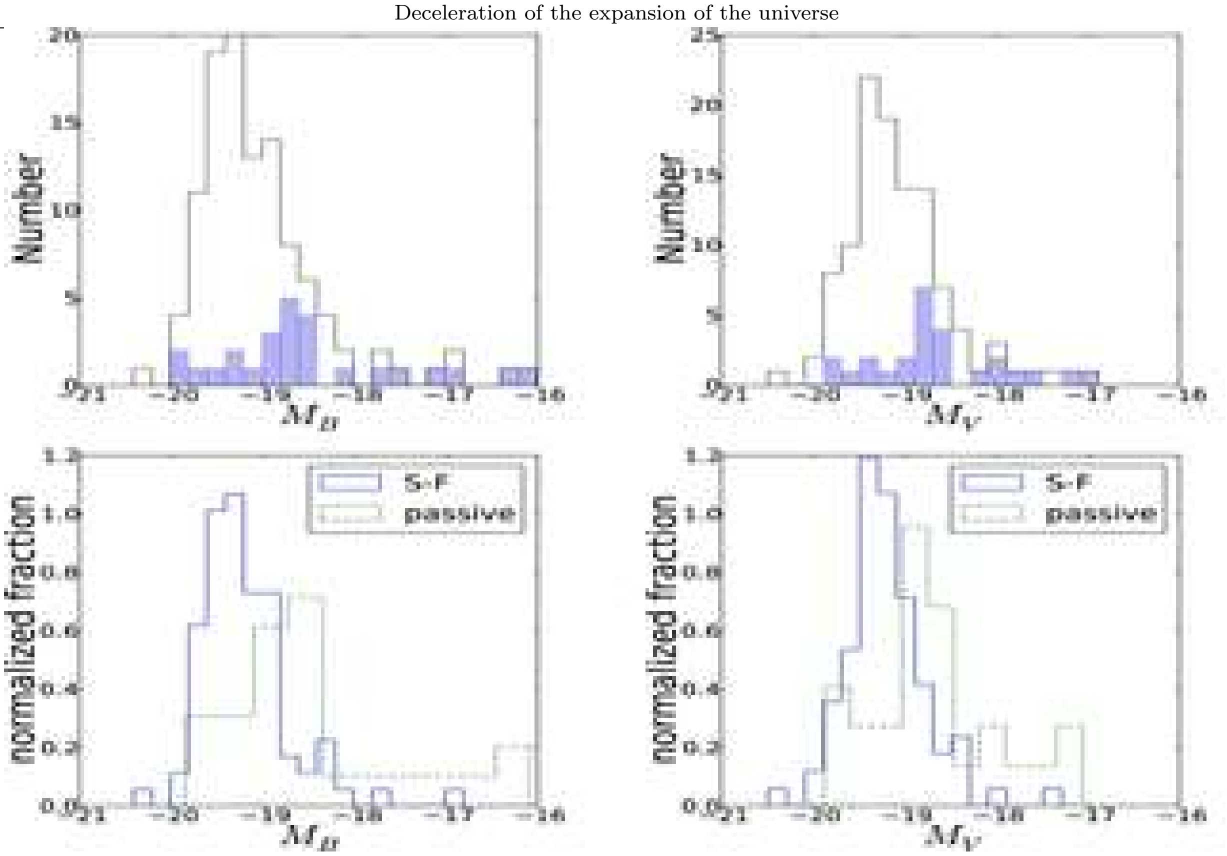

Figure 1. Distribution of absolute magnitudes of 115 type 1a supernovae. Graph copied from Ashall et al. (2016).

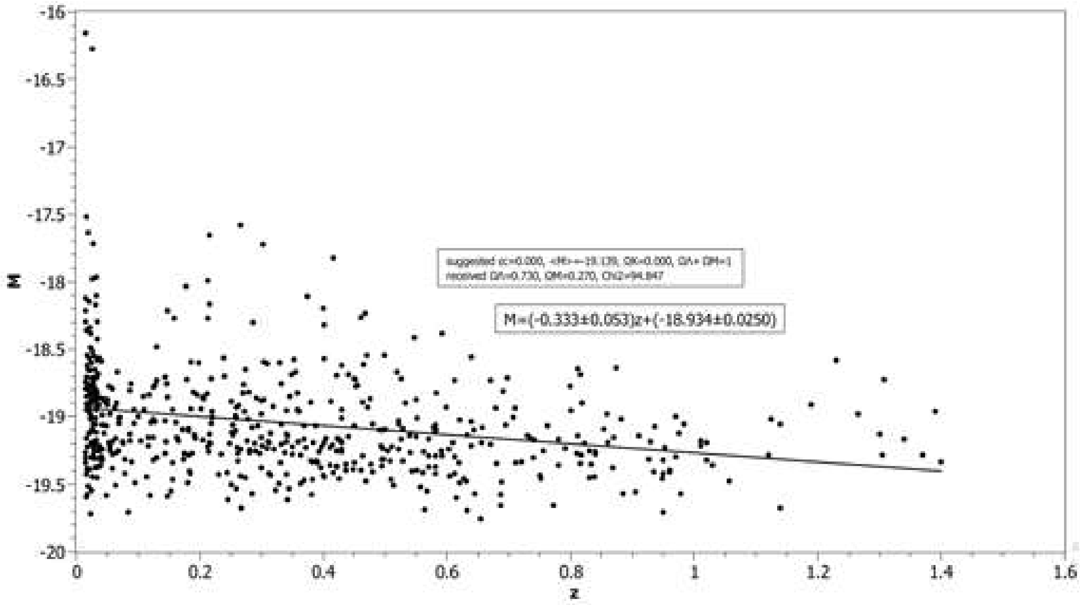

Figure 2. Dependence of the absolute magnitude of SNe1a on the redshift at $\Omega_\Lambda = 0.73$, $\Omega_M = 0.27$ for Amanullah & et al. (2010) sample.

4. Test

Amanullah & et al. (2010) investigate the case of a flat universe under the assumption that the absolute magnitudes of type 1a supernovae do not evolve.

That is, $\Omega_K = 0$, $\Omega_\Lambda + \Omega_M = 1$, $\epsilon_c = 0$.

With $M = -19.139$ ($H_0 = 72.305$) we get $\Omega_\Lambda = 0.73$, $\Omega_M = 0.27$, which were obtained in Amanullah & et al. (2010). Now let's do the "absolute magnitude test". The dependence of the absolute magnitude of M

doi:https://doi.org/10.52526/25792776-22.69.2-280

on the redshift is shown in fig. 2.

As can be seen, there is a clear relationship between the considered quantities. Thus, in this case, after the simulation, the assumption about the independence of the absolute magnitude of SNe Ia from the redshift is violated.

This gives grounds to believe that the authors found incorrect values of Ω_Λ and Ω_M.

Now let's run the simulation without fixing the absolute magnitude of the supernovae. The absolute magnitude will be obtained during the simulation. That is, we accept $\Omega_K = 0$, $\Omega_\Lambda + \Omega_M = 1$, $\epsilon_c = 0$ (as in Amanullah & et al. (2010) and we will evaluate Ω_Λ, Ω_M together with M.

The simulation gives $\Omega_\Lambda = 0.397$, $\Omega_M = 0.603$, $M = -18.903$.

Let's check the "absolute magnitude test" (Fig. 3).

As can be seen in this case, the original assumption about the independence of the absolute magnitudes of the redshift is not violated.

In addition to the "absolute magnitude test", the correctness of our result is indicated by the values of Chi^2. For the case of Amanullah & et al. (2010) obtained $Chi^2 = 94.85$, for our case $Chi^2 = 83.73$. The difference is quite big.

Thus, we can conclude that our approach is correct.

We will briefly show the results for different cases (Tables 1 and 2).

As can be seen from the tables, when the constancy of the absolute magnitudes of supernovae 1a is assumed, then the fraction of dark energy turns out to be 0.4, in contrast to 0.7, when the evolution of the absolute magnitudes of supernovae 1a is assumed, then Ω_Λ turns into 0.

When there are no restrictions on the curvature of space and the absolute magnitudes do not depend on the redshift, the Universe also consists only of gravitational matter ($\sim 40\%$ of the critical density), but has a negative curvature. This opinion reigned for approximately 50 years before 1998.

It was also found that the value of the cosmological parameters strongly depends on the absolute magnitude of supernovae.

Figure 4 shows a plot of , Ω_Λ, Ω_M versus M. This plot is built for the ΛCDM model for a flat universe ($\Omega_\Lambda + \Omega_M = 1$) and no evolution ($\epsilon_c = 0$). The graph shows the values of M corresponding to three combinations of cosmological parameters:

a) $\Omega_\Lambda = 0.7$, $\Omega_M = 0.3$ obtained at $M = -19.11$;

b) $\Omega_\Lambda = 0$, $\Omega_M = 1$ obtained at $M = -18.71$;

c) $\Omega_\Lambda = 0.397$, $\Omega_M = 0.603$ obtained at $M = -18.90$.

At the same time, as shown above, the best solution for a flat universe, without taking into account evolution, was obtained in the latter case (see Table 2).

The difference in the absolute magnitudes of supernovae 1a for combinations of a) and b) is: 19.11-18.71 = 0.4 magnitudes, while, as we saw above, the standard deviation of the distribution of absolute magnitudes of SNe Ia is 0.7 magnitudes. The magnitude difference between combinations a) and c) is only 0.2.

Thus, the dependence of the values of the parameters Ω_Λ and Ω_M on the accepted absolute value M SNe Ia is very strong, and therefore, when determining M, we must be extremely careful. As stated above, the determination of the absolute magnitude of supernovae must be simulated using the entire sample of type 1a supernovae.

5. Conclusion

The main results of this work are the following:

a. Under the assumption of the evolution of supernovae SNe 1a, the λCDM model describes the observational data better than under the assumption that the absolute magnitudes of SNe 1a are independent of redshift. In this case, a small evolution is obtained ($\Delta M = 0.304$ during the time of the corresponding z=1). Young supernovae are dimmer. Evolution is observed for both nearby and distant stars.

b. The universe turns out to be flat, even if this constraint is not initially introduced.

c. There is only gravitational matter in the universe.

d. he expansion of the universe is slowing down.

doi:https://doi.org/10.52526/25792776-22.69.2-280

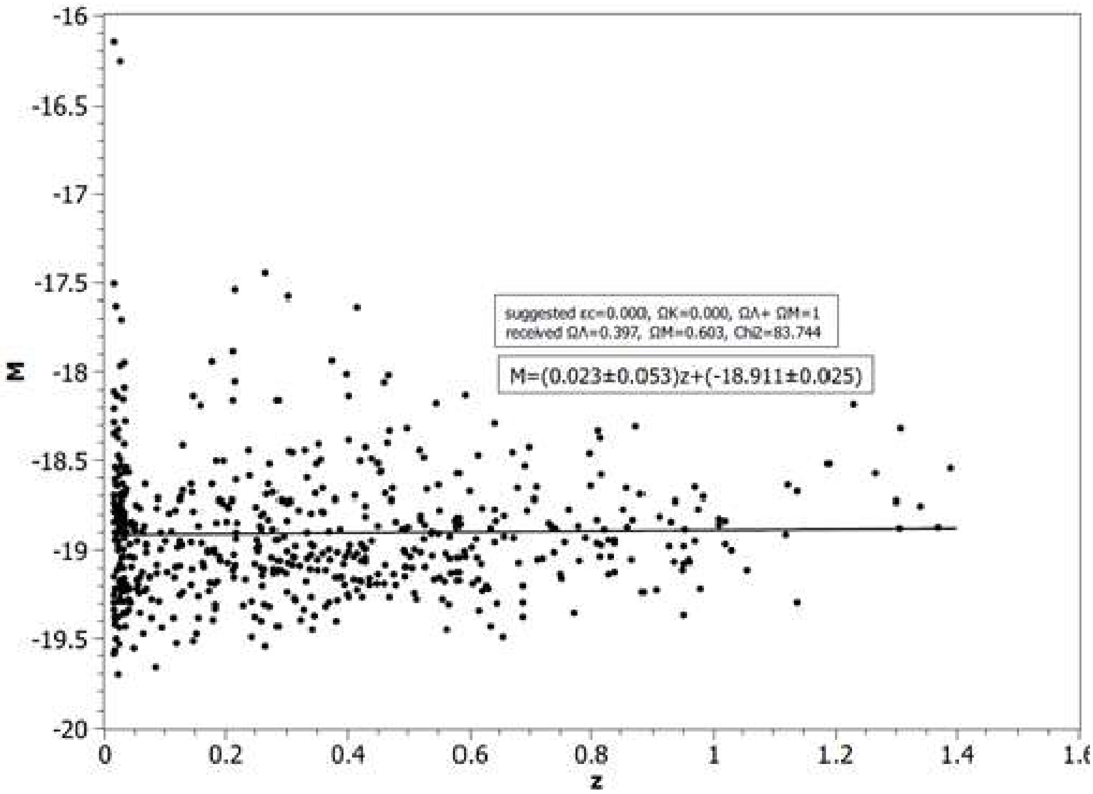

Figure 3. Absolute magnitude dependence on redshift for Amanullah & et al. (2010) sample for the case $\Omega_\Lambda = 0.397, \Omega_M = 0.603$.

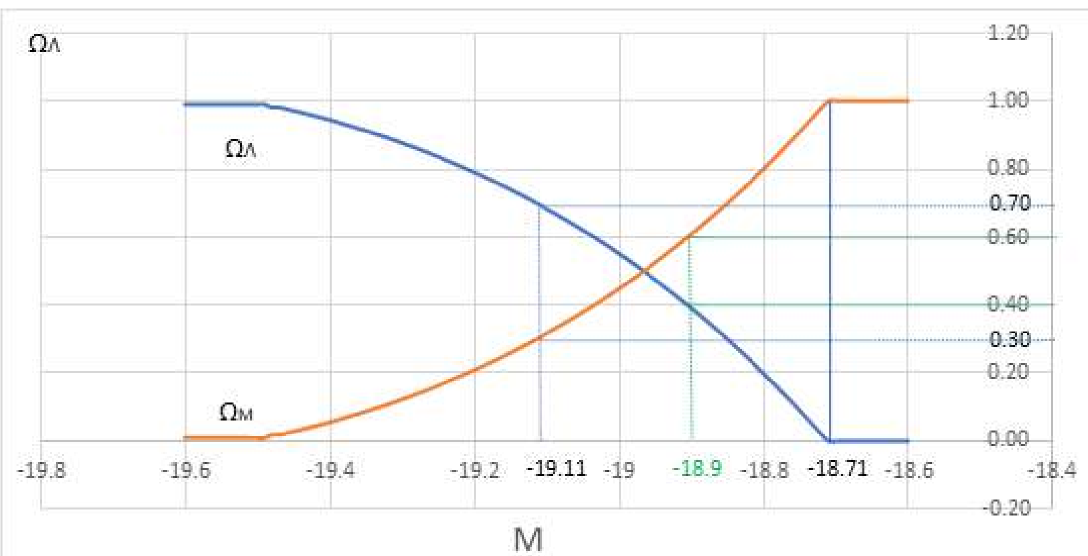

Figure 4. Plot, Ω_Λ, Ω_M versus M calculated for the ΛCDM model for a flat universe ($\Omega_\Lambda + \Omega_M = 1$). As can be seen from the figure, a change in M by only 0.4^m (from -19.11 to -18.71) leads to a change in parameters from $\Omega_\Lambda = 0.7$ and $\Omega_M = 0.3$ to $\Omega_\Lambda = 0$ and $\Omega_M = 1$.

doi:https://doi.org/10.52526/25792776-22.69.2-280

Table 1. Correlation of the absolute magnitude of supernovae 1a with the properties of host galaxies Kang & et al. (2020)

Host Property	References	Original Correlation	Direction	Converted to Age difference
Morphology	Hicken & et al. (2009)	ΔHR/Δmorph $\approx 0.14 mag/$ (Scd/Irr-E/S0)	Fainter in Later type galaxy	~0.19 mag/5.3Gyr Fainter in Younger galaxy
Mass	Sullivan et al. (2010)	ΔHR/Δmass ≈0.08 mag/ ($\Delta log M_* \sim 1$)	Fainter in Less massive galaxy	~0.21 mag/5.3Gyr Fainter in Younger galaxy
Local SFR	Rigault et al. (2018)	ΔHR/ΔlocalSFR ≈0.16 mag/ (Δ logLsSFRstep $\sim 2yr^{-1}kpc^{-2}$)	Fainter in Higher SFR environments	~0.34 mag/5.3Gyr Fainter in Younger galaxy
Population Age	Kang & et al. (2020)	ΔHR/Δage ≈0.051 mag/Gyr (YEPS)	Fainter in Younger galaxy	~0.27 mag/5.3Gyr Fainter in Younger galaxy

Table 2. The results for different cases of the Friedmann-Robertson-Walker Model

		Received					
Suggested	Evaluated	M_0	ϵ_c	Ω_Λ	Ω_M	Ω_K	Chi^2
$\epsilon_c = 0$, $\Omega_K = 0$, $\Omega_\Lambda + \Omega_M = 1$	M_0,Ω_Λ,Ω_M	-18.903	-	0.397	0.603	-	83.7439
$\Omega_K = 0$, $\Omega_\Lambda + \Omega_M = 1$	M_0,ϵ_c,Ω_Λ,Ω_M	-18.875	0.304	0.000	1.000	-	82.2258
$\epsilon_c = 0$, $\Omega_K + \Omega_\Lambda + \Omega_M = 1$	M_0,Ω_Λ,Ω_M,Ω_K	-18.881	-	0.000	0.368	0.632	83.2808
$\Omega_K + \Omega_\Lambda + \Omega_M = 1$	M_0,ϵ_c,Ω_Λ,Ω_M,Ω_K	-18.875	0.304	0.000	1.000	0.000	83.2258
$\Omega_K + \Omega_\Lambda + \Omega_M = 1$ $z = 0.0 \div 0.5$, $N = 403$	M_0,ϵ_c,Ω_Λ,Ω_M,Ω_K	-18.886	0.399	0.000	1.000	0.000	72.2283
$\Omega_K + \Omega_\Lambda + \Omega_M = 1$ $z = 0.5 \div 1.5$, $N = 154$	M_0,ϵ_c,Ω_Λ,Ω_M,Ω_K	-18.970	0.403	0.000	1.000	0.000	10.7607

Table 3. The results for the model with zero cosmological parameter ($\Lambda = 0$)

		Received			
Suggested	Evaluated	M_0	ϵ_c	q_0	Chi^2
$\epsilon_c = 0$, $\Lambda = 0$	M_0,q_0	-18.881	-	0.184	83.2808
$\Lambda = 0$	M_0,ϵ_c,q_0	-18.875	0.304	0.500	82.2258
$\Lambda = 0$, $z = 0.0 \div 0.5$, $N = 403$	M_0,ϵ_c,q_0	-18.886	0.399	0.500	72.2283
$\Lambda = 0$, $z = 0.5 \div 1.5$, $N = 154$	M_0,ϵ_c,q_0	-18.970	0.403	0.500	10.7607

doi:https://doi.org/10.52526/25792776-22.69.2-280

References

Amanullah R., et al. 2010, Astrophys. J. , 716, 712

Ashall C., Mazzali P., Sasdelli M., Prentice S. J., 2016, Mon. Not. R. Astron. Soc. , 460, 3529

Hicken M., et al. 2009, Astrophys. J. , 700, 1097

Hubble E. P., 1929, Proc. Nat. Acad. Sci., 15, 168

Kang J., et al. 2020, Astrophys. J. , 889, 8

Kelly P. L., Hicken M., Burke D. L., et al. 2010, Astrophys. J. , 715, 743

Kowalski M., et al. 2008, Astrophys. J. , 686, 749

Mahtessian A. P., Karapetian G. S., et al. 2020, AdAp, 5, 18

Mahtessian A. P., Karapetian G. S., et al. 2022, arXiv:2209.00549 [astro-ph.CO], p. 1

Perlmutter S., et al. 1999, Astrophys. J. , 517, 565

Riess A., et al. 998, Astron. J. , 116, 1009

Rigault M., Brinnel V., Aldering G., et al. 2018, arXiv:1806.03849 [astro-ph.CO], p. 1

Sullivan M., Conley A., Howell D. A., et al. 2010, Mon. Not. R. Astron. Soc. , 406, 782

doi:https://doi.org/10.52526/25792776-22.69.2-280

Communications of BAO, Vol. 69, Issue 2, 2022, pp. 287-294

Multiwavelength Space Astronomy

A. M. Mickaelian*, G. A. Mikayelyan, H. V. Abrahamyan, and G. M. Paronyan

NAS RA V. Ambartsumian Byurakan Astrophysical Observatory (BAO), Byurakan 0213, Aragatzotn Province, Armenia

Abstract

Because the Earth's atmosphere is not transparent for the most of the electromagnetic waves, Space Astronomy was born in 1960s to complement ground-based observations and to provide us with multiwavelength data from gamma-ray to radio. Most Space observatories work in gamma-ray, X-ray, UV and IR, as well as there are also optical and other Space telescopes. We will review the most important Space telescopes: their important technical parameters, scientific results and discoveries. Among them there are (by increasing wavelengths) Fermi, Swift, INTEGRAL, ROSAT, Chandra, XMM, GALEX, Hubble, Gaia, James Webb, Herschel, WISE, Spitzer, IRAS and many others. These telescopes make the Space Astronomy truly multiwavelength and the combination with ground-based data allows us to have better understanding of the Universe and phenomena going on in its all varieties.

Keywords: *Multiwavelength Astronomy, Space Astronomy, Space Telescopes, X-ray Astronomy, UV Astronomy, IR Astronomy*

Introduction

The Earth's atmosphere is not transparent to all electromagnetic wavelengths; it is transparent only for optical and radio ones, as well as a small part of infrared (IR). This is the reason why astronomers make observations also from Space using the whole spectrum of electromagnetic waves. Moreover, optical Space telescopes are also being used to get rid from the atmosphere's absorption and other negative effects. Though first radio observations were started in 1930s and observations in some other wavelengths were carried out in 1960s, however the true Multiwavelength Space Astronomy was born in 1970s-1980s, when Space telescopes in all wavelengths were launched and studied the Universe to build up multiwavelength pictures of various astronomical objects and phenomena. These were mainly USA National Aeronautics and Space Administration (NASA) and European Space Agency (ESA) missions, as well as some Japan Aerospace Exploration Agency (JAXA), Russian (Roscosmos), German Aerospace Center (Deutsches Zentrum für Luft- und Raumfahrt e. V., DLR), China National Space Administration (CNSA) and other national Space agencies' missions were accomplished.

It is also worth mentioning that the all-sky multiwavelength data at almost all wavelengths became available after 2003, when in 1996-2003 several all-sky or large area surveys (both ground-based and Space) were released, such as ROSAT, NVSS, FIRST, 2MASS, USNO-B1.0, MAPS and some others. We give in this paper an understanding on Space observatories and Space Astronomy, describe most important Space telescopes in High-Energy, UV, Optical, and IR.

High Energy Space Telescopes

Gamma-ray and X-ray astronomy are often unified as High-Energy Astronomy (HEA). In Table 1 we give the list of the most important High-Energy Space telescopes with their most important data: name, country, years of operation, energy range in keV, most important results, and number of detected sources.

In Figure 1, we give 3 most important HEA Space telescopes: Rontgensatellit (ROSAT), XMM-Newton and Chandra X-ray Observatory (CXO).

According to follow-up optical identifications of detected gamma-ray and X-ray sources, Cosmic high-energy sources are:

*aregmick@yahoo.com

doi:https://doi.org/10.52526/25792776-22.69.2-287

Table 1. Most important High-Energy Space telescopes.

Telescope	Country	Years	Energy (keV)	Results	Number of sources
Uhuru (SAS-1)	USA	1970-1973	2 – 20	Sky survey	339
HEAO-1	USA	1977-1979	0.25 – 10 000	Sky survey	842
Einstein (HEAO-2)	USA	1978-1981	0.2 – 20	Pointed deep observations	1435
EXOSAT	ESA	1983-1986	0.04 – 80	Sky survey	1210
Granat	France, Russia	1989-1999	2 – 100 000	Pointed deep observations, Sky survey	1551
CGRO	USA	1991-2000	20 – 30 000 000	Imaging, sky survey	400
ROSAT	Germany	1990-1999	0.07 – 2.4	Sky survey	124 730
ASCA (Astro-D)	Japan	1993-2001	0.4 – 10	Sky survey, spectral observations	1190
Rossi XTE (RXTE)	USA	1995-2012	2 – 250	Sky survey	321
BeppoSAX	Italy	1996-2002	0.1 – 300	Gamma bursts, broad-band spectroscopy	253
Chandra (CXO)	USA	1999-pres.	0.07 – 10	Pointed deep observations	380 000
XMM-Newton	ESA	1999-pres.	0.25 – 12	Pointed deep observations	372 728
INTEGRAL	ESA	2002-pres.	15 – 10 000	Pointed deep observations	1126
Swift	USA	2004-2008	0.2 – 150	Sky survey, gamma bursts	1256
Fermi (GLAST)	USA	2008-pres.	150 – 300 000 000	Imaging, gamma bursts	5064
NuSTAR	USA	2012-pres.	3 – 79	Deep survey for BH	498
Spektr-RG	Russia / Germany	2019-pres.	0.2 – 10	Survey, clusters of galaxies	

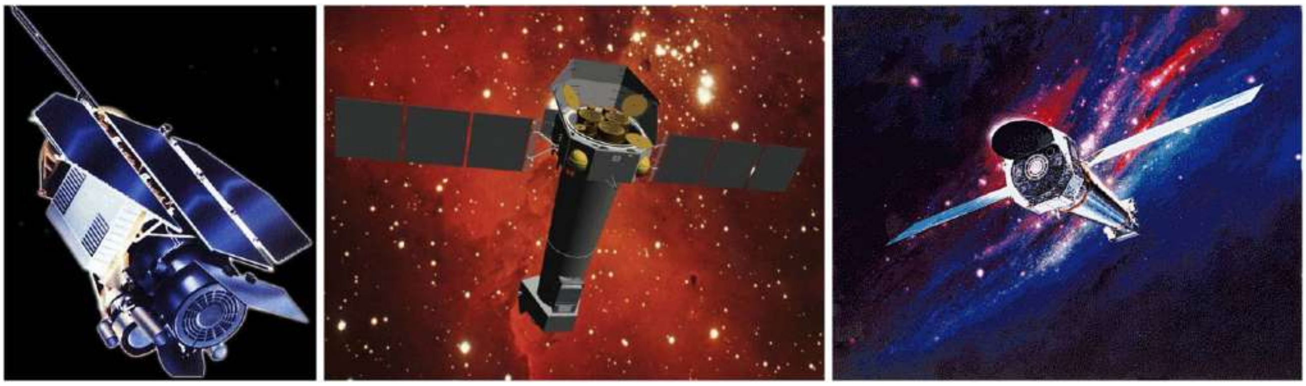

Figure 1. Three of the most important HEA Space telescopes: ROSAT, XMM-Newton and Chandra.

- Solar System bodies
- hot coronae; late-type (M) dwarfs
- white dwarfs (WD) and hot subdwarfs (sd)
- X-ray binaries; intermediate mass X-ray binaries
- cataclysmic variables (CV)
- magnetars
- Supernovae remnants (SNR)
- bright galaxies
- Active Galactic Nuclei (AGN) and Starburst (SB) Galaxies
- blazars (part of AGN)
- clusters of galaxies

Ultraviolet Space Telescopes

In Table 2 we give the list of the most important Ultraviolet (UV) Space telescopes with their most important data: name, country, years of operation, wavelength range in A, most important results, and number of detected sources.

In Figure 2, we give 3 of the most important UV Space telescopes: IUE, FUSE and GALEX.

doi:https://doi.org/10.52526/25792776-22.69.2-287

Table 2. Most important UV Space telescopes.

Space Telescope	Country	Years	Wavelength range λ ($\AA$)	Results	Number of objects
OAO 2	USA	1968-1973	1050 – 4250	Comets, Novae	
OAO 3 (Copernicus)	USA	1972-1981	1047 – 1055	HR spectra, pulsars	
Orion	USSR	1971	2000 – 3800	UV spectra	
Orion-2	USSR	1973	2000 – 3000	UV spectra	900
ANS	USA / Neth.	1974-1976	1500 – 3300	Images, spectra	3 573
International Ultraviolet Explorer (IUE)	USA / ESA	1978–1996	1150 – 3200	Images, spectra	110 033
Astron	USSR	1983-1989	1500 – 3500	Supernovae, comets	203 592
Glazar	USSR	1987	1640	UV emission of stars	
Hubble Space Telescope (HST)	USA / ESA	1990-pres.	1150 – 17000	Imaging, spectra	
EUVE	USA	1992-2001	70 – 760	All-sky survey	801
FUSE	USA	1999-2007	905 – 1195	Universal deuterium	5 061
Galaxy Evolution Explorer (GALEX)	USA	2003-2013	1350 – 2800	Sky survey	82 992 086

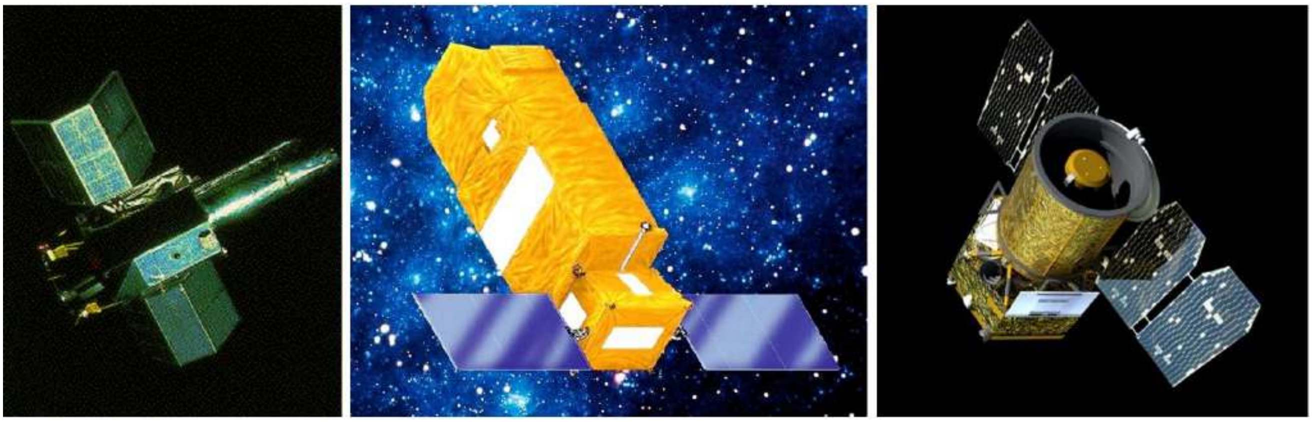

Figure 2. Three of the most important UV Space telescopes IUE, FUSE and GALEX.

Optical Space Telescopes

Though optical wavelengths are accessible from ground as well, however, the Earth's atmosphere strongly affects the astronomical observations, as the light is being absorbed and distorted due to turbulence resulting reduction of the resolution. Hence, Space observations are deeper and have much higher resolution; therefore, especially the astrometric missions have great success compared to the Earth ground-based observations. Along with HIPPARCOS and Gaia astrometric missions for all-sky surveys, optical Space telescopes Kepler, TESS and some others were aimed at detecting exoplanets, also due to high astrometric accuracy. We give in Table 3 the list of the most important optical Space telescopes with their most important data: name, country, years of operation, wavelength range in A, most important results, and number of detected objects. Note, James Webb Space Telescope (JWST), the largest Space telescope with a diameter of the mirror 6.5m and with a collecting area of 25.4 m^2, is recent and the number of detected objects is just preliminary.

Table 3. Most important optical Space telescopes.

Space Telescope	Country	Years	Wavelength range λ ($\AA$)	Results	Number of objects
HIgh Precision PARallax COllecting Sat. (HIPPARCOS)	ESA	1989-1993	visible	Astrometry	2 539 913
Hubble Space Telescope (HST)	USA / ESA	1990-pres.	1150 – 17000	Imaging, spectra	
Kepler Space Telescope	USA	2009-2013	4300 – 8900	Exoplanets	5 011
Global Astrometric Interferom. for Astrophysics (Gaia)	ESA	2013-pres.	3200 – 10000	Astrometry, spectra	1 811 709 771
Transiting Exoplanet Survey Satellite (TESS)	USA	2018-pres.	visible	Exoplanets	5 000
James Webb Space Tel. (JWST)	USA / ESA	2021-pres.	6000 – 283 000	Cosmology, exoplanets	78

In Figure 3, we give 3 of the most important optical Space telescopes: HST, Gaia and JWST.

Infrared Space Telescopes

Only the nearest part of the Infrared (IR) range is accessible from the Earth, typically up to 5.5 μm, as well as our atmosphere is somewhat transmitting also the range 8-14 μm. Anyway, the IR Space astronomy is one of the most important among all ranges, as many new discoveries have been accomplished in these wavelengths. In Table 4 we give the list of the most important IR Space telescopes with their most important data: name, country, years of operation, wavelength range in μm, most important results, and number of

doi:https://doi.org/10.52526/25792776-22.69.2-287

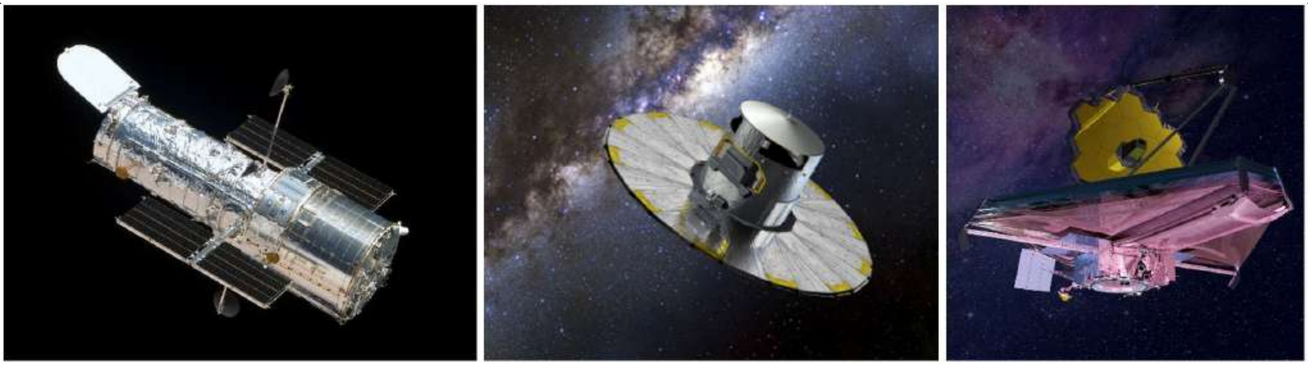

Figure 3. Three of the most important optical Space telescopes: HST, Gaia and JWST.

detected sources. Among them, there are two biggest Space telescopes: recently launched JWST with its 6.5m diameter mirror and Herschel with its 3.5m diameter mirror. Only these two Space telescopes are larger than HST (2.4m), which is operating since 1990.

Table 4. Most important IR Space telescopes.

Telescope or project	Countries	Years	λ (μm)	Results	Number of sources
Infrared Astronomical Satellite (IRAS)	USA	1983-1983	8 – 120	Sky survey	405 769
Infrared Space Observatory (ISO)	ESA	1995-1998	2.5 – 240	IR spectra	~ 30 000
Spitzer Space Telescope (SST)	USA	2003-2020	3 – 180	IR deep images and spectra	4 261 028
AKARI (Astro-F)	Japan	2006-2011	7 – 180	Sky survey	1 298 044
Herschel Space Observatory (HSO)	ESA / USA	2009-2013	55 – 672	Far IR sources	8 223 000
Wide-field Infrared Survey Explorer (WISE)	USA	2009-2013	3 – 28	Sky survey	563 921 584
JWST	USA / ESA	2021-pres.	0.6 – 283	Cosmology, exoplanets	78

In Figure 4, we give 3 of the most important IR Space telescopes: IRAS, Spitzer and Herschel.

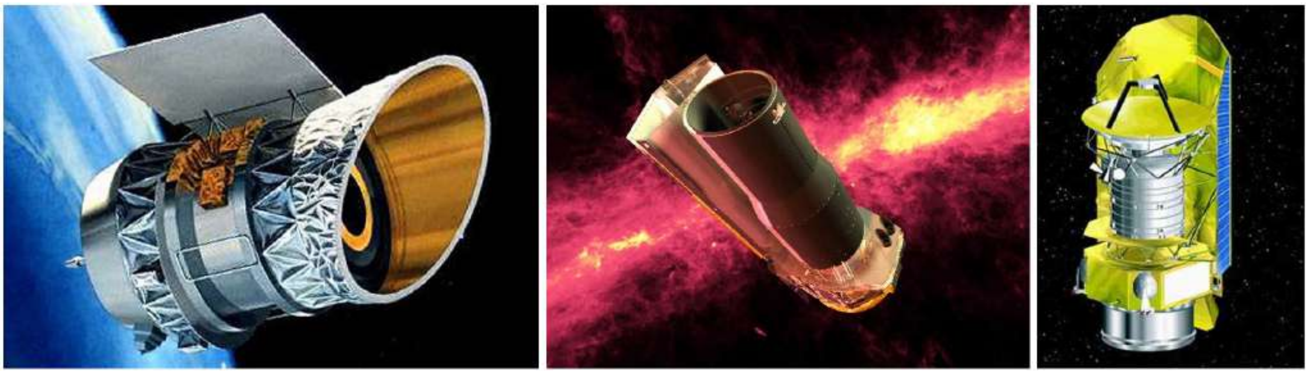

Figure 4. Three of the most important IR Space telescopes: IRAS, Spitzer and Herschel.

According to all these observations, many IR sources have been revealed and many have been identified with optical counterparts, different kinds of objects:

- In Near-IR (NIR) (wavelength range from 0.76-1 to 5 μm, temperature range from 740 to 3000-5200 K), the main emitters are cold red stars, stellar envelopes, planetary nebulae;
- In Mid-IR (MIR) (wavelength range from 5 to 25-40 μm, temperature range from 92.5-140 to 740 K), the main emitters are planets, comets and asteroids, stellar radiation heated dust, protoplanetary disks, gas-dust nebulae;
- In Far-IR (FIR) (wavelength range from 25-40 to 200-350 μm, temperature range from 10.6-18.5 to 92.5-140 K), the main emitters are cold gas radiation, central regions of galaxies, very cold molecular clouds.

doi:https://doi.org/10.52526/25792776-22.69.2-287

Microwave Space Telescopes

Cosmic Microwave Background radiation (CMB, CMBR) is the most important witness of the Big Bang, the main cosmological theory, also called theory of the Hot Universe. Space missions working at microwave range are aimed at detecting in details as much as possible the CMB, to reveal its temperature, anisotropy, etc. We give in Table 5 the list of the most important Microwave Space telescopes with their most important data.

Table 5. Most important Microwave Space telescopes.

Telescope or project	**Countries**	**Years**	λ (μm)	**Results**
Cosmic Background Explorer (COBE)	USA	1989-1993	1 – 10 000	Sky survey, CMBR
Wilkinson Microwave Anisotropy Probe (WMAP)	USA	2001-2010	3 200 – 13 000	Sky survey, CMBR
Planck Space Observatory	ESA	2009-2013	300 – 11 100	Sky survey, CMBR

In Figure 5, we give the most important Microwave Space telescopes: COBE, WMAP and Planck.

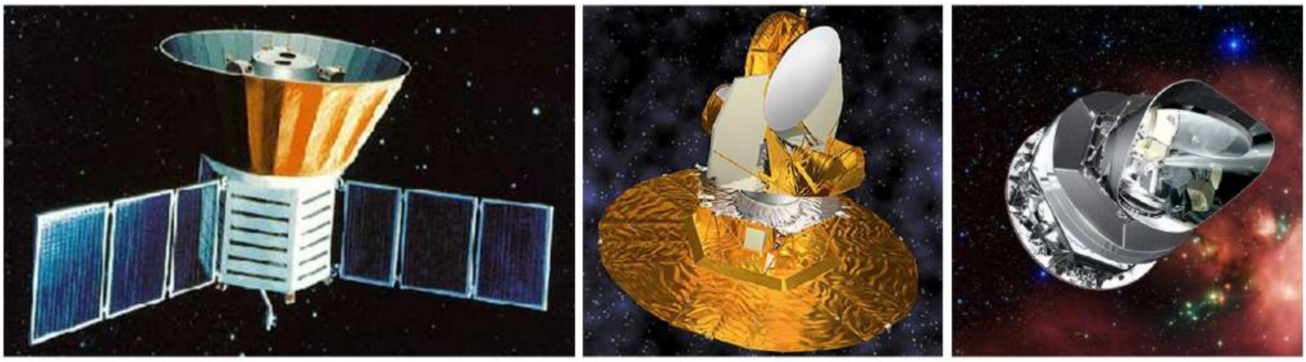

Figure 5. Most important Microwave Space telescopes: COBE, WMAP and Planck.

Scientific results at BAO based on Space telescopes data

Modern astronomy is full of discoveries based especially on Space telescopes data. Many investigations in the Byurakan Astrophysical Observatory (BAO) are also based on results from IRAS, HST, ROSAT, Spitzer, XMM, Chandra, Herschel, Gaia, and other Space telescopes. Here we give the scientific results by our "Astronomical Surveys" research team based on Space telescopes data. The following results may be outlined:

- Revelation of 1577 IRAS unidentified IR sources; 1279 galaxies (BIG objects) and 287 (BIS) (Mickaelian & Sargsyan (2004); Mickaelian & Gigoyan (2006)).
- New bright AGN (Seyferts and LINERs) and ULIRGs among BIG objects (Mickaelian et al. (2002); Mickaelian & Sargsyan (2010)). Dozens of new pairs and multiple galaxies among IRAS sources (Mickaelian (2007)). Estimation of the maximum IR luminosity of a single spiral galaxy (10^{12}L) (Mickaelian (2001)).
- Discovery of IRAS F18187+6304: a puzzling PMS emission line star with circumstellar envelope among BIS objects (Rossi et al. (2010); Gaudenzi et al. (2017a); Gaudenzi et al. (2017b)).
- Revelation of 3212 ROSAT FSC X-ray sources (Véron-Cetty et al. (2004)). New bright AGN (QSOs and Seyferts) among X-ray sources.
- Optical identification of ROSAT sources and estimation of the abundance of various types of objects among X-ray sources. Revelation of 2791 ROSAT FSC X-ray sources (BHRC objects) (Mickaelian et al. (2006)). Pairs and multiple galaxies among ROSAT sources, discovery of new types of X-ray sources: interacting galaxies.

doi:https://doi.org/10.52526/25792776-22.69.2-287

- Mickaelian's observational project on study of high-luminosity IR galaxies was carried out on IR Spitzer Space Telescope (SST) in collaboration with Cornell University (Ithaca, N.Y., USA) team (Sargsyan et al. (2008)). 32 highest IR/opt flux ratio extragalactic sources selected from IRAS FSC and observed with SST. Study of their NIR-MIR spectra. Discovery of the highest IR/opt flux ratio (40-1000) extragalactic objects.

- Mickaelian's observational project on study of IR excess galactic stars was carried out on IR Spitzer Space Telescope (SST) in collaboration with Cornell University (Ithaca, N.Y., USA) team (Hovhannisyan et al. (2009)). Study of 237 Spitzer Space Telescope (SST) stellar sources in Boötes and FLS. Discovery of 21 hot debris disk stars among Spitzer sources.

Summary

Multiwavelength Space Astronomy was a real revolution in Astronomy/Astrophysics and is still being extremely important for further advanced studies. This is especially outstanding in those wavelength ranges, where the Earth atmosphere is not transparent for photons. Many new discoveries in different wavelength ranges related to Solar System objects, stars, nebulae, star-formation regions, galaxies, clusters of galaxies, Cosmology, and exoplanets were made, as well as the combination of various wavelength data gives a new possibility for further more efficient studies of the Universe. The Astrophysical Virtual Observatories (AVOs, VOs) appeared and were developed mainly due to the development of Space Astronomy, as most of the new wavelength ranges appeared to be intensely explored after the Space era. Still, the vast majority of objects in astronomy has been discovered in the optical range (some 2.4 billion objects out of the total 3 billion in all wavelengths), however it is important to have an overall understanding for any of objects and combine gamma-ray, X-ray, UV, optical, IR, submm/mm and radio data, as well as various methods of observations and even non-electromagnetic information, leading from Multiwavelength (MW) Astronomy to real Multimessenger (MM) Astronomy.

In Figure 6, we give the distribution of ESA's Space telescopes by wavelength range, both past, operational and future ones.

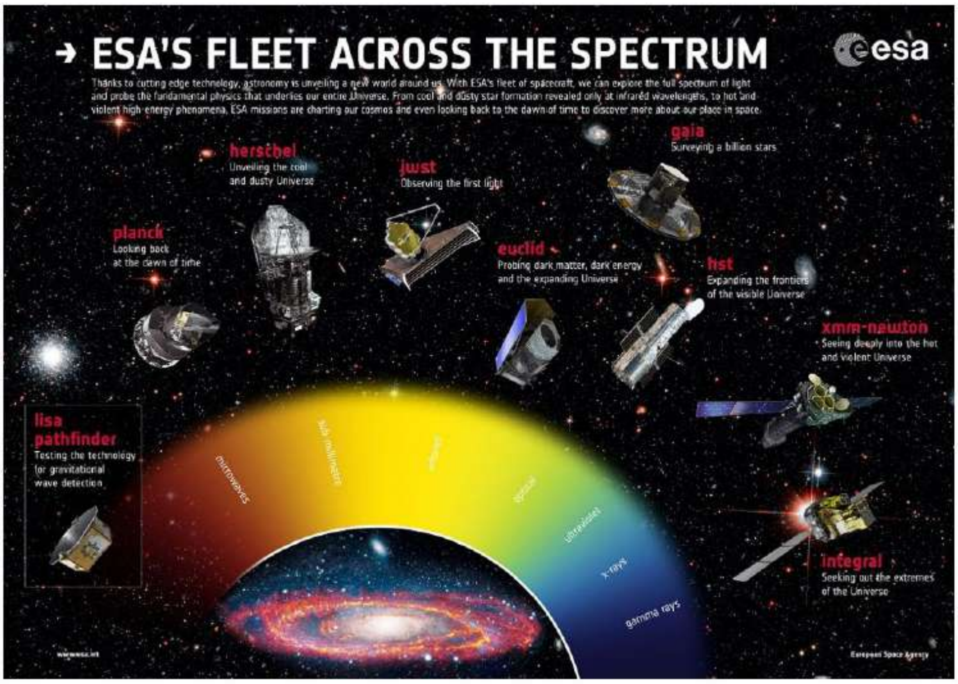

Figure 6. ESA's fleet across the spectrum; ESA's multiwavelength Space missions.

Acknowledgements

This work was partially supported by the Republic of Armenia Ministry of Education, Science, Culture, and Sports (RA MESCS) Committee of Science, in the frames of the research projects No. 15T-1C257 and 21AG-1C053. This work was made possible in part by research grants from the Armenian National Science and Education Fund (ANSEF) based in New York, USA (grants astroex-4193, astroex-4195, astroex-2347 and astroex-2597).

doi:https://doi.org/10.52526/25792776-22.69.2-287

References

1988, Infrared Astronomical Satellite (IRAS) Catalogs and Atlases.Volume 7: The Small Scale Structure Catalog. Vol. 7

1997, The HIPPARCOS and TYCHO catalogues. Astrometric and photometric star catalogues derived from the ESA HIPPARCOS Space Astrometry Mission ESA Special Publication Vol. 1200

Abdollahi S., et al., 2020, Astrophys. J. Suppl. Ser. , 247, 33

Abdollahi S., et al., 2022, Astrophys. J. Suppl. Ser. , 260, 53

Abrahamyan H. V., Mickaelian A. M., Knyazyan A. V., 2015, Astronomy and Computing, 10, 99

Ajello M., Greiner J., Kanbach G., Rau A., Strong A. W., Kennea J. A., 2008, Astrophys. J. , 678, 102

Bailer-Jones C. A. L., Rybizki J., Fouesneau M., Mantelet G., Andrae R., 2018, Astron. J. , 156, 58

Beitia-Antero L., Gómez de Castro A. I., 2016, Astron. Astrophys. , 596, A49

Bianchi L., Herald J., Efremova B., Girardi L., Zabot A., Marigo P., Conti A., Shiao B., 2011, Astrophys. Space. Sci. , 335, 161

Bottacini E., Ajello M., Greiner J., 2012, Astrophys. J. Suppl. Ser. , 201, 34

Bowyer S., Lampton M., Lewis J., Wu X., Jelinsky P., Malina R. F., 1996, Astrophys. J. Suppl. Ser. , 102, 129

Bystrov N. F., Polojentsev D. D., Potter H. I., Yagudin L. I., Zallez R. F., Zelaya J. A., 1994, Bulletin d'Information du Centre de Donnees Stellaires, 44, 3

Cutri R. M., et al., 2012, Explanatory Supplement to the WISE All-Sky Data Release Products, Explanatory Supplement to the WISE All-Sky Data Release Products

Davison P. J. N., Culhane J. L., Mitchell R. J., Fabian A. C., 1975, Astrophys. J. Lett. , 196, L23

Dezalay J. P., Barat C., Talon R., Sunyaev R., Terekhov O., Kuznetsov A., 1993, in Friedlander M., Gehrels N., Macomb D. J., eds, American Institute of Physics Conference Series Vol. 280, Compton Gamma-ray Observatory. pp 783–787, doi:10.1063/1.44220

Evans I. N., et al., 2010, Astrophys. J. Suppl. Ser. , 189, 37

Evans I. N., et al., 2014, VizieR Online Data Catalog, p. IX/45

Flores H., et al., 1999, Astrophys. J. , 517, 148

Forman W., Jones C., Cominsky L., Julien P., Murray S., Peters G., Tananbaum H., Giacconi R., 1978, Astrophys. J. Suppl. Ser. , 38, 357

Gaia Collaboration et al., 2018, Astron. Astrophys. , 616, A1

Gaudenzi S., Nesci R., Rossi C., Sclavi S., Gigoyan K. S., Mickaelian A. M., 2017a, Rev. Mex. Astron. Astrofis. , 53, 449

Gaudenzi S., Nesci R., Rossi C., Sclavi S., Gigoyan K. S., Mickaelian A. M., 2017b, Rev. Mex. Astron. Astrofis. , 53, 507

Geach J. E., et al., 2017, Mon. Not. R. Astron. Soc. , 465, 1789

Giacconi R., et al., 1979, Astrophys. J. , 230, 540

Golenetskii S. V., et al., 1991, Advances in Space Research, 11, 125

Güdel M., et al., 2007, Astron. Astrophys. , 468, 353

Haakonsen C. B., Rutledge R. E., 2009, Astrophys. J. Suppl. Ser. , 184, 138

Herschel Point Source Catalogue Working Group et al., 2020, VizieR Online Data Catalog, p. VIII/106

Hovhannisyan L. R., et al., 2009, Astron. J. , 138, 251

Ishihara D., et al., 2010, Astron. Astrophys. , 514, A1

Koss M. J., et al., 2022, Astrophys. J. Suppl. Ser. , 261, 2

Lansbury G. B., et al., 2017, Astrophys. J. , 836, 99

Malizia A., Bassani L., Bazzano A., Bird A. J., Masetti N., Panessa F., Stephen J. B., Ubertini P., 2012, Mon. Not. R. Astron. Soc. , 426, 1750

Malizia A., Bassani L., Stephen J. B., Bazzano A., Ubertini P., 2020, Astron. Astrophys. , 639, A5

Mickaelian A. M., 2001, Astrophysics, 44, 33

Mickaelian A. M., 2007, in Combes F., Palouš J., eds, Vol. 235, Galaxy Evolution across the Hubble Time. pp 225–225, doi:10.1017/S1743921306006314

Mickaelian A. M., Gigoyan K. S., 2006, Astron. Astrophys. , 455, 765

Mickaelian A. M., Sargsyan L. A., 2004, Astrophysics, 47, 213

Mickaelian A. M., Sargsyan L. A., 2010, Astrophysics, 53, 483

Mickaelian A. M., Balayan S. K., Hakopian S. A., 2002, in Green R. F., Khachikian E. Y., Sanders D. B., eds, Astronomical Society of the Pacific Conference Series Vol. 284, IAU Colloq. 184: AGN Surveys. p. 217

Mickaelian A. M., Hovhannisyan L. R., Engels D., Hagen H. J., Voges W., 2006, Astron. Astrophys. , 449, 425

Moshir M., et al. 1990, IRAS Faint Source Catalogue, p. 0

Revnivtsev M., Sazonov S., Jahoda K., Gilfanov M., 2004, Astron. Astrophys. , 418, 927

Rossi C., et al., 2010, Memorie della Societa Astronomica Italiana Supplementi, 14, 127

Sanford P. W., Ives J. C., Bell Burnell S. J., Mason K. O., Murdin P., 1975, Nature. , 256, 109

Sargsyan L., Mickaelian A., Weedman D., Houck J., 2008, Astrophys. J. , 683, 114

Tanaka Y., Inoue H., Holt S. S., 1994, Publ. Astron. Soc. Jpn. , 46, L37

Treves A., et al., 1980, Astrophys. J. , 242, 1114

Tueller J., Mushotzky R. F., Barthelmy S., Cannizzo J. K., Gehrels N., Markwardt C. B., Skinner G. K., Winter L. M., 2008, Astrophys. J. , 681, 113

Verbunt F., van Gent R. H., 2011, Astron. Astrophys. , 530, A93

Véron-Cetty M. P., et al., 2004, Astron. Astrophys. , 414, 487

Voges W., et al., 2000, IAU Circ., 7432, 3

Waskett T. J., Eales S. A., Gear W. K., McCracken H. J., Brodwin M., Nandra K., Laird E. S., Lilly S., 2004, Mon. Not. R. Astron. Soc. , 350, 785

Wesselius P. R., van Duinen R. J., de Jonge A. R. W., Aalders J. W. G., Luinge W., Wildeman K. J., 1982, Astron. and Astrophys. Suppl. Ser. , 49, 427

White N. E., Mason K. O., Sanford P. W., Murdin P., 1976, Mon. Not. R. Astron. Soc. , 176, 201

Wood K. S., et al., 1984, Astrophys. J. Suppl. Ser. , 56, 507

Yamamura I., Makiuti S., Ikeda N., Fukuda Y., Oyabu S., Koga T., White G. J., 2010, VizieR Online Data Catalog, p. II/298

von Kienlin A., et al., 2020, Astrophys. J. , 893, 46

doi:https://doi.org/10.52526/25792776-22.69.2-287

Youth project Space-π using small spacecraft for research of near-Earth space and remote sensing of the earth

S.B. Makarov *[1], S.V. Zavjalov[1], S.V. Volvenko[1], A.K. Aharonyan[2], and V.H. Avetisyan[2]

[1]Peter the Great St. Petersburg Polytechnic University, St. Petersburg, Russia
[2]Russian-Armenian University, Erevan, Armenia

Abstract

This work is devoted to the implementation of the scientific and educational project "Space-π" for the development and production of small spacecraft on the domestic digital platform in order to implement schoolchildren's projects. A very important part of this work is that a lot of school groups take part in it, not only from St. Petersburg, but from all over Russia in general, and in the future from other countries. They have the opportunity to participate via the Internet both in the processing of information and in the process of how the satellite is manufactured.

Keywords: *small spacecraft, nanosatellite, receiving-transmitting station, GLONASS*

1. Introduction

The project "SPACE-π began in Peter the Great St. Petersburg Polytechnic University (SPbPU) in 2021 and its goal was to involve schoolchildren, students and graduate students in scientific and technical activities and popularize space research, missions, technologies through team solving competitive and applied tasks. Students and schoolchildren participate in the process of development, testing of scientific and educational spacecraft into near-Earth orbit. They are engaged in processing the results obtained in the process of space missions, research and experiments.

The main scientific interests, taking into account the technological features of the project, are in the following areas:

- Earth remote sensing and space monitoring, including optical, quasi-optical, infrared and electromagnetic frequency ranges;
- Investigation of various types of radiation from the earth's atmosphere and deep space, in particular gamma radiation, electromagnetic radiation, radiation of re-reflections of the sun's rays, spacecraft;
- Studies of the state of magnetic and electric fields of the ionosphere, including fields caused by lightning discharges and non-stationary fluctuations of the atmosphere;
- Technological studies of materials and biological preparations on the effects of cosmic radiation;
- The use of cubesat technologies for organizing communication systems with ground objects, between spacecraft and the use of artificial intelligence systems to control the operation of a swarm of cubesats;
- The use of cubesats to collect large amounts of data on the organization and control of the movement of sea and river vessels, ground transport aircraft, including unmanned ones.

*makarov@cee.spbstu.ru, Corresponding author

doi:https://doi.org/10.52526/25792776-22.69.2-295

2. What is it a nanosatellite?

A nanosatellite is a smaller version of a spacecraft with all control and monitoring systems typical of large satellites. External configuration (see Fig. 1) consists of: temperature sensor, infrared sensor, MEMS triaxial accelerometer, MEMS three-axis gyroscope, MEMS triaxial magnetometer, radiation sensor, radiation recorder. Navigation equipment is based on GLONASS/GPS/BeiDou sensors. Solar panels based on GaInP/GaAs/Ge has efficiency approximate 32%.

The modular principle of building a nanosatellite makes it possible to form a scalable architecture based on a stack of printed circuit boards and modules. This approach provides fast, simple and reliable assembly of all subsystems of the nanosatellite and convenient and easy access to devices and systems installed inside the vehicle. Internal configuration of the nanosatellite is presented in Fig. 2.

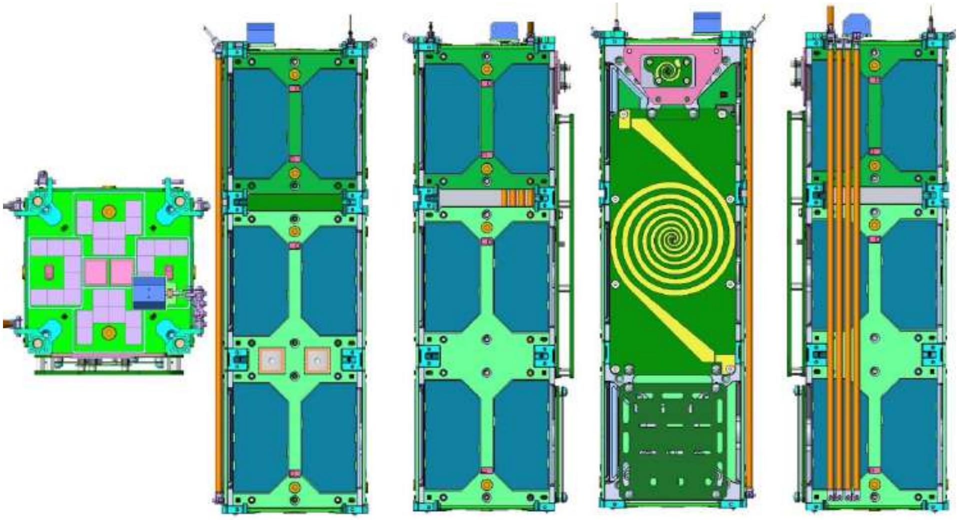

Figure 1. Appearance and content of the nanosatellite. The structure of the satellite in the sweep.

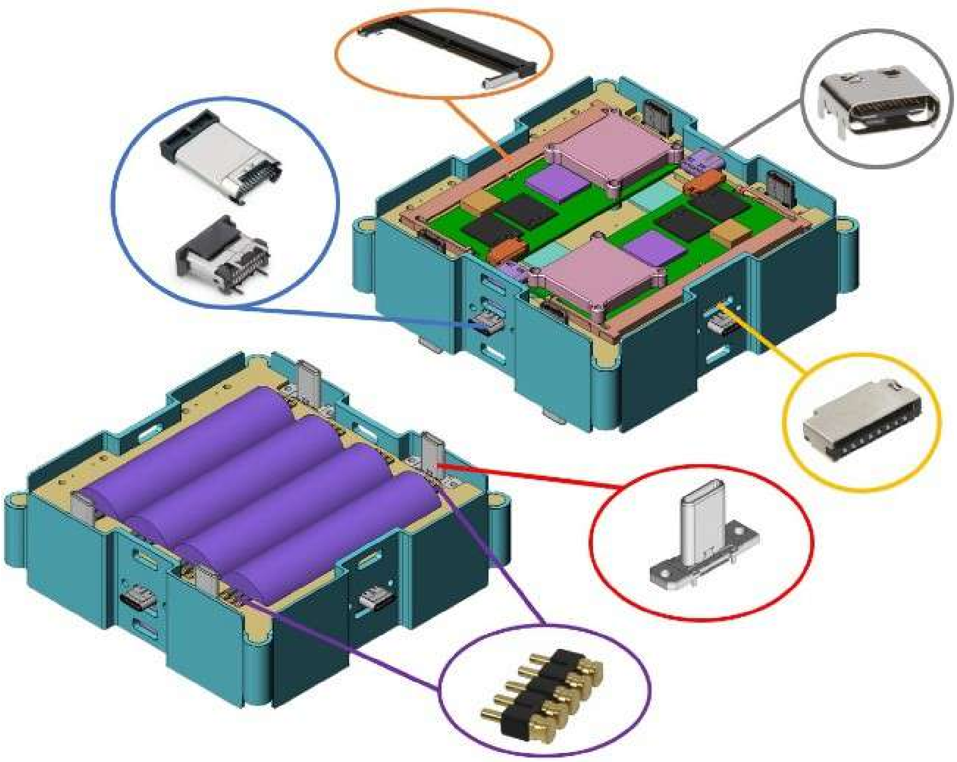

Figure 2. Internal configuration of the nanosatellite.

The modular principle of building a nanosatellite makes it possible to form a scalable architecture based on a stack of printed circuit boards and modules. This approach provides fast, simple and reliable assembly

doi:https://doi.org/10.52526/25792776-22.69.2-295

of all subsystems of the nanosatellite and convenient and easy access to devices and systems installed inside the vehicle.

The supporting frame provides reliable mechanical fixation of all subsystems of the satellite platform and the payload unit of the spacecraft, and also ensures reliable separation of the satellite from the launch container at the moment of launching into a given orbit. In addition, the frame is part of the nanosatellite's thermal regime control system.

The main part of the spacecraft is the microprocessor unit, which is the main control and management body of the satellite. The software is original and allows you to use telemetry channels to select certain satellite operation modes. The memory capacity of the microprocessor unit up to 128 GB allows you to store a large amount of data obtained in one turn of the device.

An important element of the satellite is the antenna-feeder devices. These devices provide reception of electromagnetic oscillations in a wide range of frequencies and allow this range to be divided into four parts. This provides a selective frequency response from several megahertz to units of gigahertz.

3. Control and signal reception

Reception and processing of various signals from various sources: analysis of the level of attenuation of known signals depending on the time of day, the state of the magnetic field, the ionosphere. When the spacecraft is put into orbit with the help of the Fregat upper stage, after the containment is dropped, the nanosatellite is taken out of the container. Each container contains four nanosatellites.

The main information reception center is located at the Peter the Great St. Petersburg Polytechnic University (see Fig. 3). The main channel for transmitting information is the telemetry channel. For this, a tracking antenna system is used.

Average span parameters of antenna: the average total visibility duration per day is 26.4 minutes. At the same time, this duration varies from 0.16 to 7.35 minutes, depending on the trajectory of the vehicle.

Figure 3. Control and signal reception center.

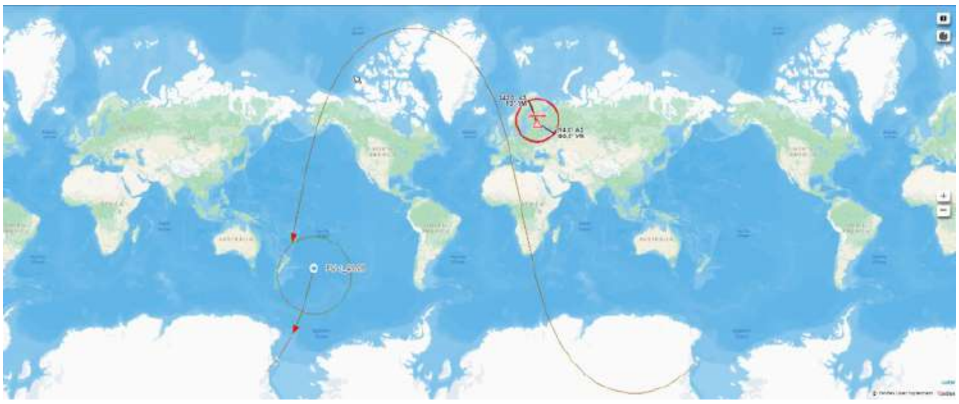

Figure 4. Data of trajectory measurements of the nanosatellite Polytech Universe 1.

It is important to note that access to the data server will be open to everyone for review and analysis of readings taken

doi:https://doi.org/10.52526/25792776-22.69.2-295

During the flight of vehicles along the trajectory (see Fig. 4) above the earth's surface, the values of the radiation power at a specific frequency are measured at certain time intervals. These results of measurements in time (points of reading information by a cubesat) are linked via the GLONASS/GPS system to a map of the earth. A set of points with geographic coordinates and radiation level data associated with them makes it possible to create a map of the distribution of electromagnetic radiation power on the earth's surface.

4. Summary

Peter the Great St. Petersburg Polytechnic University is one of the participants in the Russian educational project Space π. This is a project of the Planet Duty Program of the Innovation Assistance Fund, in which the winners of the Open Space competition of the Russian schoolchildren movement participate. The project is aimed at attracting schoolchildren to the field of science-intensive technologies related to space research. As part of the project, schoolchildren offer their own ideas for payloads for satellites, participate in their development, use data from satellites to implement their own projects. It is planned that within the framework of the project, by 2025, 100 domestic cubesats will rotate in the Earth's orbit.

Acknowledgements

This work was supported Ministry of Science and Higher Education of the Russian Federation (state assignment).

doi:https://doi.org/10.52526/25792776-22.69.2-295

Detectors for space electronics based on the quantum dots and wells

R.V. Ustimenko *[1], M.Ya. Vinnichenko †[1], H.A. Sarkisyan[2], D.B. Hayrapetyan[2], and E.M. Kazaryan[2]

[1]Peter the Great St. Petersburg Polytechnic University, Saint Petersburg, Russian Federation
[2]Russian-Armenian University, Yerevan, Armenia

Abstract

One of the promising areas of research applicable in astrophysics is the study of the properties of quantum dots (QDs) and quantum wells (QWs) in the IR region of the spectrum. The IR region of the spectrum contains a huge amount of astronomical information. Devices based on GaAs/AlGaAs QWs and Ge/Si QDs can serve as detectors and sources of IR radiation. In the current work, the photoluminescence, absorption, and transmission spectra of these nanoheterostructures were obtained in the near, mid, and far IR ranges using Fourier spectroscopy. Thus, the studied optical properties of QWs and QDs make it possible to use these structures in astrophysics as sources and detectors of IR radiation.

Keywords: *quantum wells, quantum dots, detectors, radiation sources, photoluminescence, absorption, transmission*

1. Introduction and samples

The study of the properties of quantum dots (QDs) and quantum wells (QWs) is one of the promising areas of research aimed at completely different applications: from electronics and astrophysicists to medicine and energetics. Study and creation of such structures and devices based on them is an important and urgent task.

The infrared (IR) region of the spectrum, covering wavelengths from 1 µm to 1 mm, contains a huge amount of astronomical information (Richards & McCreight (2005)). Infrared equipment measure the dominant radiative energy transfer mechanisms in the universe and provide understanding of formation and structure of planets, stars, galaxies and galaxy clusters, and measure the geometry, structure and content of the early universe.

Detectors and sources of far-IR radiation can be devices that use transitions of charge carriers between energy levels associated with shallow impurities in semiconductors. Far-IR radiation devices based on intracenter impurity transitions in doped quantum wells (QWs) are more attractive than devices based on bulk materials, since changing the nanostructure parameters can change the operating spectral range (Masselink et al. (1986)). In turn, acceptor-doped QWs have a number of advantages over n-type structures (Waugh & Dolling (1963)).

It is also possible to realize photodetectors or sources with optical pumping based on the properties of QDs associated with intraband transitions of charge carriers (Bimberg & Pohl (2011)). QD-based photodetectors have a number of advantages and features compared to the same QW detectors, for example: the ability to use the normal incidence of radiation, what contributes to the creation of matrix photodetectors (Rappaport et al. (2000)), high surface density, long lifetime of nonequilibrium charge carriers, compatibility with silicon electronics, which promotes the implementation of silicon-based integrated electronic devices (Krasilnik et al. (2011)).

*ratmirustimenko@yandex.ru, Corresponding author
†vinnimaks@mail.ru

doi:https://doi.org/10.52526/25792776-22.69.2-299

2. Experimental results

Our research was devoted to investigate the features of the photoluminescence, photoconductivity, and absorption spectra of GaAs/AlGaAs QWs doped with beryllium were studied, which are in good agreement with theoretical calculations of the energies of optical transitions of charge carriers in the structure. The ionization energy of acceptors in a QW was also experimentally determined in various ways, its value corresponds to the theoretical calculation of the energy spectrum of the investigated structure.

Similarly, during the research of the features of Ge/Si QDs, we obtained the spectra of equilibrium and photoinduced absorption and photoluminescence (PL), as well as the temperature dependence of photoinduced absorption. Several samples with different boron impurity concentrations were studied. Atomic force microscopy (AFM) photo of sample with QDs is presented in Fig. 1 on the left.

The PL spectra show two peaks, which are explained by direct and indirect interband transitions of charge carriers in QDs in real space (see Fig. 1 on the right). The peak associated with indirect transitions have a blue shift with increasing pump power, due to band bending at the Si/Ge heterointerface (see Fig. 2 on the left). As the temperature rises, a decrease in the PL intensity is observed. The peak associated with direct electron-hole recombination falls off a little faster due to the intense temperature depopulation of electronic states localized directly in the QD.

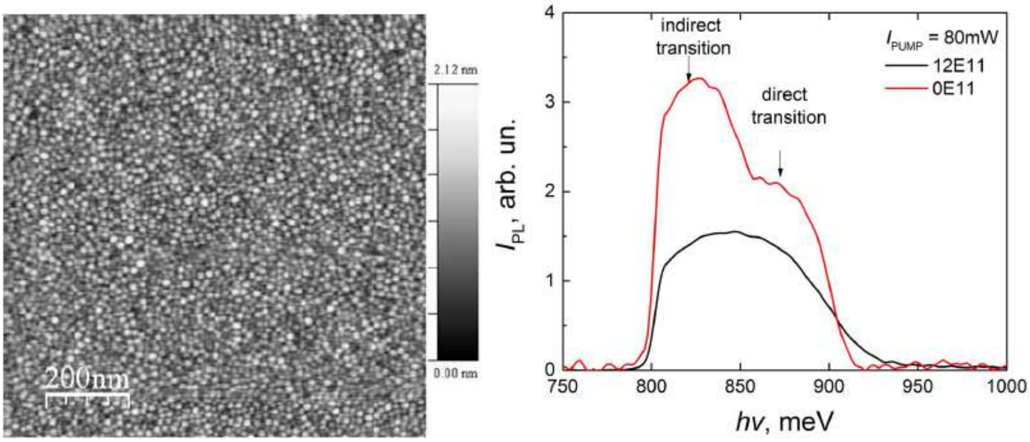

Figure 1. AFM image of Ge/Si QDs (on the left). PL spectra for different impurity concentration (on the right).

.

The spectra of photoinduced transmission at the same pump power and different impurity concentrations show peaks associated with transitions from the ground (a) and excited (c) states to the continuous spectrum, as well as intersublevel transitions (b). The intensity of peak "a" increases with an increase in the number of carriers in the ground sublevel of the valence band, so that peak "c" is lost (see Fig. 2. on the left).

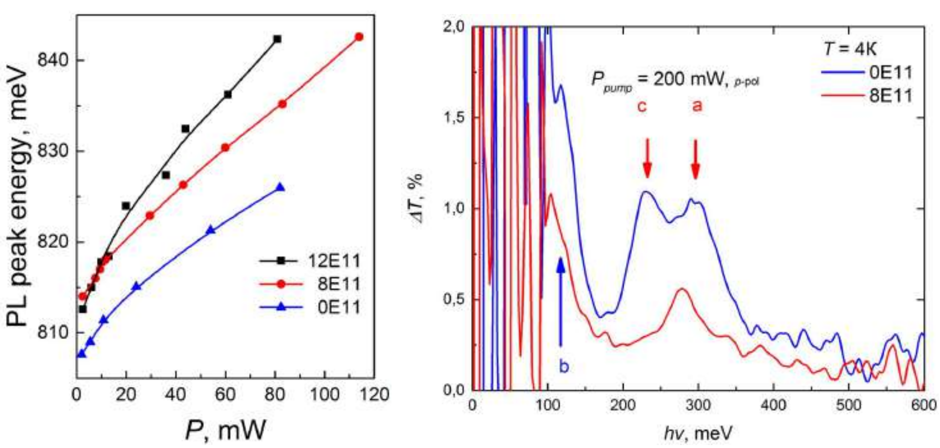

Figure 2. Dependence of the PL peak on the pump power (on the left). Photoinduced absorption spectra at the same pumping and different impurity concentration (on the right).

.

doi:https://doi.org/10.52526/25792776-22.69.2-299

3. Summary

Thus, in this work, we studied the optical properties of p-GaAs/AlGaAs QWs and Ge/Si QDs. The optical and electro-optical properties of acceptors in QWs have not been studied in detail yet due to the complex structure of the valence band and the energy spectrum of impurity states. In addition, such p-type nanostructures have prospects for development due to a number of advantages, as well as due to cheaper production and compactness compared to bulk materials and n-type. At the same time, QD structures have a wide range of applications. Devices based on Ge/Si QWs have a number of advantages over devices based on QDs. Moreover, the obtained spectra of photoinduced absorption in the far IR frequency range confirm the generalized Kohn theorem for QDs and require further study.

Acknowledgements

This work was supported by Ministry of Science and Higher Education of the Russian Federation (state assignment).

References

Bimberg D., Pohl U. W., 2011, Materials Today, 14, 388

Krasilnik Z. F., Novikov A. V., Lobanov D. N., et al. 2011, Semiconductor Science and Technology, 26, 014029

Masselink W. T., Chang Y. C., Morkoç H., et al. 1986, Solid-State Electronics, 29, 205

Rappaport N., Finkman E., Brunhes T., et al. 2000, Applied Physics Letters, 1, 3224–3226

Richards P. L., McCreight C. R., 2005, Physics Today, 58, 41

Waugh J. L. T., Dolling G., 1963, Physical Review, 132, 2410

doi:https://doi.org/10.52526/25792776-22.69.2-299

Communications of BAO, Vol. 69, Issue 2, 2022, pp. 302-307

Robotising Existing Astronomical Observatories

G. Tuparev * [1], H. R. Andreasyan, † [1,2], and Thomas M. Jackson[1]

[1]Tuparev AstroTech, Sofijski geroj 3, Sofia 1612, Bulgaria
[2]V. A. Ambartsumian Byurakan Astrophysical Observatory, National Academy of Sciences of Armenia

Abstract

Astronomical observatories can be operated either manually or remotely, but both of these options currently have many disadvantages. Manual observatories require real-time staffing by on-site astronomers and technicians, and observation time is often not used optimally. Remote observatories, on the other hand, often make it cumbersome or near-impossible to modify any observing schedules already fed into the system, making reacting to important events like gamma-ray bursts unrealistic. In addition, it is generally expected that the cheapest way to upgrade an ageing observatory is to simply build a new one, but this is not always the case. For many relatively modern observatories, it is possible to convert to a fully robotic mode of operation. In these proceedings, we describe a few straightforward ways to robotise an existing observatory and how to connect it to a network of other robotic observatories. We also discuss the use of inexpensive device controllers, the importance of emergency shut-down procedures, the introduction of local and network schedulers, and the implementation of fully automated observation planning. We finally also describe hardware and software solutions, including an example of how this is currently being applied.

Keywords: *observatories, robotics, front-end and back-end software systems*

1. Introduction

With the modern age of astronomy well underway, larger and more complex projects with significantly more extensive data sets are now commonplace. One area of astronomy which has profited from this expansion, driven by advancing electronics, engineering, and software, is the area of robotic astronomy. A robotic observatory is an observatory that can take observations by itself when given instructions or a schedule, and it can react by itself to changing observational, weather, or mechanical/electronic conditions without human intervention. This differs from manual or remote observatories which require observers to manually control or input the instructions or commands by hand, regardless of where they are located with respect to the observatory.

There are now multiple examples of robotic observatories — the MONET project (Bischoff et al., 2006, 2008, Hessman, 2001), the Zwicky Transient Facility (Bellm et al., 2019, Dekany et al., 2020), and the Las Cumbres Observatory project (Brown et al., 2013), just to name a few. Indeed, robotic observatories provide many advantages over remotely or manually operated observatories, such as lower costs for maintenance of the telescope, little or no need for an operator, and more efficient observations. They also reduce the travel needed to and from the observatory itself, have the ability to operate in conditions which would be impossible for a manual operator such as deep snow or extreme heat, and are accessible world-wide, making them very suitable for education or outreach projects.

Despite these advantages, there remains a relative lack of robotic observatories to date, driven by the common perception that it is cheaper and easier to build a new observatory when it could be more efficient and cost effective to renovate and robotise certain observatories. While some observatories may be too old to robotise (such as the Royal Observatory in Greenwich), mainly due to parts no longer being available, and some of the biggest systems may be too complex to robotise (such as the Very Large Telescope at Cerro Paranal), there are still many potential candidates currently out there. Here we show some of the steps needed and the considerations for robotising an observatory.

*gtupar@tuparev.com
†h.andreasyan@tuparev.com, Corresponding author

doi:https://doi.org/10.52526/25792776-22.69.2-302

2. Implementation

As a basis for robotising an observatory or telescope, two things are needed: A dedicated, multi-disciplinary team of astronomers, mechanical engineers and software developers, and knowledge of the observatory itself.

In order to gather this knowledge and experience, the team should extensively use the observatory in remote mode, gathering notes about the operating procedures and connecting these to possible automations. Examples of this procedure are noting and archiving weather conditions such as dew-point and rain conditions, the cabling of the de-rotator, the conditions under which auto-focusing is used, etc.

Once this experience has been developed, implementations can begin with the six steps outlined in this section and the left hand side of Figure 1, and with the three points in mind, which we dub as Tuparev's Three Laws of Robotelescopics, shown on the right hand side of Figure 1.

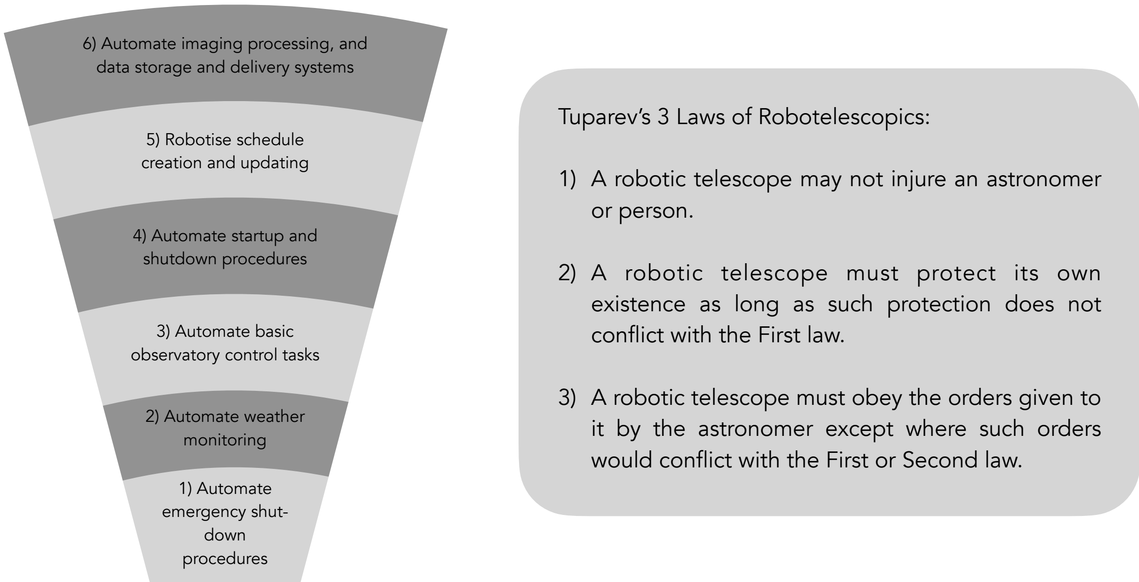

Figure 1. Left side: The 6 steps, presented here in a shell structure to reflect the software architecture, for robotising an observatory, which we outline in the following subsections. Right side: The 3 laws to keep in mind when designing the fundamentals for a robotic observatory.

2.1. Automation of the emergency shut-down procedures

The protection of the system is of relatively high priority according to the three points above, and is the first step we outline for robotising an observatory. If equipment is damaged, repair costs can be expensive or even render the observatory unsustainable. It follows that if the remote monitoring connection is lost in any way, which could potentially lead to a risk of damage to the equipment, the enclosure should close automatically. This includes loss of communication with vital systems such as weather stations or dome control.

In addition to automatic shutdown, to mitigate risks there are also other alternative fail-safes which can be implemented, such as making sure there is an emergency, uninterruptible power supply, that webcams are placed in all appropriate areas for monitoring, the automatic parking spot of the telescope is out of range of water damage if the dome does not close, or implementing passive or gravitational mechanisms for closing the dome.

doi:https://doi.org/10.52526/25792776-22.69.2-302

2.2. Automatic monitoring of the weather conditions

Second to the emergency shut-down procedures, the observatory's weather station, the monitoring it does and the communication it has with the control centre are all vital for a robotic observatory. The minimum weather parameters that should be monitored include rain, humidity, temperature, pressure (for dew-point calculations), dust, wind speed, and wind direction, as changes or the occurrence of any of these can at worst damage the telescope or at best severely reduce the observatory's performance.

These can be monitored via hardware such as cloud monitors on the dome with image analysis, online services, commercial weather sensors placed outside the dome, temperature sensors around the mirror etc. All of the information collected should be communicated to the central system, with limits set on operations dependent on the current weather conditions (e.g. a high risk of rain automatically shuts the dome, cloud to the eastern horizon means scheduled observations to the west are preferably weighted). It is also advisable to record these parameters for long-term records and observing logs.

2.3. Automating routine tasks

Following the placement of emergency procedures and weather monitoring, the automation of standard routines can be added. This focuses on the activation and control of most of the equipment via coded software routines. Basic functions include the steering of the mount, the activation of the camera, or the changing of filters in the filter wheel, which all need to be implemented for the observatory to function on the most basic level.

Once the basic activation and control functions are in place, more complex functions should be considered. Routines such as auto-focusing the camera or differentiating between taking calibration and science frames can be added to the software architecture, all of which are needed in some capacity for observations.

2.4. Startup and shutdown procedures

As a final step to automating the hardware, the startup and shutdown procedures of the observatory should be added.

Considerations for the startup mechanisms should include an initial check of weather conditions. As an example, there is no point opening the dome if it is raining or the sky is completely covered, and it should be checked again in a given time frame. This should be followed with a check of the operational status of all hardware, so the observatory is fully operational and risk-free before initiating standard startup procedures such as dome opening, cooling of the sensors and the taking of calibration images.

Frameworks should also be coded for shutdown procedures, in a somewhat reverse order, whereby final calibration images are taken, the telescope is parked and the enclosure is closed. Additional steps to consider for shutdown include getting a webcam confirmation that the shutdown mechanism has completed as an extra fail-safe before software-side tasks such as in Section 2.6 are initiated.

2.5. Robotic scheduling

Once the basic hardware procedures are automated, basic software functions can be automated too, including the scheduling which the robotic observatory will follow. Robotic schedules have a number of different parameters to account for and must contain two layers.

The initial layer of the schedule should account for a number of different target parameters, including the angular distance of the target to the zenith at any single time, the expected signal-to-noise of the target, the exposure time needed for the target, and the angular distance of each target from the previous and subsequent observations. In addition to the target constraints, there are also constraints such as sky conditions to account for, such as the moon phase and location in the sky at any one time. All of these factors should have weights and then constraint optimization algorithms applied to optimise the initial observing schedule.

Once the initial schedule is created, on-site constraints mean a secondary layer must be applied: Sky conditions such as cloud cover and distribution, or rain may hinder observations of certain targets or time slots, and rapid follow-up observations may have to be accounted for. This means constant updating of the schedule must be established to feed in unscheduled priority targets, or to re-optimise the initial schedule.

Observation scheduling must consider not just nightly observations but those over periods of weeks or months as well. To account for this, frameworks for daily feedback and logging to re-optimise schedules

doi:https://doi.org/10.52526/25792776-22.69.2-302

for subsequent nights, as well as networks of interconnected robotic telescopes are preferable for a fully optimised system.

2.6. The imaging pipeline

Once observations are taken from the optimised schedule and are readily available, automating the data analysis of the data is preferable to manual reduction for time and efficiency purposes. As robotic observatories work, on average, more efficiently than manual or remote observatories, more data is collected. This means efficient pipelines have to be created.

The basic steps should be preferably carried out on-site, as this reduces the amount of data that needs to be transferred over the network and makes archival side operations easier due to that lower volume. Such on-site processes may include deciding on the calibration images, running data reduction processes, calculating and integrating time and coordinates systems into the data, and compressing FITS files. Similarly, science analysis pipelines may also be included on-site, such as photometric measurements, line finding algorithms for spectroscopic data, or streak and transient detection.

Further steps to account for include making sure there is enough local storage space for a given amount of time (e.g. a week, month or year), so that the observatory can operate by itself for a given time frame without the need for human intervention or automatic transferring of the data to a hosting centre. These steps also need to be supported by a priority framework, whereby important event logs or important image or spectroscopic data has priority of being handled and distributed to central servers or alert services before lower priority data. Finally automatic removal of older data also needs to be implemented to avoid the discarding of new observations due to a lack of storage space.

3. Hardware requirements and configurations

We turn our attention now to the hardware needed for a robotic observatory. At it's core, a robotic observatory should contain the same equipment as a manual observatory; a dome, a mount, a telescope, an instrument such as a camera or spectrograph, a weather station, and a control computer. An external server, which can easily be located offsite, for implementing some of the automatic steps and storage is desirable, as well as a separate computing unit for analysis, especially if large amounts of data are expected to be produced so that the amount of data being transferred is reduced.

Every sensor or device should also be connected to the central control computer or server by micro-controller (a raspberry pi, for example) and be accessible on the LAN. This enables all stations to constantly send messages or "pings" confirming they are operational and, if a system malfunctions, allows for the automatic starting of emergency shut-down procedures and sends a warning message or notification to the maintenance staff astronomers. This combined system results in an ecosystem quite similar to the diagram presented in Figure 2.

4. Software architecture

In order to achieve a robust and maintainable software system, a multi-layered approach is strongly recommended. The lowest software level should connect all sensors (weather, temperature sensors associated with the enclosure and the telescope, etc.), peripheral devices (screen, webcams, etc.) with the dome, the UPS, and the internet router. Every component should periodically send an availability signal. In the case that such a signal is not received, the emergency shutdown procedure should be triggered.

Another very important task of the low-level software is logging. The observatory log should always be complete and easily searchable. The development of visual debugging tools to enable the monitoring of the messages sent between components is strongly recommended.

Higher level software should include real-time schedulers, long-term observation observatory schedulers, and optional modules that allow the automatic upload of processed images to a hosting site and communication with external network schedulers in order to negotiate the exchange of observations with other telescopes or to receive requests for high-priority observation requests (e.g. GRB observations). For more detailed information see Allan et al. (2006), Hessman et al. (2004), Tuparev et al. (2006).

The role of the real-time scheduler is to decide what observation should be scheduled next depending on the constantly changing environment and observation conditions, while the long-term scheduler should

doi:https://doi.org/10.52526/25792776-22.69.2-302

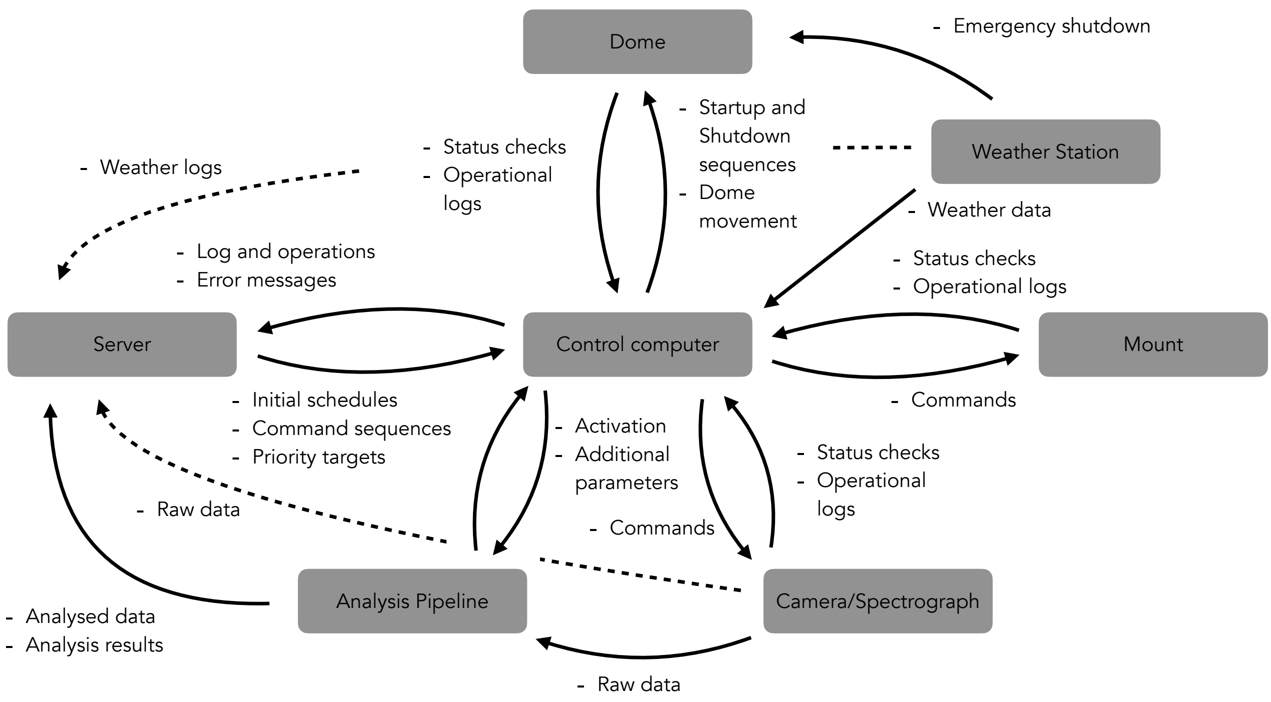

Figure 2. A diagram of the minimal hardware components and a simplified/minimal structure of the relations between each component and the operations that may be exchanged between each one.

create the observation planning for at least a few days in advance, taking into account weather condition forecasts as well as the nature of the scheduled observations and the corresponding science projects (e.g. spectroscopic observations could be avoided when the moon is visible, time-constrained observations, etc.).

5. Summary

In this work, we firstly outline the advantages of robotising existing observatories, namely that they are more efficient in observations, have significantly lower maintenance and running costs, and can generally operate in a wider range of conditions than manual or remote observatories.

We also outline the necessary steps needed to robotise an observatory given in the 6 steps outlined in Section 2, and an overview of what considerations are needed. We also present some of the relevant hardware components and considerations in Section 3 and software considerations in Section 4.

We add a final message that anyone considering robotising an observatory should a) consider the option of new equipment first, b) start slowly and take the process step-by-step, c) automate emergency procedures, d) carefully follow the six automation steps outlined here, and e) carefully architecture their software. We finally wish to state that we are happy to help and advise any organisations or individuals robotising their systems, or to provide entire robotising or archival systems services from our team.

Acknowledgements

The authors would like to thank Dr. Frederic Hessman, who discussed many of the ideas outlined here.

References

Allan A., et al., 2006, Astronomische Nachrichten, 327, 744

Bellm E. C., et al., 2019, Publ. Astron. Soc. Pac. , 131, 018002

Bischoff K., Tuparev G., Hessman F. V., Nikolova I., 2006, in Silva D. R., Doxsey R. E., eds, Society of Photo-Optical Instrumentation Engineers (SPIE) Conference Series Vol. 6270, Society of Photo-Optical Instrumentation Engineers (SPIE) Conference Series. p. 62701Q, doi:10.1117/12.671433

Bischoff K., Hessman F. V., Tuparev G., Atanasova E., Pessev P., 2008, in Stepp L. M., Gilmozzi R., eds, Society of Photo-Optical Instrumentation Engineers (SPIE) Conference Series Vol. 7012, Ground-based and Airborne Telescopes II. p. 70122X, doi:10.1117/12.788920

doi:https://doi.org/10.52526/25792776-22.69.2-302

Brown T. M., et al., 2013, Publ. Astron. Soc. Pac. , 125, 1031

Dekany R., et al., 2020, Publ. Astron. Soc. Pac. , 132, 038001

Hessman F. V., 2001, in Paczynski B., Chen W.-P., Lemme C., eds, Astronomical Society of the Pacific Conference Series Vol. 246, IAU Colloq. 183: Small Telescope Astronomy on Global Scales. p. 13

Hessman F. V., Pennypacker C. R., Romero-Colmenero E., Tuparev G., 2004, in Lewis H., Raffi G., eds, Society of Photo-Optical Instrumentation Engineers (SPIE) Conference Series Vol. 5496, Advanced Software, Control, and Communication Systems for Astronomy. pp 290–301, doi:10.1117/12.547429

Tuparev G., Nicolova I., Zlatanov B., Mihova D., Popova I., Hessman F. V., 2006, Astronomische Nachrichten, 327, 771

Communications of BAO, Vol. 69, Issue 2, 2022, pp. 308-314

New concept of ground based-space radio interferometer and modern technologies application for deployment simulation of precise petal space reflector

V.I. Bujakas and M.D. Glotov *

P.N. Lebedev Physical Institute of the Russian Academy of Sciences, Moscow, Russian Federation

Abstract

Radio interferometers make it possible to achieve high resolution of astronomical observations due to the large base of the measuring instrument. The ground-space radio telescope RadioAstron holds the record for angular resolution among radio interferometers, its maximum base was about 340 000. km. The project turned out to be very successful. The new concept is based on the experience of the RadioAstron project and proposes the use of several orbiting radio telescopes that work together in the cm and mm spectral regions. This will further increase the base of the radio interferometer and expand the viewing angle at each current moment of time. Modern technical means make it possible to launch into orbit several identical mirrors operating in the short-wavelength region of the spectrum with an effective area no worse than the effective area of the RadioAstron antenna at a wavelength of 1.35 cm. Thus, the project can be quite budgetary. Now 3D modeling and 3D printing technologies make it possible to speed up and simplify the development of physical models. The manufacture of complex parts used to take days of work. Now we can use 3D printing to make different parts in a matter of hours. In the physical model of a new petal mirror project, we used FDM and LCD printing technologies. The paper discusses examples of manufacturing petal mirror physical model components, limitations and features of these technologies.

Keywords: *ground-space radio interferometer, petal mirror, 3D printing*

1. Introduction

A new concept of ground based-space radio interferometer is proposed and discussed. The concept is based on the idea of using several small telescopes in the space arm of the radio interferometer. The problem of creating a precise space reflector for radio astronomy is considered. Previously, we proposed a new design of an accurate solid petal reflector (Bujakas (2021)). Here, the technologies used in the deployment simulation of the proposed mirror are described.

2. New concept of ground based-space radio interferometer

Advanced projects of ground based -space radio interferometers involve the creation in orbit large precise deployable reflectors. The creation of such mirrors is a complicated and expensive scientific and technical problem. It seems reasonable to consider an alternative way to create a new generation instrument. Instead of one large mirror, put into orbit a set of small precision telescopes and form a ground-space radio interferometric network based on them. The proposal is based on the results of the work of the Radioastron project telescope (Kardashev & et al. (2013)), which demonstrated the possibility of obtaining a record angular resolution using a mirror with a very low AE. This concept is illustrated in 1, 2.

*maxglotov1998@yandex.ru, Corresponding author

doi:https://doi.org/10.52526/25792776-22.69.2-308

Figure 1. Antenna array of the New Mexico Observatory.

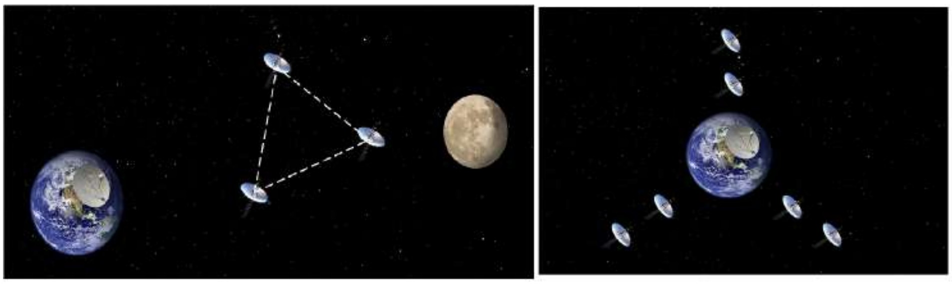

Figure 2. Variants of the ground-to-space antenna array using precise small antennas in space arm of the interferometer.

3. Modern technologies application for deployment simulation of precise petal space reflector

3.1. New petal type reflector

To create the next generation of large space telescopes operating in the short-wavelength area of the spectrum, it is necessary to deploy large high-precision mirrors in orbit. Early we proposed (Bujakas (2021)) a new deployable reflector designed to operate in the cm and mm ranges. A physical model of one of the design options is shown in 3.

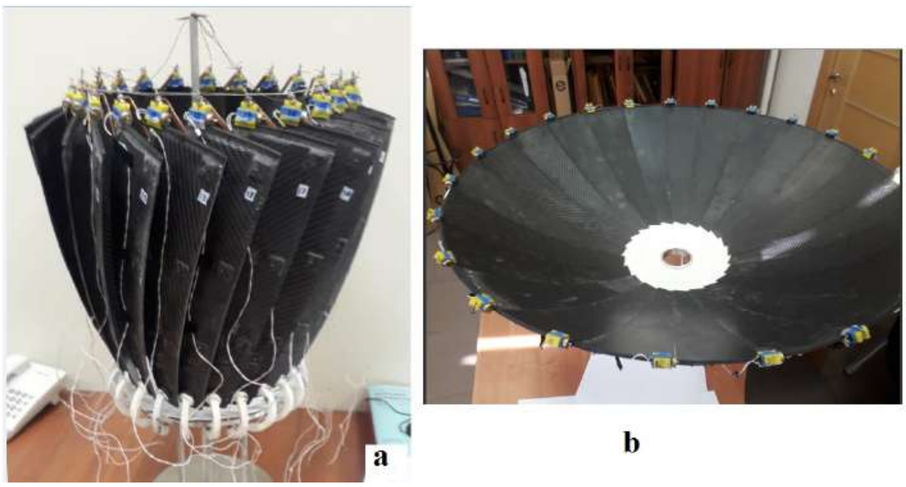

Figure 3. Physical model of a new petal reflector. a- a mirror in the folded state, b - an open mirror.

The new technical solution is based on the classic petal mirror of the Dornier Corporation (Dornier (1987)), the stages of opening of which are shown in 4. The classic design includes a central mirror and a set of petals. Each petal is connected to the base of the central mirror by a cylindrical hinge.

doi:https://doi.org/10.52526/25792776-22.69.2-308

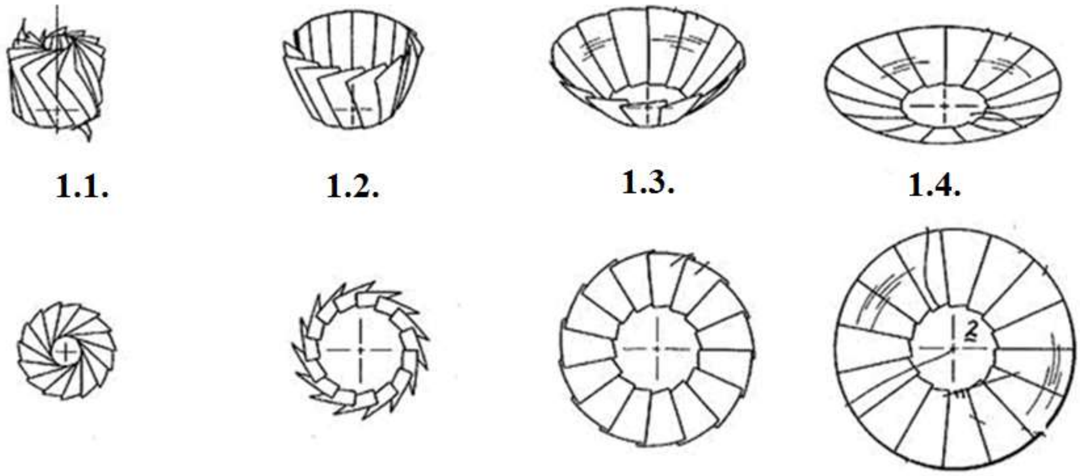

Figure 4. Deployment stages of Dornier corporation reflector.

Each petal is connected to the base of the central mirror by a cylindrical hinge. It is proved (Westphal (1990)) that there are such directions of the axes of cylindrical hinges, in which the synchronous rotation of the petals transfers the petal reflector from the folded position to the open state without engagement. Later, a modified version of the classical design was used in the RadioAstron project to create a 10-meter antenna for a space radio telescope (Kardashev & et al. (2013)). Possessing a number of advantages (compact folding, simple synchronous deployment, etc.), a classic mirror has one significant drawback. Small errors at the final stage of deployment and small errors in the installation of the axes of the cylindrical hinges connecting the petals with the central mirror lead to a significant deviation of the shape of the surface of the opened mirror along the outer edge of the petals. The latter leads to a significant loss in the quality of the open antenna. Due to an error in the deployment system, the antenna efficiency factor (AE) of the RadioAstron radio telescope in orbit (Westphal (1990)) turned out to be low (AE=0.1).

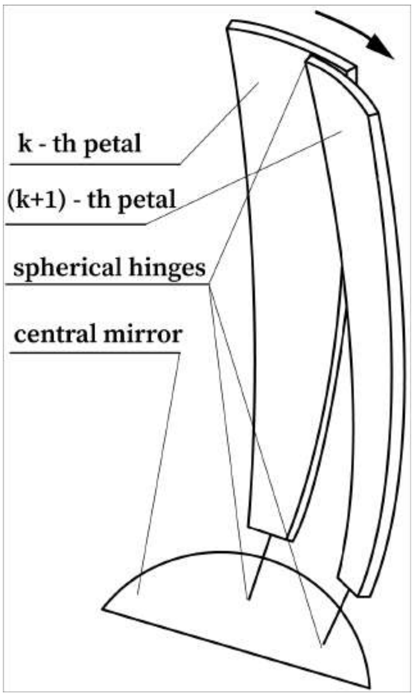

Figure 5. The kinematics of new deployment system. The left vertex of the (k + 1)-th petal is connected with the edge of the k-th petal and moves during the deployment along the edge by the actuator.

To eliminate the named shortcoming, the mirror opening scheme has been changed in the new design: the left vertex of each petal is aligned with the upper edge of the adjacent petal, the deployment is carried out by synchronous movement of the vertices along the edges (5, 6 c).

doi:https://doi.org/10.52526/25792776-22.69.2-308

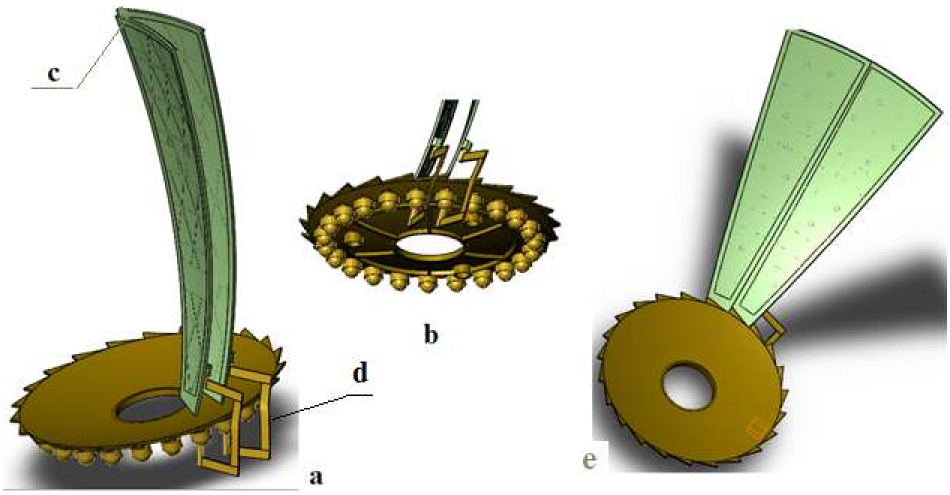

Figure 6. New design of the petal reflector. Central mirror, petals, brackets and spherical hinges. a. Petals in transport position. b. Spherical hinges on the back side of the central mirror. c. A spherical hinge connecting the vertex of one petal to the edge of an adjacent petal. d. The bracket connecting the petal with the central mirror, the bracket is rigidly connected to the petal. e. Petals in opened position.

3.2. Computer simulation

To test the proposed technical solution, a computer model of a new transformable structure was built and its research was carried out. Computer simulation was carried out in the SolidWorks package (Bujakas & Glotov (2022)). Virtual models of structural elements (petals and a central mirror) and an assembly of deployable mirror were built. The assembly includes a system of joints that guarantee statistical determinability (stress free) and geometric invariability of the structure at each moment of deployment (7, 8).

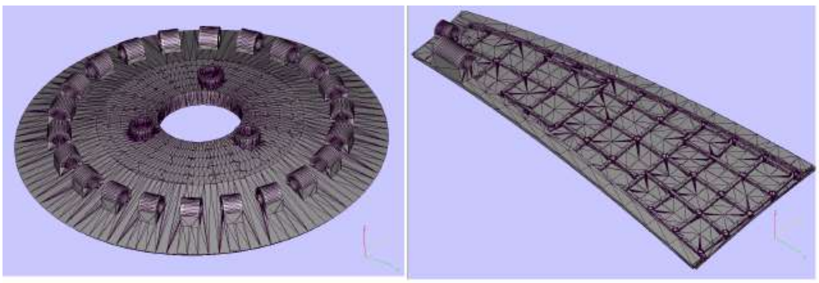

Figure 7. Virtual models of the central mirror and the petal.

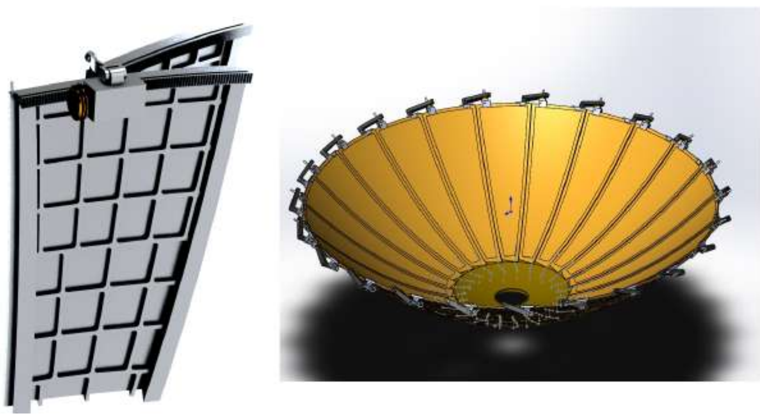

Figure 8. Virtual models of the deployment unit and assembly of petal reflector.

Computer simulation confirmed the feasibility of the proposed deployment kinematics.

doi:https://doi.org/10.52526/25792776-22.69.2-308

3.3. Physical simulation

The physical model of a transformable petal reflector is a complex structure consisting of a variety of elements and includes: a central mirror, petals, actuators, spherical hinges, gearboxes, rods of complex shap. The manufacture of structural elements required the involvement of various technologies. **Central mirror** is made of ABC plastic on CNC (9). The working surface of the mirror repeats the shape of the reference parabolic, on the reverse side, to facilitate the design and maintain rigidity, CNC milling made stiffeners.

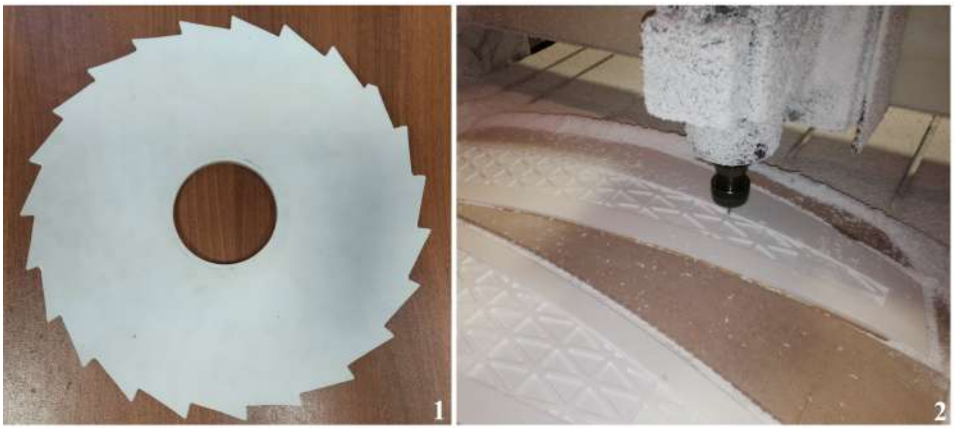

Figure 9. 1 - Central mirror of the composite parabolic reflector, 2 - Manufacturing of stiffeners of the parabolic element of the composite mirror on CNC.

Petals. The following technologies were successively tested for petals fabrication.

Figure 10. Various technologies for petals of a parabolic reflector fabrication.

Carbon fiber technology (10.1, 10.2), CNC milling technology (10.3), 3D printing technology (10.4), mold casting (10.5). The final selection was made using carbon fiber petals that met the specifications for stiffness, strength and weight.

doi:https://doi.org/10.52526/25792776-22.69.2-308

Spherical hinges. The design includes a significant number of spherical hinges that connect adjacent petals and each petal with a central mirror.

Figure 11. Spherical hinge.

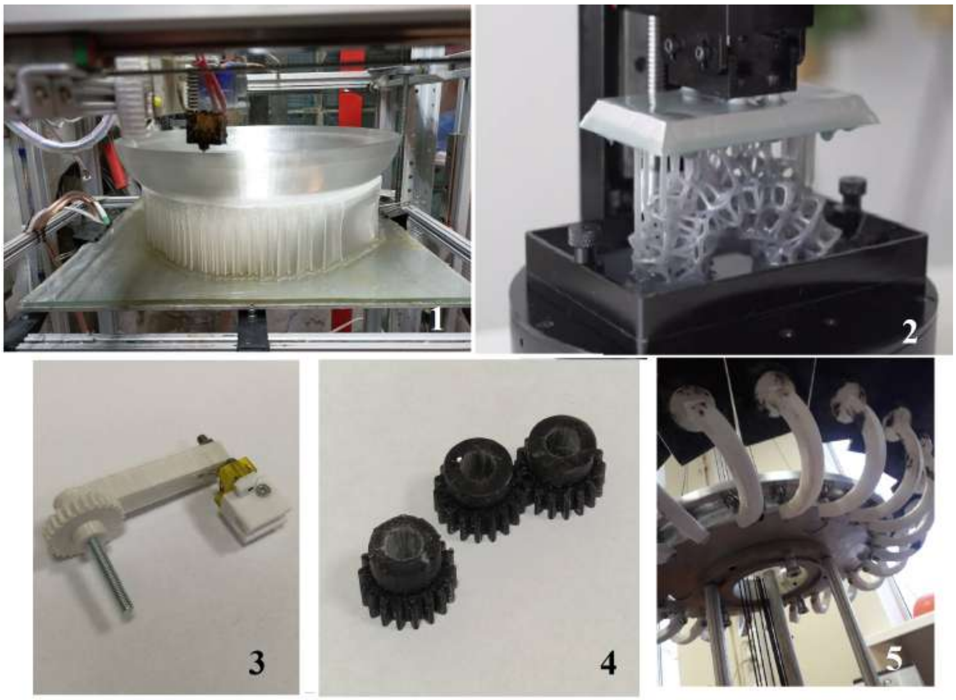

Figure 12. 3D printing technologies in physical simulation of petal reflector deployment.

Assembly of physical model on a parabolic template.

Figure 13. Assembly of a petal mirror on a parabolic template. 1 - petals, 2 - curvilinear rod connecting the petal with the base of the central mirror 3 - the base of the central mirror.

4. Conclusion

Ground-space radio interferometers with several telescopes in the space arm will significantly expand the possibilities of observational astronomy.

Modern technologies, in particular 3D printing technologies, can significantly speed up the development of physical models, perform complex details with simple means.

References

Bujakas V. I., 2021, Bulletin of the Lebedev Physics Institute, 48, 76 –78

Bujakas V. I., Glotov M. D., 2022, Proceedings of science, 425

Dornier 1987, FIRST Technology Study. Final Report RP-FA-D003

Kardashev N. S., et al. 2013, Astronomy Reports, 57(3), 153

Westphal M., 1990, US Patent 4899167.

doi:https://doi.org/10.52526/25792776-22.69.2-308

Application of radio wave reflections from meteor showers falling into the near-Earth space for organizing communications in the subpolar regions of the Earth

S.V. Zavjalov[1], S.B. Makarov *[1], I. Lavrenyuk[1], A.K. Aharonyan[2], and V.H. Avetisyan[2]

[1]Peter the Great St. Petersburg Polytechnic University, St. Petersburg, Russia
[2]Russian-Armenian University, Erevan, Armenia

Abstract

In this article we consider the possibilities of using organization of meteor-burst communication system in the subpolar regions of the Earth. Orthogonal frequency-division multiplexing (OFDM) signals as a general form of multi-frequency signals with amplitude limitation were applied. Optimal values of Peak-to-average power ratio (PAPR) reduction were found.

Keywords: *meteors, OFDM, multi-frequency signals, meteor trails*

1. Introduction

Meteors constantly fly into the Earth's atmosphere. Meteors burn up and meteor trails form in the upper atmosphere. Therefore, the meteor trail is an ionized region with a high initial linear electron density (see fig.1 on the left). There are uncompacted and overcompacted meteor trails, depending on the initial linear electron density. When a radio wave falls on a meteor trail, a mirror reflection occurs. We can use meteor trail to create communication system in polar regions.

The amplitude of the radio signal at the receiving point changes in time according to an exponential law when reflecting an uncompacted meteor trail (see fig.1 on the right). The lifetime of such a channel is on average 0.2÷0.5 s. The lifetime of a supersaturated meteor trail is already up to 10 seconds. In this case, multipath propagation of the reflected signal can be observed, leading to its deep fading at the receiving point, which does not allow analytically predicting changes in the value of the received signal over time. It follows from the practice of meteor communications that the transmission of information can be provided at a distance of up to 2000 kilometers.

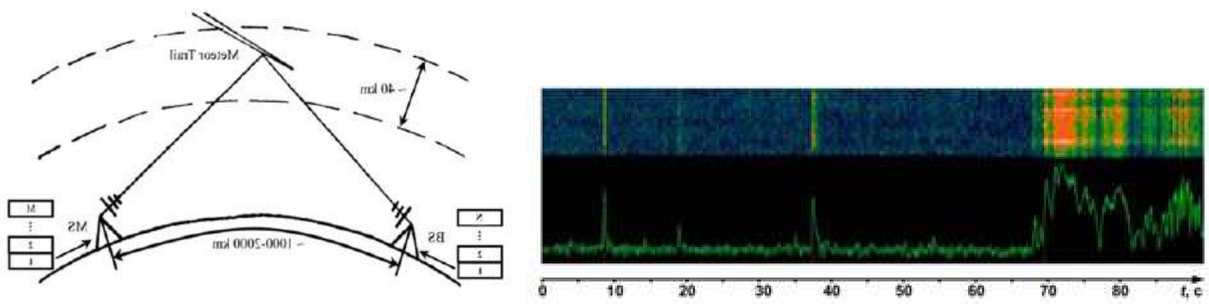

Figure 1. Meteor trails.

*makarov@cee.spbstu.ru, Corresponding author

doi:https://doi.org/10.52526/25792776-22.69.2-315

2. Formation and reception of signals.

In this project, we propose to use multi-frequency signals for organizing communications in the subpolar regions of the Earth. We consider Orthogonal frequency-division multiplexing (OFDM) signals as a general form of multi-frequency signals. Simulation model for formation and reception of OFDM signals and corresponding amplitude limiter are shown on fig. 2.

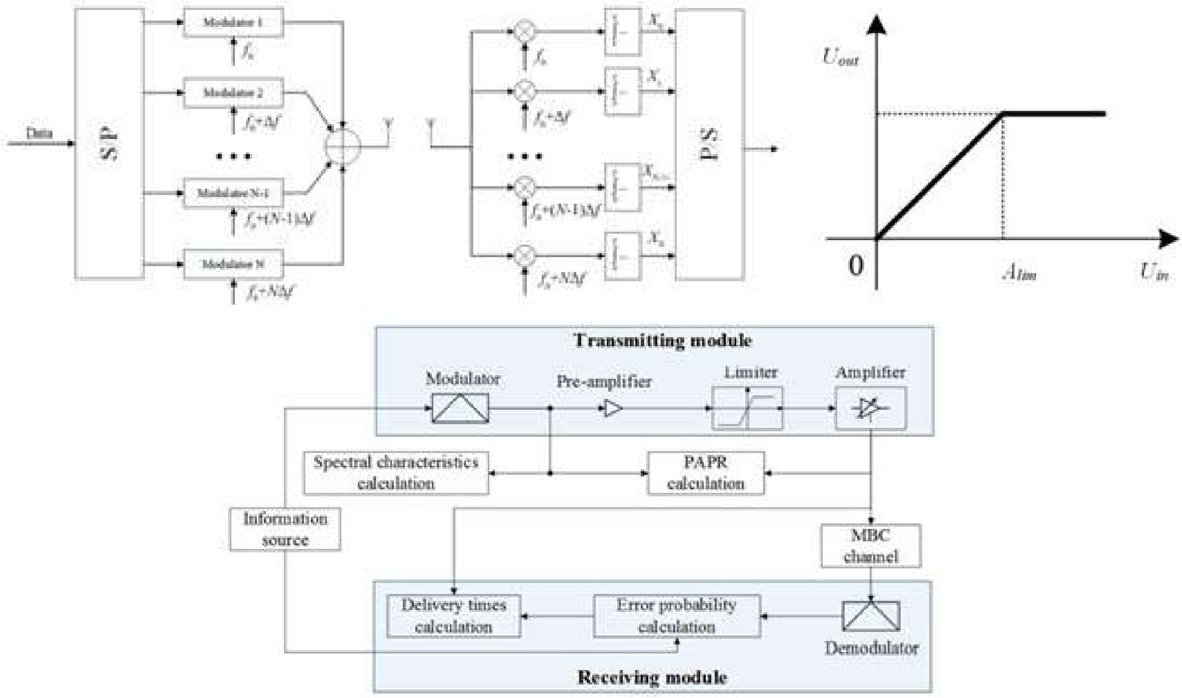

Figure 2. Formation and reception of OFDM signals (on the left), Characteristic of the limiter (on the right), Simulation model (on the bottom).

Parameters of simulation model: the number of frequency subcarriers of the OFDM signal is selected equal to 8; duration of one OFDM symbol equal to 0.1 ms; number of symbols in one packet: 100, 200, 300; duration of the package 0.01, 0.02 or 0.03 s; modulation scheme: quadrature phase shift keying (QPSK); sampling frequency $F_s = 10$ MHz.

The ratio of the Peak-to-average power ratio (PAPR) of the received signal at the output of the modulator (PAPR_{orig}) to the PAPR of the signal received at the output of the power amplifier (PAPR_{red}) is defined as the value of PAPR reduction (PR):

$$\text{PR} = \text{PAPR}_{orig}(\text{dB}) - \text{PAPR}_{red}(\text{dB}).$$

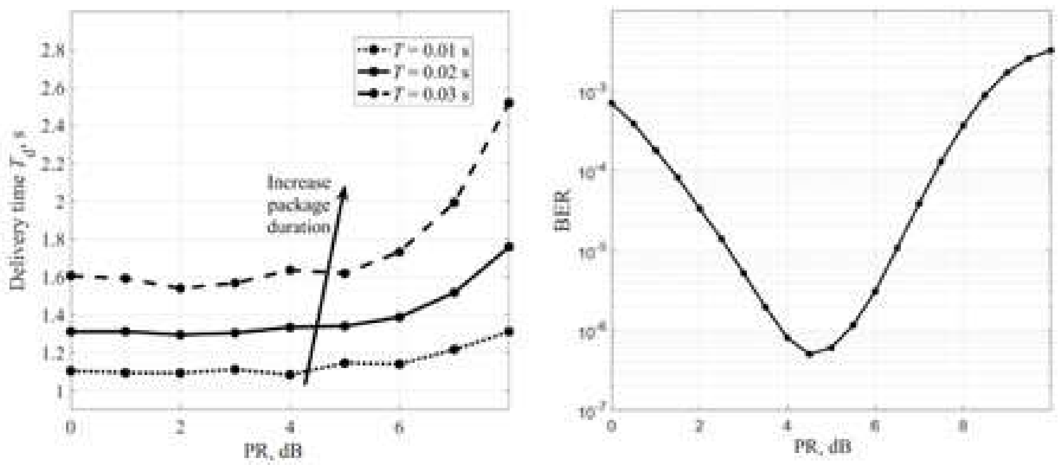

Figure 3. Dependence of delivery time on the level of PR.

doi:https://doi.org/10.52526/25792776-22.69.2-315

Fig. 3 on the left shows the dependence of the delivery time on the level of the PR values for various values of the packet duration T. We can conclude that with a decrease in PAPR by 5 dB, the delivery time is almost the same for OFDM signals.

In the considered scheme of the transmitting module there is both a limiter and an amplifier (see fig. 3). When limiting the value of the PAPR, the average power of the emitted oscillations increases, which reduces the error probability value for fixed signal-to-noise ratio values. However, with a further increase in the level of limitation, the signals from neighboring subcarrier frequencies start mutually affecting each other, which ultimately leads to an increase in the probability of error.

3. Conclusion.

The features of the organization of meteor radio communication systems are shown, the possibilities of application are considered.

The possibilities of using multi-frequency signals for the organization of meteor-burst communication are demonstrated.

Acknowledgements

This work was supported Ministry of Science and Higher Education of the Russian Federation (state assignment).

Communications of BAO, Vol. 69, Issue 2, 2022, pp. 318-323

A Modern Space Situational Awareness System

Thomas M. Jackson *[1], H. Holland †[1], G. Tuparev[1], M. Steinbatz[2], W. Promper[2], D. Weinzinger[2], and E. Doeberl[2]

[1]Tuparev AstroTech, 14 Paskal Todorov Str., Sofia 1618, Bulgaria
[2]Astro Systeme Austria, Galgenau 19, 4212 Neumarkt im Mühlkreis, Austria

Abstract

We, Tuparev AstroTech in partnership with Astro Syteme Austria, present a next-generation Space Situational Awareness (SSA) system currently being created for the tracking and characterisation of satellites and space debris in the age of big-data astronomy. Our SSA system will be based on the image processing of white-light images to detect streaks produced by satellites and space debris. These images will be obtained by a network of 20-30 custom and in-house built SSA observatory stations, which will be made operational worldwide over the coming decade. The system will use machine learning algorithms to choose the optimal part of the sky to observe at any given moment, analyse the incoming data on-site and in real-time, and deliver various standardised data packages and science-quality images to be stored on a bespoke central archive capable of storing petabytes of data. With this system, we aim to cover a greater geographical and celestial area than any previous SSA system, to create a scalable system that is both fast and efficient, and to enable access to orders of magnitude more storage capacity and information than any other system currently available, commercial or governmental.

Keywords: *Space Situational Awareness, Space Debris, All-Sky Survey, Telescope Networks, Data Archives*

1. The Current State of Space Situational Awareness

Over the next decade, more satellites are expected to be launched into Earth orbit than have been launched since Sputnik-1 in 1959. Of the current satellites in orbit, 28 percent are no longer operational (ESA, 2021), in addition to significant amounts of "space debris" (pieces from satellites which have exploded or collided). Altogether, there are ∼36500 known, uncontrolled objects with sizes greater than 10cm in orbit, with around 1 million and 130 million known pieces between 1-10cm and 1mm-1cm respectively. These pieces can collide with other objects, potentially leading to thousands more pieces of space debris being generated (e.g. Watson et al., 2021) or satellites being destroyed. This can cause a chain reaction of collisions, resulting in an exponential growth of space debris known as Kessler Syndrome (Kessler & Cour-Palais, 1978). A worst-case scenario could render the orbital space around the Earth as unusable, depriving humankind of vital services.

The detection, tracking and orbital modelling of objects, so that active satellites can be manoeuvred away from collisions, is commonly known as Space Situational Awareness (SSA). There are a number of organisations carrying out such work, both governmental and commercial, using a number of techniques in their SSA systems, all with specific advantages or disadvantages. Systems using Radar (see e.g. Apa et al., 2021, Murray et al., 2021) or Laser Ranging (e.g. Steindorfer et al., 2017, 2021) to track space debris achieve high precision in the tracking of known objects, but they are not optimal for discovering new objects. Additionally, some networks lack homogeneity and/or full geographic coverage, both of which are key to maximising the effectiveness of a system.

In the search for new objects, some organisations have turned to optical systems (e.g. Jilete et al., 2019, Park et al., 2017, Woods et al., 2012, Zhang et al., 2018), surveying the night sky using imaging data. In these images, moving satellites appear as streaks in the field of view against stars and galaxies, which are then processed using a number of techniques in order to calculate positions and orbits of satellites and space debris, including segmentation (e.g. Virtanen et al., 2016), image shifting and stacking (e.g. Yanagisawa

*tmjackson@tuparev.com
†hunterholland@tuparev.com, Corresponding author

doi:https://doi.org/10.52526/25792776-22.69.2-318

et al., 2005), filter matching (e.g. Cvrcek & Radim, 2021, Schildknecht et al., 2015), or transforms (e.g. Hickson, 2018, Nir et al., 2018). These techniques, however, may vary in their accuracy, the type of objects they are optimised for or can be quite computationally expensive and/or complex.

The ideal SSA system for discovering new space debris in the modern age therefore requires a number of characteristics: i) extensive geographical coverage, ii) effective and easy installation of the optical systems, iii) optimised algorithms for both observation scheduling and image analysis, and iv) efficient and extensive storage facilities and distribution methods. These are aspects we, Tuparev AstroTech and Astro Systeme Austria, aim to address in our new SSA system currently under construction.

2. SSA Stations

2.1. Test observatory

Our SSA test observatory is located near the village of Sandl, Austria, at an altitude of 880 metres above sea level. The observatory consists of a classical dome, ASA H400 telescope on an ASA direct drive mount, a Moravian C3-61000 CMOS camera, a weather station, a Windows control computer, and Mac Mini processing computer. The ASA H400 is a 40cm Newtonian telescope, with an f2.4 focal ratio, allowing for a wide field of view. The ASA mount can slew at speeds of up to 50 degrees a second, has a pointing accuracy of a few arcseconds, and sub-arcsecond tracking accuracy, ideal for both tracking and surveying SSA objects. The CMOS camera has 61 Mexapixels, a 2.15 degree by 1.43 degree field of view, a 0.807 arcsec pixel scale, relatively low dark current and read out noise, and can take immediate subsequent exposures.

The Windows control computer uses custom ASA software to control all equipment, including mount steering and camera control, with the entire system currently being robotised to enable fully automated observations and emergency shut-down procedures. Each device at the observatory is connected to—and is in constant communication with—the central system. In scenarios where one device is broken, or factors are present which could damage the systems (e.g. high winds or rainfall), the system automatically shuts down safely. These are all features which will be integrated into the fully deployable stations.

2.2. Rapidly deployable SSA stations

As classical observatories can take many months or years to plan, build, and bring into operation, we intend to use a new, custom designed system for rapid deployment. This in-house and purpose-built SSA station will take the core capabilities of our test observatory and package them up in such a way as to minimize the construction and installation times, all while decreasing overall cost.

Figure 1. An example of the envisioned, rapidly deployable SSA stations designed and built in-house by Astro Systeme Austria.

The basis for these stations, as seen in Figure 1, will be a standard shipping container, modified to include a raised dome for the telescope. A shipping container allows for easy transport worldwide, and cuts out the lengthy process of building the base, walls, and dome on-site. These shipping containers will contain 0.4 to 1 metre-class ASA telescopes and mounts, Moravian CMOS cameras, and control and analysis computers.

doi:https://doi.org/10.52526/25792776-22.69.2-318

On delivery to the sites, these stations will allow easy connection to power and internet, and once calibrated over a few days, should be fully automated and ready to be integrated into our SSA network.

3. Software

3.1. Observation scheduling

We intend to observe the night sky in strips, starting near the zenith and moving down as close the meridian as possible, with plans to move to an optimized, Artificial Intelligence-driven system in later stages. Each vertical strip on the sky is split into 1.43 degree segments, resulting in 28 fields per strip, each of which is the subject to 10 consecutive, 1 second exposures. This strategy captures and samples Low Earth Orbit objects, which move up to a degree per second, while also sampling geostationary objects, moving at ~ 15 arcsec per second, across the field of view. In order to maximise our observing time, we take a set of 10 bias and 10 flat-field images to construct the master frames during astronomical twilight, with observations conducted during astronomical night.

As aforementioned, we are also implementing a constraint satisfaction algorithm using artificial intelligence techniques to optimise the schedules in real-time, which will take factors into consideration such as distance of the next observation field from the zenith, moon, and previous field of observation as well as any partial-sky cloud coverage to optimise the schedule. Future versions of our scheduler will also include the ability to temporarily interrupt the observations if a tracking request for a specific object is made.

3.2. Image calibration and streak detection

Once the raw exposure files are delivered to the Mac Mini for analysis, we apply bias and flat-field corrections to each of the 10 images, producing 10 calibrated science-quality images. The 10 science images are then median-stacked to produce an "average" image of the field, which we subtract from each science image to remove background objects, such as stars or galaxies. An example of this process can be seen in Figure 2.

Figure 2. Left hand panel: One of 10 raw, consecutive images of the same field taken by the 40cm Sandl telescope and CMOS camera. This image has a satellite streak in the right hand of the image. Centre panel: The median stacked science image from the 10 raw images. Right hand panel: The summed stack of the 10 calibrated and median-subtracted science images. This removes all background stars and galaxies, leaving the streak prominently in the right hand side of the image.

The subtracted images are then summed together to increase the length and signal of any streaks present (Figure 2, right-hand panel). We then calculate the background noise via sigma clipping, mask pixels below a S/N level of 3σ (with plans to go lower in later stages), and perform a Hough transform. We find any peaks in the radius and angle (Hough) phase space, and extract the likelihood of a streak, as can be seen in Figure 3. The radius and angle values of any probable streaks are then used as a secondary mask on the science images, before applying a clustering algorithm to detect and assign any pixels belonging to the streak. From the movement of the streak across the multiple images, we can determine the position and direction of the object. This can be used to generate the TDMs and will be fed into orbital models planned for future stages of our SSA system.

doi:https://doi.org/10.52526/25792776-22.69.2-318

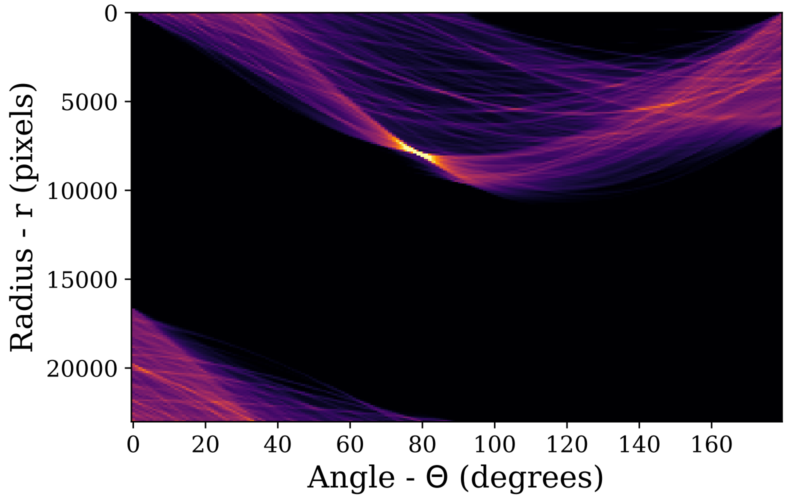

Figure 3. A heat map of the signal in radius/angle phase space (also known as "Hough space"), as run on the pure streak image (Figure 2, right hand panel). We see a definite peak at an angle of $\sim$ 70 degrees and at $\sim$ 7000 pixels away from the origin.

3.3. Data Transfer and Archive

After the streak extraction process is complete, the data products yielded are 10 science quality frames bundled in a 10 extension FITS file, and TDMs generated if a streak is detected. These are saved to monitored folders on the observatory's computer, and are then automatically added to a queue to be uploaded to the central server. If an upload is already taking place, the file will only be uploaded when all previously saved sequences have been uploaded. Since the file sizes are rather large, the science images will be generated faster than they can be uploaded, so the upload process will be continuous.

We expect an uncompressed image to take up around 250 megabytes storage space, with each of the FITS files containing 10 science quality images to be around 2.5 gigabytes. We expect a single observatory to be able to observe around 3000 individual fields per night, which results in approximately 7.5 terabytes of data collected per observatory, per night. We therefore expect observations by 20 observatories at this rate to produce upwards of 40 petabytes of data per year. Taking into account redundancy (an absolute necessity in such data systems), up to 100 petabytes of storage are expected to be necessary. This is currently in the initial design stages and will be created over the coming years, with increasing storage capacity as stations are integrated into our SSA system.

4. Data Products

We intend to have a number of data products from our system, each of which is outlined below. Some products will be delivered via push delivery, whereby clients will automatically receive urgent data rapidly, and other data products will be available for clients to request from the central data archive in pull requests.

4.1. Tracking Data Messages

The main data product of our system will be information on the positions of satellites or space debris at known times. This information will be formatted as what is known as a Tracking Data Message (TDM), and will be available in both push and pull systems. These TDMs will be available in both of the standard XML and KVN formats, and they will conform to the standards set out by the Consultative Committee for Space Data Systems, known as the CCSDS[1], which is commonly implemented by both governmental and commercial organisations.

TDMs contain both metadata and data sections. Metadata will include all mandatory information such as the SSA station information, coordinate and time frames and values, and information linking TDMs back to the original set of images. The data section of TDMs will include the Right Ascension, Declination and

[1] https://public.ccsds.org/default.aspx

doi:https://doi.org/10.52526/25792776-22.69.2-318

time values attained from our streak finding algorithms. Additionally, we intend to extract the calibrated photometry of any detected objects to provide light curves, which can then be utilised by clients to determine characteristics of the observed objects. At later stages, we intend to offer a library of light curves of known objects within our solar system.

4.2. Science Quality Images

All calibrated images will be stored on the central server, available to be pulled from the system, so that clients may run their own measurements. These images will be stored in standard FITS format, containing a top level primary HDU with information such as a unique field identifier and the number of streaks found in the images, and 10 image HDUs, one for each of the calibrated exposures of the given field. Additionally, if any streaks are found in a field, a binary table extension will be added to the FITS file that contains the unique identifiers of each of the TDMs associated with these streaks. All median stacked images of each field will also be stored on the server in a separate science server. We initially expect to make the images available for approximately 3 months before deletion, though this may increase with time and demand.

5. Scientific Potential

A data set with the size and scope as that which will be produced by our SSA system has a significant scientific potential. The all-sky coverage, homogeneity of the network, and regularity of observations are all advantageous for two particular areas: Long-term photometric catalogues and all-sky imaging.

By identifying stars and galaxies within our median stacked science images of each field of observation, we can measure the fluxes of thousands to millions of objects per night. Long-term photometric measurements can be useful for investigating astronomical objects such as variable stars and certain types of galaxies. As there is no funding time frame on this project, we have the potential to make measurements over multiple decades, which are especially suited to discovering new "changing-look" Active Galactic Nuclei (see e.g. Ross et al., 2018, Wolf et al., 2020), or previously undiscovered longer-term variable stars (see e.g. Holl et al., 2018).

We intend to take all of the median stacked images delivered to the central SSA storage server, transfer these to a science server, and continually co-add the images on top of each other (taking into account PSF effects, sky background, systematic inhomogeneities etc.). This technique has been utilised in a number of scientific surveys in recent years (e.g. Aihara et al., 2022, York et al., 2000), and can maximise the depth probed by imaging. All-sky images will then be available as in the current state (with variable depths due to different levels of stacking across the sky), or as periodically released all-sky mosaics at specific depth levels. These images could be used for characterisation of low surface brightness features (Duc et al., 2015), galaxy structure studies (e.g. Rich et al., 2017) or discovering new, faint galaxies (e.g. Greene et al., 2022).

6. Summary

In these conference proceedings, we (Tuparev Astrotech and Astro Systeme Austria) have presented an overview of our planned SSA system for tracking and characterising satellites and space debris. Our SSA system will consist of 20 to 30 custom-built stations which will be deployed worldwide over the coming decade, covering a greater geographical and celestial area than currently available commercial systems. The hardware and software systems are currently being developed and tested, with rapidly-deployable stations expected by late 2023. We aim to make our entire system fully autonomous, with automatic observation scheduling and real-time, on-site calibration, detection and extraction of satellite and space debris. The data produced from our systems will include science quality images, tracking data messages and, at later stages, orbital estimations and light curves for satellites and space debris. These data will be sent and stored on a newly-designed central data archive capable of storing multiple petabytes, and the data will be delivered either through push or pull systems according to the needs of individual clients. Altogether, we expect this system to be step above anything that has been created before, both by other private companies and by world governments, and we hope that our efforts here help to set a new standard in the world of space situational awareness for decades to come.

doi:https://doi.org/10.52526/25792776-22.69.2-318

References

Aihara H., et al., 2022, Publ. Astron. Soc. Jpn. , 74, 247

Apa R., Bonaccorsi S., Piravano L., Armellin R., 2021, in 8th European Conference on Space Debris. https://conference.sdo.esoc.esa.int/proceedings/sdc8/paper/14/SDC8-paper14.pdf

Cvrcek V., Radim S., 2021, in 8th European Conference on Space Debris. https://conference.sdo.esoc.esa.int/proceedings/sdc8/paper/80/SDC8-paper80.pdf

Duc P.-A., et al., 2015, Mon. Not. R. Astron. Soc. , 446, 120

ESA 2021, in ESA'S Annual Space Environment Report. p. 120, https://www.sdo.esoc.esa.int/environment_report/Space_Environment_Report_latest.pdf

Greene J. E., et al., 2022, Astrophys. J. , 933, 150

Hickson P., 2018, Advances in Space Research, 62, 3078

Holl B., et al., 2018, Astron. Astrophys. , 618, A30

Jilete B., Mancas A., Flohrer T., Krag H., 2019, in Revista Mexicana de Astronomia y Astrofisica Conference Series. pp 139–143

Kessler D. J., Cour-Palais B. G., 1978, J. Geophys. Res. , 83, 2637

Murray J., Kennedy T., Miller R., Matney M., 2021, in 8th European Conference on Space Debris. https://conference.sdo.esoc.esa.int/proceedings/sdc8/paper/169/SDC8-paper169.pdf

Nir G., Zackay B., Ofek E. O., 2018, Astron. J. , 156, 229

Park J., Yim H., Choi Y., Hyun J., Moon H., Park Y., Bae Y., Park S., 2017, in 7th European Conference on Space Debris. https://conference.sdo.esoc.esa.int/proceedings/sdc7/paper/535

Rich R. M., et al., 2017, in Gil de Paz A., Knapen J. H., Lee J. C., eds, Vol. 321, Formation and Evolution of Galaxy Outskirts. pp 186–189 (arXiv:1610.02775), doi:10.1017/S1743921316011881

Ross N. P., et al., 2018, Mon. Not. R. Astron. Soc. , 480, 4468

Schildknecht T., Schild K., Vannanti A., 2015, in Advanced Maui Optical and Space Surveillance Technologies Conference. p. 36

Steindorfer M. A., Kirchner G., Koidl F., Wang P., Antón A., Fernández Sánchez J., Merz K., 2017, Advances in Space Research, 60, 1201

Steindorfer M., Wang P., Kirchner G., Koidl F., 2021, in 8th European Conference on Space Debris. https://conference.sdo.esoc.esa.int/proceedings/sdc8/paper/127/SDC8-paper127.pdf

Virtanen J., et al., 2016, Advances in Space Research, 57, 1607

Wagner G., Schramm F., Riede W., Dekorsy T., Döberl E., Weinzinger D., 2021, in 8th European Conference on Space Debris. https://conference.sdo.esoc.esa.int/proceedings/sdc8/paper/79/SDC8-paper79.pdf

Wainscoat R. J., Weryk R., 2019, in 2019 IEEE Aerospace Conference. pp 1–8, doi:10.1109/AERO.2019.8742102

Watson E., Durr N., Schimmerohn M., 2021, in 8th European Conference on Space Debris. https://conference.sdo.esoc.esa.int/proceedings/sdc8/paper/115/SDC8-paper115.pdf

Wolf C., Golding J., Hon W. J., Onken C. A., 2020, Mon. Not. R. Astron. Soc. , 499, 1005

Woods D., Shah R., Johnson J., Szabo A., Pearce E., Lambour R., Faccenda W., 2012, in Ryan S., ed., Advanced Maui Optical and Space Surveillance Technologies Conference. p. 29

Yanagisawa T., Nakajima A., Kimura T., 2005, Science and Technology Series, 109, 29

York D. G., et al., 2000, Astron. J. , 120, 1579

Zhang C., Ping Y., Zhao C., 2018, in Ryan S., ed., The Advanced Maui Optical and Space Surveillance Technologies Conference. p. 17

doi:https://doi.org/10.52526/25792776-22.69.2-318

Archaeoastronomy. On "Observational Technologies" in Ancient Armenia

H.A. Malkhasyan *

NAS RA V. Ambartsumian Byurakan Astrophysical Observatory (BAO), Armenia

Abstract

The paper provides some general information on the recent studies of the "Zorats Qarer" megalithic monument, in particular, some "observational instruments" and the possible observational methodology. Several types of "observational tools" are described, namely "observational platforms" that have their own "guiding stones", stones with holes and the so-called "angular stones". Observational "stone tools" of the "mixed type" (multifunctional) were also found in the monument. Recent studies have also shown that the observations were made in 3 main positions: standing, sitting ("on the seating platform") and kneeling. With the help of the mentioned instruments, apart from the sunrise and sunset of the solstices and equinoxes, the heliacal rising and setting of bright stars, as well as their acronycal rising and cosmical setting were observed in the monument as well. In addition to the mentioned phenomena, apparent appearance and disappearance of stars at the points above the horizon were observed. The observers were also interested in the transitions of the stars in their upper and lower (for circumpolar stars) culmination points. The mentioned "technologies" were mainly used between the 9^{th} and 3^{rd} millennia BC.

Keywords: *Zorats Qarer: Archaeoastronomy: Ancient Observatories: Megalithic Monuments: Observational Technologies: Armenian Calendar History: Protohaykian Calendar: Cultural Astronomy:*

1. Introduction

It is known that in ancient times, people observed the movements of celestial bodies for calendar and religious purposes. However, the methodology details of such observations are still being studied. As it is known, a complete study of all the stones of the Zorats Qarer megalithic monument has not been conducted yet. Until recently, only the stones with holes were described as observational instruments. A complex instrument consisting of several stones was also discussed (Herouni (2006), pp. 64-67). The latter is the complex of stones numbered 60, 62 and 63. The usage of this instrument is explained as follows. It is assumed that the axis of the hole made in the upper part of No. 60 or/and 62 stone is directed to the high[1] top of No. 63. These two directions extend approximately to the South, to the points significantly higher the horizon. In these directions it is possible to observe the upper culminations of some celestial bodies (Herouni (2006), pp. 64-67). Recent studies, however, are revealing new types of observational instruments[2]. These results (Broutian & Malkhasyan, 2021, Malkhasyan, 2021b, 2022) are based solely on the 2020 measurement results with laser accuracy obtained by our expedition. Note that this report includes the complete data only on those observational instruments the study results of which have been published or are in press. In addition to the mentioned, other similar stone observational tools have been discovered, the study of which is currently in progress and promises to be no less interesting. We'll tackle some instruments briefly in this paper, leaving the details for later publications when the full results are obtained. This work also

*malkhasyan.hayk84@gmail.com

[1]The stone No. 63 has two peaks, the northern one being higher.

[2]It should be emphasized that the results obtained by us do not completely contradict to Heruni's hypothesis. However, the described directions are currently being adjusted by our measurements, after which we will also address this complex separately.

describes the possible application methods of some “observational instruments” revealed as a result of the recent thorough studies of the Zorats Qarer megalithic monument (Broutian & Malkhasyan, 2021, Malkhasyan, 2021a,b, 2022), as well as the celestial phenomena that were observed with the help of the mentioned instruments. Let us now see what observational instruments have been revealed and analyzed since 2020 and what their applications were.

2. Observational Platforms

Figure 1. Observational Platform 1.

Observational platforms are areas with some marks on the ground, intended for observations in standing or sitting positions. When viewing from the observational platform in the direction of the top of the related stone (or a protrusion, concave, etc.), the points at which the rising or setting of the celestial bodies take place are marked on the horizon. In another case, the transition of the celestial body through any point of the firmament is marked in the significantly higher positions above the horizon. The menhirs (standing stones) associated with the observational platforms are referred to as marking or guiding stones. However, in reference to the Zorats Qarer monument, it is more correct to call them guiding stones. They are the stones located in front of the observer who’s on the platform, and the top of which coincides with any point of the line of the true horizon in the eye of the observer. So far, 5 similar platforms have been found in the monument, 4 of which are intended for a standing and 1 for a sitting observer. We named the latter Seating Platform No. 14[3]. Of the remaining 4, which are numbered in the order of their discovery, only 2 have been studied so far: Platforms 1 and 2. The detailed analysis of the rest is in progress. Let us now describe the observational platforms in order.

2.1. Platform 1.

About 8 meters to the south of the central cromlech of the monument and about 7 meters to the west of the southern wing of the general row of stones, there’s a fairly flat-surfaced slab with an apparent area of about 1 square meter, placed deep in a horizontal position into the ground (Figure 1). As of today, the surface of the mentioned stone is about 10-20 centimeters above the ground and it has a certain concavity on the surface near its geometrical center which is devoid of lichens. Standing in the concave, a man with an average height can observe an interesting view in the east (with the eye level of 160 cm above the platform surface). The tops of the 4 guiding stones (No. 60, 62, 64 and 66) are aligned with the visible horizon (Figure 2). Moreover, 3 of them (No. 60, 62 and 66) coincide with certain peaks visible on the horizon, and the cut of the upper part of No. 64 stone coincides with the concave of the contour of the mountain range seen on the horizon. By moving his head only 5 centimeters, the observer can see the tops of the stones touching the horizon, thus creating 4 distinct directions (P1-60, P1-62, P1-64 and P1-66), each passing through 3 points: the observation point of the observer standing on the platform, the top of the guiding stone, and the corresponding point on

[3]Since this stone is part of a series of already numbered stones, we have left its No.14 unchanged.

the horizon (Figure 3). It is clear that one of the most likely reasons for the use of the guiding stone was the adjustment of the observation point.

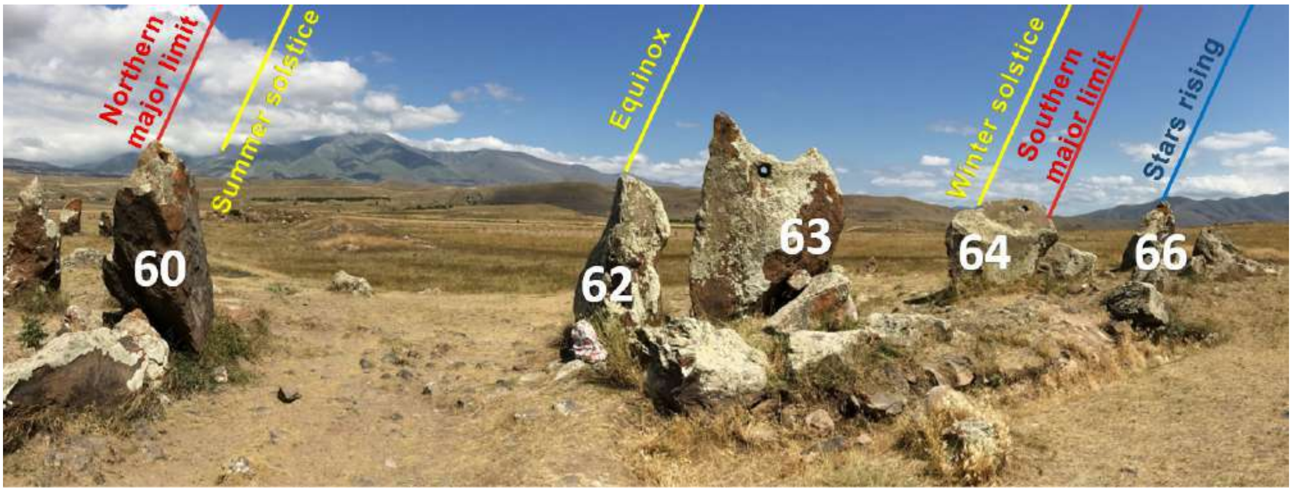

Figure 2. Eastern view from the Platform 1. Panorama.

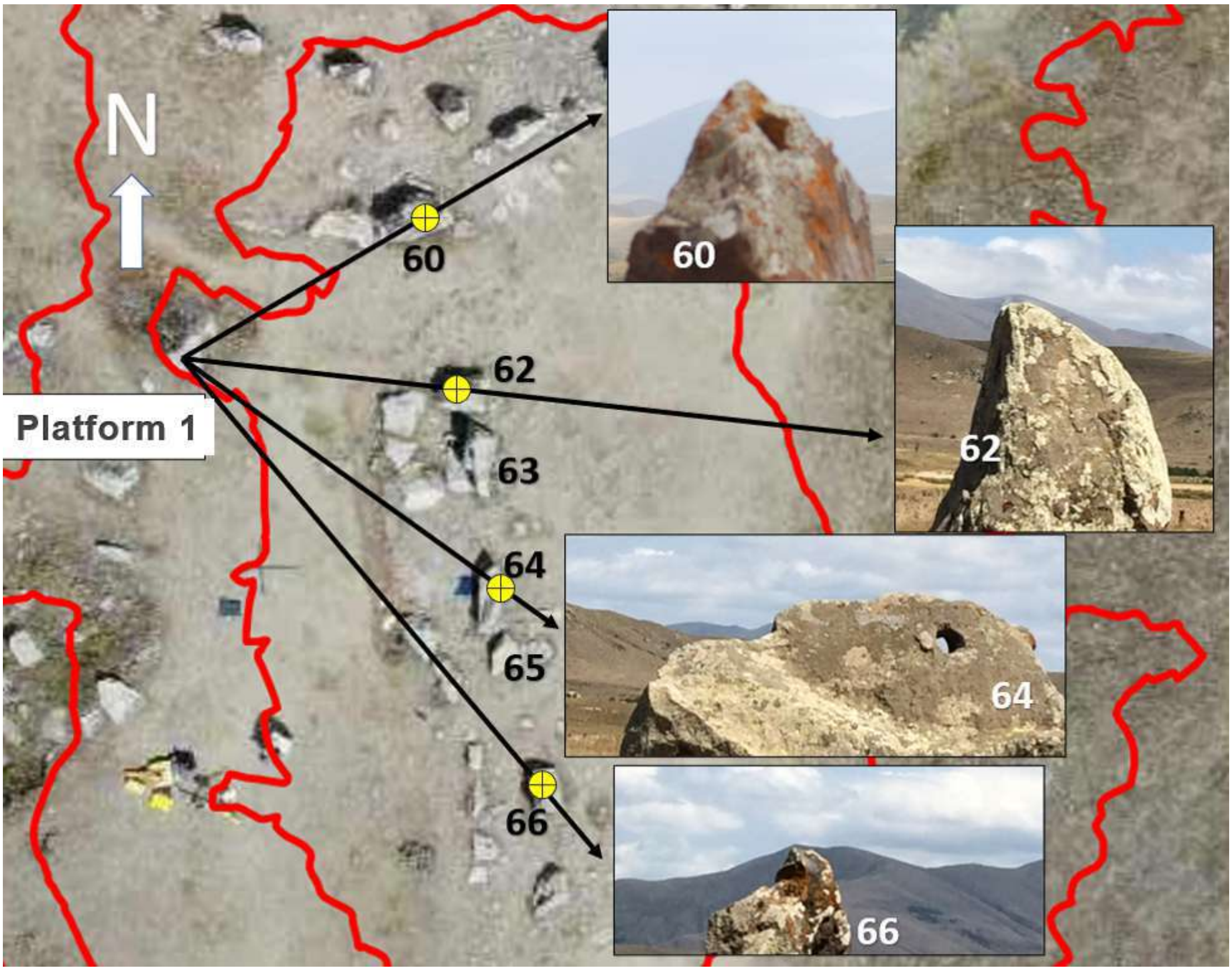

Figure 3. The simplified scheme of the 4 directions from the observation point on the Platform 1. Azimuths and Elevations of the directions are given in Table 1. The scheme is made according to the author of this article.

The study of these directions (Broutian & Malkhasyan, 2021)[4] revealed that the two of them are directed to the points of the equinox and the sunrise of winter solstice, the days of astronomical importance. The visible celestial bodies in all directions are given in Table 1.

2.2. Platform 2.

In the “northern wing” (Herouni (2006), pp. 21-22)[5] of the “Zorats Qarer” monument, we discovered another observational platform similar to Platform 1, naming it Platform 2 (Figure 4a). It is located about 16 meters to the south of No. 160 stone of the northern wing of the monument. It looks like a slab with an area of about 2.2 square meters, almost in the center of which there is a cone-shaped artificial[6] concave with a diameter of 25 centimeters and a depth of 15 centimeters.

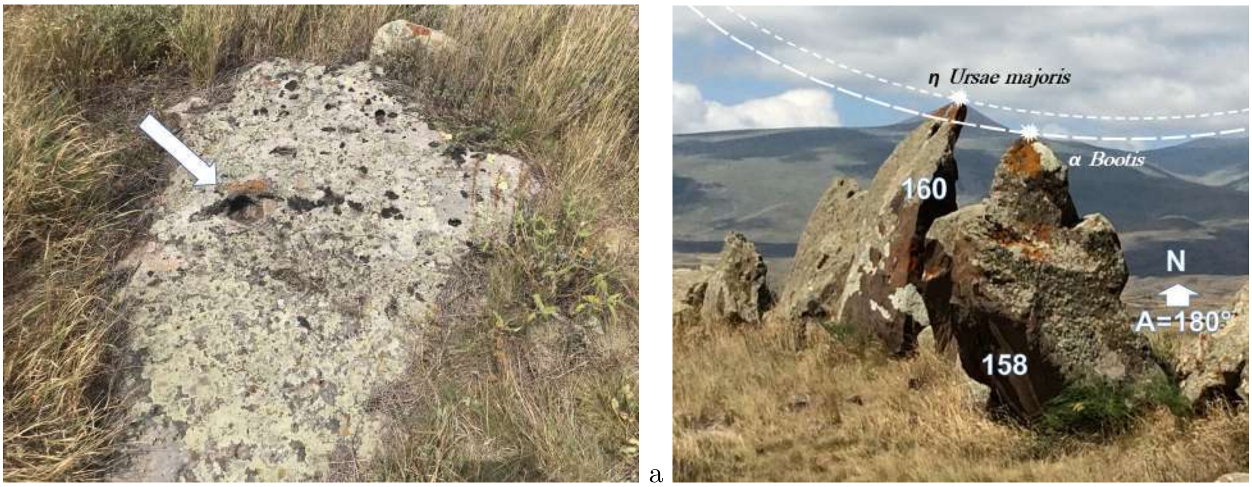

Figure 4. Observational Platform 2. a) The arrow shows the cone-shaped artificial concave in the center of the platform. b) View to the North. The brightest stars of the constellations Ursa Major and Bootes being seen in the directions. Reconstructed in Stellarium v0.20.4 (http://www.stellarium.org)

When standing in the center of this concave, a man with an average height can observe in the north the tops of 2 guiding stones (No. 158 and 160) touching the horizon (Figure 4b), as in the case of Platform 1. At the same time, the top of No. 160 stone is combined with the mountain peak that is quite clearly highlighted on the horizon (Malkhasyan, 2021b). In Figure 3, the touch of the tops of the two stones with the horizon is clearly visible. One of them, No. 160, touches the mountain top, and the other, No. 158, touches the point of the eastern slope of the same mountain where the incline changes. Unlike Platform 1, Platform 2 has some peculiarities. The first and most important difference is that the guiding stones associated with Platform 2 (No. 158 and 160) point in directions very close to the northern horizon (Figures 4 and 5). As it is known, in such directions only circumpolar stars (stars that do not set) can be observed, or in other words, stars that “touch” the horizon in their lowest position. It follows that the observation of a star at some point in the northern horizon for calendar purposes can make sense only if the apparent appearance or disappearance of the given star in the specified position has been observed. Such phenomena can occur only once a year. The other difference is that the guiding stones of Platform 1 have holes in their tops, while in the case of Platform 2, No. 158 stone doesn’t have a hole unlike No. 160. However, the two observation angles on the same No. 158 (Malkhasyan, 2021b) are especially noteworthy, which we will refer to further in the paper. Table 1 shows the stars that were observed at different times from Platform 2 in the direction of the tops of No. 158 and 160 stones (P2-158 and P2-160) (Malkhasyan, 2021b).

[4]The cited article details all the numerical data and the methods used to identify the possible time of the observable celestial bodies.

[5]The stone row which P. Herouni called ”North Wing” arranged to the north from the central cromlech.

[6]The fact that the concave is artificial is evidenced by its smooth edges and the conical depth.

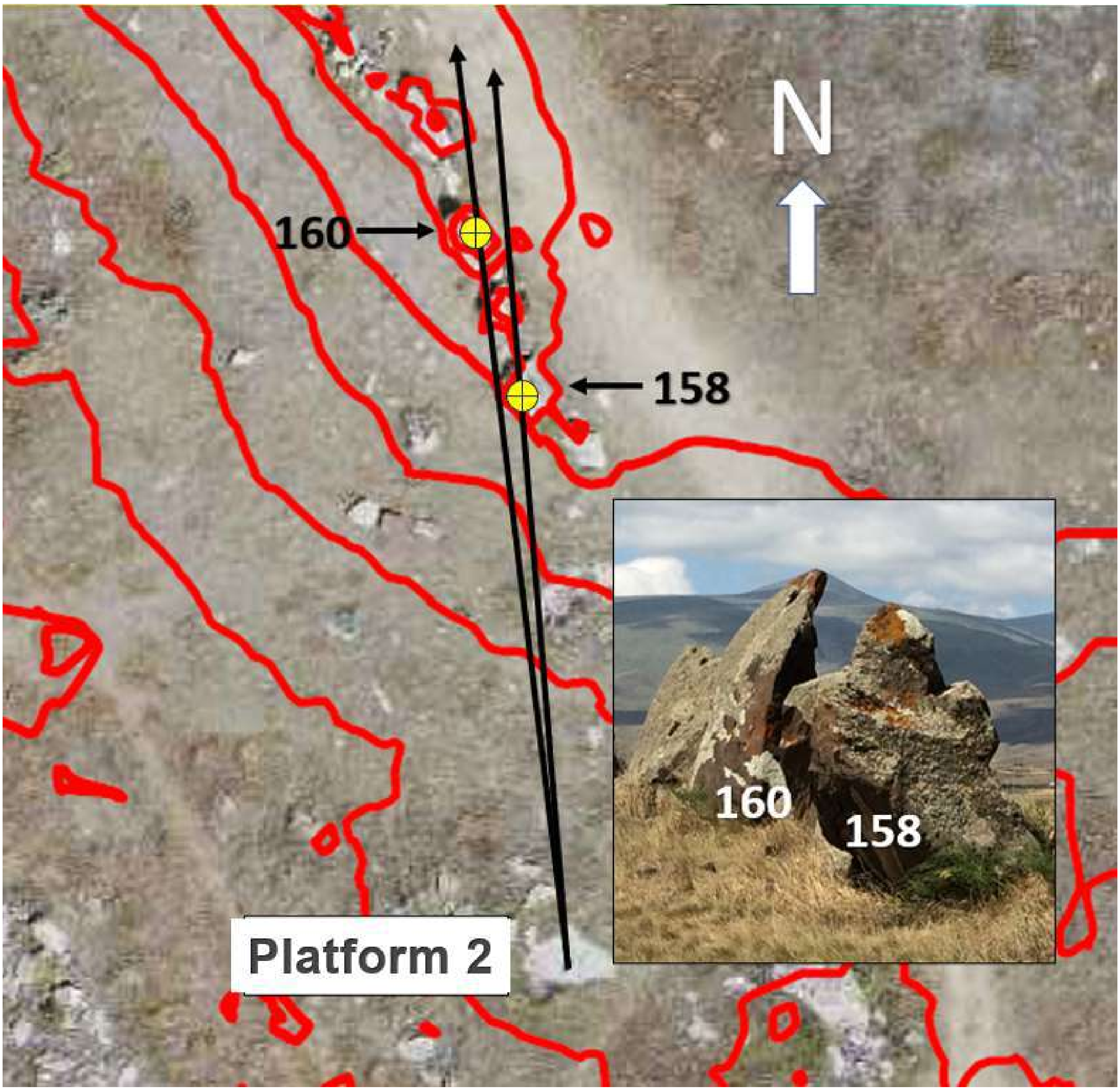

Figure 5. The simplified scheme of the directions and guiding stones No. 158 and 160. The scheme is made according to the author of this article.

2.3. Platform 3.

As it was mentioned above, only the 2 of the observational platforms found in the Monument have been studied (Platforms 1 and 2). Although a full analysis of the other two Platforms (Platforms 3 and 4) and the directions formed with their help has not been done yet, we will also give their brief description and list the associated guiding stones.

Further in the paper, we will refer to No. 29a slab[7] as Platform 3. It is somewhat different from Platforms 1 and 2. If the latter two have a more horizontal position, then Platform 3 is placed with a certain slope. However, the western part of the slab, which is positioned higher, is somewhat flattened. This is important for the reason that it is rather uncomfortable to stand in the section, and at the high point it resembles a pedestal-platform (Figure 6). Standing on this high point and looking to the

[7] In the numbering of P. Herouni, this slab is marked as number 29a and is considered one of the fallen and displaced stones of the central cromlech (Herouni, 2006).

East, the tops of 4 stones (No. 7, 19, 27 and 201) touch[8] the horizon (Figure 7. The first three stones are part of the central rhombusly “cromlech” and are placed in the ground vertically (Figure 8). It is interesting that each of them (No. 7, 19 and 27) is different from the others and from the rest of the stones in the monument. **It is also worth noting that No. 7, 19, and 27 guiding stones are the eastern, southern, and western peaks of the diagonal of the cromlech, respectively**.

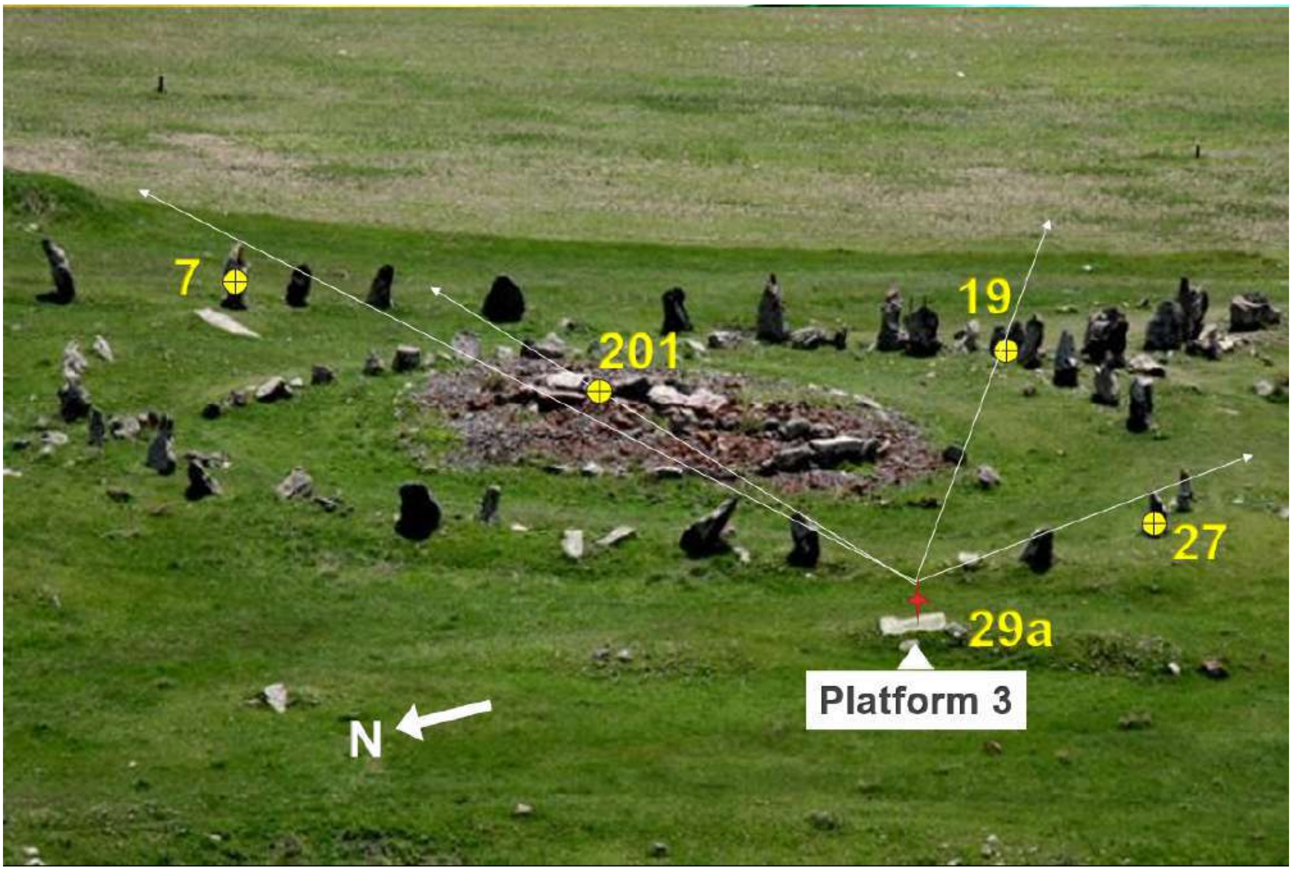

Figure 6. Observational Platform 3 and the locations of guiding stones No. 7, 19, 27 and 201. The scheme is made according to the author of this article.

Figure 7. View from the Platform 3, Panorama. the arrows show the guiding stones.

[8]The content of the stone No. 19 is slightly different. It has a hand-made cut and touches the horizon with the lower horizontal side of its cut.

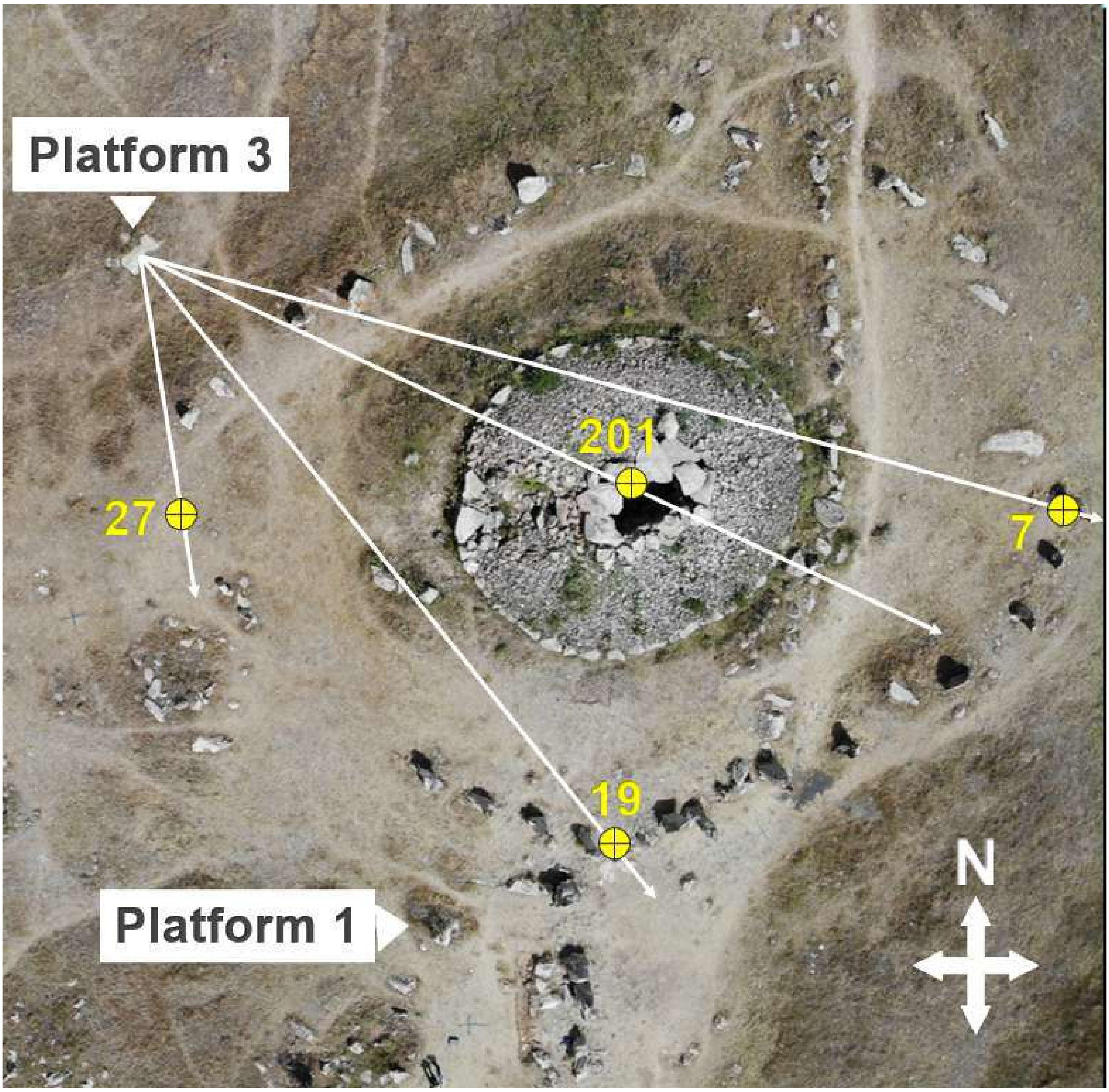

Figure 8. The locations of the Observational Platforms 1 and 2. The arrows show the directions and the yellow points marked the guiding stones. The drawing is made according to the author of this article.

As for issue No. 201, the problem here is a little different. First, this is located on the central structure (in the center of the cromlech), forming part of the roof slabs. In other words, as such, it is not part of the stone rows and it is difficult to consider its position as preliminary in any way. On the other hand, stone No. 201 also stands out from the stone rows. The peculiarity is that this stone has 3 holes in its upper part, of which only one is complete. The other two are broken, but it is obvious that they were holes before. At the same time, during the excavations in the central structure, the initial positions of the roof slabs were most likely violated. This is evidenced by some photos from the excavation process. However, on-site inspection suggests that the position of the stone No. 201 has remained unchanged in the roof structure. The question on which point of the Platform the observer was standing should be secondary, since the azimuths deviations of these parameters are quite small and such problems can be ignored. Another feature of Platform 3 is that only one of the guiding stones connected to it (No. 27) has a correspondence with its top and horizon outline, the others have some explainable features that will not be covered here. What celestial bodies have been observed and in which millennia will become clear only as a result of a systematic examination of these directions.

2.4. Platform 4.

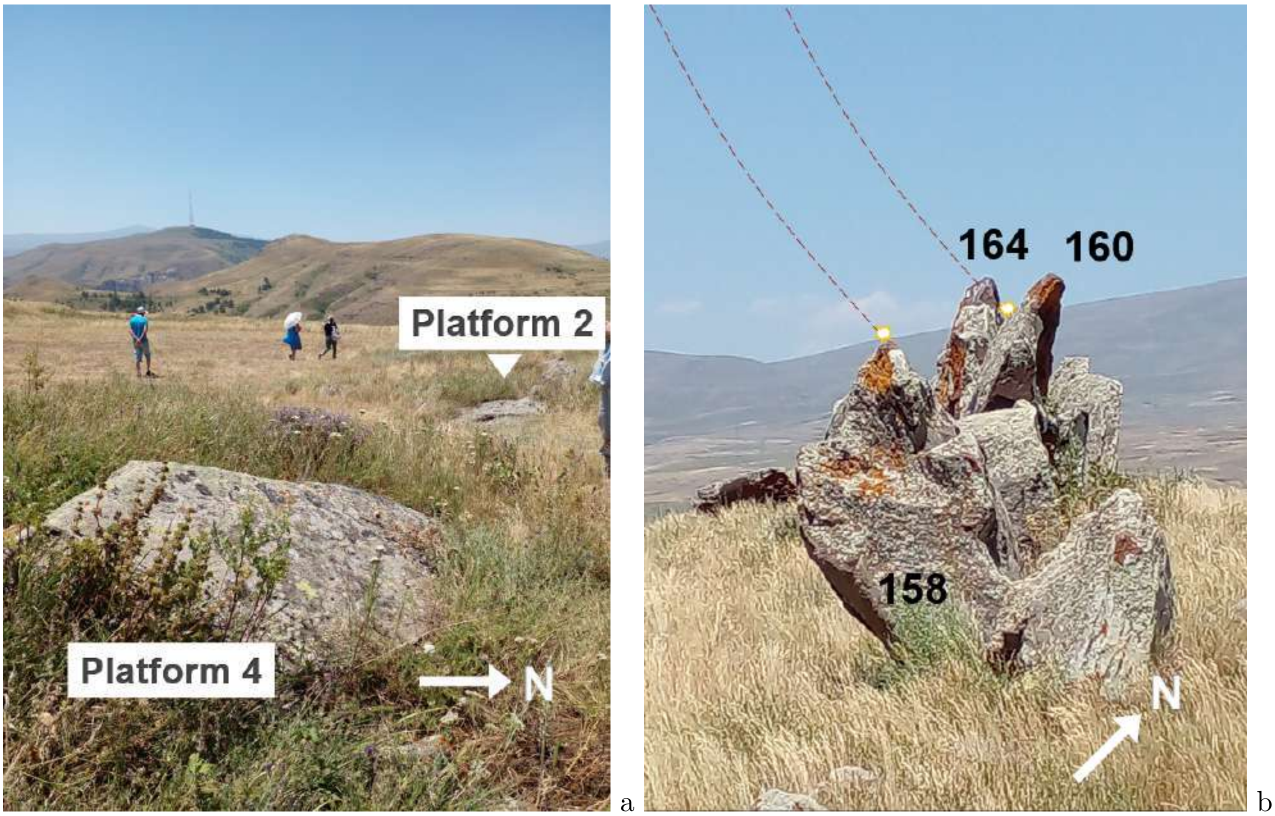

Figure 9. Observational Platform 4 and 2. a) The surface of the Platform 4 is directed to the north. b) View from the Platform 4 and guiding stones No. 158, 160 and 165.

Due to certain peculiarities, Platform 4 was discovered later, in the summer of 2021 during the reexamination of the monument. The point is that from Platform 4 the line of the horizon in the observer's field of view is quite flat, i.e., there are no obvious peaks and concaves. It was this feature that is largely reflected in the arrangement of the guiding stones associated with Platform 4, as the observer needed two guiding stones instead of one to adjust the observation point in one direction. Therefore, the following image was obtained. Platform 4 is located to the east of Platform 2, in the part of the monument where the range of stones interrupts.

It has a surface of about $2m^2$ and is placed on a slight slope, the surface of which is directed to the north (Figure 9a). Standing in its center and looking to the north, we will see the following picture. Between the Platform and the horizon 4 guiding stones are standing in 2 directions (Figure 9b). In other words, two directions are formed with the 4 guiding stones.To identify the guiding stones, we have named them proximal (closer to the viewer) and distal (closer to the horizon). No. 158 and 160 guiding stones are proximal, and No. 164 and 165 are distal (Figure 11), respectively. It should be emphasized that the stones No. 158 and 160, as mentioned above, are guiding stones for the Platform 2 as well (Figure 10). There is another feature in the case of guiding stones No. 160 and 165. The point is that if in the observer's field of the view from the platform the tops of the stones No. 158 and 165 align with each other and the horizon, then in the case of the stones No. 160 and 168 the alignment is not with the tops. In the field of view, the narrow upper parts of these stones cross each other and create a V-shaped marking on the horizon, that is, the low vertex of the V is aligned with the horizon outline (Figure 9b). It should also be noted that the 2 directions formed with the help of Platform 4 are show the points on the horizon which are very close to the North (to the north-west), where only setting of the stars can be observed (Figure 9b). Ecliptic celestial bodies never appear at these points. The analysis of the mentioned directions is also not done yet, as in the case of Platform 3.

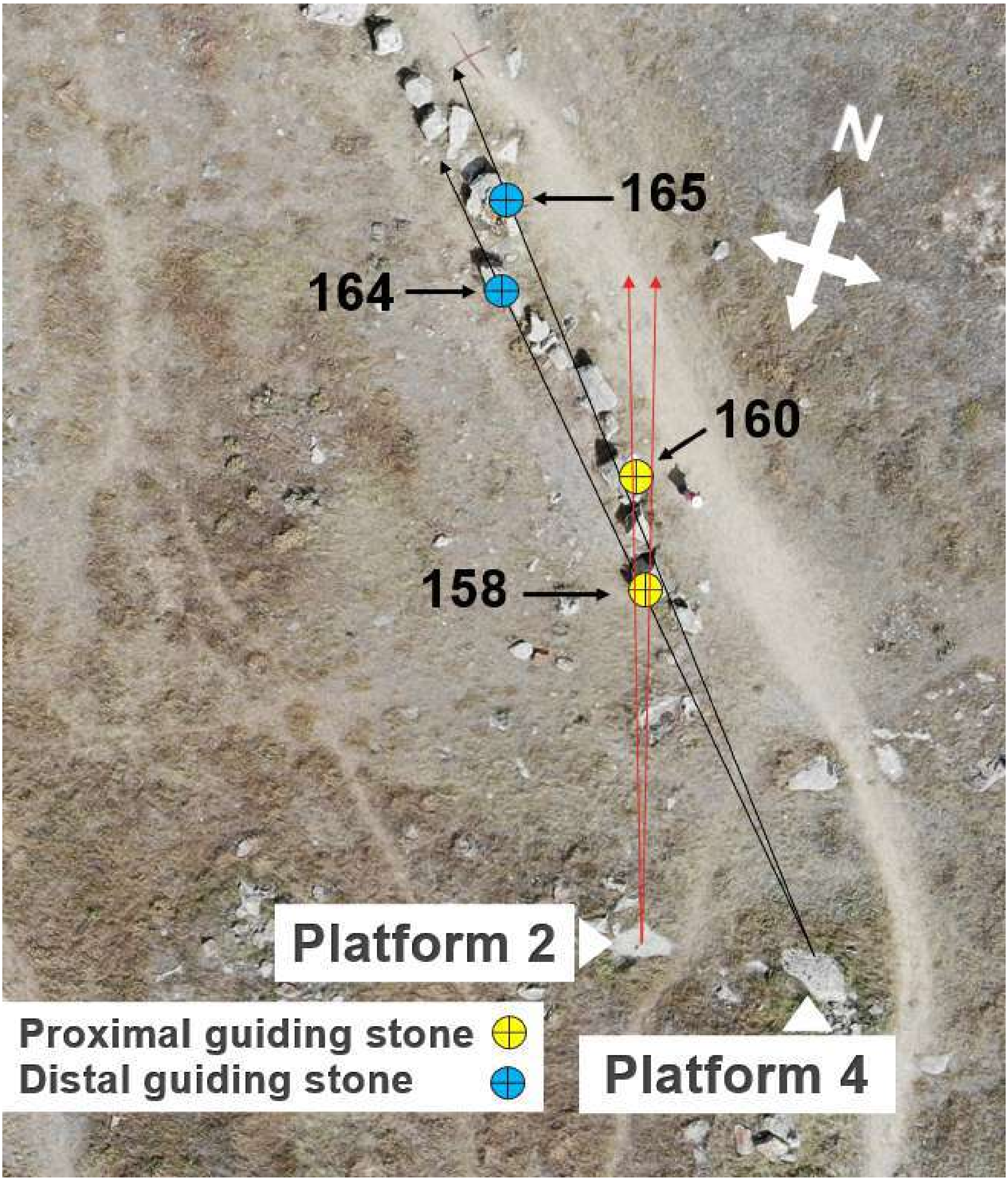

Figure 10. Observational Platforms No. 2 and 4. The red arrows show the directions formed with the help of guiding stones No. 158 and 160. The black arrows show the directions formed with help of proximal and distal Guiding stones. The drawing is made according to the author of this article.

Figure 11. Distal guiding stones No. 164 and 165. View from the west.

2.5. Seating Platform 14.

Although No. 14 seating platform is a part of the central cromlech, it is distinguished both by its form and position. It has the appearance of an irregular parallelepiped, and its upper horizontal face somewhat resembles a flat surface. During the detailed inspection of the visible part of the stone, no cut, angle or hole was found. Only the upper surface being flat is noticeable. It should be noted that the direction of the angle of the upper part of the stone No. 13, while continuing in the opposite direction, quite precisely coincides with the eye of the observer sitting on the edge of the stone No. 14 (Figure 14) (Malkhasyan, 2022). It should also be noted that in this direction also, as in the case of Platform 2, it is possible to observe only transitions of the stars, that is, ecliptic celestial bodies never appear in this direction. The observable stars in this direction (SP14-13) are given in Table 1.

3. Angular Stones.

In addition to the described observational platforms, other types of observational instruments were found in the monument, which we referred to as “angular stones” (Broutian & Malkhasyan, 2021). Only 6 of these stones have been studied so far: No. 7, 12, 13, 158, 197 and 198 (Figure 12).

The 4 of them have cut angles (7, 13, 197 and 198) and the other two have binary angles (12 and 158) (Broutian & Malkhasyan (2021), Malkhasyan (2021a,b, 2022)). In the mentioned publications,

Direction	Azimuth	Elevation	Star	Date	Phenomenon
P1-60	236° 54′	6° 40′	α Aurigae	VE (2341 BC)	HR
			Moon	*Northern major limit*	R
P1-62	276° 19′	4° 13′	Sun	VE	R
P1-64	304° 47′	1° 57′	Sun	WS	R
P1-66	321° 02′	2° 27′	γ Crucis*	AE+7 (2341 BC)	HR
			α Canis Majoris	SS-8 (5800 BC)	HR
			λ Velorum	SS+42 (5800 BC)	HR
P2-158	175° 01′	5° 59′	α Boötis	SS-5 (9000 BC)	AA
			β Ursae Minoris	VE+12 (9000 BC)	AA
P2-160	172° 30′	6° 45′	α Draconis	VE-38 (2341 BC)	AA
			η Ursae Majoris	VE+45 (9000 BC)	AA
SP14-13	232° 51′	44° 22′	α Ursae Minoris	SS+36 (5800 BC)	AA
			β Ursae Majoris	SS-34 (5800 BC)	AD
			α Cygni (Deneb)	SS-44 (9000 BC)	AA
A-197	110° 52′	21° 55′	α Aurigae	VE (2341 BC)	AA
			β Cassiopeiae*	WS-7 (9000 BC)	AA
			α Virginis**	SS-48 (9000 BC)	HS
A-198	262° 50′	19° 34′	β Persei	VE+10 (2341 BC)	AD
			β Pegasi	AE+45 (9000 BC)	AD
			α Virginis	SS (9000 BC)	AD
WA-158	101° 55′	24° 01′	α Leonis	WS-5 (2341 BC)	AD
			γ Leonis	AE+24 (5800 BC)	AD
			δ Cassiopeiae	SS+32 (5800 BC)	AD
			α Cassiopeiae	SS+27 (5800 BC)	AD
			α Cassiopeiae	SS+1 (9000 BC)	AD
			γ Cassiopeiae	SS+4 (9000 BC)	AD
EA-158	194° 56′	12° 26′	β Draconis	AE+8 (2341 BC)	AD
			α Boötis	SS-23 (5800 BC)	AD
			ε Boötis	VE-34 (9000 BC)	AD
			α Ophiuchi	SS+4 (9000 BC)	AD
			δ Cygni	AE-13 (9000 BC)	AD
SA-12	67° 30′	12° 48′	γ Orionis	VE-4 (2341 BC)	AA
			α Scorpii	AE-38 (2341 BC)	AA
			θ Scorpii	SS+8 (5800 BC)	AA
			β Geminorum	SS+48 (9000 BC)	AD
NA-12	71° 44′	11° 45′	α Hydrae	VE+15 (5800 BC)	AA
			β Tauri (γ Aur)	AE-30 (5800 BC)	AD
			α Lupi	SS-47 (9000 BC)	AA
			α Geminorum	SS+47 (9000 BC)	AD
A-7	230° 06′	62° 58′	β Ursae Majoris	SS-1 (5800 BC)	AD
			γ Cygni (Sadr)	SS-27 (9000 BC)	AA

Table 1. The observable celestial bodies. 1^{st} column - P-platform, SP-sitting platform, A-angle, WA-western angle (large), EA-eastern angle (small), NA-northern angle, SA-southern angle. 4^{th} column - *-less reliable, **-alleged. 5^{th} column - VE-vernal equinox, SS-summer solstice, AE-autumn equinox, WS-winter solstice. 6^{th} column - R-rising, HR-heliacal rising, HS-heliacal setting, AA-apparent appearance, AD-apparent disappearanc. All the azimuths, presented in the table, are calculated from the South point, as it is accepted in astronomy.

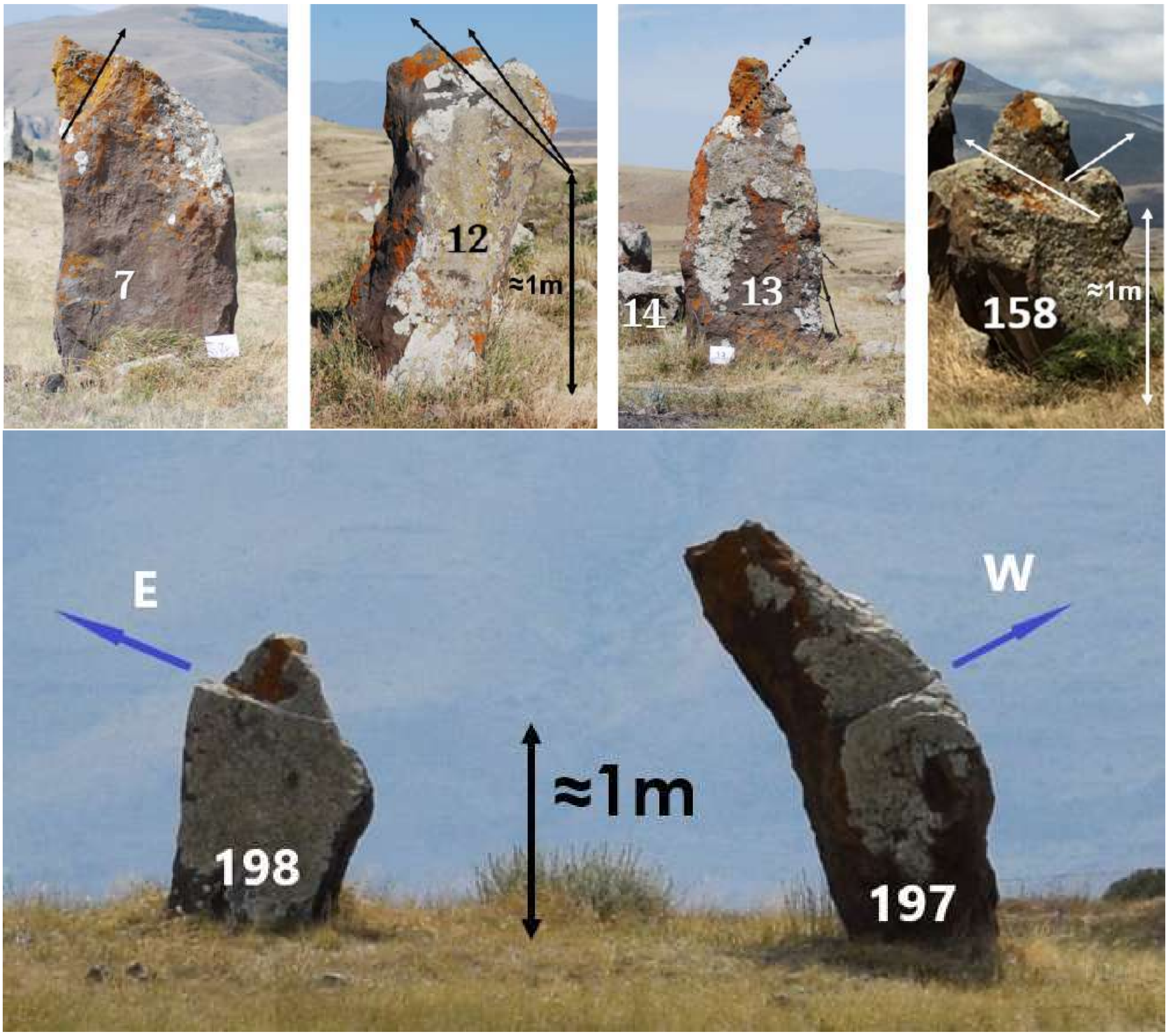

Figure 12. The photos of angular stones No. 7, 12, 13, 158, 197 and 198. The arrows show the directions of the angles.

their full descriptions and the observation principles are presented, so we will not detail them here. We would like only to note that the directions formed with the help of angular stones mark significantly high points above the horizon. The observer’s position while using these stones can be considered the other peculiarity, as it was most likely the kneeling one. In the case of stone 12, the reality of the observer’s kneeling position is substantiated in detail (Malkhasyan, 2022). In the case of the angular stone No. 13, as mentioned above, the observations were probably made in position sitting on the Platform 14. In the case of the remaining stones No. 158, 197 and 198, the angles on the stones are made at such a height that the position of the observer’s eye should be about 1 m above the ground (Figure 12). This circumstance surely implies that the most convenient position for the observer, which will allow him to adjust the height of his eyes to the specified height, will be the kneeling position. In addition, this is one of the most stable and comfortable positions used in modern shooting.

Thus, the angular stones No. 7, 197 and 198 found in the monument can be used as separate instruments. 158 with its two angles can also be considered as a separately used instrument. In addition, the angular stone No. 158 is connected to Platform 2 and Platform 4 as a guiding stone, and the angle of the stone No. 13 is actually a guide for the observer sitting on the Seating Platform 14. The picture is different in the case of stone No. 12, here the angle of the stone No. 13 serves as a guide. As mentioned, the angular stones were intended to observe the apparent appearance and disappearance of bright stars high in the sky (Broutian & Malkhasyan (2021), Malkhasyan (2021a,b, 2022)). The celestial bodies observable with the help of all mentioned angular stones (in the directions A-7, NA-12, SA-12, EA-158, WA-158, A-197 and A-198) are given in the Table 1.

4. Regarding the shape of the tops and location of the stones.

As it turned out, the listed observational instruments, especially the guiding and angular stones, apart from being mere observational tools had other functions as well. In particular, the shapes of the upper parts of some stones repeat the lines of the given part of the horizon. In case of others, we are dealing with figures formed and specially cut as a result of religious ideas. Let us give only one of such examples here. The fact (Malkhasyan, 2022) that the pair of bright stars of the Gemini constellation were visible at the same time from the pair of angles of the upper part of the stone No. 12 (Figure 13). Such coincidences are numerous and impressive in the monument. In addition, the previously revealed connection to the arrangement of the stars of the Angegh-Vulture-Swan constellation in the main plan structure of the monument (Malkhasyan (2020), Vahradyan & Vahradyan (2010)) is confirmed again. The basis for this is the probable observations of the brightest stars of this constellation (Table 1). In terms of calendar, undeniable connections are revealed between the structural-functional description of the monument and the Early Bronze Age Armenian Calendar (Malkhasyan, 2022). **The described observational instruments and the developed observational methodology allow us to confidently call this megalithic monument an observatory built for calendar and ritual-worship reasons.**

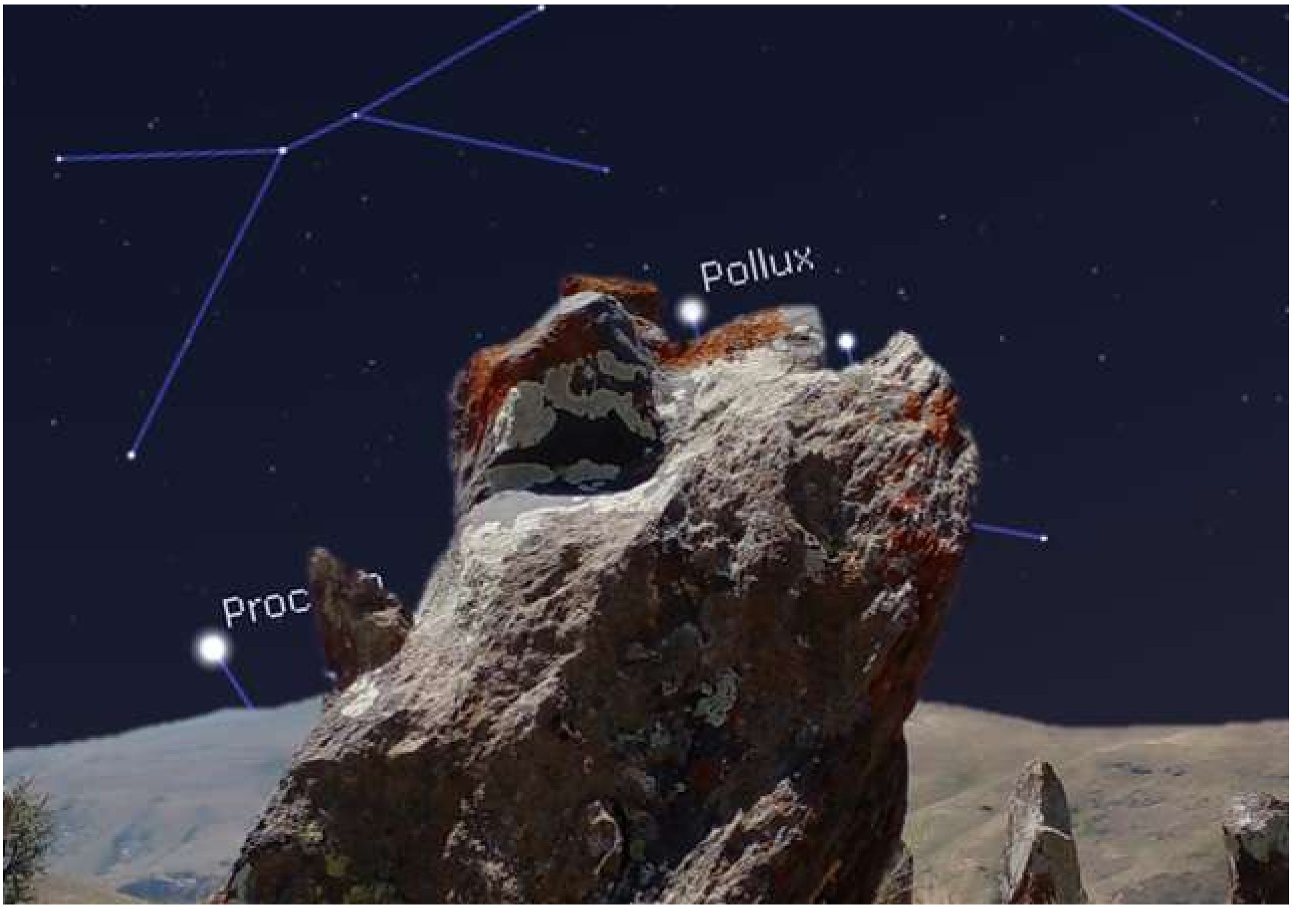

Figure 13. The brightest stars of the constellation Gemini being seen simultaneously in the directions of the angles of the stone No. 12 from the kneeling position. Reconstructed in Stellarium v0.20.4 (http://www.stellarium.org)

5. On the significance of the observed celestial bodies.

Figure 14. Observational Seating Platform 14.

In the tables (tables 1, 2, 3, 4 and 5), we have listed the celestial bodies observed with the help of the described observational equipment. However, what's more important is the purpose and significance of these observations, especially in terms of the ancient Armenian calendars. Before the mentioned studies, it was known that the beginning of the Armenian Protohaykian calendar was in 9000 BC and that the main star of this calendar was Spica of the Virgo constellation (Broutian, 2016, 2017). In addition, it was known that this calendar was closely related to the stages of grain cultivation in its structural and content features. It was also known that in 2341 BC, the Haykian calendar was founded, the main star of which was Betelgeuse of the Orion (Haykn) constellation (Broutian, 1985a,b, 1997). In other words, more than 6,500 years after the beginning of the Protohaykian calendar, the main star of the calendar was changed in order to observe its heliacal rising to keep it unchanged on the day of the beginning of the year, Navasard holiday. It was logical to assume that another change in the main star during these 6,500 years would be inevitable, but there was no information about this (Malkhasyan, 2021a). In addition, the other stars related to the same year and the days of their observations confirm again the connection of this calendar and the monument with the phases of grain cultivation.

Studies of the monument bring some clear clarifications to the above issues. In particular, the fact that Spica is the main star of the Protohaykian calendar is confirmed by observing it in the monument in 9000 BC (Broutian & Malkhasyan (2021), Malkhasyan (2021a)). In addition, the other stars related to the same year and the days of their observations confirm again the connection of this calendar and the monument with the phases of grain cultivation (Broutian & Malkhasyan (2021), Malkhasyan (2021a,b, 2022)).The obtained results also reveal that there really was a change of the main star in the Protohaykian calendar. This change took place in 5800 BC. Instead of Spica, the beginning of the year was determined by observing the heliacal rising of Sirius on the day of Navasard (Broutian & Malkhasyan (2021), Malkhasyan (2021a)). There are also other remarkable details in the mentioned publications that shed light in the dark corners of the astronomical content of the Armenian folklore and ethnographic material that has reached us from ancient times. The continuous studies of the monument are very important also in this sense.

Summary

Summarizing the listed observational instruments, methods and the observed celestial phenomena, we have come to clear conclusions that the stones of the monument were used for observational purposes in a number of ways. Yet, only several types of instruments are clearly distinguished.

1) Stones with holes
2) Observational Platforms
3) Seating Platforms

4) Angular stones

This of course does not exclude, and it is evident, that instruments of the mentioned type were possibly used in combination. Moreover, it is possible that new types of instruments will be revealed in the future. Especially since it is already clear that there are also **mixed types** of instruments. Regarding the observer's positions, three main positions have been identified:

- Standing
- Sitting
- Kneeling

As can be seen in the Table 1, the following celestial phenomena were in the center of the ancient observer's attention:

1) Sunrises and sunsets of solstices and equinoxes
2) The rising of the Moon
3) Heliacal rising and setting of bright stars
4) Acronycal rising and cosmical setting of bright stars
5) The apparent appearance and disappearance of bright stars at significantly high points above the horizon
6) The celestial bodies transitions through their upper and Lower culmination points.

The use of such technologies, as has been convincingly demonstrated (Broutian & Malkhasyan (2021), Malkhasyan (2021a,b, 2022)), refer mainly to 9^{th}-3^{rd} millennia BC (Table 1) and is directly related to the ancient Armenian calendar culture.

These conclusions further increase the already unfading scientific interest in the Zorats Qarer monument. In the upcoming publications, it is planned to describe the mentioned Platforms 3 and 4, in particular the directions formed with their help. The identification of observable celestial bodies and the chronology of observations promise to be quite interesting.

References

Broutian, Gr. 1985a. On Some Questions of Armenian Calendar: Analysis of 2341 BC. *Etchmiadzin*, **2-3**, 72–80.

Broutian, Gr. 1985b. On Some Questions of Armenian Calendar: The Main Armenian Date. *Etchmiadzin*, **1**, 51–57.

Broutian, Gr. 1997. *The Armenian Calendar*. Mother See of Holy Etchmiadzin.

Broutian, Gr. 2016. The Beginning of the Protohaykian Calendar. *Bazmavep*, **3-4**, 11–63.

Broutian, Gr. 2017. The Beginning of Protohaykian Calendar. *Pages 296–302 of: Non-stable Universe: Energetic Resources, Activity Phenomena, and Evolutionary Processes, Proceedings of an International Symposium dedicated to the 70th anniversary of the Byurakan Astrophysical Observatory held at NAS RA, Yerevan and Byurakan, Armenia 19-23 September 2016, Edited by A. Mickaelian, Astronomical Society of the Pacific, Conference Series, volume 511, San Francisco.* .

Broutian, Gr., & Malkhasyan, H.A. 2021. About Some Preliminary Results Based on the Last Measurements of “Zorats Qarer” Megalithic Monument. *Bazmavep*, **3-4**, (accepted).

Herouni, P.M. 2006. *Armenians and old Armenia*. Yerevan: “Tigran Metz”.

MALKHASYAN, H.A. 2020. The observation of Angegh-Vulture (Cygnus) constellation in Armenia 32 000 years ago. *Communications of BAO*, **67(1)**, 27–36.

MALKHASYAN, H.A. 2021a. Outline of Calendar Studies Conducted at the Byurakan Astrophysical Observatory in 1983-2021. *Communications of BAO*, **68(2)**, 407–416.

MALKHASYAN, H.A. 2021b. Some New Results of the Study of “Zorats Qarer” Megalithic Monument (Platform 2). *Bazmavep*, **3-4**, (accepted).

MALKHASYAN, H.A. 2022. On “Observational Instruments” composed of Stones No. 12, 13 and 14 of “Zorats Qarer” Monument. *Communications of BAO*, **69(1)**, 100–121.

VAHRADYAN, V., & VAHRADYAN, M. 2010. The Name of Monument Karahunge. *Bazmavep*, **1-2**, 161–177.

Optical properties of variable radio sources from NVSS and FIRST

H. V. Abrahamyan*, A. M. Mickaelian, G. M. Paronyan, and G. A. Mikayelyan

NAS RA V.Ambartsumian Byurakan Astrophysical Observatory (BAO), Byurakan 0213, Aragatzotn province, Armenia

Abstract

We have carried out a number of studies to reveal radio properties of active galaxies, namely AGN and Starbursts. A major work was related to the cross-correlation of NVSS and FIRST radio catalogues and revelation of variable radio sources. Most probably, most of them are extragalactic ones; AGN and Starbursts. We have carried out spectroscopic classification of 6301 of these objects and revealed many Seyferts, LINERs and Starbursts. We have also studied radio properties of VCV-13 AGN, Markarian galaxies and Blazars. One of the aims of our studies is to establish the radio/opt flux ratio limit between normal galaxies detected in radio and radio loud active galaxies. The ultimate goal of these studies is to combine results obtained from radio studies and derived radio properties of active galaxies with gamma-ray, X-ray, UV, optical, IR and submm/mm to have the overall multiwavelength understanding on these objects.

Keywords: *radio sources, radio flux, optical flux, absolute magnitudes.*

Radio and optical variability of radio variables sources

NVSS and FIRST radio catalogues have been cross-matched. Our principle is to take into account positional errors for individual sources, and we have applied similar to our previous research method. In the FIRST catalogue there is no information on positional errors for each source, that is why 5 arcsecond as errors for all sources is adopted. In NVSS catalogue, each source is given with its individual positional error. We have created a software through which cross-correlations are done. This software allows considering positional errors for each source individually and we have taken associations having coordinate differences between counterparts not exceeding 3σ (calculated using both σ-s from NVSS and FIRST). As a result, we have obtained 556,282 associations between NVSS and FIRST.

Our main task is the revelation of the variability of radio sources in radio wavelengths. For variability criteria, we will take into account those radio sources which have associations within less than 3σ of the positional errors and for which the second association is 2 times farther than the first one. The systematic shift (SS) between fluxes of NVSS and FIRST catalogues was considered. We counted SS between these catalogues to get rid of systematic errors that could appear due to different flux calibration. As FIRST accuracy is higher, we have shifted NVSS using SS. The first step that was accomplished is computing systematic shift (SS) for fluxes between NVSS and FIRST (SS = 0.765 mJy).

Having 6301 radio sources that have radio variability, we try to check how many of these sources are optically variable. To understand how radio variability correlates with optical one, these radio variable sources with POSS1 and POSS2 based optical catalogues are cross correlated: APM, USNO A2.0, USNO B2.0, and GSC 2.3.2. To get rid of photometric measurements systematic effects, the systematic shifts between these catalogues were counted. In the next step, the average magnitudes in POSS1 and POSS2 both for red and blue were counted. Having this result, then we have counted the shift of each magnitude from the average for each source and averaged for each catalogue.

These two methods complement each other, as in general small magnitude differences may be a reason for doubtful variability, but relative σ numbers are important to check it additionally. Having ΔB, ΔR, B_r and R_r, all sources in variability categories have been divided. For each formula, we have one category. In We build the distribution of ΔB and ΔR to have an understanding of possible breaks for ΔB and ΔR.

*abrahamyanhayk@gmail.com

doi:https://doi.org/10.52526/25792776-22.69.2-340

Two fractures are seen (at 1.5 and at 2.5 for ΔR, at 1.45 and at 2.51 for ΔB). Using these breaks, the categories by ΔB and ΔR are limited. Thus, there are 2425 radio sources which have both radio and optical variability. For each source, we have four means for understanding their variability and for each source, based on this we give variability category flags from 1 to 3. For a detailed picture of variability of these sources, 4 category flags are counted together. We give in the list of 2425 NVSS/ FIRST radio sources showing optical variability based on POSS1 and POSS2 epoch measurements.

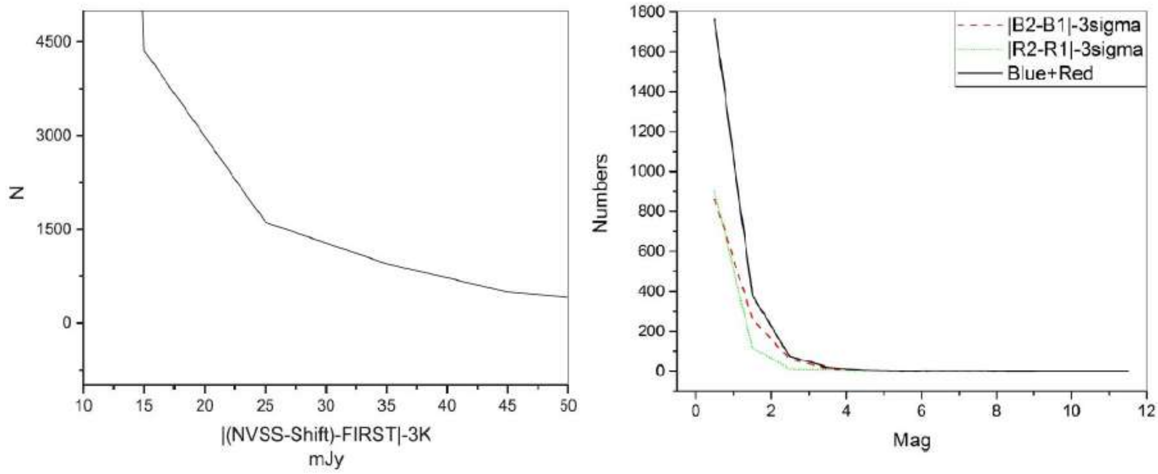

Figure 1. a)ΔF distribution, b)Distribution of ΔB and ΔR.

Optical classification

In a number of our papers, we have used the same approach to classify thousands of spectra for active galaxies from various sample. Our approach is based on BPT diagrams, however we use most recent options of such diagrams. To guarantee the best accuracy and consider all possible details, we classify the objects in several ways and then consider all obtained types and subtypes:

- By the **1st diagnostic diagram** (DD1) using line intensity ratios [OIII]/H$_\beta$ vs. [OI]/H$_\alpha$,
- By the **2nd diagnostic diagram** (DD2) using line intensity ratios [OIII]/H$_\beta$ vs. [NII]/H$_\alpha$,
- By the **3rd diagnostic diagram** (DD3) using line intensity ratios [OIII]/H$_\beta$ vs. [SII]/H$_\alpha$,
- By comparison and using the **1st, 2nd and 3rd diagnostic diagrams** simultaneously,
- **By eye** (considering all features and effects). Very often, the diagnostic diagrams do not give full understanding for all objects and only eye can reveal some details.

As it is known, the diagnostic diagrams are for classification of narrow line ratios, i. e. objects having Sy1 features (broad lines), QSOs, etc. cannot be classified by them. In addition, the classification by eye has been done in comparison with the classification by diagnostic diagrams because not all objects appear on them due to lack of line measurements data. The eye examination of spectra allows revealing broad lines (for Seyfert subtypes Sy1.0-Sy1.9), estimate (and later measure) the width of broad lines and reveal FeII lines on both sides of H$_\beta$ to identify Narrow Line Seyfert 1s, etc., as well as classifying absorption line objects. On diagnostic diagrams, for Sy/LINER separation, we have used the criteria: [OIII]/H$_\beta > 4$, and to distinguish AGN from HII, we have used the criteria: [SII]/H$_\alpha > 2/3$ and [OI]/H$_\alpha > 0.1$. For all classifications, we have used the following lines:

- **Absorption lines**: NaI 5890/5896 doublet, MgI 5175, Hydrogen Balmer lines (mostly H$_\alpha$ and H$_\beta$), etc.
- **Emission lines**: most prominent are Hydrogen Balmer series lines (H$_\alpha$ 6363, H$_\beta$ 4861, H$_\gamma$ 4340, etc.), Oxygen lines ([OIII] 4959 and 5007, [OII] 3727 and [OI] 6300), Nitrogen lines ([NII] 6548 and 6484), Sulfur doublet ([SII] 6716/6731), Helium lines HeI 5876 and HeII 4686, etc.

doi:https://doi.org/10.52526/25792776-22.69.2-340

Summary and conclusions

We have carried out a cross-correlation of NVSS and FIRST catalogues to distinguish sources which have large differences of fluxes at 1400 MHz. We have selected 6301 radio sources with flux difference at least 15 mJy. Further investigation of these radio sources led to a new sample of radio sources, which have high optical variability. The main results of our study are the cross-correlation of NVSS and FIRST radio catalogues at 1.4 GHz and construction of a large sample of 79,382 radio variable sources, including 6301 with radio variability >15 mJy flux differences between NVSS and FIRST, 1699 with flux differences >50 mJy and 260 with flux differences >200 mJy, revelation of 2425 optically variable objects out of 6301 radio sources, revelation of 1206 (19%) active galaxies out of 6301 radio sources, and compilation of a list of 619 (25.5%) out of 2425 radio sources with at the same time having optical variability (including many AGN among them).

So, we have developed a fine classification scheme for active galaxies and accordingly carried out classification of the SDSS spectra for 1864 radio variable sources.

The most important results related to the classification of active galaxies and other results are:

1) Introducing the fine classification scheme for active galaxies using SDSS spectroscopy. This became possible for the first time, as SDSS quality spectra were not available before. Detailed description of the types and subtypes of active galaxies is given, including many of them **introduced for the first time**;

2) Optical spectroscopic classification of the SDSS spectra for 1864 radio variable sources, out of which 1746 appeared to be genuine extragalactic objects. Revealing many new QSOs, Seyferts, LINERs and other active galaxies;

3) Calculating absolute magnitudes and luminosities for the sample objects. Estimation of average M and L and ranges of their values for various types of active galaxies;

4) Building colour-magnitude and colour-colour diagrams in both optical wavelengths (using SDSS photometry) and IR (using AllWISE photometry) to follow the location of different types of active galaxies on these diagrams.

Acknowledgements

The work was supported by the Science Committee of RA, in the frames of the research project No. 21AG-1C053 Revelation of the early stages of galaxy evolution by means of multiwavelength study of active galaxies" (2021-2026) and ANSEF grant PS-astroex-2597 "Search and Studies of High Luminosity X-ray Galaxies (2022-2023)".

References

Abrahamyan H. V., Mickaelian A. M., Knyazyan A. V., 2015, Astronomy and Computing, 10, 99

Abrahamyan H. V., Mickaelian A. M., Paronyan G. M., Mikayelyan G. A., Gyulzadyan M. V., 2018a, Astronomy and Computing, 25, 176

Abrahamyan H. V., Mickaelian A. M., Paronyan G. M., Mikayelyan G. A., 2018b, Izvestiya Glavnoj Astronomicheskoj Observatorii v Pulkove, 222, 5

Abrahamyan H. V., Mickaelian A. M., Paronyan G. M., Mikayelyan G. A., Gyulzadyan M. V., 2019a, Communications of the Byurakan Astrophysical Observatory, 66, 1

Abrahamyan H. V., Mickaelian A. M., Paronyan G. M., Mikayelyan G. A., 2019b, Astronomische Nachrichten, 340, 437

Abrahamyan H. V., Mickaelian A. M., Paronyan G. M., Mikayelyan G. A., 2020, Astrophysics, 63, 322

Abrahamyan H. V., Mickaelian A. M., Paronyan G. M., Mikayelyan G. A., Sukiasyan A. G., 2021, Communications of the Byurakan Astrophysical Observatory, 68, 441

Mickaelian A. M., Abrahamyan H. V., Paronyan G. M., Mikayelyan G. A., 2021a, Frontiers in Astronomy and Space Sciences, 7, 82

Mickaelian A. M., Andreasyan R. R., Abrahamyan H. V., Paronyan G. M., Mikayelyan G. A., Sukiasyan A. G., Mkrtchyan V. K., 2021b, Astronomical and Astrophysical Transactions, 32, 331

Mickaelian A. M., Abrahamyan H. V., Mikayelyan G. A., Paronyan G. M., 2022, Communications of the Byurakan Astrophysical Observatory, 69, 10

Paronyan G. M., Mickaelian A. M., Abrahamyan H. V., Mikayelyan G. A., 2020, Astrophysics, 63, 166

doi:https://doi.org/10.52526/25792776-22.69.2-340

New late-type stars found in the BAO Plate Archive

G. R. Kostandyan [*], H. V. Abrahamyan, G. A Mikayelyan, and G. M Paronyan

INAS RA V. Ambartsumian Byurakan Astrophysical Observatory (BAO), Byurakan 0213, Aragatzotn Province, Armenia

Abstract

The BAO Plate Archive low-resolution spectral plate centered $\alpha = +04^h$ $\delta = +24^0$ is analyzed to find new late-type stars. 25 new late-type stars have been detected. We have performed cross-correlations with GAIA DR3, USNO-B1.0, 2MASS, AllWISE, IRAS PSC/FSC, AKARI and SDSS. For new detected objects, we present luminosity classes estimated from Gaia DR3 and 2MASS photometry and available proper motions. The majority of the objects are red giants.

Keywords:*surveys-stars: late-type -stars, dwarf M stars, TESS and Gaia data*

1. Introduction

Byurakan Astrophysical Observatory (BAO) Plate Archive is one of the largest astronomical archives in the world. BAO archive holds some 37.000 astronomical plates, films or other carriers of observational data. It is the results of decades' hard work of Armenian astronomers and the work of BAO telescopes and other expensive equipment, as well as the results of their activities. A project on Digitization of BAO Plate Archive and creation of BAO Interactive Astronomical Database (shortly BAO Plate Archive project, BAO PAP) was aimed at preservation of BAO valuable observational material accumulated during 1947-1991 (Mikayelyan et al., 2021). The BAO Plate Archive low-resolution spectral plate centered at $\alpha = +04^h$ $\delta = +24^0$ were obtained at the Byurakan Astrophysical Observatory (BAO) on 26/27 September 1970 with the 1m Schmidt telescope, equipped with a 40 prism. Kodak IIaE emulsion was used with R filter.

2. New BAO Plate Archive late-type stars.

M-type stars are easily distinguished owing to the absorption bands of molecular TiO at wavelengths of $\lambda\lambda$ 4584, 4762, 4954, 5167, 5500, 6200, 7054, 7589, 8300, 8432 Å(Gahm, 1970, Nassau et al., 1964). Low-resolution spectral plate was analyzed with the help of standard image analysis software (FITSVIEW and SAOIMAGE ds9) and Aladin v11.0. This visualization allows us to detect red and faint candidate stars. Figure 1 shows examples of low-resolution spectral shapes for the newly discovered 10 objects on BAO Plate Archive which are M-type stars. Objective-prism low resolution spectra show the presence of the TiO molecule absorption bands at wavelengths at 7054, 7589 Å.

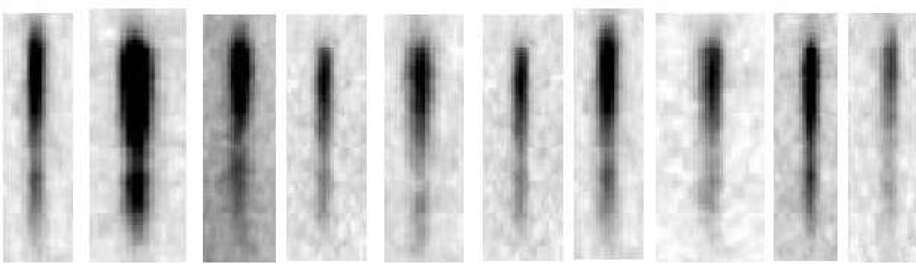

Figure 1. Low-resolution spectral shapes for the newly discovered 10 objects on BAO Plate Archive.

[*]kostandyan@bao.sci.am, Corresponding author

doi:https://doi.org/10.52526/25792776-22.69.2-343

Table 1. Gaia DR3 and 2MASS photometric data for the 12 new late-type stars

RAJ2000 "h:m:s"	RAJ2000 "d:m:s"	2MASS	J mag	H mag	K mag	G mag	BP-RP mag
04 36 42.24192	+25 55 11.7516	04364224+2555117	6.83	5.66	5.26	10.65	3.71
04 25 10.51704	+22 15 48.8268	04251051+2215488	7.44	6.45	6.06	11.04	3.43
04 30 02.96328	+22 16 13.6992	04300296+2216136	6.08	5.08	4.71	9.78	3.63
04 40 42.96000	+22 38 12.4332	04404296+2238124	4.61	3.55	3.08	9.23	4.80
04 29 55.31208	+22 58 57.9396	04295531+2258579	6.4	5.25	4.72	11.35	5.30
04 32 58.15776	+25 25 32.4480	04325815+2525324	9.53	8.42	8.00	13.07	3.39
04 26 18.33552	+24 05 21.6672	04261833+2405216	7.71	6.7	6.37	11.31	3.48
04 29 01.60248	+25 52 48.5472	04290160+2552485	8.11	7.12	6.72	11.89	3.79
04 26 30.07320	+25 53 44.5344	04263007+2553445	5.89	4.79	4.13	10.57	4.9
04 34 33.31008	+24 43 12.0252	04343331+2443120	7.16	6.06	5.59	11.49	4.69
04 36 35.13144	+25 26 42.5148	04363513+2526425	8.63	7.55	7.12	12.32	3.10
04 25 58.33440	+22 40 04.5984	04255833+2240045	8.15	7.14	6.79	11.61	3.22

3. Gaia DR3 and 2MASS photometry

Table 1 presents the Gaia DR3 and 2MASS (Two Micron All-Sky Survey) JHKs photometric data for the 12 new late-type stars (Brown et al., 2021). To discriminate dwarf/giant luminosity class, we used the traditional J-H vs. H-Ks color-color plots (Bessell & Brett, 1988). This diagram clearly shows that the majority of the new objects are red giants.

4. Summary

25 new late-type stars have been found in the BAO Plate Archive. We present luminosity classes estimated from Gaia DR3 and 2MASS photometry and available proper motions. The majority of the objects are red giants.

Acknowledgements

This research has made use of results from the SAO/NASA Astrophysics Data System Bibliographic Services, as well as the SIMBAD and VizieR databases, operated at CDS, Strasbourg, France, and Two Micron All Sky Survey, which is a joint project of the University of Massachusetts and the Infrared Processing and Analysis Center, funded by NASA and NSF.This work has made use of data from the European Space Agency (ESA) mission *Gaia* (https://cosmos.esa.int/gaia), processed by Gaia Data Processing and Analysis Consortium (DPAC, https://www.cosmos.esa.int/web/gaia.dpac.consortium).

References

Bessell M. S., Brett J. M., 1988, Publ. Astron. Soc. Pac. , 100, 1134

Brown et al., 2021, Astron. Astrophys. , 650, C3

Gahm G. F., 1970, Astron. Astrophys. , 4, 268

Mikayelyan G. A., et al., 2021, Communications of the Byurakan Astrophysical Observatory, 68, 97

Nassau J. J., Stephenson C. B., Caprioli G., 1964, Astrophys. J. , 139, 864

doi:https://doi.org/10.52526/25792776-22.69.2-343

Detailed investigation of QSO 1055+01

Mahtessian L.A. [1], Hovhannisyan M.A.*[1], Karapetyan R.A.[1,2], Amiraghyan L.A.[1,2], Grigoryan M.L.[1], and Mahtessian A.P.[3]

[1]NAS RA Institute of Applied Problems of Physics, Armenia
[2]Yerevan State University, Armenia
[3]NAS RA V. Ambartsumian Byurakan Astrophysical Observatory (BAO), Armenia

Abstract

QSO 1055+01 studies show that this extended quasar is a very, powerful, active and variable extragalactic source, with many compact sources around. We shown that the distribution of extragalactic sources around is homogenous with high density.

Keywords: *radio galaxy, quasar, homogeneous, inhomogeneous*

1. Introduction

Being a sufficiently powerful source across the entire spectrum of electromagnetic waves, including the radio range, detailed studies of QSO 1055+01 can reveal a number of cosmic phenomena that other sources are less likely to detect. In addition, there are many compact sources around this object. Considering the distance of QSO 1055+01 (d is about 4000 Mps, v=267886 km/s, z=0.89357), the apparent magnitude (m_v=16.68), and the angular size (6.74 arcsec), one can say that it has the size of a supergiant galaxy. Obviously, this is a fairly powerful object that has a significant impact on the immediate environment. The above is based on the results of numerous studies (Healey et al., 2008, Hutchings & Bianchi, 2010, Plotkin et al., 2008, Slee, 1995, Wang et al., 2016), which indicate that QSO 1055+01 is a powerful, young, rather extensive and very active source.

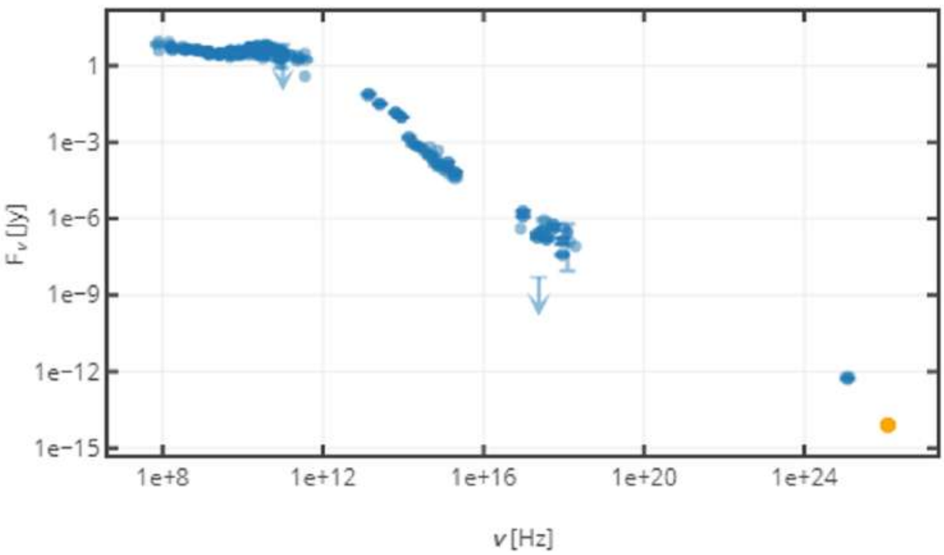

Figure 1. The spectrum of quasar 1055+01

*martik.hovhannisyan1956@gmail.com, Corresponding author

doi:https://doi.org/10.52526/25792776-22.69.2-345

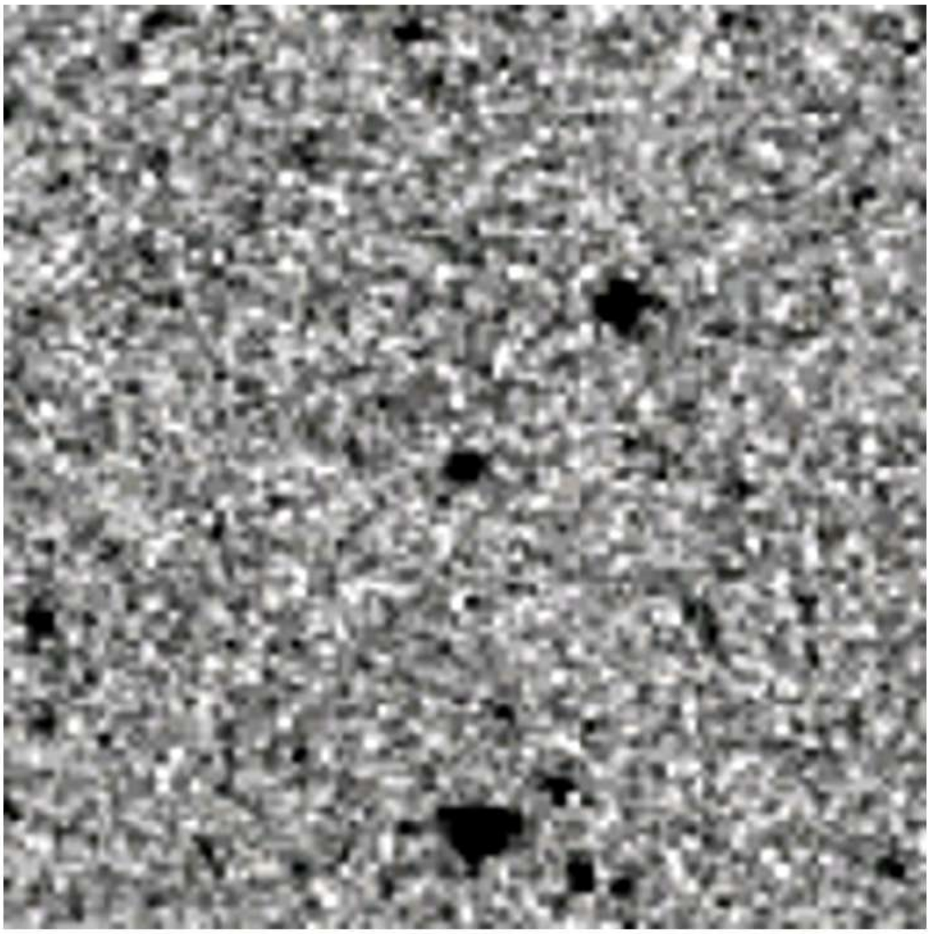

Figure 2. The optical image of quasar 1055+01

2. Quasar 1055+01 and its surroundings

The data of numerous observations of QSO 1055+01 are presented in Figure 1, where it is clearly seen that the spectrum of the radio source of the quasar in the radio range is flat from 70 MHz to 700 GHz. This indicates that the radio source is very young. As the frequency increases from the optical range to the X-ray range, the intensity decreases and further decreases at higher frequencies. This fact shows that sources emitting at low frequencies are different from sources emitting at high frequencies. Images obtained from optical observations suggest that the quasar is compact and has a diffuse component (see Figure 2). Quasar 1055+01 has strong radiation, powerfully compact and widespread components, as well as near and distance sources. Of greatest interest is the distance source, its features. Since the observational data of distant sources, due to their distance, are data of a younger age, therefore it is possible to see phenomena that are specific to young and active sources. The studies of the surroundings of the quasar 1055+01 are indeed very interesting and with the help of these studies it is possible to find out the mutual influence of the quasar and its surroundings. Figure 3 shows the distribution of galaxies around this quasar. It can be seen from the figure that the galaxies in that range are distributed in such a way that it can be said that the distribution is very close to the state of homogeneous distribution despite the fact that the number of galaxies in some range is small (Figure 8). The distribution of galaxy clusters and quasars is fully sufficient to assert that these sources are distributed evenly around the quasar and the entire range is homogeneous (Figures 4, 5, 6, and 7).

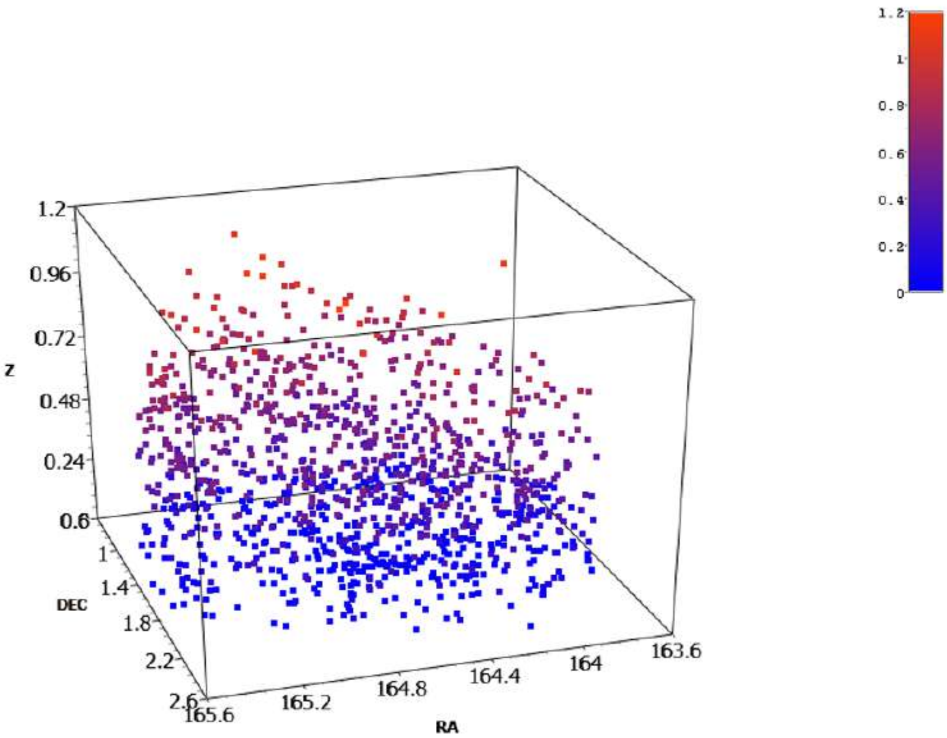

Figure 3. The dimensional distribution of galaxies

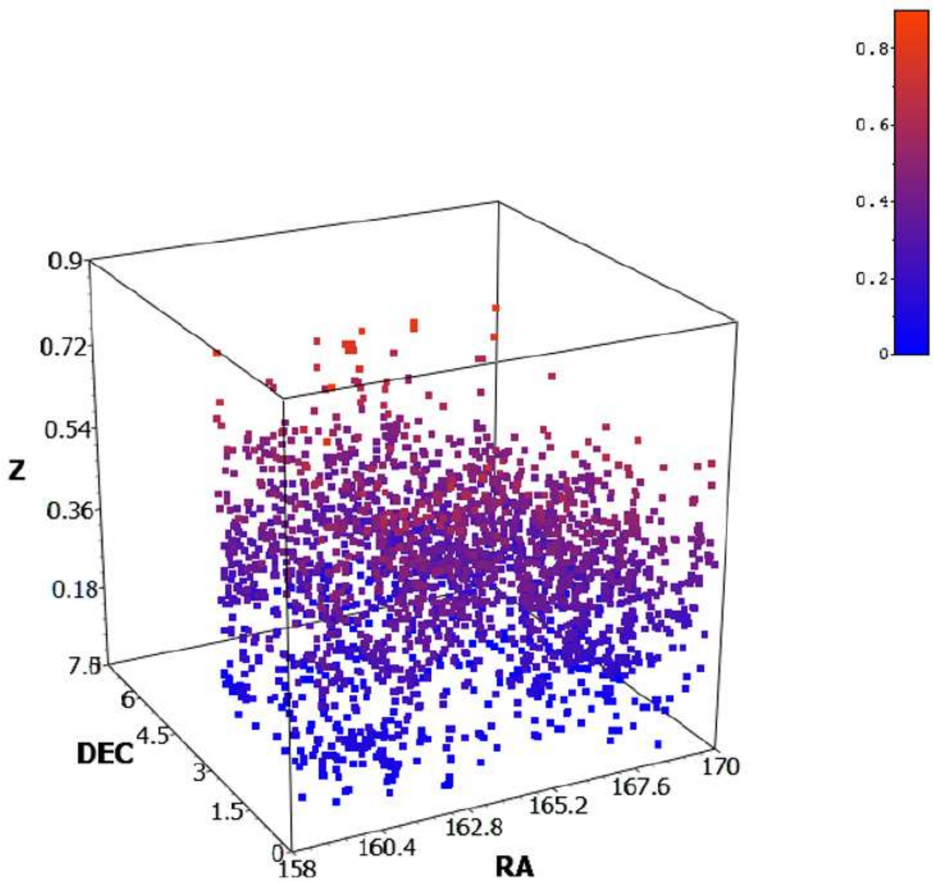

Figure 4. The dimensional distribution of galaxy clusters

doi:https://doi.org/10.52526/25792776-22.69.2-345

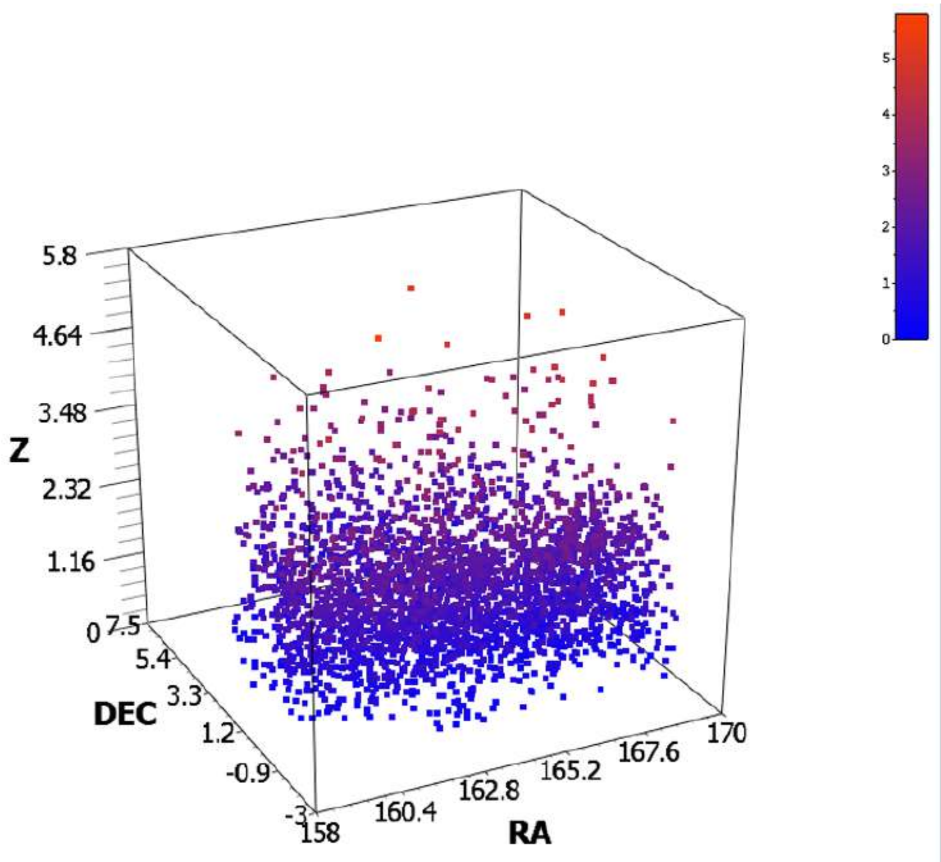

Figure 5. The dimensional distribution of quasars

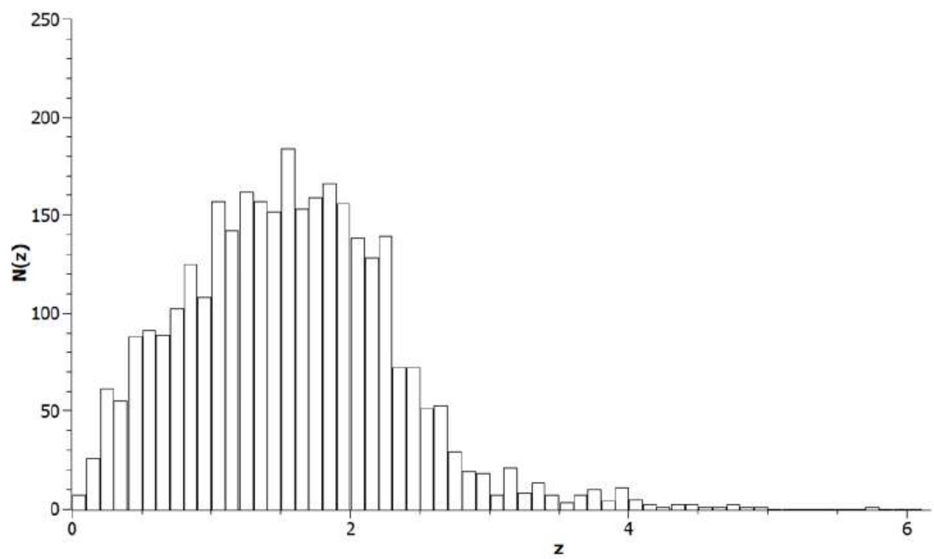

Figure 6. The distribution of redshift of quasars

doi:https://doi.org/10.52526/25792776-22.69.2-345

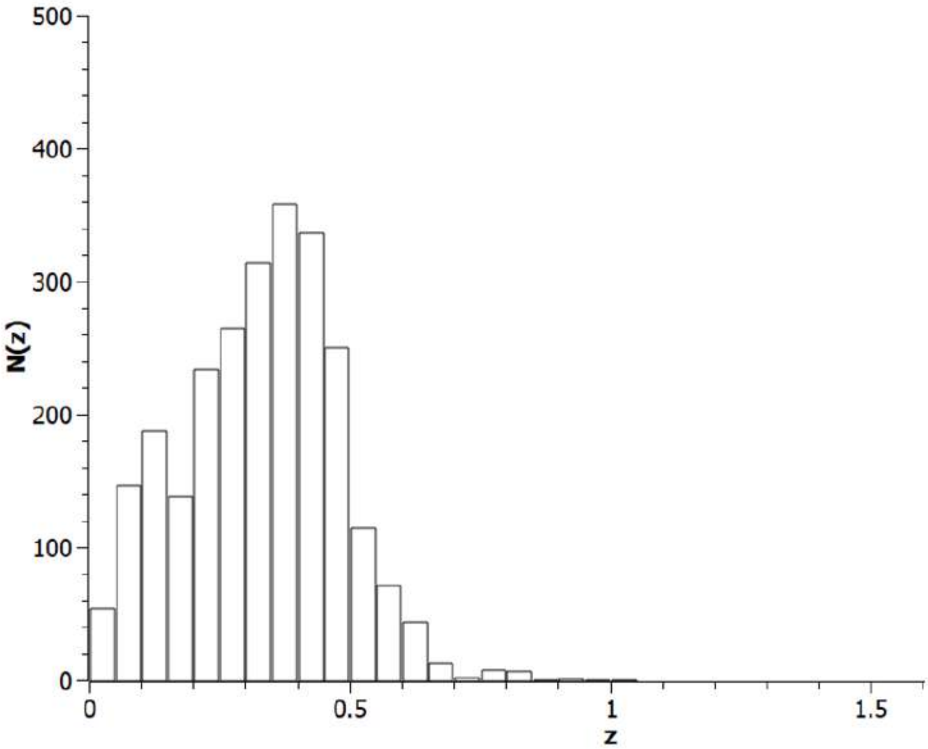

Figure 7. The distribution of redshift of galaxy clusters

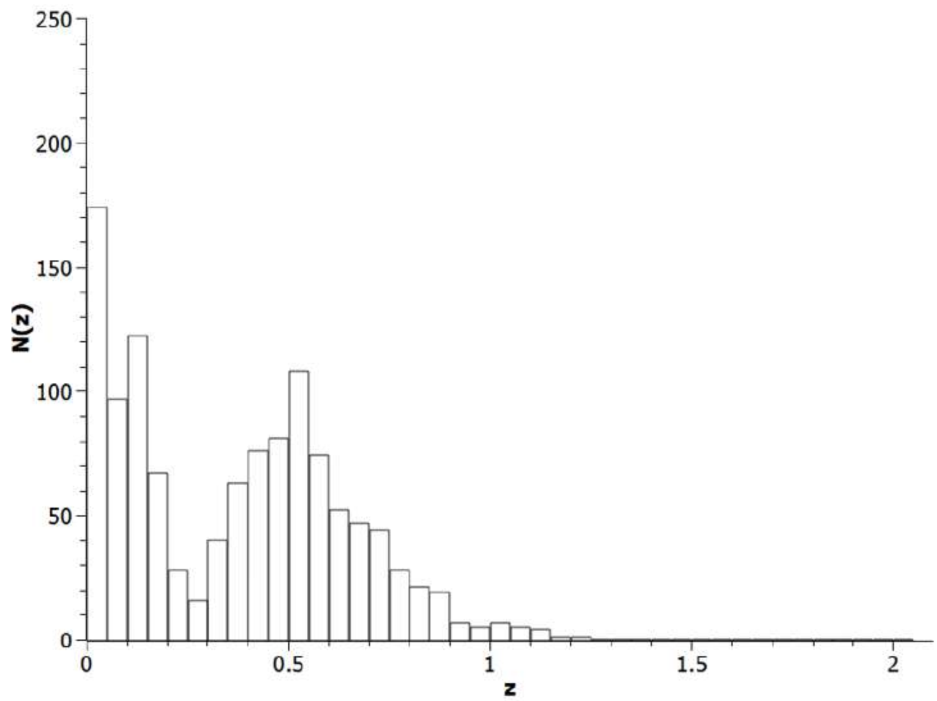

Figure 8. The distribution of redshift of galaxy

doi:https://doi.org/10.52526/25792776-22.69.2-345

References

Healey S. E., Romani R. W., Cotter G., et al. 2008, Astrophys. J. Suppl. Ser. , 175, 97

Hutchings J. B., Bianchi L., 2010, Astron. J. , 140, 1987

Plotkin R. M., Anderson S. F., Hall P. B., et al. 2008, Astron. J. , 135, 2453

Slee O. B., 1995, Aust. J. Phys., 48, 143

Wang T. S., Liu J., Qiu Y., et al. 2016, Astrophys. J. Suppl. Ser. , 224, 1

doi:https://doi.org/10.52526/25792776-22.69.2-345

Search and study of young infrared stellar clusters

N. Azatyan *

Byurakan Astrophysical Observatory, 0213 Aragatsotn Prov., Armenia

Abstract

The "bricks" of the Galactic disc are giant molecular clouds, which are birthplaces of stellar population. Therefore, there is a genetic connection between young stellar objects (YSOs) and their surrounding Interstellar Medium (ISM). The thesis is devoted to a search for young stellar clusters in the vicinity of IRAS sources and a detailed study of three selected star-forming regions: IRAS 05137+3919, 05168+3634, and 19110+1045, which includes determining the parameters of the ISM based on far-infrared data, the identification and classification of YSOs using color-color and color-magnitude diagrams, the modeling of stellar parameters, and the construction and interpretation of the luminosity functions. It is likely that the three young stellar clusters were formed under different scenarios. The age spread of the IRAS 05137+3919 and IRAS 05168+3634 regions is much larger, and, therefore, we concluded that the stellar population is formed as a result of independent condensations. The age spread of the IRAS clusters' members in the third region, which is a pair of ultra-compact HII regions (UCHIIs), namely G45.12+0.13 and G45.07+0.13, is small. The small age spread suggests that the clusters may originate from a single triggering event. Moreover, high-mass YSOs were obtained only in the G45.07+0.13 and G45.12+0.13 UCHII regions where the ISM initial density was higher and the star formation proceeded relatively quickly.

Keywords: *stars: pre-main sequence – Stars: luminosity function – Infrared: stars – radiative transfer*

1. Introduction

The star formation process continues at all stages of the evolution of our and other galaxies, including the present stage (Ambartsumian, 1947), and is one of the most important processes which provides the observational output of the galaxies. The "bricks" of the Galactic disc are giant molecular clouds, which are birthplaces of stellar population. There is a large number of observation data, which witness that the star formation process has consecutive nature (Soderblom, 2010). Therefore, the spatial distribution of YSOs in clusters and the quantitative ratio between YSOs with different masses and ages are essential for understanding the evolutionary history of a cluster itself. However, such studies have been seriously hampered by the fact that galactic clusters form in giant molecular clouds and during their formation and earliest stages of evolution are completely embedded in molecular gas and dust, and thus obscured from view. During the last two decades, the development of infrared (IR) astronomy has dramatically improved this situation providing astronomers the ability to survey and systematically study embedded clusters within molecular clouds.

Embedded stellar clusters, which are still surrounded by their progenitor molecular clouds are of particular interest to understand which properties of stellar clusters are related to their origins and which are derived from subsequent evolution (Lada & Lada, 2003). There is also a certain relationship between the properties of the stellar population of young clusters and the process of their formation. If the star-formation in clusters is triggered, the age spread of stars in the cluster should be small, while in self-initiated protocluster condensations, the individual clumps should have a larger age spread (e.g. Preibisch, 2012).

Nowdays, it is known that there is a genetic connection between YSOs and their surrounding ISM. Consequently, the study of ISM in conjunction with the study of embedded in them YSOs is very important for understanding the process of formation and evolution of the stellar population in galaxies (e.g. González-Samaniego & Vazquez-Semadeni, 2020). This necessitates an integrated approach to study of star-forming regions, which implies a determination and detailed study of the main properties of already formed young

*nayazatyan@bao.sci.am

doi:https://doi.org/10.52526/25792776-22.69.2-351

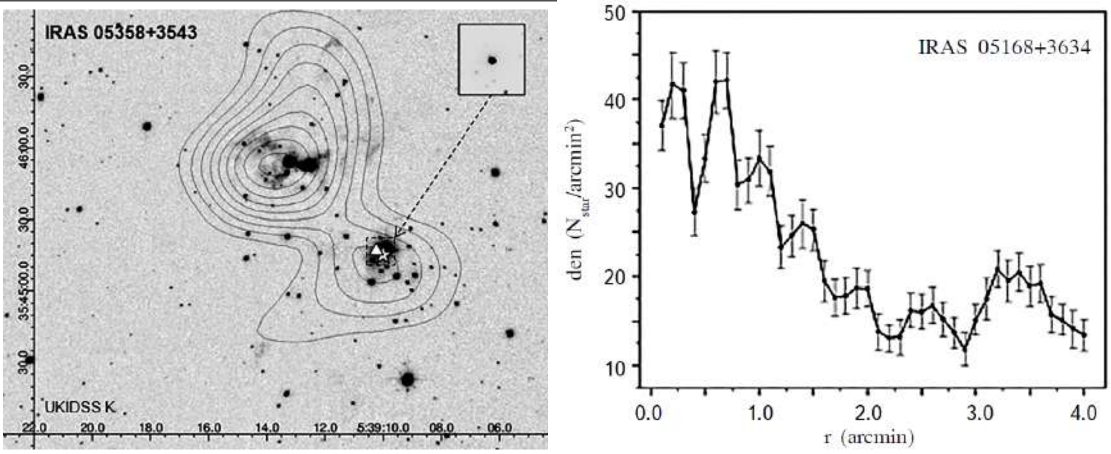

Figure 1. (*Left*) NIR images and isodenses of IRAS 05358+3543 star-forming region. IRAS and MSX sources are indicated by stars and triangles, respectively. (*Right*) Radial distribution of the stellar density relative to IRAS 05168+3634 source. Vertical lines are standard errors.

stellar clusters (density, mass function, evolutionary age distribution, etc.) and the environment (density, temperature, etc.). This approach was taken in this work.

The thesis presents the results of both a search for young stellar clusters in the vicinity of IRAS sources and a detailed study of three selected star-forming regions: IRAS 05137+3919, 05168+3634, and 19110+1045. The main selection criteria of these three regions are their considerable extent and multi-component complex structure, which implies the presence of several local nests of star formation. Besides, the preliminary studies have shown that the star-forming regions differ in their stellar composition and structural properties. All three regions, however, despite their certain differences, are united by one aspect - they are regions of active star formation. For all regions a detailed study was conducted, which includes the following topics: 1) determination of the parameters of ISM, namely the distribution of N(H_2) hydrogen column density and T_d dust temperature; 2) the search for young stellar clusters; 3) identification of the clusters' members using their infrared properties; 4) investigation of the structural properties of the young stellar clusters; 5) determination of the age and age spread of the clusters' members; 6) construction of the Luminosity Functions and Mass Functions for the clusters. This thesis is based on the papers Azatyan (2019), Azatyan & Nikoghosyan (2018), Azatyan et al. (2016, 2020, 2022), Nikoghosyan & Azatyan (2014), Nikoghosyan et al. (2020, 2021).

We have organised the paper as follows. Section 2 describes the used data; in Section 3 we present the methods; in Section 4, we analyse the stellar population in the regions. Finally, the study results are summarised in Section 5.

2. Used data

We used data covering a wide range of near- to far-infrared (NIR, FIR) wavelengths. The first dataset is the archival NIR photometric data in the J, H, and K bands of the Galactic Plane Survey DR6 (UKIDSS GPS, Lucas et al., 2008) with a resolution of $0.1''$/px, which is one of the five surveys of the UKIRT Infrared Deep Sky Survey (UKIDSS). This survey is complete to approximately 18 mag in the K band and provides a percentage probability of an individual object being a star, galaxy, or noise. In the absence of UKIDSS GPS data, we used the data of the Two Micron Sky Survey (2MASS, Cutri et al., 2003).

Archival MIR observations were obtained from the Spitzer Space Telescope under the Galactic Legacy Infrared Midplane Survey Extraordinaire (GLIMPSE) and GLIMPSE 360 programs (Churchwell et al., 2009). GLIMPSE observations were taken using the *Spitzer* Infrared Array Camera (IRAC, Fazio et al., 2004) centred at approximately 3.6, 4.5, 5.8, and 8.0 μm with a resolution of $0.6''$/px. At longer wavelengths, we used data from a survey of the inner Galactic plane using the Multiband Infrared Photometer for *Spitzer* (MIPSGAL). The survey field was imaged in 24 and 70 μm passbands with resolutions of $6''$/px and $18''$/px, respectively (Carey et al., 2009); however, only 24 μm data were available for the studied star-forming regions.

We also used Wide-field Infrared Survey Explorer (WISE, Wright et al., 2010) data in the 3.4, 4.6, 12, and 22 μm bandpasses. We used the Midcourse Space Experiment (MSX, Price et al., 2001) full plane

doi:https://doi.org/10.52526/25792776-22.69.2-351

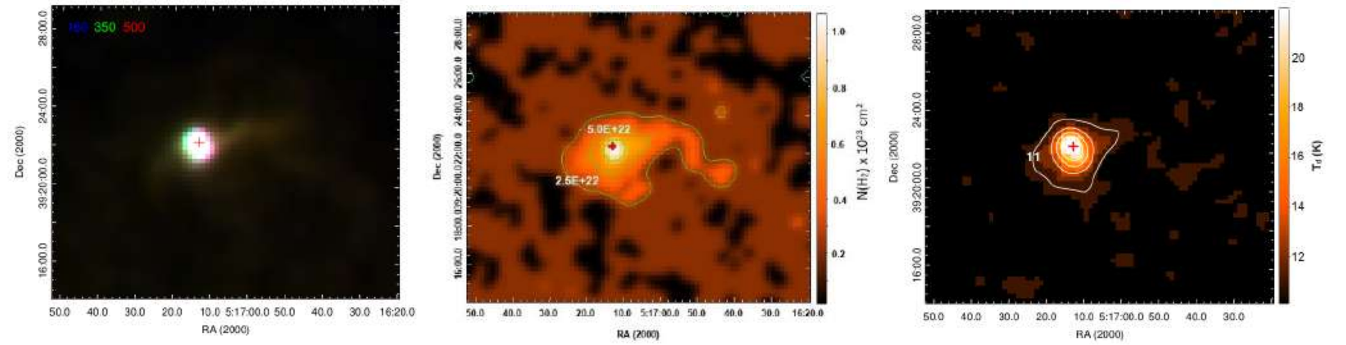

Figure 2. (*Left*) Colour-composite image of IRAS 05137+3919 star-forming region: 160 μm (blue), 350 μm (green), and 500 μm (red). (*Middle*) Column density map of the region. The external isodense corresponds to the 2.5x10^{22} cm^{-2} value and the interval between isodences is also 2.5x10^{22} cm^{-2}. (*Right*) Dust temperature of the region. The external isotherm corresponds to 11 K and interval between isotherms is 2.5 K. The position of the IRAS source is indicated by red cross.

survey data in the 8.28, 12.13, 14.65, and 21.3 μm bands.

To study gas and dust, as well as deeply embedded point sources, we used FIR observations, in the 70–500 μm range, obtained with the Photodetector Array Camera and Spectrometer (PACS, Poglitsch et al., 2010) and the Spectral and Photometric Imaging Receiver (SPIRE, Griffin et al., 2010) on board the 3.5 m *Herschel* Space Observatory (Pilbratt et al., 2010). For our analyses, we used photometric data and images from the PACS 70 and 160 μm catalogues, in addition to *Herschel* infrared Galactic Plane Survey (Hi-GAL, Molinari et al., 2016) data at 70, 160, 250, 350, and 500 μm. The corresponding Herschel half-power beamwidth (HPBW) values are 5.0″ at 70 μm, 11.4″ at 160 μm, 17.8″ at 250 μm, 25.0″ at 350 μm, and 35.7″ at 500 μm. The Infrared Astronomical Satellite (IRAS, Neugebauer et al., 1984) Point Source Catalog v2.1 (PSC) data was used. The IRAS mission performed an unbiased, sensitive all-sky survey at 12, 25, 60, and 100 μm. *Herschel* PACS and Hi-GAL data have better resolution than the IRAS PSC data. Therefore, we used the data from the Hi-GAL 70, 160 μm, or *Herschel* PACS 70, 160 μm catalogs instead of IRAS 60 and 100 μm data.

3. Methods

The thesis contains two main scientific directions, namely study of ISM and YSOs. To study gas and dust, as well as deeply embedded point sources, we used FIR observations in the 70–500 μm range since this wavelength range covers the peak of the spectral energy distribution of cold dust emission. Modified single-temperature blackbody fitting was subsequently carried out to obtain the important ISM parameters such as the hydrogen column density (N(H_2)) and the dust temperature (T_d).

To select and study the potential stellar members of the star-forming regions, we used NIR, mid-infrared (MIR), and FIR data. The identification of stellar objects was performed with GPS UKIDSS-DR6 as the main catalogue, and then other MIR and FIR catalogues were cross-matched with it within 3 σ of the combined error–matching radius. We selected objects with a <30 % probability of being noise and a magnitude of K $<$ 18.02 mag, taking into account the K band limit of the UKIDSS survey. In addition, we removed objects with zero errors of measured magnitudes in the J, H, and K bands. Since, the presence of circumstellar discs and envelopes cause an IR excess of a YSO, therefore YSO candidates were identified based on their position in colour–colour (c-c) IR diagrams. The choice of colours depends on the available data. To confirm the selected YSOs and to determine their parameters, we constructed their SEDs and fitted them with the radiative transfer models of Robitaille et al. (2007).

4. Results and Discussion

4.1. Selection of the regions

At first, we carried out the search and study of compact clusters in 20 star-forming regions from the list of Varricatt et al. (2010). In order to detect clusters and to refine their sizes in considered 20 regions,

doi:https://doi.org/10.52526/25792776-22.69.2-351

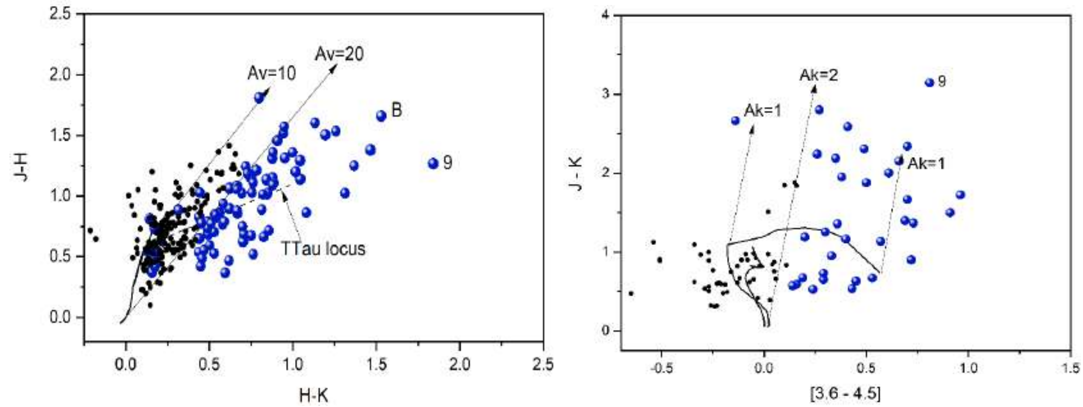

Figure 3. (*Left*) (J-H) vs. (H-K) and (*Right*) (J-K) vs. [3.6]-[4.5] c-c diagrams for IRAS 05137+3919 star-forming region. Not all non-classified objects (black circles) are presented in these diagrams. Southwest component B of CPM 15 YSO and the reddest object with number 9 are labeled.

we constructed surface and radial stellar density distribution and around each IRAS source using NIR and MIR photometric data. Figure 1 shows the examples of surface stellar density distribution map (left panel) and radial density distribution of stars (right panel) in two different star-forming regions. We have also compared the LF of the stellar objects in the clusters and their fields using the Kolmogorov-Smirnov test. We were able to detect compact clusters in 12 and 4 regions based on NIR and MIR data, respectively. This represents 80% of the overall number of regions that were studied and is substantially higher than the results based on data from the 2MASS.

4.2. Regions for detail study

Among above mentioned 16 identified clusters, we selected three star-forming regions for a detailed study, namely IRAS 05137+3919, 05168+3634, and 19110+1045, which includes the study of both the stellar population and the ISM. The main selection criteria of these three regions are their considerable extent and multicomponent complex structure, which implies the presence of several local nests of star formation. The regions are little studied, but at the same time, there is sufficient observational data for their detailed study. Besides, our preliminary studies have shown that the star-forming regions differ in their stellar composition and structural properties. These star-forming regions are also of interest because they are located at large distances, which will allow us to test the capabilities of the databases at our disposal. All three regions, despite their certain differences, are united by one aspect - they are regions of active star formation.

A young stellar cluster located in the vicinity of IRAS 05137+3919 associated with the CPM 15 YSO. Different manifestations of active star formation have been observed in this region, such as maser emissions, as well as CO and H_2 outflows. Left panel of Figure 2 shows the colour-composite image covering the IRAS 05137+3919 star-forming region. The region stands out sharply in terms of brightness. Using the modified single-temperature blackbody fitting, we have determined the main parameters ($N(H_2)$ and T_d) of cold composing gas-dust matter in the region and their maps are presented in the middle and right panels of Figure 2. The $N(H_2)$ and T_d maps show that the star-forming region stands out sharply in terms of brightness with a relatively high density and temperature. The maxima of both $N(H_2)$ ($\sim$1.0x10^{23} cm^{-2}) and T_d (22 K) almost coincide with position of the IRAS source. Towards the periphery, both parameters decrease up to 2.2x10^{22} cm^{-2} and 11 K.

The radial distribution of stars density relative to the position of IRAS 05137+3919 confirmed the existence of a cluster in the vicinity of the IRAS source with 1.5′ radius. Within this radius, the stellar density (38 stars/arcmin^2) is twice the density of the field (19 stars/arcmin^2).

The selection of YSOs in the IRAS 05137+3919 star-forming region was based on two c-c diagrams, namely (J-H) versus (H-K) and (J-K) versus [3.6]-[4.5]. Figure 3 (left and right panels) shows the positions of 253 objects located within 1.5′ radius relative to the IRAS 05137+3919 source. Totally, we selected 84 YSOs (blue circles) based on these two c-c diagrams. This is almost 1.5 times greater than the earlier estimate of the cluster members (Faustini et al., 2009). Since stellar magnitudes in the *Spitzer* 3.6 and 4.5 μm bands are available for only 33 YSOs, we were able to obtain parameters of these YSOs using the SED fitting tool. The full tables of selected YSOs with their parameters are included in the thesis. The

doi:https://doi.org/10.52526/25792776-22.69.2-351

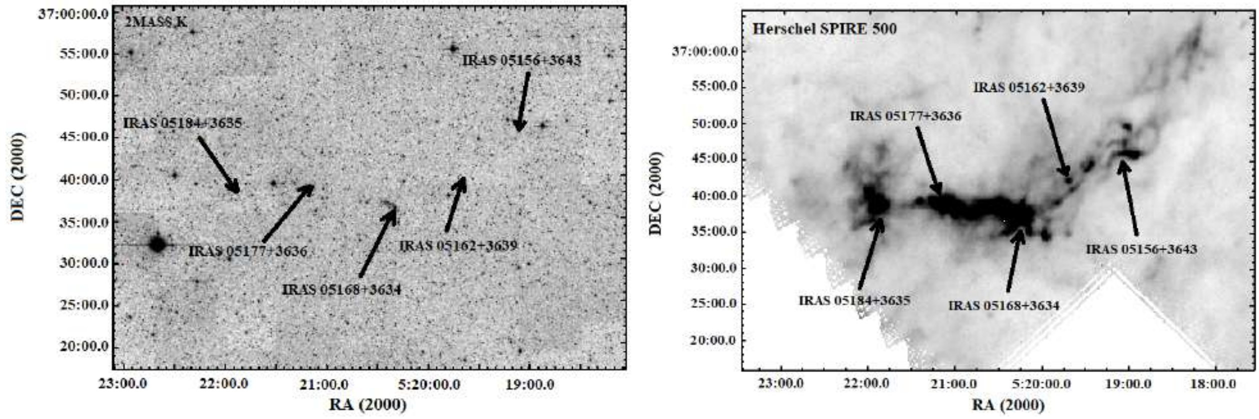

Figure 4. The IRAS 05138+3634 star-forming region at (*left*) NIR (2MASS K-band) and (*right*) FIR (*Herschel* SPIRE 500 μm) wavelength ranges. The positions of five IRAS sources are indicated by arrows.

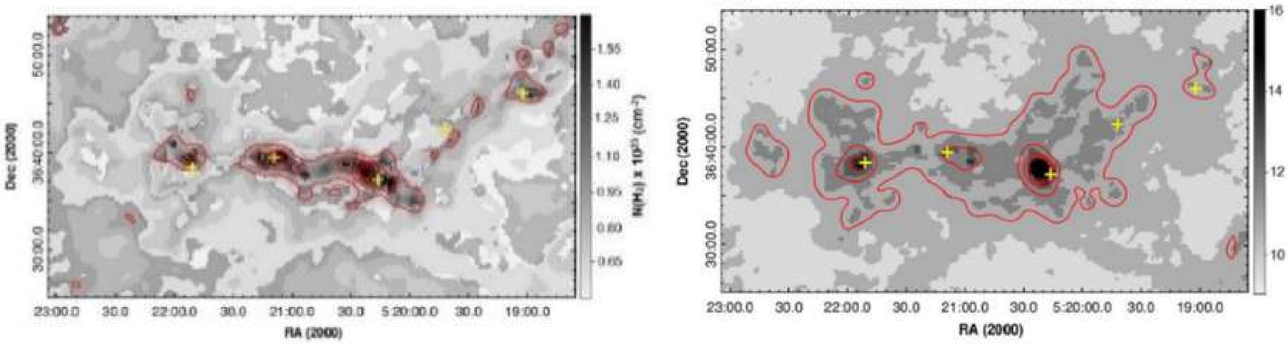

Figure 5. Maps of N(H_2) column density (*left*) and T_d dust temperature (*right*) of IRAS 05168+3634 star-forming region. The outer isodense on the N(H_2) map corresponds to $0.9\text{x}10^{23}$ cm^{-2}, and the interval between isodenses is $\sim 0.4\text{x}10^{23}$ cm^{-2}. The outer isotherm on the T_d map corresponds to 11 K, and the interval between isotherms is 1 K. The positions of IRAS sources are marked by yellow crosses.

selected YSOs are distributed nonuniformly in the star-forming region and form two subgroups; one is located around CPM 15, while the second group contains a significant number of middle-mass objects surrounded by gas-dust nebulae.

The distribution of 33 identified YSOs in colour-magnitude diagram (CMD) and histograms of their evolutionary ages clearly showed very wide spread. On the basis of these, it can be assumed that, in general, the star formation process in the considered region is sequential. In addition, based on K luminosity function (KLF) slope, the age of IRAS 05137+3919 star-forming region is estimated between 0.1 and 3 Myr. Therefore, the large age spread of IRAS 05137+3919 star-forming region give us bases to conclude that the stellar population is formed as a result of independent condensations in the parent molecular cloud.

Next young stellar cluster is located in the vicinity of IRAS 05168+3634 source. The presence of different maser emissions and ^{13}CO cores confirms its active star-forming nature. The region has a more complicated structure in the FIR wavelengths than in the NIR (see Figure 4). The complex structure of the region is clearly visible in FIR (right panel). Moving toward longer wavelengths, the cloud filaments surrounding IRAS 05168+3634 become more visible and it is obvious that the IRAS 05168+3634 star-forming region is more extended and is located within a 24 arcmin radius molecular cloud. Studying the common star-forming region in the molecular cloud, it turns out that apart from IRAS 05168+3634, there are four IRAS sources (IRAS 05184+3635, 05177+3636, 05162+3639, and 05156+3643) embedded in the same molecular cloud. Since, the distribution of stars in our field is 35 times different from the homogeneous distribution and their distribution in the field repeats the shape of the molecular cloud seen in FIR wavelengths, we concluded with a high probability that all five IRAS star-forming regions are at the same distance.

The N(H_2) and T_d maps in the left and right panels of Figure 5 show that the star-forming region clearly stands out against the background of the surrounding molecular cloud both with a higher density and temperature. The relatively hotter gas-dusty matter forms dense condensations around the IRAS objects. An exception is the IRAS 05162+3639 sub-region, near which on the N(H_2) map there is practically no

doi:https://doi.org/10.52526/25792776-22.69.2-351

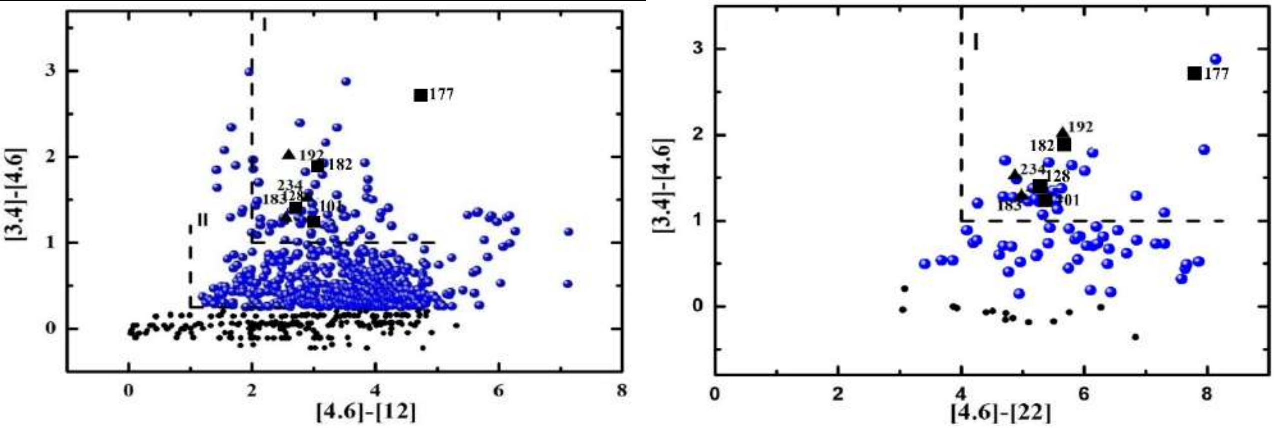

Figure 6. [3.4]–[4.6] vs. [4.6]–[12] (*left*) and [3.4]–[4.6] vs. [4.6]–[22] (*right*) c-c diagrams for the IRAS 05168+3634 star-forming region. The blue circles are selected YSOs and black circles are unclassified ones. Not all unclassified objects are presented in these diagrams. IRAS and MSX sources are indicated by triangles and squares, respectively, and they are labeled.

region with a relatively higher density and no group of YSOs has been identified around this source, but only 5 stars. In general, in the whole star-forming region T_d varies from 11 to 24 K, and $N(H_2)$ - from ~1.0 to 4.0×10^{23} cm^{-2}.

The selection of YSOs in the IRAS 05168+3634 star-forming region was based on four c-c diagrams, namely (J-H) versus (H-K), K-[3.6] versus [3.6]-[4.5], [3.4]-[4.6] versus [4.6]-[12], and [3.4]-[4.6] versus [4.6]-[22]. Figure 6 shows only two of these c-c diagrams. We added to our list those objects classified as YSOs in at least two c-c diagrams. Totally, we selected 1224 YSOs within a 24 arcmin radius. The distribution of classified YSOs in the field showed that Class II objects are distributed more homogeneously on the field than Class I objects, which are located in certain areas and show clear concentrations with sub-structures. This confirms the assumption that, unlike the Class II objects, Class I objects did not have enough time to leave their birthplaces after formation. Since the region is quite large, further investigations have only been performed on concentration areas. We estimated the size of each concentration in the molecular cloud based on map of the distribution of stellar surface density. Then, 240 YSOs of 1224 selected from c-c diagrams within the determined radii were explored in greater detail. The full tables of 240 selected YSOs with their NIR, MIR and FIR photometry and parameters (only 120 YSOs) obtained by SED fitting tool are available VizieR On-line Data Catalog[1].

The distribution of selected YSOs in K versus J-K CMDs and histograms of their evolutionary ages clearly showed very wide spread as in IRAS 05137+3919 case. KLF slopes suggested that the age of all four subregions (except IRAS 05162+3639) can be estimated between 0.1 and 3 Myr. In the case of the IRAS 05162+3639 subregion, there are not enough YSOs to construct the KLF. Therefore, the large age spread of IRAS 05168+3634 star-forming region give us bases to conclude that the stellar population is formed as a result of independent condensations in the parent molecular cloud.

Since, the results for the distance of IRAS 05168+3634 star-forming region are quite different (1.88 and 6.1 kpc), we attempt to identify the list of YSOs in the *Gaia* EDR3 database. In total, we were able to identify 65 objects, but only for 11 of them (located in all five sub-regions) the parallax measurement accuracy is high enough ($\varpi/\sigma_{\varpi} > 5$) and such a small number of objects is quite expected since YSOs are embedded in a dense ISM. The result obtained from *Gaia* EDR3 data can be considered as one more argument in favor of the fact that all sub-regions are embedded in the single molecular cloud and belong to the same star-forming region, which is located at ~1.9 kpc distance.

The last star-forming region is associated with IRAS 19110+1045 and 19111+1048 sources, referred to as G45.07+0.13 and G45.12+0.13 UCHII regions, respectively. This complex is an ideal laboratory to investigate the early stages of massive star formations and their influence on natal environments. Figure 7 presents colour-composite images covering the molecular cloud. The G45.12+0.13 and G45.07+0.13 UCHII regions stand out sharply in terms of brightness. The images also indicate that the UCHII regions are connected by a relatively colder bridge and are thus very likely a physically bound system.

The $N(H_2)$ and T_d maps of the wider region surrounding the G45.12+0.13 and G45.07+0.13 UCHII

[1]The full tables are available in VizieR On-line Data Catalog: J/A+A/622/A38

doi:https://doi.org/10.52526/25792776-22.69.2-351

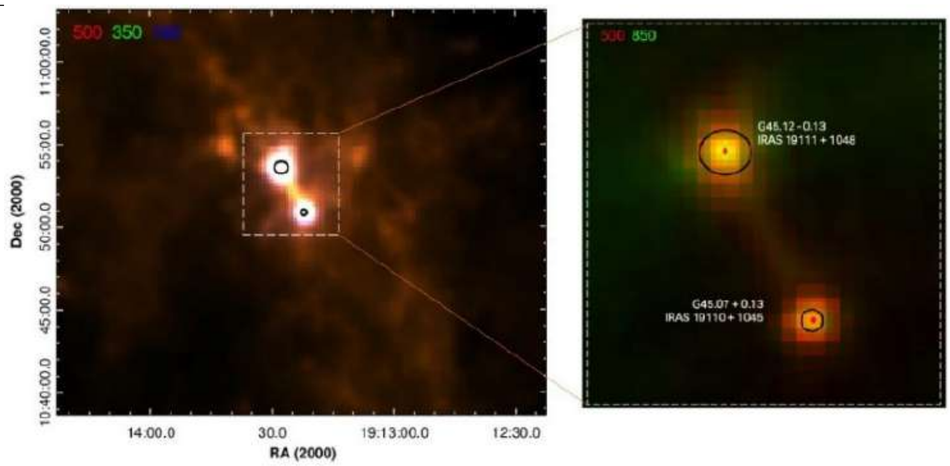

Figure 7. Colour-composite images of G45.12+0.13 and G45.07+0.13 UCHII regions. Left panel: *Herschel* 160 μm (blue), 350 μm (green), and 500 μm (red); right panel: zoomed area (white dotted square) at SCUBA 850 μm (green) and *Herschel* 500 μm (red). The positions and dimensions of the radio sources are marked by black circles. A red dot represents the position of an IRAS source.

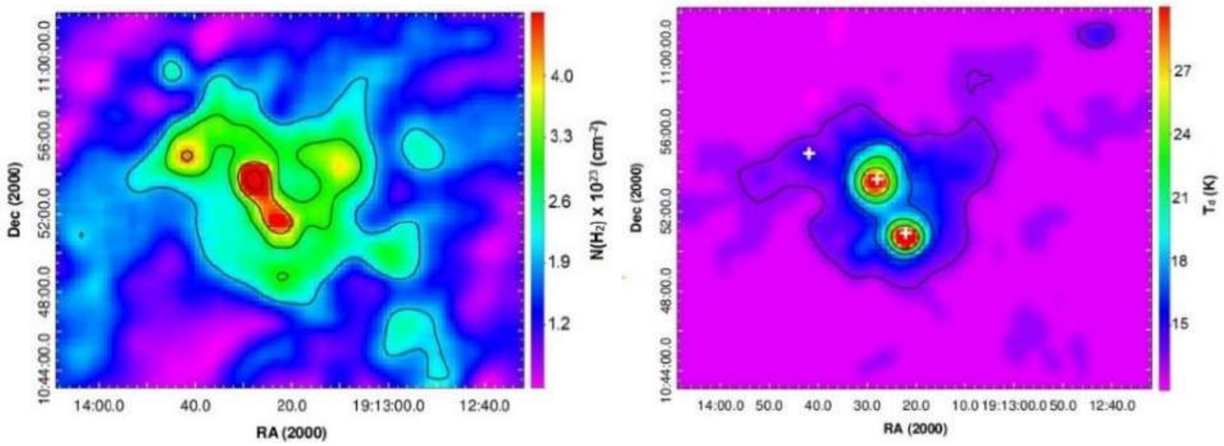

Figure 8. Maps of N(H_2) column density (*left*) and T_d dust temperature (*right*) of the region surrounding G45.12+0.13 and G45.07+0.13 UCHII objects. The outer isodense corresponds to 2.0x10^{23} cm^{-2} and interval between isodenses is 1.0x10^{23} cm^{-2}. The outer isotherm corresponds to 13 K and the interval between isotherms is 4 K. The positions of the IRAS and BGPC 6737 sources are marked by white crosses.

objects are shown in Figure 8. Both UCHII regions are distinct from the molecular cloud due to their high dust temperature and column density with an almost spherically symmetric distribution. This is fully consistent with the basic concept of UCHII regions about the presence of a hot, high mass stellar source and stellar wind, which leads to the blowing out of matter (Stahler & Palla, 2005). In general, within both regions, T_d varies from about 17 to 40 K and N(H_2) varies from about 3.0 to 5.5x10^{23} cm^{-2}. T_d drops significantly from the centres to the periphery, reaching a value of about 18–20 K. In G45.07+0.13 region, the IRAS source is somewhat offset from the density maximum. Near IRAS 19110+1045, the column density is ~3.5x10^{23} cm^{-2}. The IRAS source is located close to the dust temperature maximum ($T_d = 42$ K). In G45.12+0.13 region, the position of IRAS 19111+1048 coincides with the maxima of both the column density (5.5x10^{23} cm^{-2}) and temperature (35 K). The isotherms are slightly elongated towards the northwest, which may relate to the presence of two UCHIIs (G45.12+0.13 and G45.13+0.14). The presence of a region (bridge) with relatively high density (N(H_2) ≈ 4.3x10^{23} cm^{-2}) and low temperature ($T_d \approx 19$ K) positioned between the two UCHII regions suggests that they are physically connected.

The selection of YSOs in the IRAS 19110+1045 and 19111+1048 star-forming regions was based on six c-c diagrams, namely (J-H) versus (H-K), K-[3.6] versus [3.6]- [4.5], [3.6]-[4.5] versus [5.8]-[8.0], [3.6]-[5.8] versus [8.0]-[24], [3.4]-[4.6] versus [4.6]-[12], and [3.4]-[4.6] versus [4.6]-[22]. Figure 9 shows only two of these c-c diagrams. We added to our list those objects classified as YSOs in at least two c-c diagrams. However, since the region has two saturated areas in the MIR band around the IRAS sources (IRAS 19110+1045

doi:https://doi.org/10.52526/25792776-22.69.2-351

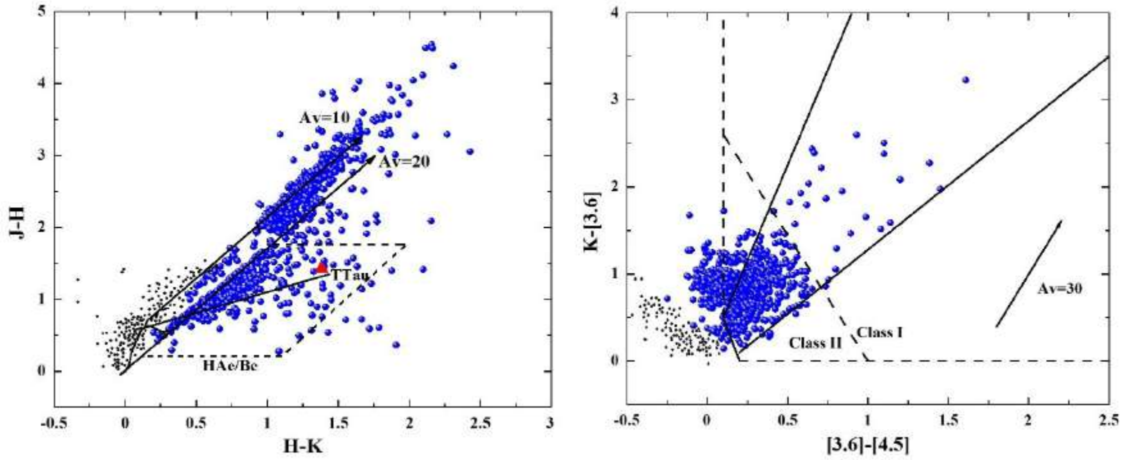

Figure 9. (J-H) vs. (H-K) (*left*) and K-[3.6] vs. [3.6]-[4.5] (*right*) c-c diagrams of the IRAS 19110+1045 and 19111+1048 star-forming regions. The blue circles are selected YSO candidates and black circles are non-classified ones. Not all non-classified objects are presented in these diagrams. IRA 19111+1048 source is indicated by a red triangle.

with 25″ radius and IRAS 19111+1048 with 50″ radius), objects within those areas classified as YSOs based on only the NIR c-c diagram were included in the list of YSO candidates. We selected 909 YSOs within a 6 arcmin radius. Excluding objects in two MIR–saturated regions (115 YSOs), we achieved relatively robust parameters for 431 of the 793 selected YSOs. We also performed a visual inspection of the YSO candidates in two MIR–saturated regions, because from our point of view, these objects are of the greatest interest as they are located in the immediate vicinity of the UCHIIs. Overall, the final list comprised 518 YSOs (423 with constructed SEDs and 95 YSOs in two saturated regions). The full tables of 518 selected YSOs with their NIR, MIR and FIR photometry and parameters obtained by SED fitting tool are available VizieR On-line Data Catalog[2]. The selected YSOs form dense clusters in both UCHII regions. Therefore, the low-density extended emission observed on the MIR images, which also stands out well on the dust temperature maps in both UCHII regions, may be due to the existence of the stellar clusters. Based on the data obtained by the SED fitting tool, the minimum and maximum estimated mass in the region is 1.7 and 22 $M_\odot$, respectively. Primarily, the lack of low-mass stellar objects can be explained by the large distance of the star-forming region. We were able to identify NIR counterpart of IRAS 19111+1048 source, which has 9.4±4.3 $M_\odot$ mass, 23 000±11 000 K temperature, and (2.5±1.2)x10^6 years evolutionary age. Unfortunately, due to the saturation of the central parts of the UCHII regions in the MIR range, we were unable to identify the YSOs associated with IRAS 19110+1045 source.

The distribution of the identified YSOs in the K versus J–K CMD is shown in the left and middle panels of Figure 10. The positions of objects in the two IRAS clusters (circles) and non-cluster objects (crosses) are different. The clusters' members and non-cluster objects exhibit low scatter relative to the isochrones. An overwhelming majority (more than 80%) of the non-cluster objects are younger than 0.1 Myr. In contrast, about 75% of objects in the IRAS clusters are older than 0.1 Myr and concentrated around the ZAMS. For improved clarity, the histograms of $(J - K)_{abs}$ are shown in the top left and middle panels. In general, the $(J - K)_{abs}$ spread of the vast majority of stellar objects from both samples is small. The distribution of evolutionary ages (by the SED fitting tool) for the non-cluster (middle right) and Control field 2 (lower right) objects has a well-defined, coincident peak and confirms the results of $(J - K)_{abs}$ histograms. In contrast, the distribution of the evolutionary ages of the objects in the clusters has two peaks (top right) which was constructed based on parameters from only 29 YSOs for which the SED fitting tool was applied. Most of the other 95 YSOs in the MIR-saturated regions are concentrated around the ZAMS and to the left of the 1 Myr isochrone. Therefore, we assumed that these objects will have a real contribution to the first peak in the evolutionary age distribution. Accordingly, this distribution will have only one well-defined peak as the histogram of $(J - K)_{abs}$. The small spread of evolutionary ages suggests that the clusters owe their origin to a triggering shock. The non-cluster YSOs are found to be uniformly distributed in the molecular cloud. Therefore, the origin of the non-cluster objects cannot be explained by the activity of the embedded massive stars in the UCHII regions. To understand the existence of the non-cluster objects, we

[2]The full table is available in VizieR On-line Data Catalog: J/other/PASA/39.24

doi:https://doi.org/10.52526/25792776-22.69.2-351

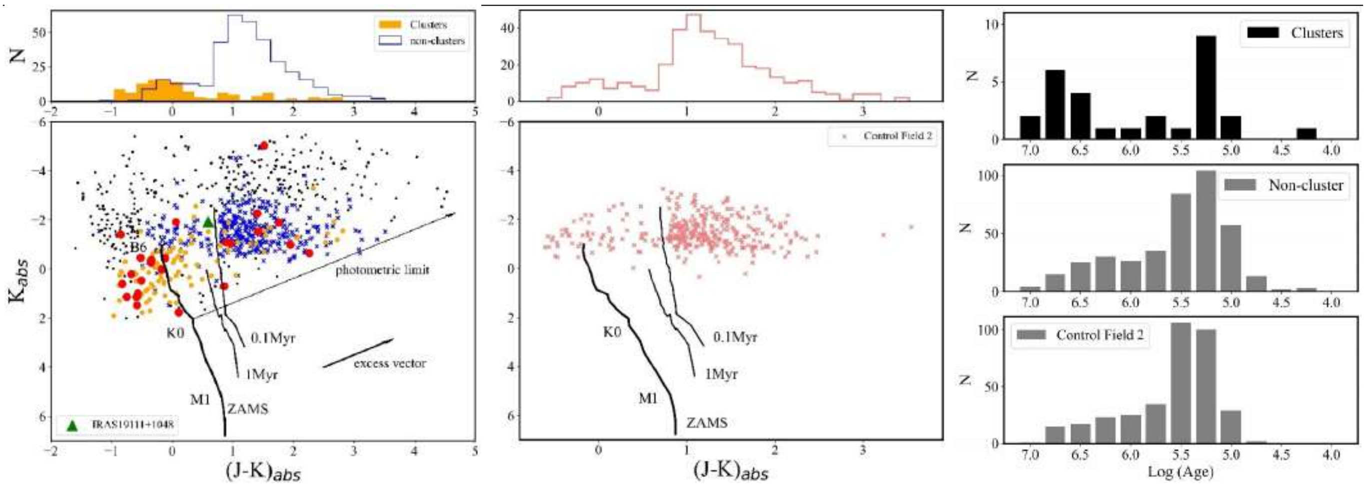

Figure 10. (*Bottom left and middle*) K versus (J–K) CMDs for identified YSOs in the IRAS 19110+1045 and 19111+1048 star-forming regions, and Control field 2, respectively. Red circles are stellar objects within the IRAS clusters with constructed SED. Objects located in the saturated regions are yellow circles. Non-cluster objects are blue crosses and no-SED objects are black dots. IRAS 19111+1048 source is indicated by a green triangle and labelled. Stellar objects located in Control field 2 are indicated by coral crosses. (*Top left and middle*) Histograms of (J - K)$_{abs}$ values. (*Right*) Histogram of evolutionary ages for members of the IRAS clusters (top), the non-cluster objects (middle), and the objects in the Control field 2 (bottom).

performed the same analysis in Control field 2 which is very close to the considered region. YSOs in Control field 2 show the same behavior as the non-cluster objects (evolutionary ages, masses, and surface stellar density). Accordingly, it is plausible that the non-cluster YSOs are part of the young stellar population of the GRSMC 45.46+0.05 molecular cloud. To understand the tracers of their origins, the star formation history of the GRSMC 45.46+0.05 star-forming region as a whole must be investigated.

5. Conclusion

At least for 20 regions, we obtained that around a middle- and high-mass YSO, in a certain stage of evolution, a group of young stars was formed and with modified selection criteria (depth of images, longer wavelength range), the percentage of detected groups should increase.

Below the main results of the detailed study of the selected star-forming regions are presented:

- Totally, we revealed 84 (05137+3919), 1224 (05168+3634), and 518 (19110+1045) YSOs.
- The selected YSOs are distributed nonuniformly in the IRAS 05137+3919 star-forming region and form two subgroups.
- The distribution of stars in the IRAS 05168+3634 field made it possible to reveal five dense subgroups around IRAS sources, which repeat the shape of the molecular cloud seen in FIR wavelengths. We concluded that IRAS 05168+3634 and other four sub-regions (IRAS 05184+3635, 05177+3636, 05162+3639, and 05156+3643) are embedded in the single molecular cloud and based on *Gaia* EDR3 parallaxes are located at ∼1.9 kpc distance.
- The age spread of the IRAS 05137+3919 and IRAS 05168+3634 star-forming regions is much larger, and, therefore, it can be concluded that the stellar population is formed as a result of independent condensations in the parent molecular cloud.
- The presence of a region (bridge) with relatively high density and low temperature positioned between the G45.12+0.13 and G45.07+0.13 UC HII regions suggests that these UC HII regions are physically connected.
- The IRAS clusters' members in G45.12+0.13 and G45.07+0.13 UC HII regions exhibit low scatter relative to the isochrones and their evolutionary age distribution shows small spread. Therefore, we concluded that their origin can be relate to an external triggering shock.

doi:https://doi.org/10.52526/25792776-22.69.2-351

- Among considered star-forming regions, massive stars were detected only in the region where star formation was probably triggered, that are IRAS 19110+1045 and 19111+1048
- We assumed that uniformly distributed non-cluster YSOs in the region surrounding IRAS 19110+1045 and 19111+1048 are part of the young stellar population of the GRSMC 45.46+0.05 molecular cloud.
- The distribution of classified YSOs in the field showed that Class II objects are distributed more homogeneously on the field than Class I objects, which are located in certain areas and show clear concentrations. This confirms the assumption that, unlike the Class II objects, Class I objects did not have enough time to leave their birthplaces after formation.

Acknowledgements

I would like to thank my supervisor – Dr. Elena Nikoghosyan for her invaluable supervision and support during the course of my PhD degree. This work was made possible by a research grant number № 21AG-1C044 from Science Committee of Ministry of Education, Science, Culture and Sports RA.

References

Ambartsumian V. A., 1947, The evolution of stars and astrophysics

Azatyan N. M., 2019, Astron. Astrophys. , 622, A38

Azatyan N. M., Nikoghosyan E. H., 2018, Communications of the Byurakan Astrophysical Observatory, 65, 228

Azatyan N. M., Nikoghosyan E. H., Khachatryan K. G., 2016, Astrophysics, 59, 339

Azatyan N., Nikoghosyan E., Harutyunian H., Baghdasaryan D., Andreasyan D., 2020, Communications of the Byurakan Astrophysical Observatory, 67, 211

Azatyan N., Nikoghosyan E., Harutyunian H., Baghdasaryan D., Andreasyan D., 2022, Proc. Astron. Soc. Aust. , 39, e024

Carey S. J., et al., 2009, Publ. Astron. Soc. Pac. , 121, 76

Churchwell E., et al., 2009, Publ. Astron. Soc. Pac. , 121, 213

Cutri R. M., et al., 2003, VizieR Online Data Catalog, p. II/246

Faustini F., Molinari S., Testi L., Brand J., 2009, Astron. Astrophys. , 503, 801

Fazio G. G., et al., 2004, Astrophys. J. Suppl. Ser. , 154, 10

González-Samaniego A., Vazquez-Semadeni E., 2020, Mon. Not. R. Astron. Soc. , 499, 668

Griffin M. J., et al., 2010, Astron. Astrophys. , 518, L3

Lada C. J., Lada E. A., 2003, Ann. Rev. Astron. Astrophys. , 41, 57

Lucas P. W., et al., 2008, Mon. Not. R. Astron. Soc. , 391, 136

Molinari S., et al., 2016, Astron. Astrophys. , 591, A149

Neugebauer G., et al., 1984, Astrophys. J. Lett. , 278, L1

Nikoghosyan E. H., Azatyan N., 2014, Astrophysics, 57, 330

Nikoghosyan E., Azatyan N., Harutyunian H., Baghdasaryan D., Andreasyan D., 2020, Communications of the Byurakan Astrophysical Observatory, 67, 187

Nikoghosyan E. H., Azatyan N. M., Andreasyan D. H., Baghdasaryan D. S., 2021, Astrophys. Space. Sci. , 366, 114

Pilbratt G. L., et al., 2010, Astron. Astrophys. , 518, L1

Poglitsch A., et al., 2010, Astron. Astrophys. , 518, L2

Preibisch T., 2012, Research in Astronomy and Astrophysics, 12, 1

Price S. D., Egan M. P., Carey S. J., Mizuno D. R., Kuchar T. A., 2001, Astron. J. , 121, 2819

Robitaille T. P., Whitney B. A., Indebetouw R., Wood K., 2007, Astrophys. J. Suppl. Ser. , 169, 328

Soderblom D. R., 2010, Ann. Rev. Astron. Astrophys. , 48, 581

Stahler S. W., Palla F., 2005, The Formation of Stars

Varricatt W. P., Davis C. J., Ramsay S., Todd S. P., 2010, Mon. Not. R. Astron. Soc. , 404, 661

Wright E. L., et al., 2010, Astron. J. , 140, 1868